

AD-A253 001



1

PHOTOREFRACTIVE MATERIALS, EFFECTS, AND DEVICES

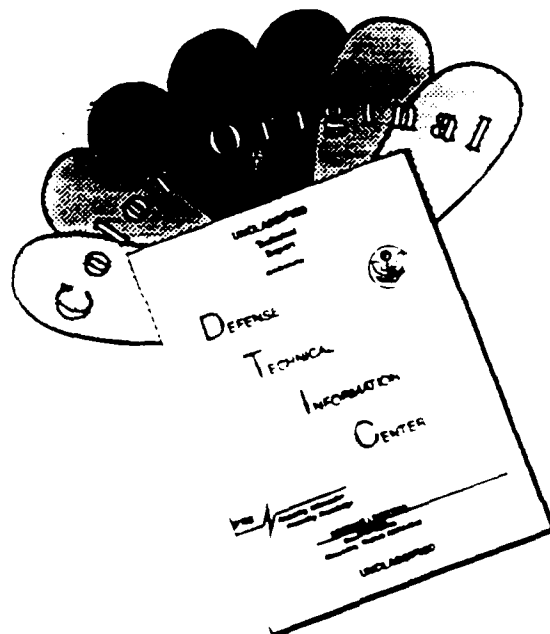
Sponsored by
Optical Society of America

In Cooperation with
IEEE/Lasers and Electro-Optics Society

**1991 TECHNICAL DIGEST
SERIES VOLUME 14**

**JULY 29-31, 1991
BEVERLY,
MASSACHUSETTS**

DISCLAIMER NOTICE



THIS DOCUMENT IS BEST QUALITY AVAILABLE. THE COPY FURNISHED TO DTIC CONTAINED A SIGNIFICANT NUMBER OF COLOR PAGES WHICH DO NOT REPRODUCE LEGIBLY ON BLACK AND WHITE MICROFICHE.

COMPONENT PART NOTICE

THIS PAPER IS A COMPONENT PART OF THE FOLLOWING COMPILATION REPORT:

TITLE: Organization of the Optical Society of America Photonic Science Topical Meeting Series. Volume 14. Photorefractive Materials Effects, and Devices Held in Beverly, Massachusetts on 29-31 July 1991.

TO ORDER THE COMPLETE COMPILATION REPORT, USE AD-A253 001.

THE COMPONENT PART IS PROVIDED HERE TO ALLOW USERS ACCESS TO INDIVIDUALLY AUTHORED SECTIONS OF PROCEEDING, ANNALS, SYMPOSIA, ETC. HOWEVER, THE COMPONENT SHOULD BE CONSIDERED WITHIN THE CONTEXT OF THE OVERALL COMPILATION REPORT AND NOT AS A STAND-ALONE TECHNICAL REPORT.

THE FOLLOWING COMPONENT PART NUMBERS COMPRISE THE COMPILATION REPORT:

AD#: AD-P006 695 thru AD-P006 807
 AD#: AD-P006 807
 AD#: AD-P006 807

| | |
|--------------------|-------------------------------------|
| Accession For | |
| NTIS CRA&I | <input checked="" type="checkbox"/> |
| DTIC TAB | <input type="checkbox"/> |
| Unannounced | <input type="checkbox"/> |
| Justification | |
| By | |
| Distribution / | |
| Availability Codes | |
| Dist | Avail and/or Special |
| A-1 | |

DTIC
ELECTE
JUL 02 1992
S A D

This document has been approved for public release and sale; its distribution is unlimited.

Summaries of papers presented at the
Photorefractive Materials, Effects, and Devices Topical Meeting

Photorefractive Materials, Effects, and Devices

1991 Technical Digest Series
Volume 14

CONFERENCE EDITION
July 29-31, 1991 — Beverly, Massachusetts



Sponsored by
Optical Society of America

Partial support provided by
Hughes Research Laboratories
Virgo Optics/Sandoz Optoelectronics

In Cooperation with
IEEE/Lasers and Electro-Optics Society

Optical Society of America
2010 Massachusetts Avenue, NW
Washington, DC 20036

Accession For

| | | |
|---------------|-------|--|
| NTIS | CRA&I | <input checked="checked" type="checkbox"/> |
| DTIC | TAB | <input type="checkbox"/> |
| Unannounced | | <input type="checkbox"/> |
| Justification | | |

By _____

Distribution / _____

Availability Codes

| Dist | Avail and/or Special |
|------|----------------------|
| A-1 | |

Articles in this publication may be cited in other publications. In order to facilitate access to the original publication source, the following form for the citation is suggested:

Name of Author(s), "Title of Paper," in Technical Digest on Photorefractive Materials, Effects, and Devices, 1991 (Optical Society of America, Washington, D.C., 1991), Vol. 14, pp. xx-xx.

ISBN Number

| | |
|--|---------------------------|
| Conference Edition | 1-55752-200-6 (softcover) |
| Postconference Edition | 1-55752-201-4 (hardcover) |
| (Note: Postconference Edition includes postdeadline papers.) | |
| 1991 Technical Digest Series | 1-55752-192-1 (hardcover) |

Library of Congress Catalog Card Number

| | |
|------------------------|----------|
| Conference Edition | 90-64486 |
| Postconference Edition | 90-64485 |

Copyright © 1991, Optical Society of America

Individual readers of this digest and libraries acting for them are permitted to make fair use of the material in it, such as to copy an article for use in teaching or research, without payment of fee, provided that such copies are not sold. Copying for sale is subject to payment of copying fees. The code 1-55752-192-1/91/\$2.00 gives the per-article copying fee for each copy of the article made beyond the free copying permitted under Sections 107 and 108 of the U.S. Copyright Law. The fee should be paid through the Copyright Clearance Center, Inc., 21 Congress Street, Salem, MA 01970.

Permission is granted to quote excerpts from articles in this digest in scientific works with the customary acknowledgment of the source, including the author's name and the name of the digest, page, year, and name of the Society. Reproduction of figures and tables is likewise permitted in other articles and books provided that the same information is printed with them and notification is given to the Optical Society of America. Republication or systematic or multiple reproduction of any material in this digest is permitted only under license from the Optical Society of America; in addition, the Optical Society may require that permission also be obtained from one of the authors. Address inquiries and notices to Director of Publications, Optical Society of America, 2010 Massachusetts Avenue, NW, Washington, DC 20036. In the case of articles whose authors are employees of the United States Government or its contractors or grantees, the Optical Society of America recognizes the right of the United States Government to retain a nonexclusive, royalty-free license to use the author's copyrighted article for United States Government purposes.

CONTENTS

| | |
|--|-----|
| Advance Program..... | v |
| MA New Materials | 1 |
| MB Wave Interactions and Instabilities | 35 |
| MC Invited Poster Preview..... | 67 |
| MD Feature Session on Optical Storage and Memories..... | 121 |
| TuA Materials and Diagnostics | 143 |
| TuB Applications..... | 171 |
| TuC Poster Session: Materials and Wave Interactions | 199 |
| TuD Plenary Session on Optical and Electronic Signal Processing | 297 |
| WA Beam Fanning and Self-Pumped Phase Conjugation..... | 301 |
| WB Defects and Charge Transport | 333 |
| WC Poster Session: Wave Interactions and Devices | 355 |
| Key to Authors and Presiders..... | 364 |

TECHNICAL PROGRAM COMMITTEE

Mark Cronin-Golomb, Cochair
Tufts University

Marvin Klein, Cochair
Hughes Research Laboratories

Materials

Vladimir Fridkin
Institute of Crystallography, USSR

Alastair Glass
AT&T Bell Laboratories

Peter Gunter
Swiss Federal Institute of Technology, Switzerland

Tom Pollak
Sanders Associates

Daniel Rytz
Sandoz Optoelectronique, Switzerland

Sergei I. Stepanov
Ioffe Institute, USSR

Physics of Photorefractive Effect

Milivoj Belic
Institut za Fiziku, Yugoslavia

Baruch Fischer
Technion-Israel Institute of Technology

Serguey G. Odulov
Ukrainian Academy of Sciences, USSR

Klaus H. Ringhofer
Universitat Osnabruck, Federal Republic of Germany

Gerald Roosen
Institut d'Optique, France

Peixian Ye
Chinese Academy of Sciences, China

Devices and Applications

Dana Z. Anderson
University of Colorado at Boulder

Jean-Pierre Huignard
Thomson-CSF, France

Kazuo Kyuma
Mitsubishi Electric Corporation, Japan

Abdellatif Marrakchi
Bellcore

Ian McMichael
Rockwell International Science Center

Henri Rajbenbach
Thomson-CSF, France

SUNDAY, JULY 28, 1991

MONDAY, JULY 29, 1991 — Continued

STUDENT CENTER

12:00 m-7:30 pm HOUSING & CONFERENCE
REGISTRATION

5:30 pm-6:30 pm DINNER

5:30 pm-8:00 pm REGISTRATION AND
INFORMAL RECEPTION

MONDAY, JULY 29, 1991

ENDICOTT STUDENT CENTER

7:00 am-8:00 am BREAKFAST

ACADEMIC CENTER AUDITORIUM

8:00 am-10:00 am

MA, NEW MATERIALS

Daniel Rytz, *Sandoz Optoelectronique, Switzerland, Presider*

8:00 am

MA1 Observation and study of the photorefractive effect in doped nonlinear polymers, D. M. Burland, S. Ducharme, W. E. Moerner, J. C. Scott, C. A. Walsh, *IBM Almaden Research Center*. The photorefractive effect has been observed, we believe for the first time, in several molecularly doped polymers as confirmed and studied by a combination of absorption, photoconductivity, electrooptic, and four-wave mixing measurements. (p. 2)

8:15 am

MA2 Characterization of a new photorefractive material: $K_{1-y}Li_{1-x}N_x$, Aharon Agranat, *Hebrew U., Jerusalem, Israel*; Rudy Hofmeister, Victor Leyva, Amnon Yariv, *California Institute of Technology*. The addition of lithium to KTN:Cu,V is demonstrated to yield high diffraction efficiency photorefractive gratings in the paraelectric phase. The beam coupling is voltage controllable by the quadratic electrooptic effect. Two beam diffraction efficiencies of 75% are observed for gratings written at 488 nm. (p. 6)

8:30 am

MA3 New type of KNSBN:Cu crystal as a high-performance self-pumped phase conjugator, Guangyin Zhang, Jingjun Xu, Simin Liu, Yuanqing Wu, *Nankai U., China*; Yongyuan Song, Huanchu Chen, *Shandong U., China*. A new photorefractive medium—Cu-doped $(0.04\text{wt}\%) (K_{0.5}Na_{0.5})_{0.2}Sr_{0.61}Nb_{0.39}O_6$ crystal—is found to have high self-pumped phase-conjugate reflectivity up to 68% at the 514.5-nm laser wavelength. (p. 10)

8:45 am

MA4 New photorefractive material KNSBN:Co, Quanzhong Jiang, Yongyuan Song, Daliang Sun, Xinliang Lu, Huanchu Chen, *Shandong U., China*. The crystal growth of KNSBN:Co and its photorefractive properties is reported. The measured photorefractive sensitivity is $10^{-3} \text{ cm}^2/\text{J}$, the two-wave coupling gain coefficient is 19 cm^{-1} , and the self-pumped phase conjugation reflectivity is 46%. (p. 14)

9:00 am

MA5 Photorefractive properties of $Bi_4Ge_3O_{12}$ crystals in the ultraviolet spectral range, G. Montemezzani, S. Pfandler, P. Gunter, *Swiss Federal Institute of Technology*. Photorefractive effects have been observed in the ultraviolet spectral region in undoped crystals of $Bi_4Ge_3O_{12}$. The relevant material parameters have been characterized. (p. 18)

9:15 am

MA6 Observation of the photorefractive effect in semi-insulating CdS, P. Tayebati, *Foster-Miller Inc.*; J. Kumar, D. Barman, U. Lowell; S. Scott, *Eagle Picher Research Laboratory*. We report what we believe to be the first observation of the photorefractive effect in cadmium sulfide. The maximum gain coefficient measured is 0.3 cm^{-1} at 633 nm. The response time is 1 ms at an intensity of 150 mW/cm^2 . (p. 22)

9:30 am

MA7 High-order diffraction in photorefractive quantum well structures, Q. N. Wang, D. D. Nolte, M. R. Melloch, *Purdue U.* Strong high-order diffraction signals caused by the second harmonic of the dielectric grating have been observed in photorefractive quantum wells in a degenerate mixing geometry. (p. 27)

9:45 am

MA8 Photorefractive properties of quantum-confined excitons, D. D. Nolte, M. R. Melloch, *Purdue U.* Band-gap engineering yields quantum well structures that have novel photorefractive processes with no analog in bulk crystals. We describe the material origins of these new photorefractive effects. (p. 31)

10:00 am-10:30 am COFFEE BREAK

10:30 am-12:30 pm

MB, WAVE INTERACTIONS AND INSTABILITIES

A. Zozulya, *Lebedev Physics Institute, U.S.S.R., Presider*

10:30 am

MB1 Red-green diffraction instability in the photorefractive mixed crystal $Bi_{12}Ti_{0.76}V_{0.24}O_{20}$, N. V. Kukhtarev, A. Gnatovskii, Z. Yanchuk, T. Semenets, L. Pryadko, Y. Kargin, *Ukrainian Academy of Sciences, U.S.S.R.*; K. H. Ringhofer, *U. Osnabruck, Germany*. Oscillation of the diffraction efficiency of a red beam reading out a grating written by green beams is explained by the interaction of interference patterns. (p. 36)

10:45 am

MB2 Buildup and decay of photorefractive wave mixing processes, Moshe Horowitz, Baruch Fischer, *Technion-Israel Institute of Technology*. The buildup and decay of photorefractive two- and four-wave mixing processes is studied. We show dependence on the coupling constant and the ratio of the signal and pump intensities. The solution for four-wave mixing with nondepleted pumps is identical to two-wave mixing with unidirectional optical feedback circuits. (p. 39)

MONDAY, JULY 29, 1991 — Continued

11:00 am

MB3 Beam fanning in coupled-wave theory of two-beam coupling, M. D. Ewbank, F. R. Vachss, R. A. Vazquez, *Rockwell International Science Center*. A simplistic representation of beam fanning of both the pump and amplified probe beams is incorporated into the coupled-wave equations governing the two-beam coupling process. These modified coupled-wave equations are solved analytically. (p. 43)

11:15 am

MB4 Instabilities in photorefractive bidirectional ring oscillators, Q. Byron He, Pochi Yeh, *UC-Santa Barbara*; Scott Campbell, Claire Gu, *Rockwell International Science Center*. We investigate the temporal stability of oscillations in a photorefractive bidirectional ring cavity. Unstable regions have been found theoretically and experimentally. (p. 47)

11:30 am

MB5 Spatial structure of scattered radiation in a self-pumped photorefractive passive ring mirror, S. A. Korolkov, A. V. Mamaev, V. V. Shkunov, *Institute for Problems in Mechanics, U.S.S.R.*; Yu. S. Kuzminov, *General Physics Institute, U.S.S.R.*; A. A. Zozulya, P. N. Lebedev *Physics Institute, U.S.S.R.* A detailed experimental investigation of scattered radiation spatial structure in a self-pumped photorefractive passive ring mirror is carried out. Experimental results agree with the predictions of a 3-D theoretical model. (p. 51)

11:45 am

MB6 Spatial solitons in photorefractive media, Mordechai Segev, Amir Saar, Amnon Yariv, *California Institute of Technology*. We show that photorefractive media can support a new type of spatial solitons, in which the diffraction is balanced by the self-scattering (two wave mixing) of the beam spatial frequency components. (p. 55)

12:00 m

MB7 Image degradation in a two-wave mixing spatial light modulator, G. Notni, R. Kowarschik, *Friedrich-Schiller U. Jena, Germany*. We report theoretical studies of image degradation and spatial resolution properties of a two-wave mixing spatial light modulator using the 2-D two-wave mixing theory. (p. 59)

12:15 pm

MB8 Resolution limit of photorefractive spatial light modulators, P. Amrhein, P. Gunter, *Swiss Federal Institute of Technology*. The resolution limit of Bragg diffraction from a photorefractive grating has been estimated theoretically and studied with a spatial light modulator using KNbO_3 crystals. (p. 63)

STUDENT CENTER CAFETERIA

12:30 pm-1:30 pm LUNCH SERVED

1:30 pm-3:00 pm FREE TIME

MONDAY, JULY 29, 1991 — Continued

ACADEMIC CENTER AUDITORIUM

3:00 pm-4:00 pm

MC, INVITED POSTER PREVIEW

Klaus Ringhofer, *Universitat Osnabruck, Federal Republic of Germany, Presider*

ACADEMIC CENTER CLASSROOMS

4:00 pm-5:30 pm

MC, INVITED POSTER SESSION

MC1 Invited Poster Paper

High-sensitivity resonant photorefractive effect in semi-insulating CdZnTe/ZnTe multiple quantum wells, A. Partovi, A. M. Glass, D. H. Olson, G. J. Zydzik, K. T. Short, R. D. Feldman, R. F. Austin, *AT&T Bell Laboratories*. We have demonstrated the photorefractive effect in the visible (570-610 nm) in a CdZnTe/ZnTe semi-insulating multiple quantum well device with < 1-mW incident power. A factor of 250 improvement in diffraction efficiency over previous results in multiple quantum wells is obtained. (p. 68)

MC2 Invited Poster Paper

Influence of cobalt doping on deep and shallow trap dependent photorefractive properties of barium titanate, M. H. Garrett, J. Y. Chang, H. P. Jenssen, C. Warde, *Massachusetts Institute of Technology*; P. Tayebati, *Foster Miller, Inc.* We report intensity dependence of electrooptic and absorptive gain, sublinear dependence of the response time on intensity and light-induced dark decays of cobalt-doped barium titanate. (p. 72)

MC3 Invited Poster Paper

Electron-hole competition in InP:Fe: the role of multiple defects, R. S. Rana, D. D. Nolte, *Purdue U.* Strong electron-hole competition, caused by multiple defect levels, induces a change in beam coupling direction and quenches four-wave mixing near 225 K in InP:Fe. (p. 76)

MC4 Invited Poster Paper

Absorption gratings with multiple levels, R. S. Cudney, R. M. Pierce, G. D. Bacher, Jack Feinberg, *U. Southern California*. Beam coupling in crystals having multiple trap levels does not vanish as the grating wavevector approaches zero; we use this to determine important parameters in BaTiO_3 . (p. 80)

MC5 Invited Poster Paper

Hot carrier enhancement of Demmer photorefractive space-charge fields in zincblende semiconductors, W. Andreas Schroeder, Thomas S. Stark, Arthur L. Smirl, *U. Iowa*; George C. Valley, *Hughes Research Laboratories*. We use a novel, picosecond transient-grating technique to measure the hot carrier enhancement of the Demmer photorefractive space-charge field in zincblende semiconductors. (p. 84)

MC6 Invited Poster Paper

Detection of low intensity optical wavefronts using noise reduction techniques in photorefractive amplifiers, H. Rajbenbach, A. Delboulbe, J. P. Huignard, *Thomson-CSF, France*. We demonstrate the detection and amplification of subpicowatt optical signals via two-wave mixing in photorefractive BSO. For these experiments, the crystal entrance face is strongly tilted with respect to the pump beam direction. (p. 88)

MC7 Invited Poster Paper

Fundamental noise limits in photorefractive systems, Frederick Vachss, Claire Gu, John Hong, Tallis Chang, *Rockwell International Science Center*. We examine the noise processes affecting holographic recording and read out in photorefractive materials. In particular, we find that the dynamic range achievable in real-time holography is fundamentally limited by fluctuations in both the charge density in the recording material and in the intensities of the writing beams. (p. 92)

MC8 Invited Poster Paper

Photorefractive noise suppression using achromatic gratings, W. S. Rabinovich, G. C. Gilbreath, B. J. Feldman, *U.S. Naval Research Laboratory*. We show that achromatic grating techniques can suppress beam fanning while still allowing two-beam coupling to occur. (p. 97)

MC9 Invited Poster Paper

Two-beam coupling with partially coherent light, Hongzhi Kong, Wieslaw Krolikowski, Mark Cronin-Golomb, *Tufts U.* The influence of partial coherence on two-beam coupling in a photorefractive material is investigated theoretically and experimentally. Improvement in the coherence properties of an amplified beam was observed in an experiment with barium titanate crystal. (p. 101)

MC10 Invited Poster Paper

Increase of mutual coherence of light beams in two-wave interactions in photorefractive crystals, N. V. Bogodaev, L. I. Ivleva, A. S. Korshunov, N. M. Polozkov, *General Physics Institute, U.S.S.R.*; V. V. Shkunov, *Institute for Problems in Mechanics, U.S.S.R.* We show that two-wave mixing of partially coherent beams may be used to increase the degree of coherence of these beams. (p. 105)

MC11 Invited Poster Paper

Four-wave mixing steady-state solutions utilizing the underlying SU(2) group symmetry, D. Fish, A. K. Powell, T. J. Hall, *King's College London, U.K.* We show that the scalar four-wave mixing equations have an underlying symmetry in the form of the SU(2) group. This formulation identifies the conserved quantities of four-wave mixing in an obvious sense rather than in the ad-hoc fashion used previously. (p. 108)

MC12 Invited Poster Paper

Why light beams follow curved paths in photorefractive phase conjugators, V. V. Eliseev, *General Physics Institute, Academy of Sciences of the U.S.S.R.*; A. A. Zozulya, P. N. Lebedev Physical Institute, *Academy of Sciences of the U.S.S.R.*; G. D. Bacher, Jack Feinberg, *U. Southern California*. We explain why light beams appear to curve in photorefractive phase conjugators. (p. 109)

MC13 Invited Poster Paper

Reflection grating photorefractive self-pumped ring mirror, V. A. D'yakov, *Moscow State U., U.S.S.R.*; S. A. Korolkov, A. V. Mamaev, V. V. Shkunov, *Institute for Problems in Mechanics, U.S.S.R.*; A. A. Zozulya, P. N. Lebedev *Physics Institute, U.S.S.R.* A reflection grating self-pumped passive ring mirror is experimentally realized in a photorefractive KNbO₃ crystal in cw regime with a relaxation time of several milliseconds. (p. 113)

MC14 Invited Poster Paper

Photorefractive crystal waveguides and their applications, Ken-ichi Kitayama, Fumihiko Ito, *NTT Transmission Systems Laboratories, Japan*. Neural processing of an 500 × 500 image seems realistic using holographic storage in 2-D photorefractive crystal waveguide (PCW) array. Phase-conjugate image replication in PCW is also demonstrated. (p. 116)

MC15 Invited Poster Paper

Image transmission through multimode fiber and photorefractive crystal, A. Gnatovskii, A. Volyar, N. Kukhtarev, S. Lapaeva, *Academy of Sciences of the Ukr.SSR, Institute of Physics, U.S.S.R.* Amplitude mask image was transmitted through 2-m multimode fiber using a correcting hologram and polarization-preserving phase conjugation in photorefractive crystals with a photogalvanic response. (p. 120)

STUDENT CENTER CAFETERIA

5:30 pm-6:30 pm DINNER SERVED

6:30 pm-7:30 pm FREE TIME

ACADEMIC CENTER AUDITORIUM

7:30 pm-9:00 pm

MD, FEATURE SESSION ON OPTICAL STORAGE AND MEMORIES

L. Hesselink, *Stanford University, Presider*

7:30 pm

MD1 Phase-coded hologram multiplexing for high-capacity optical data storage, C. Denz, G. Pauliat, G. Roosen, *CNRS Institute of Theoretical and Applied Optics, France*; T. Tschudi, *Technische Hochschule Darmstadt, Germany*. We present a deterministic phase coding method for high-capacity data storage in thick photorefractive materials. We experimentally achieved a system able to discriminate multiple images with low crosstalk. (p. 122)

7:45 pm

MD2 Multimode operations of a holographic memory using orthogonal phase codes, Yoshinao Taketomi, Joseph Ford, Hironori Sasaki, Jian Ma, Yeshaiah Fainman, Sing H. Lee, *UC-San Diego*. We describe a photorefractive memory that uses binary orthogonal phase code addressing and show how it can provide adaptive learning, selective erasure, and perform complex amplitude addition and subtraction of memory contents. (p. 126)

MONDAY, JULY 29, 1991 — Continued

8:00 pm

MD3 High-resolution volume holography using orthogonal data storage, Amnon Yariv, Victor Leyva, *California Institute of Technology*; George Rakuljic, *Optologic Corporation*. An approach for holographically storing many high-resolution images in a volume is described. Results obtained using permanently fixed holograms in a photorefractive medium are presented. (p. 130)

8:15 pm

MD4 Holographic storage capacity estimate for photorefractive media, George Fredericks, *Digital Equipment Corporation*; Adil Lahrichi, Kristina Johnson, *U. Colorado*. The practical limit on the storage capacity of photorefractive media is estimated for a given bit error rate and read out bandwidth. (p. 133)

8:30 pm

MD5 Angular selectivity of holographic gratings in BSO, S. Tao, D. R. Selviah, B. Mobasher, P. Poon, J. E. Midwinter, *University College London, U.K.* We compare the theoretical angular selectivity calculated by coupled wave theory with our experimental measurement of the same quantity for a BSO crystal. (p. 138)

8:45 pm

MD6 Diffraction efficiency dynamics in photorefractive crystals, Eric S. Maniloff, Kristina M. Johnson, *U. Colorado*. Using a self-consistent theory for the transient energy transfer and the diffraction efficiency in photorefractive crystals, we have modeled the observed dynamics. (p. 139)

TUESDAY, JULY 30, 1991

STUDENT CENTER CAFETERIA

7:00 am–8:00 am BREAKFAST

ACADEMIC CENTER AUDITORIUM

8:00 am–10:00 am

TuA, MATERIALS AND DIAGNOSTICS

Peter Gunter, *Swiss Federal Institute of Technology, Switzerland, Presider*

8:00 am

TuA1 Imaging method for nonlinear medium characteristic measurements, G. Boudebs, X. Nguyen Phu, J. P. Lecoq, M. Sylla, G. Rivoire, *Laboratoire des Proprietes Optiques des Materizux et Applications, France*. An imaging system (4f set up) is used to measure nonlinear characteristics for photorefractive materials excited with either a cw or pulsed laser. (p. 144)

8:15 am

TuA2 Origins of the photorefractive phase shift, R. S. Cudney, G. D. Bacher, R. M. Pierce, Jack Feinberg, *U. Southern California*. We isolate the effects of trap gratings to determine the real spatial phase shift of electrooptic gratings in BaTiO₃. (p. 146)

8:30 am

✓ **TuA3 Photogalvanic holographic gratings in strontium barium niobate crystals**, A. Gnatovskii, N. Kukhtarev, A. Pigida, V. Verbitskii, N. Bogodaev, N. Polozkov, *Academy of Sciences of the Ukr.SSR, Institute of Physics, U.S.S.R.* Gratings with orthogonally polarized waves were recorded in SBN with 6% diffraction efficiency for the red wavelength, corresponding to a 600-V/cm photogalvanic field. (p. 150)

8:45 am

TuA4 Electrooptic effects and domain reversal in Sr_{0.8}Ba_{0.2}Nb₂O₆, Jeffrey P. Wilde, Lambertus Hesselink, *Stanford U.* We present the results of a comprehensive electrooptic study of Sr_{0.8}Ba_{0.2}Nb₂O₆ at $\lambda = 633$ nm. The linear electrooptic coefficient r_c is measured at 25°C and 65°C; the effect of domain switching is investigated. (p. 151)

9:00 am

TuA5 Applied electric field effect on photorefractive GaAs, Duncan T. H. Liu, Li-Jen Cheng, Jae-Hoon Kim, *Jet Propulsion Laboratory*. We investigate the electrode dependence of the applied electric field effect in GaAs. In particular, the widely used silver paste is compared with other electrode materials in the same experimental conditions. (p. 155)

9:15 am

TuA6 Photorefractive properties and alternating electric field gain enhancement of vanadium doped cadmium-telluride and related compounds, Mehrdad Ziari, William H. Steier, *U. Southern California*; Marvin B. Klein, *Hughes Research Laboratories*; Sudhir Trivedi, *Brimrose Corporation of America*. We report on near-infrared photorefractive response characteristics and relevant material parameters of CdTe:V and CdZnTe:V crystals including gain enhancement by applied ac fields. (p. 159)

TUESDAY, JULY 30, 1991 — Continued

9:30 am

TuA7 Synchrotron x-ray diffraction imaging of photorefractive crystals, Gerard Fogarty, Mark Cronin-Golomb, *Tufts U.*; Bruce Steiner, *U.S. National Institute of Standards and Technology*. High-resolution x-ray diffraction images of photorefractive barium titanate, potassium niobate, and strontium barium niobate are presented that indicate the possibility of *in situ* observation of lattice deformation associated with photorefractive grating formation and of the effect and nature of optical scattering centers in these crystals. (p. 162)

9:45 am

TuA8 Homogeneity of the photorefractive effect in reduced and unreduced KNbO₃ crystals, P. Amrhein, P. Gunter, *Swiss Federal Institute of Technology*. We examine the homogeneity of the photorefractive sensitivity in three dimensions. The effects of electrochemical reduction treatment are studied in different KNbO₃ samples. (p. 166)

10:00 am–10:30 am COFFEE BREAK

10:30 am–12:30 pm

TuB, APPLICATIONS

Jean-Pierre Huignard, *Thomson-CSF, France, Presider*

10:30 am

TuB1 Phase-conjugate techniques for diode laser brightness enhancement, Stuart MacCormack, Robert W. Eason, *U. Southampton, U.K.* Near diffraction-limited output is obtained from high-power diode laser arrays using phase-conjugate geometries. Results for passive feedback and a reflection geometry MOPA are presented. (p. 172)

10:45 am

TuB2 Dynamic photorefractive optical memories, H. Sasaki, Y. Fainman, J. E. Ford, Y. Taketomi, S. H. Lee, *UC-San Diego*. We investigate an architectural approach to dynamic volume storage which circulates holograms between two photorefractive crystals using an optical amplifier that increases the effective write-erase asymmetry of the memory. (p. 176)

11:00 am

TuB3 Real-time optical intensity correlator using photorefractive BSO and a liquid crystal television, C. Soutar, Z. Q. Wang, C. M. Cartwright, W. A. Gillespie, *Dundee Institute of Technology*. An optical intensity correlator using BSO is presented. The spatially incoherent readout allows real-time addressing of the correlator via a commercial liquid crystal television. (p. 180)

11:15 am

TuB4 Multiplicative to additive speckle noise conversion via phase cancellation with photorefractive phase conjugators, Jehad A. Khoury, Anne Marie Biernacki, Mark Cronin-Golomb, *Tufts U.*; Charles L. Woods, *Rome Laboratory*. Photorefractive degenerate four-wave mixing phase conjugation is used to convert multiplicative complex speckle image noise to additive noise in the image and Fourier domains. (p. 182)

TUESDAY, JULY 30, 1991 — Continued

11:30 am

TuB5 Power stabilization in photorefractive two wave mixing by frequency tuning of laser diode, Tsutomu Shimura, Hai Yan Miao, Masahide Itoh, Hideki Okamura, Kazuo Kuroda, Iwao Ogura, *U. Tokyo, Japan*. We suppress the fluctuation of the amplified signal output power by controlling the detuning between the index grating and interference fringe. (p. 186)

11:45 am

TuB6 New thresholding device using a double phase-conjugate mirror with phase-conjugate feedback, Parviz Tayebati, Lawrence H. Domash, *Foster-Miller, Inc.* We present a new thresholding device consisting of a double phase-conjugate mirror (DPCM) combined with a phase-conjugate mirror resulting in superior thresholding characteristics compared with those of a DPCM alone. (p. 190)

12:00 m

TuB7 Laser-induced interference filters in photorefractive materials, P. M. Petersen, T. Skettrup, *Technical U. Denmark*; P. M. Johansen, *U. Aalborg, Denmark*. We investigate the properties of a laser-induced interference filter in BaTiO₃. Two coherent laser beams induce the filter and control the reflection of a third laser beam. (p. 195)

12:45 pm CLAM BAKE (at Endicott Beach)

Food served from 12:45 pm–1:45 pm

ACADEMIC CENTER CLASSROOMS

4:00 pm–5:30 pm

TuC, POSTER SESSION: MATERIALS AND WAVE INTERACTIONS

TuC1 Experimental comparison of the ac field and moving grating techniques for BTO and BSO crystals, E. V. Mokrushina, V. V. Prokofev, S. L. Sochava, S. I. Stepanov, *A. F. Ioffe Physical-Technical Institute, U.S.S.R.* Two-beam gain in BTO and BSO for recording in an ac field is shown to be higher or lower than that for recording of a moving grating in a dc field, depending on the photocarrier diffusion length. (p. 200)

TuC2 Polarization properties of Bi₂SiO₂₀ crystals, T. Panchenko, A. Kudzin, Y. Potapovich, G. Snejnol, *Dnepropetrovsk State U., U.S.S.R.* Quasidipole and the space-charge formation mechanisms of thermoelectret and photoelectret states in the 300–800 K temperature range are determined thermally stimulated depolarization current method. Electric field distribution, exclusion and injection processes in Bi₂SiO₂₀ crystals are considered. (p. 205)

TuC3 Hologram recording in GaAs through EL2 intracenter absorption, Andrei L. Khromov, Michael P. Petrov, *A. F. Ioffe Physico-Technical Institute, U.S.S.R.* The first use of EL2 intracenter absorption in hologram recording in GaAs is reported. A qualitative model of the phenomenon and the possibility of gaining experimental insight into the microscopic structure of the EL2 point defect are discussed. (p. 209)

TuC4 Single crystal growth of photorefractive sillenites, V. V. Volkov, Yu. F. Kargin, V. M. Skorikov, *Academy of Sciences of the U.S.S.R., Kurnakov Institute of General and Inorganic Chemistry*. $\text{Bi}_{12}\text{TiO}_{20}$, $\text{Bi}_{12}\text{ZnO}_{58}$, $\text{Bi}_{12}\text{GaO}_{39}$, and $\text{Bi}_{12}\text{FeO}_{39}$ single crystals have been prepared. The hetero-valent substitution, transmission, optical activity and linear electrooptic data are presented. (p. 212)

TuC5 Temperature dependence of the two-beam coupling gain coefficient of photorefractive GaP, K. Kuroda, Y. Okazaki, T. Shimura, M. Itoh, *U. Tokyo, Japan*. We observed the decrease of gain around 150 K, due to the screening effect of holes photoionized from shallow acceptors. Photochromic effect is also observed. (p. 216)

TuC6 Nonsteady-state photoEMF in crystals with long relaxation times of photoconductivity, I. A. Sokolov, S. I. Stepanov, A. F. Ioffe *Physical Technical Institute, U.S.S.R.* We report the investigation of the nonsteady-state photoEMF in photoconducting $\text{Bi}_{12}\text{Si(Ti)O}_{20}$ crystals and measurements of average lifetimes of photocarriers, Maxwell relaxation times, average photoconductivity, and diffusion length. (p. 220)

TuC7 Charge transport in high resistivity photorefractive crystals $\text{Bi}_{12}\text{SiO}_{20}$, ZnSe, and GaAs, A. V. Ilinskii, *Academy of Sciences of the U.S.S.R. A. F. Ioffe Physical-Technical Institute*. After reviewing earlier studies we find that there are two electric field screening regimes that depend on experimental conditions (kind of crystal, temperature). (p. 224)

TuC8 Transport-induced grating interferometry: application to photorefractive $\text{Bi}_{12}\text{TiO}_{20}$, Ping Xia, J. P. Partanen, R. W. Hellwarth, *U. Southern California*. We have developed a technique to measure interferometrically all relevant experimental parameters which describe charge-transport-induced refractive index gratings in photoconductive insulators. (p. 228)

TuC9 Determination of the mobility and transport properties of photocarriers in BGO by the time-of-flight technique, M. Tapiero, A. Ennouri, J. P. Zielinger, J. P. Vola, *IPCMS, France*; J. Y. Moisan, *CENT Lannion, France*; J. C. Launay, *CNRS Chemistry of Solids Laboratory, France*. The mobility and transport properties of photoelectrons in BGO are determined by the classical time-of flight technique using a nitrogen laser for pulse excitation. (p. 232)

TuC10 Conduction band and trap limited mobilities in $\text{Bi}_{12}\text{SiO}_{20}$, P. Nouchi, J. P. Partanen, R. W. Hellwarth, *U. Southern California*. We used our holographic time-of-flight technique to measure a trap-limited mobility $\mu_t = 0.24 \pm 0.07 \text{ cm}^2/(\text{Vs})$ in $\text{Bi}_{12}\text{SiO}_{20}$. We developed a shallow-trap model and inferred a conduction band mobility $\mu_c = 7 \pm 3 \text{ cm}^2/(\text{Vs})$. (p. 236)

TuC11 Breaking of the electrooptic and dielectric tensor symmetries by space-charge electric fields, G. Pauliat, P. Mathey, G. Roosen, *CNRS Institute of Theoretical and Applied Optics, France*. We derive analytical expressions for the photorefractive electrooptic and dielectric coefficients and demonstrate that their symmetries are not those of the electrooptic and dielectric tensors. (p. 240)

TuC12 Influence of piezoelectric and photoelastic effects on impulse hologram recording in photorefractive crystals, R. Litvinov, S. Shandarov, *Institute of Automatic Control Systems and Radioelectronics, U.S.S.R.* The additional contribution of piezoelectric and photoelastic effects to perturbations of optical properties of the medium during hologram recording in photorefractive crystals by short light impulses is considered. The numerical calculations for orientation cut (110) of cubic BSO crystals are also performed. (p. 244)

TuC13 Elastooptic and rotooptic contributions to the photorefractive effect, Marko Zgonik, *U. Ljubljana, Yugoslavia*; Peter Gunter, *Swiss Federal Institute of Technology*. The answer is provided to the clamped-unclamped EO coefficients dilemma. Refractive index modulation must be calculated from the crystal deformation in the form of a static plain wave. The correct elastooptic contribution is obtained from unsymmetrized displacement gradients. (p. 248)

TuC14 Simultaneous diffraction of two light waves in cubic optically active photorefractive piezocrystals, V. V. Shepelevich, N. N. Egorov, *Mozyr Pedagogical Institute, U.S.S.R.* The influence of piezoelectric and photoelastic properties of cubic photorefractive crystals on the simultaneous diffraction of two light waves by a holographic grating is investigated theoretically and experimentally. (p. 252)

TuC15 Photogyration and photoinduced structure distortions in doped LiNbO_3 and LiTaO_3 , S. M. Kostitskii, *Kemerovo State U., U.S.S.R.* The appearance of gyrotropy due to the influence of light is discussed. This effect is determined by the electrogyration under the photovoltaic field's influence. The distortions—which lower the symmetry in a unit cell—were detected, and they cause forbidden activity of A_2 phonons in the Raman spectra. (p. 256)

TuC16 Photorefractive self-pumped phase conjugators in the presence of loss and high modulation depth, James E. Miller, Steffen D. Koehler, Elsa M. Garmire, *U. Southern California*; Marvin B. Klein, *Hughes Research Laboratories*. Self-pumped phase-conjugate mirrors are examined in the presence of linear absorption and nonlinear photorefractive response at high modulation depths, which is important in semiconductors. (p. 260)

TuC17 Perturbative analysis of the higher-order photorefractive effect, R. Saxena, T. Y. Chang, *Rockwell International Science Center*. Analytic expressions are derived for second- and third-order photorefractive effects. The dependence on spatial frequency, applied field, and velocity of the moving grating is examined. (p. 264)

TuC18 Effect of large signals in photorefractive media, A. K. Powell, D. Fish, G. R. Barrett, T. J. Hall, *King's College London, U.K.* We show new results for applied ac fields and model the effect of large signal saturation on the performance of an optical resonator system based on the ring-passive phase conjugation. (p. 267)

TuC19 Large signal gain effects in photorefractive $\text{Bi}_{12}\text{TiO}_{20}$ at 633 nm, M. B. Klein, F. P. Strohkendl, B. A. Wechsler, *Hughes Research Laboratories*; G. A. Brost, *Rome Laboratory*; J. E. Millerd, E. M. Garmire, *U. Southern California*. We find that the two-wave mixing gain coefficient in $\text{Bi}_{12}\text{TiO}_{20}$ with an applied ac field varies strongly with the pump/probe intensity ratio. We interpret these data using a finite difference method to model the photorefractive grating formation. (p. 268)

TuC20 Numerical analysis of photorefractive grating formations at large modulation, George A. Brost, *Rome Laboratory*. Photorefractive grating formations in BSO were modeled by a finite difference method. These numerical solutions predict the photorefractive behavior at large modulation index. (p. 272)

TuC21 Dynamic solutions and instabilities of the four-wave mixing interaction utilizing the underlying SU(2) group symmetry, G. R. Barrett, A. K. Powell, T. J. Hall, *King's College London, U.K.* The temporal nature of anisotropic four-wave mixing has been studied and shown in certain conditions, to exhibit chaotic behavior when an electric field is present. The effect of any material absorption on the chaotic nature is also demonstrated. (p. 276)

TuC22 Holographic recording and parametric scattering from orthogonally polarized beams in BaTiO_3 , L. Holtmann, E. Kratzig, *U. Osnabruck, Germany*; M. Goukov, S. G. Odoulov, *Ukr. S.S.R. Academy of Sciences Institute of Physics, U.S.S.R.*; B. Sturman, *Institute of Automation and Electrometry, U.S.S.R.* We report what we believe to be the first observation of anisotropic selfdiffraction from gratings arising in BaTiO_3 when two copropagating orthogonally polarized waves (ordinary and extraordinary) impinge in the crystal at an arbitrary angle in the plane perpendicular to the optical axis and discuss the possible origins of this effect. (p. 277)

TuC23 Parametric scattering of light in photorefractive LiNbO_3 crystals, K. N. Zabrodin, A. N. Penin, N. M. Rubinina, *Moscow State U., U.S.S.R.* We study the temporal dynamics of degenerate parametric scattering and discuss some of the new scattering properties observed. (p. 281)

TuC24 Forward phase-conjugate waves in degenerate four-wave mixing in a photorefractive crystalline slab, H. Y. Zhang, X. H. He, *Beijing U., China*; S. H. Tang, *National U. Singapore*. Both backward and forward phase conjugate waves have been observed in degenerate four-wave mixing (DFWM) in a $\text{LiNbO}_3\text{:Fe}$ crystalline slab. Investigation shows that the observed forward phase conjugate wave consists of two main contributions. (p. 285)

TuC25 Photoinduced charge transport in optical damage resistant $\text{LiNbO}_3\text{:Me}$ (Me = Mg,Zn), T. R. Volk, M. A. Ivanov, F. Ya. Shchapov, *Institute of Crystallography, U.S.S.R.*; N. M. Rubinina, *Moscow State U., U.S.S.R.* In low-doped $\text{LiNbO}_3\text{:Me}$ the Me^{2+} ions are electron trapping levels resulting in sub-linear dependence of photoconductivity on light intensity. The Fe^{3+} loses its acceptor properties at [Me] exceeding the thresholds leading to a sharp increase of photoconductivity and to photorefractive decrease. (p. 289)

TuC26 Optical damage resistant impurities in LiNbO_3 (Mg,Zn), T. R. Volk, *Institute of Crystallography, U.S.S.R.*; N. M. Rubinina, *Moscow State U., U.S.S.R.*; S. Stizza, *U. Camerino, Italy*. In optical damage resistant $\text{LiNbO}_3\text{:Me}$ (Me = Mg,Zn) . . . at threshold Me concentrations (%5.5 mol.% Mg or 7.7 mol.% Zn) the extrema of nonlinear optical parameters and step-like changes of ESR and IR spectra and of charge transport are observed. The Me location in LiNbO_3 lattice is discussed. (p. 293)

STUDENT CENTER CAFETERIA

5:30 pm–6:30 pm DINNER SERVED

6:30 pm–7:30 pm FREE TIME

ACADEMIC CENTER CAFETERIA

7:30 pm–8:30 pm

TuD, PLENARY SESSION ON OPTICAL AND ELECTRONIC SIGNAL PROCESSING

Alastair Glass, *AT&T Bell Laboratories, Presider*

7:30 pm Plenary Paper

TuD1 Electronics Optics and the Photorefractive Effect, Richard C. Williamson, *MIT Lincoln Laboratories*. (p. 298)

8:00 pm Plenary Paper

TuD2 Optics, Electronics and the Photorefractive Effect, Dimitri Psaltis, *California Institute of Technology*. (p. 299)

8:30 pm DISCUSSION

WEDNESDAY, JULY 31, 1991

STUDENT CENTER CAFETERIA

7:00 am-8:00 am BREAKFAST

ACADEMIC CENTER AUDITORIUM

8:00 am-10:00 am

WA, BEAM FANNING AND SELF-PUMPED PHASE CONJUGATION

Jack Feinberg, *University of Southern California, Presider*

8:00 am

WA1 Reflection grating mutual conjugator in the geometry of two interconnected ring mirrors, A. V. Mamaev, *Institute for Problems in Mechanics, U.S.S.R.*; A. A. Zozulya, P. N. Lebedev Physics Institute, U.S.S.R. We present an investigation of a reflection grating mutual conjugator in the geometry of two interconnected passive ring mirrors in photorefractive $\text{KNbO}_3\text{:Fe}$ with a characteristic relaxation time of the order of several milliseconds. (p. 302)

8:15 am

WA2 Crystal noise limited holographic interferometry in BSO, R. C. Troth, J. C. Dainty, *Imperial College, U.K.*; S. L. Sochava, S. I. Stepanov, *Academy of Sciences of the U.S.S.R.* A. F. Ioffe Physicotechnical Institute. Results of the noise and sensitivity characteristics of two $\text{Bi}_{12}\text{SiO}_{20}$ crystals are presented with respect to their use in an anisotropic self-diffraction real-time holographic interferometer. (p. 306)

8:30 am

WA3 Double phase-conjugated mirror and double color-pumped oscillator using band-edge photorefractivity in InP:Fe , N. Wolffer, P. Gravey, G. Picoli, V. Vieux, *CNET Lannion, France*. We have measured typical DPCM and DCPO conversion efficiencies of 50% in InP:Fe , down to 965 nm, with an external field of 10 kV/cm. (p. 310)

8:45 am

WA4 Application of beam fanning in a photorefractive BaTiO_3 crystal: measurement of light scattering at zero degrees by a single glass fiber, G. G. Padmabandu, Choonghoon Oh, Edward S. Fry, *Texas A&M U.* Beam fanning in a photorefractive BaTiO_3 crystal has been used to measure the forward light scattering from glass fibers; the results are in agreement with theory. (p. 314)

9:00 am

WA5 Frequency shift in a mutually pumped phase conjugator of BaTiO_3 , Dadi Wang, Zhiguo Zhang, Peixian Ye, *Chinese Academy of Sciences, Institute of Physics*. We report on an experimental study of the self-frequency shift in a mutually pumped phase conjugator and show its dramatic dependence on the pumping power. (p. 317)

WEDNESDAY, JULY 31, 1991 — Continued

9:15 am

WA6 Parametric oscillation in photorefractive crystals with local response in unclosed optical cavities, A. P. Mazur, A. D. Novikov, S. G. Odoulov, M. S. Soskin, *Ukr. SSR Academy of Science Institute of Physics, U.S.S.R.* Steady-state oscillation in local-response photorefractive crystals in unclosed cavities is demonstrated. With a proper choice of pump angles and pump frequency, detuning the phase conjugation of one beam is possible. (p. 320)

9:30 am

WA7 Anisotropic diffraction in photorefractive volume holograms, Ching-Cherng Sun, Ming-Wen Chang, *Taiwan National Central U., China*. We report theoretical and experimental investigations on the diffraction efficiency, angle sensitivity, and optimal reconstructing angle of volume holograms in a photorefractive BaTiO_3 crystal. (p. 324)

9:45 am

WA8 Low-frequency noise and photoinduced scattering in photorefractive crystals, B. I. Sturman, *Institute of Automation and Electrometry, U.S.S.R.* A new interpretation of strong photoinduced scattering in crystals with a predominant local photorefractive response is suggested, based on amplification of LF noise of a laser or crystal. (p. 328)

10:00 am-10:30 am COFFEE BREAK

1030 am-12:00 m

WB, DEFECTS AND CHARGE TRANSPORT

Thomas Pollak, *Sanders Associates, Presider*

10:30 am

WB1 Identification of light-induced charge-transfer processes in BaTiO_3 by combined ESR and optical measurements, O. F. Schirmer, E. Possenriede, H. Krose, P. Jacobs, *U. Osnabruck, Germany*. By simultaneously monitoring the changes in the ESR and optical absorption of defects in BaTiO_3 under illumination, their charge-conversion thresholds and the associated charge-transfer paths are identified. (p. 334)

10:45 am

WB2 Spectroscopy of light sensitive defect/impurity centers in photorefractive BaTiO_3 , Robert N. Schwartz, Barry A. Wechsler, Ross A. McFarlane, *Hughes Research Laboratories*. We review our electron paramagnetic resonance (EPR), photo-EPR, and optical spectroscopy studies that probe the nature of defects and impurities that are present in BaTiO_3 , and we examine their role in the photorefractive effect. (p. 338)

11:00 am

WB3 Two-center model explains photorefractive properties of $\text{KNbO}_3\text{:Fe}$, L. Holtmann, G. Kuper, K. Buse, S. Loheide, H. Hesse, E. Kratzig, *U. Osnabruck, Germany*. Measurements of photoconductivity, light-induced absorption, diffraction efficiency, and grating phase in $\text{KNbO}_3\text{:Fe}$ are interpreted in terms of a two-center charge-transport model. (p. 341)

WEDNESDAY, JULY 31, 1991 — Continued

11:15 am

WB4 Electron-hole transport in photorefractive media, M. C. Bashaw, T.-P. Ma, R. C. Barker, *Yale U.* For most regimes, single- and two-level electron-hole transport models give significantly different results. For a regime to be described, they give similar results. (p. 345)

11:30 am

WB5 Determination of the effective trap density of Ta:KNbO₃ at 823 nm, A. E. Clement, G. C. Gilbreath, *U.S. Naval Research Laboratory*; S. N. Fugera, *Sachs-Freeman Associates, Inc.* Reduction in the effective trap density is computed in poled Ta:KNbO₃ and BaTiO₃ at 823 nm using experimental data where computational methods are compared. (p. 347)

11:45 am

WB6 Photorefractive and photochromic effects in barium titanate, M. H. Garrett, J. Y. Chang, H. P. Jenssen, C. Warde, T. M. Pollak, *Lockheed Sanders*. We report on the intensity dependence of photorefractive properties of barium titanate that also exhibits the photochromic effect which enhances the sensitivity at the illuminating wavelength. (p. 351)

STUDENT CENTER CAFETERIA

12:00 m-1:00 pm LUNCH SERVED

ACADEMIC CENTER CLASSROOMS

1:00 pm-2:30 pm

WC, POSTER SESSION: WAVE INTERACTIONS AND DEVICES

WC1 Picosecond nonlinear optical responses in photorefractive crystals, H. Liu, R. J. Reeves, R. C. Powell, *Oklahoma State U.* Picosecond-pulse excitation was used to elucidate the properties of fast nonlinear optical processes that are precursors to the space-charge field photorefractive effect. (p. 356)

WC2 Self-pumped phase conjugation in barium titanate with high-intensity nanosecond pulses, M. J. Damzen, N. Barry, *Imperial College, U.K.* Experimental results are presented of corner-pumped and ring-passive phase conjugation of nanosecond pulses. Intensity-dependent hole-electron competition strongly affects reflectivity and crystal dynamics. (p. 360)

WC3 Nanosecond photorefractive effects in KNbO₃, I. Biaggio, M. Zgonik, P. Gunter, *Swiss Federal Institute of Technology*. 75-ps pulses at 532 nm are used to write photorefractive gratings. The build-up of the grating for different experimental setups and material treatments are studied. (p. 364)

WC4 Spectral pulse distortion from two-beam coupling of subpicosecond pulses in a photorefractive crystal, X. Steve Yao, Jack Feinberg, *U. Southern California*. We measure and discuss the pulse shape distortion caused by beam coupling using trains of subpicosecond pulses in BaTiO₃. (p. 368)

WEDNESDAY, JULY 31, 1991 — Continued

WC5 Feature extraction by a self-organizing photorefractive system, Claus Benkert, Verena Hebler, Ju-Seog Jang, Shakil Rehman, Mark Saffman, Dana Z. Anderson, *U. Colorado*. We present a photorefractive system that learns to distinguish between features in a set of input pictures in a self-organizing manner. (p. 372)

WC6 Self-organizing photorefractive frequency decoder, Mark Saffman, Claus Benkert, Dana Z. Anderson, *U. Colorado*. We demonstrate a self-organizing photorefractive circuit. The circuit decodes a beam containing two optical frequencies into two beams, each containing one frequency. (p. 376)

WC7 All-optical associative memory based on a nonresonant cavity with image bearing beams, M. Ingold, M. Duelli, P. Gunter, *Swiss Federal Institute of Technology*; M. Schadt, F. Hoffman-LaRoche, Ltd., *Switzerland*. Associative recall of simple patterns is demonstrated in a multistable, content-addressable cavity. The photorefractive KNbO₃ crystal performs image comparison and nematic liquid crystal image discrimination. (p. 380)

WC8 Detection of the transient motion of a scattering surface by two-wave mixing in a photorefractive crystal, R. K. Ing, *Ultra Optec, Inc., Canada*; J.-P. Monchalain, *National Research Council of Canada*. Two-wave mixing in BaTiO₃ is used to detect the phase shift induced on a signal beam by ultrasonic surface motion following pulsed laser excitation. (p. 384)

WC9 Velocity filtering using complementary gratings in photorefractive BSO, Ghazanfar Hussain, Robert W. Eason, *U. Southampton, U.K.* A technique for velocity filtering and feature extraction has been demonstrated which exploits the recording of complementary gratings in photorefractive BSO. (p. 388)

WC10 Phase-locked detection of a running interference pattern in photorefractive SBN, O. P. Nestiorkin, Ye. P. Shershakov, B. Ya. Zeldovich, *Chelyabinsk Polytechnic Institute, U.S.S.R.*; N. V. Bogodaev, L. I. Ivleva, N. M. Polozkov, *General Physics Institute, Academy of Sciences of the U.S.S.R.* Recording of a static photorefractive hologram by a running interference pattern is achieved in SBN crystal with an externally applied ac field. The influence of self-diffraction through degenerate interaction is studied. (p. 392)

WC11 Time-integrating self-pumped phase conjugator, Erik Oldekop, Azad Siahmakoun, *Center for Applied Optics Studies*. A time-integrating filter with self-pumped phase conjugation is used to remove time-varying speckles from images. (p. 396)

WC12 Photorefractive deamplification for artifact noise reduction, Jehad Khoury, Mark Cronin-Golomb, *Tufts U.*; Charles L. Woods, *Rome Laboratory*. Nonlinear optical thresholding in the Fourier plane reduces additive signal-dependent noise. An order of magnitude reduction of artifact noise is demonstrated using photorefractive two-beam coupling. (p. 400)

WC13 Stability of information readout by self-pumped phase conjugation in barium titanate, F. C. Lin, D. Sun, G. Leu, M. A. Fiddy, T. Yang, Y. Y. Teng, *U. Lowell*. Experimental data are interpreted on optical signal recall by self-pumped phase conjugation in barium titanate (BaTiO₃) crystal in terms of temperature, illumination configuration, and spatial frequency content of the information. (p. 404)

WC14 Effects of grating erasure on beam fanning and self-pumped phase conjugation, Gary L. Wood, William W. Clark III, Edward J. Sharp, *CECOM Center for Night vision and Electro-Optics*; Gregory J. Salamo, *U. Arkansas*. The time response for photorefractive beam fanning and self-pumped phase conjugation is determined as a function of erasure exposure time for both coherent and incoherent erasure beams. (p. 408)

WC15 Intensity dependent thresholding and switching in the photorefractive bridge mutually pumped phase conjugator, Stephen W. James, Robert W. Eason, *U. Southampton, U.K.* Total intensity dependent reflectivity has been obtained from the bridge mutually pumped phase conjugator, allowing the observation of optical thresholding and switching. (p. 412)

WC16 Extraordinary polarized light does not always yield the highest reflectivity from self-pumped BaTiO₃, Stephen W. James, Robert W. Eason, *U. Southampton, U.K.* The inclusion of an ordinary polarized component in the input to a self-pumped phase conjugator in BaTiO₃ can double the phase-conjugate reflectivity. (p. 416)

WC17 Self-pumped phase conjugation in cerium-doped barium titanate, Chitra Guruswamy, Doyle A. Temple, *Louisiana State U.* Measurements of self-pumped phase conjugate reflectivity have been performed on cerium-doped barium titanate. The results indicate that cerium doping enhances the phase conjugate reflectivity. (p. 420)

WC18 Multiple grating optical processing in barium titanate, S. A. Boothroyd, P. H. Beckwith, L. Chan, J. Chrostowski, *National Research Council of Canada*. Photorefractive gratings representing different images are written in barium titanate with a controlled phase relationship via a spatial light modulator; the output demonstrates logic operations. (p. 423)

WC19 Acoustooptic modulator correction by holograms in photorefractive crystals, A. Gnatovskii, N. Kukhtarev, V. Maglevanii, A. Pigida, V. Verbitskii, *Academy of Sciences of the Ukr.SSR Institute of Physics*. Real-time correction of the aberrations caused by an acoustooptic modulator was achieved in a photogalvanic lithium niobate crystal by a simple two-wave mixing scheme. (p. 427)

WC20 Phase conjugation with saturable gain and saturable absorption, Milivoj Belic, Dejan Timotijevic, *Institute of Physics, Yugoslavia*; Robert W. Boyd, *U. Rochester*. Stable and unstable solutions to different models of two-wave and four-wave mixing in photorefractive media with saturable gain and saturable absorption are obtained. (p. 428)

WC21 Instabilities in coupled photorefractive ring cavities and self-pumped phase conjugators, Li-Kuo Dai, Yih-Shun Gou, *National Chiao Tung U., China*; Claire Gu, *Rockwell International Science Center*; Pochi Yeh, *UC-Santa Barbara*. We investigate the temporal instabilities of self-oscillations in coupled unidirectional photorefractive ring resonators. Results, including self-pulsation and chaos, are presented and discussed. (p. 432)

WC22 Analytic and numeric results on subharmonics in BSO, A. Bledowski, J. Otten, K. H. Ringhofer, *U. Osnabruck, Germany*; B. Sturman, *U.S.S.R. Academy of Sciences Siberian Branch, Institute of Automation and Electrometry*. By analytic and numerical methods, we find hysteresis of the solutions of Kukhtarev's materials equations for holography in photorefractive crystals and instability against period doubling. (p. 436)

WC23 Spatial subharmonic generation in BaTiO₃, A. Novikov, S. Odoulov, *Ukr. S.S.R. Academy of Sciences, Institute of Physics, U.S.S.R.*; R. Jungen, T. Tschudi, *Technische Hochschule Darmstadt, Germany*. Parametric amplification of the spatial subharmonic in BaTiO₃ due to nonlinear mixing of three copropagating waves with orthogonal polarizations is predicted and studied experimentally. (p. 440)

WC24 Instability of spatial subharmonic in hologram recording in a photorefractive crystal, O. P. Nestiorkin, *Chelyabinsk Polytechnic Institute, U.S.S.R.* The process of hologram recording by a running interference pattern in photorefractive crystal with an applied dc field is considered. Conditions are found under which the spatial subharmonic grating is generated as a result of instability. (p. 444)

WC25 Spatial subharmonic generation at intermode interaction in planar waveguides, V. Popov, E. Shandarov, S. Shandarov, *Institute of Automatic Control Systems and Radioelectronics, U.S.S.R.* Amplification of the weak signal beam by exciting waves at the intermode interaction $TE_{p-1} - TE_p$ in the planar optical waveguide in photorefractive LiNbO₃:Ti:Fe is considered. (p. 448)

WC26 Light-induced scattering in planar photorefractive waveguides, A. Bashkurov, G. Glazov, I. Itkin, S. Shandarov, *Institute of Automatic Control Systems and Radioelectronics, U.S.S.R.* Analysis of the formation of noisy holograms in planar waveguides while nonstationary holographic amplification of a input noise picture by a powerful exciting wave has been performed. The generalized parameters characterizing degradation of waveguide properties have been also found. (p. 452)

WC27 Photorefractive parametric interaction of volume and leaky optical waves in planar waveguide on lithium niobate, V. M. Shandarov, *Institute of Automatic Control Systems and Radioelectronics, U.S.S.R.* The effect of leaky TE-mode beam scattering into higher-order leaky mode beams because of volume and leaky wave parametric interactions in planar optical waveguide LiNbO₃:Ti:Fe is discovered and experimentally studied. (p. 456)

WC28 Photorefractive waveguides fabricated by excimer laser ablation and ion implantation, K. E. Youden, Robert W. Eason, *U. Southampton, U.K.*; M. C. Gower, *Rutherford Appleton Laboratory, U.K.* We discuss the growth and properties of thin film epitaxial BGO waveguides, deposited on ZrO₂ by excimer laser ablation, and ion-beam implanted waveguides in SBN. (p. 460)

Monday, July 29, 1991

New Materials

MA 8:30am–10:00am
Academic Center Auditorium

Daniel Rytz, *Presider*
Sandoz Optoelectronique, Switzerland

**Observation and Study
of the Photorefractive Effect in Doped Nonlinear Polymers**

D. M. Burland, S. Ducharme, W. E. Moerner, J. C. Scott, and C. A. Walsh

IBM Research Division, Almaden Research Center

K95/801, 650 Harry Road, San Jose, CA 95120-6099

92-18685



AD-P006 695

408-927-1501



Many applications of photorefractivity have been proposed: a virtually unlimited array of image processing techniques including phase conjugation and novelty filtering, simulations of neural networks and associative memories, and high density efficient holographic optical storage. Until very recently, all materials showing the photorefractive effect have been inorganic crystals¹. A problem currently impeding the wide-spread exploitation of the photorefractive effect has been the fact that inorganic materials exhibiting the effect tend to be difficult and thus expensive to prepare and, because of their crystalline nature, to be incompatible with current integrated packaging processes. There is thus a continuing and critical need for new classes of photorefractive materials with improved processability and performance.

It is instructive to compare various classes of potential photorefractive materials using a diffraction efficiency figure-of-merit $Q \approx n^3 r_{eff} / \epsilon$, where n is the optical index of refraction, r_{eff} is the effective electro-optic coefficient, and ϵ is the DC dielectric constant. For inorganic crystals, it is well-known that the ratio r_{eff} / ϵ does not vary much from material to material. This is simply a consequence of the fact that the optical nonlinearity in these systems is driven chiefly by the large ionic polarizability which has the consequence of increasing ϵ along with r_{eff} . A variety of organic materials, crystalline and polymeric, have been investigated for their nonlinear optical

properties². These materials have *large electro-optic coefficients not accompanied by large DC dielectric constants*. This means that the internally developed space charge field necessary for the photorefractive effect will not be screened by internal polarization fields as effectively in organic materials as in inorganic ones.

Recently, the first example of photorefractivity in an organic crystal was reported³ for the organic nonlinear COANP crystal doped with TCNQ. Just as in the inorganic crystal case, it is, in general, difficult to grow high optical quality doped organic crystals. Polymeric materials, on the other hand, can be doped with various molecules of quite different sizes with relative ease. In addition, polymers may be formed into a variety of thin-film and waveguide configurations tailored to the specific application.

We have obtained, for the first time to our knowledge, firm evidence of photorefractivity in molecularly doped nonlinear optical polymers⁴. The fundamental approach that was followed in searching for photorefractivity in polymers was to start with nonlinear(NLO) polymeric materials with a known electric-field-poling-induced electro-optic activity. These NLO polymers were then doped with charge transport agents to provide the required photoconductivity. Indeed, insulating polymers can be readily made photoconductive by the addition of charge transport agents as is regularly done in the photoconductors used in electrophotographic printers and copiers⁵.

Photorefraction (at 647.1 nm) in systems of this type was established by a combination of hologram erasability, correlation with photoconductivity and electro-optic response, and enhancement by external fields in numerous samples (178 to 533 μm thick) of the epoxy based nonlinear optical polymers (BisA-NPDA)⁶ or (NA-APNA)⁷ mixed with hole transport agents such as p-diethylaminobenzaldehyde-diphenyl hydrazone (DEH). Diffraction efficiencies up to 0.1% (NA-APNA) and 0.006% (BisA-NPDA) were observed at bias fields of 84 kV/cm and 126 kV/cm, respectively.

The calculated space-charge field in one sample of the BisA-NPDA mixture was 26 kV/cm (quite comparable to values reported for inorganic photorefractive crystals) at 126 kV/cm and a grating spacing of 1.6 μm ; the estimated photorefractive trap density was $2 \times 10^{15} \text{cm}^{-3}$. A useful property of these materials is that electric field poling of the nonlinear chromophores is partially reversible and thus continuous realignment of the nonlinear molecules in the polymer permits external control of grating readout independent of the internal space-charge field formed.

The photorefractive effect in amorphous polymers differs in many important ways from the corresponding effect in inorganic crystals. Photoconductivity, a process at the heart of the photorefractive effect, is very different in polymeric systems. The current band and hopping models of the photorefractive effect need to be modified to take this difference into account.

Furthermore, geminate charge carrier recombination⁸, a little understood process limiting charge carrier generation quantum yields, is much more important in low dielectric constant polymers than it is in inorganic systems. In organic systems in general, the electron-hole pair initially created by molecular autoionization subsequent to photon absorption may recombine before the mobile species, in most cases the hole, has a chance to escape from the Coulomb well created by the pair. This process is under investigation in the photorefractive polymers described above using a sub-picosecond transient grating experiment to probe the temporal process of creation, annihilation and transport of charge carriers.

1. See P. Günter and J.-P. Huignard, eds., *Photorefractive Materials and Their Applications I and II*, (Springer Verlag, Berlin 1988,9).

2. See D. S. Chemla and J. Zyss, eds., *Nonlinear Optical Properties of Organic Molecules and Crystals I and II*, (Academic, Orlando, 1987).

3. K. Sutter, J. Hullinger, and P. Günter, *Sol. St. Commun.* **74**, 867 (1990).
4. S. Ducharme, J. C. Scott, R. J. Twieg, and W. E. Moerner, Postdeadline Paper, OSA Annual Meeting, Boston, MA, November 5-9, 1990; appearing in *Phys. Rev. Lett* (1991).
5. D. M. Burland and L. B. Schein, *Phys. Today* **39**, 1 (1986).
6. M. Eich, B. Reck, D. Y. Yoon, C. G. Willson, and G. C. Bjorklund, *J. Appl. Phys.* **66**, 3241 (1989).
7. D. Jungbauer, B. Reck, R. Twieg, D. Y. Yoon, C. G. Willson, and J. D. Swalen, *Appl. Phys. Lett.* **56**, 2610 (1990).
8. A. Twarowski, *J. Appl Phys.* **65**, 2833 (1989)



Characterization of a New Photorefractive Material: $K_{1-y}Li_yTa_{1-x}Nb_x$

Dr. Aharon Agranat, Rudy Hofmeister, Victor Leyva, and Dr. Amnon Yariv
California Institute of Technology, Pasadena, CA 91125, 818-356-4826

Introduction

The use of photorefractive materials to store volume holograms for optical computing and optical memories has long been an active area of research¹. In addition, these materials have been considered in the implementation of optical neural networks.

Crystals from the solid solution series $K_{1-y}Li_yTa_{1-x}Nb_x$ were among the first to be recognized as photorefractive. Nevertheless, most work has been concentrated on the end-members of the series, potassium tantalate² and potassium niobate (KN)^{3,4}. KLT as well as KTN have also seen some research^{5,6,7}. Since the other members of the solid-solution series are considered difficult to grow, they have received little attention.

We were able to grow large optical-quality crystals of KLTN with the dopants copper and vanadium by carefully proportioning the ingredients in the flux. Our primary motivation for adding lithium to KTN was to increase the para/ferroelectric phase transition closer to room temperature.

KLTN has a perovskite structure with the general composition ABO_3 . In its highest symmetry phase it is cubic and, for small lithium concentrations, undergoes transitions to tetragonal, orthorhombic, and rhombohedral structures with decreasing temperature. In our experiments the crystal was maintained just above the cubic/tetragonal transition.

In the cubic phase the material's photorefractive properties are described by the quadratic electrooptic effect⁸. When an external field is applied to the crystal an index grating is written with

$$\begin{aligned} n_1 &= \Delta n(E_0 + E_{sc}) - \Delta n(E_0) \\ &= \frac{n_0^3}{2} g \epsilon_0^2 \epsilon^2 (2E_0 E_{sc} + E_{sc}^2) \\ \rightarrow n_{1,eff} &= n_0^3 g \epsilon_0^2 \epsilon^2 E_0 E_{sc} \end{aligned}$$

Where E_{sc} is the space charge field due to the interfering light beams. The E_{sc}^2 term can be ignored because it has the wrong spatial frequency. The beam coupling has the property that it can be switched externally by the applied field.

Experimental Discussion

Material Properties

The sample used in the following discussion was a 6.8x 4.9x 2.9mm piece cut from a crystal grown by us using the "top seeded solution growth method." Using electron probe analysis, the composition was determined to be $K_{.960}Li_xTa_{.857}Nb_{.129}Cu_{.004}V_{.0025}$. Quantitative measures of the lithium concentration remain to be done.

Phase Transitions

Since the diffraction efficiency, given by

$$\eta = e^{-\alpha L} \sin^2(n_1 \pi L) \quad (2)$$

is a strong function of the dielectric constant ϵ , we wish to operate the crystal near its phase transition where ϵ is large. We monitored the dielectric constant as a function of temperature by measuring the capacitance of the crystal, where $C = \epsilon_r \epsilon_0 A/d$. The results are shown in figure 2a and are compared to those obtained from a KTN crystal with a similar tantalum:niobium ratio, figure 2b. The cubic/tetragonal transition temperature has been raised approximately 50° to 178°K, and the remaining transitions are comparatively weak or absent. The full width at half maximum (FWHM) for this sample is also increased to approximately 10°. This effect has been attributed to the increased polarizability of the lithium ions⁹.

92-20681



Diffraction Experiments

The diffraction experiments were performed as in figure 3. The writing beams were from an Argon ion laser at 488nm. They were ordinary-polarized to prevent beam interaction. The diffraction efficiency of the grating thus written was monitored with a weak extraordinary-polarized HeNe beam at 633nm. The 633nm beam was verified not to erase the grating. The writing continued until the maximum diffraction was achieved.

After the gratings were written, the diffraction efficiency was determined as a function of applied field. The results are illustrated in figure 4. The three curves shown are for gratings which were written at +1450V/cm, 0V/cm, and -1450V/cm. From the data it is clear that a compensating DC field is induced in the crystal under the influence of the writing field, and that it is approximately one fifth the magnitude of the writing field. This allowed readout of the stored grating in the quadratic phase without an applied field. When the grating was optically erased with the argon beams, some residual diffraction (~1%) remained which was not optically erasable and could only be removed by heating the crystal to room temperature.

The highest diffraction efficiency observed for 488nm writing beams was 75%. For 514nm writing beams the maximum value was reduced to 30%, and at 633nm the diffraction was almost undetectable. From the data we calculate a maximum two beam coupling constant of $\Gamma = 1.75/\text{cm}$. The writing times for maximum diffraction roughly followed $\tau_{\text{write}} \approx 6\text{sec}/I$, where I is the intensity incident on the crystal in Watts/cm².

From the writing time and the calculated index modulation of $n_1 = 8.54 \times 10^{-5}$, we estimate a sensitivity for this KLTN of 7.24×10^{-5} . In all cases the erase time for the gratings was longer than the write time. Very near to the phase transition, the erase/write time asymmetry was up to two orders of magnitude. None of the gratings were diminished measurably after 24 hours at low temperatures.

Summary

We have demonstrated the growth of a new photorefractive material, KLTN, and have characterized its photorefractive properties. The crystal was of good quality with a phase transition at 178°K. It displayed a strong quadratic photorefractive effect with a sensitivity of 7.24×10^{-5} . The maximum diffraction efficiency observed was 75% with a corresponding coupling constant of $\Gamma = 1.75/\text{cm}$. The writing times were given by $\tau_{\text{write}} = 6\text{sec}\cdot\text{cm}^2/\text{W}$, and there was a strong read/write time asymmetry. The photorefractive process was shown to be voltage controllable. Based on this work, KLTNs seem to be highly promising materials for volume hologram storage applications.

1. D. Von der Linde and A.M. Glass, *Appl. Phys.* 8, 85 (1975).

2. S. Rod, F. Borsa, and J.J. van der Klink, *Phys. Rev. B*, 38, 4, 2267-2272 (1988)

3. A. Reisman, S. Triebwasser, and F. Holtzberg, *J. Am. Chem. Soc.*, 77, 4228-4230 (1959)

4. E. Wiesendanger, *Ferroelectrics*, 6, 263-281 (1974)

6. Van der Klink and D. Rytz, *J. Cryst. Growth*, 56, 673-676 (1982)

6. A. Agranat, V. Leyva, and A. Yariv, *Opt. Lett.* 14, 1017-1019 (1989)

7. R. Orlowski, L.A. Boatner, and E. Kraetzig, *Opt. Comm.* 35, (1) 45-48 (1980)

8. A. Agranat, K. Sayano, and A. Yariv, *Digest of the OSA topical meeting on photorefractive materials, effects, and devices* (OSA, Washington, D.C. 1987), paper PD-1

9. J.J. van der Klink, D. Rytz, F. Borsa, and U.T. Höchli, *Phys. Rev. B*, 27, (1) 89-101 (1983)

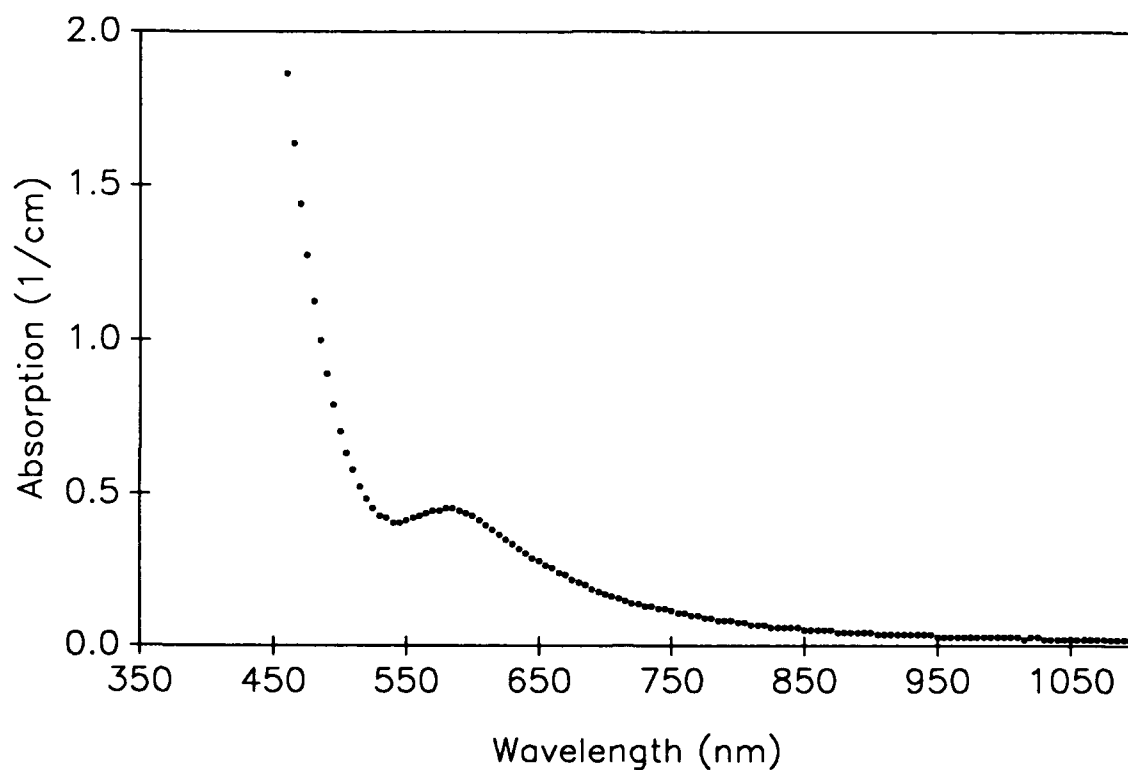


Figure 1 Absorption spectrum of the as-grown KLTN:Cu,V.

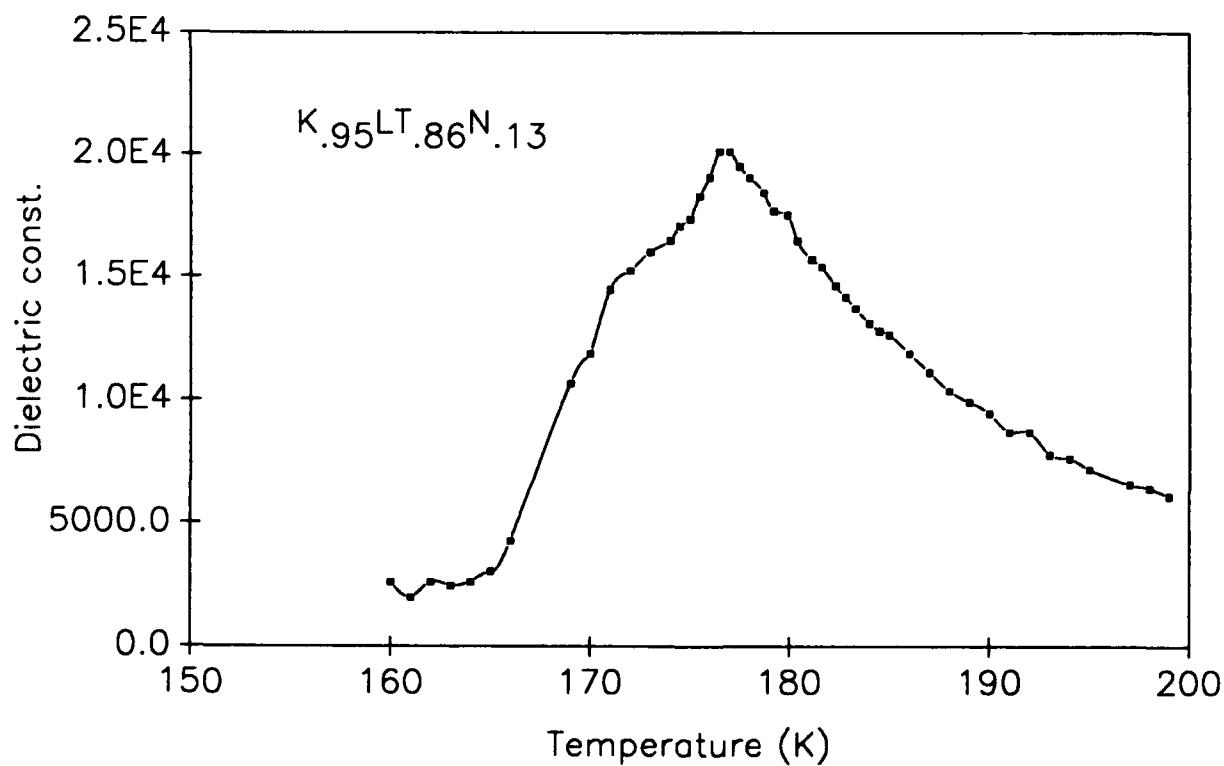


Figure 2 Dielectric constant of the KLT_{0.867}N_{0.133}. The phase transition is approximately 50 degrees higher than a comparable KTN.

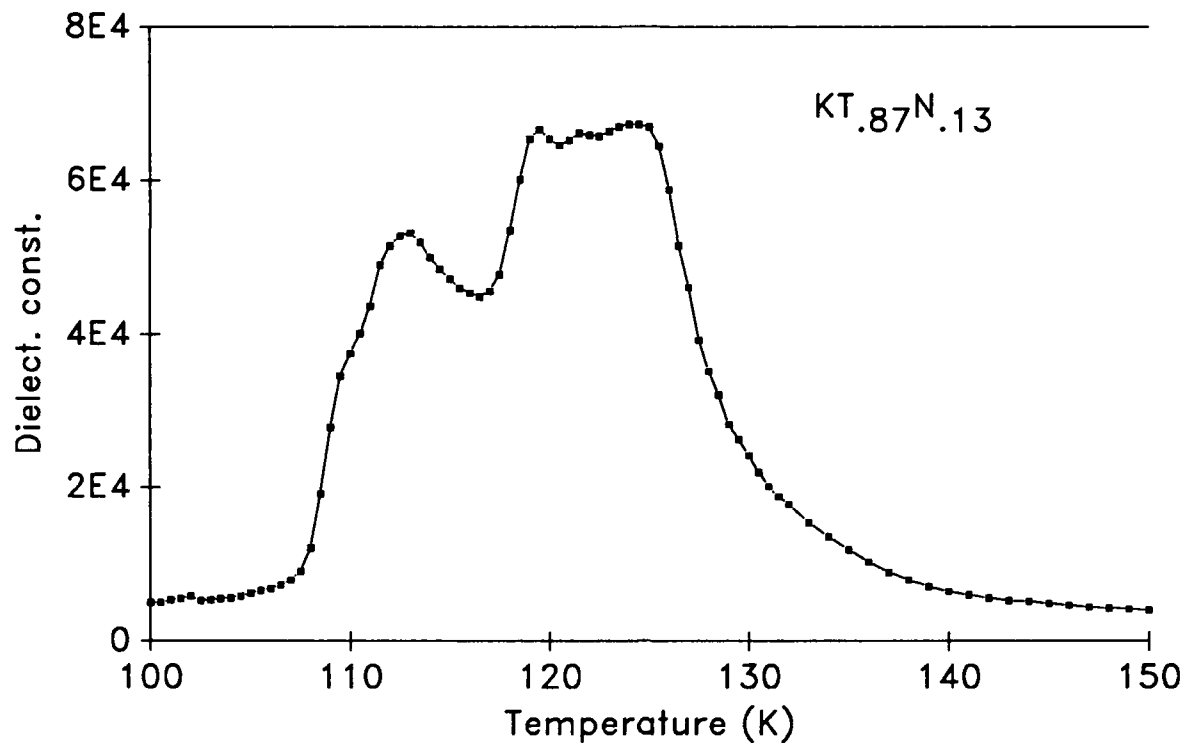


Figure 3 Dielectric constant of a $KT_{.86}N_{.13}$.

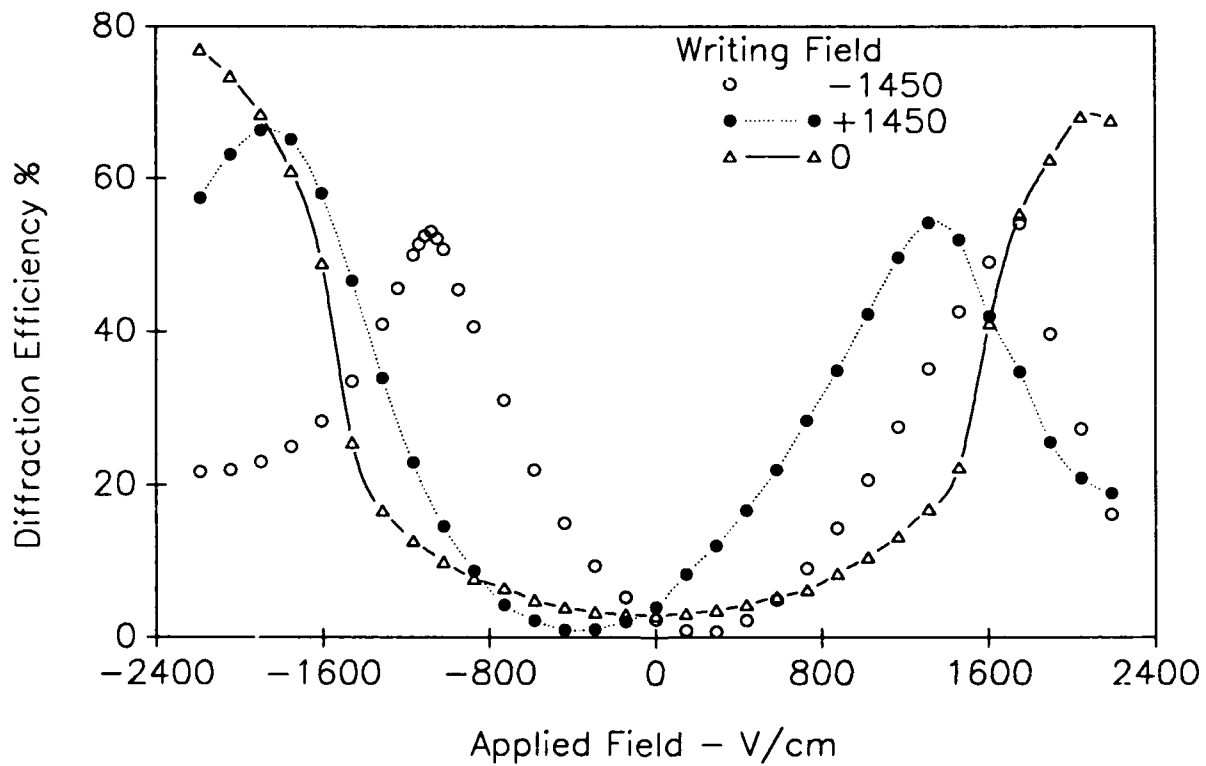


Figure 4 Two beam coupling diffraction efficiency, for gratings written at +1450V/cm, 0V/cm, and -1450V/cm.

The New Type of KNSBN:Cu Crystal as High-performance Self-Pumped Phase-Conjugator

Zhang Guangyin, Xu Jingjun, Liu Simin, Wu Yuanqing

Physics Department, Nankai University

Tianjin 300071, China

Song Yongyuan, Chen Huanchu

Institutes Crystal Materials, Shandong University

Jinan 250100, China

AD-P006 697



Summary

In KNSBN several crystallographic sites can be partially empty, which allow crystal composition to be tailored. The magnitude of longitudinal (r_{61}) and transverse (r_{33}) electro-optic coefficient depend greatly on the ratios of Ba/Na and K/Na. So either r_{33} or r_{61} can be made large, absorption and response wave range can be controlled in the desired spectral range by changing the dopant and its concentration. According to these the crystal with partially-filled composition Cu-doped $(\text{K}_{0.5}\text{Na}_{0.5})_{0.2}(\text{Sr}_{0.1}\text{Ba}_{0.9})_{0.1}\text{Nb}_2\text{O}_6$ is grown. We get the reflectivity R up to 68% of self-pumped phase-conjugate wave (SPPCW) in this kind of KNSBN:Cu (Cu-doped 0.04wt%) at the laser wavelength $\lambda = 614.5\text{nm}$, $I_1 = 30\text{mw}$, $\theta = 5^\circ$ (the experimental

92-18686



arrangement of SPPCM shown in Fig.1), which is much higher than that in KNSBN, KNSBN: Ce crystals with fully-filled

composition. ⁽¹⁾ Through our

investigation of three samples :

1. Cu-doped 0.1wt%, $5 \times 4 \times 3 \text{ mm}^3$; 2.

Cu-doped 0.06wt%, $6 \times 4 \times 4 \text{ mm}^3$; 3. Cu

-doped 0.04wt%, $4 \times 5 \times 6 \text{ mm}^3$, we

know that R is the largest at the

wavelength λ at which the

absorption edge of Cu dopant band

of the sample stands, as shown in Fig.2, Tab.1 and Tab.2. From

the experimental results we conclude that in order to produce

the high-reflectivity SPPCW at the working wavelength the

dopant concentration and absorptioin coefficient must be made

properly low.

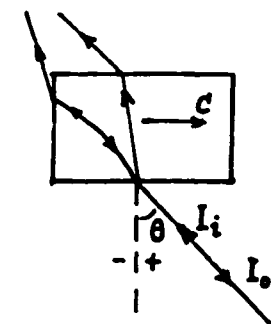


Fig.1 The experimental

arrangement of SPPCM.

Tab 1 Relationship of R

vs Cu-doped concentration

p at $\lambda = 514.5 \text{ nm}$

| | | | |
|-------|------|------|------|
| p (%) | 0.04 | 0.06 | 0.1 |
| R (%) | 68.0 | 52.3 | 29.7 |

Tab 2 relationship of R vs

wavelength λ in sample #3

| | | | | |
|----------------|-------|-------|-------|-------|
| λ (nm) | 514.5 | 496.5 | 488.0 | 476.5 |
| R (%) | 68.0 | 47.4 | 38.2 | 21.4 |

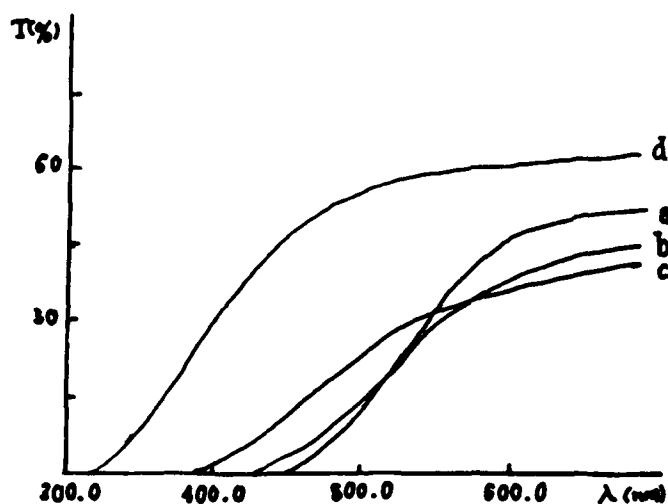


Fig.2 Transmission spectra for sample #1(curve a), #2(curve b), #3(curve c), an undoped one(curve d), not corrected for Fresnel losses.

Based on the experimental results that there is no loop and self-bending channels exit in the crystal while the self-pumped phase-conjugate wave appears, we think that the backscattering and its effective amplification, then successive four-wave mixing interaction in self-bending channels are supposed to be responsible for the formation of SPPCW. Its reflectivity is high enough to be almost equal to the maximum $R \sim 70\%$ ^[2] in BaTiO_3 , besides its advantages over BaTiO_3 in growth, processing and its convenience in usage because there is no limit for it to work necessarily above 15°C , unlike for BaTiO_3 . So this kind of SPPCM is more convenient, economical and practical in application than BaTiO_3 , and this new type of

crystals is very competitive to become one of the leading photorefractive materials as the self-pumped phase-conjugate mirrors in application.

References

- [1]. Juan Rodriguez , et al., Applied Optics 26 (1987), 1732
- [2]. H. Rajbenhach, J. P. Huignard, and P. Gunter
Springer Series in Electronics and Photonics, Vol. 30,
Nonlinear Photonics, 151 (Springer-Verlog Berlin
Heidelerg 1990)



A NEW PHOTOREFRACTIVE MATERIAL KNSBN:Co

Quanzhong JIANG, Yongyuan SONG, Daliang SUN, Xinliang LU and Huanchu CHEN

(Institute of Crystal Materials, Shandong University, Jinan, P. R. C., 250100, Tele.: 643861-2451)

1. INTRODUCTION

Potassium sodium strontium barium niobate (KNSBN) has been developed in our country for the first time. It is a new ferroelectric with A-sites thoroughly occupied by K^+ , Na^+ , Sr^{2+} and Ba^{2+} ions. Comparing to $BaTiO_3$, KNSBN crystals have no phase transition at room temperature, but have large hardness coefficient and 180° ferroelectric domains that are easy to be polarized. KNSBN will be one of the most prospective photorefractive materials that can be used in holographic storage, image amplification and optical phase conjugation. The purpose of this paper is to describe the crystal growth and photorefractive properties of KNSBN:Co.

2. CRYSTAL GROWTH

$Co_z(K_{x/2}Na_{1-x/2})(Sr_{1-y}Ba_y)_{0.9-2z}Nb_2O_6$ (KNSBN:Co, $x=0.5$, $y=0.39$) crystals were grown by pulling method using MCGS-3 system. The starting materials are 99.99% $BaCO_3$, $SrCO_3$, Nb_2O_5 , K_2CO_3 , Na_2CO_3 , and Co_2O_3 , which were mixed according to the crystal composition as $z=0.003$, 0.006 and 0.02 . The growth conditions are:

Growth temperature: $1550^\circ C$
 Pulling rate : 3--5mm/h
 Rotation : 10--15rpm
 Atmosphere : Air
 Pulling direction : 001

From the appearances of the as-grown crystals, it can be seen that the amount of Co ions severely affects the growth habits of them. For crystal $z=0.003$, it appears eight facets with good symmetry, which are (110), (100) and their symmetrical facets, and is very similar to the undoped KNSBN ($z=0$). For crystal $z=0.006$, the cross section perpendicular to C-axis is square, and at the places equal to its edges, there are (210), (110) and their symmetrical facets. Only two facets of (100) appears for crystal $z=0.02$.

3. TRANSMISSION SPECTRA

Fig.1 shows the transmission properties of KNSBN:Co. From it we can see that, although the value of z is changed, increasing absorption to the light of 675nm appears for all of the three doped samples. So, a new energy level has been formed in the band gap for the dopants of Co ions, and new centers for free charge carrier stimulation and recombination can modify the photorefractive properties of KNSBN.

92-18630



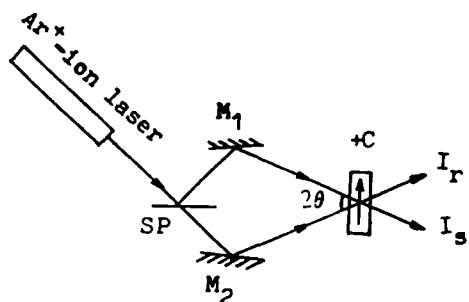


Fig.2 Experimental set-up for two-wave coupling.SP,beam splitter;M,mirror.

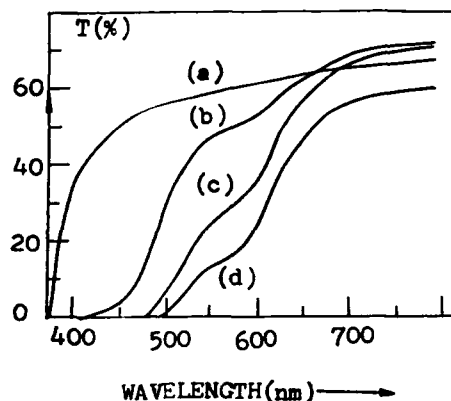


Fig.1 Transmission spectra a)undoped,b)z=0.003,c)z=0.006 and d)z=0.02.

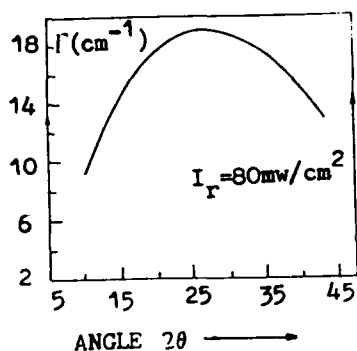


Fig.3 The relation between the gain and the angle 2θ .

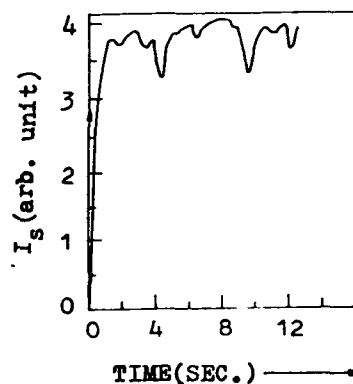


Fig.4 The time response property of KNSBN:Co in two-wave coupling.

4. TWO-WAVE COUPLING IN KNSBN:Co

Two-wave coupling usually means the energy transformation between two coherent beams inside a photorefractive material. The change of the energy density of the signal beam can be represented by :

$$I_s(I_r \neq 0)/I_s(I_r = 0) = (1+m)e^{\Gamma d} / 1+me^{\Gamma d}$$

Where d is the thickness of a sample, Γ is the gain coefficient and $m=I_s(0)/I_r(0)$. In our experiments, $m=0.001$, then:

$$\Gamma = d^{-1} \ln(I_s(I_r \neq 0)/I_s(I_r = 0))$$

Fig.2 shows the arrangement for two-wave coupling. An extraordinary Ar^+ -ion laser beam ($\lambda=488\text{nm}$) was used and a detector connected to a X-Y recorder was used to record the time response property. Fig.3 shows the relation between

the gain for the crystal of $z=0.003$ and the angle 2θ formed by the two-beams outside the sample. The Debye constant is determined to be $5.75 \times 10^4 \text{ cm}^{-1}$ and the effective charge density is estimated to be in the order of 10^{17} cm^{-3} . Fig. 4 is the time response property and the oscillating at the saturation state is caused by the sparking at the surface of the sample.

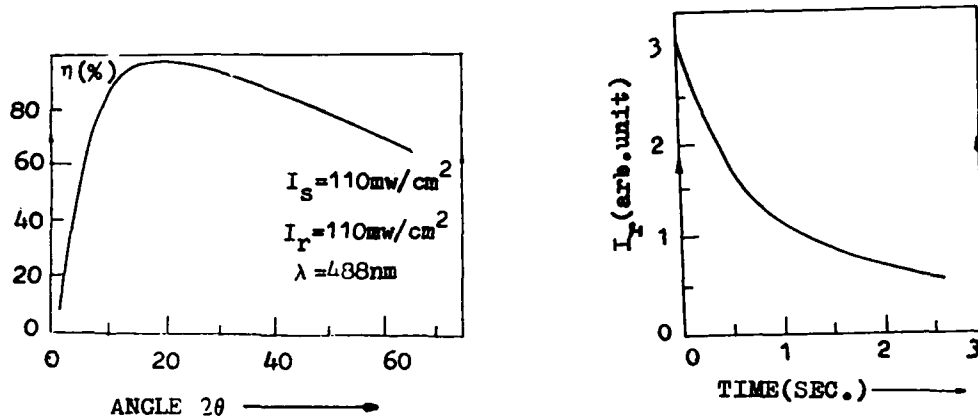


Fig.5 The relation between the diffraction efficiency and the angle 2θ . Fig.6 The time response property of storage in KNSBN:Co.

5. HOLOGRAPHIC STORAGE PROPERTIES OF KNSBN:Co

Photorefractive materials can play an important role in volume holography and real-time associative memory. The relation between the diffraction efficiency and the angle 2θ formed by the reference beam and the signal beam is shown in Fig.5, and the response property is shown in Fig.6. The photorefractive sensitivity is estimated to be in the order of $10^{-3} \text{ cm}^2/\text{J}$, two-orders of magnitude higher than that of LiNbO_3 .

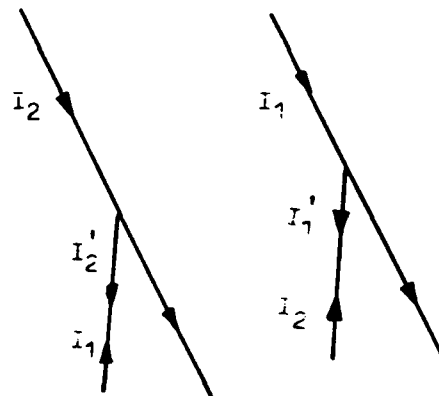


Fig.7 The diagram for our purpose to produce a phase conjugation beam.

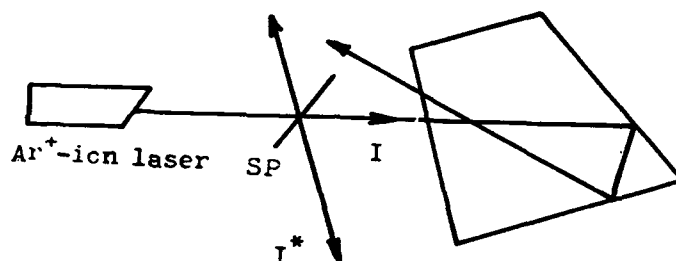


Fig.8 Experimental set-up for our purpose. SP, beam

6. SELF-PUMPED PHASE CONJUGATION EXPERIMENT IN KNSBN:Co.

Photorefractive materials provides a convenient way to realize optical phase conjugation. The purpose for our experiments is described as follows:

When a beam of light goes through a photorefractive material, a beam fan can be formed for the coupling between the beam and the noise, that is to say, there are so many gratings, which have different grating vectors, that the phase matching condition is automatically reached when another beam is to read the gratings. Because of the coupling between the reading beam and the diffracted beam, one of the grating is strengthened and the strong phase conjugation beam can be output. Fig.7 is the diagram explanation for our purpose, $I_1(I_2)$ is the fanning light of $I_1(I_2)$. The experiment diagram is shown in fig.8. The self-pumped phase conjugation reflectivity of 46% is determined using Ar-ion laser ($\lambda=514.5\text{nm}$).

7. CONCLUSION

In our experiments, high optical quality crystals have been got and the centers responsible for photorefractive effect is determined to be Co ions. High photorefractive sensitivity, large gain coefficient and large self-pumped phase conjugation reflectivity enable KNSBN:Co crystals to be used in many aspects of optical image processing.

REFERENCES

1. Huanchu CHEN et al., Physics, 10(1981)729.
2. R. R. Neurgaonker et al., Optical Engineering, 5(1987)392
3. Kebin XU et al., Chinese laser, 16(1989)532.



Photorefractive properties of $\text{Bi}_4\text{Ge}_3\text{O}_{12}$ crystals in the ultraviolet spectral range

G. Montemezzani, St. Pfändler and P. Günter

Institute of Quantum Electronics, Swiss Federal Institute of Technology

ETH Hönggerberg HPF E 20, CH- 8093 Zürich (Switzerland)

(Phone: 41-1 377 22 96; Fax: 41-1 371 59 89)

To the best of our knowledge, only preliminary studies of photorefractive effects in the ultraviolet (UV) spectral range have been reported up to now, e.g. in KH_2PO_4 [1], RbZnBr_4 [2] (both at low temperatures), and in LiNbO_3 [3, 4] and LiTaO_3 [5] in the near UV. Photorefractive materials operating in the UV however could be very useful for all types of coherent optical beam interactions, e.g. beam amplification, dynamical holography, phase-conjugation or photolithographic applications where the use of shorter wavelengths leads to an increased resolution.

$\text{Bi}_4\text{Ge}_3\text{O}_{12}$, the material used in this work belongs to the cubic point group $\bar{4}3m$ and has a large transparency range extending from about 300 nm to about 6 μm . In the visible spectral range, photorefractive effects have been observed recently in Cr doped $\text{Bi}_4\text{Ge}_3\text{O}_{12}$ by Moya et al. [6], who first proposed the material as a candidate for UV photorefraction.

In this work we report on the observation of photorefraction in undoped $\text{Bi}_4\text{Ge}_3\text{O}_{12}$ and present a detailed characterization of photoinduced refractive index changes, the absorption constant, the photoconductivity and the dispersion of the electro-optic coefficients all in the UV spectral range.

The samples investigated in this study were cubes with faces perpendicular to the crystallographic $[\bar{1}10]$, $[110]$ and $[001]$ axes and dimensions of $4.88 \times 5.01 \times 5.26 \text{ mm}^3$. They were cut from a boule of pure $\text{Bi}_4\text{Ge}_3\text{O}_{12}$ and the $(\bar{1}10)$ faces were polished to optical quality. Preliminary piezoelectric tests allowed to determination of the $[\bar{1}10]$ and of the $[110]$ directions in accordance with the *Standards on Piezoelectric Crystals* [7]. The photorefractive investigations were performed by using either the laser line at $\lambda = 351.1 \text{ nm}$ or the line at $\lambda = 334.5 \text{ nm}$ from a Spectra Physics Ar⁺-ion laser operating in the mid UV region.

The absorption coefficient α of our undoped $\text{Bi}_4\text{Ge}_3\text{O}_{12}$ samples is $\alpha = 0.06 \text{ cm}^{-1}$ at $\lambda = 351 \text{ nm}$ and 0.13 cm^{-1} at $\lambda = 334 \text{ nm}$. $\text{Bi}_4\text{Ge}_3\text{O}_{12}$ possesses only three non vanishing and equal electro-optic coefficients, $r_{41} = r_{52} = r_{63}$. The value of r_{41} is 0.96 pm/V at $\lambda = 633 \text{ nm}$. Towards shorter wavelengths we have measured a slight decrease of r , for instance, at $\lambda = 351 \text{ nm}$ we get

92-18687



$r_{41} = 0.57$ pm/V. The room temperature dark conductivity of the material is $\sigma_d = 5 \cdot 10^{-14}$ ($\Omega \text{ cm}$) $^{-1}$ and, as it is the case for the photoconductivity (Figure 1, inset), depends linearly on the voltage applied along the [001] direction. As it is shown in Fig.1, the photoconductivity σ_{ph} is linearly increasing with intensity at all wavelengths and becomes particularly large in the UV. The value of $\phi\mu\tau$, the product of ϕ , the quantum efficiency for generating a free charge carrier per absorbed photon, μ , the average carrier mobility and τ , the lifetime of a free charge carrier before recombination in a deep trap, can be extracted from the photoconductivity measurements. The obtained values at different wavelengths are contained in table 1. The photoconductivity measurements reported above indicate that in $\text{Bi}_4\text{Ge}_3\text{O}_{12}$, similarly to the fastest photorefractive materials like KNbO_3 and $\text{Bi}_{12}\text{SiO}_{20}$, the drift length $L_E \equiv \mu\tau E_0$ of the free charges can reach values comparable to the fringe spacing. For example, a drift length larger than $0.2 \mu\text{m}$ is obtained at $\lambda = 334.5$ nm for an applied field of 10 kV/cm .

| Table 1: Photoconductivity data of $\text{Bi}_4\text{Ge}_3\text{O}_{12}$ | |
|---|--|
| λ [nm] | $\phi\mu\tau$ [$10^{-10} \text{ cm}^2/\text{V}$] |
| 514 | 0.09 |
| 458 | 0.2 |
| 351 | 5 |
| 334 | 20 |

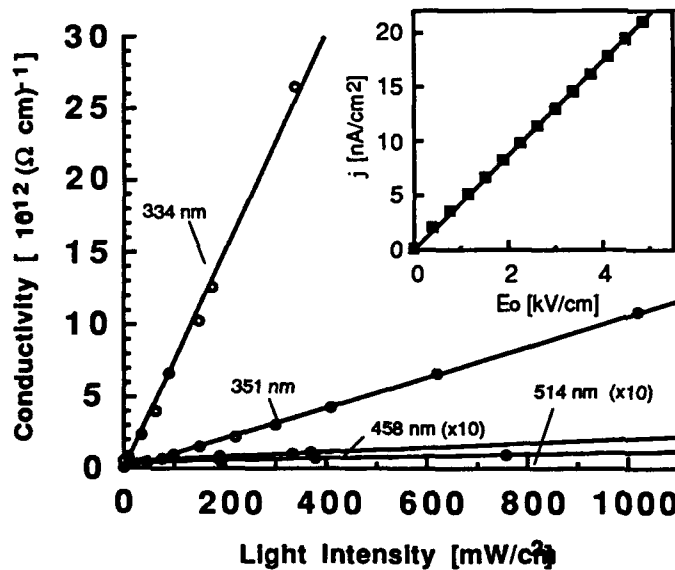


Fig. 1: Intensity dependence of the conductivity σ for illumination at different wavelengths. Inset: Current-field characteristics at $\lambda = 351 \text{ nm}$ for an illumination intensity $I_0 = 0.41 \text{ W/cm}^2$.

Holographic investigations in our samples were performed in geometrical configuration where the grating wavevector \mathbf{K} of the light fringes was parallel to the crystal [001] axis and the polarizations of the pump, the signal or the weak He-Ne probe beam were all parallel to the crystal [110] axis. The recording, erasure or the dark decay of the refractive index grating can be described by a simple exponential law. The time constant τ observed during the dark decay

is of the order of $\tau \approx 30\text{-}40$ s and agrees satisfactorily with the dielectric relaxation time $\tau_{\text{die}} \equiv \epsilon\epsilon_0/\sigma_d \approx 27$ s as obtained from the measured dark conductivity σ_d . According to the much higher conductivities observed under illumination, the recording and erasure time constants observed in our samples are much shorter. Fig.2 shows the intensity dependence of recording and erasure times. Since the straight lines have unity slope, τ depends inversely proportional on the light intensity. By extrapolating the straight lines on Fig.2 to an intensity of 1 W/cm^2 we get $\tau \approx 60$ ms at $\lambda=351$ nm and $\tau \approx 14$ ms for $\lambda=334$ nm.

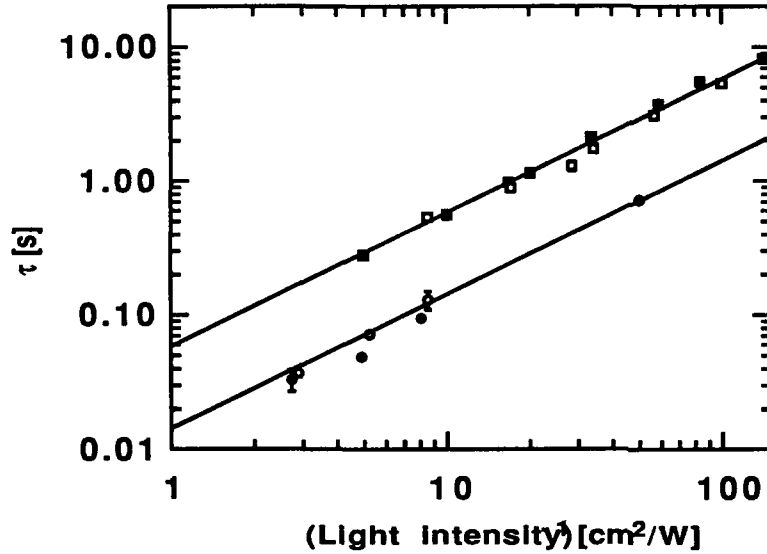


Fig.2: Recording (full symbols) and erasure times (open symbols) of the photorefractive gratings in $\text{Bi}_4\text{Ge}_3\text{O}_{12}$ measured by Bragg diffraction.

■ : $\lambda=351.1$ nm,
 $\Lambda=2.5$ μm ,
 ○ : $\lambda=334.5$ nm, $\Lambda=0.8$ μm .

Applied electric field
 $E_0=0$.

The saturation diffraction efficiencies observed in our samples reached a value of about 1 percent /cm corresponding to a refractive index change of about $2 \cdot 10^{-6}$. This is less than normally obtained in most of the ferroelectric photorefractive crystals like i.e. BaTiO_3 , KNbO_3 , LiNbO_3 . However, since large and low cost crystals of $\text{Bi}_4\text{Ge}_3\text{O}_{12}$ can be grown, the small refractive index changes are not a fundamental obstacle for the use of this crystal for holography.

We performed two-wave mixing experiments in order to determine the effective trap density N_{eff} and the sign of the majority charge carriers. In our experimental configuration the exponential gain coefficient Γ is given by

$$\Gamma = + \frac{2\pi n^3 r_{41}}{\lambda \cos \theta} \frac{E_q^2 E_D + E_D^2 E_q + E_q E_o^2}{(E_q + E_D)^2 + E_o^2} \quad (1)$$

where E_o is the externally applied electric field and E_q and E_D are the well known fields [8].

The measured gain coefficients for different grating spacings Λ are shown in Fig.3 together with a fit to the data with equation (1). For our $\text{Bi}_4\text{Ge}_3\text{O}_{12}$ crystals we obtain

$N_{\text{eff}} = 2.1 \cdot 10^{15} \text{ cm}^{-3}$ and we find that holes are the majority charge carriers responsible for the build-up of the space-charge field.

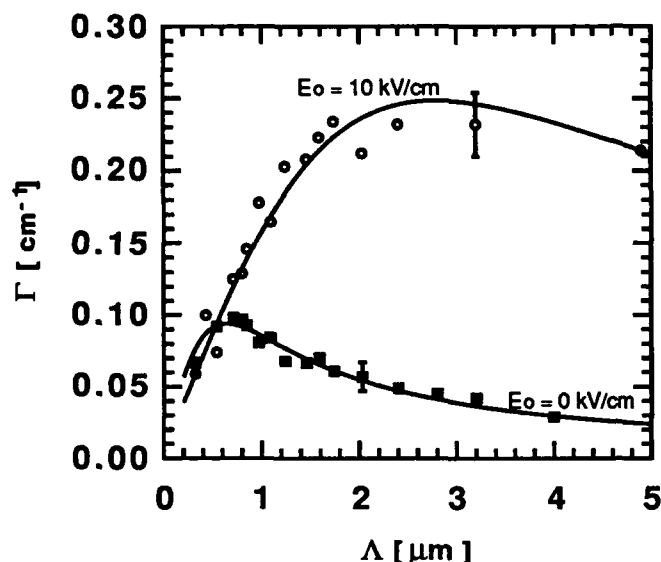


Fig.3: Exponential gain coefficient Γ measured in two-wave mixing experiments as a function of the grating spacing Λ for $\lambda = 351 \text{ nm}$.
 ■ : externally applied field $E_0 = 0$; ○ : $E_0 = 10 \text{ kV/cm}$. The curves are fits using eq.(1) with $N_{\text{eff}} = 2.1 \cdot 10^{15} \text{ cm}^{-3}$.

It should be noted that the observed exponential gains Γ exceed by up to a factor of 4 the absorption coefficient $\alpha = 0.06 \text{ cm}^{-1}$ at the recording wavelength of $\lambda = 351 \text{ nm}$. Effective amplification factors $\exp((\Gamma - \alpha)d)$ larger than unity are therefore possible and have been observed already in the 0.49 cm long crystals. $\text{Bi}_4\text{Ge}_3\text{O}_{12}$ therefore seems attractive for coherent image amplification and other nonlinear optical applications in the UV spectral range. In addition, $\text{Bi}_4\text{Ge}_3\text{O}_{12}$ crystals belong to the group of materials having fast recording times and could thus find applications also in dynamic holography using UV lasers.

References

- [1]. V. M. Fridkin, B. N. Popov, and K. A. Verkhovskaya, *Appl. Phys.* **16**, 313 (1978).
- [2]. T. Nakamura, V. Fridkin, R. Magomadov, M. Takashige, and K. Verkhovskaya, *J. Phys. Soc. Jpn.* **48**, 1588 (1980).
- [3]. R. Orlowski, E. Krätzig, and H. Kurz, *Opt. Commun.* **20**, 171 (1977).
- [4]. J. P. Huignard, J. P. Herriau, and F. Micheron, *Spring Meeting of the Electrochemical Society*, Washington, D.C., May 2-7, 1976, Extended Abstracts, No. 428, pp 1064-1070.
- [5]. E. Krätzig and R. Orlowski, *Appl. Phys.* **15**, 133 (1978).
- [6]. E. Moya, L. Contreras, and C. Zaldo, *J. Opt. Soc. Am. B* **5**, 1737 (1988).
- [7]. *Standards on Piezoelectric Crystals*, *Proc. IRE* **37**, 1378 (1949).
- [8]. N. V. Kukhtarev, V. B. Markov, S. G. Odulov, M. S. Soskin, V. L. Vinetskii, *Ferroelectrics* **22**, 949 and 961 (1979).

**Observation of the Photorefractive Effect in
Semi-insulating CdS**

AD-P006 700



P. Tayebati

Foster-Miller Inc.,

350 second Ave, Waltham, MA, 02154, Tel: 617-890 3200

J. Kumar, D. Barman

Department of Physics, University of Lowell,

Lowell, MA, 01854, Tel: 508- 934 3788

S. Scott

Eagle Picher Research Laboratory,

Miami, OK, 74354, Tel: 918-542 1801

Abstract

We report the first observation of the photorefractive effect in Cadmium sulfide. The maximum gain coefficient measured is 0.3 cm^{-1} at 633 nm. The response time is 1 ms at an intensity of 150 mW/cm^2 .

92-18688



Summary

Considerable attention has been devoted to the identification of fast and sensitive photorefractive materials in the last decade. Materials such as $\text{Bi}_{20}\text{SiO}_{20}$, GaAs, InP:Fe, GaP and CdTe:V are characterized by relatively large diffusion lengths and fast response times at incident intensities of few tens of mw/cm^2 . However, with the exception of GaP [1] none of these materials can be used in the wavelength range of 600-700 nm.

Cadmium Sulfide (CdS) has been extensively investigated as a photoconductor [2,3] but to the best of our knowledge investigations on its photorefractive properties have not yet been reported. This paper reports the observation of moderate gain (0.3 cm^{-1}) in low loss (0.14 cm^{-1}) single crystals of CdS at a wavelength λ of 633 nm. At the same wavelength CdS is at least an order of magnitude more sensitive than GaP [1] and in contrast to this material it offers net gain. The behavior of the gain coefficient as a function of grating period for ordinary and extraordinary polarizations has been investigated assuming a one charge carrier model. The photorefractive grating response time has also been determined.

Figure 1 shows the absorption spectrum of the crystal used in the experiment. As expected, the ordinary and extraordinary polarizations have different absorbances $A = \alpha L$ near the band edge, but at longer wavelengths they become almost identical. Here L is the thickness of the crystal and α the absorption coefficient. It is interesting to note that the maximum gain coefficient measured in the crystal at this wavelength is more than twice the value of the absorption coefficient (without the application of an external field). The dark resistivity of the crystal used in our experiments about $5 \times 10^8 \Omega \text{ cm}$. The crystal is strongly photoconducting at 633 nm and 670 nm. Incident intensity of a few tens of $\mu\text{W}/\text{cm}^2$ causes the resistivity to drop by nearly three orders of magnitude.

The experimental setup used for measuring the two-beam coupling gain is well known and we shall only discuss conditions relevant to our experiment. A 5 mW, 633 nm wavelength beam of HeNe laser was used to obtain a signal and a pump beam with input intensity ratio $\beta = I_s(0)/I_p(0)$ of about 0.38 and polarizations \hat{e}_1 and \hat{e}_2 respectively. These beams were crossed inside a 1.4 mm thick CdS crystal. The crystal was oriented such that the c-axis of the crystal is in the same direction as the grating wavevector $\vec{k} = |k| \hat{k}$. By chopping the pump beam and monitoring the signal beam on an oscilloscope the magnitude of the optical

gain coefficient and the response time of the grating decay / formation was determined. The ratio of the intensity modulation of the signal beam ΔI_s to the total signal beam intensity emerging from the crystal after travelling a distance L is given by,

$$\frac{\Delta I_s}{I_s} = \frac{\exp\left(\frac{\gamma_{eo} L}{\cos(\theta_{in})}\right) - 1}{1 + \beta \exp\left(\frac{\gamma_{eo} L}{\cos(\theta_{in})}\right)}$$

Where θ_{in} is the internal half angle between the two beams and γ_{eo} is the electrooptic gain coefficient given by,

$$\gamma_{eo} = -\frac{2\pi}{n\lambda} r_{eff} \frac{E_1}{im} \hat{e}_1^* \cdot \hat{e}_2$$

where the space charge field E_1 is given in terms of the effective trap density N_E and room temperature energy $k_B T$ and e is the magnitude of the electronic charge [4].

$$E_1 = -im \frac{k_B T}{e} \frac{k}{1 + \frac{k^2}{k_0^2}}, \quad k_0^2 = \frac{e^2}{\epsilon k_B T} N_E$$

In figure 2, we plot the two-beam coupling gain determined for ordinary and extraordinary input beam polarizations. For these polarization orientations and the geometry described

above the values of $r_{eff} = \hat{e}_1^* \cdot [\underline{\epsilon} \cdot (\underline{R} \cdot \hat{k}) \cdot \underline{\epsilon}] \cdot \hat{e}_2$ are given by,

$$r_{eff} = n_o^4 r_{13} \quad (\text{ordinary polarization}),$$

$$r_{eff} = n_o^4 r_{13} \left(\sin^2(\theta_{in}) - \frac{n_e^4 r_{33}}{n_o^4 r_{13}} \cos^2(\theta_{in}) \right) \quad (\text{extraordinary polarization}).$$

Where ϵ is the permittivity tensor of the crystal and R is the linear electrooptic tensor. The values of ordinary and extraordinary indices of refraction in CdS at 633 nm are $n_o=2.46$ and, $n_e=2.48$ [5]. By simultaneous fitting of these formulae into the electrooptic coupling data, we determine various parameters of the material. Independent parameters were chosen to be r_{13} , k_o^2 and the ratio r_{33}/r_{13} . The best fit is determined when effective trap density $N_E=0.8 \times 10^{15} \text{ cm}^{-3}$, $r_{13} = 0.7 \text{ pm/V}$ and $r_{33}/r_{13} = 3.7$ (or $r_{33} = 2.59 \text{ pm/V}$) (see curve (b)). In order to determine the accuracy of these parameters, we fitted the data by fixing the ratio r_{33}/r_{13} at two values of 2.75 and 5.0 respectively and allowing the other two parameters to vary. We found that the effective trap density did not change more than 4% but r_{13} was determined to be 0.93 pm/V ($r_{33} = 2.55 \text{ pm/V}$) in the first instance and 0.53 pm/V ($r_{33} = 2.6 \text{ pm/V}$) in the second case. These two fits are also plotted and labeled as (a) and (c) respectively. Using this method we determine values of the r coefficients to be $r_{13} = 0.7 \pm 0.2 \text{ pm/V}$ and $r_{33} = 2.59 \pm 0.08 \text{ pm/V}$. These values are slightly different from the values measured by direct methods $r_{33} = 2.4 \text{ pm/V}$ and $r_{13} = 1.1 \text{ pm/V}$ [5].

In summary we report the first observation of photorefraction in CdS single crystals. The maximum gain coefficient at 633 nm is 0.3 cm^{-1} which is more than twice the value of the absorption coefficient in the sample. The effective trap density obtained for the crystal by fitting the grating period dependence of the gain is $8.0 \times 10^{14} \text{ cm}^{-3}$. The photorefractive response time of the crystal is about 1 ms at an intensity of 150 mW/cm^2 (available from low power Helium Neon or red diode lasers). This makes CdS the most sensitive photorefractive material in this wavelength regime.

References

1. Photorefractive effect in GaP, K. Kuroda, Y. Okazaki, T. Shimura, H. Okamura, M. Chihara, M. Itoh, and I. Ogura, Optics Letters, Nov. 1, 1990, Vol. 15, No. 21, p. 1197.
2. "Photoconductivity of Solids", R. H. Bube, John Wiley and sons, Inc.
3. "Concept in Photoconductivity and Allied Problems", Albert Rose, R. E Krieger Publishing Co. Huntington, New York, 1978.
4. N. V. Kukhtarev, V. B. Markov, S. G. Odulov, M. S. Soskin, and V. L. Vinetskii, "Holographic storage in electrooptic crystal. I. steady state," Ferroelectric 22, 949 (1979).
5. Handbook of Laser Science and Technology, Volume IV, Optical Materials, Part 2: Properties, Editor, Marvin J. Weber. CRC press, Inc.

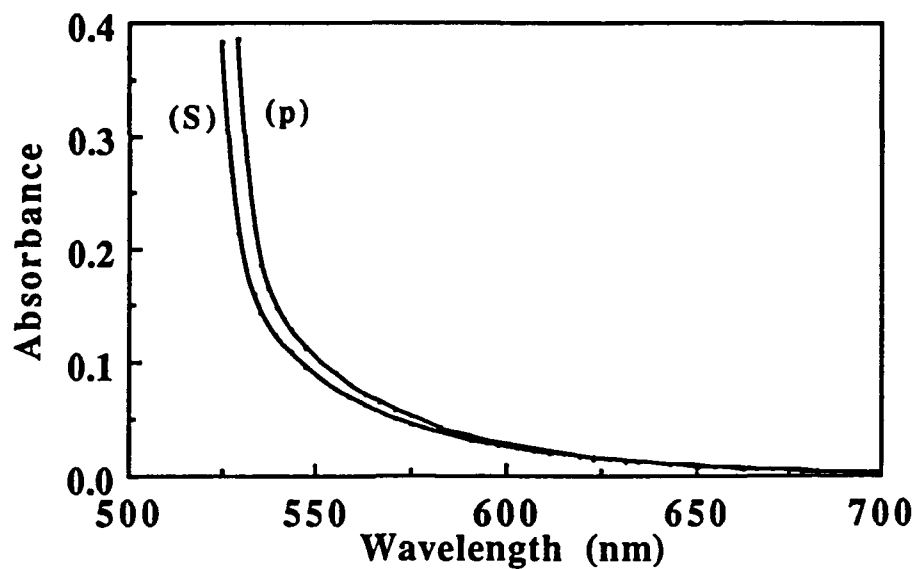


Figure.1 Absorbance of extraordinary (p) and ordinary polarizations (s) in CdS.

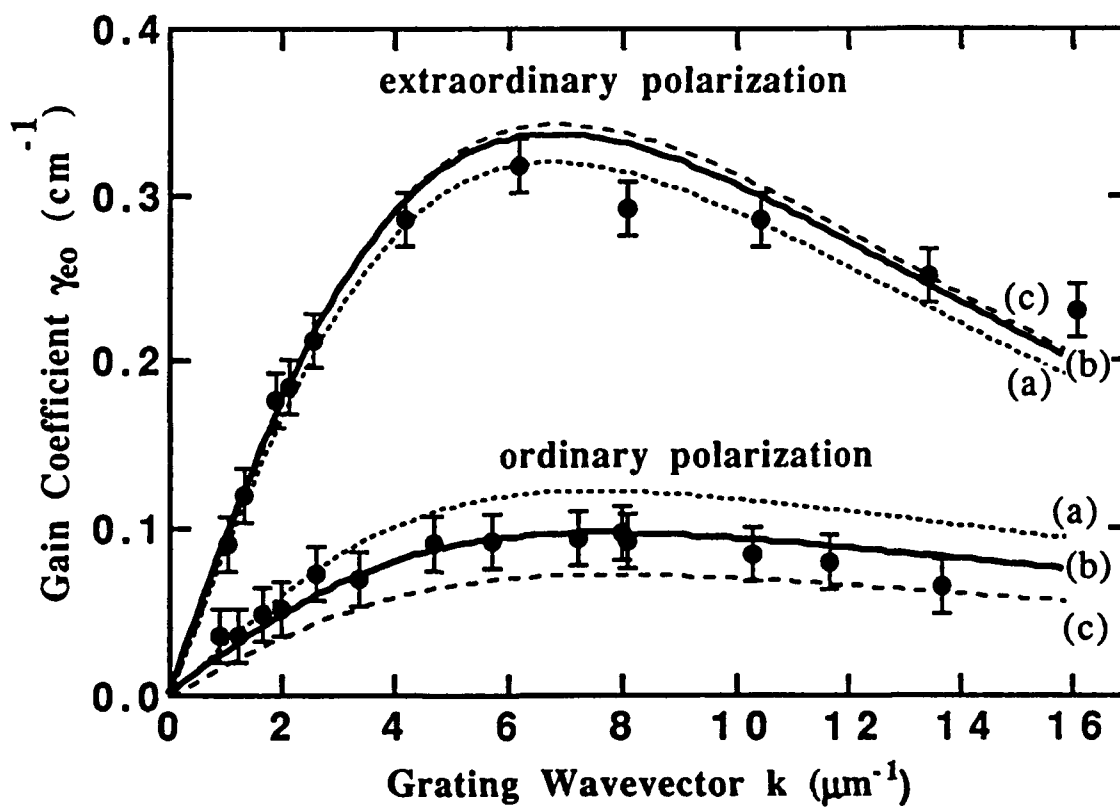


Figure. 2 Two-beam coupling electrooptic gain coefficient γ_{eo} .



High-Order Diffraction in Photorefractive Quantum Well Structures

Q. N. Wang and D.D. Nolte

Dept. of Physics, Purdue University, W. Lafayette, IN 47907

M.R. Melloch

School of Electrical Engineering, Purdue University, W. Lafayette, IN 47907

Recently, the high speed of semiconductor materials was combined with the large optical nonlinearity of the Franz-Keldysh effect near the quantum confined exciton absorption within semi-insulating multiple quantum well structures (SIMQW)[1]. The diffraction efficiency of four wave mixing obtained in the SIMQW with an optical interaction length of $1.05 \mu\text{m}$ is comparable with the diffraction efficiency for a semiconductor bulk sample with an optical interaction length of several mm operating under similar conditions. Thus, SIMQW become a ideal candidate to study the diffraction process in the Raman-Nath regime[2]. Here, we report two effects of the second order diffraction in a SIMQW sample under applied field: 1) the direct observation of a strong second order diffraction signal; 2) the intensity of the degenerate four wave mixing signal depends on the direction of applied field when the fringe spacing becomes large.

The diffraction process is in the Raman-Nath regime[2], and multiple diffraction become possible, if $Q = (2\pi \lambda_p l)/(n \Lambda^2) < 1$, where l and n are the thickness and the refractive index of the medium respectively, λ_p and Λ are the wavelength of the probing beam and the fringe spacing of the grating respectively. In the small-signal regime, the total diffraction efficiency into the m^{th} order by a complex index of refraction grating, $\Delta n'(x) = (\Delta n + i\lambda_p \Delta \alpha / 4\pi) \cos(Kx)$, is given by[2]

$$\eta_m = \frac{1}{m!^2} \left[\left(\frac{\pi \Delta n l}{\lambda_p} \right)^2 + \left(\frac{\Delta \alpha l}{4} \right)^2 \right]^m \quad (1)$$

where Δn , $\Delta \alpha$ are the modulation of the index of refraction and absorption coefficient respectively, and $K = 2\pi/\Lambda$ is the spatial frequency of the grating.

The optical interaction region of our SIMQW sample is composed of 60 periods of GaAs wells (75 \AA thickness) and $\text{Al}_{0.3}\text{Ga}_{0.7}\text{As}$ barriers (100 \AA thickness), with a total optical interaction length of $1.05 \mu\text{m}$ and a total sample thickness of $2 \mu\text{m}$. It was made semi-insulating by proton implantation. This process introduces deep level defects which provide traps to store charge and pin the Fermi level midgap to make the entire

92-18689



sample semi-insulating. The electro-optical properties of the sample were characterized in the Franz-Keldysh geometry with the applied field parallel to the quantum wells. The infrared light source in our experiment is a Ti:sapphire laser which is tunable from 800 nm to 850 nm, covering the exciton absorption range of the SIMQW.

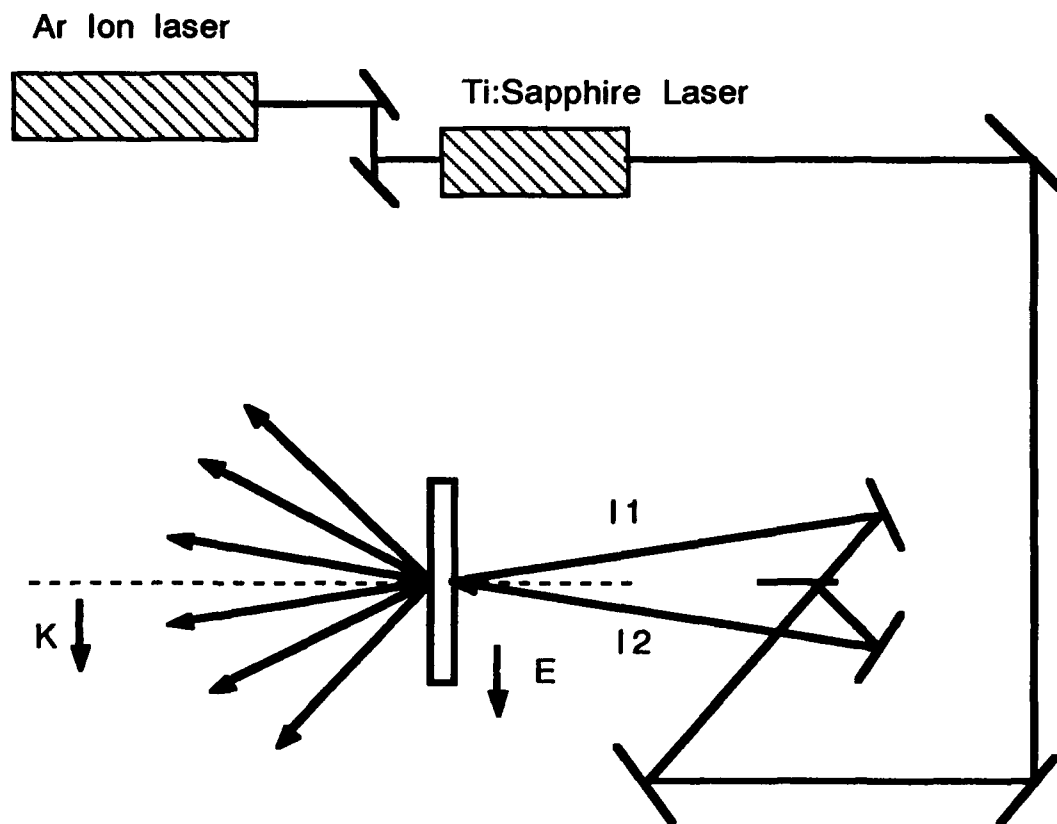


Fig. 1. Experimental set up of the multi-wave mixing process. Applied AC field is 5kV/cm.

Our multi-wave mixing experimental setup is shown in Fig. 1. The SIMQW is illuminated symmetrically with respect to the normal vector of the quantum well plane by two coherent laser beams, each beam polarized perpendicular to the plane of incidence and parallel to the quantum well layers. The intensities of the two beams are approximately the same (0.36 W/cm^2). The intersection angle between the laser beams is $2\theta = 8.2^\circ$, corresponding a fringe spacing Λ of the interference pattern of $\Lambda = \lambda / (2 \sin \theta) = 5.9 \text{ } \mu\text{m}$ for a wavelength of 840 nm. A biased AC field of 5 kV/cm is applied across the sample in the direction indicated on Fig. 1 at a frequency of 290 Hz. To justify the diffraction regime in our measurement, take the typical values of our measurements: $l = 2 \text{ } \mu\text{m}$, $\lambda = 840$

nm, $n=3.6$ for GaAs wells and $\Lambda=5.9 \mu\text{m}$. Thus $Q=0.08$, putting us in the strong Raman-Nath regime.

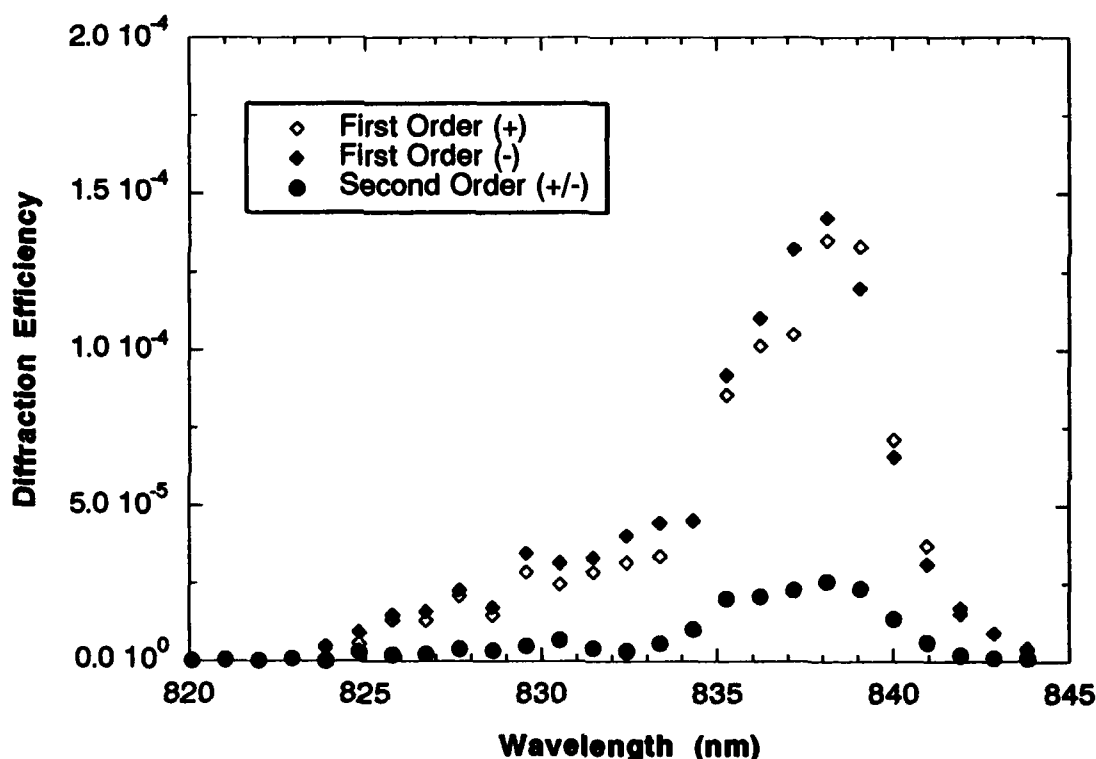


Fig. 2. The first and second order diffraction efficiencies.

The diffraction signals of the first and second order were observed for both beams. The first order and second order diffraction efficiency for beam 1($m=1,2$) is shown in Fig. 2. The first order diffraction efficiency depends on the direction of the applied field, while the measurement of differential transmission and intensity of second order diffraction shows no indication of field-direction dependence. There are two physical origins of the strong second order diffraction signal: 1) the first order diffraction of the probing beam through a dielectric grating with a spatial frequency of $2K$; 2) the multiple diffraction process through a dielectric grating with a spatial frequency of K . The effect of the later can be estimated from equation (1), which yields a gain of 10^{-8} for $m = 2$, and is therefore negligible. Thus, there exists a dielectric grating with twice the spatial frequency of the light intensity pattern.

The ratio between the second and the first order diffraction efficiency is approximately $1/6$, which implies

$$\frac{\eta_2}{\eta_1} = \frac{|4\pi\Delta n_2 + i\Delta\alpha_2\lambda_p|^2}{|4\pi\Delta n_1 + i\Delta\alpha_1\lambda_p|^2} \approx \frac{1}{6} \quad (2)$$

where the subscripts 1,2 indicate the Fourier components of dielectric gratings with spatial frequencies of K and $2K$ respectively. The Franz-Kelydish effect is a quadratic effect. A Fourier analysis of the E -field in the sample and E^2 is easy to make by keeping $2K$ harmonic components:

$$E = E_0 - (E_1 \cos(Kx + \varphi_1) + E_2 \cos(2Kx + \varphi_2)) \quad (3)$$

$$E^2 = E_0^2 + 0.5(E_1^2 + E_2^2) - 2E_0E_1 \cos(Kx + \varphi_1) + E_1E_2 \cos(Kx + \varphi_2 - \varphi_1) - 2E_0E_2 \cos(2Kx + \varphi_2) - 0.5E_1^2 \cos(2Kx + 2\varphi_1) \quad (4)$$

In order to explain the experimental results, E_2 must be considered. A rough estimate of E_1/E_2 is possible by neglecting the effects of the fourth and sixth term in eq.(4). As a result, we have

$$\frac{\eta_2}{\eta_1} = \left(\frac{E_2}{E_1}\right)^2 \approx \frac{1}{6} \quad (5)$$

This means a 40% strength of E_2 compared with E_1 . The effect of the direction of field on the diffraction efficiency of the first order diffraction can be understood as the interference effect between two beams: the first order diffraction signal of I_1 ($m=1$) and the second order diffraction signal from I_2 ($m=-2$). This effect is similar to the two-wave mixing process in SIMQW[3]. When the direction of the E field changes, the relative phase between these two beams also change, so that the detected signal changes.

In conclusion, we have observed a second-order diffraction signal with a diffraction efficiency comparable with the first order diffraction in degenerate four-wave mixing. This large high-order diffraction is generated from the large second harmonic component of the dielectric grating in the SIMQW. When the fringe spacing became large, the condition for thin grating diffraction can be satisfied by the dielectric grating with high spatial frequencies.

References

1. D. D. Nolte, D.H. Olson, G.E.Doran, W.H.Knox and A.M. Glass, J.Opt. Soc. Am B. 7, 2217(1990)
2. A.Yariv and P.Yeh, Optical Waves in Crystals (Wiley, New York, 1984).
3. Q. Wang, D. D. Nolte, M. R. Melloch(to be published)



The Photorefractive Properties of Quantum-Confined Excitons

D. D. Nolte

Dept. of Physics, Purdue University, W. Lafayette IN 47907

M. R. Melloch

School of Electrical Engineering, Purdue University, W. Lafayette IN 47907

Multiple-quantum-well structures in semiconductors have strong spatial inhomogeneity. Bandgaps in these multilayer samples vary by several tenths of eV over monolayer distances. These dramatic spatial changes in bandstructure have significant consequences for the photorefractive effect, creating new effects that have no analog in bulk photorefractive materials. The ability to design new materials and devices, and control desired photorefractive properties, has few limitations. Several processes give photorefractive quantum well structures unique advantages. Two charge separation processes, in particular, contribute to the novel effects: 1) bandgap energies can be selectively tuned to isolate optical absorption to some layers, but not others; 2) carriers in quantum wells tunnel into barrier regions with larger bandgaps, generating metastable defect occupancies with associated electric fields. These processes couple with one of the strongest advantages of quantum well structures: quantum-confined excitons. Quantum-confined excitons in semiconductors exhibit large quadratic electro-optic effects. The quadratic electro-optic effect combines with the charge separation processes to yield ultra-high sensitivity photorefractive effects with large diffraction efficiencies[1] and beam coupling gains. In this paper, we present the theory of photorefractive effects in quantum well structures, concentrating on the role of spatial inhomogeneity in the nonlinear optical behavior.

Quantum-confined excitons have two distinct quadratic electro-optic effects: the quantum-confined Franz-Keldysh effect; and the quantum-confined Stark effect. The Franz-Keldysh effect occurs when the electric field is in the plane of the quantum wells. The electro-optic mechanism is the lifetime broadening of the exciton transition. The Stark effect occurs when the electric field is perpendicular to the quantum wells. The electro-optic mechanism is the shift of the transition energy. The Stark effect is potentially a much stronger electro-optic effect, leading to the largest photorefractive effects. Photorefractive gratings are probed with wavelengths near the excitonic absorption wavelength. The pump beam wavelength is not restricted, however, but can be any excitatory wavelength, even visible wavelengths.

The key to the quantum well photorefractive properties are the deep level defects. The quantum well samples are made semi-insulating by proton implantation. The implant damage creates deep level defects that pin the Fermi level midgap. The electron states on the deep defects are highly localized. The typical radius of the defect wavefunctions is approximately $\sim 5\text{\AA}$. This wavefunction radius is much smaller than the quantum well or barrier widths ($\sim 100\text{\AA}$). Therefore, strong spatial variation of the defect occupancy is possible, depending on whether the defect is positioned in a well region, or in the center of the barrier region. The spatial dependence of the defect occupancy also depends on the wavelengths of the mixing photons. An example is shown in Fig. 1. The probe photons excite electron-hole pairs only in the quantum wells. The photocarriers from the probe can recombine directly, or can tunnel into the barriers before trapping. The rapid decay of the electron and hole wavefunctions into the barriers rapidly reduces the capture rate into defects in the barriers. Defects in the



center of the barriers are essentially inaccessible to tunneling carriers. Space-charge trapped in the barriers will therefore not be erased rapidly by the probe photoconductivity. The transport and trapping features shown in Fig. 1 are generic for any photorefractive quantum well structure. However, the different means by which electric fields may be applied, or the different exciting wavelengths that can be used, provide a large degree of flexibility in what types of photorefractive behavior will be observed.

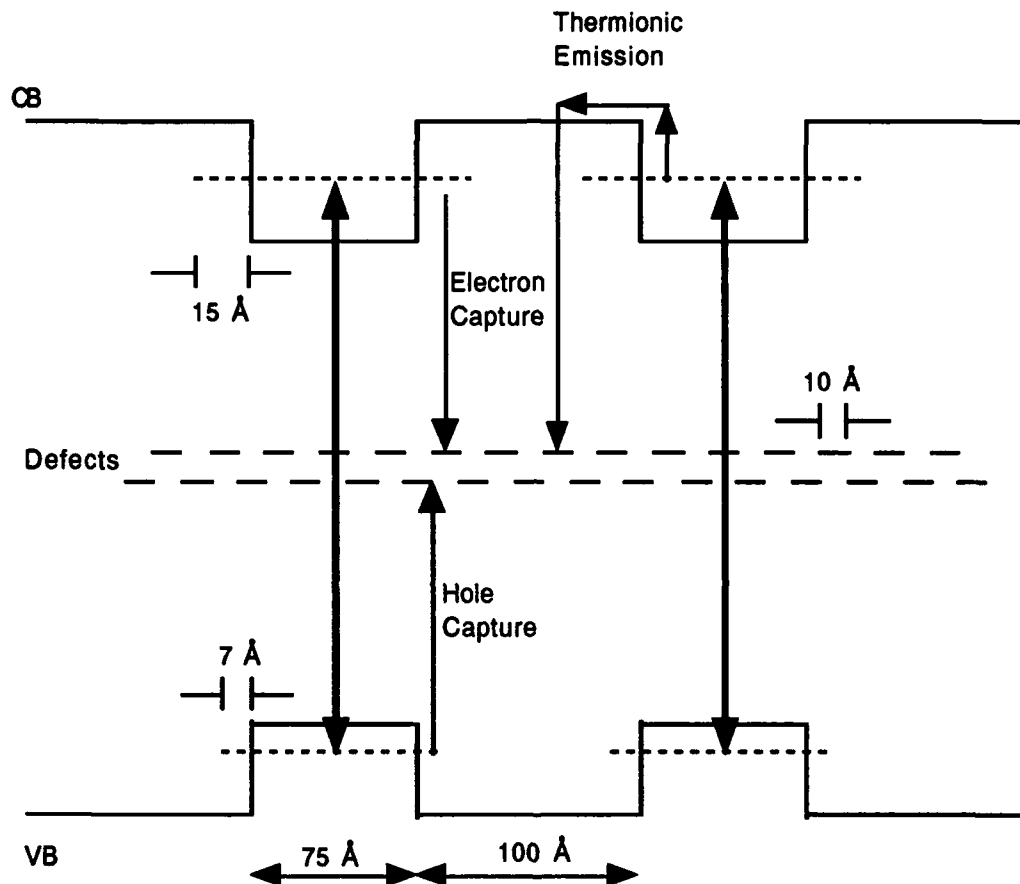


Fig. 1 Vertical transport in multiple quantum wells. Electrons and holes generated in the quantum wells transport into the barriers by tunneling or by thermionic emission, before they trap at deep defects.

When the electric field is applied in the plane of the quantum wells (Franz-Keldysh effect), the transport equations for transport parallel to the field are very similar to the usual equations used for bulk photorefractive crystals. The novel photorefractive effects therefore come from transport perpendicular to the applied field, as shown in Fig. 1. In this paper, we illustrate the novel transport effects by discussing robust infrared gratings in the Franz-Keldysh geometry. When pump laser beams from a HeNe laser write an interference pattern, the pump light is above the bandgaps of both the wells and barriers. Therefore, in the bright interference fringes, carriers are generated in both the wells and the barriers. The carriers generated in the barrier regions trap at defects in the barriers in the usual manner as with bulk crystals,

generating space-charge gratings with their associated electric fields. The probe laser, tuned to the exciton absorption, experiences large photorefractive gratings due to the quadratic electro-optic effect of the quantum-confined excitons. The probe is diffracted in nondegenerate four-wave mixing by the grating. However, the probe photoconductivity is isolated to the quantum wells and cannot erase the space-charge stored in defects in barriers. Probe laser intensities can therefore be considerably larger than the pump beams, without erasing the gratings. The dielectric relaxation of the space charge fields generated by the pump laser, caused by the photoconductivity of the probe, can be expressed through the position-dependent saturation intensity $\beta(x, \xi)$

$$\beta(x, \xi) \sim \frac{I_{pr}(x)}{I_{pu}(x)} \frac{\lambda_{pr}}{\lambda_{pu}} \frac{\alpha_{pr}}{\alpha_{pu}} \left(4 e^{-2k_b a} \cosh^2(k_b \xi) + e^{-\Delta E/k_b T_e} \right)$$

where the first term in the parenthesis is from tunneling into the barrier, and the second term is from thermionic emission over the barrier, a is the half-width of the barrier, k_b is the inverse decay length of the carrier wavefunctions into the barriers, T_e is the electron temperature, and I_{pr} and I_{pu} are the probe and pump intensities respectively. The diffracted probe signal as a function of probe intensity is obtained by

$$I_{diff} \propto I_{pr} \left[\frac{1}{2 a L} \int_0^L \int_a^a \frac{d\xi}{(1 + \beta(x, \xi))} dx \right]^2$$

The second-power comes from the quadratic electro-optic effect and the quadratic dependence of diffraction efficiency on index and absorption gratings. The theoretical diffracted signal as a function of probe intensity is shown in Fig. 2 for two barrier thicknesses, and two temperatures. The dielectric relaxation due to thermionic emission is comparable with tunneling into the barriers. For 150 Å barriers, the probe beam intensity can exceed the pump intensity by almost a factor of 100 at the peak in the excitonic absorption when the diffracted signal is maximized. Extremely weak pump beam intensities can therefore be used to control strong probe signals.

This example of "robust" gratings is one illustration of the photorefractive consequences of the spatial inhomogeneity and vertical transport in quantum well samples. Many other effects are anticipated. In particular, the vertical transport, through tunneling, is a mechanism for charge separation perpendicular to the grating vector. Space charge fields will therefore be built up between the wells and the barriers. One result of this may be a new mechanism for generating a phase shift between the intensity grating and the index grating. This phase shift is necessary for photorefractive gain. Preliminary work[2] on two-wave mixing using the Franz-Keldysh effect in semi-insulating AlGaAs/GaAs quantum wells has lead to large phase shifts and gains $\Gamma > 400 \text{ cm}^{-1}$ under DC applied fields. The source of the phase shift may not be due to space-charge limitations, but may represent a differential tunneling of electrons and holes into the barriers. If so, then this new transport mechanism will be

of significant importance for future photorefractive applications that require beam amplification.

These novel photorefractive effects combine with the large electro-optic properties of quantum-confined excitons to create a promising new class of materials. Ultimately, when using the quantum-confined Stark effect, very large diffraction efficiencies will be expected. These diffraction efficiencies challenge the efficiencies of some of the ferroelectric oxides and should form the basis of novel photorefractive materials and devices.

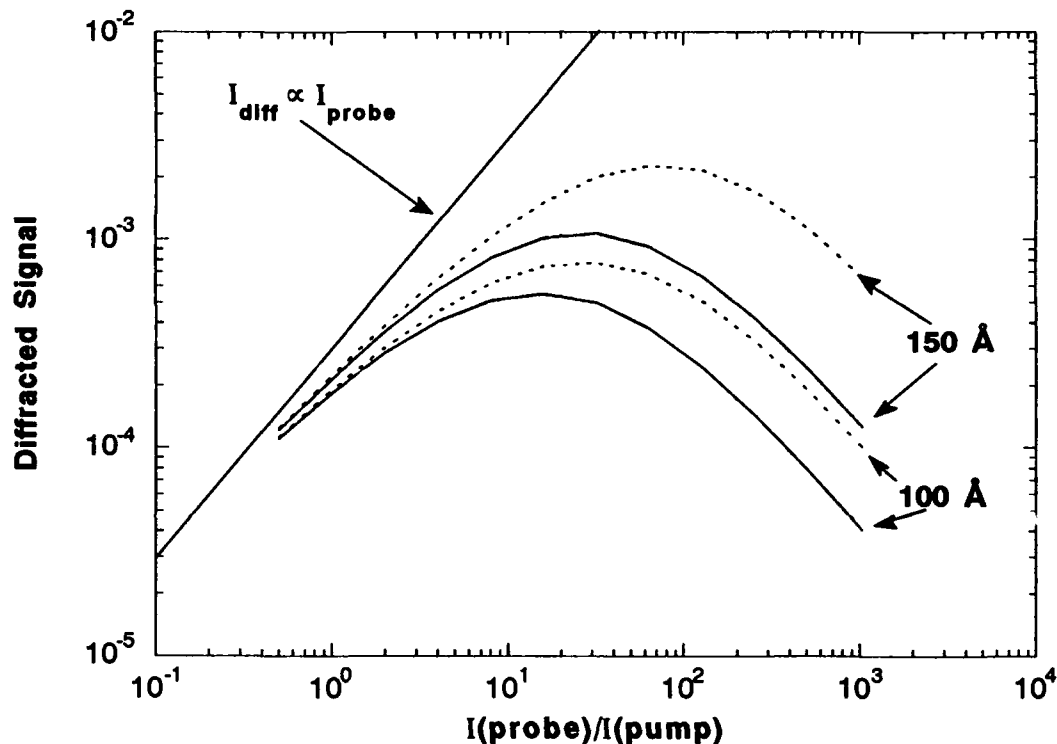


Fig. 2 Theoretical diffracted signal as a function of the probe beam intensity. The material parameters were for $\text{Al}_{0.3}\text{Ga}_{0.7}\text{As}/\text{GaAs}$ multiple quantum wells with the barrier widths given. The dotted curves are for $T = 200$ K, and the solid curves are for $T = 300$ K.

Refs:

- [1] D. D. Nolte, D. H. Olson, G. E. Doran, W. H. Knox and A. M. Glass, The Resonant Photodiffractive Effect in Semi-insulating Multiple Quantum Wells, *J. Opt. Soc. of Am. B7* , 2217 (1990)
- [2] Q. Wang, D. D. Nolte and M. R. Melloch, to appear in *Appl. Phys. Lett.*

Monday, July 29, 1991

Wave Interactions and Instabilities

MB 10:30am–12:30pm
Academic Center Auditorium

A. Zozulya, Presider
Lebedev Physics Institute, USSR

AD-P006 703

Red-green diffraction instability in the photorefractive mixed crystal $\text{Bi}_{12}\text{Ti}_{0.76}\text{V}_{0.24}\text{O}_{20}$

N. V. Kukhtarev, A. Gnatovskii, Z. Yanchuk,
T. Semenets, L. Pryadko and Y. Kargin
Institute of Physics
Ukrainian Academy of Sciences
252650 Kiev, Prospekt Nauki 46, U.S.S.R.

K. H. Ringhofer
Fachbereich Physik der Universität
PF 4469, D-4500 Osnabrück, F.R.G.

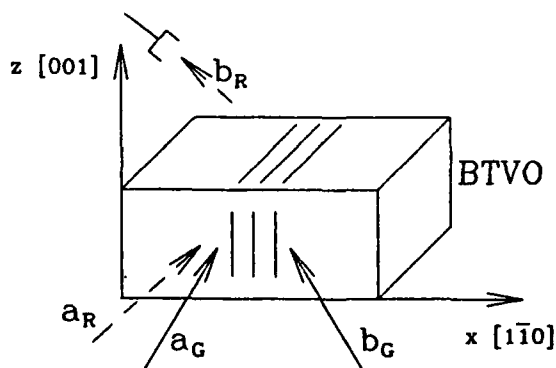


Figure 1: Geometry for observation of red-green diffraction instability.

We have investigated the new doubly color sensitive photorefractive crystal $\text{Bi}_{12}\text{Ti}_{0.76}\text{V}_{0.24}\text{O}_{20}$ by writing a hologram in green ($\lambda = 0.51 \mu\text{m}$, cw-argon laser) and reading it out in red ($\lambda = 0.63 \mu\text{m}$, cw-HeNe laser). It was found that the diffraction efficiency for the red beam is chaotically oscillating in time with a period of about 0.1 s between zero and some maximum. The diffraction efficiency for the red beam decayed smoothly after the green beam was switched off.

92-18691

These oscillations exist also for values of the diffraction efficiency as low as 0.1%, and therefore can not be explained by overmodulation of the refractive-index grating.

We propose an explanation of this instability based on the interplay of the selfenhancement effect [1,2,3] with the kinetics of the hologram formation by green and red interference patterns. For an orientation of the grating vector $\vec{q} \parallel [110]$ (see Fig. 1) the equations for the slowly-varying amplitudes of the red waves are [2,4]:

$$\begin{aligned}\frac{da_{x,z}}{dy} &= -ir \Delta E b_{z,x} \pm G a_{z,x} \\ \frac{db_{x,z}}{dy} &= -ir \Delta E^* a_{z,x} \pm G b_{z,x}\end{aligned}\quad (1)$$

where $r = \pi \kappa^3 r_{14} / (\lambda \cos \theta)$, r_{14} is the electrooptic coefficient, and G is the specific optical activity. Similar equations can be written for the green waves, taking into account dispersion of r and G . The amplitude of the electric-field holographic gratings E can be found from the equation

$$\tau \frac{d \Delta E}{dt} = i E_D \frac{\Delta I_R + \Delta I_G}{I_0} - \Delta E \quad (2)$$

where $\Delta I_{R,G}$ stand for the interference pattern in red and green, E_D is the diffusion field, and I_0 is the total intensity. To describe the experiment we start from the steady-state holographic grating in green which according to eqn. (2) for the grating amplitude gives

$$\Delta E = i E_D \frac{\Delta I_G}{I_0}. \quad (3)$$

When the red reading wave is switched on, the transmitted and the diffracted red waves form an interference pattern

$$\Delta I_k = r E_D \Delta I_G \left[\frac{G}{\gamma^2} (I_x - I_z) \sin^2 \gamma y - (A_x A_z^* + \text{c.c.}) \frac{\sin 2\gamma y}{2\gamma y} \right] \quad (4)$$

where $\gamma^2 = G^2 + |r \Delta E|^2$, $I_{x,z} = |A_{x,z}|^2$, and $A_{x,z}$ are the input values of $a_{x,z}$. This red interference pattern may write its own holographic grat-

ing. One can see from eqn. (4) that the space shift between the red ΔI_R and the green ΔI_G patterns depends on the polarization of the reading wave because of optical activity and changes through the crystal depth y . When the "out of phase" condition $\Delta I_R \approx -\Delta I_G$ is met, the green pattern is washed out by the red one which leads to the disappearance of the diffracted red wave and the red interference pattern. Then the green light pattern writes a new hologram and this oscillating process can proceed further. This physical picture of a new type of red-green diffraction instabilities will be further investigated by numerical calculations in progress.

References

- [1] D. L. Staebler and J. J. Amodei, J. Appl. Phys. 43, 1042, 1972
- [2] N. V. Kukhtarev, Ukr. Fiz. J. 23, 1947, 1978 (in Russian)
- [3] J. Otten and A. Ozols and M. Reinfeldt and K. H. Ringhofer, Opt. Comm. 72, 175, 1989
- [4] N. V. Kukhtarev, Topics in Applied Physics vol. 61, Springer-Verlag Berlin, Heidelberg 1988.

ON THE BUILDUP AND DECAY OF PHOTOREFRACTIVE WAVE MIXING PROCESSES

Moshe Horowitz and Baruch Fischer
 Department of Electrical Engineering
 Technion - Israel Institute of Technology
 Haifa 32000, ISRAEL

AD-P006 704



SUMMARY

92-18692



Photorefractive media have been used for many novel applications in image processing. One interesting use is the novelty filter which is an all optical processor based on the response of two wave mixing (2-WM) or four wave mixing (4-WM) [1,2]. It is obvious that the temporal dynamics of the wave mixing process is essential to understand such processes. However, since the overall photorefractive dynamics, including the wave mixing part, is described by complicated non-linear partial differential equations, it is hard to obtain a general solution. The study has been largely limited to steady state behavior and the response of the photorefractive material only, without taking into account the dynamics of the wave coupling effects.

In the first part of our paper we study photorefractive 2WM. We first derive an analytic solution for writing and erasure of a grating in the photorefractive material using the undepleted pump approximation. This solution is based on Cronin-Golomb's theory [1], except that we apply boundary conditions in the time domain, rather than the frequency domain as he does. We thus obtain a simple analytic solution for the cases of turning on or off the input signal. Unlike the solutions presented in earlier work, we emphasize the dependence of the dynamic solution on the coupling of the waves in the photorefractive material. We compare our analytic solution with experimental measurements of 2WM in $BaTiO_3$. It allows us to estimate the gain coefficient and time constant of the material simply and precisely.

In the figures below we describe part of the results. Figure 1 shows the temporal change of the normalized output intensity from the crystal after turning off the signal at $t = 0$, as a function of the amplification coefficient, γl , where l is the length of the interaction zone. It shows the

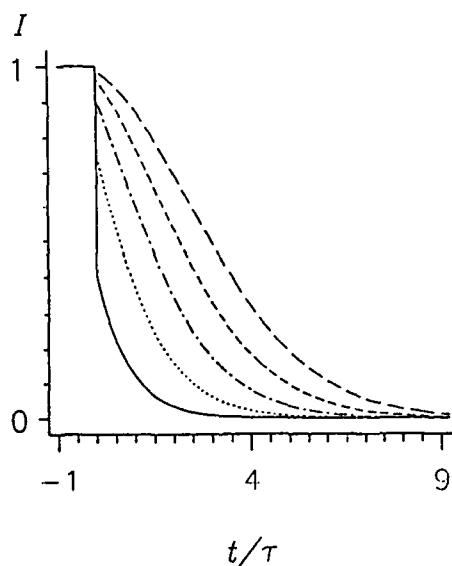


Fig. 1 Theoretical curves for 2-WM, describing the normalized signal beam intensity versus time after turning off the signal at $t = 0$ for various positive coupling constants: $\gamma l = 1, 2, 3, 4, 5$. The lowest curve (fastest decay) corresponds to the lowest $\gamma l (= 1)$; and increasing the γl decreases the decay rate.

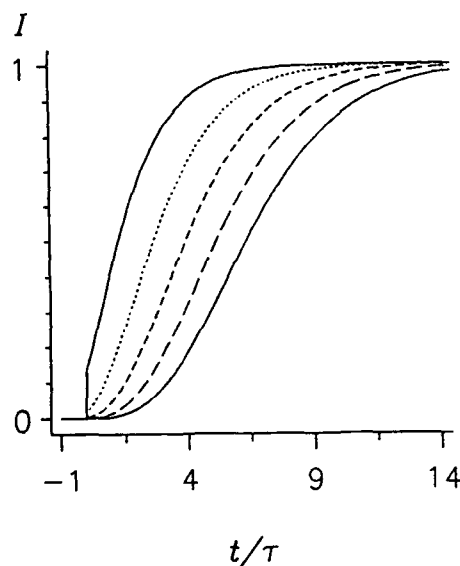


Fig. 2 Theoretical curves for 2-WM, describing the normalized signal beam intensity versus time after turning on the signal at $t = 0$ for various real positive coupling constants: $\gamma l = 1, 2, 3, 4, 5$. The uppermost curve (fastest buildup rate) corresponds to the lowest $\gamma l (= 1)$; and increasing the γl decreases the buildup rate.

response of a photorefractive amplifier ($\text{Re } \gamma l > 0$). It can be seen that as the amplification (γl) increases, the normalized response becomes slower and hence, the amplification bandwidth decreases. This behavior is explained by the fact that at high amplifications, even before the input signal is turned off, the energy in the signal in the interaction zone in the crystal is drawn mostly from the pump beam, which is scattered by the grating inside the material. Because the grating strength is not altered at the moment the input signal is turned off, the signal inside the crystal remains strong initially, and therefore, the output signal drops off slowly. The buildup rate for an opposite coupling constant (when the crystal serves to attenuate the signal ($\text{Re } \gamma l < 0$), is also strongly dependent on γl (not shown in the figures) and response times much faster than the time constant of the material (τ) may be obtained. For the buildup behavior, Fig. 2 shows the output signal after the input signal is turned on at $t = 0$, for a number of different positive values of γl . There is a qualitative similarity to the results shown in Figure 1, particularly in the fact that the larger the value of γl , the slower will be the change in the output after the input is turned on.

These results show that we can control the response time of a photorefractive device, such as a novelty filter, that is based on 2-WM [1,2], by controlling the amplification coefficient through appropriate choice of the mixing angle.

In the experiment we measured the temporal response of the output signal after turning the input signal on or off. We used a poled BaTiO_3 crystal illuminated by an argon ion laser operating at 515 nm. Figs. 3 and 4 compare the experimental and theoretical results for three different values of γl . The fitting of the theory to the experimental data was based on common values of τ and γl for both the buildup and the erasure processes together for each geometry.

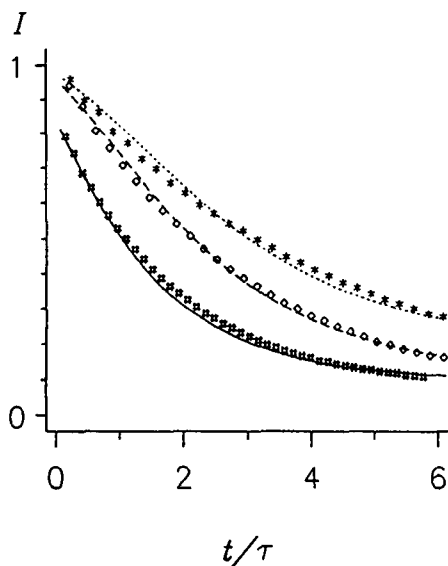


Fig. 3 Experimental and theoretical dependence of the output signal in 2-WM after turning it off. The fitted coupling constants are (the same as in the former figure for the buildup) : $\gamma l = 1.72$ (lowest curve), 2.78, 3.3 (uppermost curve).

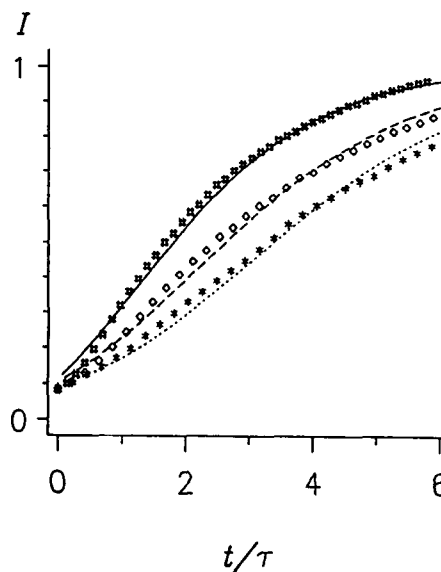


Fig. 4 Experimental and theoretical dependence of the output signal in 2-WM after turning it on. The fitted coupling constants are : $\gamma l = 1.72$ (uppermost curve), 2.78, 3.3 (lowest curve).

Next, we present a numerical solution to the 2WM problem for cases in which the signal intensity is not negligible in comparison with the pump. We take into account the nonlinearity of the wave coupling, while assuming the material's response to be linear. This numerical solution permits for the first time the calculation of the dependence of the writing and erasure times on the ratio of intensities of the signal and pump beams. It also predicts an unusual phenomenon of photorefractive grating buildup after the signal beam has been turned off.

Figures 5 and 6 show the temporal response of the the signal normalized outputs after the input signal is turned off or turned on for the pump depleted regime. τ is the time constant after turning on or off the signal. The time needed to erase the grating will depend on the modulation depth of the grating recorded in the material, which in turn is a function of the beams ratio. In steady state the strength of the grating is proportional to the modulation depth of the light intensity in the crystal. For a very weak or strong signal this modulation depth decreases, so that the erasure time is shorter.

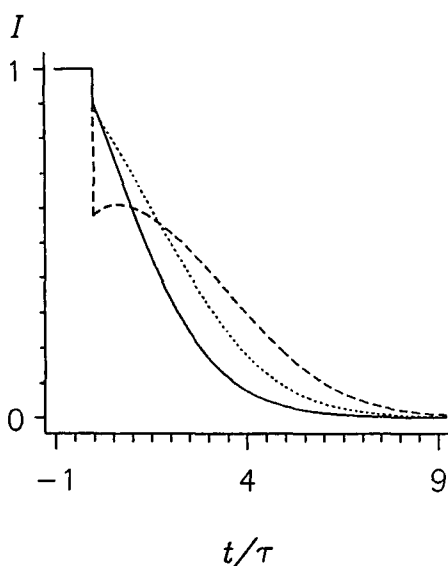


Fig. 5 Theoretical curves for 2-WM, describing the normalized signal (a) and pump (b) intensities versus time for $\gamma l = 3$ after turning off the signal at $t = 0$, for various ratios of pump to signal intensities: $I_1/I_4 = 10^6$ (solid curves), 100 (dotted curves), 4 (dashed curves).

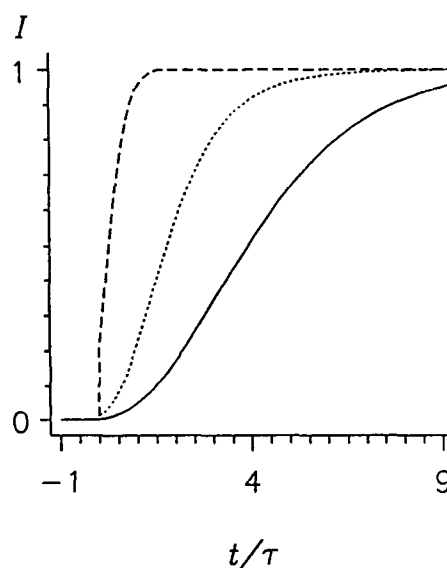


Fig. 6 Theoretical curves for 2-WM, describing the normalized signal (a) and pump (b) intensities versus time for $\gamma l = 3$ after turning on the signal at $t = 0$, for various ratios of pump to signal intensities: $I_1/I_4 = 10^6$ (solid curves), 100 (dotted curves), 4 (dashed curves).

Figs. 6 shows that the stronger the input signal, the faster is the buildup of the output signal. The decrease in buildup time stems in part from the fact that a stronger input signal reduces the grating amplitude required to attain maximum scattering of the pump beam into the output signal, since the possible energy transfer from the pump to the signal in this case comes to be limited not by the strength of the grating, but by depletion of the pump. Moreover, the buildup rate of the grating increases with increasing modulation depth between the pump and signal beams in the crystal. Thus, during most of the buildup process, the buildup rate of the grating is high, while the grating amplitude required for energy transfer from the pump to the signal is dropping, and therefore, the signal buildup time decreases.

These results explain the long buildup time measured in Ref. [4] for fanning relative to that of the output signal. The difference stems from the fact that the strength of the scattered light that gives rise to the fanning is much less than the strength of the input signal to the crystal.

In the second part of the article we show an analogy between four-wave mixing (4WM) and 2WM in a unidirectional ring cavity, in the undepleted pump approximation. It is obtained by comparing the time dependent equations of the two configurations. Fig. 7 describes the circuit for the case of the externally pumped four-wave mixing. A similar scheme can be obtained for the Double phase conjugate mirror [3]. The comparison demonstrates that there is an effective feedback mechanism in 4WM even when there is no positive external feedback circuit. This analogy is used to study the 4WM schemes and to obtain its stability properties.

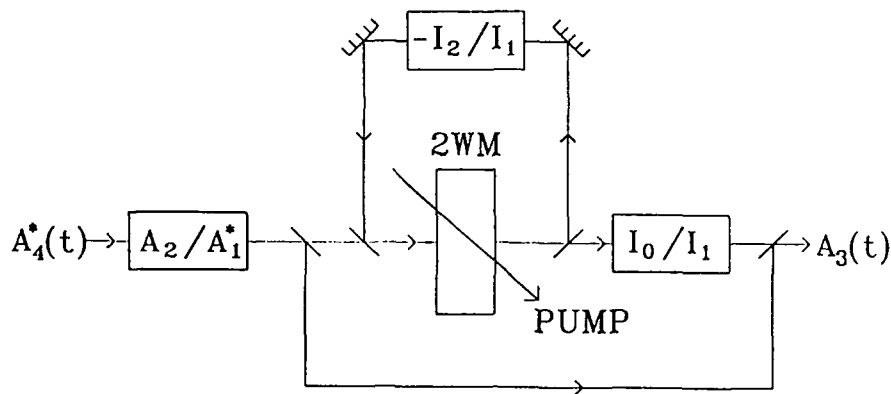


Fig. 7 The circuit for the standard case of the undepleted 4WM (the phase conjugate mirror), which provides the analogy with two-wave mixing in a unidirectional ring resonator. (A factor of 2 for each 3 dB beam-splitter is not included in the scheme).

REFERENCES

1. M. Cronin-Golomb, A.M. Biernacki, C. Lin, H. Kong: Opt. Lett. *12*, 1029 (1987); M. Cronin-Golomb, in Technical Digest of Topical Meeting in Photorefractive Materials, Effect and Devices (Optical Society of America, Washington, D.C., 1987), p. 142.
2. J. Feinberg, D. Z. Anderson IEEE J. Quant. Electr. *QE-25*, 635, (1989).
3. B. Fischer, S. Sternklar and S. Weiss, : IEEE, J. Quant. Electr. , *25*, 550 (1989).
4. H. Rajbenbach, A. Delboulbe, J.P. Huignard: Opt. Lett. *14*, 1275 (1989).

Beam Fanning in Coupled-Wave Theory of 2-Beam Coupling

M. D. Ewbank, F. R. Vachss and R. A. Vazquez

Rockwell International Science Center

1049 Camino Dos Rios

Thousand Oaks, CA 91360

(805) 373-4443

AD-P006 705



SUMMARY

Simple coupled-wave theory^{1,2} accounts for depletion of the pump beam due to energy transfer (i.e., amplification) to the probe beam. Ignoring absorption, the probe gain g can be expressed as¹

$$g = \frac{I_1(z)}{I_1(0)} = \frac{1+r_{pp}}{1+r_{pp}e^{-\Gamma z}} \quad (1)$$

where $I_1(0)$ is the incident probe intensity, Γ is the two-beam-coupling coefficient and r_{pp} is the incident pump-to-probe beam ratio given by

$$r_{pp} = \frac{I_2(0)}{I_1(0)} \quad (2)$$

with $I_2(0)$ being the incident pump intensity. Equation (1) remains valid even when the pump-to-probe ratio r_{pp} is not sufficiently large (only the approximation for the probe gain $g \approx e^{\Gamma L}$ becomes invalid when r_{pp} is not much greater than $e^{\Gamma L}$). Similarly, the pump depletion d can be expressed as¹

$$d = \frac{I_2(z)}{I_2(0)} = \frac{1+r_{pp}}{r_{pp}+e^{\Gamma z}} \quad (3)$$

These expressions for the probe gain and pump depletion have proven inadequate in describing the two-beam-coupling process, particularly when the coupling coefficient Γ is very large (recently, Γ 's exceeding 60cm^{-1} have been reported^{3,4})

As is well-known in the photorefractive field, when the two-beam-coupling coefficient Γ is large, beam fanning⁵ is very pronounced and can significantly deplete the pump⁶ and probe beams. Attempting to quantify the effect of beam fanning on two-beam coupling is complicated by the fact that beam fanning originates from scattering centers in the photorefractive crystal which

92-18693



results in a collection of many beams with different wavevectors. In order to incorporate beam fanning into the coupled-wave analysis in a tractable manner, we assume the crudest possible arrangement for the beam fanning: a single wavevector. Scattering from both the pump and probe beams throughout the interaction region (from $z=0$ to $z=L$) contributes to this fanning beam, as well as two-beam coupling between the fanning beam with the pump and probe beams.

Neglecting linear absorption and letting $I_1(z)$, $I_2(z)$ and $I_3(z)$ represent the intensities of the probe, pump and fanning beams, respectively, the coupled-wave equations can be written as

$$\frac{dI_1}{dz} = \frac{+\Gamma I_1 I_2}{I_0} - fI_1 - \frac{\Gamma I_1 I_3}{I_0} \quad (4)$$

$$\frac{dI_2}{dz} = \frac{-\Gamma I_1 I_2}{I_0} - fI_2 - \frac{\Gamma I_2 I_3}{I_0} \quad (5)$$

$$\frac{dI_3}{dz} = +fI_1 + fI_2 + \frac{\Gamma I_1 I_3}{I_0} + \frac{\Gamma I_2 I_3}{I_0} \quad (6)$$

where Γ is the two-beam-coupling coefficient and f is a phenomenological fanning scattering coefficient (related to the scattering cross-section and the density of scattering centers) describing the scattered light from the pump and probe beams into the fanning beam. Here, for simplicity, we have assumed the same coupling strength Γ for the pump-probe interaction as for the fanning-pump and fanning-probe interactions. Also, the fanning scattering coefficient f for the pump is assumed to be identical to that for the probe. The total intensity I_0 is given by

$$I_0 = I_1 + I_2 + I_3 = I_1(0) + I_2(0) \quad (7)$$

where $I_1(0)$ and $I_2(0)$ are, again, the incident probe and pump intensities. As indicated, I_0 is constant in the absence of absorption.

The coupled-wave equations modelling two-beam coupling with fanning (Eqs. (4) - (6)) have exact analytic solutions, which can be written as

$$g_f = \frac{I_1(z)}{I_1(0)} = \frac{(f+\Gamma)^2(r_{pp}+1)}{(fe^{(f+\Gamma)z}+\Gamma)(f+\Gamma+fr_{pp}+\Gamma r_{pp}e^{-(f+\Gamma)z})} \quad (8)$$

$$d_f = \frac{I_2(z)}{I_2(0)} = \frac{(f+\Gamma)(r_{pp}+1)}{(f+\Gamma+fr_{pp})e^{(f+\Gamma)z} + \Gamma r_{pp}} \quad (9)$$

$$\frac{I_3(z)}{I_1(0)} = \frac{f(e^{(f+\Gamma)z}-1)(r_{pp}+1)}{fe^{(f+\Gamma)z} + \Gamma} \quad (10)$$

where, as before, r_{pp} the incident pump-probe intensity ratio given in Eq. (2). Note that the fanning beam intensity $I_3(z)$ is arbitrarily normalized by the incident probe beam intensity since there is no incident fanning beam. Clearly, in the limit of no scattering from the pump and probe beams into the fanning beam (i.e., $f \rightarrow 0$), the probe gain g_f given by Eq. (8) reduces to well-known form for the probe gain g given by Eq. (1). Furthermore, in the limit of $f \rightarrow 0$, the pump depletion d_f given by Eq. (9) also reduces to the appropriate form as given by Eq. (3).

With this model for incorporating beam fanning in the two-beam-coupling process, the dependence of the probe gain g_f can be calculated as a function of pump-probe ratio r_{pp} for various fanning scattering coefficients f from Eq. (8). The results are shown in Fig. 1, using a coupling coefficient of $\Gamma=50\text{cm}^{-1}$ and an interaction length of $L=0.50\text{cm}$. As illustrated in Fig. 1, the case of no fanning ($f=0$) requires a pump-probe ratio r_{pp} of $\sim 10^{12}$ to reach the saturated gain value of $\sim 10^{11}$. Increasing the fanning scattering coefficient f has two obvious consequences: a) the saturated gain value decreases substantially and b) the threshold for gain saturation occurs at a lower pump-probe beam ratio. Both of these features are apparent in recent two-beam-coupling data obtained in SBN:60:Ce, as will be discussed. Figure 2 gives the dependence of probe gain g_f on interaction length L and illustrates that for a given set of coupling and scattering coefficients, the probe gain g_f is maximized for only the optimal interaction length. Again, we will present evidence of this behavior from experiments performed on a wedged BaTiO₃, where two-beam-coupling gains were measured directly as a function of interaction length.

Despite the simplistic model employed for the beam fanning (i.e., a single wavevector, identical coupling and scattering coefficients, etc.), the strong correlation between theory and experiment indicates that the fundamental effect of beam fanning on the two-beam-coupling process is at least qualitatively described in this fashion.

REFERENCES

1. P. Yeh, Opt. Comm. 45, 323 (1983).
2. D. Rak, I. Ledoux and J.P. Huignard, Opt. Comm. 49, 302 (1984).
3. M.D. Ewbank, R.A. Vazquez, R.S. Cudney, G.D. Bacher and J. Feinberg, OSA Tech. Dig. (Boston, Nov. 1990) paper FS1, p251.
4. R.A. Vazquez, M.D. Ewbank and R.R. Neurgaonkar, OSA Tech. Dig. (Boston, Nov. 1990) paper FS6, p252.
5. J. Feinberg, JOSA 72, 46 (1982).
6. M. Cronin-Golomb and A. Yariv, J. Appl. Phys. 57, 4906 (1985).

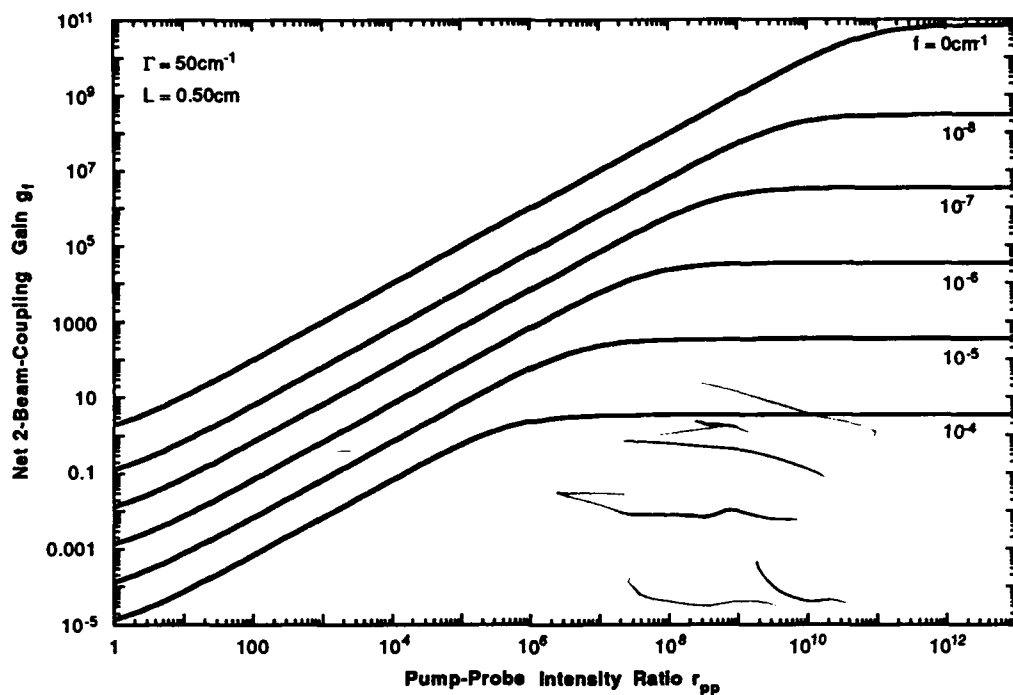


Figure 1 -- Dependence of probe gain g_f on pump-probe ratio r_{pp} parameterized by the fanning scattering coefficient f , as calculated from Eq. (8).

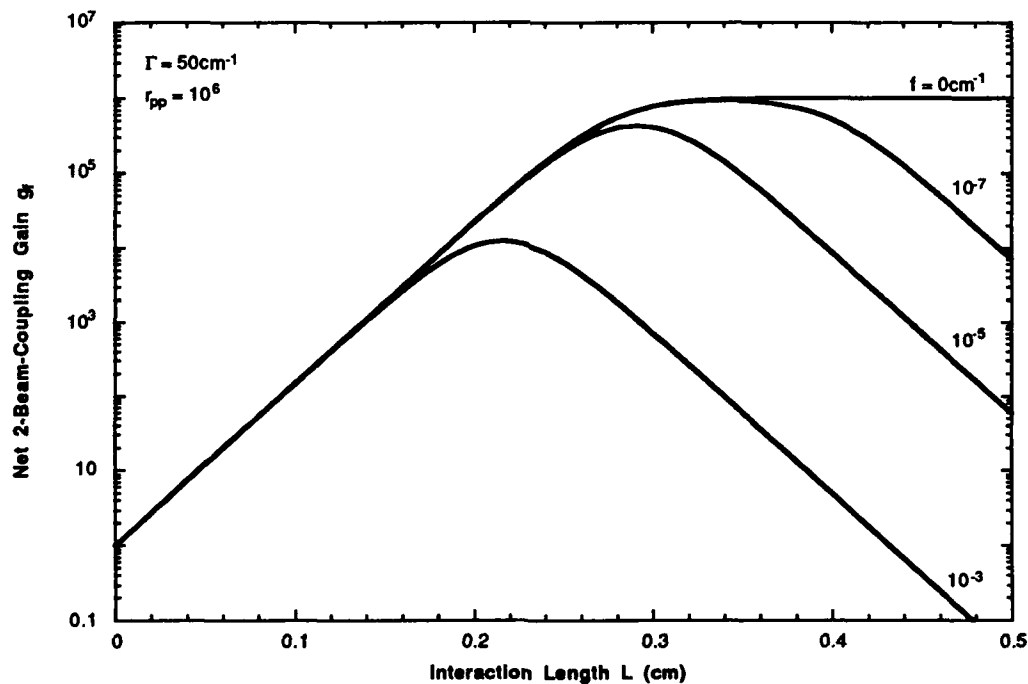


Figure 2 -- Dependence of probe gain g_f on interaction length L parameterized by the fanning scattering coefficient f , as calculated from Eq. (8).

Instabilities in photorefractive bidirectional ring oscillators

Q. Byron He, Scott Campbell*, Claire Gu*, and Pochi Yeh†

Department of Electrical and Computer Engineering
University of California, Santa Barbara
Santa Barbara, CA 93106
Tel (805) 893-8278

* Rockwell International Science Center
Thousand Oaks, CA 91360

AD-P006 706



SUMMARY

Photorefractive bidirectional ring oscillation was demonstrated experimentally some time ago [1]. Recently, a theory for the bidirectional oscillation in photorefractive ring resonators was proposed [2]. Interesting properties, such as intensity thresholding effect, may find applications in the fields of optical computing and optical neural networks [3]. Although, the steady state oscillations are understood, the stability of those oscillations has not been addressed. In this paper we present the linear stability analysis of photorefractive bidirectional ring oscillation under mean-field approximation and experimental confirmation of unstable oscillations.

Referring to Fig. 1, two counter-propagating beams A_1 and A_4 are incident on a photorefractive crystal which is placed in a ring cavity. The optical waves are coupled by the following equations and boundary conditions:

$$\left(\frac{\partial}{\partial z} + \frac{1}{c} \frac{\partial}{\partial t}\right) A_1 = -\frac{1}{2} \gamma G A_2, \quad (1)$$

$$\left(\frac{\partial}{\partial z} + \frac{1}{c} \frac{\partial}{\partial t}\right) A_2^* = \frac{1}{2} \gamma G A_1^*, \quad (2)$$

$$\left(\frac{\partial}{\partial z} - \frac{1}{c} \frac{\partial}{\partial t}\right) A_3 = \frac{1}{2} \gamma G A_4, \quad (3)$$

$$\left(\frac{\partial}{\partial z} - \frac{1}{c} \frac{\partial}{\partial t}\right) A_4^* = -\frac{1}{2} \gamma G A_3^*, \quad (4)$$

$$\tau \frac{\partial G}{\partial t} + G = \frac{A_1 A_2^* + A_3 A_4^*}{|A_1|^2 + |A_2|^2 + |A_3|^2 + |A_4|^2}, \quad (5)$$

92-18694



and

$$A_2(0, t) = \sqrt{R} A_2(L, t - \Delta t), \quad (6)$$

$$A_3(L, t) = \sqrt{R} A_3(0, t - \Delta t), \quad (7)$$

where γ is the photorefractive coupling constant, $c' = \frac{c \cos \theta}{n}$ is the phase velocity of optical wave in the crystal, τ is the photorefractive time constant, $R = 1 - T$ is the product of mirror reflectivities, $\Delta t = \frac{\mathcal{L} - L}{c}$ is the transit time of the cavity, and \mathcal{L} is the total length of the cavity. We assume that the cavity is perfectly tuned and consider the diffusion dominated photorefractive effect only.

Under the mean-field approximation [4] where $\gamma L \rightarrow 0$, $T \rightarrow 0$, while the ratios $\xi = \frac{\gamma L}{T}$ and $u = \frac{c' \tau T}{2(L + c' \Delta t)}$ remain constants, the above equations can be written as

$$\frac{dx_1}{dt'} = -\frac{c' \tau}{L + c' \Delta t} \left\{ \frac{T}{2} x_1 - \frac{\gamma^* L}{2} y^* \right\}, \quad (8)$$

$$\frac{dx_2}{dt'} = -\frac{c' \tau}{L + c' \Delta t} \left\{ \frac{T}{2} x_2 + \frac{\gamma L}{2} y \right\}, \quad (9)$$

$$\frac{dy}{dt'} = -y + \frac{q x_1^* + x_2}{1 + q + q|x_1|^2 + |x_2|^2}, \quad (10)$$

where

$$x_1 = \frac{\bar{A}_2(L)}{\bar{A}_1}, \quad x_2 = \frac{\bar{A}_3(0)}{\bar{A}_4}, \quad y = \bar{G}, \quad q = \frac{I_1}{I_4} \quad t' = \frac{t}{\tau}.$$

We can find the steady-state solutions and examine their stabilities through linear stability analysis. In steady state, besides the trivial solution for all the effective coupling ξ and beam ratio q , we find that when $\xi > 1$ and $q > q_{th} = \frac{\xi+1}{\xi-1}$, there exists a non-trivial solution $|x_1^{ss}|^2 = |x_2^{ss}|^2 = \frac{\xi(q-1)-q-1}{q+1}$, which corresponds to the bidirectional oscillation in the resonator. The results of linear stability analysis of above solutions are illustrated in Fig 2. When $\xi < 3$, the ring resonator exhibits stable steady-state which depends on the beam ratio q , i.e. when $q > q_{th}$ (and $\xi > 1$), stable bidirectional oscillation builds up in the ring, when $q < q_{th}$, cavity ceases to oscillate. However when $\xi > 3$, there always exists a region near q_{th} in which both trivial and non-trivial solutions are unstable. Beyond this region, stable oscillation can again be maintained. Within the unstable region, cavity outputs flip flop between zero and the oscillation state and are sensitive to any minor disturbances. Since the transitions from stable state to instability occur via saddle bifurcations, no self-pulsation or other instability are expected.

Experimental study was conducted in the setup as shown in Fig. 3. A single-domain $BaTiO_3$ was placed in the ring cavity and pumped by two counter-propagating beams, one of which was frequency shifted 140 MHz by an A-O modulator to prevent the formation of reflection grating. Without beam 4, the ring resonator oscillated unidirectionally at the stable single-transverse mode. Adding beam 4, bidirectional oscillations were monitored by two power meters, one at each side of the output beam splitter. The oscillation outputs with respect to various beam ratios are shown in Fig. 4. Near the lower threshold beam ratio, oscillations became unstable. The cavity remained oscillating for a short while, ceased to oscillate quickly and kept alternating between these two states. Oscillations beyond this region were again stable showing the distinct intensity thresholding effect.

In summary, we have found theoretically and experimentally the instability regions of a photorefractive bidirectional ring oscillator. This research was supported in part by Office of Naval Research under contract N00014-91-J-1028.

† Pochi Yeh is also a principal technical advisor at Rockwell International Science Center

REFERENCES

1. J.O. White, M. Cronin-Golomb, B. Fischer, and A. Yariv, Appl. Phys. Lett. 40, 450 (1982).
2. C. Gu, and P. Yeh, to be published in J. Opt. Soc. Am. B, (1991).
3. C. Gu, and P. Yeh, Topical Meeting on Optical Computing, OSA Tech. Digest, 6, 68 (1991).
4. See, for example, L.A. Lugiato, Progress in Optics, V21, 71 (1984).

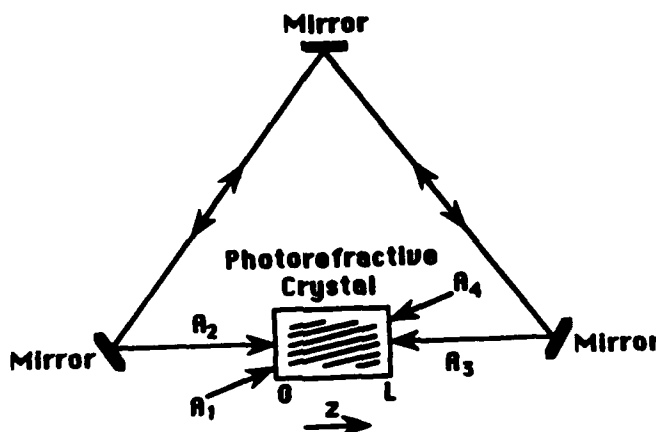


Fig.1 Bidirectional photorefractive ring resonator.

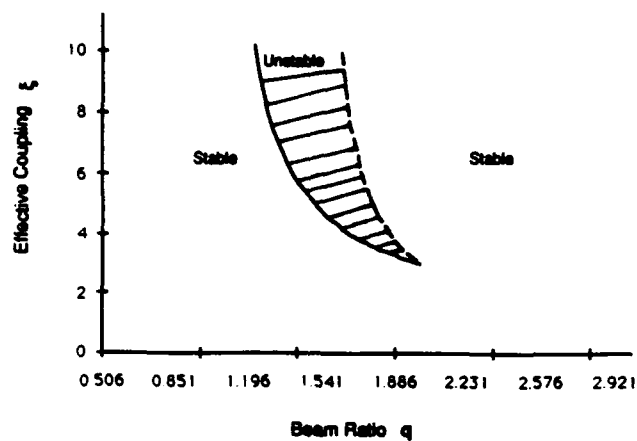


Fig.2 Instability region in the parameter space (ξ , q).

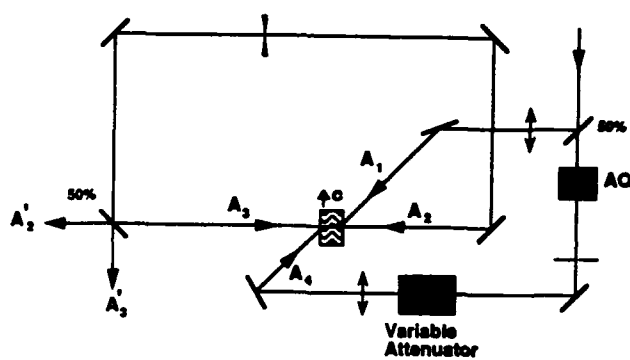


Fig.3 Experimental setup.

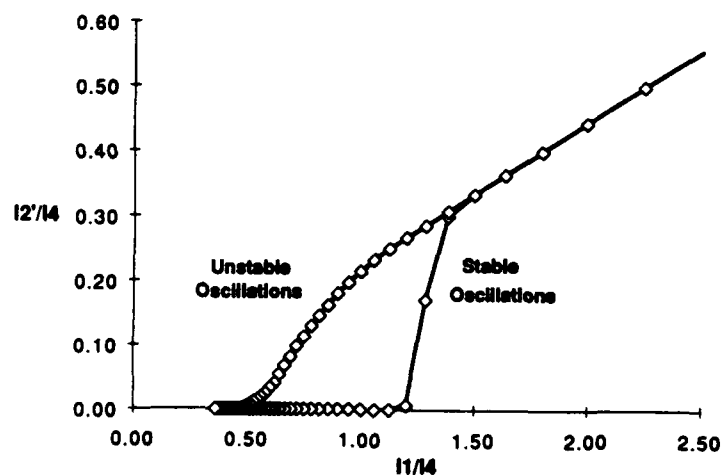


Fig.4 Experimental results.



SPATIAL STRUCTURE OF SCATTERED RADIATION IN A SELF-PUMPED
PHOTOREFRACTIVE PASSIVE RING MIRROR

S. A. Korol'kov, Yu. S. Kuz'minov*, A. V. Mamaev, V. V. Shkunov
and A. A. Zozulya**

Institute for Problems in Mechanics, pr. Vernadskogo 101, Moscow
117526, USSR

* General Physics Institute, Vavilov st. 38, Moscow 117942, USSR

** P. N. Lebedev Physics Institute, Leninsky pr. 53, Moscow
117924, USSR

We present detailed experimental investigation of scattered radiation spatial structure in the geometry of a transmission grating photorefractive passive ring mirror (Fig.1) and compare our results with the predictions of Ref.[1]. According to the theory, behaviour of a ring mirror in the limit of large Fresnel numbers is determined by two scale variation coefficients: $\alpha_{//}$ and α_{\perp} . Scale variation coefficient $\alpha_{//}$ is the ratio of the width of the pumping beam 4 in the plane of intersection to that of the pumping beam 2 (see Fig.1). For $|\alpha_{//}| < 1$ beam 4 is narrower and for $|\alpha_{//}| > 1$ wider, than beam 2. The same with the scale variation coefficient α_{\perp} , but for the direction, perpendicular to the intersection plane. The theory gives the following predictions:

1) To obtain phase conjugation in the geometry under consideration the width of secondary pumping beam 4 in the interaction region in the direction perpendicular to the intersection plane should be

92-18695



less, than that of primary pumping beam 2: $\alpha_{\perp} < 1$. The relation between the widths of pumping beams 2 and 4 in the intersection plane may be arbitrary.

2) Quality of conjugation increases with the increase of scale variation coefficients $\alpha_{//}$ and α_{\perp} , but for $\alpha_{\perp} \Rightarrow 1$ higher transverse modes may be excited along with the main one due to the closeness between their thresholds. 3) For $\alpha_{\perp} > 1$ scattered beam is not conjugate to the pump. Its radius of curvature in the direction, perpendicular to the intersection plane, is given by the theory.

4) Selection of the conjugate component for any values of $\alpha_{//}$, α_{\perp} may be achieved by rotating the cross-section of the beam, propagating along the feedback loop, through an angle, differing from zero or 180° .

In experiment we used a He-Ne laser ($\lambda = 0.63\mu\text{m}$) and SBN:Ce photorefractive crystal. To change values of $\alpha_{//}$ and α_{\perp} separately, cylindrical optics was used. Experimental results, presented in Figs.2-4, demonstrate full agreement with the predictions of a three - dimensional theory [1].

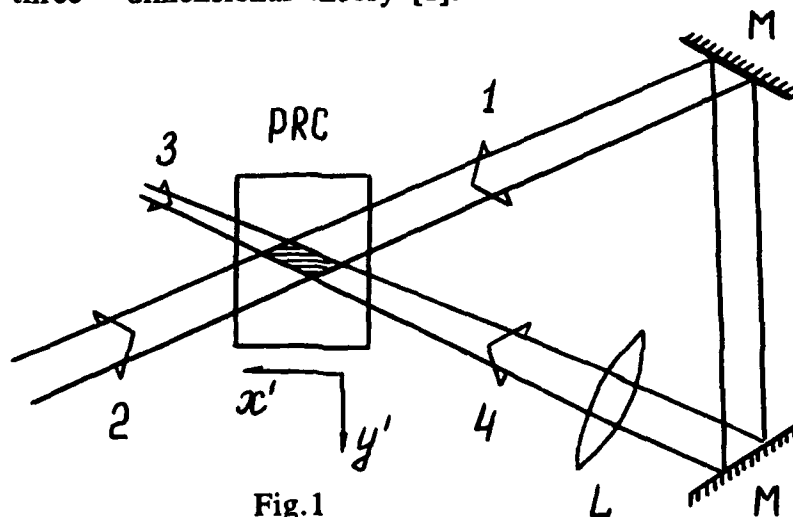


Fig.1

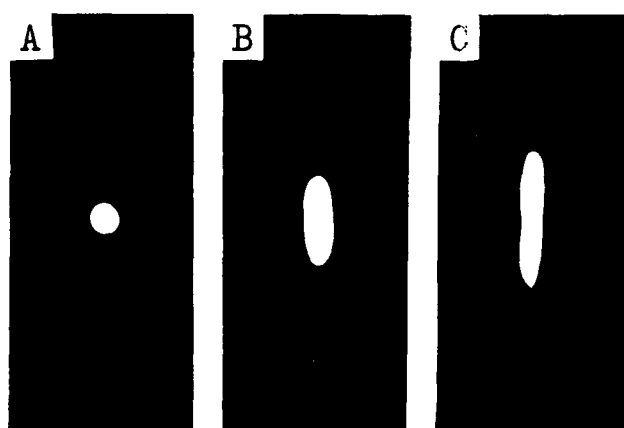


Fig.2

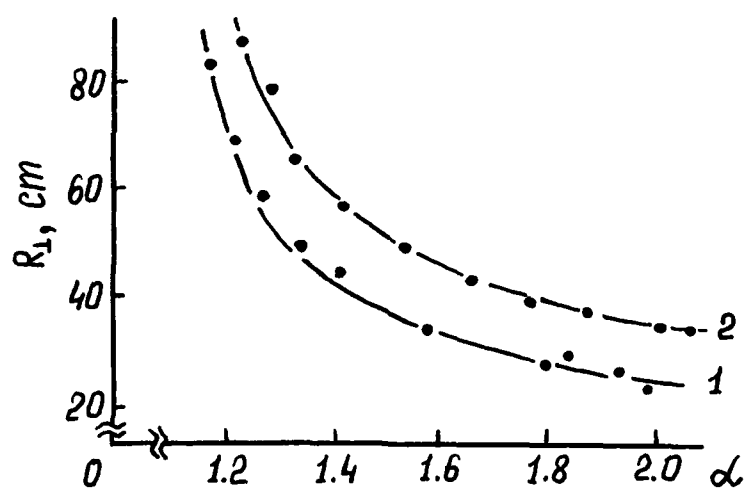


Fig.3

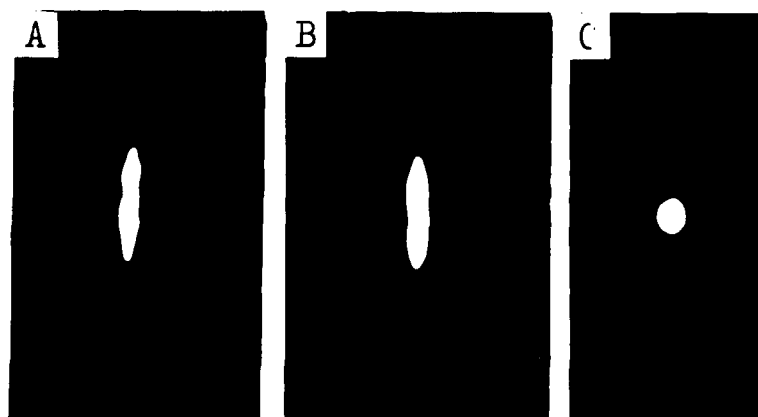


Fig.4

References

1. A. A. Zozulya, V. P. Silin, V. T. Tikhonchuk, Zh. Eksp. Teor. Fiz. 92, 788 (1987) [Sov. Phys. JETP 65, 443 (1987)].

Figure captions

1. Geometry of a passive ring mirror.

Fig.2. Structure of the backscattered beam in a far-field zone versus $\alpha = \alpha_{//} = \alpha_{\perp}$. The value of α increases from the left to the right; a) - $\alpha < 1$, b) and c) - $\alpha > 1$.

Fig.3. Radius of curvature of the wave-front of the backscattered beam in the direction, perpendicular to the intersection plane, versus $\alpha_{\perp} = \alpha_{//} = \alpha > 1$ for two values of total feedback loop length L : 1) $L \approx 48\text{cm}$ and 2) $L \approx 56\text{cm}$. Dots - experimental, solid lines - theoretical.

Fig.4. Structure of the backscattered beam in a far - field zone: a) $\alpha_{\perp} = \alpha_{//} = \alpha \approx 1.5$; b) $\alpha_{//} \approx 0.6$, $\alpha_{\perp} \approx 1.5$; c) $\alpha_{//} \approx 1.5$, $\alpha_{\perp} \approx 0.6$.

**SPATIAL SOLITONS IN PHOTOREFRACTIVE MEDIA****Mordechai Segev, Amir Saa'r and Amnon Yariv****California Institute of Technology
Pasadena, CA 91125. Tel. (818) 356-4823**

Light solitons in space (spatial solitons) have been under an intensive theoretical and experimental research in the last three decades. The solitons evolve from nonlinear changes in the refractive index of the material, due to the light intensity distribution. When the modulation of the index confines the light beam in such a way that diffraction is compensated for exactly, the beam becomes self-trapped, and is called a spatial soliton. The nonlinear effects, which are responsible to soliton formation, are in general Kerr-like effects, causing local index changes proportional to the local light power. The index changes needed for spatial solitons require high power densities, and often exceed 1MWatt/cm^2 (see ref.[1]).

We present here a new type of solitons in space, generated by the photorefractive (PR) effect in the medium. The solitonic waveform modulates the refractive index due to the PR effect, compensates for the diffraction exactly, and causes the light beam to propagate with no spatial change. This specific index modulation is introduced by interference gratings between the pairs of the spatial components (which compose the light beam), that are translated into phase gratings by the PR effect. Since the efficiency of this effect is independent of absolute light intensity, our solitons can be generated even at very moderate light power densities. Moreover, the same solitonic waveform can propagate unchanged in the medium, at very high or very low light intensities.

The PR solitons are the steady state solutions of the nonlinear wave equation, which describes beam propagation in PR media, and takes into account both diffraction and mutual interaction between each pair of spatial components of the beam. We

92-18696

develop this equation here, in a rigorous formalism, from the paraxial wave equation. The soliton solution occurs when the waveform is unchanged along the direction of propagation. Full compensation for the diffraction requires nonlinear phase coupling between the spatial (plane wave) components, but allows no intensity coupling, which may deform the beam and destroy the soliton. This condition can be fulfilled by choosing a proper material symmetry and an externally applied electric field.

Beam propagation in a PR medium is conveniently represented in the spatial frequency space, by the following equation:

$$(1) \quad \frac{df(q,z)}{dz} = i \beta(q) f(q,z) - \frac{1}{F_0} f(q,z) \int_{-k}^k |f(q',z)|^2 \gamma(q,q') dq'$$

where $f(q,z)$, the spatial frequency (angular) distribution of the beam complex amplitude $A(y,z)$, is given by the relation:

$$(2) \quad f(q,z) = \int_{-k}^k A(y,z) e^{iqy} e^{i\sqrt{k^2-q^2} z} dy$$

where $q=2\pi n \cdot \sin(\alpha)/\lambda$, and α is the propagation angle of the spatial component (plane wave) q , with respect to the optical axis z .

F_0 is the absolute power (Watts), and is given by:

$$(3) \quad F_0 = \int_{-k}^k |f(q,z)|^2 dq = 2\pi \int_{-\infty}^{\infty} |A(y,z)|^2 dy$$

$\gamma(q,q')$ is the complex coupling coefficient between the spatial components q and q' , and $\beta(q)$ is the term responsible to the linear diffraction and is equal to:

$$(4) \quad \beta(q) = \sqrt{k^2 - q^2} - \frac{q^2}{2k}$$

In the absence of the nonlinear PR interaction, the nonlinear term is omitted, and Eq. (1) is identical to the Fourier transform of the paraxial wave equation, with the well known Gaussian beam solutions.

The solitons experience no change with z , therefore $dA(y,z)/dz=0$. It occurs when:

$$(5) \quad f(q,z) = \psi(q) e^{i\sqrt{k^2 - q^2} z}$$

and for the existence of a spatial soliton, from eq. (1), we require:

$$(6) \quad -i \frac{q^2}{2k} = \frac{1}{F_0} \int_{-k}^k |\psi(q')|^2 \gamma(q,q') dq' \quad \text{for all } q.$$

Equation (6) is an integral equation, classified as Fredholm equation of the first kind. Given the material and the configuration, the only unknown is the spatial power spectrum function $|\psi(q)|^2$. Since the power spectrum is a real function, a solution can be obtained only if $\gamma(q,q')$ has an imaginary part. The symmetry properties of Eq. (6) must be considered as well, since diffraction is a symmetrical process, and the term q^2 is an even function of q .

The simplest solution to (6), is achieved for a symmetric and pure imaginary coupling coefficient $\gamma(q,q')$. This condition is fulfilled if the external field E_0 obeys to the relation :

$$(7) \quad |E_d| \ll |E_0| \ll |E_p|$$

Where E_d is the diffusion field, and E_p is the maximum trap field, as defined in ref [2]. At this field, the dominant transport

mechanism for the excited charges in the conduction band of the PR material, is drift, and the real part of $\gamma(q,q')$ is negligible.

We calculate the power spectrum waveform numerically. We emphasize, that since Eq. (6) is defined for the power spectrum, the phase of the PR soliton does not contribute, and can be chosen arbitrarily. Moreover, any waveform with a spatial power spectrum that satisfies Eq. (6), will propagate unpertrubed in the PR medium, and maintain its original phase fronts. An outcome of this property leads to another interesting characteristic of the PR solitons: they do not collapse into the solitonic waveform. The soliton should be launched properly into the nonlinear medium, and experiences no spatial change. Nevertheless, the efficiency of the PR interaction can be tuned by changing the external electric field, to compensate for the diffraction for a specific soliton solution $\Psi(q)$. Another way of controlling the PR solitons, is by light - using background illumination to reduce the modulation depth of the stored index gratings in the PR material (see ref. [3]).

In conclusion, we have introduced a new kind of spatial solitons, which results from interaction between the nonlinear PR effect and diffraction. This soliton demonstrates interesting properties not shared by "conventional" solitons, such as independence of both the absolute light power and phase.

References

- (1) J.S.Aitchinson, A.M.Winer, Y.Silberberg, M.K.Oliver, J.L.Jackel, D.E.Leaird, E.M.Vogel and P.W.Smith, Opt. Lett. 15, 471 (1990).
- (2) M.Cronin-Golomb, B.Fischer, J.O.White and A.Yariv, IEEE J.Quant. Elect. QE-20, 12, (1984).
- (3) M.Segev, Y.Ophir and B.Fischer, Appl. Phys. Lett. 56, 1086, (1990).

Image-degradation in a two-wave mixing spatial-light modulator

G. Notni and R. Kowarschik

Friedrich-Schiller University Jena, Faculty of Physics and
Astronomy, Institute of Applied Optics, O - 6900 Jena,
Max - Wien Platz 1, Germany, Tel. Jena / 82 25293

1. Introduction

Optical real-time image processing by spatial light modulators (SLM's) that utilize photorefractive crystals has attracted much attention /1/. The two-wave mixing SLM is based on the selective spatial erasure of the uniform phase volume hologram created by the two plane coherent beams using an incoherent image bearing beam $I_{inc}(\vec{r})$ resulting in an additional spatial modulation of the refractive index distribution $n_1(\vec{r})$ (commonly with a greater spatial period than the grating period of the hologram). The parameters of these Bragg-type SLM's are strongly determined by the diffraction properties of the nonuniform volume gratings and are analyzed here by means of the two-wave mixing coupled-wave formalism in its two-dimensional description /2/.

2. Theoretical background

Following the standard analysis of steady state plane-wave TWM, generalizing these equations including amplitude profiles of the interacting finite waves $A_1(\vec{r})$, $A_2(\vec{r})$, and a refractive index, $n_1(\vec{r})$, spatially modulated by the incoherent erasing beam and using the assumptions of the 2D-coupled wave theory, we get the following 2D-nonlinear coupled-wave equations

92-18697

$$\sin\theta \frac{\partial A_1}{\partial x} + \cos\theta \frac{\partial A_1}{\partial z} + i \frac{\pi}{\lambda} n_1(\vec{r}) e^{-i\phi} \frac{A_1^* A_2^* A_2}{I_0} + \alpha_0 A_1 = 0 \quad (1)$$

$$-\sin\theta \frac{\partial A_2}{\partial x} + \cos\theta \frac{\partial A_2}{\partial z} + i \frac{\pi}{\lambda} n_1(\vec{r}) e^{i\phi} \frac{A_1^* A_1 A_2}{I_0} + \alpha_0 A_2 = 0$$

These are rather general equations describing completely the TWM in the plane wave nonuniform case with arbitrary boundaries. In a SLM $n_1(\vec{r})$ is given by

$$n_1(\vec{r}) e^{-i\phi} = r_{\text{eff}} \frac{n_0^3}{4} E_{\text{sc}}(\vec{r}) \quad (2),$$

with r_{eff} , the effective electro-optic coefficient. The spatial dependence of the space-charge field $E_{\text{sc}}(\vec{r}) = m_{\text{eff}}(\vec{r}) E_{\text{sat}}$ results from the nonuniform erasure due to the incoherent image, where E_{sat} is the value of the space-charge field for no erasure. The modulation ratio $m_{\text{eff}}(\vec{r})$ in the material is given by

$$m_{\text{eff}}(\vec{r}) = \frac{1}{1 + \frac{\alpha_{\text{inc}} \lambda_{\text{inc}} I_{\text{inc}}(\vec{r})}{\alpha_0 \lambda_0 I_0(\vec{r})} \exp((\alpha_0 - \alpha_{\text{inc}})d)} \quad (3),$$

with α_0 and α_{inc} the absorption coefficient for the coherent and incoherent beam, respectively.

3. Numerical results

Using the 2D-Runge-Kutta method /3/ we calculated the intensity distribution of the depleted pump (transmitted) beam $I_1(l)$ and of the amplified signal (diffracted) beam $I_2(m)$. The diffraction geometry is shown in Fig.1. As an incoherent test object we choose a binary light distribution.

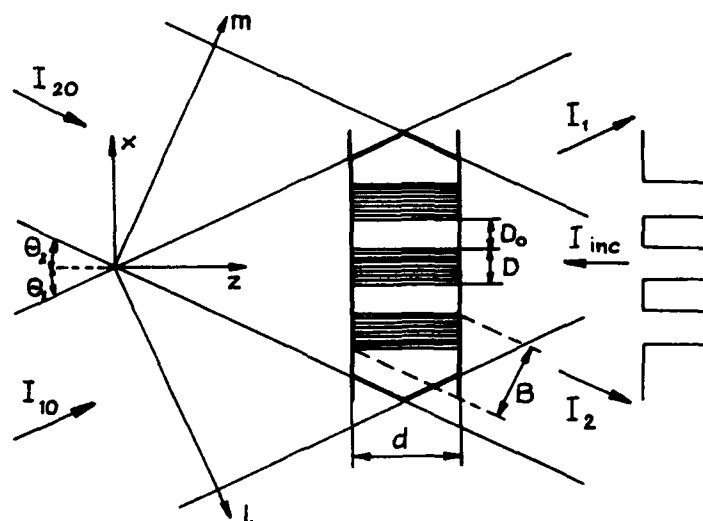


fig.1 TWM-SLM in a planar finite transmission grating geometry
(m , l are the beam coordinates; the dashed regions represent nonerased zones with high modulation)

Numerical examples for the spatial intensity distribution of the converted images :

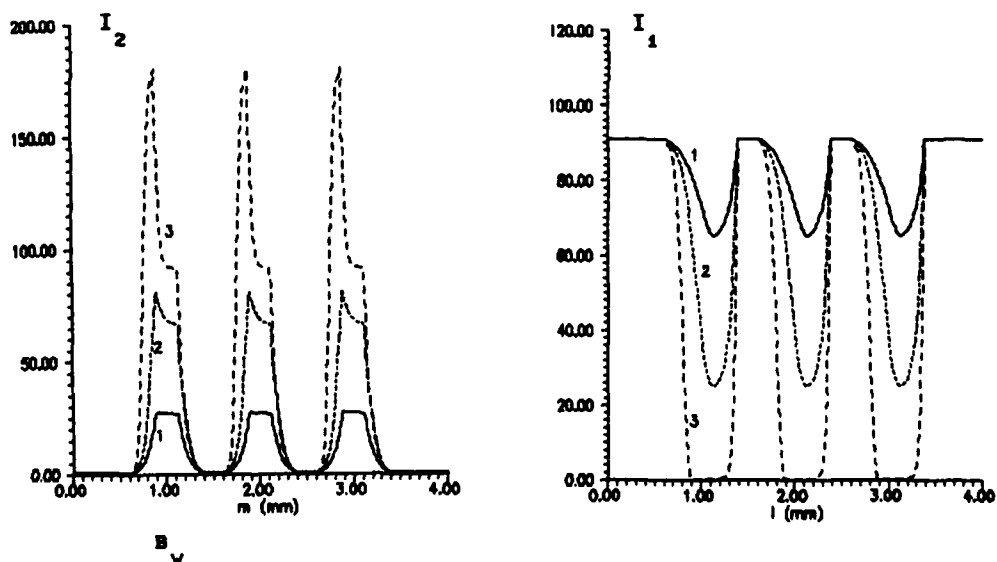


fig.2 parameters: $D = 0.5 \text{ mm}$, $D/D_0 = 1$, $I_{10}/I_{20} = 100$
 $\theta_2 = 5^\circ$, $d = 5 \text{ mm}$, beam width = 4 mm ,
 curve 1: $n_1 = 10^{-4}$, curve 2: $n_1 = 1.5 \cdot 10^{-4}$, curve 3: $n_1 = 3 \cdot 10^{-4}$

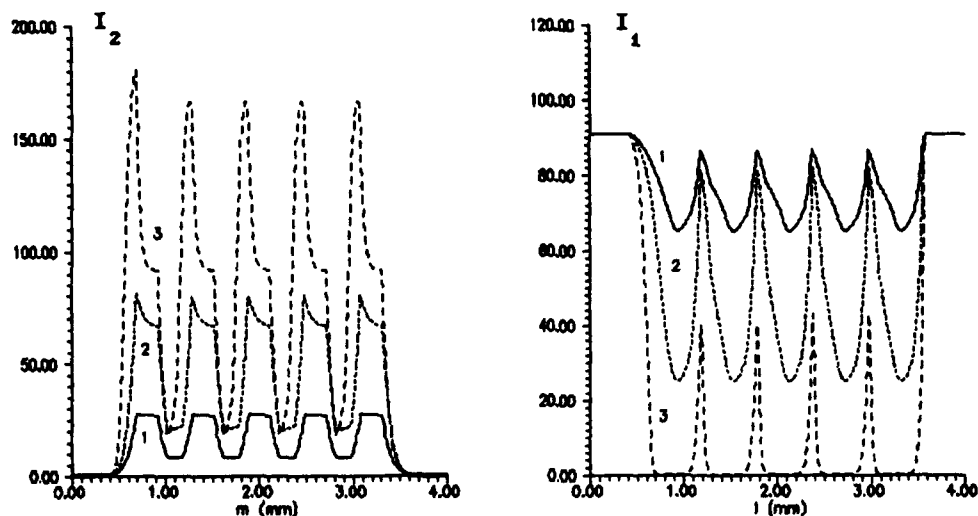


fig.3 parameters: see fig.2 and $D/D_0 = 5$

4. Main results

- The amplified beam is strongly degraded showing an asymmetric peaking in the direction of the coupling, which is smaller for lower gain coefficients ($\Gamma_0 d < 1.5$).
- A good quality (here a binary structure) appears in the transmitted beam only for great gain coefficients ($\Gamma_0 d > 4$).
- The inclination $\theta_2 = 5^\circ$ yields to a trapezian like structure (broadening) of each amplified beamlet with a basis width $B_v = 0.76$ mm which corresponds to the value B predicted by the geometrical limit with $B = D \cos \theta_2 + d \sin \theta_2$.
- In the case of $d \tan \theta_2 > D_0$ ($\theta = \theta_1 = \theta_2$) a decrease of the contrast in both beams appear also for an erasure contrast of 1.

5. References

- /1/ Y.W.Yu, D.Psaltis, A.Marrakchi, A.R.Tanguay, Jr., and R.V. Johnson, Topics in Applied Physics Vol.62 (Springer Verlag 1989)p.275
- /2/ G.Notni and R.Kowarschik, IEEE J.Quant.Electr. (accepted)
- /3/ G.Notni and R.Kowarschik, J.Opt.Soc.Am. A6(1989)1682



Resolution limit of photorefractive spatial light modulators

P. Amrhein and P. Günter

Institute of Quantum Electronics, Swiss Federal Institute of Technology, ETH-Hönggerberg,
CH-8093 Zürich, Switzerland (Phone: 0041 / 1 / 377 23 37)

The experimental set-up of our photorefractive incoherent to coherent converter¹ is shown in figure 1. With two interfering Ar-ion-laser beams ($\lambda=514.5$ nm) we write a phase hologram into a photorefractive KNbO_3 crystal. Using anisotropic Bragg diffraction² we choose the direction of the diffracted beam ($\lambda=632.8$ nm) perpendicular to the crystal surface. The input image is projected into the crystal plate anti-parallel to the diffracted beam. A short wavelength transmitting dichroitic beam splitter is used to separate the incoherent light from the diffracted beam. This set-up shows highest resolution³.

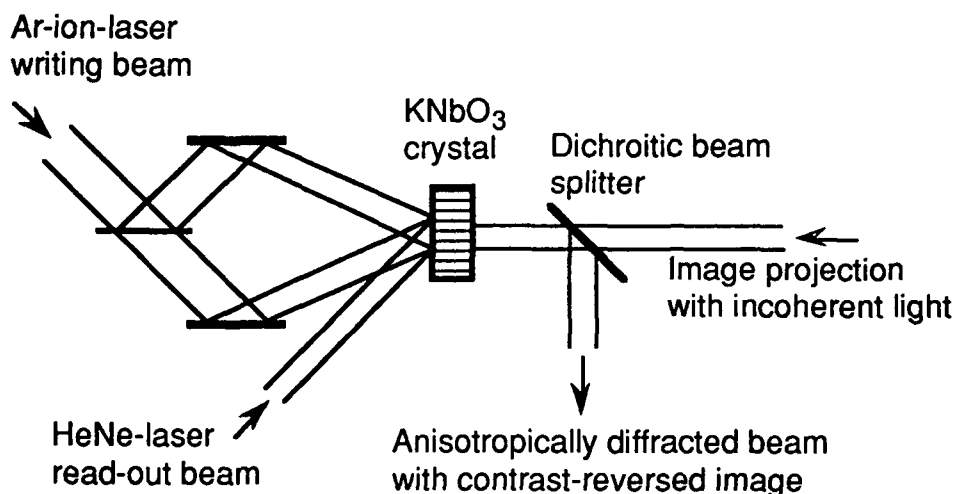


Fig.1 Experimental set-up for the photorefractive incoherent to coherent optical converter with KNbO_3 . Anisotropic Bragg diffraction is used.

We estimate the theoretical resolution limit of Bragg diffraction from finite holographic gratings. The method used consists of Fourier transform of the non-uniform photorefractive grating and the subsequent phase-sensitive integration over all waves Bragg diffracted from the partial (yet uniform) gratings.

92-18698



We start with a sinusoidal phase grating (grating vector \mathbf{K}_g parallel to z) that has nonzero amplitude only in two next-neighboring narrow regions (pixel) with a width of $2L$. The hologram is extended to infinity in x -direction and has a thickness d in y -direction. The two-dimensional Fourier transform of such a refractive index modulation $\Delta n(y, z)$ is

$$\Delta n(k_y, k_z) = 2 \Delta_0 \frac{\sin(k_y d/2)}{k_y} \frac{2 \sin(k_z L) \cos(2 k_z L)}{k_z} \quad (1)$$

where Δ_0 is the amplitude of the refractive index change and $\mathbf{k}=(k_y, k_z)$ is the variation of the grating vector \mathbf{K}_g . The Fourier components $\Delta n(k_y, k_z)$ describe uniform sinusoidal phase gratings. For each grating we can apply the theory of Kogelnik⁴ to get amplitude and phase of the Bragg diffracted waves

$$E(k_y, k_z) = v \frac{\sin\left(\sqrt{v^2 + \xi^2}\right)}{\sqrt{v^2 + \xi^2}} \exp(-i\xi) \quad (2)$$

where v is proportional to $\Delta n(k_y, k_z)$ and ξ is proportional to the deviation from the Bragg condition δk . The total field amplitude of the diffracted wave at the end surface of the crystal is derived by integrating over these fields multiplied with an additional phase factor $\phi(k, z)$ describing the wave propagation through the crystal

$$E_{\text{diff}}(z) = \iint E(k_y, k_z) \exp(-i \phi(k_y, k_z, z)) dk_y dk_z \quad (3)$$

The diffracted intensity pattern $I(z)$ which can be observed experimentally is the product $I(z) = E_{\text{diff}}(z) E_{\text{diff}}^*(z)$. The integral is solved numerically for different parameters. We define the resolution limit R in linepairs per unit length (the inverse of twice a pixel width) as $R = (4L)^{-1}$ where L follows from the condition that the diffracted intensity $I(z)$ between the peaks of the two pixels is lower than 50 percent of the peak values.

The phase of the diffracted waves and hence the diffracted intensity pattern depend strongly on the crystal thickness d . Figure 2 shows $R(d)$ for our experimental conditions. It is straightforward to notice that the best resolution is achieved with thin crystals. This is true also for all other (geometrical) factors limiting the resolution³. Increasing the resolution with thinner crystals, however, leads to a substantial decrease of diffraction efficiency.

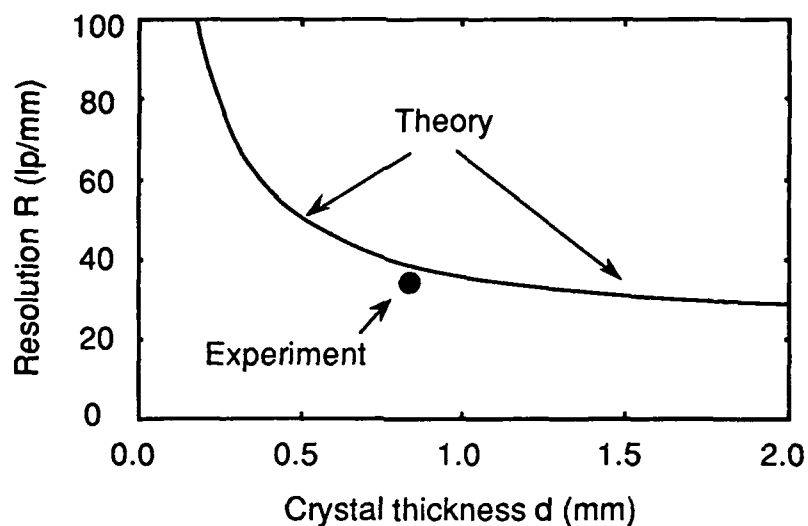


Fig.2 Resolution limit R as a function of crystal thickness d for KNbO_3 for anisotropic Bragg diffraction. Parameters: $n/\lambda=3.6$, read-out wavelength $\lambda=632.8$ nm and diffraction efficiency $\eta=0.01$.

In our experiment we used a KNbO_3 crystal plate with thickness $d=0.83$ mm. We observed a maximum resolution of 35 linepairs per mm which is near to the theoretical limit. Figure 3 shows 3 different examples of converted images. For a writing intensity of 50 mW/cm^2 the diffraction efficiency was $\eta=1\%$ and the writing time constant $\tau=0.1$ s.



Fig.3 Contrast reversed images with a resolution of 35 linepairs per mm. The size of the crystal area used for one image is $3 \times 3 \text{ mm}^2$.

It is known that in KNbO_3 crystals the writing process can become faster than 1 ms after electro-chemical reduction ⁵. On the other hand the large resolution allows the construction of photorefractive spatial light modulators with 1000 x 1000 pixels within a crystal area of less than 15 x 15 mm. KNbO_3 crystals of this size can be grown easily.

REFERENCES

- [1] A. Marrakchi, A.R. Tanguay Jr., J. Yu and D. Psaltis, " Physical characterization of the photorefractive incoherent-to-coherent optical converter ", *Optical Engineering* **24** (1), 124 (1985)
- [2] E. Voit, " Anisotropic Bragg diffraction in photorefractive crystals," in Electro-optic and photorefractive materials, P. Günter, ed., Vol. **18** of Springer Series in Proceedings in Physics (Springer Verlag, Berlin, 1987), p. 246
- [3] P. Amrhein and P. Günter, " Resolution limit for isotropic and anisotropic Bragg diffraction from finite holographic gratings ", *J.Opt.Soc.Am.B* **7** (12), 2387-2392 (1990)
- [4] H. Kogelnik, " Coupled wave theory for thick hologram gratings ", *Bell Syst. Tech. J.* **48** (9), 2909 (.969)
- [5] E. Voit, M.Z. Zha, P. Amrhein and P. Günter, " Reduced KNbO_3 crystals for fast photorefractive nonlinear optics ", *Appl.Phys.Lett.* **51** (25), 2079 (1987)

Monday, July 29, 1991

Invited Poster Preview

MC 3:00pm–4:00pm
Academic Center Auditorium

Klaus Ringhofer, *Presider*
Universitat Osnabruck, Federal Republic of Germany

AD-P006 711

High sensitivity resonant photorefractive effect in semi-insulating CdZnTe/ZnTe multiple quantum wells

A. Partovi, A.M. Glass, D.H. Olson, G.J. Zydzik, K.T. Short
 AT&T Bell Laboratories, Murray Hill, New Jersey, 07974
 (201) 582-2847

R.D. Feldman, R.F. Austin
 AT&T Bell Laboratories, Holmdel, New Jersey, 07733

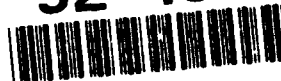
Although the photorefractive sensitivity of the semiconductors is many orders of magnitude larger than the oxides, their small Pockels electro-optic coefficient has been a serious drawback. By taking advantage of the quadratic effects near the band-edge, nonlinearity and sensitivity of semiconductor photorefractives can be dramatically improved. Recently, two-beam-coupling gain coefficients of 16.3 cm^{-1} in GaAs [1] and 26.0 cm^{-1} in InP [2] have been reported near the band-edge. Quantum confinement of excitons in multiple quantum wells (MQWs) provides an additional enhancement of the resonant electro-optic nonlinearities. We have recently demonstrated how enhanced photorefractive sensitivity can be obtained in semi-insulating MQW devices [3]. These devices were made semi-insulating through ion-implantation to provide sufficient density of traps for the photorefractive process as well as relieving the need for any pixelation.

Here we report on a II-VI MQW photorefractive device where the electric field is applied perpendicular to the quantum well layers. Sensitive operation in the visible (570-613 nm) and 250 times improvement in diffraction efficiency over previous results [3] have been achieved. This MQW device has many advantages over bulk photorefractive semiconductors. In this device: 1) QCSE which is a larger nonlinearity than the Franz-Keldysh effect or Pockels linear electro-optic effect, can be used. 2) Application of a small voltage results in very large fields due to the small interelectrode distance (structure thickness $\sim 1 \mu\text{m}$). 3) Since the direction of carrier transport is perpendicular to the grating wavevector, slowing down of device operation due to long carrier drift lengths does not occur.

The device consists of a $\text{Cd}_x\text{Zn}_{1-x}\text{Te}$ MQW sample placed between dielectric layers and transparent electrodes. These MQWs show sharp room-temperature exciton peaks as well as enhanced excitonic oscillator strength and excitonic saturation intensities over III-V MQWs [4]. We have recently shown that very large QCSE changes in the absorption coefficient ($\Delta\alpha \sim 7000 \text{ cm}^{-1}$) are possible in such structures [5]. The dielectric layers serve as a barrier against carrier drift. This device is similar to the Pockels Readout Optical Modulator (PROM) [6] but here, by utilizing the large excitonic nonlinearities of MQWs, very short interaction lengths are necessary and very high resolution can be obtained. The semi-insulating MQW serves as both the photoconductor and the nonlinear media and provides diffraction limited resolution without need for pixelation of the device.

The device is operated by applying an ac square-wave voltage to the electrodes. The dielectric relaxation time of the semi-insulating MQW layer is given by:

$$\tau_d = \frac{\epsilon}{(\sigma_d + \sigma_p)} \quad (1)$$

92-18699

where ϵ is the permittivity of the material and σ_d and σ_p are respectively the dark conductivity and photoconductivity of the material. For an ac field with period shorter than the dielectric relaxation time, τ_d , the carriers in the MQW structure do not have sufficient time to accumulate at the dielectric barriers and screen the applied field. Increasing the incident light intensity on the structure produces carriers that reduce τ_d and screen the applied field. In this way, an intensity variation such as the variation due to interference of two intersecting laser beams can be transformed to a corresponding electric field variation across the MQW layer. Through the QCSE, this modulation of the electric field changes the absorption coefficient and refractive index of the material. Absorption and refractive gratings are thereby produced.

The change in the absorption coefficient ($\Delta\alpha$) was measured by passing a single laser beam at the exciton peak ($\lambda = 590$ nm) from a cw dye laser through the device. Figure 1 shows $\Delta\alpha$ as a function of the frequency of the applied voltage for various beam powers. With increased light intensity, the necessary frequency to obtain the full QCSE increases as expected from Eq. (1). As can be seen from Fig. 1, at a frequency such as 10 kHz, the QCSE and therefore the absorption of the device can be easily controlled by the incident intensity. Very large absorption changes ($\Delta\alpha \sim 3500$ cm⁻¹) can be obtained with mW of change in incident power. Since the material is semi-insulating, cross-talk between two adjacent parts is minimized and no pixelation is necessary.

To record diffraction gratings in the device, two beams of 0.5 mW power at $\lambda = 590$ nm were intersected in the sample while an ac field was applied to it. The angle between the beams was 3.6° resulting in an interference pattern with a period $\Lambda_g = 9.4$ μ m. Illumination of the device with this interference pattern produces a corresponding nonuniform QCSE absorption change thereby creating an absorptive grating. A corresponding refractive grating is also formed. This thin grating causes self-diffraction of the two laser beams into many Raman-Nath orders. Figure 2 shows the diffraction efficiency (ratio of first order diffracted beam to the beam travelling directly through the sample) of the device as a function of the magnitude of a 50 KHz applied ac voltage. The diffraction efficiency increases rapidly with increasing voltage. At a voltage of only 50V, a diffraction efficiency of 0.2% is obtained. Our maximum diffraction efficiency of 0.25% is 250 times the previously obtained results with the field applied parallel to the MQW layers [3]. This improvement is due to the larger nonlinearities possible in MQWs with the field perpendicular to the layers. Change in absorption due to QCSE as a function of voltage was also measured with a single laser beam. This data is also shown in Fig. 2.

Figure 3 shows the measured diffraction efficiency as a function of wavelength. Diffraction at wavelengths up to 613 nm is observed. These results at long wavelengths are due to index gratings and occur at a low absorption region. By using moving grating techniques to produce a phase shift between the grating and the intensity pattern, two beam-coupling gain should be possible in this region. Using the value of diffraction efficiency at 611 nm, we estimate a gain coefficient of 2000 cm⁻¹ to be possible with moving grating techniques.

From the values of absorption change possible in our device, we expect diffraction efficiencies of several percent to be possible in our device. We believe our current value of 0.25% may have been limited by lateral diffusion of accumulated carriers at the semiconductor-dielectric interface. With improvements in design of device structure larger diffraction efficiencies should be possible.

REFERENCES:

1. A. Partovi, A. Kost, E.M. Garmire, G.C. Valley, and M.B. Klein, Appl. Phys. Lett., **55**, 1087 (1989).
2. J.E. Millerd, S.D. Koehler, E.M. Garmire, A. Partovi, A.M. Glass, and M.B. Klein, Appl. Phys. Lett., **57**, 2776 (1990) and J.E. Millerd, S.D. Koehler, E. M. Garmire, and A. Partovi, OSA annual meeting, paper FI3, Boston, MA. (1990).
3. A.M. Glass, D.D. Nolte, D.H. Olson, G.E. Doran, D.S. Chemla, and W.H. Knox, Opt. Lett., **15**, 264 (1990).
4. D. Lec, J.E. Zucker, A.M. Johnson, R.D. Feldman, and R.F. Austin, Appl. Phys. Lett., **57**, 1132 (1990).
5. A. Partovi, A.M. Glass, D.H. Olson, R.D. Feldman, R.F. Austin, D.H. Lee, A.M. Johnson, and D.A.B. Miller, Appl. Phys. Lett., **58**, 334 (1991).
6. B. A. Horwitz and F.J. Corbett, Opt. Eng., **17**, 353 (1978).

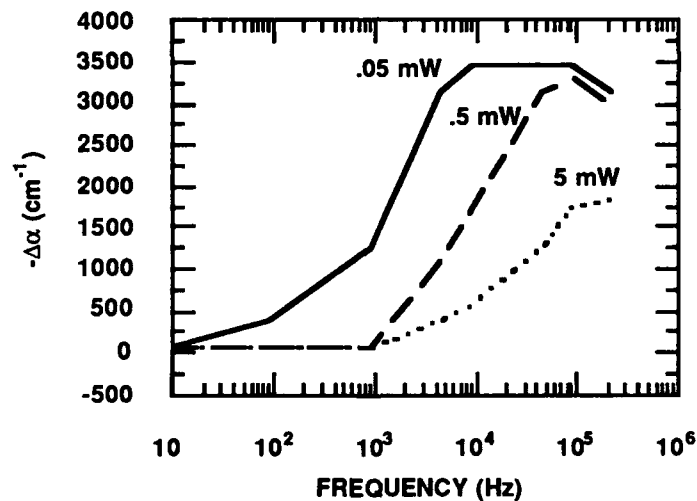


Figure 1 - Change in the absorption coefficient of the photorefractive device at $\lambda = 590$ nm due to quantum confined stark effect as a function of the frequency of the applied 60V (peak-zero) square voltage for various incident beam powers. The beam diameter is 0.74 mm. The device consists of a II-VI MQW structure sandwiched between 1500 Å Vycor dielectric layers and transparent electrodes. The $\text{Cd}_x\text{Zn}_{1-x}\text{Te}$ MQW consists of 130 periods of 51 Å wells ($x=0.34$) and 122 Å barriers ($x=0$) grown on a buffer layer consisting of 1700 nm of $\text{Cd}_{0.1}\text{Zn}_{0.9}\text{Te}$ grown on top of 700 nm of ZnTe. The buffer layer is designed to minimize the strain in the MQW structure.

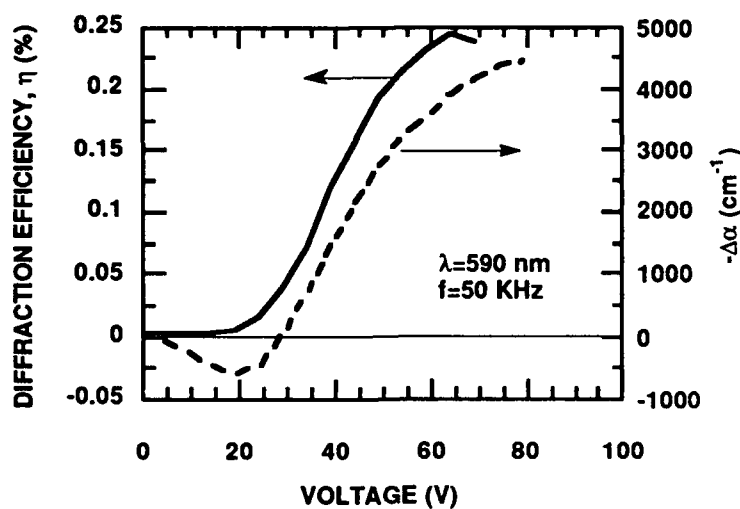


Figure 2 - Diffraction efficiency at $\lambda = 590$ nm as a function of the applied 50 kHz applied square voltage amplitude. The amplitude is peak-zero. Absorption change due to QCSE as a function of the voltage is also shown.

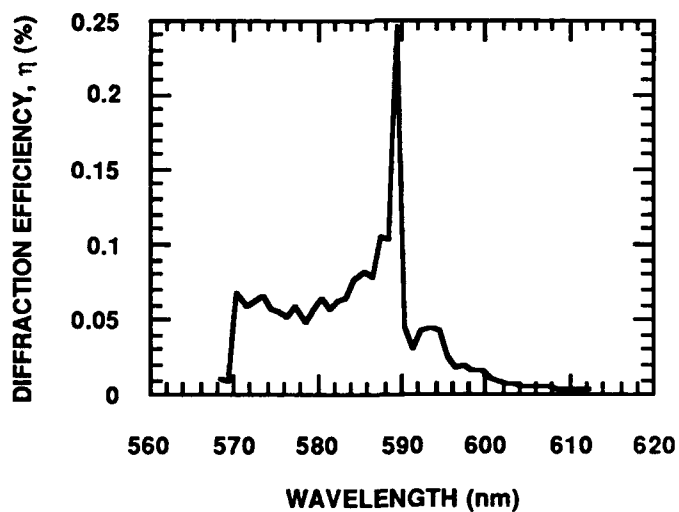


Figure 3 - Diffraction efficiency as a function of wavelength for 75 V (peak-zero) applied voltage. The frequency of the ac voltage is optimized at each wavelength.



The Influence of Cobalt Doping on Deep and Shallow Trap Dependent Photorefractive Properties of Barium Titanate

M. H. Garrett, *J. Y. Chang, †P. Tayebati, H. P. Jenssen and †C. Warde

Massachusetts Institute of Technology

†Department of Electrical Engineering and Computer Science, the *Materials Science and Engineering Department and the Crystal Physics Laboratory, 77 Massachusetts Ave. Rm 13-3157, Cambridge, MA 02139, (617) 253-6622

1.0 Introduction

The photorefractive properties of cobalt-doping barium titanate have been recently reported by Rytz et al. [1]. High beam coupling gains were reported therein. Similarly, we have grown a series of cobalt-doped p-type barium titanate crystals, (undoped, 17 ppm, 50 ppm and 75 ppm), that also have relatively large beam coupling gains, e.g. for Ella and k_{gllc} the gain is 7.4 cm^{-1} at 514.5 nm in the 75 ppm sample. We have further characterized these crystals by determining the sublinear dependence of the response time on intensity, the asymmetry of the beam coupling gain for $\pm C$ -axis crystal orientations, (i.e. electrooptic and absorptive coupling), intensity dependence of the gain, and light-induced dark decays. Experimental results indicate that, as the cobalt concentration is increased, the photorefractive character of the crystals change from "type B" to "type A" as defined by Mahgerefteh and Feinberg [2]. Type A crystals have filled hole-shallow traps and type B crystals have partially filled hole-shallow traps and thus low and high dark conductivity respectively.

2.0 Deep and Shallow Trap Theory

Our experimental results can be explained with the photorefractive model of Tayebati and Mahgerefteh [3] briefly outlined here. The possible deep and shallow trap charge gratings, N_1 and M_1 respectively, due to a sinusoidal intensity modulation m , where $m \ll 1$, are,

$$-eN_1 = -meN_E \frac{k_g^2}{(k_g^2 + k_0^2)} - meM_E \frac{1}{(1 + s_T I_0 / \beta)} \frac{k_{0D}^2}{(k_g^2 + k_0^2)} \text{ and,}$$

$$eM_1 = -meM_E \frac{1}{(1 + \beta / s_T I_0)} \frac{k_g^2}{(k_g^2 + k_0^2)} + meM_E \frac{1}{(1 + s_T I_0 / \beta)} \frac{k_{0D}^2}{(k_g^2 + k_0^2)} \quad (1)$$

I_0 is the intensity, β is the thermal excitation rate of the shallow traps, s_T is the excitation cross-section of shallow traps, and N_E and M_E are intensity dependent effective deep and shallow trap densities. The Debye screening wavevector is defined as,

$$k_0^2 = k_{0D}^2 + k_{0T}^2, \quad (2)$$

where k_{0D} and k_{0T} are the deep and shallow trap effective trap densities respectively both of which are intensity dependent because of the redistribution of charge between deep and shallow levels. Absorption of light by filled shallow-traps may result in a shallow-trap charge-grating.

The spatial modulation of the absorption (producing absorption gratings and a corresponding index grating that diffracts light) is given by,

$$\hbar\omega(s_D N_1 - s_T M_1), \quad (3)$$

and the space-charge field,

$E_1 = -ie / k\epsilon(N_1 - M_1)$, is intensity dependent where,

$$E_1 = -im \frac{k_B T}{e} \frac{k}{1 + k^2 / k_0^2} \eta(I), \quad (4)$$

and the intensity dependent term has a value between 0 and 1 where,

$$\eta(I) = \frac{1}{k_0^2} \left[k_{0D}^2 + \frac{k_{0T}^2}{1 + \beta / s_T I_0} \right]. \quad (5)$$

We note that as $k_g \rightarrow 0$ the space-charge field vanishes but the absorption gratings remain finite since the second terms of equations (1) do not vanish.

92-18700



In addition, this model [3] gives expressions for sublinear photoconductivity (or the sublinear dependence of the response time on intensity) and light-induced dark decays of the space-charge field.

3.0 Characterization Measurements

The effect of cobalt-doping on barium titanate's absorption spectrum is to induce a broad absorption shoulder that starts at the band edge (~ 3.0 eV), extends into the visible and diminishes in the near-infrared as shown in Figure 1.

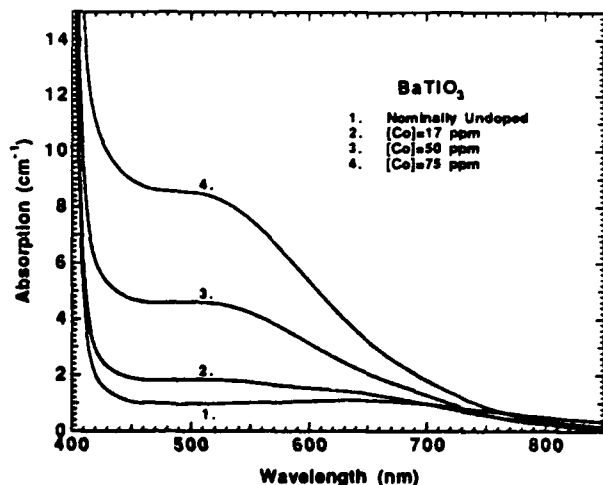


Figure 1. Absorption spectra of Co-doped BaTiO₃.

Recent analysis by Mahgerefteh and Feinberg [2], Brost and Motes [4] and Tayebati and Mahgerefteh [3] indicate that the sublinear dependence of the response time on intensity is explained by a model that includes deep and shallow traps. The response time as a function of intensity for the series of cobalt-doped crystals was determined by measuring the light-induced decay of the space-charge field with a weak, diffracted, He-Ne probe beam. In Figure 2 is a log-log plot of the inverse of the response time as a function of intensity. Over the intensity range measured a straight line fits the data and indicates that the exponent of the intensity dependence changes from $x=0.57$ to $x=0.90$ with increasing cobalt-doping. ($x=1$ indicates only deep traps.)

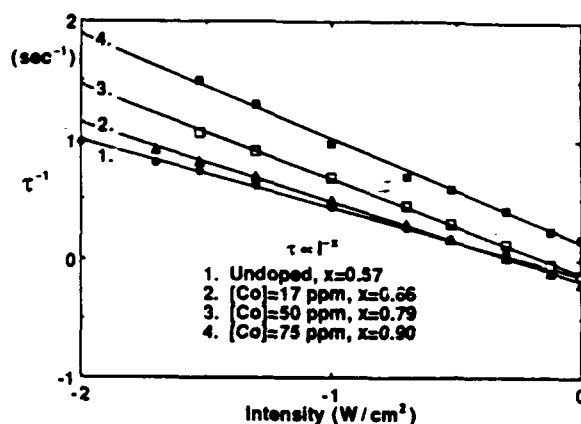


Figure 2. Intensity dependence of the response time for the series of cobalt-doped BaTiO₃.

One effect of shallow traps is revealed by the intensity dependence of the space-charge field (eqn. (4)) or beam coupling gain. Shown in Figure 3 is the electrooptic beam coupling gain measured for E₁₁₁ and k₁₁₁. The undoped crystal has a strong intensity dependence and, with higher cobalt-doping, gradually changes to little or no intensity dependence.

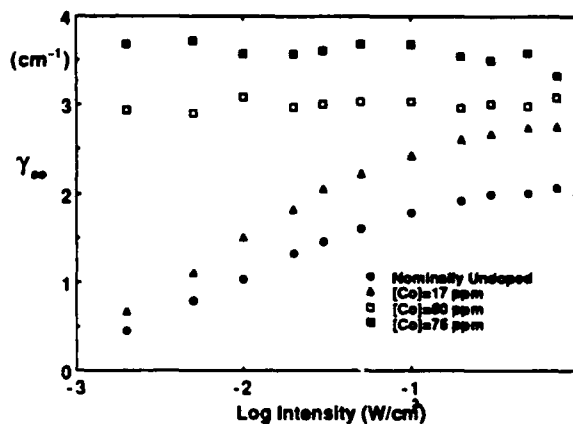


Figure 3. Intensity dependence of the electrooptic beam coupling gain.

Previous beam coupling models [e.g. 5,6] predict gain symmetry for $\pm C$ -axis orientations of the crystal. The beam coupling gain and its dependence on grating wavevector was determined by measuring the effective gain in a way which allowed us to ascertain the contributions to beam coupling from electrooptic and absorptive gain [7,8]. We used a technique similar to Pierce et al. [8] but determined the absorptive "gain" in the same crystallographic orientation as the electrooptic

coupling. When measuring the effective gain light-induced absorption changes were avoided by having the pump and signal beams continuously illuminate the crystal. Initially the pump beam was rapidly vibrated to make it incoherent with the signal beam while the signals' transmission was measured. The vibration was then terminated making the beams coherent and beam coupling ensued where the effective gain is given as,

$$\gamma_0^\pm \equiv \frac{I_c(L)}{I_{inc}(L)} = \frac{I_c \text{ with Coherent Pump}}{I_c \text{ with Incoherent Pump}} \quad (5)$$

and, for an undepleted pump and small modulation, is equal to,

$$\gamma_0^\pm = \exp[\pm \gamma] l / \cos \theta$$

$$= \exp[\pm \gamma_{eo} + \gamma_{abs}] l / \cos \theta. \quad (6)$$

Where, l is the crystal thickness and θ is the internal half-angle between the beams. We note that $\pm \gamma$ is the gain coefficient which is the sum of the electrooptic gain coefficient, $\pm \gamma_{eo}$, (whose sign is dependent on the orientation of the crystallographic C-axis and sign of the majority charge carriers), and γ_{abs} the absorptive "gain" coefficient from trap gratings [7,8]. There is an asymmetry in the beam coupling, i.e. $+\gamma \neq -\gamma$, and we determine the electrooptic and absorptive components of the coupling from,

$$\gamma_{eo} = (\gamma^+ + |\gamma^-|) / 2 \text{ and}$$

$$\gamma_{abs} = (\gamma^+ - |\gamma^-|) / 2 \quad (7)$$

(To reduce errors from physically reorienting the crystal we simply exchange the roles of the pump and signal beams by changing their relative intensities with the crystal in a fixed position, where their beam ratio is 800).

Shown in Figure 4 are the electrooptic and absorptive gain dependence on grating wavevector. For clarity the absorptive gain is given only for the undoped and we note that both the electrooptic and absorptive gain increase with increasing cobalt concentration but zero-crossing is found in the Co-doped samples.

4.0 Analysis

The intensity dependence of the gain, not predicted by previous beam coupling models

[e.g. 5,6], is evidence of deep and shallow trap effects as shown in Figure 3. Shallow and

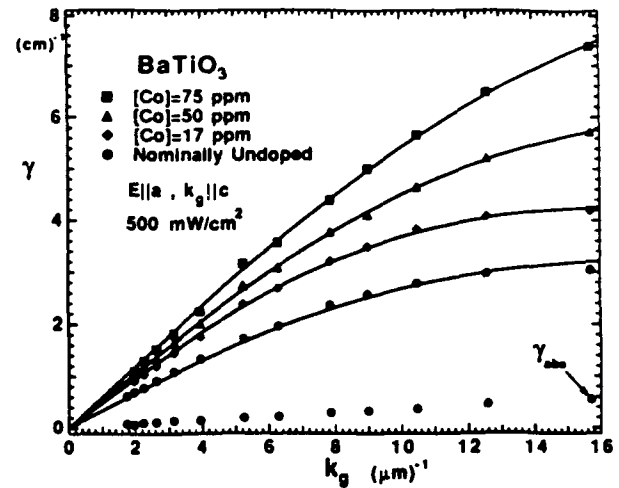


Figure 4. Electrooptic and absorptive gain dependence on grating wavevector.

deep trap effects are especially evident in the sublinear dependence of the response time ($x=0.57$, Fig. 2) for the type B undoped crystal (high dark conductivity). As the cobalt concentration is increased the coefficient of the sublinear dependence of the response time on intensity increases and the 75 ppm sample behaves like a "type A" crystal with low dark conductivity. This reduction of the dark conductivity leads to an increase in the space-charge field strength resulting in the largest electrooptic beam coupling gain for the 75 ppm crystal. We note that this sample also has the largest peak absorptive gain.

Mahgerefteh and Feinberg [2] describe the change in the dark conductivity as due to a filling of hole-shallow-traps with electrons and thus there is very little hole photoexcitation or thermal ionization into or out of the shallow traps in a type A crystal. By analogy with reference [2] cobalt doping must fill the shallow levels with electrons. This implies that increases in absorptive gain with increasing cobalt concentration must arise from light-induced changes in the charge distribution within the deep levels and not from charge redistribution between deep and shallow levels.

The influence of shallow traps on the photorefractive properties of barium titanate can also be examined, as proposed by Tayebati and Mahgerefteh [3], using light-induced dark decays. This experiment was performed to determine the magnitude of erasure of the deep

trap gratings from shallow trap thermal ionization. Shown in Figure 5 is the normalized diffraction efficiency as a function of time, before and after the grating writing beams were shuttered off, for the series of Co-doped crystals.

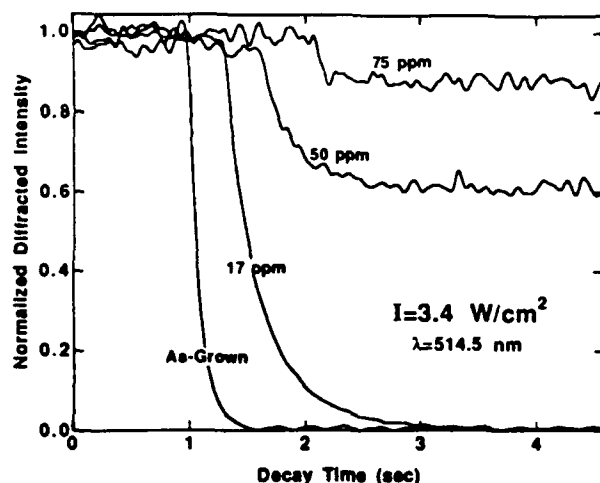


Figure 5. Light-induced dark decays of BaTiO₃:Co.

Qualitatively, it is apparent from Figure 5 that the dark decay of the space-charge field decreases with increased cobalt-doping. That is, the thermalization of charge from shallow traps, leading to the erasure of the deep-charge-grating, is greatest in the undoped sample and least in the 75 ppm Co-doped crystal. This result is consistent with the model of Mahgerefteh and Feinberg [2] where electron filled hole-shallow-traps of the type A crystal, (the filling apparently increases with increasing cobalt doping), would not participate in the light-induced dark decay. However, it is also possible that the deep-trap-density is increasing proportionately greater than the shallow-trap-density, as evidenced by the increase in absorption coefficient at the exciting wavelength and diminishes at longer wavelengths (see Fig. 1), leading to a relatively smaller dark decay in the space-charge field.

Electron paramagnetic resonance (EPR) data and analysis by Rytz et al. [1] indicates that cobalt forms a complex with an oxygen vacancy, Co³⁺-V_O, which have deep levels in the band, at 2-2.3 eV (620-540 nm). If oxygen vacancies are responsible for shallow-hole-traps then the addition of cobalt causes the simultaneous reduction in the shallow-trap population with the recompense of the creation

of deep levels. We find that the total effective trap density is an increasing function of cobalt-doping as shown in the following table:

| Sample | $\eta(I)$ | k_0 (μm^{-1}) | N_T (cm^{-3}) |
|---------|-----------|------------------------------|----------------------------|
| undoped | 0.38 | 17.2 | 6.4×10^{16} |
| 17 ppm | 0.51 | 17.6 | 6.67×10^{16} |
| 50 ppm | 0.56 | 23.1 | 1.15×10^{17} |
| 75 ppm | 0.63 | 30.6 | 2.02×10^{17} |

Table 1. Intensity dependent factor $\eta(I)$, Debye screening wavevector k_0 and total effective trap density N_T .

Further experiments, e.g. light-induced dark decays as a function of writing intensity, are being conducted to quantify the deep and shallow trap population as a function of cobalt concentration.

Since the absorption increases substantially with increasing cobalt concentrations and exceeds the gain for our 75 ppm crystal, additions of cobalt have limited usefulness when accessing only the r_{13} electrooptic coefficient but should lead to a substantial increase in the gain for a 45°-cut crystal.

Acknowledgment

This work supported by NASA under agreement NAG 1-996.

[§]P. Tayebati, Foster Miller, Inc., 350 Second Ave., Waltham, MA 02154

1. D. Rytz, B. A. Wechsler, M. H. Garrett, C. C. Nelson and R. N. Schwartz, J. Opt. Soc. Am. B 7(12), 2245 (1990).
2. D. Mahgerefteh and J. Feinberg, Phys. Rev. Lett. 64, 2195, (1990).
3. P. Tayebati and D. Margerefteh, J. Opt. Soc. Am. B, May, (1991).
4. G. A. Brost and R. A. Motes, Opt. Lett. 15, 1194 (1990).
5. Kukhtarev, V. B. Markov, S. G. Odoulov, M. S. Soskin and V. L. Vinetskii, Ferroelectrics 22, 949 (1979).
6. J. Feinberg, D. Heiman, A. R. Tanguay, Jr., and R. W. Hellwarth, J. Appl. Phys. 51(3), 1297 (1990).
7. A. V. Knyaz'kov and M. N. Lobanov, Sov. Tech. Phys. Lett. 11, 365, (1985).
8. R. M. Pierce, R. S. Cudney, G. D. Bacher and J. Feinberg, Opt. Lett. 15, 414 (1990).



Electron-Hole Competition in InP:Fe -- The Role of Multiple Defects

R. S. Rana and D. D. Nolte

Department Of Physics

Purdue University

W. Lafayette, IN 47907

92-18701



The photorefractive effect has now been identified and studied in many semi-insulating III-V compound semiconductors [1]. In general, it can be well described by a Single Defect Model (SDM) with one or two types of charge carriers. However, discrepancies arise between theory and the experimental results due to the presence of additional defects. In understanding the role of multiple deep defects in the photorefractive effect, temperature plays a key role. Each different defect has a specific energy position within the bandgap of the material. Thermal emission of carriers trapped at defect sites is a strong (exponential) function of defect energy and the sample temperature. The thermal relaxation of nonequilibrium defect occupancies, and the subsequent effect on the photorefractive effect, can be studied by monitoring the two-wave mixing (2WM) gain and four-wave mixing (4WM) diffraction efficiency as functions of temperature, providing a natural tool to characterize the material. We find that multiple defect levels in InP:Fe lead to dramatic changes in the photorefractive behavior. Reduced gain reported at room temperature can be shown to arise from an additional defect in InP other than isolated Fe.

We have performed 2WM and 4WM experiments on InP:Fe samples as functions of temperature and applied DC field. The pump laser is a Nd:YAG with an emission wavelength of 1.06 microns. The index grating is formed by two coherent beams interfering inside the semi-insulating sample. In 2WM experiments, the signal beam amplification after its interaction with nonlinear medium, is experimentally characterized by the measurement of γ_0 , defined as :

$$\gamma_0 = \frac{I_s (\text{With pump})}{I_s (\text{Without pump})} = e\Gamma L$$

(assuming no pump depletion), where Γ is the beam coupling coefficient and L is the interaction length, which is 8 mm for our sample. In 4WM experiments the index grating is probed by a third laser beam originating from a second YAG:Nd laser with a wavelength of 1.32 microns. The

magnitude of the holographic grating is measured as the diffracted intensity of the probe beam. The thermal measurements were obtained by placing the sample in a Janis Supravertemp cryostat. The grating spacing in the material for these experiments was 4.5 microns.

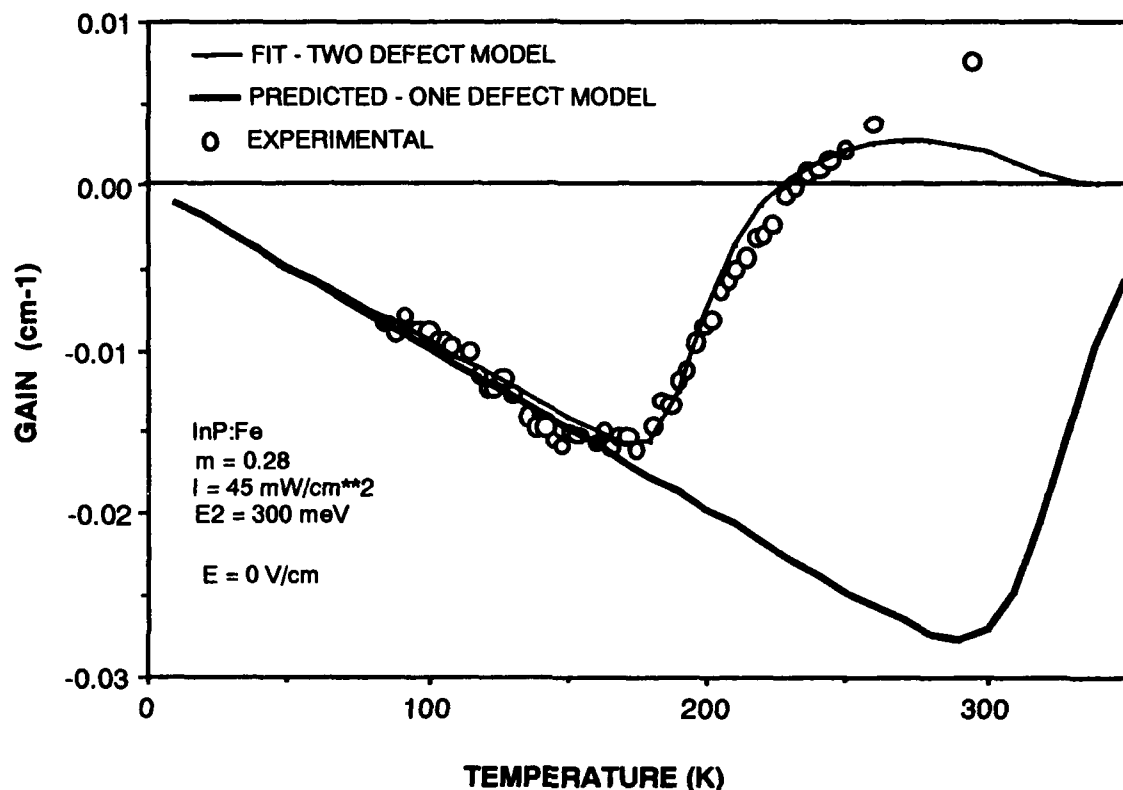


Fig. 1 The 2WM gain as a function of temperature for InP:Fe. A fit to experimental data predicts an additional electron trap with a binding energy of 300 meV.

The photorefractive gain measured as a function of temperature for InP:Fe is shown in Fig(1). At room temperature, the photorefractive effect is dominated by electrons [2], and the gain is positive. As the sample is cooled down, the gain starts to decrease and becomes negative below 225 K, indicating a change in the direction of energy coupling between the two laser beams and establishing holes as the dominant photocarriers at low temperature. This behavior cannot be explained based on the SDM because in this model the occupation of the iron level, $N_{Fe^-} = N_{sd} - N_{sa}$, where N_{sd} , N_{sa} refer to shallow donors and acceptors concentrations, does not change with temperature. The solid curve in Fig(1) is the predicted gain based on

the SDM and obtained by numerically solving the photorefractive rate equations for the experimental conditions described above. It is obvious, therefore, that more than one defect level is participating in the photorefractive effect. In order to explain this discrepancy, we assumed that a shallower electron trap occurs in the material with a binding energy of 300 meV. In this Two Defect Model (TDM), it is easy to understand the change in the sign of the dominant photocarriers and the direction of energy coupling with temperature, because the non-equilibrium occupation of the electron trap can change significantly with temperature. An excellent fit to the experimental data obtained by numerically solving the photorefractive rate equations in the TDM with simultaneous charge transport by electrons and holes [3], is also shown in Fig(1). We used standard parameters in the fit [4].

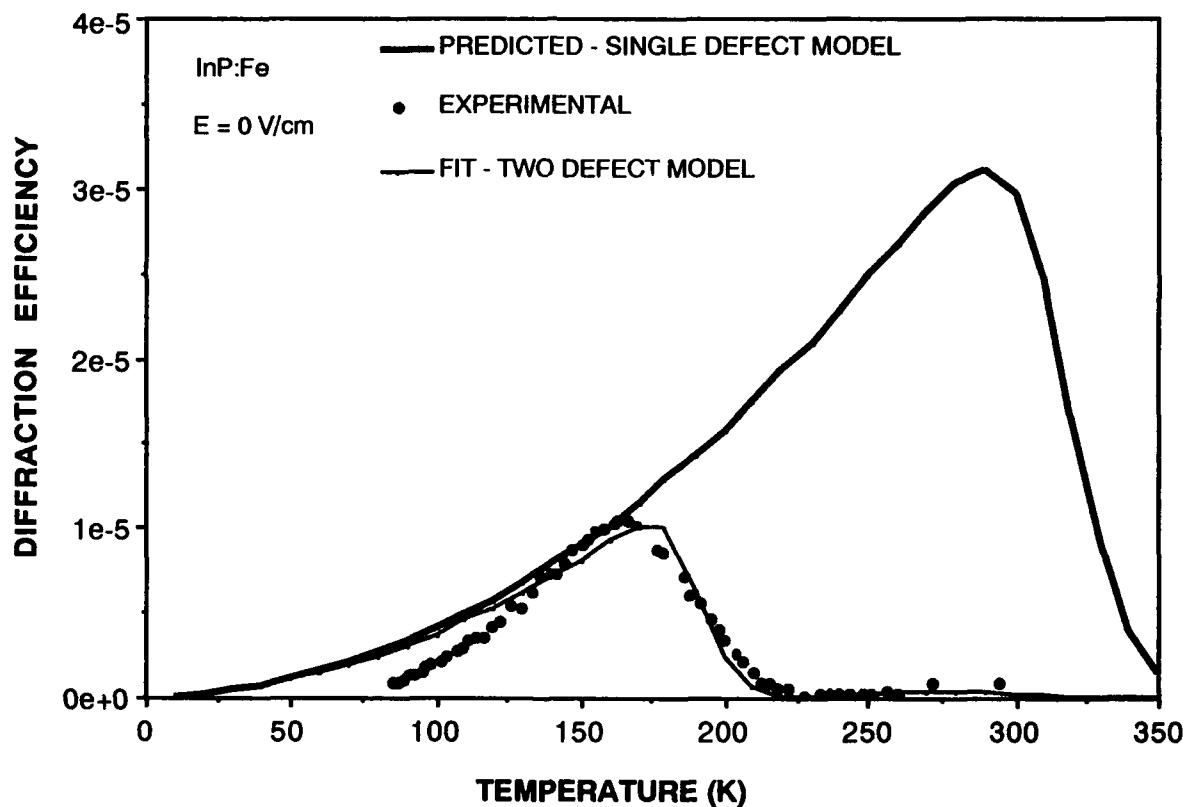


Fig. 2 Diffraction efficiency as a function of temperature. The two solid curves represent predicted diffraction efficiencies from SDM and TDM.

The temperature dependance of the diffraction efficiency is shown in Fig(2). The pump beam power was 45 mW/cm² and the probe beam was

sufficiently small so that no erasure of the diffraction grating occurred during read-out. The diffraction efficiency exhibits a marked temperature dependence, with a peak at about 170 K. At about 225 K the diffracted signal is completely quenched because of the cancellation of the index grating due to equal contributions from electrons and holes. This is consistent with 2WM data. The diffraction efficiency goes through another smaller peak before it drops off again at high temperature due to dielectric relaxation. This behavior is in sharp disagreement with the prediction from the SDM. The results of SDM and TDM are compared with experimental data in Fig(2). An excellent fit to the data is obtained from TDM for exactly the same parameters that were used for 2WM data. The drop off of the diffraction efficiency at low temperature is due to the non-equilibrium screening of the photorefractive effect [5].

In conclusion, we have demonstrated that multiple defect levels can lead to dramatic effects, altering the photorefractive behavior to such an extent that the direction of beam coupling can change sign. When measurements are made only at room temperature, it is not possible to isolate the effects from additional defect levels in the material. Temperature-dependent photorefractive measurements provide a wealth of information on the material, and can explain room temperature experimental results. In particular, the reduced gains reported in InP:Fe at room temperature are likely due to multiple defects.

References:

- [1] P. Günter and J. P. Huignard, eds., Photorefractive Materials And Applications I, II, vol. 61, 62, Springer-Verlag series.
- [2] A. M. Glass, M. B. Klein and G. C. Valley, Electron. Lett. 21, 4326 (1985)
- [3] R. S. Rana and D. D. Nolte (to be published)
- [4] G. C. Valley et al., J. Appl. Phys. 64, 12 (1988)
- [5] D. D. Nolte, D. H. Olson and A. M. Glass, Phys. Rev. Lett. 63, 891 (1989)



Absorption Gratings with Multiple Levels

R. S. Cudney, R. M. Pierce, G. D. Bacher, and Jack Feinberg

*Departments of Physics and Electrical Engineering,
University of Southern California, Los Angeles, CA 90089-0484, Tel. (213) 740-1134*

92-18702

Absorption gratings can cause significant beam coupling in photorefractive crystals;^{1,2} in the case of BaTiO₃, we found gains as large as 1 cm⁻¹.³ This coupling is caused by the variation in absorption created by the spatially periodic distribution of empty and full trap sites throughout the crystal and it requires only one active level. There is also evidence that there are two or more photo-active levels in BaTiO₃, as well as in other photorefractive crystals. In BaTiO₃, these extra levels explain the sublinear intensity dependence of the photoconductivity,^{4,5} as well as light-induced absorption.^{6,7} Here we study the effects that multiple photo-active levels have on absorption grating coupling. We derive expressions for the two-beam absorption coupling gain vs. the magnitude of the grating wavevector k_g and show that it does not vanish as k_g tends to zero, in contrast to the single photo-active level case. This effect is verified experimentally and is used to evaluate the donor-to-acceptor density ratio in a BaTiO₃ crystal.

The extension of the band conduction model to include an arbitrary number of trap levels is straightforward: a rate equation is added for each new active level, and Gauss's law and the continuity equation are modified appropriately to account for these new trap sites. Consider the case of two-beam coupling due to absorption gratings. In the steady-state, for low modulation, single charge-carrier type, and with a negligible photogalvanic effect, the intensity of the weak beam will grow (or decrease, according to the particular crystal) exponentially with distance. The gain per unit length $\gamma_{\text{abs}}(k_g, I)$ is a complicated function of the optical intensity I ; nevertheless, for a given intensity the dependence on k_g takes a remarkably simple form,

$$\gamma_{\text{abs}}(I, k_g) = \frac{\Gamma_{\text{abs}}(I) (k_g/k_0(I))^2 + \Phi(I)}{1 + (k_g/k_0(I))^2} |\hat{e}_1 \cdot \hat{e}_2^*|^2. \quad (1)$$

where the term $|\hat{e}_1 \cdot \hat{e}_2^*|^2$ is the dot product of the polarizations of the beams. The term containing k_g^2 in the numerator of Eq. (1) arises from the diffusion of mobile charge carriers. $\Gamma_{\text{abs}}(I)$ is a function of the densities of the different photo-active levels, their recombination, optical and thermal excitation rates, and the difference of the optical cross-sections for trap sites that are full or empty.

The term $k_0(I)$ is the effective inverse screening length. For the special case of a single active level it is independent of the optical intensity, but the inclusion of more than one level makes it intensity dependent. Its definition is found in Ref (8) .

The coupling also includes an "offset" term $\Phi(I)$, which is the absorption grating coupling that prevails when k_g is made arbitrarily small. It is caused by holes that are excited from one trap site level and recombine into another *without* migrating. Since this charge transfer process does not rely on diffusion it is not proportional to k_g^2 . If there is only a single active level the term $\Phi(I)$ cannot appear. This offset is the grating analog of the bulk light-induced absorption.^{6,7} The possibility of this term was first suggested by Tayebati⁹ and also by Knyaz'kov and Lobanov¹⁰ for the special case of two active levels.

We measured the two-beam absorption grating coupling in BaTiO₃ using a geometry where the electro-optic coupling is zero. This was accomplished by aligning the crystal's c-axis perpendicular to the grating wavevector, and by polarizing both beams in the plane of incidence. Details of the experimental procedure are given in Ref (3). Fig. 1 shows the two-beam coupling gain per unit length γ_{abs} in a BaTiO₃ crystal ("Free"). Here we fixed the wavelength at $\lambda = 488$ nm and varied the crossing angle between the two optical beams. The solid lines in Fig. 1 are fits to Eq.(1). It is clear that the coupling strength does not approach zero in the vicinity of $k_g = 0$ as it would in the single-level model; furthermore, the coupling is seen to flip from gain to depletion. Fig. 2 shows the absorption grating gain in the same crystal at 3 different wavelengths. In all cases the gain changes similarly with intensity, but the size of $\Phi(I)$ decreases with increasing wavelength. At $\lambda = 515$ nm, $\Phi(I)$ is so small that we missed it in our previous work.³

In order to compare the intensity dependence of the offset $\Phi(I)$ to our theoretical model, we must choose the number of active levels. The simplest case is to assume only one active donor level and one active acceptor level. We also assume only hole conduction and we ignore thermal excitation from the deep donor level but not from the shallow acceptor level. Even with these approximations there are four free parameters, which forced us to acquire a large number of data points over a wide range of intensity in order to make a meaningful theoretical fit. We measured the absorption grating two-beam coupling gain coefficient at $\lambda = 488$ nm in the "Free" crystal at a very small crossing angle (half-internal crossing angle $\theta_{int} = 0.16^\circ$); at this small angle the offset $\Phi(I)$ dominates the coupling. Figure 3 shows this data and the theoretical curve fit. The fitted parameters are $N_A/N_D = 0.97 \pm 0.02$, $I_C = 0.95 \pm 0.06$ W / cm², $\gamma_A s_D / \gamma_D s_A = 0.031 \pm 0.006$, and $N_D(\Delta\sigma_D - \Delta\sigma_A) = -6.2 \pm 0.5$ cm⁻¹, where N_A and N_D are the densities of the acceptor and donor sites, I_C is the intensity at which the optical and thermal hole excitation from the acceptor level are equal, s_A , s_D , γ_A , γ_D are the optical excitation and recombination coefficients from the acceptor and

donor levels, and $\Delta\sigma_A$ and $\Delta\sigma_D$ are the differences of cross-sections between empty and full donor and acceptor sites. Note that our crystal is almost perfectly compensated: $N_A \approx N_D$.

The same set of parameters must also describe the bulk light-induced absorption for the two-active level model described above. Fig. 4 shows the absorption of a weak probe beam vs. the intensity of an incoherent pump beam, and the solid line is the theoretical fit to the two-level model. The values of the fitting parameters agree very well with those obtained with the measurement of $\Phi(I)$: $N_A/N_D = 0.96 \pm 0.02$, $I_C = 0.73 \pm 0.06$ W/cm², $\gamma_A s_D / \gamma_D s_A = 0.033 \pm 0.007$, and $N_D(\Delta\sigma_D - \Delta\sigma_A) = -7.6 \pm 0.7$ cm⁻¹.

The effects of the absorption grating offset also appear in electro-optic measurements. We checked this by aligning the c-axis of the crystal parallel to the grating wavevector and by polarizing the beams in the plane of incidence. The observed coupling is the sum of the electro-optic and the absorption grating couplings γ_{eo} and γ_{abs} , which for small values of k_g is given by

$$\gamma = \gamma_{eo} + \gamma_{abs} \approx \text{const.} \times k_g + \Phi. \quad (2)$$

Figure 5 shows two sets of data taken in "Free" at $\lambda = 488$ nm and $\lambda = 458$ nm. The solid lines are linear fits to Eq. (2). The values of the Φ obtained from these fits agree with those obtained from the absorption grating data.

In conclusion, we predict that for a single type of charge carrier the absorption grating coupling vs. k_g is always of the form of Eq. (1), regardless of the number of photo-active levels. The "offset" of this coupling, Φ , is due to the diffusionless redistribution of charge among the different photo-active levels and is the grating analog to bulk light-induced absorption. By measuring the intensity dependence of this offset and by assuming a two-photo-active level model we were able to determine important parameters in a BaTiO₃ crystal, such as the ratio of donors to acceptors.

References

1. A. V. Alekseev-Popov, A. V. Knyaz'kov, and A. S. Saikin, *Sov. Tech. Phys. Lett.* **9**, 475 (1983).
2. R. B. Bylsma, D. H. Olson, and A. M. Glass, *Opt. Lett.* **13**, 853 (1988).
3. R. M. Pierce, R. S. Cudney, G. D. Bacher and J. Feinberg, *Opt. Lett.* **15**, 414 (1990).
4. L. Holtmann, *Phys. Stat. Sol. (a)* **113**, K89 (1989).
5. D. Mahgerefteh and J. Feinberg, *Phys. Rev. Lett.* **64**, 2195 (1990).
6. A. Motes and J. J. Kim, *J. Opt. Soc. Am. B* **4**, 1379 (1987).
7. G. A. Brost, R. A. Motes, J. R. Rotge, *J. Opt. Soc. Am. B* **5**, 1879 (1988).
8. D. D. Nolte, D. H. Olson and A. M. Glass, *Phys. Rev. Lett.* **63**, 891 (1989).
9. P. Tayebati, Ph.D. Dissertation, University of Southern California, (1989).
10. A. V. Knyaz'kov and M. N. Lobanov, *Topical Meeting on Photorefractive Materials, Effects and Devices II*, BP1-1 (1990).

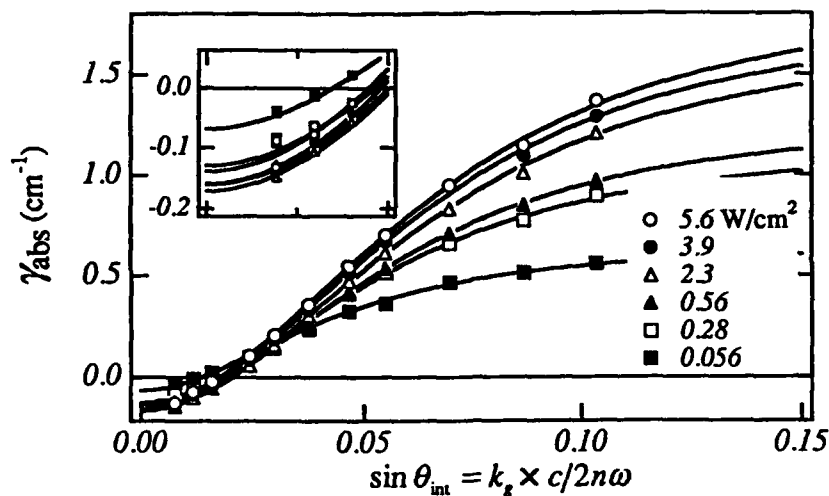


Fig. 1. Absorption grating gain per unit length vs. crossing angle at different intensities.

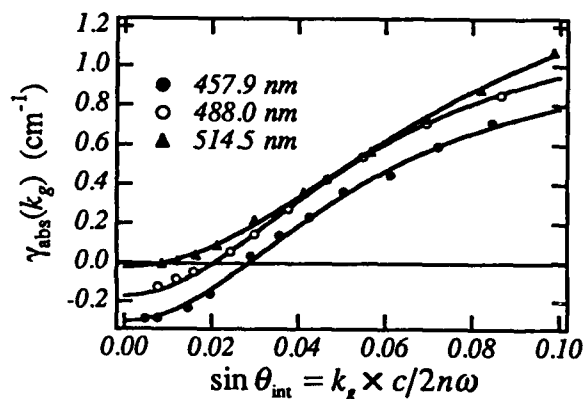


Fig. 2. Absorption grating gain per unit length vs. $\sin \theta_{int}$ at a fixed intensity at different wavelengths.

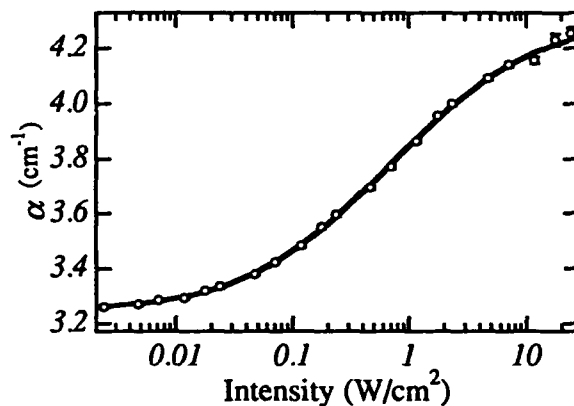


Fig. 4. Bulk absorption vs. intensity at $\lambda=488$ nm.

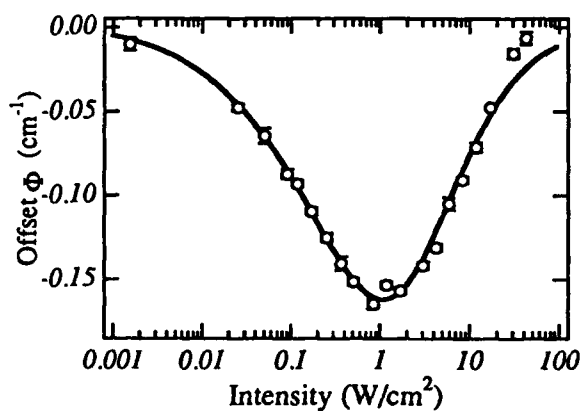


Fig. 3. Absorption grating gain per unit length vs. intensity at $\theta_{int}=0.16^\circ$ and $\lambda=488$ nm.

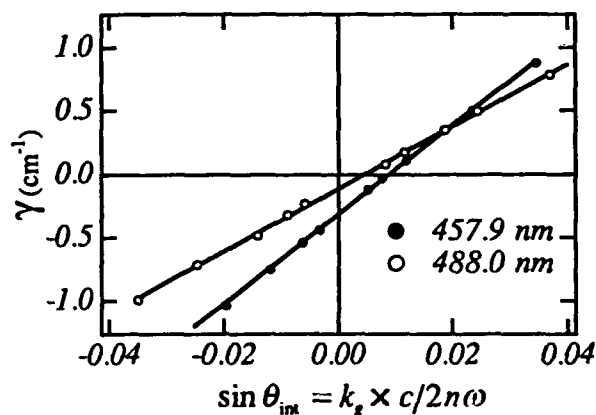


Fig. 5. Absorption plus electro-optic gain per unit length vs. $\sin \theta_{int}$ at a fixed intensity at two wavelengths.

AD-P006 715

**Hot Carrier Enhancement of Dember Photorefractive
Space-Charge Fields in Zincblende Semiconductors**

W. Andreas Schroeder, Thomas S. Stark, Arthur L. Smirl

Center for Laser Science and Engineering, University of Iowa, 124 AMRF, Iowa City, IA 52242
(319) 335 4580

and

George C. Valley

Hughes Research Laboratories, 3011 Malibu Canyon Road, Malibu, CA 90265

92-18703

SUMMARY

We use a novel, nondegenerate, polarization-sensitive, transient-grating technique¹ to monitor the picosecond dynamics of the photorefractive effect in undoped CdTe and InP:Fe at 960 nm. The technique circumvents the limited temporal resolution of the two-beam coupling geometry by using a time-delayed third probe pulse (with a duration of <5 psec) to read the gratings written in the semiconductor. The technique also exploits the crystal symmetry of zincblende semiconductors by using an optically induced anisotropy in the crystal index of refraction² to separate the photorefractive gratings from the stronger, co-existing instantaneous bound-electronic and free-carrier gratings. In both semiconductors, the photorefractive effect is associated with the Dember field between mobile electron-hole pairs, in contrast to the more conventional photorefractive space-charge field connected with the separation of a mobile carriers species from a stationary, but oppositely charged, mid-gap state. In the undoped CdTe sample, which possesses no optically-active mid-gap levels, the electron-hole pairs are produced by two-photon absorption of 1.3 eV photons across the 1.44 eV band-gap of the semiconductor. The resultant ~ 1 eV excess carrier energy, which allows hot carrier transport to dominate the initial formation of the space-charge field, causes up to an order of magnitude enhancement in the photorefractive effect on picosecond timescales. After the carriers have cooled and the initial overshoot in the space-charge field has decayed, the photorefractive effect is observed to decay as the Dember field is destroyed by ambipolar diffusion of the electron-hole pairs across the grating period. In InP:Fe on the other hand, the electron-hole pairs are produced predominantly by direct single-photon band-to-band absorption into the band-tail of the semiconductor (band-gap ~ 1.35 eV), since the iron dopant only dominates the linear absorption at longer wavelengths. This means that the carriers are generated with little excess energy. Consequently, no hot carrier enhancement of the photorefractive effect was observed, and once

formed, the Dember space-charge field decayed directly by ambipolar diffusion.

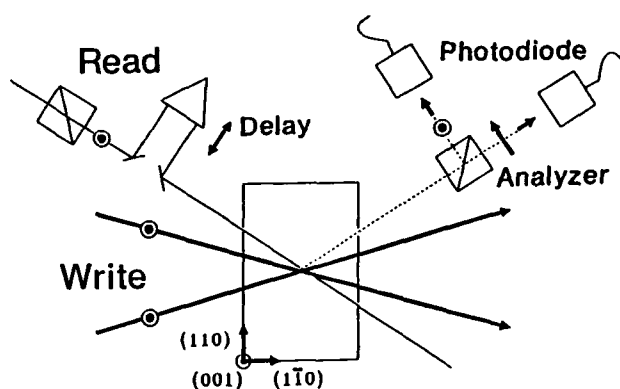


Figure 1
Experimental configuration.

The transient-grating technique¹, which is illustrated schematically in Fig. 1, has the advantage over the more conventional counter-propagating four-wave mixing geometry in that it maintains a high temporal resolution (<5 ps) with a background-free diffracted signal over long interaction lengths. The gratings were written by two s-polarized, 1 ps pulses at 960 nm generated by a synchronously amplified Styryl 13 dye laser system. A fraction of the 960 nm radiation was Raman shifted in benzene to produce a <5 ps, s-polarized $1.06 \mu\text{m}$ "readout" pulse, which was phase-matched to the $1.7 \mu\text{m}$ grating period written in the semiconductor. With semiconductor samples oriented as shown in Fig. 1, the signal diffracted from the photorefractive grating, which is p-polarized, was isolated from the s-polarized signal diffracted from the non-photorefractive (bound-electronic and free-carrier) gratings by placing an analyzer in the diffracted readout path. The photorefractive nature of the p-polarized diffracted signal was confirmed by showing that, as expected, this component of the diffracted signal disappeared when the sample was rotated by 90° so that the (001) crystallographic axis was parallel to the grating wavevector².

The measured diffraction efficiency of the photorefractive grating as a function of probe delay is shown in Fig. 2 for both InP:Fe and undoped CdTe at a writing fluence of $\sim 2 \text{ mJ/cm}^2$. Both results show an initial rise that roughly follows the accumulation of carriers during the photoexcitation process. In addition, in both cases we attribute the final decay of the photorefractive grating to a destruction of the Dember space-charge field by ambipolar diffusion at the lattice temperature, since we have shown that this decay rate is the same as that of the electron-hole free-carrier grating. The CdTe results, however, show an additional transient feature immediately following the carrier generation, which represents up to an order of magnitude enhancement in the photorefractive effect over that associated with the Dember field at the lattice temperature. We attribute this initial peak in the photorefractive response to an "overshoot" in the Dember space charge field while the carriers are hot. As the carriers cool, the space-charge field "recovers" by decaying to

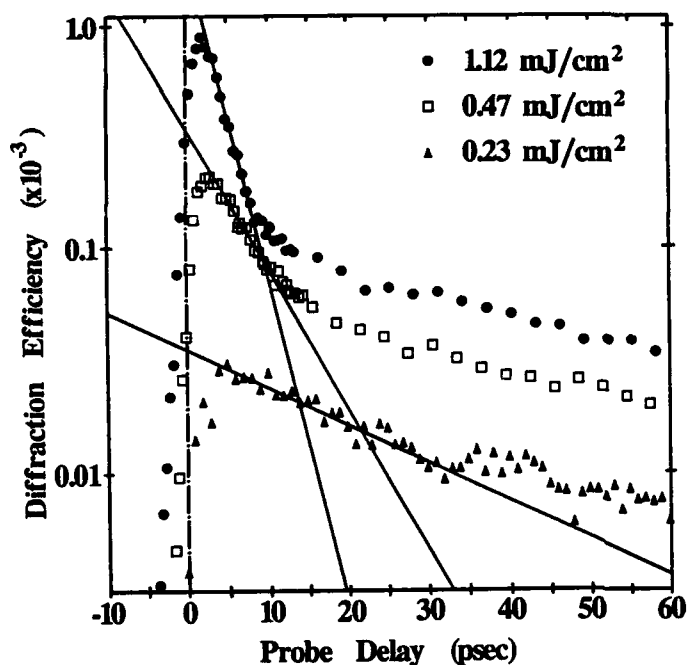


Figure 2

Photorefractive grating diffraction efficiencies versus probe delay for undoped CdTe and InP:Fe at a writing fluence of ~ 2 mJ/cm².

the value required for the ambipolar decay of the Dember field at the lattice temperature. Figure 3 shows that the decay of the overshoot in the Dember field is a strong function of the writing fluence - being of the order of (or shorter than) our temporal resolution at fluences > 1 mJ/cm², while approaching the final ambipolar decay rate for fluences less than ~ 0.2 mJ/cm². We emphasize that

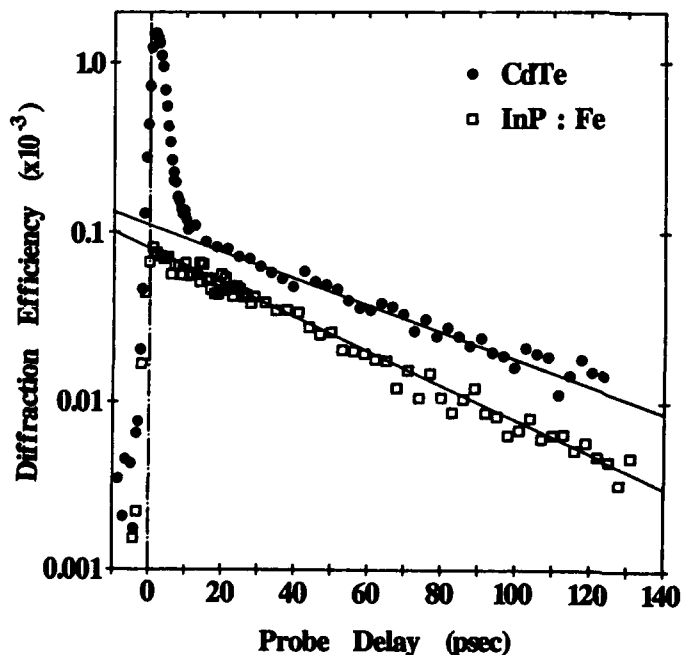


Figure 3

Photorefractive grating diffraction efficiencies versus probe delay for three different writing fluences in undoped CdTe.

we do not observe a similar transient feature in the photorefractive response of InP:Fe at any writing fluence.

The transient overshoot in the space-charge field E_{sc} can be understood by considering the effect that the excess carrier temperature has on the mobilities and diffusivities (and hence transport dynamics) of thermalized hot carriers. The magnitude of E_{sc} is determined by competition between the drift ($e\mu_j n_j E_{sc}$) and the diffusion currents ($eD_j \nabla n_j$) for the electrons ($j = e$) and holes ($j = p$), where n_j is the carrier density. True ambipolar transport, where the two carrier species move together, is established by the exact balance of these four currents. The diffusion coefficients D_j and mobilities μ_j are related by the Einstein relationship: $\mu_j k_B T_j = eD_j$, where T_j is the carrier (not the lattice) temperature and k_B is Boltzmann's constant. Consequently, at elevated carrier temperatures, the diffusion coefficient increases in magnitude relative to the mobility. Thus initially, the diffusion current dominates the drift current until, in response, an anomalously large space-charge field develops in an effort to balance the enhanced diffusion current. As the carriers cool (\sim ps), the diffusion coefficient (and diffusion current) decreases in magnitude relative to the mobility (and drift current), so that the Demmer space-charge field is reduced to its room temperature value in order to restore the current balance required for ambipolar diffusion. This recovery time, however, is limited by the dielectric relaxation time $\tau_{di} = \epsilon / (e\mu_e n_e)$, where ϵ is the permittivity of the medium. Thus, if τ_{di} is less than the carrier cooling time τ_c , the "hot" space-charge field will decay initially in a time τ_c . Alternatively, if τ_{di} is greater than τ_c , then the overshoot in the Demmer field will decay with a time constant given by τ_{di} . Consequently, as observed with the undoped CdTe sample (Fig. 3), the decay of the transient enhanced photorefractive response is expected to be fluence dependent since the dielectric relaxation time τ_{di} is a function of the generated carrier density n_j .

We emphasize that we also observe similar hot carrier enhancements of the photorefractive responses of GaAs:EL2 and CdTe:V, because in these semiconductors, at a wavelength of $\sim 1 \mu\text{m}$, the carriers are generated with significant excess energy both from the mid-gap states and by two-photon absorption.

References

1. W. A. Schroeder, T. S. Stark, M. D. Dawson, T. F. Boggess, A. L. Smirl and G. C. Valley, *Optics Lett.*, **16**, 159 (1991).
2. P. Yeh, *J. Opt. Soc. Am. B*, **4**, 1382 (1987).

AD-P006 716

**DETECTION OF LOW INTENSITY OPTICAL
WAVEFRONTS USING NOISE REDUCTION TECHNIQUES IN
PHOTOREFRACTIVE AMPLIFIERS**

H. Rajbenbach, A. Delboulbé and J.P. Huignard
Thomson-CSF, Laboratoire Central de Recherches
Domaine de Corbeville, 91404 Orsay Cedex, France

Noise reduction techniques in photorefractive amplifiers are centrally important for numerous applications in image processing, pattern recognition and detection of ultra-low optical wavefronts. Recently original techniques for reducing the optical noise were proposed and experimentally demonstrated⁽¹⁻³⁾. Rotating the crystal is a very general method which successfully removes the amplified scattered noise and the multiple interface parasite reflections. In this paper, we propose an alternative for which no mechanical movement is required. As will be detailed in the following, this new noise reduction method is mostly suited to photorefractive materials which exhibit a strong resonance of the two-wave mixing gain around the optimum angle between the injected signal and the pump beam.

The principle of noise reduction is based on the observation that a large contribution of the beam fanning originates from optical oscillations between the crystal faces. These oscillations build up, because the exponential gain coefficient Γ is large enough to overcome the bulk absorption and interface reflection losses⁽⁴⁾. The condition for these oscillations can be written as $\Gamma > \Gamma_{th}$, where

$$\Gamma_{th} = 2\left(\alpha - \frac{\text{Log}R}{l}\right);$$

Γ_{th} is the two beam coupling threshold exponential gain coefficient, α is the crystal absorption, R is the reflection coefficient on the crystal interface and l is the interaction length. Typical values for the above parameters in materials such as BSO, GaAs and BaTiO₃ in their optimum gain configurations are $\Gamma \sim 8$ - 20 cm^{-1} , $\alpha \sim 1 \text{ cm}^{-1}$, $R = 0.2$ and $l = 1 \text{ cm}$. In such conditions the oscillation threshold is easily attained ($\Gamma_{th} \sim 5 \text{ cm}^{-1}$ with the above data) and numerous oscillations modes build-up between the crystal faces. The principle of noise reduction in bandpass-type photorefractive amplifiers is shown in Fig.1. The pump beam P_0 and a signal S_0 illuminate the crystal in a two wave mixing configuration. The crystal input face is tilted by an angle ϕ with respect to the

92-13704

pump beam. Let Γ_ϕ be the exponential gain coefficient associated to the interaction between the pump beam and the interface oscillating modes around the angular direction ϕ . Then the oscillations are not allowed to build up if $\Gamma_\phi < \Gamma_{th}$. On the other hand, the angle θ between the pump beam and the injected signal beam is chosen for maximum two beam coupling gain. In other words, high signal-to-noise ratios are expected when the two following conditions are met simultaneously : (i) the pump-to-signal angle belong to the bandwidth of the amplifier while (ii) the oscillating noise directions are rejected out of the amplifier bandwidth. Due to its very narrow angular bandpass characteristics, we have performed noise measurement experiments with a photorefractive BSO crystal. The crystal aperture is 5 x 5 mm and the interaction length is 1 cm. An electric field $E_0 = 9$ kV/cm is applied along the (001) direction. The incident pump beam illumination is $I_0 = 7.5$ mW/cm² from a CW single longitudinal mode Argon-ion laser operating at 514.5 nm wavelength. The optical noise is measured with a large aperture detector shown in Fig.1. Its total intensity variation as a function of the angular position of the crystal is shown in fig.2. The lower curve corresponds to the case where antireflection coated glass plates are bounded to the crystal with an index matching oil (residual reflection $\sim 7\%$). All the measurements are performed with light polarized perpendicular to the applied electric field and incident pump beam. The main characteristics that can be drawn from these curves are twofold. First, the optical noise intensity is lower with antireflection glass plates on the crystal. Second the optical noise drops drastically when the crystal is strongly tilted. In addition, largest noise intensity always occurs for slightly tilted crystals. These behaviors can be understood in terms "oscillating noise modes" that build up between the two external crystal faces. When the crystal is tilted or antireflection coated, the number of oscillating Fabry-Perot modes that reach the threshold condition ($\Gamma_\phi > \Gamma_{th}$) decreases, resulting in an overall decrease of the optical noise in the output plane. It is noticeable that maximum of noise occurs for $\phi = 1^\circ$. This value is close to the optimum signal-to-pump angle $\theta \sim 1^\circ$ that produces high gain in two-beam coupling with BSO. A 6° tilt is sufficient to suppress most of the noise at the output. Similar experiments performed with tilted BaTiO₃ were not successful with respect to reducing the optical noise. This correlated well with the large acceptance angle of BaTiO₃ amplifiers that enables off-axis oscillating noise modes to build-up in the crystal. In addition, the large gain of our crystal ($\Gamma > 15$ cm⁻¹) may also produce beam fanning without the need of any feedback effect, i.e., with a single pass amplification of scattered light.

To demonstrate low-noise amplification of very weak signals carrying spatial information, a test object slide is inserted across the signal beam path in a nearly degenerate two-beam coupling configuration (moving grating recording). To improve the homogeneity across the amplified image, a diffusing screen is placed in front of the test slide. The resulting intensity at the entrance face of the crystal is $I_s = 35 \text{ nW}$ (fig.3a). The photorefractive BSO crystal is sandwiched between the two AR coated glass plates. Finally, the pump-to-signal angle is adjusted for maximum coupling ($\theta = 2^\circ$) and an electric field $E_o = 8.4 \text{ kV/cm}$ is applied to the crystal. For untilted crystal, the amplified image is buried in a strong background noise (Fig.3b). The crystal is then tilted with $\phi = 5^\circ$. In addition to a tilt in the horizontal direction, a tilt in the vertical direction ($\phi' = 9.5^\circ$) further improves the signal-to noise ratio. Fig.3c shows the amplified image. The measured input-output gain is about 30 and all the background noise has been removed.

The amplification of ultra-weak signals is a straightforward application of this noise reduction technique. We will present the detection of optical wavefronts in the picowatt range.

References :

- (1) H.Rajbenbach, A. Delboulbé, J.P. Huignard - Opt. Lett. 14, 1275 (1989).
- (2) J. Joseph, P.K.C. Pillar, K. Singh - Opt. Comm. 80, 84 (1990).
- (3) M. Ewbank - Proceeding of the Optical Society of America annual meeting, paper FS 1, p 251 (1990).
- (4) A. Novikov, S. Odulov, O. Oleinik, B. Sturman - Ferroelectrics, 75, 295 (1987).

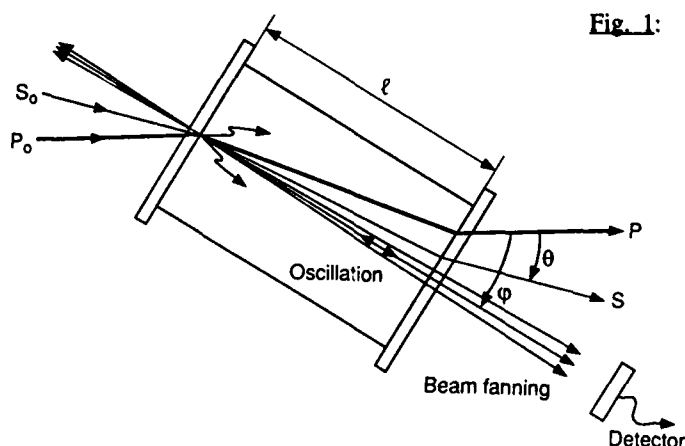


Fig. 1: Two-wave mixing in a tilted photorefractive crystal. The optical noise due to Fabry-Perot oscillator between the crystal faces can be suppress in sufficiently narrow angular bandwidth amplifiers. The signal beam S_o is

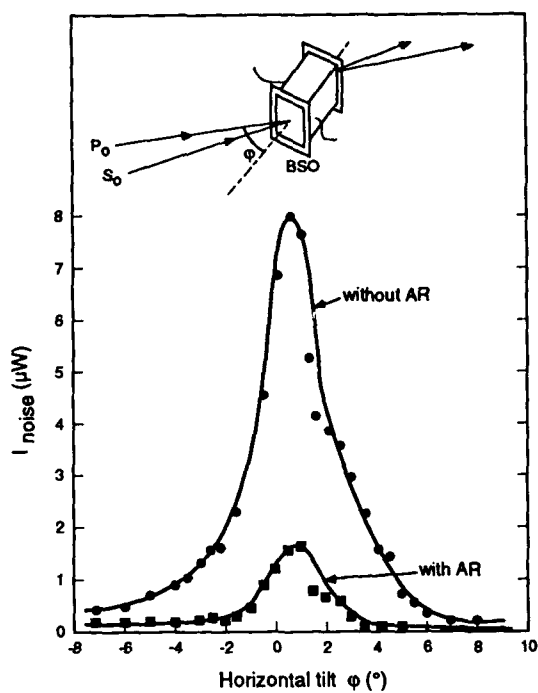


Fig. 2 : Noise power in photorefractive BSO versus tilt of the crystal. Top curve : without antireflection coated glass plate bottom curve: with antireflection coated glass plate.

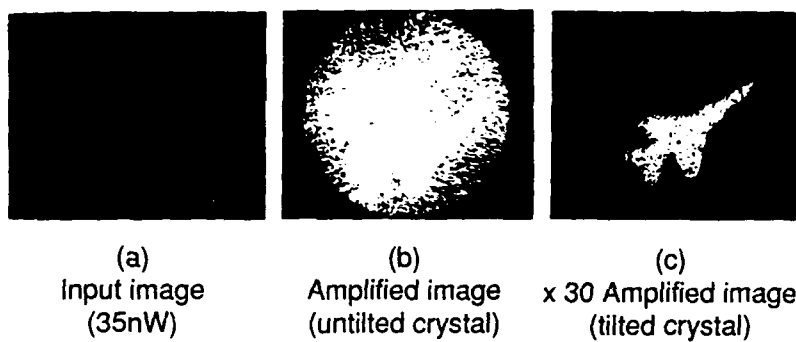


Fig. 3: Low-noise image amplification with tilted BSO crystal
 (a) input image
 (b) amplified image without tilt
 (c) amplified image with tilt

AD-P006 717



**Fundamental Noise Limits
in Photorefractive Systems**

Frederick Vachss

Claire Gu

John Hong

Tallis Chang

**Optical Information Processing Department
Rockwell International Science Center
Thousand Oaks, CA**

92-18705



When photorefractive materials are included as elements in image and signal processing systems, the dynamic range of the photorefractive element has a significant impact on the overall performance of the system. Evaluating the limits on this dynamic range is of particular importance if we hope to provide a realistic comparison of photorefractive devices such as spatial light modulators ^{1,2} or integrating correlators ³ with similar devices based on competing opto-electronic technologies. We must thus determine the range of signal beam intensities which may be used to write a holographic grating with a reference beam of some fixed intensity, or in other words, the maximum beam ratio that will cause a detectable refractive index grating to be written within the photorefractive material.

Before beginning our description of the noise sources affecting the performance of photorefractive devices, we must clarify what we mean by "noise". In most common photorefractive holograms the limit on achievable dynamic range is due to deterministic sources of light obscuring the signal. The most predominant among these is scattering from defects both on the surface and within the volume of the photorefractive crystal. In particular, in materials with high two beam coupling gain the amplification of such scattered light resulting in beam fanning severely restricts the observability of weak holograms written in the material ⁴. The effects of such deterministic "noise" sources can be reduced, however, by using (or developing) relatively defect-free materials and through various lock-in detection techniques. Even if such methods are used and these sources of signal bias are completely removed, however, there exist fundamental limits on the observability of weak holograms in photorefractives due to the statistics of the material itself and of the light used to write the grating. The determination of these fundamental limits is the goal of this paper. While an accurate estimate of these limits requires a detailed analysis of the various noise processes operating in the material, we will describe these processes here in a non-rigorous fashion to show the regimes in which they become significant. We have carried out a rigorous probabilistic analysis of these processes elsewhere, but the essential results thus obtained are equivalent to those presented here.

Assuming our hologram is written using a reference beam of some fixed intensity I_R and a much weaker signal beam of intensity $I_S \ll I_R$, two effects become increasingly noticeable as I_S is decreased. First, since the modulation depth of the interference pattern,

$$m \equiv 2 (I_R I_S)^{1/2} / (I_R + I_S) \approx 2 (I_S / I_R)^{1/2} , \quad (1)$$

is decreased the amplitude of the space charge field within the material is decreased proportionally. When this amplitude is so small that the variation in charge over a grating period approaches e , the charge of a single carrier, clearly the continuum model of charge build-up used in the standard photorefractive band transport model ⁵ is inaccurate. When this regime of operation is reached, statistical fluctuations in the locations of charge trapping centers cause commensurate fluctuations in the space charge field. In particular we find that these fluctuations result in noise of comparable magnitude to the output signal diffracted from a photorefractive hologram when the ratio between the signal and reference intensities reaches a value of

$$I_S / I_R \approx m^2 / 4 \sim (N_A V)^{-1} \quad (2)$$

where N_A is the effective trap density in the photorefractive material and V is the volume of the grating being read. The minimum detectable beam ratio is thus expressed as a function of the total number of charge trapping sites present in the grating volume.

In addition to the effects of charge discretization, another noise source becomes significant in the regime of weak grating modulation. When the modulation depth is reduced sufficiently so that the number of photons from the signal beam arriving at the photorefractive crystal during the time required for holographic recording is small, statistical fluctuations in this intensity will affect the recording process. Specifically, photon noise of this sort will overwhelm the diffracted output signal when the total number of signal photons arriving at the crystal during a recording time approaches unity, or

$$I_S A \tau / h\nu \sim 1 \quad (3)$$

where A is the cross-sectional area of the grating, τ the photorefractive recording time and $h\nu$ the photon energy. We note, however, that the recording time may be expressed as ⁶:

$$\tau = \tau_{di} \times f \quad (4a)$$

where f is a dimensionless factor dependent on the charge transport properties of the material, but close to unity when the characteristic electric fields within the material due to drift and diffusion are small. Here τ_{di} is the material's dielectric relaxation time given by :

$$\tau_{di} = h\nu \epsilon \gamma N_A / (4\pi \mu e \alpha I_0) \quad (4b)$$

where ϵ , μ and α are the dielectric constant, mobility and optical absorption of the material, respectively, γ is the charge carrier recombination coefficient and $I_0 \approx I_R$ is the total optical intensity.

Combining these results we may thus re-express (3) as:

$$I_S / I_0 \sim 4\pi \mu e / (\epsilon \gamma f N_A V) \quad (5)$$

which expresses the minimum writing beam ratio as a material dependent parameter divided by the total number of trap sites in the grating volume - and is in fact equivalent to the result given in (2) above apart from the dimensionless leading factor, $4\pi \mu e / (\epsilon \gamma f)$. Thus depending on the value of this leading factor, either the fluctuations in the signal intensity or the charge density will provide the limiting noise source.

In particular, we find that in materials such as BSO with relatively long recombination times, this leading factor is correspondingly large and expression (5) above provides the operating limit. Conversely, materials such as BaTiO₃ with very rapid recombination times are dominated by charge discretization noise and operate under the limit given in (2). Using expression (2) we thus find that for materials such as BaTiO₃ we may expect a minimum detectable beam ratio as low as

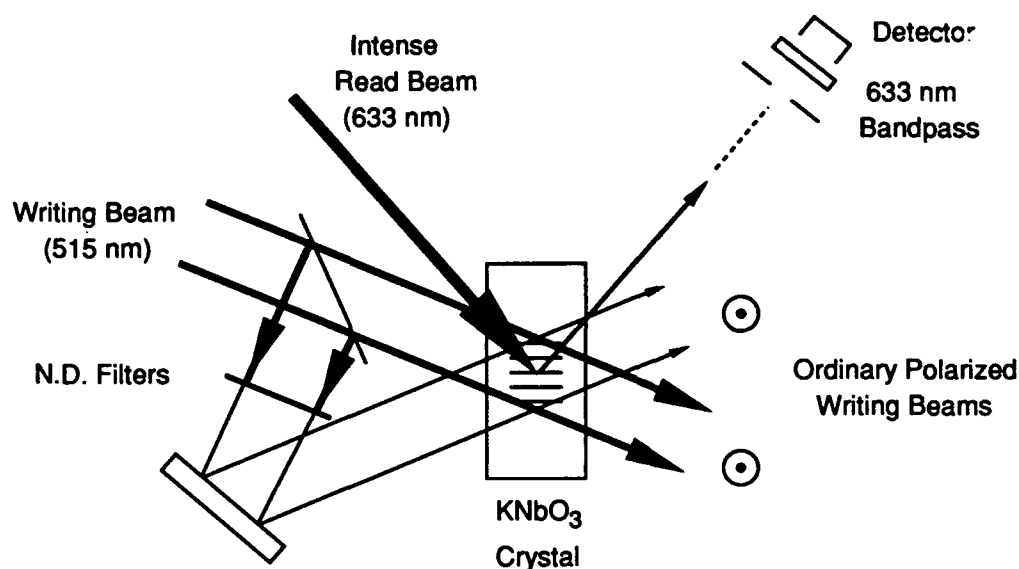
10^{-16} if a full 1 cm^3 grating volume is used, but only $10^{-13} - 10^{-14}$ if unexpanded beams (resulting in a reduced grating volume) are used. In practice, however, experimental conditions must be very carefully controlled if gratings written with such extreme beam ratios are to be detected.

In attempting to find the minimum detectable beam ratio experimentally one must eliminate all sources of stray light normally regarded as noise. Specifically, specular reflection from crystal edges must be avoided by routing all beams through the central portion of the material. Similarly, the fluctuation limited performance we describe can only be achieved if relatively defect-free crystals are used to minimize scattering from the material. In a related requirement, amplified scattering due to photorefractive beam fanning must be minimized. This in turn requires that the writing beams be polarized in an orientation reducing the effective electro-optic coefficient (and hence the photorefractive two-beam coupling gain) to a minimum.

In addition to these restrictions on the recording procedure, care must be taken in the process through which the output light diffracted from the photorefractive grating is detected if low modulation depth holograms are to be observed. In particular, the beam used to read out the hologram should be of a wavelength only weakly absorbed by the material. This has a two-fold advantage. First, any light scattered from the writing beams may now be blocked by placing a band-pass filter in the diffracted output beam path. Second, a relatively intense read beam may be used without disturbing the grating and hence I_{OUT} , the intensity of the diffracted output beam, may substantially exceed the weak I_S . Additional noise due to low intensity fluctuations in I_{OUT} is thus avoided. As a final requirement, to minimize the effect of scattered light, the detector into which I_{OUT} is directed should only sample a solid angle corresponding to the diffraction limited cone propagating from the grating aperture (i.e. on the order of λ^2/A where λ is the wavelength of the read beam and A is the area of the grating). Any larger detection angle increases detected noise without appreciably increasing the signal and any smaller unduly limits the detected output power.

These recording and detection conditions were implemented in an experimental set-up as depicted in Fig. 1, on the following page. Here an expanded and collimated 515 nm beam from an Ar+ laser is split into two components - one of which is severely attenuated by a set of neutral density filters. These two beams are then interfered in the center section of a photorefractive crystal (KNbO_3 and BaTiO_3 in successive trials), with both beams ordinary polarized to minimize fanning. The resultant photorefractive grating is then probed by an unexpanded 633 nm beam from a HeNe laser yielding an effective grating volume of about 1 mm^3 . The diffracted output light is detected by a photomultiplier tube after passage through a 1 mm diameter aperture 1 m from the crystal followed by a 633 nm bandpass filter. The signal to noise ratio is determined by blocking and unblocking the weak pump beam and comparing the steady state signal at the detector.

Following this procedure, the minimum beam ratio we have been able to detect is roughly $(I_S / I_R) \sim 10^{-10} - 10^{-11}$ in both materials. Assuming that KNbO_3 like BaTiO_3 is charge discretization limited, however, the theoretical minimum for the grating volume used here is on the order of 10^{-13} . This 2 order of magnitude discrepancy thus implies that the grating detectability observed here is not limited by the fluctuation processes described in equations (2) and (5).



Specifically, we believe the noise source limiting our detection is related to the low light level reaching the detector. In our experiment the 633 nm read wavelength was chosen to reduce grating erasure yet remain in a range to which our detectors were sensitive. Unfortunately, as both photorefractive materials we have used remain somewhat photosensitive at this wavelength, it was necessary to keep the read beam intensity at roughly the level of the reference, I_R . This resultingly weak output beam intensity I_{OUT} thus reaches the noise limit of our photodetector before the intrinsic photorefractive noise levels are reached. Future experiments in which more intense read beams at near infrared wavelengths are used in conjunction with detectors sensitive in this range are planned to circumvent this limitation. In the interim, the experimental and theoretical results we have presented provide a good idea of the typical and ultimate limits, respectively, on the dynamic range that may be achieved in photorefractive holographic devices.

Acknowledgments

The authors gratefully acknowledge the support of the US Air Force through Rome Laboratories under contract # F30602-89-C-0181

References

1. Y. Shi, D. Psaltis, A. Marrakchi, A. R. Tanguay, "Photorefractive Incoherent-to-Coherent Converter", *Appl. Opt.* **22**, 3665 (1983).
2. F. Vachss, J. Hong, P. Yeh, "Temporal Integration Using the Photorefractive Square-Law Converter", *Proc. SPIE* **1291**, 68 - 74 (1990).
3. J. Hong, J. Yu, S. Hudson, D. Psaltis, "Photorefractive crystals as adaptive elements in acousto-optic filters", *SPIE Proceedings* **789**, 39 (1987).
4. H. Rajbenbach, A. Delboulbe, J. P. Huignard, "Noise Suppression in Photorefractive Image Amplifiers", *Opt. Lett.* **14**, 1275 - 1277 (1989).
5. N. V. Kukhtarev, V. B. Markov, S. G. Odulov, M. S. Soskin, V. L. Vinetskii, "Holographic Storage in Electro-optic Crystals, I: Steady State", *Ferroelectrics* **22**, 949 - 960 (1979).
6. G. C. Valley, M. B. Klein, "Optimal Properties of Photorefractive Materials for Optical Data Processing", *Opt. Eng.* **22**, 704 - 711 (1983).

Photorefractive Noise Suppression using Achromatic Gratings

by

W. S. Rabinovich, G. C. Gilbreath[†] and B. J. Feldman

Laser Physics Branch

Naval Research Laboratory

Washington, DC 20375

AD-P006 718



Abstract

We show that achromatic grating techniques can suppress beam fanning while still allowing two beam coupling to occur.

Summary

Photorefractive beam fanning is a well known effect in which a collimated beam of light is scattered into a broad fan as it propagates through a crystal which exhibits high two wave mixing gain^{1, 2}. Beam fanning can be a very strong effect, removing almost all the light from the initial beam. It has been proposed² that the fan originates from scattering off defects in the crystal, which then become amplified by the two beam coupling process. Beam fanning can be beneficial, for instance, in allowing self-pumped phase conjugation³. But it can also be an undesirable competing nonlinear effect. For example, it may prevent high gain image amplification by two beam coupling, by robbing the pump and signal beams of light⁴. In this letter, we demonstrate that two beam coupling, using achromatic gratings, can suppress beam fanning that would otherwise occur.

Achromatic grating techniques are used to create high visibility fringes using broadband sources⁵. A diffraction grating splits a broadband beam into diffraction orders. Two orders, generally either the +1 and -1 or 0 and 1, are allowed to pass and the others are blocked. Either achromatic lenses, or a second grating, are used to recombine the beams. Because of the linear dispersion of the grating, all colors produce an interference pattern of the same spacing and phase.

In previous work⁶, we showed that an achromatic system (using the +1 and -1 orders) with an argon-ion laser operating on all lines could produce nearly the same two beam coupling gain as a single line (514.5 nm) argon-ion laser of the same intensity. Using the +1 and -1 orders of the diffraction grating produces a perfectly achromatic volume hologram, but, in order for the achromaticity to be preserved inside the crystal, the angle between the bisector of the pump and signal beams and the crystal surface normal must be zero⁶. An alternative is to use the +1 and 0 orders of the diffraction grating. This produces a pattern that is achromatic only in a plane, and would normally not be efficient for creating volume holograms. However, Cronin-Golomb⁷ showed that, by rotating the crystal and grating in the plane of incidence, this lack of volume achromaticity can be approximately compensated for by the crystal dispersion.

[†] G. C. Gilbreath is with the Communications Systems Technology Branch, Naval Research Laboratory.

92-18706



If we adopt the viewpoint that beam fanning arises from scattering², then its development is as follows: Light from the initial beam scatters from a defect in the crystal. The scattered light

interferes with the initial beam and forms an interference pattern. The light generates carriers, which then diffuse, creating a volume phase grating in the crystal. Both the initial beam and the scattered beam are automatically Bragg matched to this grating. If the beam has been scattered towards the c-axis, it will be amplified by two beam coupling. As the scattered beam grows from noise, the fringe visibility grows, further increasing the gain from the noise-generated gratings. Eventually, a broad fan, that consumes much of the light of the original beam, is formed.

If, however, the initial beam consists of two colors, the situation may be different. Both colors will scatter off a defect, each creating its own Bragg grating which will be superimposed in the crystal. The light scattered from these gratings may destructively interfere, since the grating created by one color will not be Bragg matched to the other. If the grating formation rate of the two colors are balanced, then neither color may succeed in diffracting light from the initial beam into the scattered beams, and beam fanning will be suppressed. If one color does have a faster grating formation rate, then it will fan (though more slowly), but fanning in the other color may be suppressed.

Normally, this suppression of beam fanning would be of little practical utility, since most applications of photorefractive materials require the creation of a volume hologram, and two multicolor beams will not ordinarily form a hologram. The achromatic technique offers a way out of the difficulty. Using this method a volume hologram *can* be created with multicolor beams⁶. Further, since the conditions for creating an achromatic grating are very special, it is unlikely that they will occur accidentally upon scattering off a defect. Hence beam fanning may be suppressed, while the creation of the desired volume hologram will not.

To test this hypothesis, we set up the experiment shown in Fig. 1. An argon-ion laser operating on all lines was the source. Using notch filters, and variable attenuators, a beam, consisting of 488 nm and 514.5 nm light only, was created, with a controllable ratio of the two colors, and a fixed total intensity. The laser light was then split into pump and signal beams using the achromatic arrangement proposed by Cronin-Golomb⁷. The signal beam was the zeroth order of the grating and the pump was the first order. The diffraction grating had a spacing of 5 μm , and its tilt angle, along with that of the photorefractive crystal, was 28°. The crystal, BaTiO₃, supplied by Sanders, was rotated so that the projection of the K vectors of the pump and signal beams were anti-parallel to the c-axis. The mean external half angle between the beams was 2.85°. The pump and signal beams had equal intensities of 6 mW/cm², diameters of 1.2 mm, and were polarized in the plane of incidence. The interference pattern formed in the crystal had a spacing of 5 μm . The dimensions of the crystal were 5 mm x 5 mm x 7 mm.

Fig. 2 shows the effective gain of the signal beam as a function of time. All measurements were taken by allowing both the pump and the signal beam to enter the crystal at time=0. The effective gain is defined as the signal intensity at a given time divided by its intensity at time=0. Between runs, the gratings in the crystal were erased by illuminating it with a Helium-Neon laser whose beam was translated to prevent the formation of beam fanning gratings. Near the end of each run, the pump beam was blocked. This allowed measurement of the final effective gain, and the degree of extinction of the signal beam. When the light entering the crystal was monochromatic

(blue:green = 0:1, Fig. 2 a) no two beam coupling gain was observed, because the extinction due to beam fanning predominated. As the ratio of blue to green light became more nearly 1:1, Fig. 2d, the signal beam exhibited gain for a longer period of time. In the end, however, for all cases except 1:1, beam fanning ultimately depleted the two beam coupling gain. Even in the 1:1 case, a small amount of fanning was observed. This may be due to wavelength dependence in the grating formation rate. When there was more blue than green, as in the 1.25:1, Fig. 2e, case, fanning again depleted gain. The final gain coefficient, Γ , measured was highest for the 1:1 case, at 2.25 cm^{-1} , indicating that fanning reduced the two beam coupling gain in other cases, in addition to extinguishing the signal beam.

The beam fanning suppression was quite visible in the transmitted beam profiles. Fig. 3 shows the signal beam profile for both the monochromatic and two color achromatic cases. The first photographs show the profiles at the beginning of the run, and the second set, one minute later. In the monochromatic case, the fanning has extinguished the left half of the beam, but in the two color achromatic case, the beam retains its profile

A similar set of experiments was carried out in Ce:SBN:60 using the +1 and -1 orders of the diffraction grating. Suppression of beam fanning was again found, indicating that this technique may find general application.

In conclusion, we have demonstrated that beam fanning can be suppressed, while at the same time allowing two beam coupling, using an achromatic grating arrangement. This technique may have further application to the reduction of noise effects in image amplification, which may also result from two beam coupling off of scattering defects. Achromatic gratings may also suppress other stimulated scattering processes in photorefractive materials.

Acknowledgments

This work was funded in part by the Office of Naval Research.

References

- [1] Jack Feinberg, D. Heiman, A.R. Tanguay, Jr. and R. W. Helwarth, J. Appl. Phys. **51**, 1297, (1980).
- [2] V. V. Voronov, I. R. Dorosh, Yu. S. Kuz'minov and N. V. Tkachenko, Sov. J. Quantum Electron. **10**, 1346, (1980).
- [3] M. Cronin-Golomb, B. Fischer, J. O. White, A. Yariv, IEEE JQE, **QE-20**, 12, (1984).
- [4] G. C. Gilbreath, A. E. Clement, S. N. Fugera and G. J. Mizell, S.P.I.E. Proc., **1049** (1991)
- [5] B. J. Chang, R. Alferness and E. N. Leith, Appl. Optics **14** (1975) 1592
- [6] W. S. Rabinovich, C. G. Gilbreath and B. J. Feldman, accepted for publication in Opt. Comm.
- [7] M. Cronin-Golomb, Optics Lett. **14** (1989) 1297.

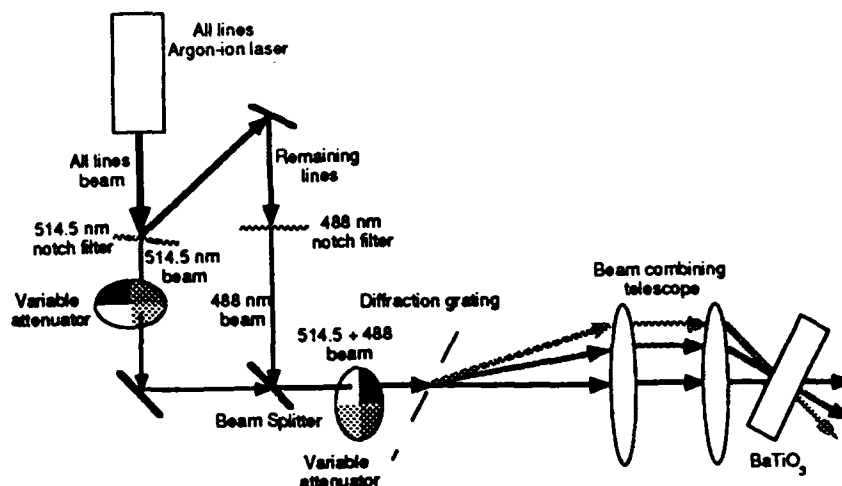


Fig. 1. Experimental Configuration used to study suppression of beam fanning using achromatic photorefractive coupling.

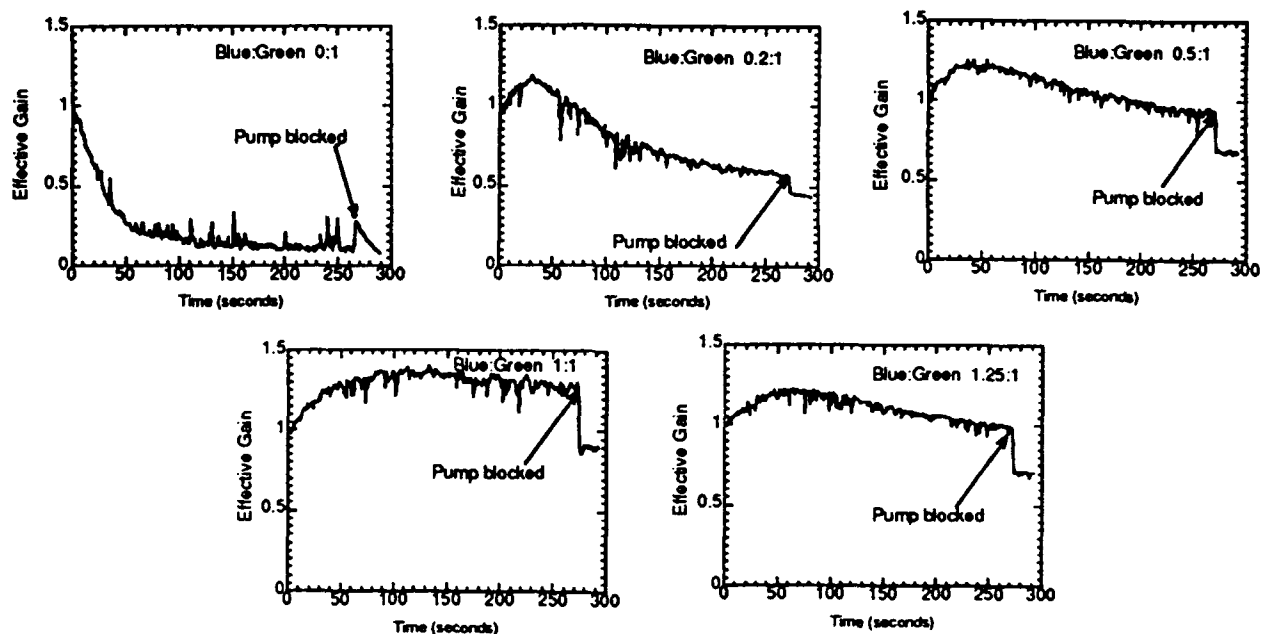


Fig. 2. Gain in signal beam as a function of time for various degrees of monochromaticity.

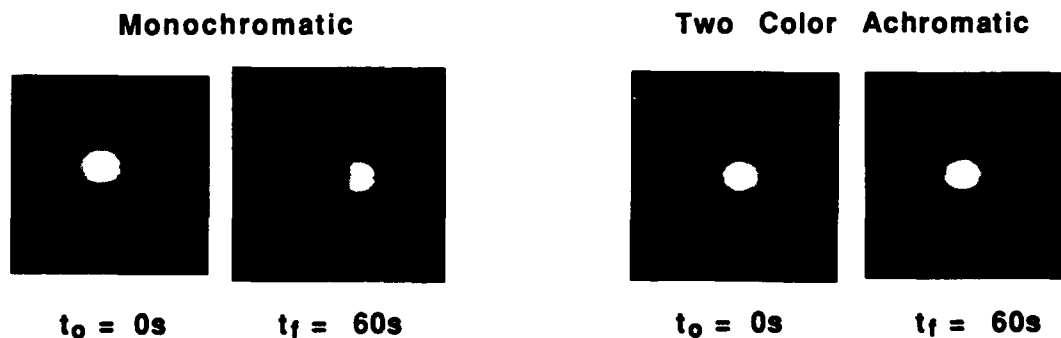


Fig. 3. Effect of fanning on beam profiles.



TWO-BEAM COUPLING WITH PARTIALLY COHERENT LIGHT

Hongzhi Kong, Wiesław Królikowski and Mark Cronin-Golomb
Electro-optics Technology Center, Tufts University,
Medford MA 02155

Introduction

In photorefractive two-beam coupling the interference of two optical beams creates a refractive index grating resulting in energy transfer between the two beams. In models describing this effect it is usually assumed that both beams have perfect spatial coherence. For some applications such as achromatic volume holography [1], multimode fiber gyroscopes and optical phase conjugation through turbulence, spatial coherence effects may become important in the coupling process. Reduced spatial coherence leads to lower contrast interference fringes in an interference fringe region smaller than that of the perfectly coherent case. In recent work, we have made a quantitative study of the influence of these effects on coupling under the assumption that the coherence properties of the interacting beams do not change during the coupling [2]. In the present work, we include the influence that beam coupling has on spatial coherence of the interacting beams. It is worth noting that the problem of spatial coherence in nonlinear wave mixing has been studied earlier [3-5]. However, all of these studies referred to the case of fast Kerr medium. Photorefractive materials are much slower and cannot follow fast changes of the phases of interacting beams. Thus description of the mixing process will be different.

Experimental

An experiment was arranged to study the possible change of beam coherence due to the coupling. The experimental setup used in our studies is shown in Fig.1. The laser beam from an Argon-ion laser ($\lambda=514\text{nm}$) is focused by lens L1 on a rotating disk of ground glass and the degree of coherence of the beam is controlled by changing the spot size on the ground glass. The partially coherent beam is collimated by lens L2 and separated by the beam splitter BS1 into a strong (pump) and a weak (signal) beams which subsequently interfere in a photorefractive barium titanate crystal. The crystal's orientation ensures the energy transfer from pump to signal. The amplified signal beam is then directed into an interferometer. The resultant interference fringes are imaged with a CCD camera and scanned with a 512×512 frame grabber with 256 gray levels. The fringe visibility is calculated from the scanned data. The visibility of the fringes gives direct information on coherence properties of the signal beam. If the beam were completely coherent, our arrangement would lead to a constant visibility in the fringe area. For partial coherence, the fringe visibility is the largest in the intersection center and drops symmetrically towards the sides [2]. With this apparatus, we were able to observe beam coherence changes due to the coupling process.

The measurements of the visibility were performed in two cases: without coupling (pump beam blocked) and with photorefractive coupling. The results are presented in Fig.2 where visibility of the fringes is shown as a function of position in the interference region. Both graphs reflect typical interference pattern of partially coherent beams. As is seen in Fig.2, we observed that 1): the coupling may cause changes in beam coherence, 2): the change is more significant in the wings rather than in the center and 3): the coupling tends to improve the beam coherence. The coherence properties of signal beam changes because energy transfer is distributed throughout the entire region of interaction. Therefore, various parts of the pump wave front contribute to the total light amplitude at every point of the signal beam, changing its statistical properties. This in turn lead to changes in correlation between any two points of the signal.

92-18707



Model

We used very simple model without diffractive propagation effects to describe interaction of partially coherent beams in photorefractive materials. Two optical beams (pump P and signal S) cross inside photorefractive crystal. For simplicity, we assume that region where beams overlap is completely inside the medium. The existence of suitable coordinate transformations means that we can also assume without loss of generality that the beams cross at right angles (beam S propagates along x axis and beam P along y axis). The crystal's orientation ensures that energy transfer occurs from pump to the signal. We represent both beams by their slowly varying amplitudes

$$\begin{aligned} P(x,y)\exp i(ky - \omega t) \\ S(x,y)\exp i(kx - \omega t) \end{aligned} \quad (1)$$

In the overlapping region the beams write a refractive index grating whose amplitude is proportional to the modulation index of the interference pattern

$$Q(x,y) = \frac{\langle S(x,y)P^*(x,y) \rangle}{\langle P(x,y)P^*(x,y) \rangle + \langle S(x,y)S^*(x,y) \rangle} = \frac{\langle S(x,y)P^*(x,y) \rangle}{I_P(x,y) + I_S(x,y)} \quad (2)$$

where brackets mean time or ensemble average. The averaging reflects the statistical properties of the beams (partial spatial coherence). The creation of the index grating in the crystal is slow compared to the fast phase variations of the input beams. If the crystal were sufficiently fast such as Kerr medium we could drop the averaging symbol in Eq.2. In the case of photorefractive material the averaging symbol can be dropped only for fully coherent light beams. We assume that pump beam is much stronger than the signal ($I_S \ll I_P$) and does not change amplitude in the interaction (also its statistical properties remain the same). Thus we can drop signal intensity from definition of $Q(x,y)$ (Eq.2) and arrive at the following equation describing evolution of the signal beam:

$$\frac{\partial S(x,y)}{\partial x} = \gamma Q(x,y)P(x) \quad (3)$$

where γ is a coupling constant.

Integration of this equation gives an expression for the grating amplitude

$$Q(x,y) = Q_0(x,y) + \gamma \int_0^x \frac{Q(x',y)\langle P^*(x')P(x) \rangle}{I_P(x)} dx' \quad (4)$$

where

$$Q_0 = \frac{\langle S_0(x,y)P^*(x,y) \rangle}{I_P(x,y)} \quad (5)$$

represents the refractive index modulation without interaction. The averaged quantity appearing in Eq.

(4) may be calculated from the known statistical characteristics of the pump beam using the theory of partial coherence:

$$\langle P(x)P^*(x') \rangle = \mu_p(x, x') \quad (6)$$

Therefore, in the Eq.4 only function $Q(x, y)$ is unknown. This equation may be easily solved numerically. The resultant expression for Q may be used in the integral of Eq.3 to find the normalized degree of coherence of the output signal beam

$$\mu_s(y_1, y_2) = \frac{\langle S(x, y_1)S^*(x, y_2) \rangle}{\sqrt{\langle S(x, y_1)S^*(x, y_1) \rangle} \sqrt{\langle S(x, y_2)S^*(x, y_2) \rangle}} \quad (7)$$

We find that it is given by the following expression

$$\mu_s(y_1, y_2) = \frac{\langle S_0(x, y_1)S_0^*(x, y_2) \rangle + 2\gamma_r \int_0^x Q(\hat{x}, y_2)Q^*(\hat{x}, y_1)I_p(\hat{x})d\hat{x}}{\sqrt{I_{s0}(y_1) + 2\gamma_r \int_0^x |Q(\hat{x}, y_1)|^2 I_p(\hat{x})d\hat{x}} \sqrt{I_{s0}(y_2) + 2\gamma_r \int_0^x |Q(\hat{x}, y_2)|^2 I_p(\hat{x})d\hat{x}}} \quad (8)$$

where γ_r is a real part of the coupling constant and I_{s0} is incident signal's intensity.

We see that when the coupling is absent ($\gamma_r = 0$) Equation (8) gives a coherence function for input signal beam. We used formula (8) to calculate the coherence function for the amplified signal beam assuming coupling constant $\gamma\ell = 1.65$ (ℓ is interaction length) and the same Gaussian form of the coherence functions for pump and initial signal beam. This calculation showed that the coherence of the signal beam increased during interaction in a way similar to that observed in the experiment.

This study was supported by National Sciences Foundation through Presidential Young Investigator Award and by the U.S. Army Research Office, Durham, North Carolina.

References:

1. M. Cronin-Golomb, Opt. Lett. 14, "Achromatic volume holography using dispersive compensation for grating tilt", 1297 (1989).
2. H.Kong C.Wu, and M.Cronin-Golomb, "Photorefractive two-beam coupling with reduced spatial coherence", submitted to Optics Letters.
3. M.Zahid and M.S.Zubairy, Coherence properties of second-harmonic beam generated by a partially coherent pump", Opt. Commun. 76, 1 (1990).
4. B.Crosignani and A.Yariv, "Degenerate four-wave mixing in the presence of nonuniform pump wave fronts", J.Opt. Soc. Am. A, 1, 1034 (1984).
5. G.Lera and M.Nieto-Vesperinas, "Phase conjugation by four-wave mixing of statistical beams", Phys. Rev. A, 41, 6400 (1990).

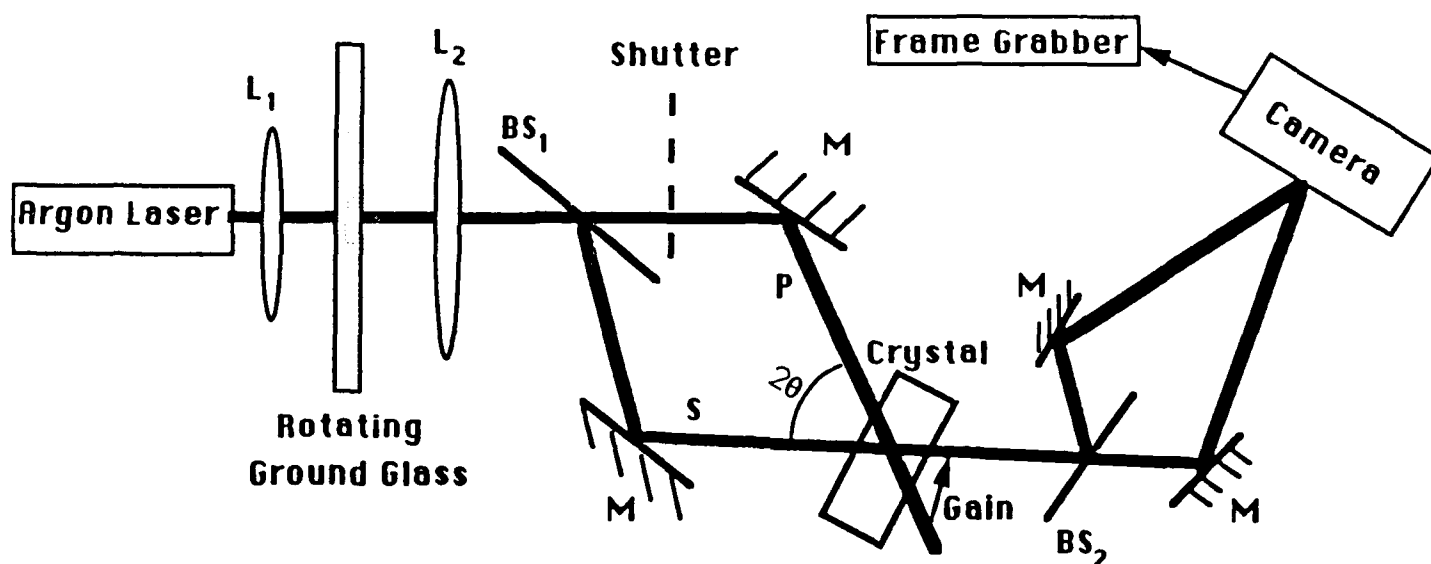


Fig.1 Experimental setup.

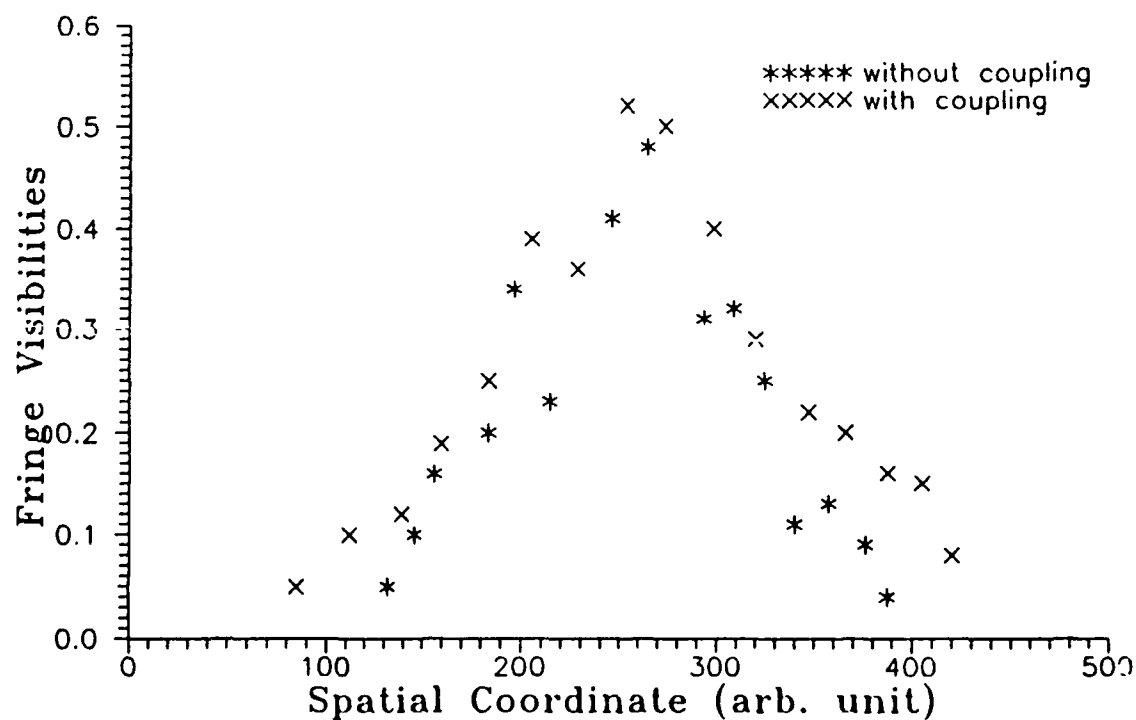


Fig.2 Experimental data of fringe visibility vs. spatial position.



Increase of mutual coherence of light beams
in two-wave interaction in photorefractive crystals.

N. V. Bogodaev, L. I. Ivleva, A. S. Korshunov, N. M. Polozkov
General Physics Institute, Vavilov str. 38, Moscow 117942, USSR
and V. V. Shkunov

Institute for Problems in Mechanics, pr. Vernadskogo 101, Moscow
117526, USSR

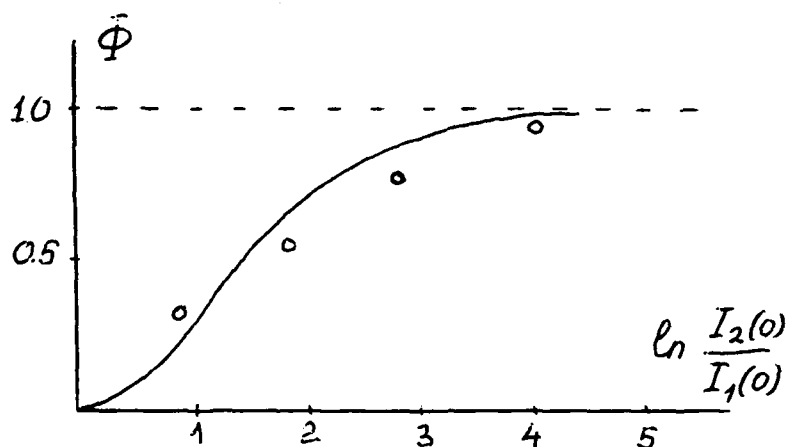
Two-wave mixing allows one to change effectively intensities, phases, space profiles, polarizations and time evolution of interacting beams [1,2]. We will show, that two-wave mixing of partially coherent beams may be used to increase degree of coherence of these beams. The physics of the effect under discussion is as follows: two partially coherent beams write a refraction index grating in a nonlinear medium whose position and profile are practically stationary. Scattering of strong beam on this grating in the direction of the weak one means that this weak beam acquires an addition, that is coherent with the strong beam, thereby increasing degree of coherence of the beams. Similar effects were discussed in connection with scattering of different frequency components at the common running grating [3] and with interaction of different polarization components [4,5].

In our theoretical approach we used one-dimensional plane-wave model, describing two-wave mixing with transmittive grating recording. Degree of coherence of two beams for any value of coordinate z inside the crystal along direction of their



propagation is most conveniently characterized by their normalized correlation function $\phi(z)$: $\phi^2 = |\langle E_1 E_2^* \rangle|^2 / I_1 I_2$, where E_j and I_j ($j = 1, 2$) are the amplitudes and the intensities of these beams, $\langle \rangle$ means averaging over time, both beams are moving from $z = 0$ to $z = 1$. Beam intensity ratio is characterized by parameter $P(z) = 4I_1 I_2 / (I_1 + I_2)$. Let beam 1 be amplified and input beam intensity ratio be small: $I_1 \ll I_2$. Consider dependence of $\phi(z)$ and $P(z)$ on coordinate, assuming, that the nonlinear coupling coefficient Γ is large enough. First both ϕ and P grow with coordinate. Then intensities of the beams at some point z_M become equal $P = 1$ and the correlation function ϕ reaches its maximum value $\phi_M = [1 - P_0(1 - \phi_0)]^{1/2}$, where $\phi_0 = \phi(0)$, $P_0 = P(0)$. Further increase of coordinate results in the decrease of coherence function ϕ , that is, to the decrease of degree of coherence of the beams.

In experiment we used a He-Cd laser ($\lambda = 0.44\text{mm}$) and a Ce-doped SBN photorefractive crystal. Initial laser beam was split into two parts, that were made partially coherent by introducing a delay $\Delta l = 2.5\text{m}$ in one of the beams. Initial degree of coherence was equal to $\phi_0 = 0.24$. The beams were fed in the crystal at an angle $\theta = 30^\circ$ between them in the air. Both beams were polarized in the plane of intersection, optical axis of the crystal was parallel to its entrance face and lay in the same plane. Fig. 1 presents experimental (dots) and theoretical (solid line) dependence of coherence function ϕ on input beam intensity ratio. Theoretical curve demonstrates good agreement with the experiment.



References

1. V. L. Vinetskii, N. V. Kukhtarev, S. G. Odulov and M. S. Soskin, Uspekhi Fizicheskikh Nauk, **129**, 113 (1979).
2. Photorefractive Materials and Their Application I, II - Berlin; Springer Verlag, 1989, 1990.
3. G. P. Dzhotyan and Yu. E. Dyakov, Vestnik MGU, Fizika i Astronomiya, **18**, 70 (1977).
4. I. M. Bel'dyugin and E. M. Zemskov, Kvantovaya Elektronika **4**, 1114 (1977).
5. G. I. Kochemasov and V. Nikolaev, Kvantovaya Elektronika **4**, 115 (1977).

Four-Wave Mixing Steady-State Solutions Utilising the Underlying SU(2) Group Symmetry

D. Fish, A. K. Powell and T. J. Hall
Physics Dept, King's College London
Strand, London WC2R 2LS

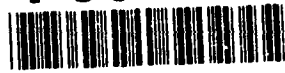
Abstract

A method of solution for the scalar four wave mixing equations has been known for many years [1]. We show that these equations have an underlying symmetry in the form of the SU(2) group. This formulation identifies the conserved quantities of four wave mixing in an obvious sense rather than in the ad-hoc fashion used previously. The method also solves the equations in terms of beam amplitudes rather than beam ratios.

The main advantage of this method is that solutions can be found in terms of three real quantities i.e. the three Euler angles. This means the dynamical problem can be solved in terms of the three real quantities rather than four complex beam amplitudes.

The steady state solution is still interesting though and will be the subject of the presentation. The solution can be formulated in terms of three vectors due to the unitary and hermitian traceless nature of the matrices involved. The results show that the solutions are more complex than previously thought.

[1] Mark Cronin-Golomb, Baruch Fisher, Jeffrey O. White and Amnon Yariv, IEE J. Quant. Elect. Vol QE-20 No 1 12 (1984)



Why Light Beams Follow Curved Paths in Photorefractive Phase Conjugators

V.V. Eliseev

*General Physics Institute, Academy of Sciences of the USSR,
38 Vavilov Street, Moscow, 117924, USSR*

A. A. Zozulya

*P. N. Lebedev Physical Institute, Academy of Sciences of the USSR,
Leninsky pr. 53, Moscow, 117924, USSR*

G. D. Bacher and Jack Feinberg

*Departments of Physics and Electrical Engineering
University of Southern California, Los Angeles, CA 90089-0484
Telephone: (213)740-1134*

In recent years a variety of photorefractive phase conjugators have been demonstrated that rely on stimulated light beams.¹⁻⁶ These self-pumped and mutually-pumped phase conjugators are all closely related⁷ and differ only in the number and angle of their input beams. Here we propose a detailed though necessarily simplistic description of how light beams spring up inside a photorefractive crystal, and why under some conditions these stimulated light beams appear to follow curved paths inside the crystal. We show that these curves are composed of a number of straight line segments which spring up by stimulated scattering in the photorefractive crystal.

Figure 1 is a photomicrograph of stimulated beams inside a Cat conjugator.¹ The stimulated beams have collapsed into narrow filaments (for reasons that will not be discussed here). These filaments appear to follow curved paths but upon close inspection are seen to consist of a series of straight line segments connected by distinct bends. We show that two separated regions inside the crystal, each having its own pair of counterpropagating waves, can "find" each other with new light beams, provided that the total round-trip reflectivity of a small seed wave between these regions is greater than unity. Our model predicts a sequence of such couplings, so that the path of the filaments eventually resembles a curved trajectory.

92-18709



Consider the double phase-conjugate mirror with a single interaction region.² All of the stimulated conjugators can be modeled as a sequence of such devices.⁷ In this basic device, two (preferably mutually incoherent) laser beams with incident optical intensities I_R and I_L intersect inside the crystal as shown in Fig. 2a. The particular grating that diffracts beam R into the phase-conjugate of beam L will also diffract beam L into the phase conjugate of beam R, by time-reversal symmetry.² In order for these phase conjugate beams to appear, the nonlinear coupling coefficient $\gamma_0 l \equiv \Gamma_0$ must exceed a threshold $\Gamma_{0,th}$.²

However, slightly above this threshold, this configuration of one interaction region is unstable against the excitation of arbitrarily weak beams scattered between the regions of the nonlinear medium that are pumped by two counterpropagating waves, as shown in Fig. 2b. The threshold for this instability occurs when the round-trip reflectivity of a weak seed wave between the regions 1 and 2 in Fig. 2b exceeds unity.⁸

For simplicity we will assume here that the coupling is the same in all three regions. Figure 3 shows the calculated threshold for phase conjugation vs. the incident beam ratio $q = I_R/I_L$ when there is only one interaction region, and also for the case in which the system has already bifurcated once and has three interaction regions. Note that a single interaction region will become unstable for coupling strengths only slightly larger than the single region threshold, and so will bifurcate into three interaction regions. For example, at $q = 1$, the single region threshold (no bifurcations) is at $\Gamma_{th}^{(0)} = 2$, while the three-region threshold (single bifurcation) is only slightly larger: $\Gamma_{th}^{(1)} = 2.026$. For even larger values of Γ the geometry of Fig. 2b may in turn undergo further bifurcation, since this configuration is now equivalent to two simple double phase-conjugate mirrors coupled together. This process will continue, with new beams springing up to connect new interaction regions, and so carve out a path made of many straight-line segments that approximates a curved trajectory.

We analyze the 3-region geometry of Fig. 2b by modifying the boundary conditions used to solve the four-wave mixing equations of Ref 8. Instead of the usual boundary condition where the amplitude of the conjugate wave A_3 starts from zero, $A_{3,in} = 0$, we let the conjugate wave be seeded by scattered light, so that $A_{3,in} = \sqrt{\epsilon} A_{2,in}$. Physically, this seed is due to the scattering of the wave A_2 from crystal defects into the direction of wave A_3 , and the "seeding" parameter $\epsilon \ll 1$ controls the amplitude of this scattering. These seed beams will become especially important when the coupling strength Γ becomes large, and they will determine the asymptotic behavior of the system.

As the bifurcations develop, the overall transmission T of the device changes, where T is defined as the ratio of the intensity input on one side of the crystal divided by the intensity exiting on the other side. For the case of equal intensity input beams ($q=1$) the dependence of T on the coupling strength Γ is shown in Fig. 4. Here the effect of the extra light path is clearly evident: it causes the sharp jump in the transmission as Γ increases above $\Gamma_{th}^{(1)}$ and the first bifurcation appears. The appearance of this bifurcation increases the overall transmission of the device. For any finite value of ϵ , the diffraction efficiency of the new gratings asymptotically approaches 1 for large coupling strength Γ , but the form of the approach depends critically on the value of the seed. As Γ increases, an increasing amount of light is channeled between regions 1 and 2, so that the A-shaped pattern in Fig. 2b begins to resemble the \wedge geometry of Fig. 2c. Note that Fig. 2c can also be viewed as two mutually-pumped phase conjugators sharing a common set of beams, and both the dynamic behavior and the stationary states of this system have been shown to be critically dependent on the values of the seeding coefficient ϵ .^{9,10}

In summary, we have presented a simple model to explain the bending of light beams in various self-pumped and mutually-pumped phase conjugators. This model explains the curved beam paths as a series of straight line segments that result from a sequence of couplings between different regions inside the crystal, each pumped by counterpropagating waves. Further, we have shown that including a small but finite amount of scattered light is crucial in describing this self-bending. It should prove possible to obtain a more physically realistic picture of this process by including the dependence of the coupling strength on both the crossing angle and the orientation of the gratings inside the crystal. Also we note that there are often a multitude of possible bifurcation paths which will compete for the available light energy, and that the primary path of the light could oscillate between them.

References

1. J. Feinberg, Opt. Lett. **7**, 486 (1982).
2. S. Weiss, S. Sternklar, B. Fischer, Opt. Lett. **11**, 528 (1986); Opt. Lett. **12**, 114 (1987).
3. M.D. Ewbank, Opt. Lett. **13**, 47 (1988).
4. M.D. Ewbank, R.A. Vasquez, R.R. Neurgaonkar, and J. Feinberg, JOSA B **7**, 2306 (1990).
5. Wang, Zhang, Zhu, Zhang, and Ye, Opt. Comm. **73**, 495 (1989).
6. R.W. Eason and A.M.C. Smout, Opt. Lett. **12**, 51 (1987); Opt. Lett. **12**, 498 (1987).
7. M. Cronin-Golomb, Opt. Lett. **15**, 897 (1990).
8. M. Cronin-Golomb, B. Fischer, J.O. White and A. Yariv, IEEE J. Quant. Electr. **20**, 12 (1984).
9. A.V. Mamaev, A.A. Zozulya, Opt. Comm., 1990, in press
10. V.T. Tikhonchuk, M.G. Zhanuzakov, A.A. Zozulya, Opt. Lett., 1990, in press.



Figure 1. Photomicrograph of stimulated beams in a Cat conjugator.

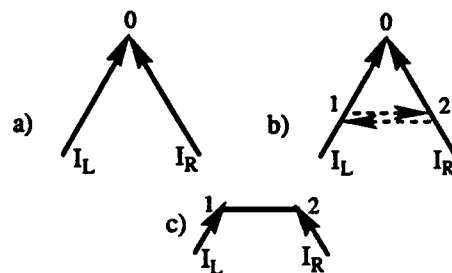


Figure 2. a) Double phase conjugate mirror.
b) Bifurcation begins.
c) Bifurcation complete.

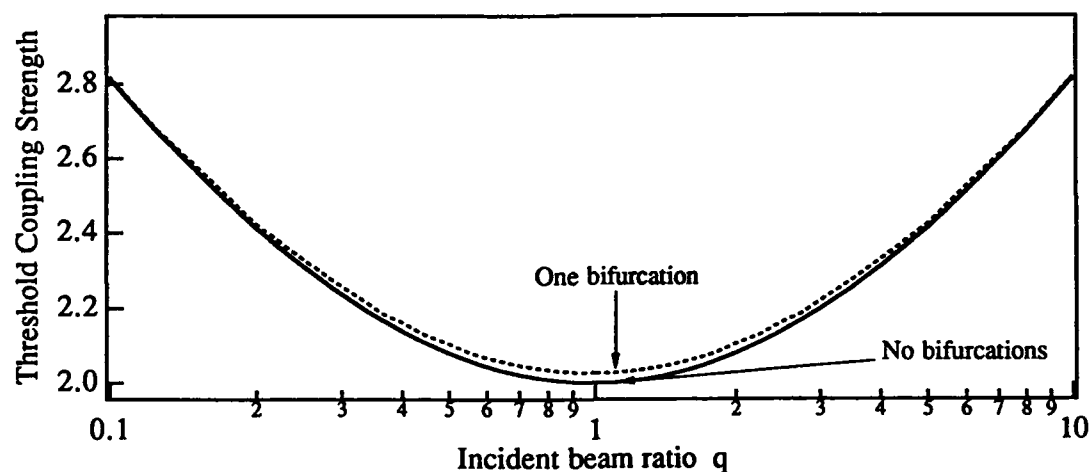


Figure 3. Threshold of oscillation for phase conjugator with no bifurcations and with one bifurcation.

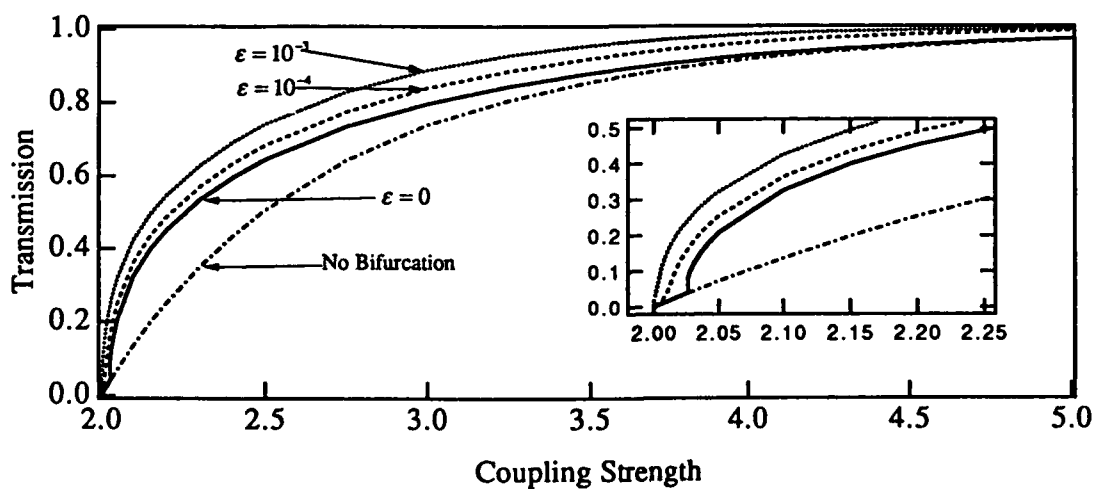


Figure 4. Phase-conjugate transmission with no bifurcations, and with a single bifurcation, for seeding coefficient $\epsilon = 0, 10^{-4}, 10^{-1}$.

REFLECTION GRATING PHOTOREFRACTIVE SELF-PUMPED RING MIRROR

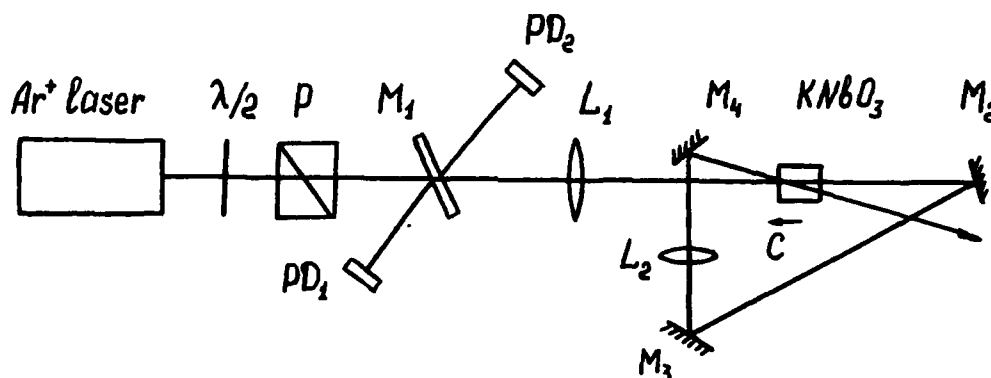
V.A. D'yakov^{*}, S.A. Korol'kov, A.V. Mamaev, V.V. Shkunov
and A.A. Zozulya^{**}

Institute for Problems in Mechanics, pr. Vernadskogo 101, Moscow,
117526, USSR

^{*} Moscow State University, Leninskie Gory, Moscow, 119899, USSR.

^{**} Lebedev Physics Institute, Leninsky pr. 53, Moscow, 117924,
USSR

We report on the first to our knowledge experimental realization of a reflection grating passive ring mirror in a photorefractive medium. The experimental arrangement is shown in Fig.1.



92-18710

Fig.1

We used an argon ion laser at 488nm operating at several longitudinal modes with the laser radiation coherence length ≈ 5 cm. A halfwave plate $\lambda/2$ and the polarizer P (Glan prism) served

to change incident power of laser radiation. After passing through the semitransparent mirror M_1 the beam was focused by the lens L_1 in the photorefractive $\text{KNbO}_3\text{:Fe}$ crystal of the length $\approx 6.5\text{mm}$ along the c-axis. The diameter of the incident beam in the crystal was $\approx 0.2\text{mm}$. After passing through the crystal the beam was redirected by the metal mirrors $M_2 - M_4$ and again entered the crystal from the same face, as the primary beam. The angle between these pumping beams was about 3 degrees in the air. The lens L_2 placed in the feedback loop made the diameter of this second beam approximately equal to that of the primary one. Both beams were linearly polarized in the plane of their intersection. The length of the feedback loop was about 75cm, that was less, than the round-trip laser cavity length ($\approx 205\text{cm}$). Detectors PD_1 and PD_2 served to monitor the power of incident and reflected radiation correspondingly. The dynamics of the nonlinear reflectivity of the phase-conjugate (PC) mirror under consideration is shown in Fig.2,

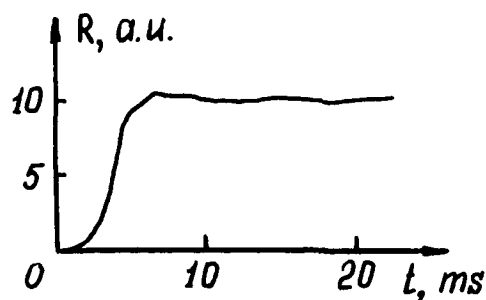


Fig.2

demonstrating characteristic relaxation time of several milliseconds. Depending on the details of experiment, we were able to realize both the case, when only one common reflection grating was recorded and the case, when all reflection gratings

(including $2k_0$ gratings between the antiparallel beams) were operative. Nonlinear reflectivity in the first case was about 10% and in the second case about 45%.



Photorefractive Crystal Waveguides and their applications

Ken-ichi Kitayama and Fumihiko Ito
 NTT Transmission Systems Laboratories
 1-2356 Take, Yokosuka-shi, 238-03 Japan
 Phone 81 468 59 3161, Fax 81 468 59 3396

I. Introduction

Photorefractive crystal waveguide(PCW) is a novel approach to enhance the photorefractive effects.¹⁻⁴ The waveguide geometry provides a tight optical field confinement and long interaction length of waves, resulting in increasing diffraction efficiency and angular sensitivity of hologram. It also allows to synthesize a high-density matrix array. Key issues to gain the practical applicability are how to overcome the drawbacks of PCW such as the finite aperture and modal phase dispersion which affects both image fidelity and holographic storage capacity.

In this paper, the solutions to the above problems of PCW are presented. Both neural image processings by storing holographic synaptic matrix in 2-D PCW array and distortion-free image replication by phase conjugation in PCW are investigated. LiNbO_3 and BaTiO_3 waveguides are used in the experiments.

II. Photorefractive crystal waveguides(PCW)

Multiple wave interaction

In Fig.1, holographic recordings in bulk crystal and PCW are compared. In PCW, the space saving factor becomes $(1/N)^2$, and the interaction increases by M times over the entire distance compared with the bulk crystal. This is a key to enhancing both angular sensitivity and diffraction efficiency of PCW holography.

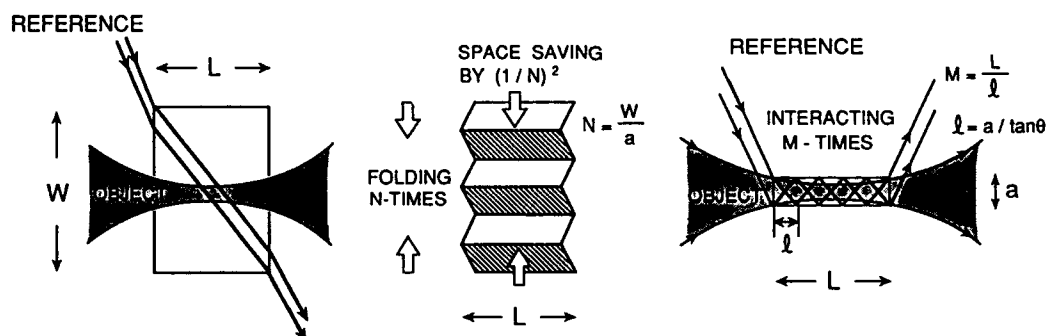


Fig.1 Interaction of object and reference beams in holographic recordings: (a) in bulk crystal and (c) in PCW. Features of PCW including compactness and multiple interaction of the beams.

Preparation of PCW

LiNbO_3 crystal fibers in Fig.2(a) are prepared by the resistance-heated pedestal method.⁴ BaTiO_3 waveguide in Fig.2(b) is prepared for the first time by cleaving from a single bulk crystal. The length is around 5 mm.

92-18711



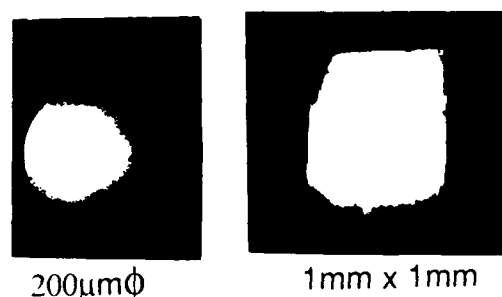
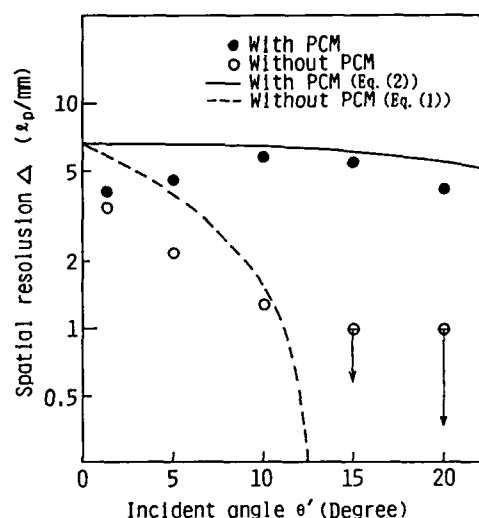


Fig.2 Cross-sectional views of (a) LiNbO₃ fiber by resistance-heated pedestal method and (b) BaTiO₃ waveguide from bulk crystal.

Fig.3 Experimental and theoretical spatial resolution plotted against incident angle of object beam. Dashed and solid lines without and with PCM, respectively.



III. PCW holography

Spatial resolution

Finite aperture and modal phase dispersion are the major causes to limit spatial resolution of PCW holography. The spatial resolution Δ of Fourier hologram recorded in PCW is

$$\Delta = \frac{2f\lambda}{(a - 2L \tan\theta) \cos\theta'} \quad (1)$$

where a denotes the diameter of the waveguide, and θ and θ' the incident angle of the reference beam in the crystal and the air, L the waveguide length, f the focal length of Fourier lens, and λ the wavelength. In Fig.3, the calculated Δ of Eq.(1) by dashed line and the experimental result using BaTiO₃ waveguide are shown against θ' . For higher-order modes, Δ deteriorates.

A distortion-free reconstruction of hologram recorded in PCW is realized by using phase conjugation.⁵ Then, the spatial resolution Δ of Fourier transformed hologram is restored to

$$\Delta = \frac{2f\lambda}{a \cos\theta'} \quad (2)$$

In the experiment, a BaTiO₃ photorefractive crystal is placed just behind the output endface of the PCW, and is used as self-pumped PCM. The phase conjugate reference wave reflected by PCM backpropagates on its original path and reconstructs the hologram. As shown in Fig.3, the experimental result shows that the compensation of the modal dispersion is achieved as is predicted by the theory based upon Eq.(2) plotted by a solid line. This suggests that for PCW holographic storage it is possible to utilize as many modes as required to bear high spatial frequency components of Fourier hologram.

Two-dimensional PCW array for neural nets

A novel approach to optically store and reconstruct 4th-rank synaptic weight matrix T_{ijk} of neural nets in 2-D PCW array is proposed in Fig.4. The synaptic matrix which connects 2-D input

and output images becomes 4th-rank. This will be an only and most realistic method to scale up T_{ijkl} . The synaptic matrix is obtained as $T_{ijkl} = \sum_m u_{ij}^{(m)} v_{kl}^{(m)}$ being $u_{ij}^{(m)}$ the target vector. T_{ijkl} is generated by optically performing the outer-product of the input and target vectors, and is recorded in the waveguide at (k,l) position of the array only for $v_{kl} \neq 0$. The summation with respect to (m) is optically accomplished by overwriting the corresponding hologram. The target image is duplicated through the multiple Fourier transform system. In the reconstruction process, the system output u'_{ij} is obtained as $u'_{ij} = \sum_k \sum_l T_{ijkl} v_{kl}$ by illuminating PCW with the input image where v_{kl} is the input vector. The phase conjugate wave of v_{kl} which is reflected by PCM placed behind the PCW array, reconstructs u'_{ij} . The summation of the optically reconstructed matrix elements is automatically taken at the position of the output plane. The PCM also works for compensating the modal phase dispersion.

The density of plane Fourier hologram is given by $(2\lambda F)^{-2} \cos\theta'$ bits per unit cross-sectional area where F is an F number of the Fourier lens. In the case of $F=1$ and $\lambda=0.5 \mu\text{m}$, the storage capacity as large as $500 \times 500 \text{ bit/mm}^2$ might be possible. The overall storage capacity of the array consisting of 500×500 PCWs becomes 63 Gbit. Furthermore, the capacity could be increased by the angular-multiple recording. The angular sensitivity of the hologram governs the angular multiplicity AM as

$$AM = \frac{L_{\text{eff}}}{\lambda} (1 - \sqrt{\frac{n+1}{2n}}) \quad (3)$$

where L_{eff} is the effective waveguide length $(1 - \exp(-\alpha L))/\alpha$, and α is the loss of the waveguide per unit length. From Eq. (3), the multiplicity becomes typically in the order of 10^2 .

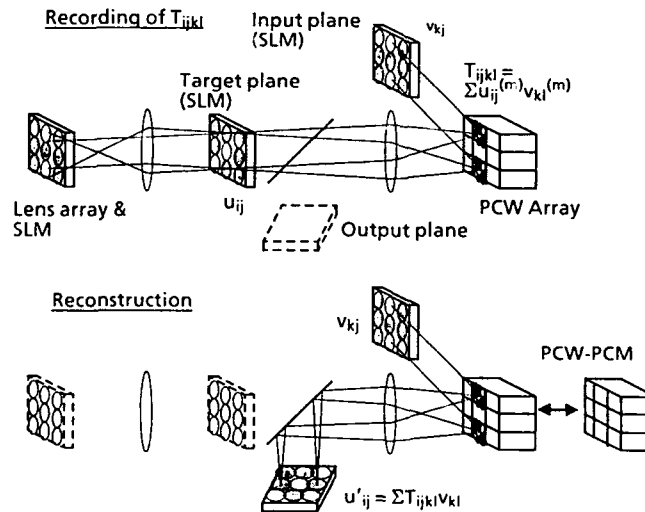


Fig.4 Holographic storage of 4th-rank synaptic matrix in 2-D PCW array. PCW:photorefractive crystal waveguide, PCM:phase conjugation mirror, SLM:spatial light modulator.

By considering the reduction of diffraction efficiency due to the

multiple recording, AM of 10 will be attained with ease, resulting in the total storage capacity of the system of approximately 600 Gbit.

IV. PCW phase conjugation

Generation by 4-WM

The generation of the phase conjugate by 4-WM can be observed in PCW. The input image will be replicated at the input with a high fidelity. A preliminary experiment is conducted for the first time by using a BaTiO_3 waveguide. From Fig.5, the generation of phase conjugate wave is verified due to the fact that the fidelity of the reflected field(b) is improved compared to the transmitted image at the output(a).

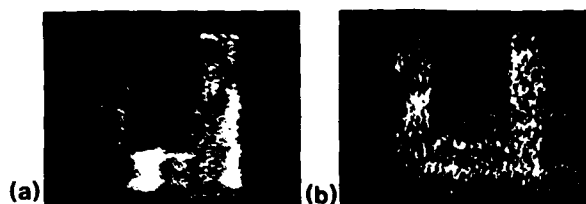


Fig.5 Experimental results of phase conjugation by 4-WM in BaTiO_3 PCW. (a)transmitted image at the output end and (b)replicated image at the input by phase conjugation.

Constraints for perfect image replication

From the theory,^{6,7} there are three major constraints under which a perfect replication of Fourier transformed hologram is obtained in a multimode waveguide:

- (i)The "cross" mode coupling between the different modes of the input and reflected fields must be negligible.
- (ii)The mode-to-mode variations of coupling coefficient must be negligible.
- (iii)The effect of the higher-order modes in the pump beams must be insignificant.

Our study theoretically clarifies that the validities of the above constraints are not perfectly guaranteed under practical conditions. This will be detailed on-site.

V. Conclusion

Up to 500x500 image processings based upon neural nets seems realistic by using 2-D PCW array holographic storage system in which PCM is incorporated. Another application of distortion-free image replication by phase conjugation in PCW has also been successfully demonstrated by using BaTiO_3 .

References

1. L. Hesselink and S. Redfield, Opt. Lett. 13, 877(1988).
2. B. Fischer and M. Segev, Appl. Phys. Lett. 54, 684(1989).
3. L. Hesselink, International J. of Optoelectronics 5, 103(1990).
4. H. Yoshinaga, K. Kitayama, and H. Oguri, Appl. Phys. Lett. 56, 1728(1990).
5. A. Yariv, Appl. Phys. Lett. 28, 88(1976).
6. A. Yariv, J. AuYeung, D. Fekete, and D. M. Pepper, Appl. Phys. Lett. 32, 635(1978).
7. R. W. Hellwarth, IEEE J. Quantum Electron. QE-15, 101(1979).

IMAGE TRANSMISSION THROUGH MULTIMODE FIBER AND THE PHOTOREFRACTIVE CRYSTAL

A.Gnatovskii, A.Volyar, N.Kukhtarev and S.Lapaeva

Institute of Physics, Academy of Sciences of the Ukr.SSR
Prospekt Nauki 4z, 252650, USSR

We describe the results of the image transmission through the multimode optical fiber and photorefractive crystal $\text{LiNbO}_3:\text{Fe}$. Experiments were done with HeNe laser ($\lambda = 0.633\mu\text{m}$), with multimode fiber of $70\mu\text{m}$ diameter, the aperture number 0.17 and 2m long. After passing an optical fiber light wave E_1 were mixed with another coherent wave E_2 at the photorefractive crystal. Amplitude mask was introduced in E_2 wave and a dynamic hologram was recorded in the crystal through photogalvanic effect [1]. Retrieval of this hologram was done by another counterpropagating wave E_3 , which lead to diffracted wave E_4 conjugated to E_1 with 10% diffraction efficiency after 3min. of hologram writing. To reproduce polarization state of the input waves special orientation of the crystal should be used: crystal C axis is perpendicular to the plane of incidence, polarization of E_2 wave is 45° and of E_1 is -45° to the crystal C-axis. Then phase conjugate wave modulated by mask propagate in reversed direction through fiber, and after filtering from the speckle pattern by diffraction on another correcting holograms, reproduce mask image in the image plane.

This is first, to our knowledge, successful one-way transmission of the image through 2m long multimode fiber.

1. N.Kukhtarev, T.Semenets, A.Volyar and S.Lapaeva, "Polarization recovery during PC in the photorefractive crystals", to be published

Monday, July 29, 1991

Feature Session on Optical Storage and Memories

MD 7:30pm–9:00pm
Academic Center Auditorium

L. Hesselink, *Presider*
Stanford University



Phase-coded hologram multiplexing for high capacity optical data storage

C. Denz¹, G. Pauliat, G. Roosen

Institut d'Optique Théorique et Appliquée, Unité associée au CNRS
Centre Scientifique, Bat. 503, B.P. 147, 91403 Orsay Cedex, France
Tel.: 331/69416855; FAX: 331/69413192

T. Tschudi

Institut für Angewandte Physik, Technische Hochschule Darmstadt
Hochschulstr. 6, 6100 Darmstadt, Germany
Tel.: 49-6151/162022; FAX: 49-6151/164123

Introduction

Reconfigurable volume holograms are important for a wide range of multiple data storage applications, including optical interconnection systems, image processing and neural network models. Therefore, there has been much previous work on multiplexing techniques to obtain a large number of stored images which can be recalled independently. But even the most promising of these multiplexing techniques, angular multiplexing using the selectivity of the Bragg-condition, revealed to be limited primarily because of cross-correlation noise. Moreover, mechanically changing the incident angle of the reference beam^{1,2} requires a high reliability in the positioning and is therefore inherently slow. To overcome these problems, an intensity spatial light modulator can be used to define the various angular multiplexed incident directions³. However, this solution is energy consuming.

Out of these reasons, we present in this paper an alternative approach implementing a phase coding method of the reference beam. Phase encoding has been discussed for interconnecting vector arrays in thin holograms⁴ and, more recently in a different context, to perform array interconnections by correlation of a reference beam with a supplementary phase-coded input beam⁵.

In contrast to these investigations, we use a reference beam phase coding method in thick volume holographic media, taking thus full advantage of the selectivity of the Bragg-condition in volume storage media. In our method, all images are stored with pure and deterministic orthogonal phase references, each of it divided into $n \times n = N$ pixels. During recording, all these reference pixels overlap the image beam in the recording medium and the angular spacing between two adjacent pixels is chosen to be large enough to satisfy the Bragg-selectivity. As an advantage of that method no alignment problems occur during writing and readout-cycles. Moreover, orthogonal phase code addressing provides easy, reliable, and immediate reference wave images. Especially, theoretically no crosstalk and therefore noiseless reconstruction appears because the reconstructions of the undesired images interfere destructively to produce zero intensity. In our theoretical approach we calculate the storage capacity of our multiplexing method. We show, that the maximal number of holograms able to be stored is equal to that obtainable in angular multiplexing. Experimentally, we realized for the first time a system using purely phase coded reference waves to store four images, which could be recalled with low crosstalk. Moreover, to quantify the features of the system realized, we investigated the recall of two simple images.

Phase encoding in thick media

Among the several phase coding methods which can be used efficiently in volume holographic media, deterministic phase encoding seems to be the most promising one, because it ensures a high signal-to-noise ratio. In contrast, for random phase encoding crosstalk may become significant when the number of stored holograms grows too large. The deterministic phase encoding technique we are developing allows to store M images in a thick recording medium and to retrieve each image separately with low crosstalk. This number M will be precised below. The corresponding scheme of the recording arrangement is depicted in fig. 1. During the recording procedure, the image beam, whose complex amplitude $0.5 \cdot (A_q \cdot \exp(jk \cdot r) + cc.)$ carries the information of the q^{th} image, simultaneously interferes with all N pixels of the reference beam. This can be interpreted as an interference with N different reference beams.

¹ permanent address: Institut für Angewandte Physik, Technische Hochschule Darmstadt, Hochschulstr. 6, 6100 Darmstadt, Germany



Each of these references is encoded with a phase modulation carrying the complex amplitude

$0.5 \cdot (P_\ell \cdot \exp(j\varphi_\ell^q) \cdot \exp(jk_\ell \cdot r) + cc)$. Here, the set of adjustable phases $(\varphi_1^q, \dots, \varphi_N^q)$ represents the address of the q^{th} image.

Assuming that the recording medium is a photorefractive crystal, we can derive an expression for the diffracted amplitude $0.5 \cdot (R \cdot \exp(jk \cdot r) + cc)$ during readout of the holograms with the N reference beams and the address $(\varphi_1^q, \dots, \varphi_N^q)$ using the coupled wave analysis and the material equations:

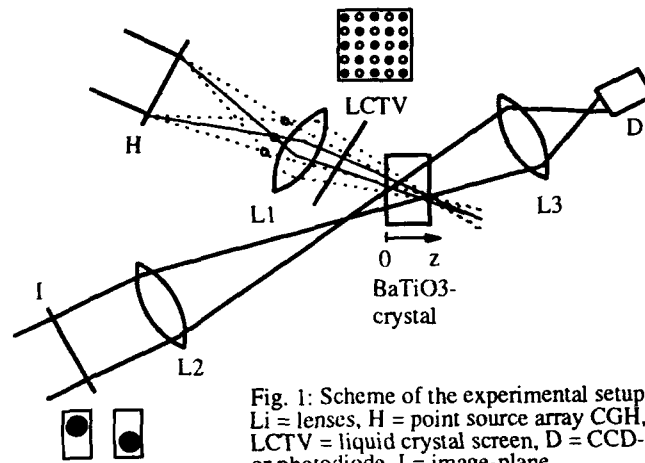


Fig. 1: Scheme of the experimental setup; Li = lenses, H = point source array CGH, LCTV = liquid crystal screen, D = CCD-camera or photodiode, I = image-plane

$$\frac{\partial R}{\partial z} = j \cdot \exp(j\psi) \cdot \sum_{q=1}^M \sum_{\ell=1}^N \frac{\pi n^3}{\lambda} \cdot \frac{r_{\text{eff}}^\ell}{2} \cdot E_{\text{sc}}^\ell \cdot \frac{P_\ell \cdot P_\ell^*}{(I_q + I_R)} \cdot \exp(j(\varphi_\ell^p - \varphi_\ell^q)) \cdot A_q \quad (1)$$

In eq. (1) we used usual notations. The effective electrooptic coefficient r_{eff}^ℓ and the space charge field E_{sc}^ℓ depend on the reference beam we consider. $I_q = 0.5 \cdot A_q \cdot A_q^*$ is the intensity of the q^{th} image beam, $I_R = 0.5 \cdot \sum P_\ell P_\ell^*$ the total intensity of the reference beams.

If we assume now a perfect system, the terms r_{eff}^ℓ , E_{sc}^ℓ and P_ℓ are independent of the special reference beam we consider and are equal to r_{eff} , E_{sc} and P . With $I_0 = 0.5 PP^*$, eq. (1) simplifies to:

$$\frac{\partial R}{\partial z} = j \cdot \exp(j\psi) \cdot \frac{\pi n^3}{\lambda} \cdot r_{\text{eff}} \cdot E_{\text{sc}} \cdot I_0 \cdot \sum_{q=1}^M \frac{A_q}{(I_q + N \cdot I_0)} \cdot \sum_{\ell=1}^N \exp(j(\varphi_\ell^p - \varphi_\ell^q)) \quad (2)$$

In order to retrieve the p^{th} image ($R \equiv A_p$) without crosstalk, we have to address the system with phase codes fulfilling the condition:

$$\sum_{\ell=1}^N \exp(j\varphi_\ell^p) \cdot \exp(-j\varphi_\ell^q) = 0 \quad \text{if } p \neq q \quad (3)$$

This equation can be solved using matrix algebra methods so that the problem reduces to find matrices X_{ij} with $X_{ij} \cdot X_{ij}^* = I$, where I is the unity matrix. Because in that solution all row vectors of X_{ij} are orthogonal, we must choose orthogonal phase codes to retrieve the p^{th} image without crosstalk. If N is a power of 2 and if the phases φ_i^q are chosen equal to 0 or π , then N orthogonal phase addresses can be constructed using the Walsh-Hadamard transform.

Thus the number M of images which can be stored in the recording volume medium is equal to N and is only limited by the Bragg-selectivity. This limitation is the same which appears using the usual angular multiplexing technique. If we assume exponential writing and readout behaviour with the same time constants for the refractive index modulation, the requirement that all holograms should have the same diffraction efficiency at the end of the recording cycle leads to a recursive equation giving a simple expression for the maximal number of holograms which can be stored

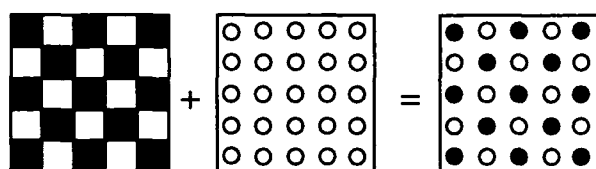
$$M \approx \Delta n_{\text{max}} / \Delta n_1 \quad (4)$$

where Δn_{max} is the index modulation required for maximal diffraction efficiency obtained for single image recording and Δn_1 is the index modulation for minimal diffraction efficiency, which still can be detected relative to noise.

Up to now, we considered a perfect system (eq. (2), (3)), where no crosstalk exists between images. However, when we switch to real systems (eq. (1)), crosstalk may become a limiting factor, which arises from different origins. Among them, the nonuniformity in the photorefractive diffraction efficiency ($r_{\text{eff}}^i \cdot E_{\text{sc}}^i \neq r_{\text{eff}}^j \cdot E_{\text{sc}}^j$) and in the reference beam intensity ($|P_i|^2 \neq |P_j|^2$) and the imperfections of the phase modulator ($\varphi_i^q = \varphi_0^q \pm \epsilon$) play an important role. The amount of crosstalk resulting from these origins will be discussed at the conference and a technique to reduce it will be proposed.

Experiments

The reference beam is phase coded using the combination of a computer generated matrix-array hologram (CGH) with a commercially available liquid crystal TV (LCTV) (see fig. 1). The hologram is used to create a 6×6 array of converging waves and is imaged onto the crystal. Thus we ensure that all phase code pixels of the array are superposed completely in the crystal volume. The LCTV as phase modulating element is placed behind the CGH in such a way that phase encoding takes place where the beams are still separated. Phase-only modulation can be achieved in these LC-cells when the inherent birefringence effect (associated with the molecule) is altered as the structure of the LC starts to deform. This effect appears when the applied field is above a certain threshold field. For high applied fields, the twisted structure starts to untwist itself and the polarization modulation takes place too, leading to a hybrid operation mode of the LCTV. For optimum phase modulation effect, the polarization direction of the incident light must be aligned parallel to the molecule director on the LCTV's front surface⁶.



LCTV phase encoding Hologram spots Resulting phase mask

Fig. 2: Binary phase encoding mask obtained by the combination of a liquid crystal TV and a computer generated hologram creating a matrix of separated converging waves.

In our experiments, hybrid modulation occurred even for low applied fields, such that a phase-nearly modulation with the two binary values 0 and π was obtained using the maximum and minimum output grey levels of the LCTV. Therefore, a quarter-wave and a half-wave-plate were necessary behind the LCTV-screen to ensure phase-only modulation. A supplementary polarizer behind these waveplates selects again extraordinary polarization to take best advantage of the large electrooptic effect in BaTiO_3 . For convenience, these three elements are not shown in fig. 1.

The phase coding mask was created from a host computer connected to a frame grabber, which sent the coding image to the LCTV screen. The resulting phase address of the reference beam after passing through both elements is shown in fig. 2.

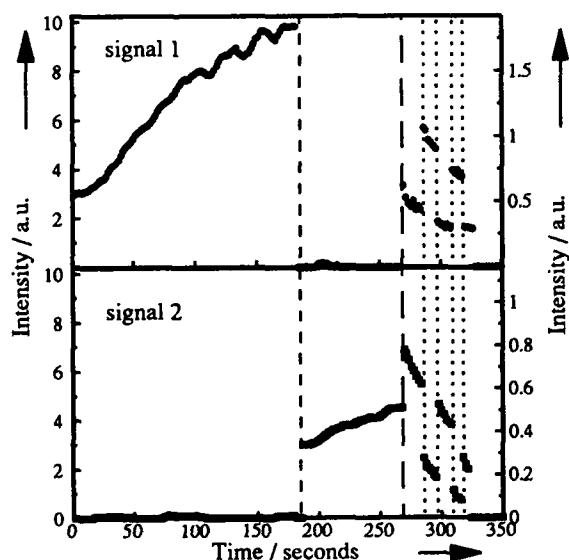


Fig. 3: Writing and readout cycles with the binary phase-coding method for two vertically separated spots as simple input images. Left side: Writing cycle of the two images, right side: alternative retrieval of both images with the corresponding phase codes.

To control the reliability of the phase-shift, a Mach-Zehnder interferometer was used, monitoring the interference fringes shifts for maximum and minimum grey scale levels relative to the signal beam on a photodiode array. Again, for simplicity that part of the setup is not shown in fig. 1. We observed deviations in the range of a few percent from ideal $0/\pi$ phase-shifts due to temporal fluctuations of the grey scale level of each pixel in the LCTV. Thus, although theoretically all crosstalk contributions should interfere destructively and vanish, these imperfections of our phase encoder give rise to a certain amount of crosstalk.

As photorefractive medium, a single domain, as-grown BaTiO_3 has been used, illuminated by an Ar^+ -laser operating on a single frequency mode. The crystal was oriented in such a way that the direction of the energy exchange between the two writing beams were from the reference to the signal beam.

To investigate the readout properties and reliability of our system quantitatively, we choose two simple images as input: two vertically separated spots (see fig.1). Thus, crosstalk and temporal writing, readout and erasure properties of the interconnection holograms could be observed properly.

Fig. 3 shows the writing and readout cycle for these two images, detected by two photodiodes. As phase coding addresses, the matrix was divided into two fields, carrying the phase 0 or π . During the writing

cycle (fig. 3, left side), each image is recorded sequentially, but the length of each exposure is different. The first hologram is recorded long enough to reach saturation. The recording time of the second one is adapted so that after recording both holograms have the same diffraction efficiency. The values of the diffraction efficiency are relatively low compared to what we obtain without phase encoding. This fact arises, because the phase fluctuations in the phase coding mask decrease the degree of coherence between both writing beams.

After recording being accomplished, the image beams (A_1 , A_2) were blocked and both phase codes (ϕ_1^1 , ϕ_1^2) were used to retrieve alternatively the corresponding image (right side of fig. 3). We found a crosstalk of $\text{signal-1}(\phi_1^2)/\text{signal-2}(\phi_1^2) \approx \text{signal-2}(\phi_1^1)/\text{signal-1}(\phi_1^1) \approx 20 \pm 5\%$ for both images. This is also due to the fluctuation effects of the pixels of the LCTV that exist during both, recording and readout cycles.

In a next step several different images were written and selectively read out. Here, a 2×2 matrix of orthogonal phase fields was chosen as encoding pattern. Fig. 4 shows four images and their retrieval with the corresponding phase mask, demonstrating that they can be recalled and distinguished properly.

At the moment, investigations are in progress to define the phase coding element necessary to realize a system with 1000 images stored with our phase coding method.

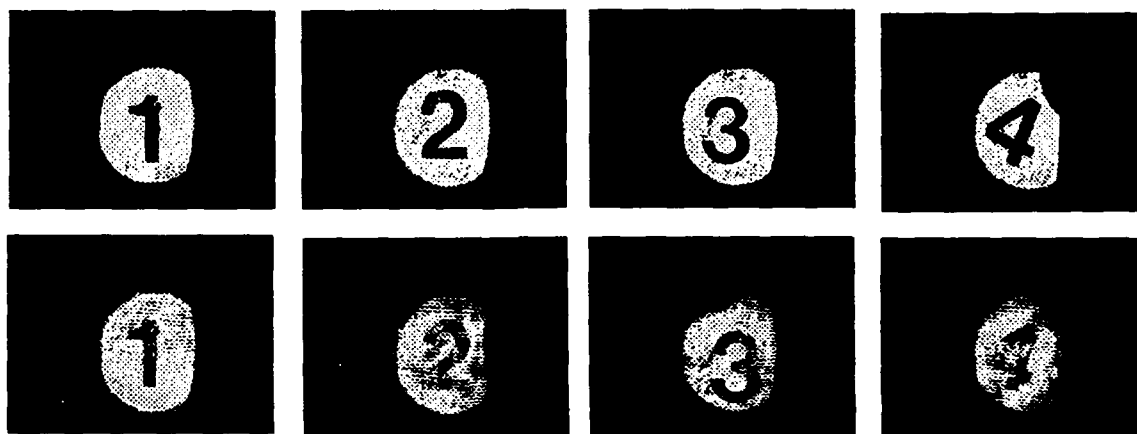


Fig. 4: Input (a) and recalled images (b) stored with the binary phase-codation system shown in fig. 1.

Conclusion

In conclusion, we have investigated a deterministic phase-coding method for high capacity optical image storage in photorefractive materials taking full advantage of the Bragg-selectivity of volume materials. Compared to other multiplexing techniques as angular multiplexing, that method allows high storage capacity without alignment problems. Moreover, easy, light efficient as well as immediate image retrieval without any time delay is possible. Experimentally, we realized a system which is able to discriminate four images with low crosstalk. Current limitations of the system arise mainly from the phase modulator, a commercially available LCTV. We suggest, that with a reliable phase coding element, much lower crosstalk values can be achieved and the system will be able to store and recall multiple images.

Acknowledgements

The authors like to thank E. Jäger, Technische Hochschule Darmstadt for the computer generated hologram and Dr. J. Albers, Universität Saarbrücken for the BaTiO₃-crystal. Parts of this work were supported by the Deutsche Forschungsgemeinschaft, Sonderforschungsbereich 185 and by the European French-German Cooperation Project PROCOPE.

References

- [1] L. d'Auria, J.P. Huignard, C. Slezak, E. Spitz, Appl.Opt. 13 (1974) 808.
- [2] D.L. Staebler, W.J. Burke, W. Phillips, J.J. Amodei, Appl.Phys.Lett. 26 (1975) 182.
- [3] E.S. Maniloff, K.M. Johnson, Opt.Eng. 29 (1990) 225
- [4] P. Healey, D. Smith, Annual Meeting OSA 1987, paper THV 3
- [5] J.E. Ford, Y. Fainman, S.H. Lee, Opt.Lett. 15 (1990) 1088
- [6] E.C. Tam, F.T.S. Yu, A. Tanona, D.A. Gregory, R.D. Juday, Opt.Eng. 29 (1990) 1114.



Multi-mode operations of a holographic memory using orthogonal phase codes

Yoshinao Taketomi, Joseph Ford, Hironori Sasaki, Jian Ma, Yeshaiah Fainman and Sing H. Lee

University of California San Diego, Electrical & Computer Engineering Dept., La Jolla CA 92093

Introduction

Holographic memories offer the advantages of high storage density, distributed storage, and fast parallel access. These characteristics can be important for parallel opto-electronic computers such as neural networks. The memory can be used to hold a training set which is repetitively displayed during learning. In addition, if partitioning is used to solve problems requiring more neurons than the actual number of processors, the memory can also be used to hold connection weight and threshold information. In this paper, we present results from a photorefractive memory using incremental recording scheduling and binary orthogonal phase codes image addressing. We show how this approach allows modification of the content and diffraction efficiency of the stored images, and how multiple images can be combined by complex amplitude addition and subtraction during reconstruction.

Memory design

The photorefractive memory¹ uses an incremental recording schedule to initially load the images. Each image and reference pair illuminates the crystal for a recording increment which is short compared to the crystal's response time. All of the images to be recorded are cycled through repetitively. The crystal's recording sensitivity is highest for index modulations much lower than the saturation level. Initially, some of the increase in diffraction efficiency during a recording increment remains even after all the other images have been recorded, and all of the recording gradually increase in diffraction efficiency after each cycle. After a certain number of cycles, saturation is reached. In contrast to the scheduled recording approach², only one parameter --the recording increment-- is necessary, and no detailed knowledge of the crystal's recording dynamics is needed. This may become important for crystals which have either field or material nonuniformities across their aperture. The saturation efficiency for incremental recording is identical to that reached by a scheduled recording cycle. Depending on the increment chosen and the number of cycles used, the recording energy required can also be reduced. However, to implement incremental recording, the interference pattern produced by each hologram-reference pair must be reproduced exactly, to within much less than a fringe width. To make this possible, we use a phase only reference image, keeping the crystal and all optical components rigidly fixed.

The phase only reference image consists of a set of phased plane waves, each separated from the others by more than the Bragg selectivity requirement. All of the reference beams have unit amplitude. The reference images are made distinct by choosing a set of phases on each plane-wave component. We require that each phase code reconstruct only it's corresponding hologram. That is, that

$$\sum_{j=1}^N R_{ij} R_{kj} = \begin{cases} N & (i=k) \\ 0 & (i \neq k) \end{cases} \quad (1)$$

where R_{ij} represents the coded reference beam of the j^{th} pixel of the i^{th} code. In general, there are N solutions of this equation for an N pixel code. For the particular case of binary (zero and pi) phases, the solution set is the Walsh functions, shown in Figure 1. These functions are regular, and can be generated by a simple binary tree logic structure from a $\log_2 N$ bit address. Using this binary phase reference beam allows the same memory addressing capacity as angle-multiplexed intensity modulators, but with full energy efficiency.

92-18713



Experimental demonstration

The experimental system is shown in Figure 2. Iron-doped LiNbO_3 was the recording media. The phase codes were displayed using a glass plate with the patterns shown in Figure 1(a) ion-beam etched into it. The one-dimensional codes were mechanically translated in front of a microlens and pinhole array, using a computer controlled stage. The images were recorded on transparencies, moved into position by another translation stage. Finally, the exposures were made with a computer controlled electromechanical shutter. Fixed patterns, rather than spatial light modulators (SLM), displayed the phase code and images because for the initial demonstration we wanted to test only the phase coding and not SLM response. The resulting memory output for 4 of 16 images is shown in Figure 3. A more quantitative result is given in Figure 4, where raster scans of 16 patterns with no overlap showed that the average signal to crosstalk ratio was 100 to 1, with a worst case ratio of 30 to 1. This corresponds to expectations, given the slight nonuniformity of the phase code intensities.

Multimode memory operation

The phase code address has N orthogonal settings, as shown in Figure 1, but 2^N possible states. The other $2^N - N$ address correspond to combinations of the N memory addresses. In the case of $N=16$, the number of address becomes 65536. The memory output will be a linear superposition of the complex amplitudes of the memory contents. Figure 5 shows how the basic orthogonal codes can be combined to produce the reference images which will recall the sum and differences between any two memories. In general, the address representing a combination of M different memories has integer values ranging from $-M$ to M . However, if the number of phase code pixels is large, the address can be truncated to binary phase only and still retain most of the information. We will present simulation and experimental investigations of this behavior. Using this capability, a memory containing a well-chosen basis set of patterns can be used to generate a large number of images. As a trivial example, sixteen single line segments can produce the 26 letters and 10 numbers of an alphanumeric display.

Summary

We have described a photorefractive holographic memory design using orthogonal phase code addressing and incremental recording. The requirement for using incremental recording is that system must be able to display image and reference pairs repetitively, accurately reproducing the fringe patterns. In exchange for this, the system is capable of monitoring the diffraction efficiency of each memory, making corrections and adjustments. For example, if a memory is no longer desired, the identical image can be recorded with complement of it's phase code to selectively erase only that memory³. The phase code addresses can be generated using a binary tree logic structure, allowing memory access limited only by the SLM speed. In addition, the phase code addressing approach can be used to generate additional images, multiply combining the memory contents through complex weighted addition and subtraction. Our presentation will include experimental and computer simulation investigations of this capability.

References

- [1] Y. Taketomi, J. E. Ford, H. Sasaki, J. Ma, Y. Fainman, S. H. Lee, and J. Feinberg, *Tec. Dig. of the Topical meeting of the Opt. Soc. Amer. on Optical Computing, 1991*, 6 p.268 (1991).
- [2] D. Psaltis, D. Brady, and K. Wagner, *Appl. Opt.* **27**, p.1752 (1988).
- [3] J. P. Huignard, J. P. Herriau, and F. Micheron, *Ferroelectrics* **11**, p.393 (1976).

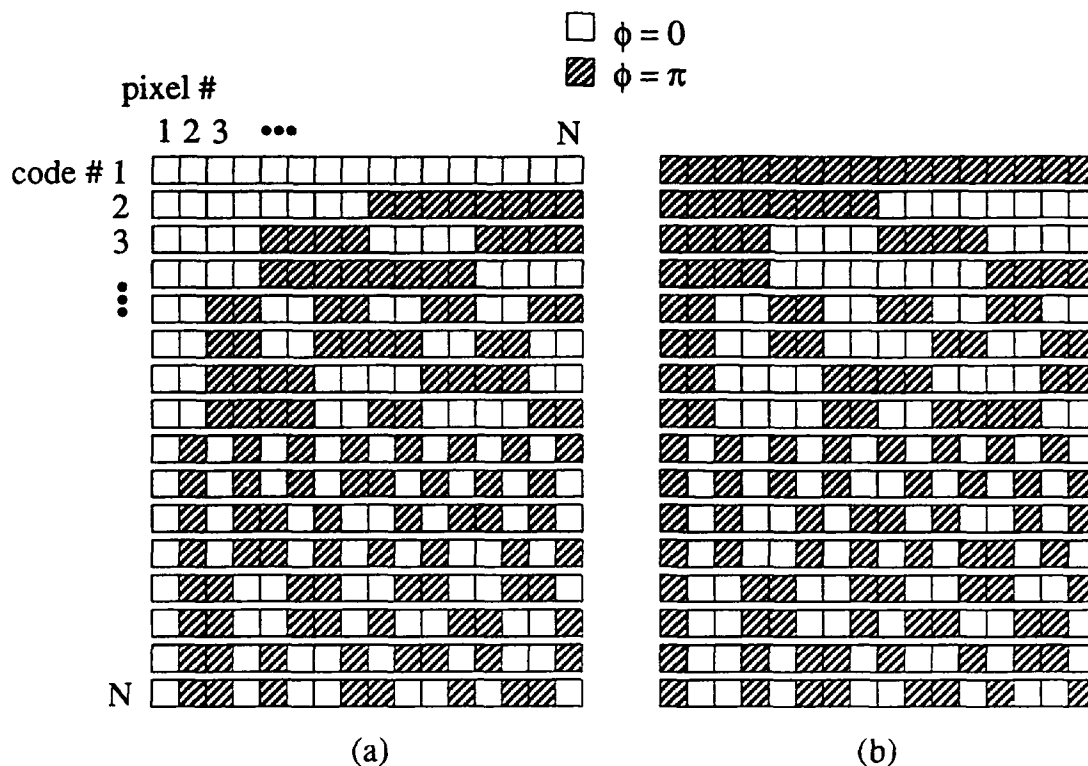


Figure 1. Binary orthogonal phase codes (a) and the complements (b). Orthogonality is maintained even after the complimentary codes are introduced.

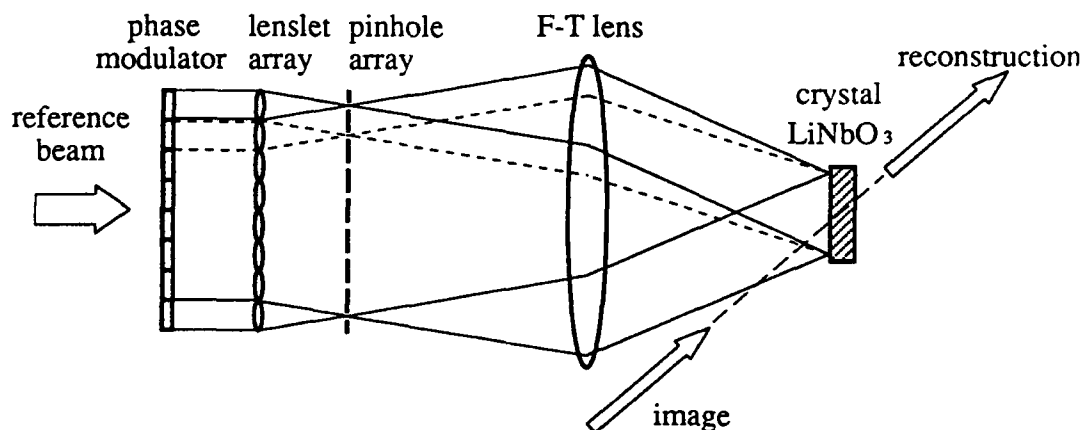


Figure 2. Experimental set-up. The reference beam is modulated by a 1-D phase modulator, then focused by the lenslet array and filtered by the pin-hole array. The phase modulated points are Fourier transformed into multiple overlapping plane waves which cover the entire crystal aperture.

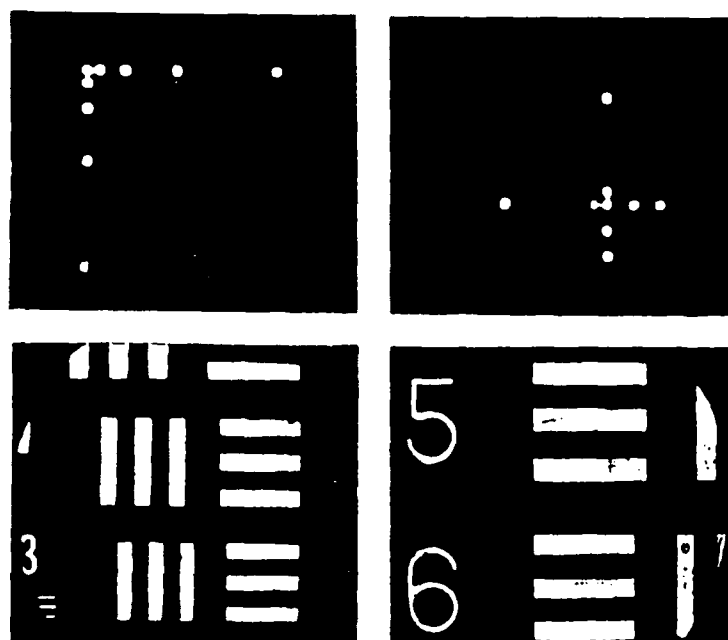


Figure 3. Reconstructed images (4 out of 16 superimposed holograms).

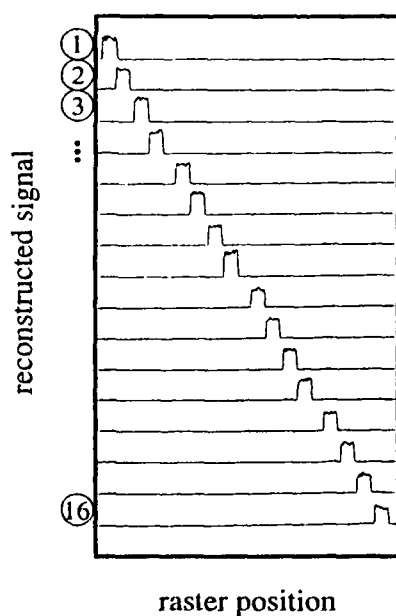


Figure 4. Raster scan results of the reconstructed images using binary orthogonal phase codes. The images were chosen to have no overlapped portions to check the orthogonality of the codes. The results show high signal to crosstalk ratio, with 30 to 1 in the worst case and 100 to 1 on average.

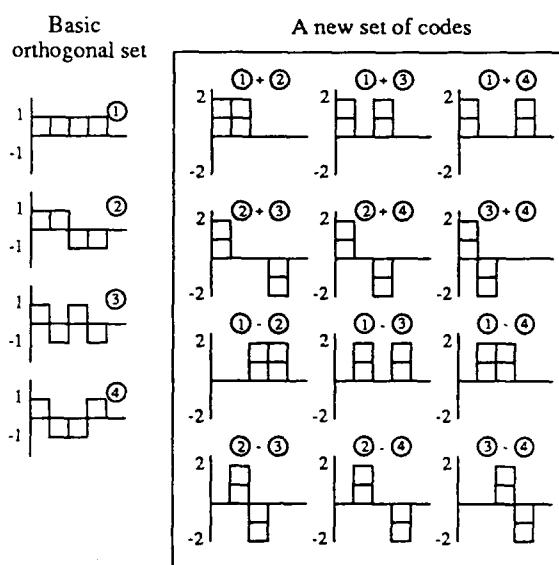


Figure 5. A new set of amplitude and phase modulated codes can be generated by addition or subtraction of original binary orthogonal phase codes.



High Resolution Volume Holography using Orthogonal Data Storage

Amnon Yariv, George Rakuljic, Victor Leyva

Holographic volume data storage has long been an intriguing subject of research interest. The main reason for this interest is the promise of enormous data storage capacities. In a 1cm^3 volume, storage of 10^{12} bits or more is possible using visible light (1). However, to date, all attempts at attaining and demonstrating a volume holographic data storage system of this density have fallen far short of this theoretical limit (2-6). Although materials limitations contributed to this shortcoming, of more fundamental importance, however, were the problems associated with the angular multiplexing schemes used to holographically access the volume of the storage medium (7-9).

The angular multiplexing scheme often used is one in which many two-dimensional patterns or images are sequentially recorded with successively angle-multiplexed reference waves. Holograms stored in this manner suffer from excessive noise and crosstalk, thereby significantly reducing the storage capacity of the recording medium (8-10). These difficulties arise from the inherent, inefficient "use" of K space by the angular multiplexing method.

Often, photorefractive materials were used as the holographic storage media (11). However, such materials previously lacked an effective and efficient fixing mechanism for the permanent retention of the stored information (1, 12). Although researchers using lithium niobate in the past, for example, have been able to permanently fix their holograms, the resultant hologram diffraction efficiencies were small, especially when many information containing holograms were stored (13,14).

The Optologic orthogonal data storage system overcomes these two problems in a basic fashion. The system is based on two fundamental discoveries: (1) an enhanced fixing scheme which allows permanent storage of high diffraction efficiency holograms in a photorefractive material; and (2) the orthogonal data storage scheme which permits the theoretical maximum storage capacity of $\sim V/\lambda^3$ bits to be realized by holographically recording numerous, very high

92-18714



definition (diffraction limited) 2D images in a photorefractive medium using wavelength multiplexing. The latter is done by a fundamental spreading of the stored information not only throughout the physical volume of the storage medium, but also throughout the available K space. The large storage capacity of the orthogonal data storage system is a result of both the increased hologram fixed diffraction efficiencies (signal) and the simultaneous reduction of hologram noise and crosstalk that is realized with this system.

In particular, we have demonstrated the orthogonal data storage approach by storing more than 50 permanently fixed, high diffraction efficiency holographic images with no crosstalk in a 2mm thick LiNbO_3 crystal. The spatial resolution of each hologram was better than 2 microns. The lifetime of the fixed gratings was determined from elevated temperature measurements to be over 70 years at room temperature.

References

1. P.J. van Heerden, Appl. Opt. 2, 393 (1963).
2. S. Hunter, F. Kiamilev, S. Esener, D.A. Parthenopoulos, and P.M. Rentzepis, Appl. Opt. 29, 2058 (1990).
3. P.D. Henshaw, S.A. Lis, and N.R. Guivens, Jr., "Compact 4-D Optical Neural network Architecture," Final report, Contract No. F49620-89-C-0120, April 1990.
4. L. Hesselink and S. Redfield, Opt. Lett., 877 (1988).
5. L. Solymar and D.J. cooke, Volume Holography and Volume Gratings (Academic Press, London, 1981).
6. W.J. Burke, P. Sheng, and H.A. Weakliem, "Intrinsic Noise Sources in Volume Holography," Final Report, Contract No. N00014-75-C-0590, December 1975.
7. B.D. Guenther, Army Research Office, private communication.
8. T. Jansson, Optica Acta 27, 1335 (1980).
9. K. Blotekjaer, Appl. Opt. 18, 57 (1979).
10. W.J. Burke, "Signal/Noise Ratio of Holographic Images," Final Report, Contract No. N00019-75-M-0494, October 1975.
11. A.M. Glass, opt. Eng. 17, 470 (1978).
12. P. Gunter, Physics Reports (Review section of Physics Letters) 93, 199 (1982).
13. W. Meyer, P. Wurfel, R. Munser, and G. Muller-Vogt, Phys. Stat.

- Sol. (a) 53, 171 (1979).
14. D.L. Staebler, W. Phillips, and B.W. Faughnan, "Materials for Phase Holographic Storage," Final Report, Contract No. N00019 72 C 0147, March 1973.
 15. H. Kogelnik, Bell Syst. Tech. J. 48, 2909 (1969).
 16. A. Yariv, Quantum Electronics (Wiley, New York, ed. 2, 1975).



Holographic Storage Capacity Estimate for Photorefractive Media

George Fredericks

Digital Equipment Corporation
1175 Chapel Hills Drive
Colorado Springs, CO 80920
(719) 260-2715

Adil Lahrichi, Kristina Johnson

University of Colorado
Optoelectronic Computing Systems Center
Dept. of Electrical and Computer Engineering
Boulder, CO 80309
(303) 492-8238

March 15, 1991

Abstract:

The practical limit on the storage capacity of photorefractive media is estimated for a given bit error rate and read out bandwidth.

92-18715

1 Introduction

A fundamental argument based on the number of multiple exposure volume holograms that can be distinguishably recorded and retrieved in a photorefractive database places an upper limit on of about a terabit per cubic centimeter on the storage density¹. However, the practical limit is much smaller and depends on the bit error rate (BER) and read out band that are desired.

The BER that will be experienced on reading one set of equal diffraction efficiency multiple exposure volume holograms will depend on the signal to noise ratio at the output detector. The signal will depend on the laser power in the read beam and the diffraction efficiency of the hologram. The noise will consist of intrinsic detector noise and crosstalk noise.

The crosstalk noise analysis depends on the method used to address multiple holograms or pages of information. One method is Bragg selection or angular addressing. In this case each hologram is recorded with different angles between object and reference beams. This produces holograms with different grating vectors. Read out of a particular page then occurs when the reference beam satisfies the Bragg condition with the grating vector of the hologram containing that page. Crosstalk can occur when light is scattered from the read out beam from crystalline imperfections. When a large number of pages with closely spaced Bragg angles have been recorded, the scattered light will have a very high probability of addressing another page giving rise to crosstalk noise.

Another way to record multiple pages in a photorefractive crystal is to keep the angle between the object and reference beams the same while recording each page but apply a different spatial modulation pattern to the reference beam for each page². If these modulation codes are chosen to be orthogonal, they will serve as page addresses. When one of these patterns is applied to the reference beam during read out, the page that was recorded with that pattern will be reconstructed. In this case, scattering from crystalline imperfections will contribute much less noise in the detector plane. But the lack of perfection on the spatial light modulator that applies the addressing patterns to the reference beam will provide another mechanism for crosstalk. It is this sort of crosstalk that will be modelled here.

2 The crosstalk Model

In the case we are considering here, crosstalk comes about because the spatial light modulator (SLM) can not apply a pure orthogonal addressing pattern to the reference beam. The beam will be predominately modulated with the desired pattern. But because of SLM imperfection there will be a small admixture of all the other patterns. During writing a page, this will cause a small amount of overwriting of other pages. These effects are fairly simple to model in the case where the addressing patterns are simple amplitude patterns such as (1,0,0,...), (0,1,0,...) etc. and the only non ideality in the SLM is a finite contrast ratio. But when phase patterns are used, the SLM non-idealities include small random phase shifts. To model this crosstalk noise, we use a simple one parameter model that assumes that the average signal power at each detector in the output plane to be

$$P_d = \left(\frac{\eta_d P_L}{N_b} \right) (1 - \xi) \quad (1)$$

where η_d is the diffraction efficiency of the holograms, P_L is the readout laser power reaching the photorefractive crystal, N_b the number of bits per page, and ξ is a parameter that measures the crosstalk. The ξ parameter is a measure of crosstalk or the tolerance of error in the applied orthogonal codes. It can also be viewed as the SLM merit factor. For instance, ξ is equal to zero for a perfect SLM that displays the desired pattern without any mixture of the other patterns, and ξ is equal to 1 for an SLM that is so bad that it could not display even a small fraction of the desired pattern. Therefore, the SLM crosstalk measure parameter ξ is always equal to a value between 0 and 1 ($0 < \xi < 1$). The crosstalk noise power reaching each detector is then:

$$P_\xi = \left(\frac{\eta_d P_L}{N_b}\right)\xi \quad (2)$$

The signal to noise ratio is then:

$$\frac{S}{N} = \frac{2M^2\left(\frac{eP_d\eta}{h\nu}\right)^2}{M^{2+\chi}\left(\frac{3e^2(P_d+P_\xi)\eta\Delta\nu}{h\nu} + 2e i_d \Delta\nu\right) + \frac{4kT\Delta\nu}{R_L} + 2M^2\left(\frac{eP_\xi\eta}{h\nu}\right)^2}, \quad (3)$$

The first term on the bottom on the right hand side of Eq.3 is the detector shot noise. The second term is the Johnson noise and the third term is the crosstalk noise. M represents the gain factor for the case when an avalanche photodiode is used. It is equal to 1 when a regular photodetector is used. χ is the excess noise factor. i_d is the dark current, e is the electronic charge and h is the plank's constant. R_L is the resistance of the detector, η_d is the quantum efficiency, and T is the absolute temperature. Finally $\Delta\nu$ is the system bandwidth or the inverse of the time the detector array integrates photons while reading out one page. Once the BER or the probability of error p_e is chosen, the signal to noise ratio (SNR) can be obtained by solving Eq.4:

$$p_e = \frac{1}{2}\left(1 - \operatorname{erf}\left(\frac{\sqrt{\frac{S}{N}}}{2\sqrt{2}}\right)\right). \quad (4)$$

Then this SNR value in conjunction with Eqs. 1 and 2 can be used to recast Eq.3 into a quadratic equation that can be solved for the quantity:

$$\Omega = \left(\frac{\eta_d}{N_b}\right) \quad (5)$$

The relationship between the number of multiple exposure holograms, N_p , that can be superimposed with equal diffraction efficiency in iron doped $LiNbO_3$ is given by⁴,

$$N_p = \sqrt{\frac{400.0}{\eta_d}} \quad (6)$$

This dependence of N_p on η_d is generally valid for $N_p > 50$, and does not account for losses through the photorefractive crystal. Eqs. (5) and (6) can be combined to yield

$$N_p N_b = \frac{400}{\Omega N_p}. \quad (7)$$

Eq.7 gives the total storage capacity of the photorefractive crystal as a function of the number of pages stored in the crystal.

3 Discussion

A computer model using the analytical results of the last section was written to evaluate the maximum storage capacity of photorefractive crystals. To evaluate this storage capacity, an array of avalanche photodiodes (Hamamatsu S2381) APD has been selected at the output. The characteristic of the APD at a wavelength $\lambda = 514nm$ are fixed; dark current $i_d = 0.1nA$, the output resistance $R_L = 50\Omega$, the quantum efficiency $\eta = 0.5$, the excess noise factor $\chi = 0.3$, and the avalanche multiplicative gain is fixed to $M = 100$. The read laser power is chosen to be $P_L = 40.0mW$.

The functional dependence of the storage capacity on crosstalk for a $BER=10^{-6}$ is shown in fig.1. It is monotonically decreasing with increasing crosstalk. This plot shows also beyond a certain value of ξ (0.95 in this case), the crosstalk is so high that accurate detection of the stored information can not be achieved. The plot in Fig.2. shows that the storage capacity increases with increasing read out time as pointed out by Blotekjaer⁵. Finally, the plot in Fig.3. shows that the storage capacity decreases with increasing number of pages for different crosstalk values. Thus, to attain high storage capacity values, one should consider storing a small number of highly dense pages instead of a larger number of less dense pages.

4 Conclusion

Crosstalk noise sets the limit on the capacity of storage of information in photorefractive crystals. It has been shown that the storage capacity increases with increasing read out time of a page. Finally, to increase the storage capacity of photorefractive crystals one should consider storing a small number of very dense pages.

5 References

1. P. J. van Heerden, "Theory of Optical information Storage in Solids," Appl. Opt. 2, 393 (1963)
2. D. Z. Anderson and D. M. Lininger, "Dynamic Optical Interconnects: Volume holograms as two-port operators," Appl. Opt. 6, 5031 (1987)
3. A. Yariv, "Optical Electronics," CBS College publishing, 1985
4. E. S. Maniloff and K. M. Johnson, "Maximized Photorefractive Holographic Storage," Submitted to Journal of Applied Physics, (1990)
5. K. Blotekjaer, "Limitations on Holographic Storage Capacity of Photochromic and Photorefractive Media," App. Opt. 18, 57 (1979)

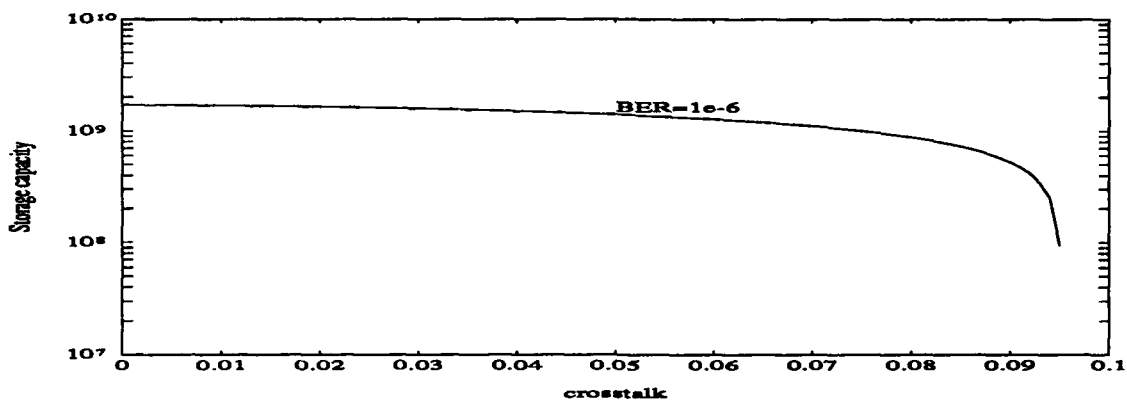


Fig1. Storage capacity versus crosstalk noise

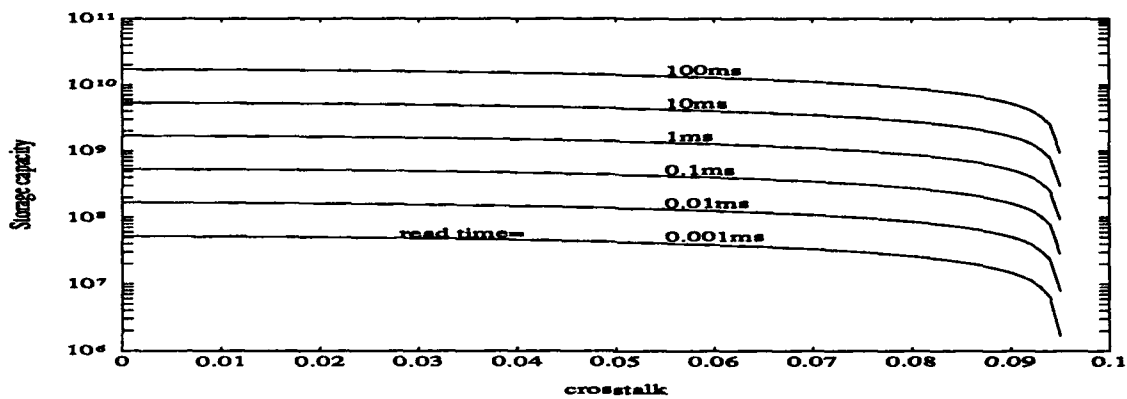


Fig.2 Storage capacity versus Crosstalk noise for different read out times

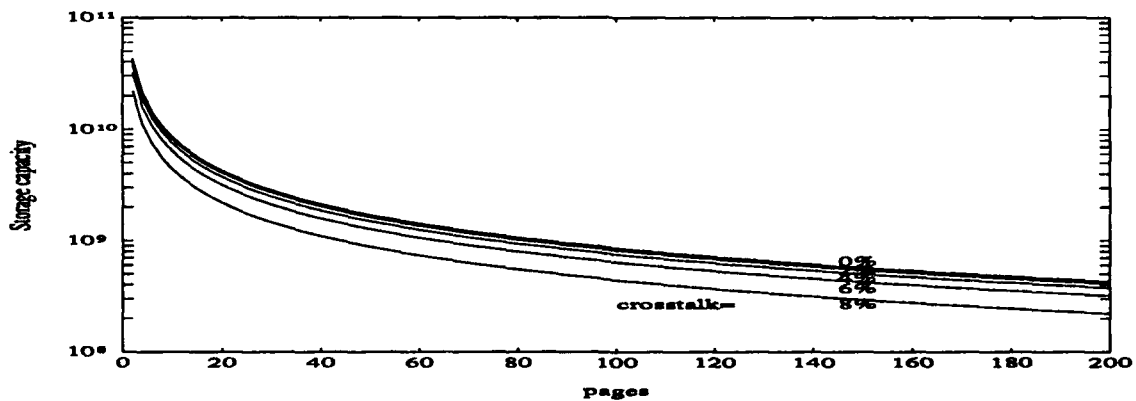


Fig3. Storage capacity versus the number of pages

Angular Selectivity of Holographic Gratings in BSO

Tao, S., Selviah, D.R., Mobasher, B., Poon, P. and Midwinter, J.E.

Department of Electronic and Electrical Engineering

University College London

Torrington Place London WC1E 7JE, U.K.

Abstract

Optics offers the promise of large number of weighted parallel interconnects for use in optical neural networks. However, to date the maximum number of holographic interconnects stored in any photorefractive crystal was 500 in Fe:LiNbO₃. It has not yet been established what are the fundamental limits to the maximum number of angularly multiplexed gratings. One relevant parameter is the angular selectivity of a holographic grating. In this paper we compare the theoretical angular selectivity calculated by coupled wave theory with our experimental measurement of the same quantity for a crystal of BSO. BSO has the advantage for optical interconnects that it has a higher sensitivity than Fe:LiNbO₃, so lower power laser can be used for recording.



Diffraction Efficiency Dynamics in Photorefractive Crystals

Eric S. Maniloff and Kristina M. Johnson

Department of Electrical and Computer Engineering
Center for Optoelectronic Computing Systems
University of Colorado, Boulder, CO 80309

1. Introduction

Due to their large potential storage capacity, photorefractive crystals are an attractive medium for a variety of optical computing architectures[1]. The actual capacity of such storage systems is determined by the minimum acceptable diffraction efficiency for a given system design[2] and the maximum number of holograms that can be recorded with this efficiency in photorefractive crystals.

If the intensity fringes that are responsible for recording the hologram are assumed to be static in both crystal thickness and time, an analytic expression for the temporal dynamics of the index can be obtained [3]. If this index variation is then used in the coupled wave equations, an analytic expression for the diffraction efficiency dynamics is obtained[4]. However, according to the coupled wave equations, the recording fringes are only static in both modulation and phase for local response (grating phase equal to 0) and unity modulation depth. This approach is therefore self-consistent only for this specific case.

A more general approach was formulated in 1977 by Khukhtarev et al[5] in which both the coupled wave equations and the space charge field dynamics were simultaneously calculated. Using this model, transient gain was predicted, however, the affects of this transient gain on the diffraction efficiency dynamics was not investigated.

Using this type of approach we present here a theoretical model for the dynamics of the diffraction efficiency. A comparison with experimental data for holograms recorded in Lithium Niobate is presented for both the diffraction efficiency and the recording intensities at various modulation depths. The diffraction efficiencies predicted by this theory can be several times larger than previous predictions, in agreement with the experimental results. Further deviations from the theoretical predictions obtained using the static fringe assumption will also be presented.

92-18716



2. Diffraction Efficiency Results

Due to the variation in the grating phase with recording time, transient energy transfer can be observed in photorefractive crystals with a local response[5]. Using a notation similar to that of Heaton and Solymar[6], the equations governing the recording of the space charge field are:

$$\frac{\partial R}{\partial x} = i \Gamma E_1^* S \quad (1)$$

$$\frac{\partial S}{\partial x} = i \Gamma E_1 R \quad (2)$$

$$\frac{\partial E_1}{\partial t_n} + A E_1 = B E_q^* R^* S \quad (3)$$

where R and S are the recording waves, E_1 is the space charge field, and A , B , Γ , and E_q include the material parameters and applied field. These equations can be solved numerically to obtain the recording intensities and recorded space charge field. The diffraction efficiency is then obtained by solving equations 1 and 2 for a single incident beam.

For large applied or photovoltaic fields the grating phase in photorefractive crystals is close to zero. In this case, due to the large phase coupling, transient energy exchange is observed. This energy exchange serves to increase the effective modulation depth in the crystal, and hence increases the observed diffraction efficiency. In previous analyses [4], the maximum predicted diffraction efficiency for a recording beam ratio of 10:1 is 30%.

The experimentally measured diffraction efficiency and the amplification of the weak input beam measured in iron-doped Lithium Niobate are plotted in Figure 1 for a beam ratio of 10:1. One of the two recording beams was blocked periodically during recording in order to monitor both the diffraction efficiency and the transient gain. Therefore, the solid line in this plot represents the amplified weak beam, and the spikes represent the diffraction efficiency. Both of these values are normalized with respect to the total transmitted power.

A theoretical fit to the diffraction efficiency and the transient gain are shown in Figure 2. To obtain this fit, the photovoltaic field

was treated as an applied field, and was used as a fitting parameter. Experimental and theoretical results will be presented over a range of beam ratios demonstrating the various types of coupling observed in Lithium Niobate.

Although the agreement between the experiment and theory is excellent over the range of the experiments, for longer recording times much more complicated dynamical behavior is predicted by this model. Since equations 1-3 are nonlinearly coupled in both time and thickness it is not surprising that complicated behavior is predicted. Figure 3 shows the predicted values for one of the recording intensities versus time and thickness for a long recording time. The predictions of this model for the intensities, space charge field, and phases will be discussed in this large coupling regime. In addition, expansion of this theory to include absorption and scattering will be presented.

3. Conclusions

Simplified models for photorefractive dynamics fail to predict the full range of possible dynamical effects. Using a self-consistent model we have obtained an accurate fit to the full range of observed dynamics in Lithium Niobate.

References

1. See for example, Conference Record 1990 Topical Meeting on Optical Computing, SPIE, Bellingham, 1990.
2. A. Lahrichi, G. Fredricks, K. Johnson, and E. Maniloff, "Signal to Noise Limitations on the Capacity of Holographic Interconnect Networks", submitted to JOSA A.
3. G. Valley and M. Klein, "Optimal Properties of Photorefractive Crystals for Optical Data Processing", *Opt. Eng.* **22** (1983).
4. N. Khukhtarev, "Kinetics of Hologram Recording and Erasure in Electrooptic Crystals", *Sov. Tech. Phys. Lett.* **2** (1976).
5. N. Khukhtarev, V. Markov, and S. Odulov, "Transient Energy Transfer During Hologram Formation in LiNbO₃ in External Electric Field", *Opt. Comm.* **23** (1977).
6. J. Heaton and L. Solymar, "Transient Energy Transfer during Hologram Formation in Photorefractive Crystals", *Optica Acta*, **32** (1985).

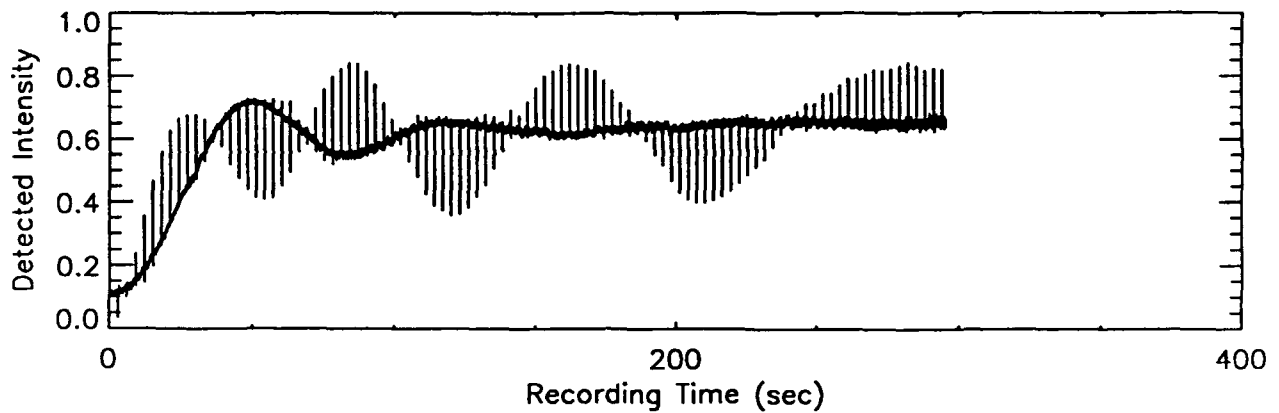


Fig. 1 Experimentally measured diffraction efficiency and intensity gain. The solid line shows the intensity gain, and the spikes show the diffraction efficiency.

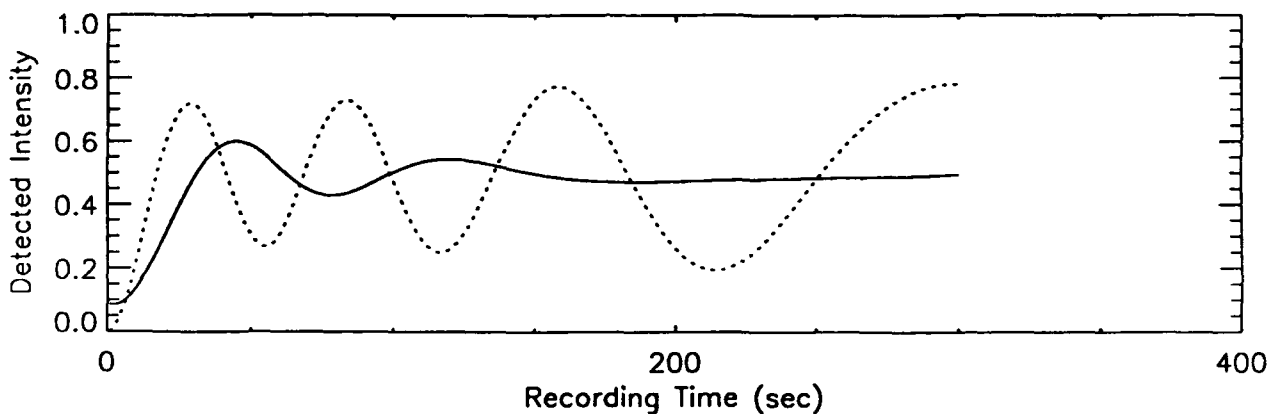


Fig. 2 Theoretical diffraction efficiency and intensity gain, the solid line shows the intensity gain and the dotted line shows the efficiency.

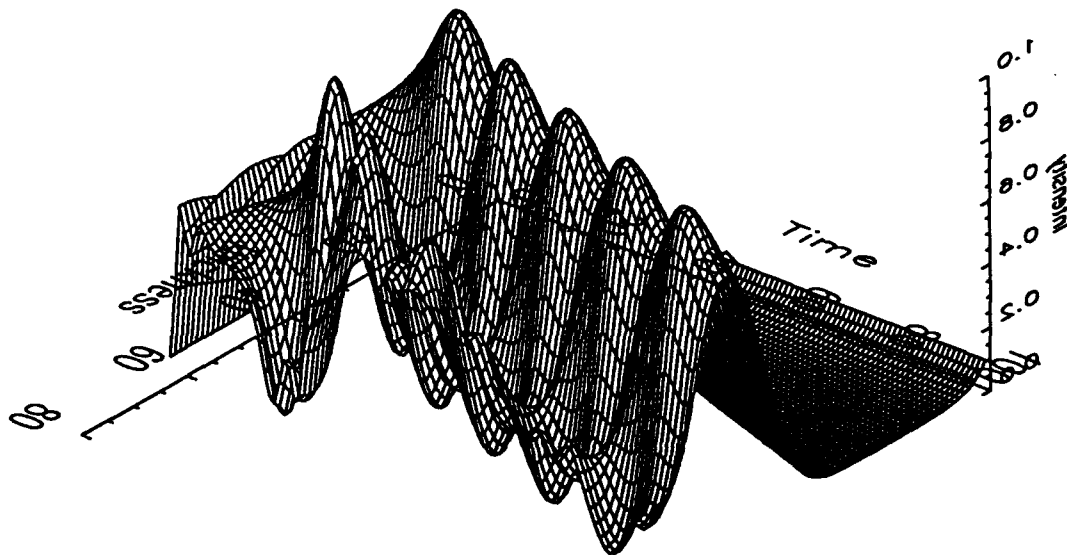


Fig 3 One of the recording intensities versus recording time and thickness.

Tuesday, July 30, 1991

Materials and Diagnostics

TuA 8:00am–10:00am
Academic Center Auditorium

Peter Gunter, *Presider*
Swiss Federal Institute of Technology, Switzerland

AD-P006 729



AN IMAGING METHOD FOR NON LINEAR MEDIUM CHARACTERISTIC MEASUREMENTS.

G. BOUDEBS, X. NGUYEN PHU, J. P. LECOQ, M. SYLLA, G. RIVOIRE.

LABORATOIRE DES PROPRIETES OPTIQUES DES
MATERIAUX ET APPLICATIONS

4 Bvd LAVOISIER BP 2018 49016 ANGERS CEDEX Phone 41.73.53.20

A non linear medium is placed in the focal plane of a $4f$ set up (fig.1). The Fourier spectrum $S(u)$ induces phase and amplitude changes inside the material [1].

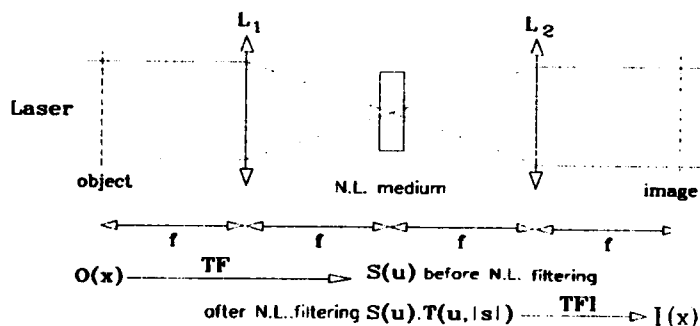


fig. 1

Such self induced non linear effects produce two modifications in the image $I(x)$:

- 1 - intensity variation due to non linear absorption,
- 2 - shape changes due to non linear refractive index variation.

The study of these modifications allows the measurement of the non linear material characteristics.

This method is used to study photorefractive materials excited either with CW or with pulsed laser.

A two slit object $O(x)$ is chosen in our experiment. When non linear refractive index changes (Δn_{NL}) are increasing, supplementary slits are observed in the image plane (fig. 2). Their number and intensity are connected to Δn_{NL} [2].

92-18717



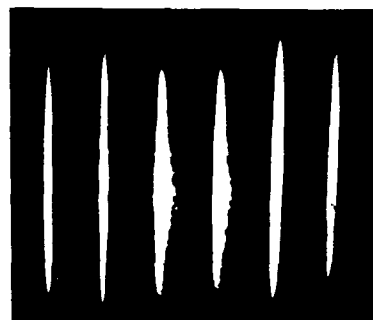


fig 2a: Slits image without
N.L. filtering

fig 2b: slits image in presence
of Fe:LiNbO₃ illuminated
with CW laser

The image formation process involved by using the set up fig. 1 is modeled and simulated on computer. The results are compared with the experimental data. The comparison between the simulated and experimental results allows the determination of the non linear characteristics.

Measurements were made using Fe:LiNbO₃ crystals excited by CW green laser and BSO, BGO crystals excited by picosecond pulses.

The method is particularly interesting for the measurement of real parts of the third order susceptibility tensor components especially when they are associated with high imaginary parts (due to non linear absorption). The precision obtained is better than in the classical methods such as four wave mixing or Jamin interferometry.

References

- [1] NGUYEN PHU XUAN et Al
Optics communications, (1988), 68, 4, 24.
- [2] BOUDERS GEORGES et Al
Opto 91, (26 mars 1991).



Origins of the Photorefractive Phase Shift

R. S. Cudney, G. D. Bacher, R. M. Pierce, and Jack Feinberg

*Departments of Physics and Electrical Engineering,
University of Southern California, Los Angeles, CA 90089-0484, Tel. (213) 740-1134*

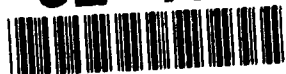
There is a spatial phase shift between a sinusoidal light intensity pattern and the resulting refractive index grating formed in a photorefractive crystal. For crystals where diffusion is the dominant mechanism for charge migration, this spatial shift is $1/4$ of the grating spacing. Any deviation from this value implies some other transport mechanism, such as an applied or internally developed electric field, or the photogalvanic effect, in which optically excited charges preferentially move in one direction in the crystal. Due to its relevance to beam coupling, this spatial shift has been studied extensively using a variety of methods, most of them interferometric in nature¹⁻⁵. However, interferometric methods only reveal the phase of the complex beam coupling coefficient, which is not necessarily the spatial phase shift of the electro-optically induced grating. Other effects, such as trap grating coupling, can affect the phase of the total coupling coefficient, and thereby prevent a measurement of the spatial phase shift.

Trap gratings are formed when light redistributes charge among different trap site levels.⁶⁻⁸ This produces a spatially varying population of empty and full trap sites. If the polarizability of the empty and full sites are different, then a grating is written by the trap sites themselves, without requiring the electro-optic effect. For two-beam coupling in the undepleted pump regime, the amplitude of the weak probe beam changes exponentially with distance with a complex coupling coefficient g_{traps} given by

$$g_{traps}(k_g, I) \equiv |g_{traps}| e^{i\phi_{traps}} = \frac{A(I)k_g^2 + B(I)}{1 + k_g^2/k_0^2(I)}. \quad (1)$$

Here $A(I)$ and $B(I)$ are complex-valued functions of the total light intensity I , the trap densities of the different levels, the trap polarizabilities, and the excitation and recombination rates. $k_0(I)$ is the effective inverse screening length, which in general is intensity dependent. In Eq. (1) we have assumed a single type of charge carrier, no externally applied fields and no photogalvanic effect. Under these conditions the spatial phase shift of the trap gratings is exactly 0° (or 180°); however, since the polarizabilities of the traps are intrinsically complex (with the real and imaginary part representing the index of refraction and the absorption, respectively), g_{traps} is also complex. The

92-18718



imaginary part of g_{traps} alters the amplitude of the weak probe beam (energy transfer from or to the reference beam) while the real part alters its phase.

We measure the real and imaginary part of g_{traps} in barium titanate using a frequency modulation technique.³⁻⁴ Fig. (1) shows the basic experimental set-up: a laser beam is split into a reference beam and a less intense probe beam which intersect and write a grating inside the crystal. The probe beam's phase is modulated sinusoidally with a very small amplitude by an electro-optic modulator.

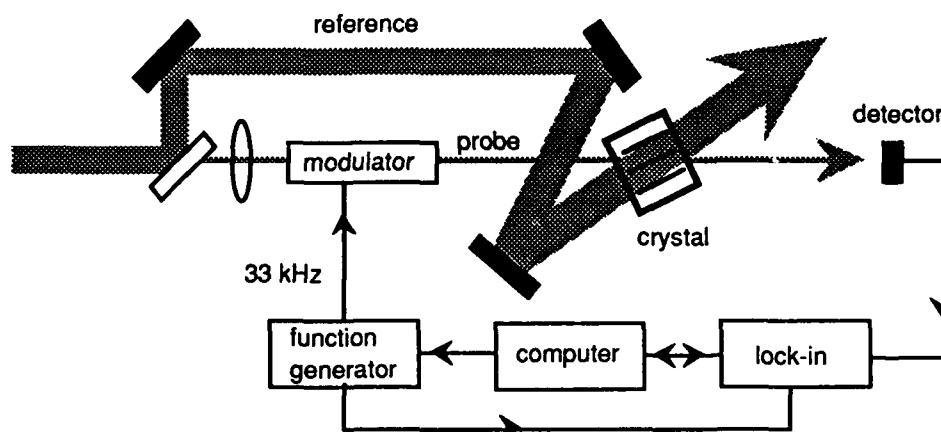


Fig 1. Experimental set-up.

If the modulation frequency Ω is high enough, the crystal will not be able to follow the rapid variations of the interference pattern. However, the frequency modulated probe beam will beat with the diffracted portion of the reference beam, producing sidebands at harmonics of Ω . The relative intensity of the different harmonics will depend on the phase of g_{traps} and on the magnitude of the phase modulation μ . For $\mu \ll 1$ and $|g_{traps}z| \ll 1$ the components of the transmitted probe beam intensity oscillating at Ω and 2Ω are given by

$$\frac{I_p(\Omega)}{I_p^0} = -2\mu \text{Im}[g_{traps}z] \sin(\Omega t) \quad (2)$$

$$\frac{I_p(2\Omega)}{I_p^0} = \frac{\mu^2}{2} \text{Re}[g_{traps}z] \cos(2\Omega t) \quad (3)$$

where I_p^0 is the output intensity of the probe beam without coupling and z is the interaction length.

In order to isolate the coupling due to trap gratings in barium titanate, we aligned the c-axis perpendicular to the plane of incidence of the optical beams, which gives a null effective electro-optic coefficient for two-beam coupling. In this configuration there is no preferential direction for

charge transport, irrespective of the underlying mechanism, so the trap gratings must be spatially in phase with the light intensity pattern. Fig. (2) shows the phase of g_{traps} vs. k_g at different wavelengths in a barium titanate crystal (called "Free"):

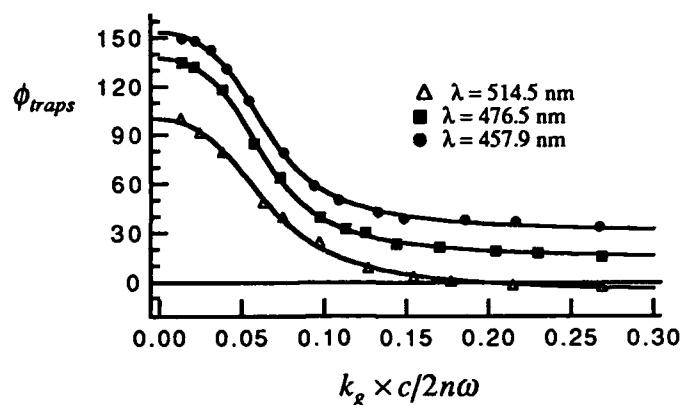


Fig. 2. Phase of trap grating coupling vs. k_g at different wavelengths ($I = 1 \text{ W/cm}^2$).

The solid lines are curve fits to ϕ_{traps} using Eq. (1). For a crystal with a single active level, the phase of the coupling coefficient should be constant; it represents the phase of the difference in polarizability between the full and empty sites of the active level. Fig. (2) clearly shows that ϕ_{traps} in "Free" is not constant with k_g . We interpret this as an indication that there is more than one photo-active level present in this sample of barium titanate.

We repeated the same experiment using ordinary beams but with the c-axis parallel to \mathbf{k}_g . Now we see beam coupling from both trap and electro-optic gratings. In addition, this crystal orientation allows photogalvanic currents and fields to break the symmetry of charge transport, and thereby create an arbitrary spatial shift between the electro-optic grating and the light interference pattern. Eqns. (2) and (3) are still valid, provided that g_{traps} is changed to the total complex coupling coefficient $g_{total} = g_{traps} + g_{eo}$, where g_{eo} is the complex electro-optic coupling coefficient. Fig. (3a) and (3b) show the real and imaginary parts of g_{total} measured at an external half-crossing angle $= 1.2^\circ$, and Fig (3c) shows the inferred phase shift ϕ_{total} . In order to isolate the phase of g_{eo} we measured the trap coupling separately and subtracted it from g_{total} ; the results are shown in Fig. (4). In Fig. (4c) a phase shift of 0° would correspond to purely diffusive transport (i.e., the usual 90° phase shift). Two conclusions can be made from Fig. (3) and (4): i) the spatial shift is intensity dependent and ii) the effects of the trap grating coupling are not negligible and must be taken into account to get the correct spatial phase shift.

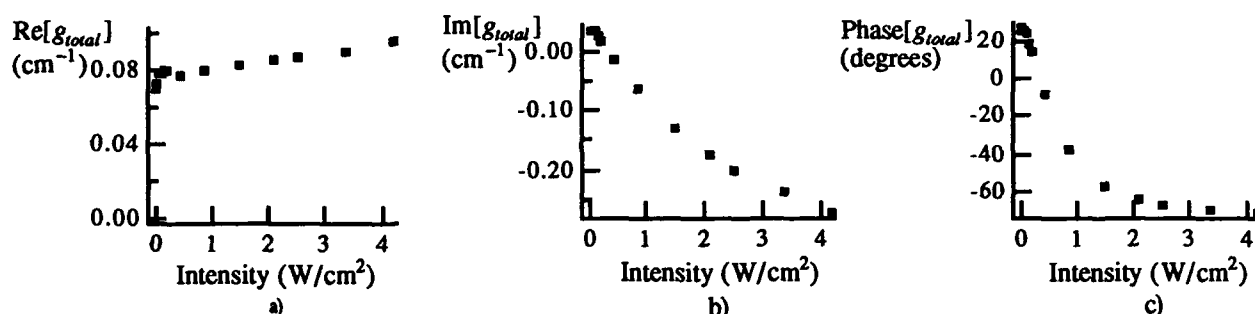


Fig. 3. Real part, imaginary part and phase of the trap plus electro-optic coupling coefficient vs. intensity at an external half-crossing angle $=1.2^\circ$ and $\lambda = 515$ nm.

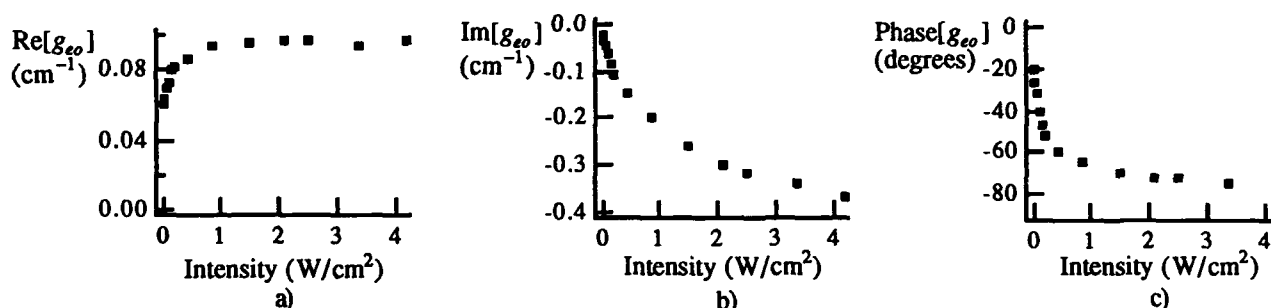


Fig. 4. Real part, imaginary part and phase of just the electro-optic coupling coefficient vs. intensity at an external half-crossing angle $=1.2^\circ$ and $\lambda = 515$ nm.

What causes the spatial shift? It is tempting to ascribe it to a constant photovoltaic field; however, the sign of the externally measured field is opposite to that inferred from our phase shift measurements and the magnitude of the field is too small; furthermore, if dark conductivity is negligible, then the drift produced by the photovoltaic field should be balanced by the photogalvanic current that produced the field in the first place. We tried painting silver electrodes on the c-faces of the crystal and joining them with a wire in order to eliminate any uniform electric field. No noticeable difference in the phase shift was observed, so we conclude that a uniform field does not build up. We believe the phase shift is caused by the photogalvanic *current* itself, which produces a phase shift in the correct direction.

1. V. Kondilenko, V. Markov, S. Odulov, and S. Soskin, *Optica Acta* **26**, 239 (1979).
2. I. McMichael and P. Yeh, *Opt. Lett.* **12**, 48 (1987).
3. R. S. Cudney, G. D. Bacher, R. M. Pierce and J. Feinberg, OSA Meeting, Technical Digest **11**, ThU5 (1988).
4. P. Magno García, L. Cescato, and J. Frejlich, *J. Appl. Phys.* **66**, 47 (1989).
5. K. Sutter and P. Günter, *J. Opt. Soc. Am.* **7**, 2274 (1990).
6. A. V. Alekseev-Popov, A. V. Knyaz'kov, and A. S. Saikin, *Sov. Tech. Phys. Lett.* **9**, 475 (1983).
7. R. B. Bylsma, D. H. Olson, and A. M. Glass, *Opt. Lett.* **13**, 853 (1988).
8. R. M. Pierce, R. S. Cudney, G. D. Bacher and J. Feinberg, *Opt. Lett.* **15**, 414 (1990).
9. A. M. Glass, D. von der Linde, and T. J. Negran, *App. Phys. Lett.* **25**, 233 (1974).

PHOTO GALVANIC HOLOGRAPHIC GRATINGS IN THE STRONCIUM BARIUM NIOBATE CRYSTALS (SBN: Ce).

*A. Gnatovskii, N. Kukhtarev, A. Pigida,
V. Verbitskii, N. Bogodaev, N. Polozkov.*

Institute of Physics, Academy of Science of the Ukr. SSR.
Prospect Nauki 46, Kiev, 252650, USSR.

Photogalvanic holographic gratings were recorded in the photorefractive crystal $\text{Sr}_{0.39}\text{Ba}_{0.61}\text{NbO}_3:\text{Ce}$ (0.05 weight %) by HeNe laser ($\lambda = 0.633\mu\text{m}$). When holographic grating vector was perpendicular to the \vec{c} axis hologram writing with orthogonally polarized waves were realized with diffraction efficiency of 6% (for thickness 1.0 mm). Intermode scattering [1] was observed in accordance to calculations and photoinduced holographic electric field was estimated to be about 600 V/cm. Photogalvanic holographic grating, recorded with orthogonally polarized waves may be used for phase conjugation with polarization restoration [2,3], and for processing of laser beams.

1. N. Kukhtarev, Photorefractive Effect and Materials, Topics on Applied Physics, Springer Verlag, 1988, v. 61, p. 99-129.
2. I. McMichael, P. Yeh and Backwith, Opt. Lett, 1987, v. 12, p. 507.
3. I. Volkov, A. Volyar, N. Kukhtarev et al. Optica i spectroscopia (Russian) 1988, v. 64, N 4, p. 927-930.

Electro-Optic Effects and Domain Reversal in $\text{Sr}_{0.61}\text{Ba}_{0.39}\text{Nb}_2\text{O}_6$

Jeffrey P. Wilde and Lambertus Hesselink

Department of Applied Physics
 Stanford University, Stanford, CA 94305
 (415) 723-4940

AD-P006 731Abstract

We present the results of a comprehensive electro-optic (EO) study of $\text{Sr}_{0.61}\text{Ba}_{0.39}\text{Nb}_2\text{O}_6$ at $\lambda = 633$ nm. The experiments are conducted in the transverse field configuration, hence the effective linear EO coefficient r_c is measured. Uniformly poled samples yield $r_c = 230 \pm 20$ pm/V at 25°C and $r_c = 1600 \pm 150$ pm/V at 65°C . However, the EO behavior is found to substantially degrade when attempting domain reversal. Imaging a crystal through crossed polarizers during the reversal process shows a very non-uniform birefringence distribution in the vicinity of the original $-c$ electrode face.

Introduction

$\text{Sr}_x\text{Ba}_{1-x}\text{Nb}_2\text{O}_6$ (SBN) is a ferroelectric tungsten bronze crystal that, when uniformly poled, possesses a large linear EO effect for temperatures below the Curie point ($T_c = 75^\circ\text{C}$ for $x=0.61$). The magnitude of the effect is strongly dependent on the composition as shown by Lenzo *et al.* [1] in their early studies of crystals with $x = 0.25, 0.50$ and 0.75 . In this paper the primary interest centers around the congruent composition, $x = 0.61$. For SBN:61 at 25°C , Neurgaonkar and Cory [2] report $r_{33} = 420$ pm/V while the interferometric measurements of Ducharme *et al.* [3] give $r_{33} = 235 \pm 21$ pm/V and $r_{13} = 47 \pm 5$ pm/V. To our knowledge, EO measurements as a function of temperature have only been previously conducted by Fox [4] for SBN:70.

Photorefractive crystals that are also ferroelectric have been shown to offer some interesting holographic recording properties when the spontaneous polarization (P_s) is varied with an applied electric field. Applications include rapid switching of the two-beam coupling direction [5] and magnitude [6], control over latent and active states of a pre-recorded hologram [7], and "electrical fixing" of a hologram for sustained non-destructive readout [8]. The reversibility of P_s is a central feature of these applications. Typically, the domain reversal process is quantified by measuring P_s vs. E hysteresis loops. A number of researchers have found that beginning with an unpoled crystal, the shape of a hysteresis loop can change dramatically after only a few (< 5) switching cycles for both SBN:50 [9,10] and SBN:75 [11]. The most notable change occurs during the very first reversal. For SBN:50 at room temperature, the initial value of P_s is $\sim 30 \mu\text{m}/\text{cm}^2$. After just four reversals, P_s is reduced to a fairly stable value of $\sim 5 \mu\text{m}/\text{cm}^2$ [10]. Borchardt *et al.* [11] attribute this degradation to an interface effect at the metal-crystal electrodes. Their claim is based on the following observations: 1) after repeated switching, the crystal can be returned to its original state by polishing the electrode surfaces to remove $\sim 100 \mu\text{m}$ of material and applying new electrodes.

92-18719

and 2) using LiCl aqueous electrodes, instead of metal (Au, Ag, Nb, Sb) electrodes, provides substantially less degradation of the switching.

In this paper we report measurements of the effective linear EO coefficient r_c at 25°C and 65°C. We also monitor the degradation of the EO effect upon attempted domain switching. Images of a crystal taken before and after the reversal process clearly show a pronounced interface effect and provide a visual confirmation of the work in Ref. [11].

EO Effect in SBN

Single crystals of SBN belong to the point symmetry group 4mm at room temperature, and this symmetry class has three nonzero linear EO coefficients: $r_{13} = r_{23}$, $r_{42} = r_{51}$ and r_{33} . In the standard transverse configuration, E is applied along the [001] c -axis and light propagation is along [100]. The birefringence, to first order in E , is then given by,

$$\Delta n = (n_e - n_o) - \frac{1}{2} n_e^3 r_c E, \quad (1)$$

where $r_c = r_{33} - (n_o^3/n_e^3)r_{13}$. The transmitted intensity I of a crystal placed between crossed polarizers (oriented at 45° with respect to the crystallographic axes) is [12],

$$I = I_o \sin^2 \left(\frac{\Gamma}{2} \right), \quad (2)$$

where I_o is the peak transmittance and Γ is the optical phase retardation given by,

$$\Gamma = \Gamma_o + \Gamma_1 r_c E. \quad (3)$$

For light with a vacuum wavelength λ and a sample interaction length L , we have $\Gamma_o = (2\pi/\lambda)(n_e - n_o)L$ and $\Gamma_1 = (\pi/\lambda)n_e^3 L$.

Experimental Results

The SBN:61 crystals used in this study were grown by the Czochralski method using facilities at the Center for Materials Research, Stanford University. The crystals contain striations that are approximately perpendicular to the c -axis and observed predominantly with extraordinary polarized light. Based on interferograms made from thin sections, we find the striae correspond to $\Delta n_e \simeq 5 \times 10^{-4}$ at room temperature. We estimate, using data from Ref. [1], that this index variation results from a $\pm 0.5\%$ change in the local composition, but low-level impurities may also be involved. The optical striae scattering is highly dependent on the input angle, and a number of samples were prepared (approximate cubes with dimensions between 3-5 mm) that exhibited a reasonably "clean" transmittance for near-normal incidence. Evaporated metal electrodes were formed with 100 Å of Cr followed by 4000 Å of Au.

To perform the EO experiments, a sample is first mounted between 1 cm² copper plates and electrically connected to the plates by a thin layer of air-drying silver paste. The sample and mount are then placed in a cuvette containing high-dielectric silicone oil that can be

uniformly heated by an aluminum enclosure to which power resistors are connected. The value of r_c is measured by linearly ramping the applied electric field at a rate of 2.5 kV/cm-min and performing a least-squares fit, using Eq. 2, to the first few intensity cycles. Because SBN is naturally birefringent ($n_e - n_o = -0.03$ at 25°C [13]), it is important to minimize the effects of any sample variation (thickness and/or composition). This is done by using a focused He-Ne laser beam with a free-space waist of 70 μm and a Rayleigh range of 24 mm. A low incident intensity of $\sim 1 \text{ mW/cm}^2$, taken at the beam waist, is used to prevent any measurable beam fanning. The beam is chopped at a 1 kHz rate for lock-in detection.

Results for a uniformly poled crystal at 25°C are shown in Fig. 1a and yield $r_c = 233 \text{ pm/V}$. At 65°C the same experiment produces a "chirped" signal (shifting to smaller r_c with increasing E) owing to the strong dependence of the dielectric constant ϵ_c on the E -field [4]. However, least-squares fitting gives $r_c = 1600 \pm 150 \text{ pm/V}$ in the limit $E \rightarrow 0$. Some of the uncertainty is attributed to variations in thermocouple placement, leading to possible measured temperature differences of $\pm 1^\circ\text{C}$ from one sample to the next. It is possible that the striae may also affect the measurements, but the resulting error should be bounded by the $\pm 0.5\%$ uncertainty in x . The degree to which space-charge layers at the electrodes affect the results is still unknown.

The EO signal during (scan1) and after (scan2) domain reversal is shown in Fig. 1b. Rapid switching is seen to occur near -4 kV/cm, followed by a clear degradation in the EO effect. The degradation persists despite repeated switching attempts with both E -field polarities. Imaging a sample before and after switching (Fig. 2) shows that, after switching, the field-induced birefringence is limited to a thin layer ($< 500 \mu\text{m}$) adjacent to the original - c face. Only after heating above T_c and re-poling, could the sample be returned to a condition of uniform P_s . These results are consistent with the earlier switching studies and indicate that domain reversal using an E -field applied with metal electrodes is significantly corrupted by an interface phenomenon. The detailed nature of the interface physics is uncertain, but these findings have important implications for photorefractive applications that require some type of domain switching.

References

1. P. V. Lenzo, E. G. Spencer and A. A. Ballman, *Appl. Phys. Lett.* **11**, 23 (1967).
2. R. R. Neurgaonkar and W. K. Cory, *J. Opt. Soc. Am. B* **3**, 274 (1986).
3. S. Ducharme, J. Feinberg and R. R. Neurgaonkar, *IEEE JQE QE-23*, 2116 (1987).
4. A. J. Fox, *J. Appl. Phys.* **44**, 254 (1973).
5. D. M. Gookin, *Opt. Lett.* **12**, 196 (1987).
6. J. Ma, L. Liu, S. Wu, Z. Wang, L. Xu and B. Shu, *Appl. Phys. Lett.* **53**, 826 (1988).
7. J. B. Thaxter and M. Kestigian, *Appl. Opt.* **13**, 913 (1974).
8. F. Micheron and G. Bismuth, *Appl. Phys. Lett.* **23**, 71 (1973).
9. R. B. Maciolek and S. T. Liu, *J. Elect. Mat.* **2**, 191 (1973).
10. T. W. Cline, Ph. D. Thesis, The Pennsylvania State University, (1977), pp. 21-25.
11. G. Borchardt, J. Von Cierninski and G. Schmidt, *Phys. Stat. Sol. A* **76**, K1 41 (1983).
12. A. Yariv and P. Yeh, *Optical Waves in Crystals* (Wiley, NY, 1984), p. 131.
13. A. S. Bhalla, R. Guo, L. E. Cross, G. Burns, F. H. Dacol and R. R. Neurgaonkar, *Phys. Rev. B* **36**, 2030 (1987).

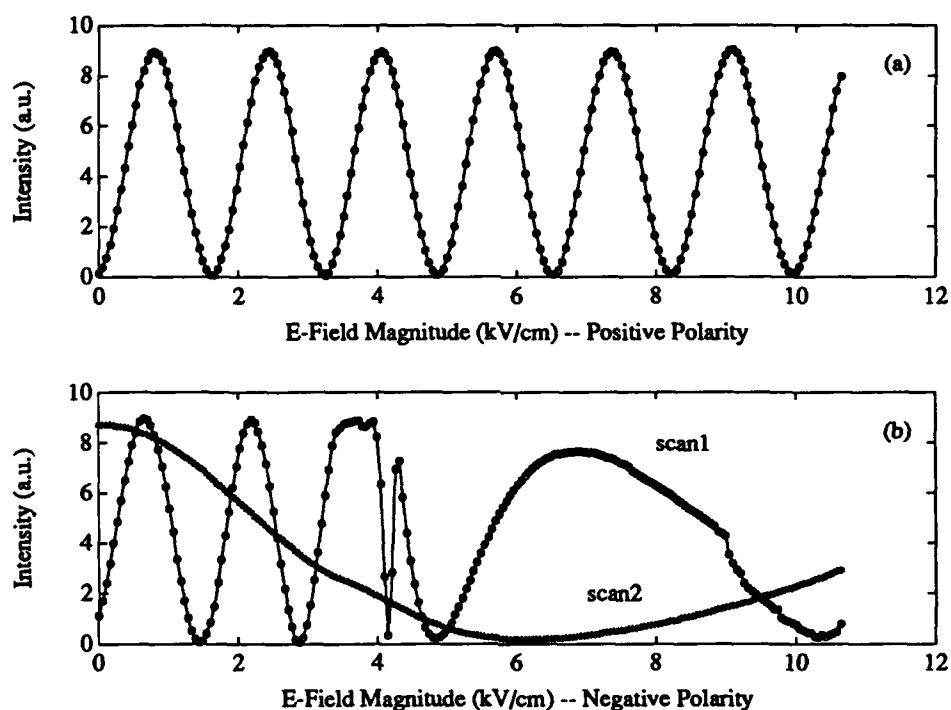


Figure 1: Transmitted intensity as a function of E at 25°C: (a) uniformly poled sample, and (b) same sample during (scan1) and after (scan2) domain switching. The trace in (a) was taken immediately prior to the traces in (b).

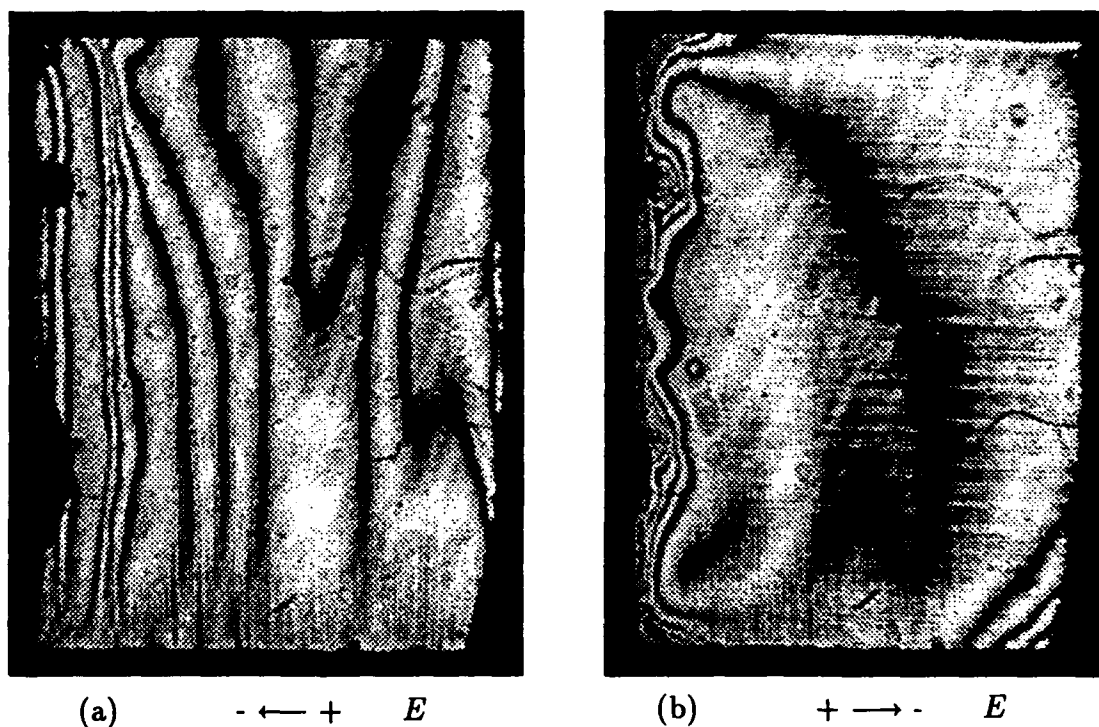


Figure 2: Images of a crystal through crossed polarizers in the presence of an applied electric field: (a) uniformly poled state ($E = +10$ kV/cm), and (b) after domain switching ($E = -10$ kV/cm).



Applied Electric Field Effect on Photorefractive GaAs

Duncan T. H. Liu, Li-Jen Cheng, and Jae-Hoon Kim

Jet Propulsion Laboratory

California Institute of Technology

Pasadena, California 91109, USA

INTRODUCTION

Compound semiconductors such as GaAs are known to be very fast photorefractive materials. However, due to their relatively small electro-optic coefficient, their diffraction efficiency is much smaller than that of most oxide materials such as BaTiO₃. Even so, easily detectable signal with fairly good signal to noise ratio can be usually achieved in a GaAs based application without the aid of an external electric field due to the cross-polarization coupling¹ capability of GaAs and the high sensitivity of modern video cameras. For example, in a recently demonstrated real-time optical image correlator², the correlation output was normally strong enough to saturate the vidicon camera used. On the other hand, in some applications such as the ring oscillator, the double phase conjugate mirror, and the self-pumped phase conjugator, a sufficiently large net two-beam coupling gain is needed. In compound semiconductors, net gain had been achieved by applied electric field techniques. However, in general, these techniques have two side effects, namely the Schottky-barrier effect³ and the low-frequency current



oscillation effect⁴. Depending on the particular requirement of an application, these effects may or may not be a problem. But, they are not desired in general. In this paper, we report the results of a study on the electrode material dependence of the Schottky-barrier effect in the undoped GaAs crystal. In particular, the widely-used silver-paste electrodes are compared with thermally-evaporated alloy electrodes.

SCHOTTKY EFFECT IN GaAs WITH APPLIED ELECTRIC FIELD

It is well known that Schottky barrier is a potential barrier that occurs near the junction of a metal and a semiconductor as this junction is reverse biased. It can be used to make useful electronic components such as Schottky diodes. On the other hand, it is an undesired effect in photorefractive semiconductor crystals because it makes the electric field and so the photorefractive effect non-uniform inside the crystal.

The strength of the Schottky effect depends on the kind of metal and the type of semiconductor used as well as on how the metal is attached to the semiconductor crystal. In most works, the silver paste electrodes are used because they are simple to make. The Schottky effect in a GaAs:Cr crystal with silver-paste electrodes was previously reported³ in which a very strong Schottky effect was observed and the relation between the width of the Schottky barrier and the applied voltage was found to agree with the semiconductor device theory. To reduce the Schottky effect, an

Ohmic contact is needed. An effort was made earlier to achieve this goal using InZn contacts on undoped GaAs⁵. The contact was deposited on the GaAs crystal by thermal evaporation and then annealed at 460 C for a few minutes. The electric field was found to be quite uniform in this crystal when the average electric field reaches about 8 kV/cm.

EXPERIMENT

In our investigation, an undoped GaAs sample with silver-paste electrodes is compared to samples with other electrode materials such as InZn, AuGe, and Au under equal conditions. These samples were obtained from the same boule and cut to the same size, namely 10 mm x 5 mm x 5.5 mm. To compare them, DC electric field and DC electric field with moving grating enhanced two beam coupling experiments were performed. The Schottky effect on two-beam coupling in these samples was monitored by a video camera. The results indicate that the Schottky effect in the sample with InZn, AuGe, and Au electrodes is much less strong than in the sample with silver-paste electrodes. Furthermore, the beam coupling coefficient in the strong field region was measured for each sample as an index for the relative electric field in the Schottky barrier region. The gain coefficient of the sample with silver-paste electrodes was found to be about 7 cm^{-1} at 5 kV which is as high as that reported previously³, while the gain coefficient of the sample with InZn electrodes was found to be only about 4 cm^{-1} at the same voltage. This difference in the

gain coefficient is large because the Schottky barrier is much narrower in the sample with silver-paste electrodes than in the sample with InZn electrodes, an indication that InZn electrodes behave more like an Ohmic contact on the particular GaAs samples used than the silver-paste electrodes. The influence of Schottky effects and low-frequency current oscillation on the optical processing will be discussed.

REFERENCES

1. Duncan T. H. Liu and Li-Jen Cheng, J. Opt. Soc. Am B 6, 1554 (1989) and the references therein.
2. Duncan T. H. Liu, Li-Jen Cheng, Tien-Hsin Chao, Jeffrey W. Yu, and Don A. Gregory, SPIE Proceedings Vol. 1347 "Optical Information-Processing Systems and Architectures II," 156 (1990).
3. B. Imbert, H. Rajbenbach, S. Mallick, J. P. Herriau, J. P. Huignard, Opt. Lett. 13, 327 (1988).
4. H. Rajbenbach, J. M. Verdiell, and J. P. Huignard, Appl. Phys. Lett. 53, 541 (1988).
5. D. T. H. Liu, L. J. Cheng, M. F. Rau, and F. C. Wang, Appl. Phys. Lett. 53, 1369 (1988).



Photorefractive properties and alternating electric field gain enhancement of vanadium-doped cadmium telluride and related compounds

Mehrdad Ziari and William H. Steier

Department of Electrical Engineering, Center for Photonic Technology
University of Southern California, Los Angeles, California 90089-0483

Marvin B. Klein

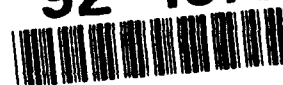
Hughes Research Laboratories, 3011 Malibu Canyon Road, Malibu, California 90265

Sudhir Trivedi

Brimrose Corporation of America, 7720 Belair Road, Baltimore, Maryland 21236

Recent studies of the photorefractive response of CdTe have demonstrated it to be a highly sensitive material with a broad near infrared sensitivity extending to beyond $1.5\ \mu\text{m}$ ^[1,2]. Desirable parameters, such as large electrooptic coefficient, small dielectric constant, large carrier mobility and availability in semi-insulating form, makes CdTe a potential material of choice for many applications^[3]. This study focuses on photorefractive characterization of Bridgeman grown crystals with the goal of providing the information that can lead to the optimization of key photorefractive parameters. We have observed gain and broad sensitivity (1 - $1.5\ \mu\text{m}$) in vanadium doped CdTe and $\text{Cd}_{0.96}\text{Zn}_{0.4}\text{Te}$ samples. Mixed alloys such as CdZnTe and CdMnTe allow band gap engineering such that the sensitivity range could be tuned toward the visible and be matched to the wavelength of interest. An applied alternating (AC) field gain enhancement technique is used to demonstrate net gain which is a prerequisite for coherent amplification and self-pumped phase conjugation.

The advantages of CdTe as a photorefractive material have been suggested in the past^[3] and vanadium was later shown to be a proper dopant^[4], capable of producing the necessary deep centers. Recent studies^[2] demonstrated a response at $1.5\ \mu\text{m}$, a wavelength of interest for optical communications and eye-safe applications, and compared the grating formation fluence and the index change per absorbed energy or photon to that of other semiconductors such as GaAs, GaAs:Cr and InP:Fe. Our measurements confirmed that CdTe has the highest sensitivity of any known photorefractive semiconductor.

92-18721

This study was further extended and other samples were characterized. Two-wave mixing experiments suggest effective trap densities in the $1-5 \times 10^{15} \text{cm}^{-3}$ range for most crystals. The optical loss coefficients of different CdTe:V samples at the wavelength of $1.5 \mu\text{m}$ are between 0.5 to 2.0cm^{-1} . The difference in the absorption coefficient can be correlated with the effective trap density such that the samples with lower trap densities consistently exhibit reduced optical losses. This could be attributed to different incorporation of vanadium in the growth process. All samples benefited from large electrooptic coefficient (r_{41}) and low electron-hole competition (ξ). The estimated ξr_{41} value for all our samples is around 4.5 pm/V . The photorefractive carrier is determined to be electrons at the wavelengths of 1.064 , 1.318 , and $1.523 \mu\text{m}$. The intensity dependence of the beam coupling gain implies a low value for the equivalent dark irradiance ($I_d \sim 100 \mu\text{W/cm}^2$) which is consistent with the large dark resistivity and is favorable for low power CW applications.

The two-beam coupling gain in semiconductors can be further enhanced by many techniques, such as DC field and a moving grating^[5], application of an alternating (AC) square or sinusoidal field^[6,7,8], temperature tuning^[9] in InP, operation at the band-edge with a DC field^[10] and finally combinations of the above techniques^[11]. The applied AC field technique has some inherent advantages over the other approaches. It provides a large gain uniformly across the sample, and can be used far from the band edge, where the field induced electroabsorptive and the background losses are low. The AC field gain enhancement is a non-resonance effect and therefore is far less sensitive to temperature and intensity variations. The transport properties of CdTe allow higher electric fields to be applied before drift velocity saturation effectively reduces the mobility of the carrier. The decrease in mobility and lifetime can reflect upon many gain enhancement techniques in a negative manner^[12] and would result in gain reduction.

We used a high voltage (0-6kV) square wave generator ($f = 100-200 \text{ KHz}$) to enhance the beam coupling gain. A set of preliminary measurements showed a gain coefficient of $\Gamma = 3.3 \text{ cm}^{-1}$ at $1.318 \mu\text{m}$ wavelength, a fringe spacing of $5.5 \mu\text{m}$, and an applied field of 10 kV/cm . This translates into a net gain of larger than 2.5 cm^{-1} , such that a 0.4 cm sample could produce a ΓL value of larger than unity. The measured gain as a function of applied voltage falls below the theoretical predictions. The deviation, however, can be explained by the finite rise time and fall time of the nominally square pulse^[5]. The theoretical treatment in Ref. 5 suggest an appreciable decrease in the enhancement factor for our pulse shape ($t_{\text{rise}}/\text{Pulse period} \sim 0.15$). Our observed gain is large as compared to experiments with AC fields in GaAs^[7] and InP^[8] and can be further improved by using larger fringe spacings. A comparison with the experimental findings of Ref. 8 suggest that our observed gain is sufficiently large for achieving self-pumped phase conjugation.

We have undertaken the study of photorefractivity in II-VI alloys of CdTe:V and observed beam-coupling gain at $1.138 \mu\text{m}$ in a $\text{Cd}_{0.94}\text{Zn}_{0.4}\text{Te:V}$ [10^{19}cm^{-3}] sample, which to the best of our knowledge, is the first observation in ternary II-VI compounds. The bulk alloying capability can lead to development of materials whose band gap and sensitivity range can overlap the wavelength of application. The absorption spectrum of this sample is fairly flat and rises sharply at the band edge. The absorption coefficient at $1.3 \mu\text{m}$ is estimated to be less than 0.1 cm^{-1} . The beam coupling at this wavelength suggest an effective trap density of $\sim 2 \times 10^{15}$ and a slightly reduced value of 3 pm/V for the χ_{r41} coefficient. The resistivity which was measured using the van der Pauw or a simple two point resistive method to be $\rho \sim 10^6 - 10^7 \Omega\text{-cm}$ is less than CdTe:V. The intensity dependence of gain and grating formation time revealed a reduced sensitivity for this sample which could be explained by its low absorption and higher dark conductivity. Photoluminescence and scanning electron microscopy (SEM) is being performed on this crystal to understand the nature of vanadium incorporation in the crystal growth. This study will be extended to other materials such as CdMnTe and ZnTe.

In conclusion, we find vanadium doped CdTe a promising material in the near infrared region. The sensitivity range can be extended by alloying CdTe with larger band gap semiconductors. Applied AC fields result in sufficiently large net gains that can be used for phase conjugation and coherent amplification.

Reference:

1. M. Ziari et al " Photorefractive Properties of CdTe at $1.5 \mu\text{m}$ ", IEEE Digest of Nonlinear Optics: Materials, Phenomena and devices conference, Kuai, Hawaii ,1990
2. A. Partovi, J. Millerd, E. Garmire,. M. Ziari, W. H. Steier, Marvin B. Klein and Sudhir Trivedi, Appl. Phys.Lett., **57**, 846 (1990)
3. A. M. Glass and J. Strait in *Photorefractive Materials and Their Applications I* (Springer-Verlag, Berlin,1988) Ch. 8.
4. R. B. Blysm, P. Bridenbaugh, D. Olson, and A. M. Glass, Appl. Phys. Lett. **51**, 889 (1987)
5. K. Walsh, A. K. Powell, C. Stace, and T. J. Hall. J. Opt. Soc. Am. B. **7**, 288 (1990)
6. B. Imbert, H. Rajbenbach, S. mallick, J. Herriau, and J. Huignard, Opt. Lett. **13**, 327 (1988)
7. M. B. Klein, S. McCahon, T. F. Boggess, and G. Valley, J. Opy. Soc. Am. B **5**, 2467 (1988)
8. R. B. Bylsma, A. M. Glass, D. Olson, and M. C. Golomb, Appl. Phys. Lett. **54**, 1968 (1989)
9. G. Picoli, P. Gravey, C. Ozkul, and V. Vieux, J. Appl. Phys. **66**, 3798 (1989)
10. A. Partovi, A. Kost, E. Garmire, G. Valley, and M. Klein, Appl. Phys. Lett. **56**, 1089 (1990)
11. J. Millerd, S. Koehler, E. Garmire, and A. Partovi, *OSA Annual Meeting Digest 1990*, p. 239
12. G. C. Valley, H. Rajbenbach and H. J. Bardeleben, Appl. Phys. Lett., **56**, 364 (1990)



Synchrotron X-ray Diffraction Imaging of Photorefractive Crystals. Gerard Fogarty and Mark Cronin-Golomb, *Electro-Optics Technology Center, Tufts University, Medford, Massachusetts (617 381 3136* and Bruce Steiner, *The National Institute of Standards and Technology, Gaithersburg, Maryland (301) 975 5977*

Signal processing in photorefractive crystals is complicated by photorefractive amplified scattering (fanning). The scattering centers responsible for seeding the fanning noise may be presumed to be traceable to crystal lattice irregularities. These defects have not yet been examined in any great detail, and the relative importance of various specific imperfections and the role they play in the crystal optics are not known. An understanding of these defects should lead to improvement in signal processing through growth of more satisfactory photorefractive crystals. We have set out to address these problems through direct, *in situ* observation of photorefractive crystals and their gratings in barium titanate by high resolution monochromatic synchrotron x-ray diffraction imaging. The results that we report here indicate the nature of the principal limiting imperfections and demonstrate the feasibility of direct observation of photorefractive gratings and scattering centers.

X-ray beams are now available for the first time that make possible lattice imaging with a spatial resolution of about 1 micrometer and angular resolution of the order of one arc second. Intense x-ray beams with a divergence less than an arc second are provided by suitably designed monochromators on synchrotron storage rings with small optical source size. The large storage ring at the National Synchrotron Light Source at Brookhaven provides the most satisfactory beam to date, with a divergence of 1.5 arc seconds at a point on a sample twenty meters from the source. This is further improved by the monochromator on Beam Line X23A3.

We have observed six carefully selected crystals of barium titanate in order to determine their overall uniformity and thus their suitability for real time high resolution x-radiation diffraction imaging. The results characterize the current state of barium titanate crystal perfection and indicate that real time observation of optically induced photorefractive gratings is possible.

The overall uniformity of lattice orientation in all six of the crystals is within the acceptance angle of the crystal for the beam, a few arc seconds. Thus with the subarc second beam available, diffraction is observed from virtually the entire surface of individual domains in each crystal in Bragg geometry, as in Figure 1. In Laue geometry (transmission), which places much higher restrictions on the diffraction condition because of the elimination of most kinematical diffraction, diffraction is observed in the best crystal, Figure 2.

Ninety degree domains are clearly imaged in various orientations. Some are oriented in $\langle 100 \rangle$ directions, while others are oriented in $\langle 110 \rangle$ directions as they intersect the $\langle 100 \rangle$ surfaces, as seen in Figure 1. Some crystals contained two or three large domains. Other crystals display the narrow intrusion of long, thin domains into what is otherwise a single domain matrix, such as in Figure 3. The presence of multiple domains clearly will prevent diffraction in Laue geometry. This is therefore a primary criterion for selection.

92-18722



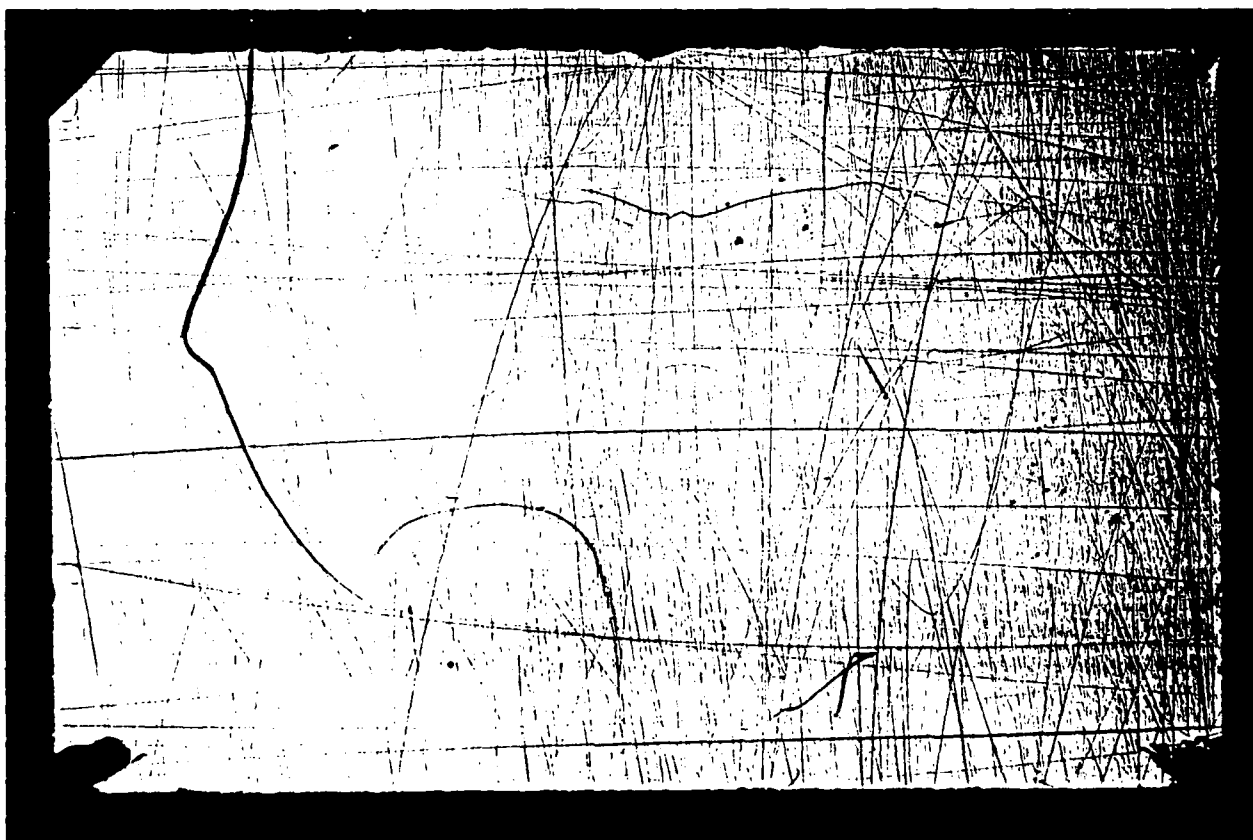


Figure 1. High resolution image of (224) diffraction at 10 keV from barium titanate crystal with corner domain, in Bragg geometry.

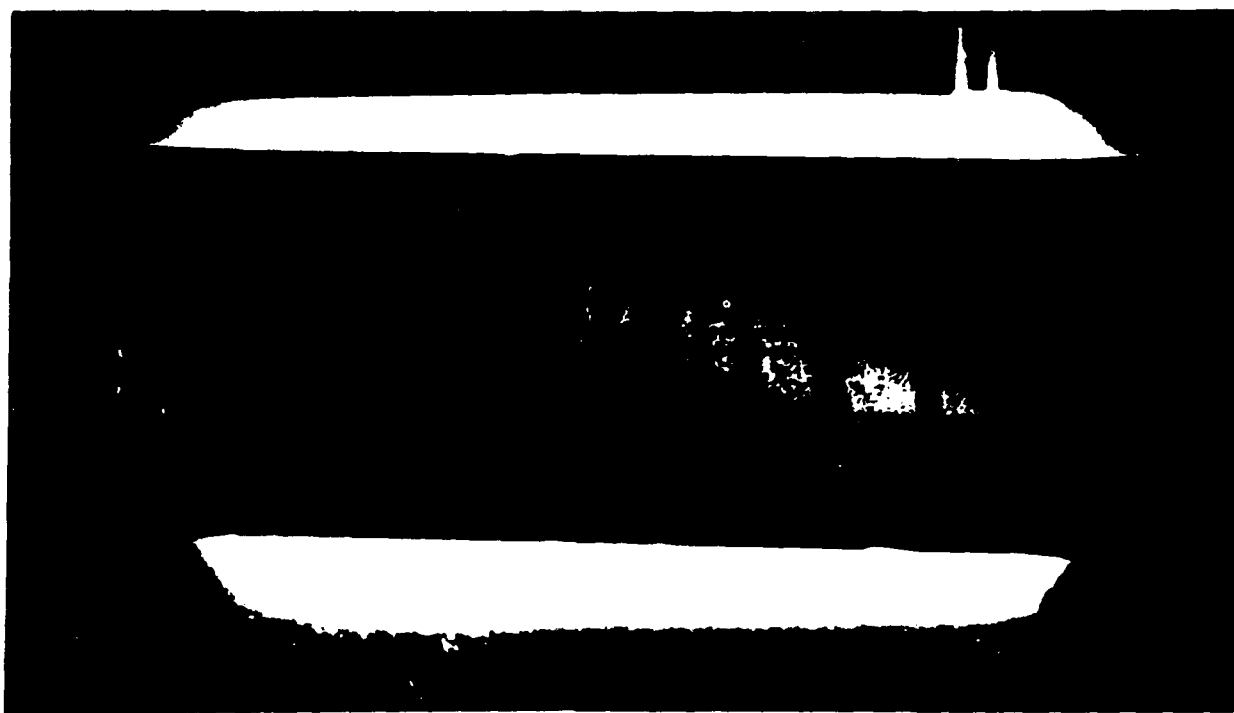


Figure 2. High resolution diffraction image of (040) diffraction at 10 keV from another barium titanate crystal in Laue geometry.

In addition, however, many crystals display deviation in lattice orientation within individual domains. In some crystals, two relatively large areas of a single domain may be slightly misoriented with respect to one another by a few arc seconds, as in Figure 4. In others crystals, the relative misorientation may be restricted to small parts of the entire domain. These deviations are far more pervasive than the separation of a crystal into 90 degree domains and will inhibit diffraction in Laue geometry.

Surface imperfections are more serious than had been anticipated. The surface of barium titanate appears to be far more difficult to polish than are the surfaces of other optical materials, with the result that surface treatment requires particular attention. Dense networks of residual scratches, especially visible in Figures 1 & 3, are found in most crystals after normal surface preparation. Even with particular care taken in polishing, different types of surface can be distinguished.

Of particular interest is the effect that surface scratches have on the surrounding orientation of the lattice over a distance of the order of a millimeter. Misorientation is at least several arc seconds, which is sufficient to preclude diffraction in Laue geometry, as in parts of Figure 2.

With very special care, single domain crystals of barium titanate with satisfactory subdomain orientational uniformity and surface quality are indeed available. In them, optically induced lattice changes should be observable. In these carefully prepared and highly selected crystals, the role of other defects in the establishment of optical gratings should be observable directly in real time.

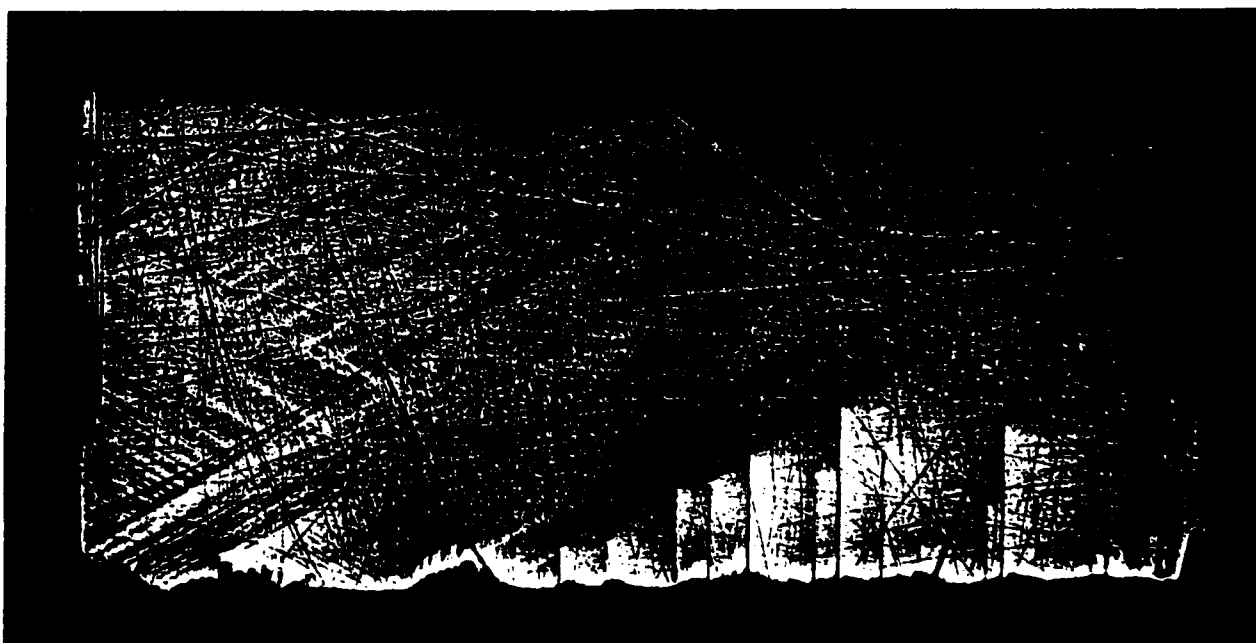


Figure 3. High resolution image of (400) diffraction at 10 keV from barium titanate crystal with thin domain structure, in Bragg geometry.

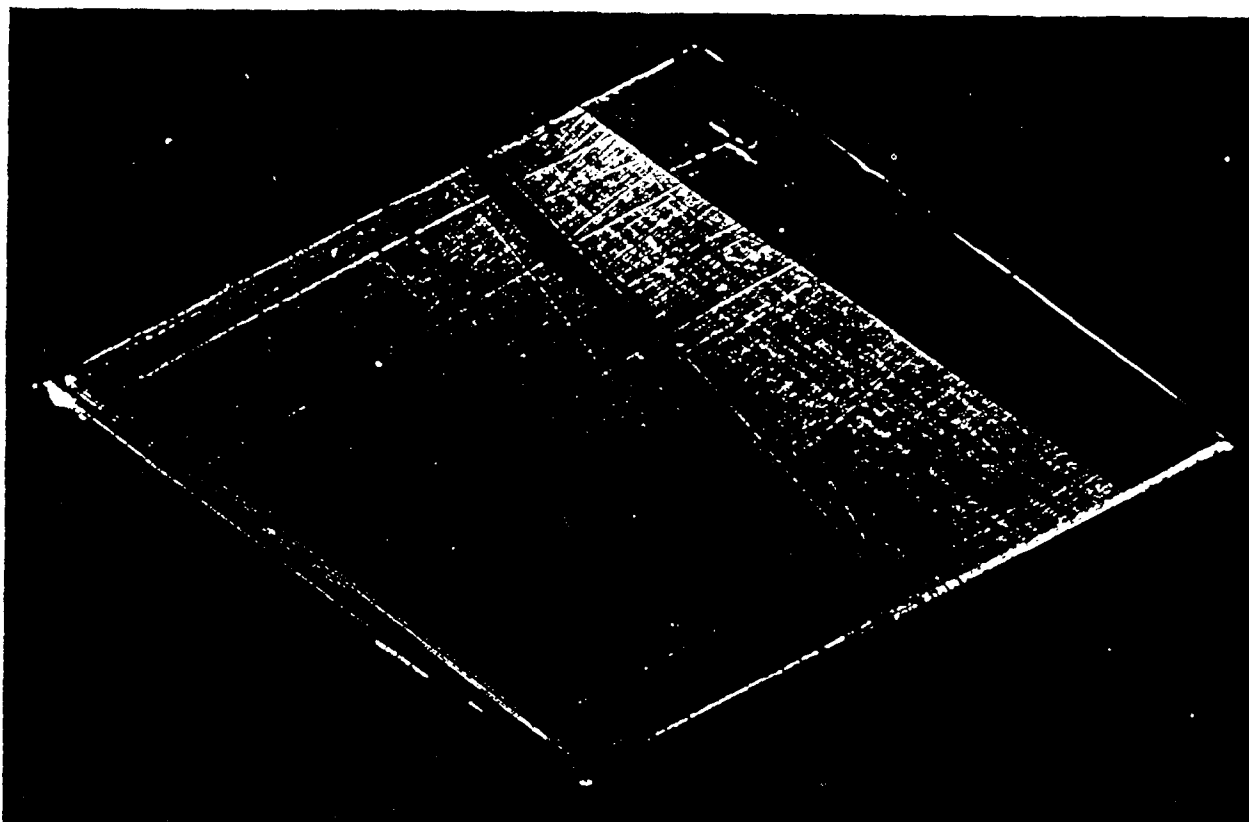


Figure 4. High resolution image of (224) diffraction at 10 keV from a barium titanate crystal with subdomain misorientation, in Bragg geometry.

We have also performed preliminary experiments on the growth of ferroelectric domains in barium titanate. In some instances, display of the domain structure of barium titanate, which can orient in barium titanate, single, with the tungsten bronze structure, show even greater lattice orientation and smaller cell length than in barium titanate.

We are grateful to David Anderson, Barry Weir, and other members of the group, collaboration in the selection and polishing of the barium titanate, to Fred Meyer for the photo microscope, and to Robert B. Johnson for the electron microscope.

AD-P006 735

Homogeneity of the photorefractive effect in reduced and unreduced KNbO₃ crystals

P. Amrhein and P. Günter

Institute of Quantum Electronics, Swiss Federal Institute of Technology, ETH-Hönggerberg,
CH-8093 Zürich, Switzerland (Phone: 0041 / 1 / 377 23 37)

It is obvious that the homogeneity of the photorefractive sensitivity has strong influence on devices such as optically driven spatial light modulators (SLM) ¹⁻³. These applications involve two-dimensional image information and need position-independent transfer functions. The photorefractive homogeneity is based on the distribution of the photorefractive donor centers and traps in the crystal. Therefore it is affected by the crystal growth conditions and subsequent crystal treatments such as poling and electro-chemical reduction ^{4,5}.

It has been shown that the photorefractive sensitivity of KNbO₃ is very high in the visible and that the grating build-up time can be lowered by several orders of magnitude by an electro-chemical reduction treatment ⁴. Response times of less than 1 ms have been achieved for writing intensities of 100 mW/cm². The conductivity of freshly grown samples is dominated by holes, whereas reduced samples are electron-conductive ⁵. The electro-chemical reduction method applies an electric field along the spontaneous polarization of the ferroelectric KNbO₃ sample at temperature of 200°C. During this material treatment inhomogeneities can appear especially in Fe-doped crystals (see figure 3b). With the method described in this paper these inhomogeneities are examined.

In our experiment we use two interfering argon ion laser beams (plane waves, wavelength 514.5 nm) to produce a sinusoidal phase grating in the photorefractive KNbO₃ crystal. This hologram is read out by a HeNe laser beam (wavelength 632.8 nm) using anisotropic Bragg diffraction. The active electro-optic coefficient is $r_{51}=105$ pm/V. For a plane wave read-out beam (as seen in figure 1) and an additional incoherent signal beam this set-up can be used as a spatial light modulator. A cylindrical lens with large focal length ($f=150$ mm with aperture < 3 mm) is put into the read-out beam to focus it into the crystal. The focal line is chosen to lie in the crystal, perpendicular to the plane of incidence (see figure 1). The convergence of the read-out beam does not disturb the diffraction pattern since the angular selectivity of the Bragg condition selects only a small angular part of the incident

92-18723

light distribution for diffraction. Applying such a lens instead of a narrow diaphragm has the advantages of higher read-out intensity and suppression of diffraction effects.

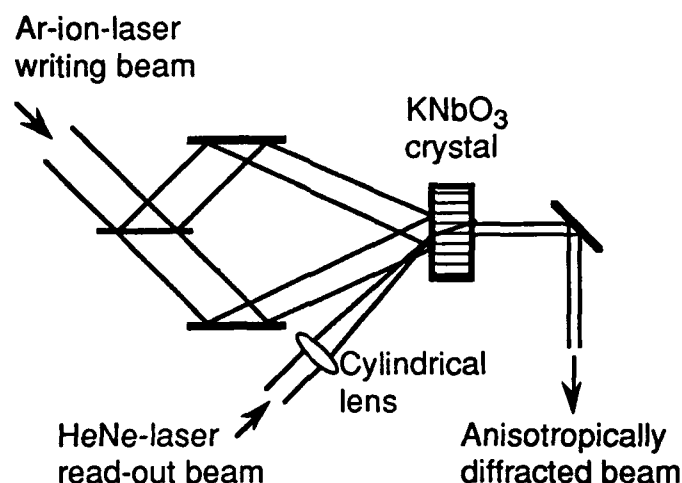


Fig.1 Set-up to examine the photorefractive homogeneity of a KNbO_3 crystal. The anisotropic Bragg diffraction efficiency of a cylindrically focused read-out beam is monitored as a function of its lateral position.



Fig.2 Diffraction patterns : a) Fixed read-out position b) Sequence of diffraction patterns by scanning the read-out beam over the crystal.

A typical two-dimensional diffraction pattern is shown in figure 2a, where the width of the diffracted beam is the thickness d of the crystal multiplied by the cosine of the internal read-out angle. It is an image of the plane illuminated by the read-out beam. Obviously the diffraction efficiency is inhomogeneous. There is a large homogeneous lower part separated by a sharp (and dark) line from the upper part, where the diffraction efficiency is higher near the

surfaces of the crystal. If the crystal is scanned by shifting the read-out beam laterally, the whole crystal is monitored. Figure 2b shows several photographs taken during a scan. Note that the black line with shifts and changes its form as a function of the lateral position.

The shape information of the separation line (typical for this sample) can be described by its positions at the crystal surface and the extremal position in the center. By collecting these values for all separation lines of a complete scan one is able to reconstruct a two-dimensional pattern (see figure 3a). The correlation of this artificial image with an image produced with a plane read-out beam (figure 3b) is astonishingly good. This means that the two-dimensional inhomogeneity can be explained with interference effects of diffracted light from different depths in the crystal. A full understanding will be reached when discussing the dominance of electron- and hole-conduction in this sample. In the upper part of the crystal (near the cathode) the diffraction efficiency at the surfaces is higher than in the central part. As a consequence these two diffracted waves lead to a lowered diffraction efficiency compared to the case of a homogeneous photorefractive effect as well as to additional interference effects when slightly changing the read-out angle. This behaviour again corresponds to the experiment (figure 3b).

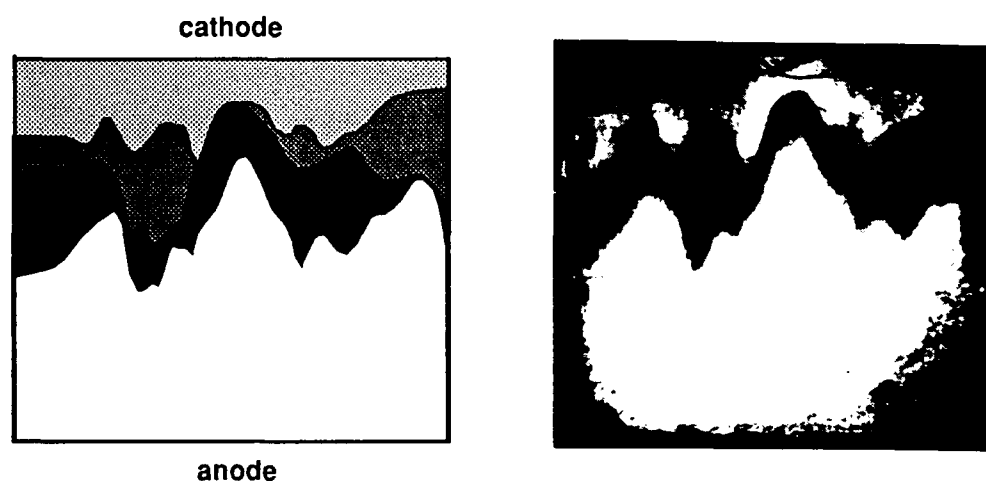


Fig.3 Diffraction patterns of a plane wave : a) Estimated from the data of figure 2b. b) Experimental result.

Note that with our simple experimental set-up we are able to monitor the diffraction efficiency of a photorefractive crystal as a function of position in all three dimensions. This is a very useful test for the crystal quality to be applied after crystal growth and/or different crystal treatments such as poling, reduction or annealing. It may be also interesting to study

surface effects (e.g. enhanced diffraction efficiency), the distribution of defects and the spatial position and orientation of domain walls within the crystal.

Most interesting is the inhomogeneous zone (separation region) between these two parts. The two wave mixing gain is measured as a function of position in the crystal along a direction parallel to the spontaneous polarization. Figure 4 demonstrates the transition from the crystal region near the cathode with electron conduction dominance to the region near the anode, where holes are the dominant charge carriers. It can be interpreted with a linear change of the gain which corresponds in first approximation to the behaviour one expects when assuming that the separation line is indeed separating the electron conduction region from the hole conduction region.

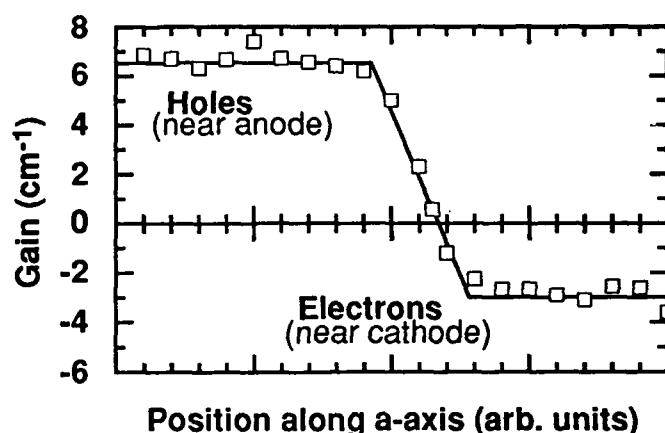


Fig.4 Two wave mixing gain (no applied field) in the separation region along a line starting from the anode towards the cathode (The electrodes were used to reduce the crystal).

REFERENCES

- [1] Y. Shi, D. Psaltis, A. Marrakchi and A.R. Tanguay Jr., "Photorefractive incoherent-to-coherent optical converter", *Appl.Opt.* **22** (23), 3665 (1983)
- [2] E. Voit, C. Zaldo and P. Günter, "Optically induced variable light deflection by anisotropic Bragg diffraction in KNbO_3 ", *Optics Letters* **11**, 309 (1986)
- [3] P. Amrhein and P. Günter, "Resolution limit for isotropic and anisotropic Bragg diffraction from finite holographic gratings", *J.Opt.Soc.Am.B* **7** (12), 2387 (1990)
- [4] E. Voit, M.Z. Zha, P. Amrhein and P. Günter, "Reduced KNbO_3 crystals for fast photorefractive nonlinear optics", *Appl.Phys.Lett.* **51** (25), 2079 (1987)
- [5] C. Medrano, E. Voit, P. Amrhein and P. Günter, "Optimization of the photorefractive properties of KNbO_3 " crystals, *J. Appl.Phys.* **64**, 4668 (1988)

Tuesday, July 30, 1991

Applications

TuB 10:30am–12:30pm
Academic Center Auditorium

Jean-Pierre Huignard, *Presider*
Thomson-CSF, France

AD-P006 736

Phase conjugate techniques for diode laser brightness enhancement

Stuart MacCormack and Robert W. Eason
 Department of Physics and Optoelectronics Research Centre
 University of Southampton
 Southampton SO9 5NH
 United Kingdom

Diode laser arrays provide a compact, high power, high efficiency source of monochromatic light and are finding many applications in all solid-state mini and micro-laser systems. Unfortunately, the preferred modes of operation of free-running, conventional gain-guided laser arrays involve the simultaneous oscillation of many array transverse modes¹. This results in an undesirable broadened twin-lobe output in the far field which is generally several times the diffraction limit of the emitting region. This leads to poor focussability which in turn severely limits the efficiency of launching into optical fibers, coupling into planar waveguides and longitudinal pumping of solid-state micro-lasers.

Photorefractive materials and their unique abilities, namely low-power self-pumped phase conjugation and two-beam coupling, present themselves as ideal materials for use in diode laser array combination and brightness enhancement techniques.

In this paper we present results for two brightness enhancement techniques involving phase conjugate feedback from a BaTiO₃ self-pumped phase conjugate mirror (SPPCM) into a high power diode laser array.

1) Single lobe emission from a diode laser array coupled to a SPPCM

Optical phase conjugation is an ideal technique for external self injection locking configurations since the stringent requirements of accurate mirror alignment and exact retroreflection of the array output are automatically satisfied in the phase conjugation process. The coupling of laser diode arrays to several different forms of phase conjugate mirrors have previously been described², and recently mode-locking and frequency tuning of a laser array coupled to a photorefractive SPPCM has been demonstrated³. In all these cases the output powers available were severely limited due to the competition between the external cavity selected mode and free running array modes which occurs at higher output powers.

The array used was a commercial, 1 W gain-guided device (SDL 2462-P1) operating around a wavelength of 808 nm. In order to initiate the self pumped phase conjugation process we found it necessary to externally lock the array to single longitudinal mode operation by means of a conventional injection locking procedure⁴. The experimental set up was as shown in figure 1. The output of a single mode diode laser (Sharp LTO 17 MD) was injected down the path of one lobe of the free running array profile, at an angle of approximately +4° to the array normal, via a Faraday isolator in order to prevent output from the array returning along this path and causing instabilities in the master laser. This resulted in the array emission appearing in the opposite lobe and the array switching to a single longitudinal mode operation (figure 2(a)). The array output beam was then picked off and directed to an external ring SPPCM which consisted of a 5x5x5 mm³ BaTiO₃ crystal and two high reflectivity mirrors. A lens of focal length 125 mm was used to ensure that the spot sizes of the beams crossing within the crystal were correctly matched and an optical flat used to monitor the phase conjugate reflectivity of the loop.

Initially, the array far field pattern consisted of a large spike at an angle of -4° to the array normal containing a large fraction of the output power. After a characteristic response time of approximately 5 seconds, the phase conjugate reflectivity of the SPPCM grew and an additional spike appeared at an angle of +4° to the array normal, resulting from the amplification of the phase conjugate of the injection locked output beam. For a phase conjugate reflectivity of 2.5% both lobes were of equal

92-18724

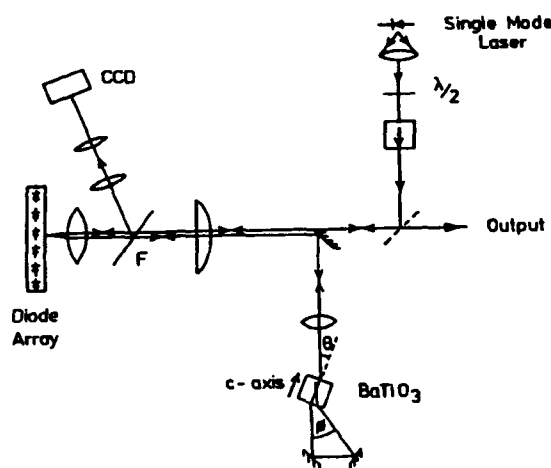


Figure 1 Experimental configuration for single-lobe emission from a diode laser array coupled to SPPCM.

intensity and the SPPCM reflectivity appeared to become saturated (figure 2(b)). The injecting beam was then blocked and the majority of the array output instantaneously transferred into the $+4^\circ$ lobe (figure 2(c)), which resulted in the array output being easily accessible in a single beam. With no apparent broadening in the far field spike, it was possible to increase the array current to $2.1 I_a$ (corresponding to an array output power of 450 mW) at which point the self injection locking process became unstable and there was a washout of the SPPCM grating followed by the array returning to its free running far field pattern. The full-width, half-maximum of the far field spike generated under the phase conjugate self injection locking scheme was measured to be 0.67° which corresponds to 2.2 times the diffraction limit for the array emitting region, 75% of the array output power being contained in this spike.

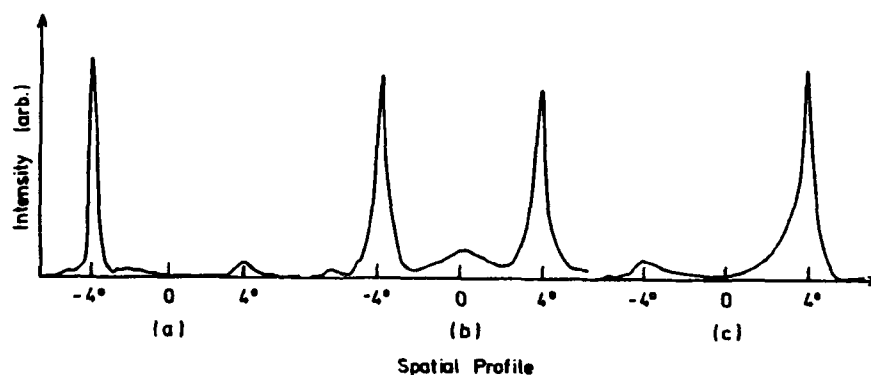


Figure 2 Far-field patterns of array for (a) conventional injection locking process, (b) injection locking with SPPCM feedback, and (c) array coupled to SPPCM with no external injection locking.

The longitudinal mode spectrum of the array was monitored at each different stage of the procedure. For all situations when the single mode laser was being injected there was a pronounced array single longitudinal mode operation with side mode suppression well in excess of 20 dB. On blocking the injecting beam, the longitudinal mode spectrum became erratic with many modes growing and fading over a time period of a few minutes before the mode pattern settled into a very stable six mode output which was almost identical to that of the free running array pattern. The asymmetric nature of the far-

field lobe when coupled to the SPPCM suggests that the array is simultaneously operating on a number of array transverse modes. A theoretical model based on preferential feedback for the higher order array transverse modes has been shown to be in good agreement with experimentally observed data. Unlike the results presented in reference 2 we observed no tendency for the laser to operate on a single longitudinal mode whilst coupled to the SPPCM.

The output from this system was very stable ($<1\%$ intensity fluctuations) and relatively insensitive to external vibration. Once the SPPCM had been established, single lobe operation was maintained until the feedback process was actively prevented.

2. Reflection geometry diode laser phase conjugate master-oscillator power-amplifier (MOPA)

The conventional PC MOPA⁵ involves the injection of a single-mode diode laser beam into a diode array amplifier and phase conjugation of the output back through the amplifier, thus removing all the optical path errors accumulated on the first pass. The diode amplifier in this case was a back and front facet anti-reflection coated diode array. These devices are technically difficult to manufacture, requiring good optical access to both front and rear facets, and considering the very large output divergence perpendicular to the array junction, this presents significant problems in adequately heat sinking the active region. (A previous report⁵ noted the failure of several stripes of the amplifier device during operation of their PC MOPA.) Using a reflection geometry PC MOPA we avoid the need for optical access to both facets of the array amplifier diode array, and as such greatly reduce the problems associated with heat sinking of this device in addition to improvement in the array power extraction efficiency.

A schematic of the experiment is shown in figure 3. The master oscillator used was a Sharp LTO16 MD which operated on a single longitudinal and single transverse mode at a wavelength of 804 nm. The power amplifier was a commercial ten-stripe, gain guided laser diode array (SDL-2430-G) with no special coatings. It was mounted on a temperature controlled heatsink and the temperature adjusted such that the wavelength of the peak of the array gain curve matched that of the master oscillator. The injection locking and subsequent SPPCM geometry was similar to that used in the previous experiment. The Faraday isolator used (Optics for Research IO-5-NIR) rejected the remaining array output at a small angle to the master oscillator beam axis, allowing it to act as the output coupler for the diode array amplifier. This output was monitored using a CCD camera and video analyzer.

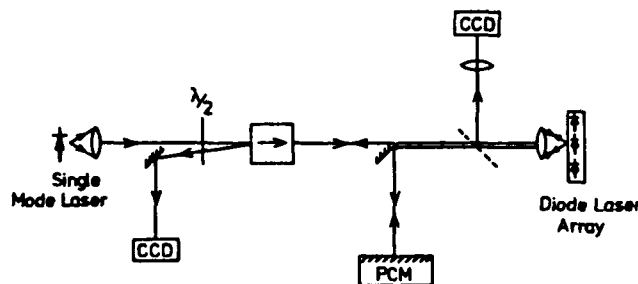


Figure 3 Experimental configuration for reflection geometry PC MOPA.

Under the conditions of small signal injection locking, a diode laser array can be adequately modelled as a broad area Fabry-Perot amplifier with slight perturbation due to the multi-stripe geometry. Because of the multi-pass nature of the Fabry-Perot amplifier scheme, as opposed to a double pass of the conventional PC MOPA, the injected signal beam fills all the active gain region, efficiently saturating all the available gain of the array amplifier. The diode array was operated close to threshold so as to suppress the self-oscillation and free running modes of the array in order that it would simulate the operation of a diode array amplifier as closely as possible.

When the master oscillator output was initially injected at an angle of $+4^\circ$ into the diode array

cavity, the system acted as a conventional injection locking scheme, generating a diffraction limited lobe in the far field containing in excess of 65% of the array output. For the initial investigations, the array was operated at $1.2 I_{th}$, corresponding to a free running array output of 45 mW. The injection locked lobe was spatially separated and directed towards the phase conjugate mirror. After a characteristic response time, the phase conjugate reflectivity began to grow and an additional lobe appeared in the far field at an angle of -4° , corresponding to the amplification of the phase conjugate beam. The phase conjugate lobe intensity then grew at the expense of the injection locked lobe intensity, until the phase conjugate reflectivity of the system became saturated at a value of $\sim 20\%$. At this point the power in the phase conjugate lobe was roughly equal to that in the injection locked lobe. When saturation of the phase conjugate reflectivity had been reached, the intensity of the output from the system contained in the phase conjugate lobe remained constant to better than 1%. If the phase conjugate reflectivity was disrupted by, for example, a small movement of the crystal, the same characteristic growth in the output from the system was repeated as the phase conjugate grating reformed.

Figure 4 shows the far field pattern of the array when the master-oscillator beam was injected with and without the phase conjugate feedback present. The phase conjugate output lobe shows a full-width, half-maximum of 0.61° which compares to the diffraction limit of 0.59° for an uniformly illuminated aperture $100\mu\text{m}$ wide. At higher injection powers, the phase conjugate lobe began to broaden slightly, growing to a maximum value of 1.8 times the diffraction limit for an injection power of 9 mW at the array facet. The longitudinal mode spectrum was monitored in the MOPA configuration and showed a predominantly single mode operation with frequencies with a side mode suppression of 14 dB. On increasing the array injection current, the twin lobe structure was maintained but the central regions of the far-field pattern began to fill in as the free-running modes of the array began to compete. At an injection current of $1.5 I_{th}$, corresponding to an array output power of 100 mW, ~ 0.24 of the array output was outside of the two locked lobes. This problem could easily be solved by anti-reflection coating the front facet of the array, thus preventing the appearance of the undesirable self oscillation.

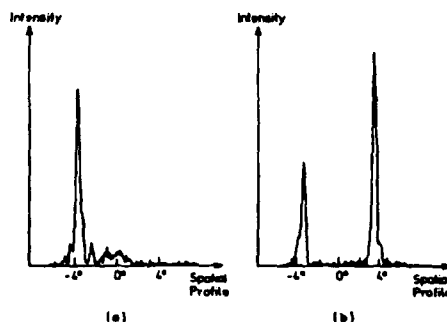


Figure 4 Array far-field patterns for (a) conventional injection locking, and (b) operation as PC MOPA. The right hand spike represents the diffraction limited PC MOPA output and the left hand spike represents the input into the SPPCM.

In conclusion, we have demonstrated two phase conjugate techniques for the generation of near diffraction limited outputs from high power diode laser arrays. Significant improvements in the outputs available from these schemes can be achieved by optimisation of the laser array output coupler reflectivity and we hope to demonstrate this in the near future.

References

1. J.M. Verdiell, and R. Frey, IEEE J. Quantum Electron. QE-26, 270 (1990).
2. M. Segev, S. Weiss, and B. Fischer, Appl. Phys. Lett. 50, 1397, (1987).
3. M. Segev, Y. Ophir, B. Fischer, and G. Eisenstein, Appl. Phys. Lett. 57, 2523 (1990).
4. L. Goldberg, H.F. Taylor, J.F. Weller, and D.R. Scifers, Appl. Phys. Lett. 46, 236 (1985).
5. R.R. Stephens, R.C. Lind, and C.R. Giuliano, Appl. Phys. Lett. 50, 647 (1985).



Dynamic photorefractive optical memories

H. Sasaki, Y. Fainman, J. E. Ford, Y. Taketomi, S. H. Lee
University of California, San Diego, Dept. of Elec. and Comp. Eng.
La Jolla, CA 92093

1. Introduction

The extremely large storage density of volume holographic memories is applicable to numeric and neural network optical computing. Such photorefractive memories can be used to provide optical storage of binary bit-plane or gray scale images as well as weighted interconnects for optical digital and neural network computing. However, success in applying optical memories to computing will strongly depend not only on the memory's large capacity and short random access time, but also on the memory's dynamic characteristics.

Our objective is to construct a dynamic photorefractive memory that provides (i) nondestructive readout, i.e., after a large number of readings, the memory can be refreshed by rewriting the still useful information from one crystal into another, and (ii) write/erase capability, that is, while rewriting the useful part of the information from one crystal to the other, we can also replace some of the old information that must be erased by the new information introduced from the input to the memory.

Different approaches have been undertaken to optimize the photorefractive memories with respect to dynamic characteristics as erasability and storage lifetime¹⁻⁵. These existing approaches utilize the photorefractive material properties. The selective erasure approach³ is based on the superimposed recording of a π -phase shifted image on the image that must be erased. The disadvantages of the selective erasure approach are due to a decrease of the signal-to-noise ratio from the coherent accumulation of scattered light and the gradual optical erasure of stored information by the readout wave. Thermal⁴ or electrical⁵ fixation approaches have been employed to reduce the readout erasure problem, but as a consequence they limit the ability to erase and rewrite new information. To overcome the disadvantages of these material-based approaches to read, write and erase memories, we are investigating a system approach called dynamic or circulating memory⁶.

2. Principle of the dynamic memory system

The dynamic memory approach is diagrammed schematically in Fig. 1. The input images are stored sequentially in one of the two photorefractive crystals (PRC1) until the total memory capacity of that crystal is reached. After many readouts the stored information in PRC1 will be degraded. We then transfer the useful part of the information from PRC1 into PRC2. If the storage capacity of PRC2 is not reached after the transfer, additional input images can be recorded in PRC2. The first crystal then is optically erased to prepare it for the next cycle, when the memory capacity of the second crystal is reached. The two crystals are functionally identical, exchanging tasks periodically. A thresholding optical amplifier intensifies the input to be stored, the

92-18725



reconstructed output, and the images being transferred from one crystal to the other.

In contrast to the approach of Ref. 7, where a buffer hologram was used to synthesize a single high diffraction efficiency hologram, the approach under investigation produces a dynamic multi-image memory using an optical amplifier and a pair of photorefractive crystals as memory devices. Using two separate crystals and an optical amplifier produces important advantages. First, it allows the transfer of independent holograms (with different reference beams) without recording the unwanted cross terms which would otherwise be generated. Second, the amplifier allows us to reduce the minimum acceptable diffraction efficiency of the holograms while maintaining the required output intensity, with a resulting increase in memory capacity. Finally, this approach allows us to use a weak readout beam on one crystal while recording with an intense writing beam in the second, artificially introducing an effective write-erase asymmetry into the system. Without such an asymmetry it would be impossible to circulate the stored information at high diffraction efficiencies for many cycles.

3. Experimental results

We have conducted preliminary experiments to evaluate the performance of the dynamic memory by analyzing the quality of the stored images during transfer. The experimental arrangement is shown schematically in Fig. 1. This system consists of an optical amplifier A and two photorefractive crystals of LiNbO_3 . A Liquid Crystal Light Valve (LCLV) is used as an amplifier. Because of the binary modulation characteristics of an LCLV, it can also perform thresholding. The input binary image is written on the back surface of the LCLV and modulates the writing beam. The output image from the LCLV is captured by a CCD camera and stored in a hard disk of a personal computer for analysis.

After a binary image is recorded in crystal PRC1, it is reconstructed by a weak reference beam. The reconstructed image is thresholded and intensified by amplifier A and stored in crystal PRC2. The same transfer procedure from PRC2 to PRC1 follows. Each time the image is transferred, it is recorded with a unique reference beam angle. To ease the alignment required from the optical system we have used spatial domain masking, ensuring the image lies on the same position of the LCLV at each transfer cycle. The output of the system after multiple transfers is shown in Fig. 2. The distortion in the image occurs because of the spatial nonuniformity of the available LCLV. The average intensity of the image is maintained after many iterations.

4. Conclusions

We have introduced the principle of the dynamic photorefractive optical memory architecture, and performed preliminary experimental results. More complete experiments are being conducted. The results will be presented and compared with the theoretical analysis of the dynamic memory system.

References

1. D. Psaltis, D. Brady and K. Wagner, Appl. Opt., **27**, 1752 (1988).
2. J. Ford, Y. Taketomi, D. Bize, Y. Fainman, R. Neurgaonkar and S. Lee, Proc. SPIE, **1148**, 12 (1989).
3. J. P. Huignard, J. P. Heriau and F. Micheron, Appl. Phys. Lett., **26**, 256 (1975).
4. W. Burke, D. Stacbler, W. Phillips and G. Alphonse, Opt. Eng., **17**, 308 (1978).
5. J. P. Heriau and J. P. Huignard, Appl. Phys. Lett., **49**, 1140 (1986).
6. Y. Fainman, Proc. SPIE, **1150**, 120 (1989).
7. D. Brady, K. Hsu, and D. Psaltis, Opt. Lett., **15**, 817 (1990).

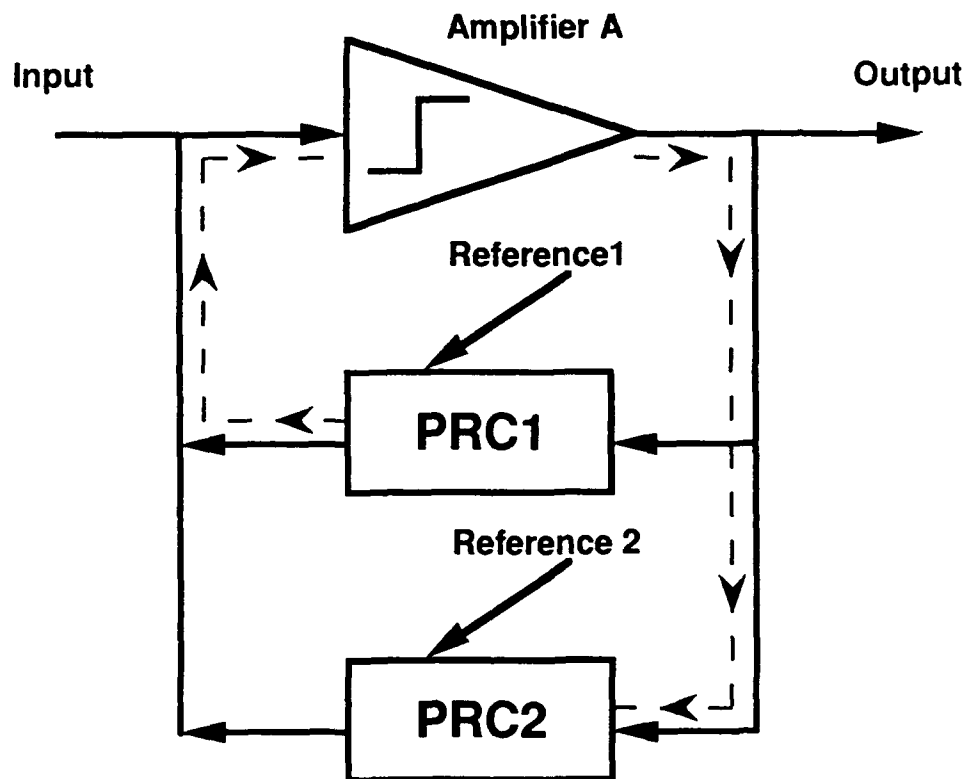
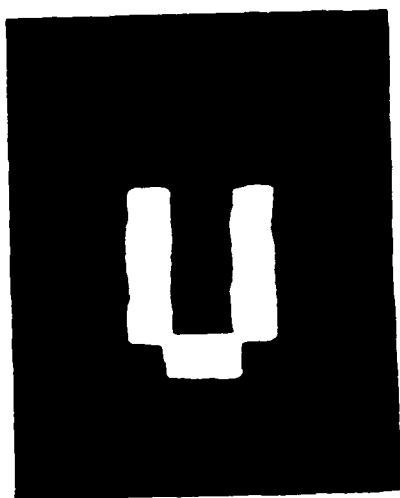
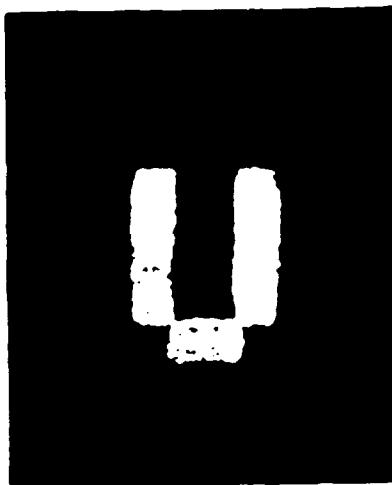


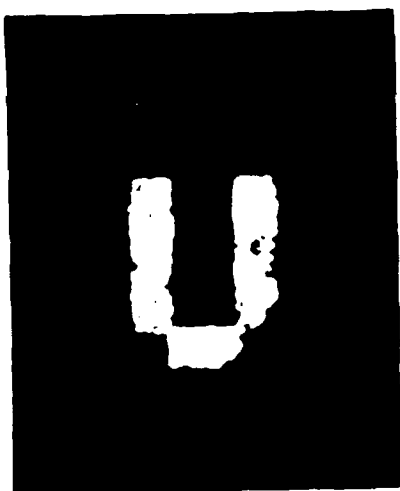
Figure 1: Schematic diagram of the dynamic photorefractive optical memory. A is a thresholding optical image amplifier. Images are stored and transferred between crystals PRC1 and PRC2 via the amplifier A. The dashed line shows the transfer of an image from PRC1 to PRC2.



(a)



(b)



(c)

Figure 2: Outputs of the memory. (a) original image; (b) after five transfers; and (c) after ten transfers.



Real-Time Optical Intensity Correlator using Photorefractive BSO and a Liquid Crystal Television

C. Soutar, Z.Q. Wang, C.M. Cartwright and W.A. Gillespie

Dept. of Electronic and Electrical Engineering,
Dundee Institute of Technology, Bell Street, Dundee. U.K. DD1 1HG

The use of photorefractive $\text{Bi}_{12}\text{SiO}_{20}$ (BSO) as a dynamic holographic medium in optical processing systems has been the subject of much activity. Typical operations carried out include edge enhancement [1], novelty filtering [2] and the correlation of optical signals [3]. However the use of BSO in coherent correlator systems is hindered by positional problems [3,4] as the crystal must be inserted at the Fourier plane of the transforming lens(es) to a high degree of accuracy (to within 0.5 % of the focal length of the lens as determined in ref 3).

In a previous paper we demonstrated that an optical intensity correlator is free from these positional constraints [5]. This correlator consists of Fresnel holographic filters (FHF's) in conjunction with spatially incoherent readout. The in-plane shift of the holographic filter does not significantly affect the correlation results, and the off-plane shift tolerance extends to several millimetres. This increased tolerance in positioning eases the implementation of an intensity correlator based on BSO. Further, due to the spatially incoherent nature of the readout system, any spatial phase variation of components in the readout portion of the system will have no influence on the correlation output. This allows an inexpensive liquid crystal television (LCTV) to be used as a spatial light modulator to address the holographic filters, despite its inherent phase inhomogeneities caused by the transparent electrodes and liquid crystal molecular distribution.

We present results of an optical intensity correlator using a single crystal of BSO within which 'real-time' Fresnel holographic filters are written. This produces an updateable hologram as the reference of the correlator which is interrogated at frame-rates by the LCTV. The particular merits of this system are assessed and experimental results are presented to show that the system tolerates poor alignment while producing satisfactory character recognition.

The experimental configuration for the optical intensity correlator is shown in Fig. 1. Experimental results are shown for a multichannel optical parallel processor using conventional high-contrast photographic film as the input objects (Fig. 2). This is extended to real-time processing by using a single letter to write a single-channel holographic filter to which various letters are presented sequentially using the LCTV. Although the discrimination of this system is lower than a coherent correlator system, it was sufficient to distinguish objects of similar form such as the letters O and G. It is anticipated that the discrimination may be improved either by digitally pre-processing the video signal fed to the LCTV or by edge-enhancement of the recorded object by non-linear recording of the hologram in BSO.

References

1. J.P. Huignard and J.P. Herriau *Appl. Opt.* **17**, 2671 (1978)
2. J.A. Khoury, G. Hussain and R.W. Eason *Opt. Comm.* **71**, 138 (1989)
3. L. Pichon and J.P. Huignard *Opt. Comm.* **36**, 277 (1981)
4. N. Collings *Optical Pattern Recognition* (Addison-Wesley 1988)
5. Z.Q. Wang, W.A. Gillespie, C.M. Cartwright and C. Soutar
(submitted to *Opt. Comm.* February 1991)

92-18726



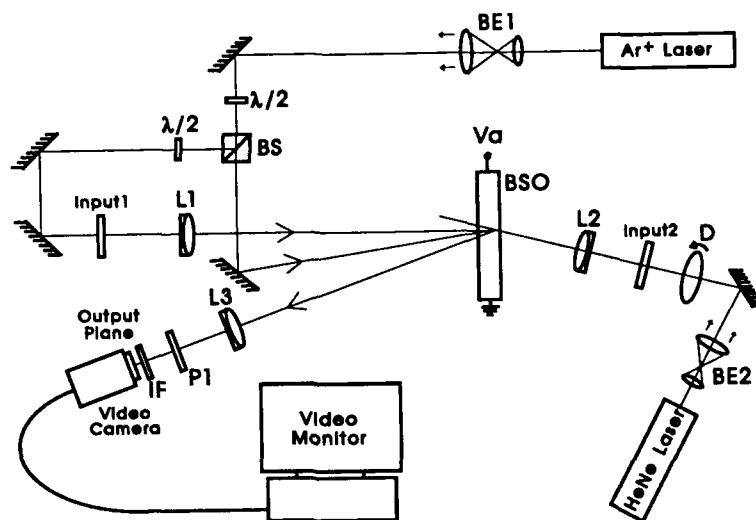


Fig. 1. Experimental configuration for optical intensity correlator.
D, rotating diffuser; L1-3, 40 cm focal length plano-convex lenses

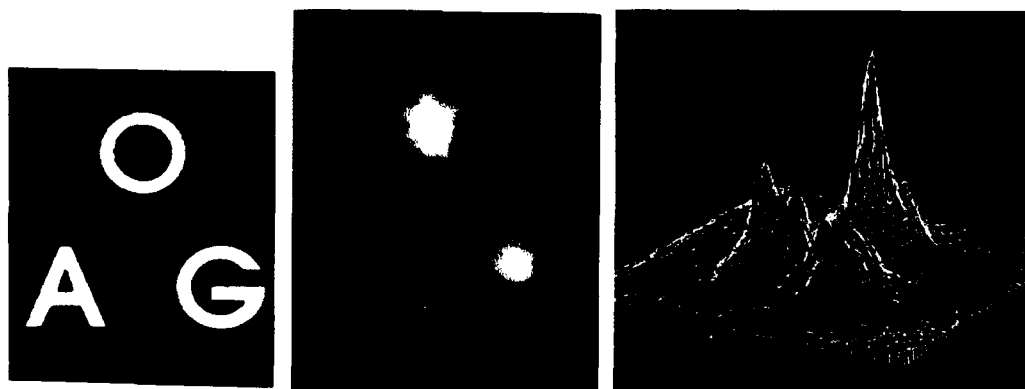


Fig 2 (left to right) a) Input1 used for multi-channel optical intensity correlator b) Output when the letter 'O' is presented to the optical correlator c) Three-dimensional representation of the output.



Multiplicative to Additive Speckle Noise Conversion via Phase Cancellation
with Photorefractive Phase Conjugators

J. A. Khoury¹, A. M. Biernacki^{1,2}, Charles L. Woods³, M. Cronin-Golomb¹

¹ Tufts University Electro-Optics Technology Center

Medford, Massachusetts 02155

(617) 381-3136

² The Charles Stark Draper Laboratory, Inc.

Cambridge, Massachusetts 02139

(617) 258-4414

³ Solid State Sciences Directorate, Rome Laboratory

Hanscom AFB, Massachusetts 01731

(617) 377-4922

A new technique for dealing with multiplicative complex speckle noise on coherently imaged amplitude objects is presented. This technique uses phase cancellation via quadratic nonlinearity to convert the multiplicative noise into additive noise on the Fourier spectrum. This is accomplished using a noisy image as the pump and a clean planar reference beam as the probe in a degenerate four-wave mixing phase conjugator. The counterpropagating pump is provided by the phase conjugate of the noisy image from a total internal reflection self-pumped phase conjugator whose input is the noisy image transmitted through the first crystal. The phase conjugate output is read off from the clean probe; the remaining noise on the Fourier spectrum of the output image is additive and can be removed by nonlinear filtering in the Fourier plane [1].

A number of other techniques have been described in the literature [2-3] that compensate for the effect of multiplicative speckle on images. A majority of these techniques are based on the reduction of the temporal coherence or on signal averaging (for example, using moving apertures or rotating diffusers). The drawbacks of these techniques are that reduction of temporal coherence restricts the applicability of coherent optical processors, and averaging methods are not typically real-time. Digital processing of speckle images may be achieved by subtracting an average of prior speckle measurements from an image, or by applying homomorphic filtering. In this latter technique, the multiplicative noise effect is logarithmically transformed into an additive effect and then can

92-18727



be subtractively removed. One technique for conversion of multiplicative speckle noise to additive noise [4] entails recording the speckled image in an intensity detector with hard-clipping logarithmic response, such as certain types of logarithmic film. One reason the latter technique is so successful is in the effective removal of the phase, as the phase of information is not recorded in intensity measuring film.

In the technique described in this paper, the output of the externally pumped phase conjugator is proportional to the product of the pump and clean reference amplitudes. This output carries the squared amplitudes of the image/noise product. Theoretical and experimental results show the effects of this technique on both the image and its Fourier spectrum. We consider the multiplication of the beams that occurs in the phase conjugator, where A_1 is the noisy input, A_2 is the phase conjugated return beam, and A_3 is the clean planar reference beam. If A_1 or A_2 is represented in terms of the product of the image information, S , and the complex speckle noise, N , the phase elements of A_1 and A_2 will cancel:

$$\begin{aligned} \text{If } A_1 = S \cdot N \text{ and } A_2 \approx A_1^* \approx S^* \cdot N^* \\ \text{and } A_3 \text{ is constant, then in the crystal plane} \\ \text{the output is } A_1 A_2 A_3 \approx |S|^2 |N|^2 A_3. \end{aligned}$$

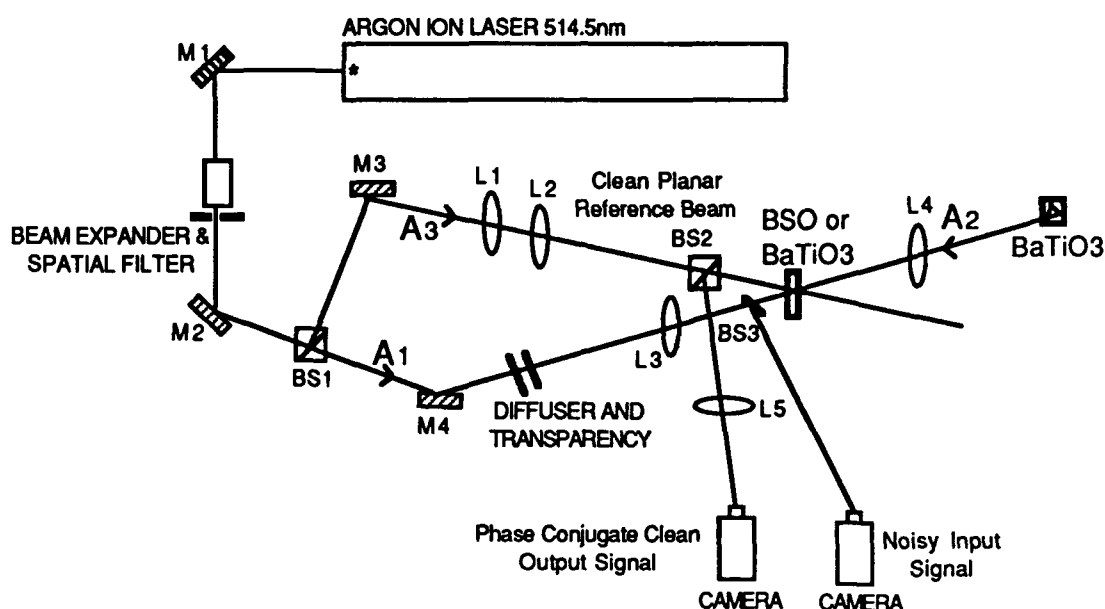
We make the assumption that we are dealing with binary amplitude objects; for objects containing significant greyscale, the squaring operation changes the dynamic range of the greyscale without affecting resolution. For the purposes of this discussion we will set $S' = |S|^2 A_3$. The Fourier transform of the output is then given by

$$FT \{ S' \cdot |N|^2 \} = FT \{ S' \} * FT \{ |N|^2 \}$$

The noise $|N|^2$ has a strong dc component, giving its Fourier spectrum a delta function at the origin and a new spectral distribution corresponding to the spatial extent of the noise.

$$\begin{aligned} \text{F.T.} \{ |N|^2 \} &= \delta(0,0) + N'(v_x, v_y) \\ FT \{ S' \cdot |N|^2 \} &= S'(v_x, v_y) * (\delta(0,0) + N'(v_x, v_y)) \\ &= S'(v_x, v_y) + (S'(v_x, v_y) * N'(v_x, v_y)) \end{aligned} \quad , \text{ therefore}$$

The noise remaining on the signal is now additive and can be dealt with via nonlinear filtering, as stated previously.



In the experimental setup pictured illumination was provided by an argon ion laser operated at 514.5 nm with an intracavity etalon. The beam is spatially filtered to clean the beam, and split with a 50/50 beamsplitter to produce two beams. One of these is used as a clean planar reference beam. The other beam is passed through a diffuser plate of ground glass to impose the multiplicative complex noise component on the phase component to the signal. The image information is imposed on the beam by an Air Force resolution chart, providing an amplitude image corrupted by the interference effects imposed by the speckle noise character of the diffuser plate. A lens images a resolution chart pattern of three diagonal bars into a photorefractive crystal (BSO in the first experiment, BaTiO₃ in the second attempt). The image beam and the reference beam interfere in the crystal, and the transmitted image beam emerging from the first crystal is focussed into a second crystal in such a way as to initiate total internal reflection self-pumped phase conjugation. The phase conjugate return beam from this second crystal provides a counterpropagating pump of proportional to a the phase conjugate of the original noisy signal, such that their product in the crystal is real. This also satisfies the Bragg matching condition necessary to obtain an exact counterpropagation of the noisy information. The device output is the product of the uniform plane wave amplitude and the noisy image input pump and the phase conjugated signal counterpropagating pump, giving a phase conjugate output bearing the amplitude variations of the input beam multiplied by a constant from the reference. Our output is a slightly degraded image from the effect of a thick crystal used for the first phase conjugator. A thinner crystal would lead to improved resolution.

A demonstration of the conversion of multiplicative speckle noise to additive noise in the Fourier transform plane has been described. In the output of the device at the Fourier transform the distribution of the noise can be flat or drop off with increasing spectral orders, depending on the spectral distribution of the speckle and the signal. In transfer of the amplitude of the signal beam to the clean probe (which acts as a carrier), the device resembles an amplitude squaring spatial light modulator in the sense that the noisy signal is the input to a multiport device, and the output of that device is a different signal, carrying some dc bias or offset, with the effects of multiplicative noise converted to easily dealt with additive noise and the phase of the signal stripped away. The system described in this paper can be applied more globally to perform beam cleanup on any dominantly phase-distorted amplitude image, as it is single pass technique. One significant limitation imposed on what can be processed by the system is the due to the phase cancellation mechanism of the system; only the amplitude of the signal is preserved. This does restrict the class of input information, but not prohibitively, due to the practical limitations on many commercially available spatial light modulation devices and the kind of imagery available to be processed in many optical systems.

REFERENCES

- 1.) J. Khoury, C.L. Woods, M. Cronin-Golomb, "Noise Reduction Using Adaptive Spatial Filtering in Photorefractive Two-Beam Coupling", Manuscript to be published in Optics Letters, 1991
- 2.) G.O. Reynolds, J.B. DeVelis, G.B. Parrent, Jr., B.J. Thompson, *The New Physical Optics Notebook: Tutorials in Fourier Optics*, SPIE Optical Engineering Press, Bellingham, Washington (1989).
- 3.) A.K. Jain, *Fundamentals of Digital Image Processing*, Prentice Hall, Englewood Cliffs, New Jersey (1989).
- 4.) H. Kato, J.W. Goodman, "Nonlinear Filtering in Coherent Optical Systems Through Halftone Screen Processes", *Applied Optics*, 14, 1813-1824, 1975



Power stabilization in photorefractive two wave mixing by
frequency tuning of laser diode

Tsutomu SHIMURA, Hai Yan MIAO, Masahide ITOH, Hideki OKAMURA,
Kazuo KURODA, and Iwao OGURA

Institute of Industrial Science, the university of Tokyo
7-22-1, Roppongi, Minato-ku, Tokyo 106, Japan
3-3402-6231

In photorefractive two wave mixing (TWM) using a BaTiO_3 , output power of amplified signal beam is often fluctuating. The amplification factor is very sensitive to disturbances such as mechanical vibration and fluctuation of the wavelength of the laser. It becomes a serious problem when we use TWM in optical information processing systems. We tried to stabilize the output power of the probe beam using a laser diode (LD) and feedback loop.

An experimental setup is shown in fig.1. LD driver has a feedback loop that controls the injection current of the LD to keep the signal from the photodiode PD constant. In this system, dominant effect for the power stabilization is not power modulation of LD but frequency change. For stabilization, this system controls the gain of the TWM by changing the phase shift ϕ between the interference fringe and index grating in BaTiO_3 . The TWM coupling constant γ is proportional to $\sin\phi$.¹⁾ The phase of the fringe shifts according to the change of wavelength and the path difference of the arms of signal and pump beam.

First, under the constant LD power and wavelength without feedback, we made an index grating by two beams. The phase shift ϕ is $\pi/2$ in BaTiO_3 when the feedback loop is open. After the index grating was build up, we closed the feedback loop. Then the system controlled the LD injection current and shifted ϕ from $\pi/2$ to make γ proper value and stabilize the signal output power of



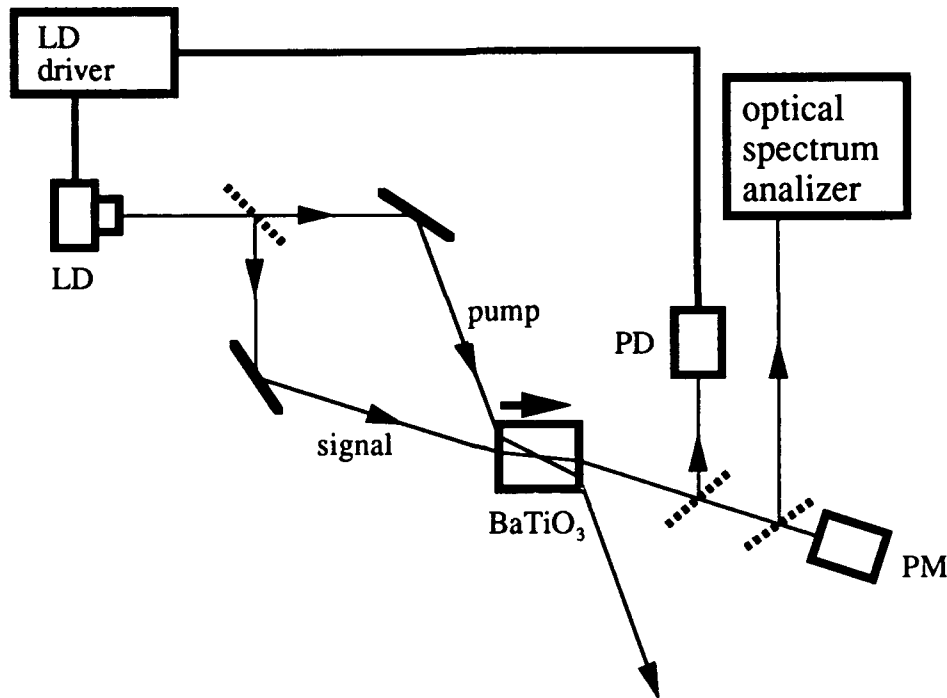


Fig.1 Experimental setup. LD: laser diode, PD: photodiode, PM: power meter.

which level was set. Because the function $\sin\phi$ is symmetric about $\pi/2$, there exist two values for ϕ . But $d(\sin\phi)/dI > 0$ is needed for stable condition, then only one value is permitted. Under this condition, when the output power decreases by some causes, mechanical vibration for example, the LD driver increases the injection current. Then $\sin\phi$ that is the gain γ and output power of LD increase, and the output power of TWM is stabilized. If the pass difference is large enough, increase of output power is small compare to that of γ .

In this system, because ϕ is not equal to $\pi/2$, index grating in the crystal is rewritten continuously. We must, therefore, consider time-dependent beam coupling process to analyze this system.²⁾ But within the period shorter than time constant of grating formation, a steady state analysis mentioned above is valid.

Experimental results are shown in fig.2. LD used in our system was sharp LT024MF and case temperature was stabilized at $22 \pm 3 \times 10^{-3} ^\circ\text{C}$. LD driver was Melles Griot 06 DLD 001. Input and output power and the wavelength of the signal without feedback loop are shown

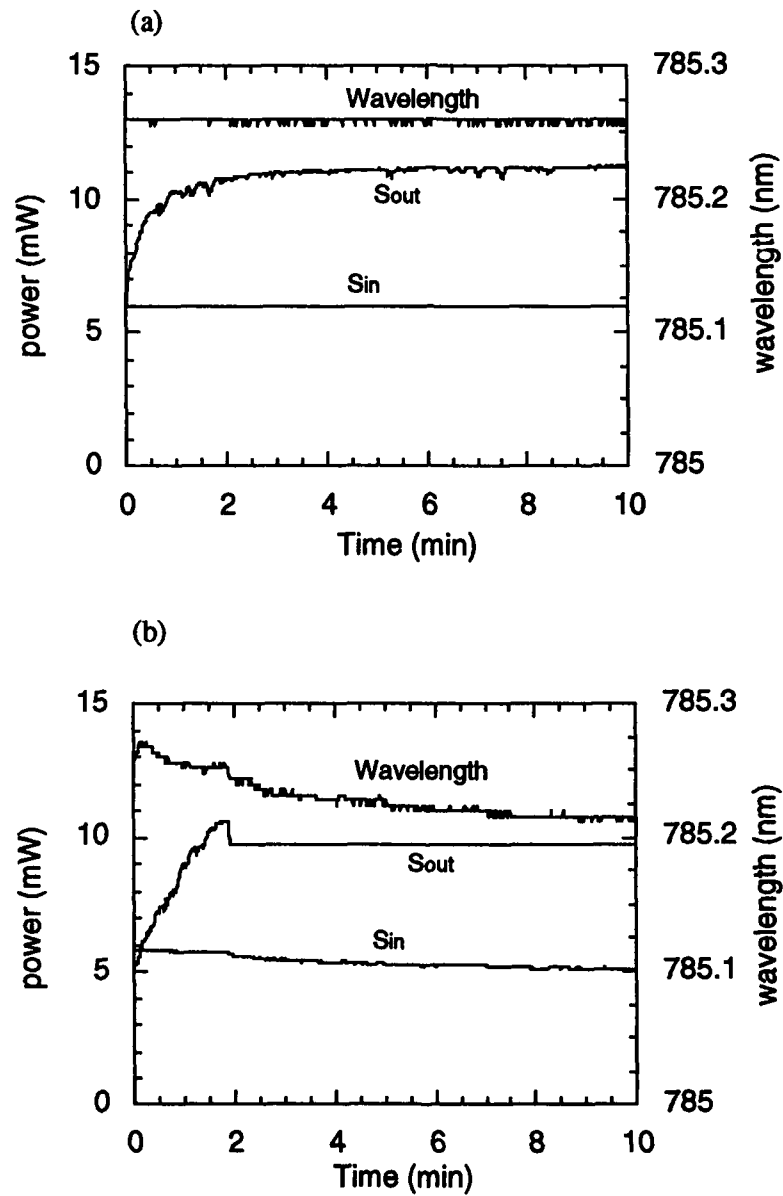


Fig.2 Signal input and output power of the crystal and wavelength. Feedback loop is oper. (a), closed: (b). Sin and Sout indicate input and output signal power respectively.

in fig.2(a). Input power and wavelength are constant, but output power fluctuates. Same data when feedback loop is closed are shown in fig.2(b). The output power was stabilized over 8 minutes. Output fluctuation was 0.8 % rms. It is seen that the input signal power and wavelength are changed to stabilize the output power. Power stabilized state does not last infinitely because the index grating is rewritten and the fringe moves according to it in order to make ϕ be proper value. Tuning range of LD is limited by mode hopping and the fringe can not follow the moving of the grating at last.

Input and output signal power when set level of stabilization was changed stepwise is shown in fig.3. The output power was changed in steps although the change of the input power was quite small. This result indicates that the effect of phase shift is dominant to control the output power.

References

- 1) P. Yeh, IEEE J. Quantum Electron., **25** (1989) 484.
- 2) S. Weiss and Baruch Fischer, Opt. Quantum Electron., **22** (1990) S18.

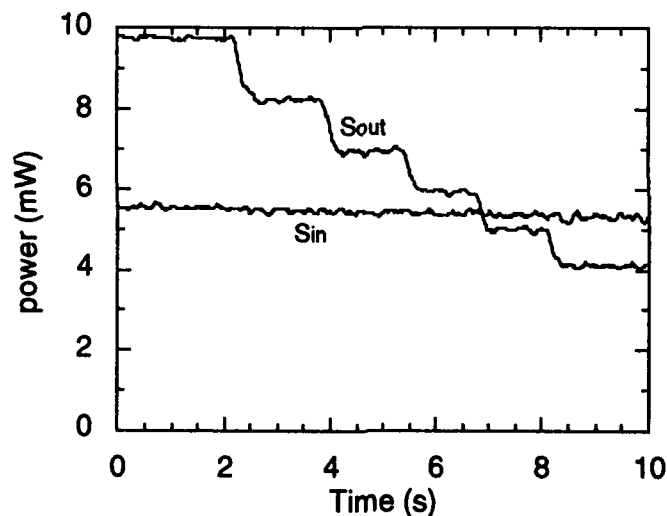


Fig.3 Signal input and output power when set level of stabilized power changed in steps.

AD-P006 741



**New Thresholding Device using a Double Phase Conjugate
Mirror with Phase Conjugate Feedback.**

Parviz Tayebati and Lawrence H. Domash

Foster-Miller Inc.

350 Second Ave,

Waltham, MA 02154, USA, Tel: (617) 890-3200

Abstract

We present a new thresholding device consisting of a double phase conjugate mirror (DPCM) combined with a phase conjugate mirror resulting in superior thresholding characteristics compared to that of a DPCM alone.

92-18729



Summary

Optical intensity thresholding is a long-standing problem with applications in almost all optical computing systems proposed today. A DPCM is a photorefractive device with thresholding characteristics [1, 2]. In this device two incoherent laser beams enter a photorefractive medium and spontaneously set up a photorefractive grating from which they scatter and generate phase conjugates of each other. Figure 1 shows such a device using a 45° cut BaTiO₃ crystal. The ratio q of the intensity of the signal beam I_1 to the intensity of the reference beam I_2 determines the phase conjugate reflectivity.

Theoretically, phase conjugation occurs when this ratio is either smaller than $(1-b)/(1+b)$, or larger by the inverse of same factor [1]. Here b is the solution of,

$$\tan(\gamma L b) = -b ,$$

γ is the gain coefficient and L is the interaction length. Typical behavior of this device is illustrated by curve (a) in Figure 3. In this paper we suggest that feeding back some of one of the phase conjugate outputs of the DPCM to the corresponding input, greatly enhances the thresholding characteristics of the device. The feedback is in the form of phase conjugate of the phase conjugate signal. The schematic of the device is shown in Figure 2. Input signal I_1 enters the DPCM after reflecting off a beam splitter BS2. At the onset of oscillations, a small phase conjugate signal is generated. A part of the phase conjugate signal is split (using BS2) and fed into a phase conjugator which phase conjugates the signal for a second time and feeds it back into the DPCM. This positive feedback moves the system well above the threshold. Alternatively, the system may be viewed as a resonator with two phase conjugating mirrors where a sufficient seed signal I_1 stimulates cavity oscillations. The feedback phase conjugate mirror in our experiments was a four-wave mixing system in which the counter propagating beams were provided by a pump and its phase conjugate signal obtained in a self pump phase conjugator. This conjugator was independently introduced by Chiou et al. and referred to as the "Kitty conjugator" [3]. We calculate the steady-state response of our system by treating it as a resonator with two phase conjugation mirrors. Equations describing the system are,

$$E_6 = r_2 E_3^* .$$

$$r_1 = (I_5/I_4)^{1/2} = \{b^2[1+q^{-1}]^2 - [1-q^{-1}]^2\}^{1/2}/2, \quad [1]$$

$$E_4 = r_b E_1 + t_b^2 r_2 E_5$$

Where t_b and r_b are the transmittivity and the reflectivity of the beam splitter inside the resonator, r_1 is the reflectivity of the DPCM and r_2 is the reflectivity of the feedback phase conjugator and is assumed to be a constant. The overall reflectance $R=(r_b E_5/E_1)^2$ is plotted as a function of the input ratio ($q=I_1/I_2$) in Figure 3. The parameters are $b=0.85$ (for $\gamma L=-3$) and $r_b=0.7$. With $r_2=0$, i.e with no phase conjugate reflectivity the system is just as a DPCM. Curves (b) and (c) show the response of the system with $r_2=0.25$ and 0.5 respectively. These plots indicate much sharper thresholding with phase conjugate feedback.

We measured the phase conjugate signal at the output with and without the feedback loop. Figure 4 shows reflectance R of the device with and without the phase conjugate reflectivity. In Figure 5 the output at the monitor is plotted as a function of the input beam ratio q . The sharp transition at $q=0.1$ indicates the thresholding capability of the device as predicted by the theory. Above this transition, the phase conjugate signal stays almost constant throughout the range of input intensity covered in our experiments. This leads us to suggest that the device may be used as a thresholding device with a built in *binarizing* capability. We will present preliminary image processing capability of this device.

This research was performed under a Phase II SBIR program sponsored by SDIO and managed by the Office of Naval Research. The interest and encouragement of the contract monitor, Wm. Miceli, is acknowledged. We also acknowledge useful conversations with M. Cronin-Golomb.

References

1. M. Cronin-Golomb and A. Yariv, Proc. SPIE 700, 301 (1986).
2. S. Weiss, S. Sternklar, and B. Fischer, Opt. Lett. 12, 114 (1987)
3. A. E. Chiou, T. Y. Chang, M. Khoshnevisan, Optical Society of America, 1990 Annual Meeting, technical digest, paper MHH5, p.40.

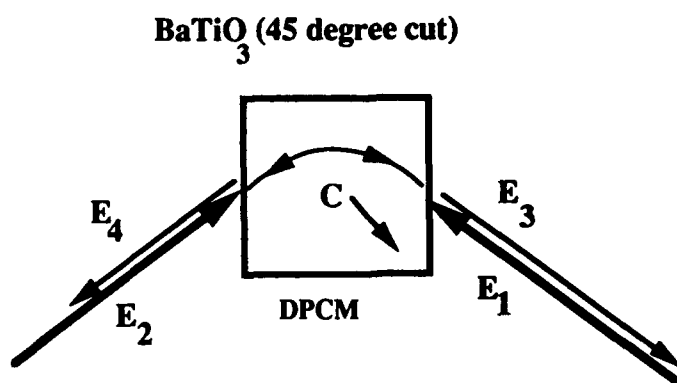


Figure 1.

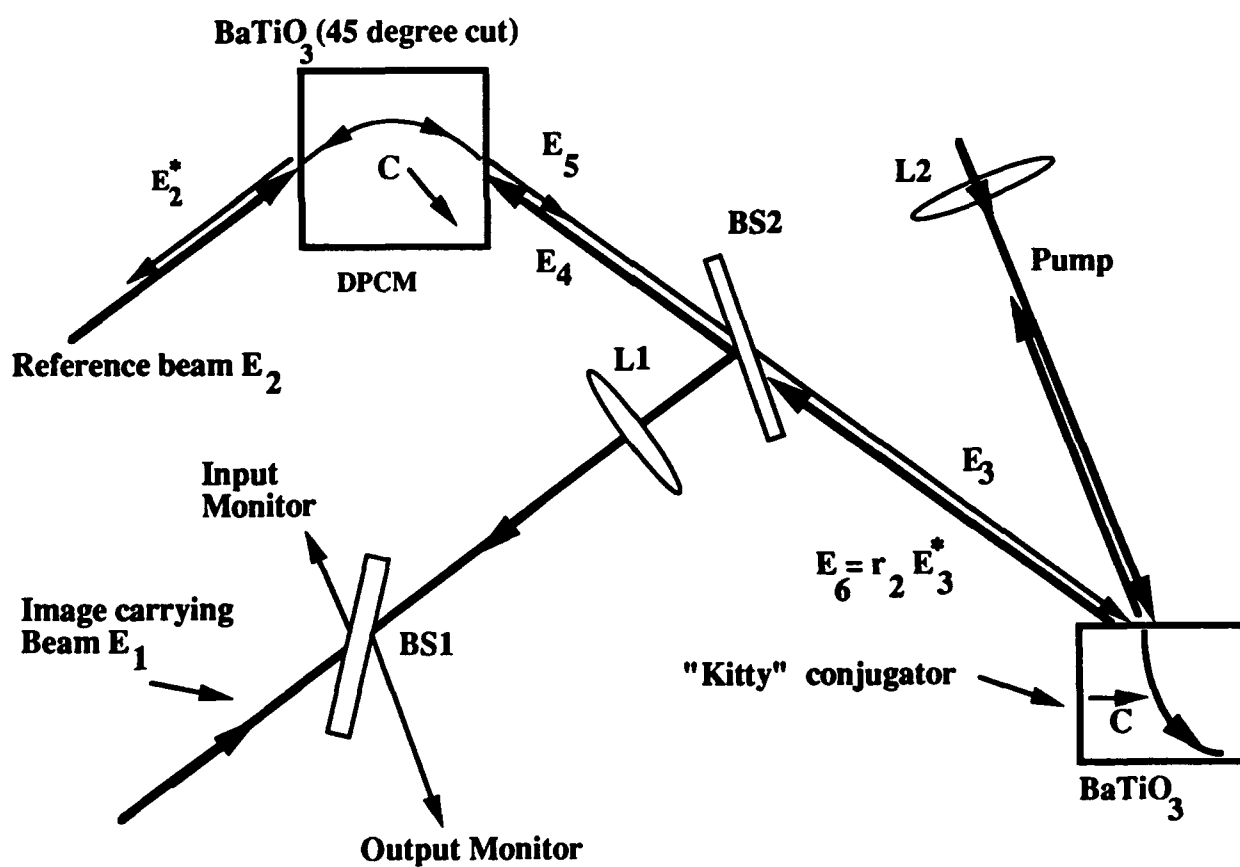
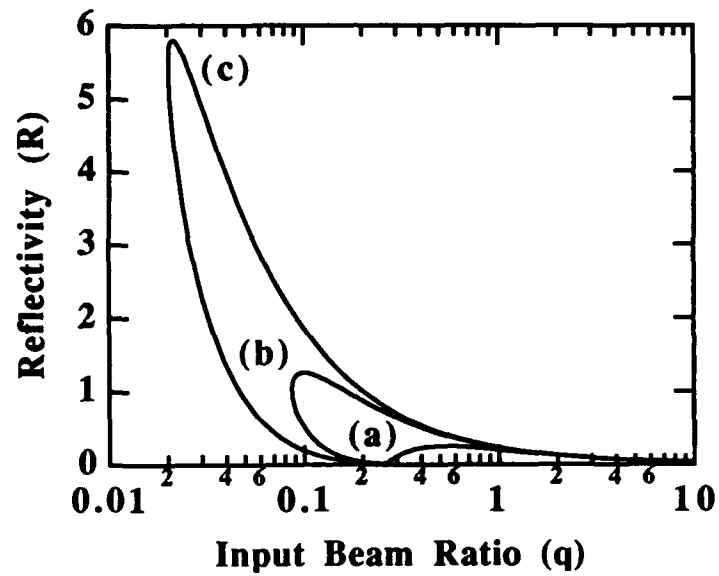
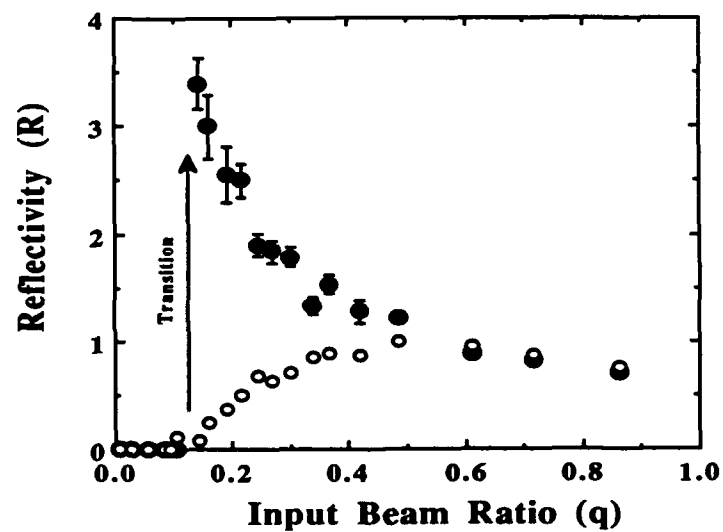
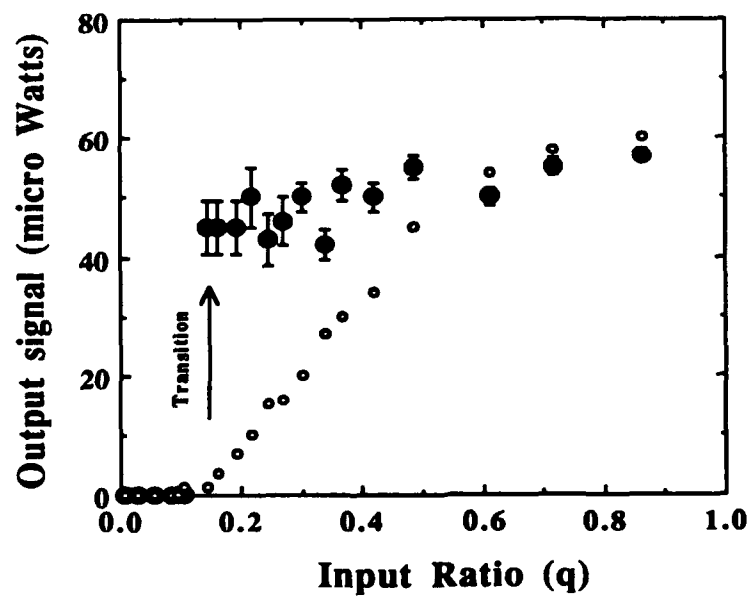


Figure 3Figure 4Figure 5



Laser-Induced Interference Filters in Photorefractive Materials

P.M.Petersen*, P.M.Johansen**, and T.Skettrup*

* Physics Laboratory III, Technical University of Denmark, DK-2800 Lyngby,
Denmark, tel. 45 42881611

**Institute of Physics, University of Aalborg, DK-9220 Aalborg,
Denmark, tel. 45 98158522

Summary

We investigate the properties of a laser-induced interference filter in photorefractive BaTiO_3 . The filter has several control parameters for the reflectance and its high wavelength selectivity makes the filter suited as output mirror of a tuneable single mode infrared semiconductor laser. Furthermore, the interference filter represents a unique simple method for probing higher spatial harmonics in the photorefractive grating.

The photorefractive interference filter has only been investigated very briefly in the literature¹. The configuration for the interference filter is shown in Fig. 1. Two coherent laser beams E_1 and E_2 are incident on the BaTiO_3 crystal. Due to the photorefractive effect² these two beams induce a sinusoidal index of refraction of period Λ in the BaTiO_3 crystal. A third beam E_3 propagating in the x-direction will experience layers of alternate high and low index. This situation is analogous to the multilayer dielectric mirror with alternating quarterwave layers of high and low index, the theory of which is described, for example, in ref.3. In the present situation the thickness of layers of different index is $\Lambda/2$. If this thickness is equal to an odd number of quarter-waves for the probe beam E_3 then the reflected waves from all layers will interfere constructively at the front surface of the BaTiO_3 crystal and a strong reflected signal E_3^R from the filter can be obtained.

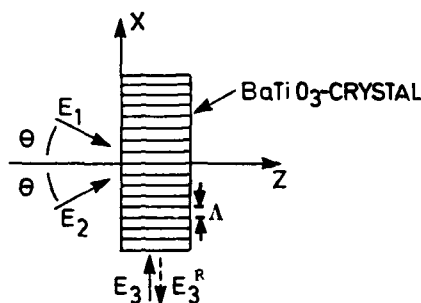


Fig. 1 Configuration for the photorefractive interference filter. Two coherent laser beams E_1 and E_2 induce the filter and control the reflection of a third laser beam E_3 . E_3^R is the reflected wave. θ is the incident angle with respect to the crystal normal. Λ is the fringe spacing.

In our work we extend the theory of interference filters from Ref.3 to the case of

92-18730



photorefractive filters. We assume that the two beams E_1 and E_2 induce an index profile of the form:

$$n(x) = n_0 + n_1 \sin(Kx) \quad (1)$$

where $K = 2\pi/\Lambda$ is the grating vector and Λ is the fringe spacing. The reflectance of the filter is given by³:

$$R = \frac{|E_3|^2}{|E_3|^2} = \frac{\kappa^2 \sinh^2 sL}{s^2 \cosh^2 sL + (\Delta k/2)^2 \sinh^2 sL} \quad (2)$$

where $\kappa = \pi n_1/\lambda$, $s^2 = \kappa^2 - (\Delta k/2)^2$, $\Delta k = 2\pi(2n_0/\lambda - 1/\Lambda)$, λ is the wavelength of the probe beam E_3 , and L is the grating interaction length. For a photorefractive medium the index change is given by⁴:

$$n_1 = 2n_0^3 r_{\text{eff}} \frac{\sqrt{\beta}}{1+\beta} \left[\frac{E_0^2 + E_D^2}{(1 + E_D/E_q)^2 + E_0^2/E_q^2} \right]^{1/2} \quad (3)$$

where E_D , E_q , and E_0 are the electric fields of diffusion, space charge, and externally applied dc electric field, r_{eff} is the effective electro-optic coefficient, and β is the incident intensity ratio (I_2/I_1) of the exciting beams. Eq.(3) is valid for small phase changes. For larger phase changes beam coupling becomes important and the index change n_1 will be a function of the z -position. The reflectance R in Eq.(2) has a peak value $R_{\text{max}} = \tanh^2(\kappa L)$ at $\Delta k = 0$ and a sharp cutoff with oscillatory sidebands. In Fig.2 we have shown the reflectance versus mistuning ΔkL calculated from Eq.2 with typical values for BaTiO_3 : $n_1 = 0.00005$ and $L = 5$ mm.

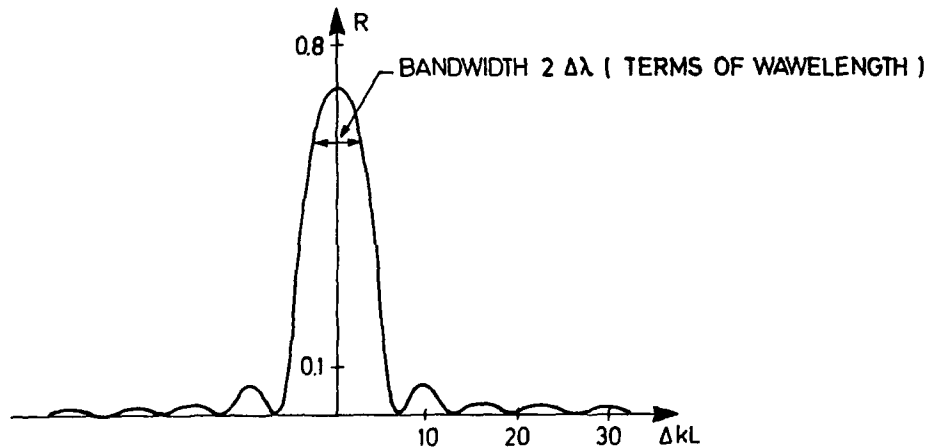


Fig.2 The reflectance versus mistuning for the photorefractive filter calculated from Eq.(2) with typical experimental values for BaTiO_3 .

The bandwidth of the filter is determined by the requirement that the parameter s must be real. This condition gives the following wavelength selectivity:

$$\Delta\lambda/\lambda = 2|n_1/n_0| \quad (4)$$

By inserting the previous given typical values for BaTiO_3 and $n_0=2.48$, $\lambda=632.8\text{nm}$ we obtain $\Delta\lambda/\lambda=4 \cdot 10^{-5}$ which shows the high wavelength selectivity of the photorefractive filter. The center wavelength $\lambda=2\Lambda n_0$ of the filter can be controlled by the angle 2θ between the two exciting beams E_1 and E_2 according to $\Lambda = \lambda_c/(2\sin(\theta))$ where λ_c is the wavelength of the exciting beams. This tuning property is important for many applications. For example, it is possible to frequency tune an infrared semiconductor laser with a photorefractive interference filter as output mirror. Furthermore, the reflectance R can be dynamically controlled by the modulation ratio of the two exciting beams E_1 and E_2 .

The reflectance of the filter is given by Eq.(2) when λ is close to $2\Lambda n_0$. Λ is typical of the order of some micro meters in a photorefractive medium like BaTiO_3 and consequently the wavelength of the probe beam must be in the infrared. However, the zones with high reflectance will exist for all wavelengths for which each layer(of thickness $\Lambda/2$) is equal to an odd number of quarter-waves for the probe beam. Therefore, there will also be high reflectance zones for wavelengths $\lambda/n_0 = 2\Lambda, 2\Lambda/3, 2\Lambda/5, 2\Lambda/7, 2\Lambda/9, \dots$ -and due to the fact that Λ can be controlled by the angle θ the filter can also be used in the whole visible region. The analysis for these higher order zones is the same as for the fundamental zone and therefore the reflectance for the higher order zones are also given by Eq.(2) when modified with a mistuning parameter $\Delta k = 2\pi(2n_0/\lambda - (2p+1)/\Lambda)$ where p is an integer.

In Fig.3 we have shown the experimental reflectance R versus external angular mistuning $\Delta\theta$ of the probe beam E_3 for a BaTiO_3 crystal with dimensions $5 \times 5 \times 5 \text{mm}^3$. Two counter propagating extraordinary polarized beams E_1 and E_2 with powers $P_1=0.4\text{mW}$ and $P_2 = 0.2\text{mW}$ from a HeNe-laser are exciting the filter in the BaTiO_3 crystal. The external

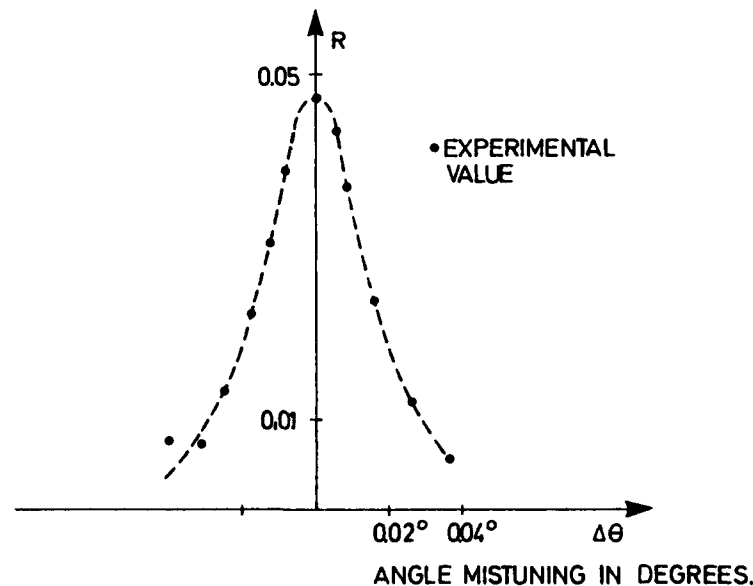


Fig.3 The experimental reflectance R versus angular mistuning of the probe beam E_3 .

angle between the direction of propagation for E_1 and the c-axis of the BaTiO_3 crystal is 68 degrees. A 0.01mW probe beam E_3 from a HeNe-laser is propagating in the same direction as E_2 and is reflected in the interference filter. The experimental reflectance R in Fig.3 shows the high angular selectivity of the filter. However, the magnitude of R is lower than expected from Eq.(2). This is probably due to beam fanning in BaTiO_3 which is detrimental for the filter performance. Furthermore, we have neglected absorption losses in Eq.(2).

The method outlined in the present work provides a simple way of probing the onset of higher spatial harmonics in the photorefractive grating. Higher spatial harmonics in the space-charge field exist both with and without an applied frequency detuning in one of the exciting beams E_1 and E_2 . The onset of such higher harmonics is crucially dependent on the modulation ratio m of the two exciting beams. In the case where the intensity distribution is moving it has been shown⁵ that each higher harmonic has its own distinct resonance. In our work we use the interference filter technique to probe the onset of each higher harmonic in BaTiO_3 as a function of modulation ratio m and grating wave vector.

References.

- (1) P.Mills and E.Paige, "Holographically formed, highly selective, infra-red filter in iron-doped lithium niobate" *Electron.Lett.* vol.21, pp.885-886, 1985.
- (2) M.Cronin-Golomb, B.Fisher, J.White, and A. Yariv, "Theory and application of four-wave mixing in photorefractive media". *IEEE J. Quantum Electron.*, vol.QE-20, pp.1-29, 1984
- (3) P.Yeh, "Optical waves in layered media" J.Wiley and Sons, New York 1988.
- (4) N.Kukhtarev, V.Markov, S.Odulov, M.Soskin, V.Vinetskii, "Holographic storage in electrooptic crystals", *Ferroelectrics* vol.22, pp.949-964, 1979
- (5) F.Vachss and Hesselink. "Selective enhancement of spatial harmonics of a photorefractive grating", *J.Opt.Soc.Am.B*, vol.5, pp.1814-1821, 1988.

Tuesday, July 30, 1991

Poster Session: Materials and Wave Interactions

TuC 4:00pm–5:30pm
Academic Center Classrooms



Experimental Comparison of the "AC Field" and
"Moving Grating" Techniques for PTO and PSC Crystals.

E.V. Mokrushina, V.V. Prokof'ev, S.L. Sochava, S.I. Stepanov
A.F. Ioffe Physical Technical Institute
Academy of Sciences of the USSR, 194021, Leningrad, USSR

There are two techniques of nonstationary holographic recording which are widely used for PWCs with long drift lengths of photocarriers. These are recording of a moving interference pattern in an external DC electric field [1] and recording of a fixed pattern in an AC field [2]. Both of them allow the efficiency of the drift mechanism of recording in the external electric field to be increased and the recorded hologram to be transformed into a shifted one. The theory [3] predicts equal efficiencies of two wave energy exchange for these two techniques. In practice, the "moving grating" technique is traditionally employed for $\text{Bi}_{12}\text{SiO}_{22}$ (BSO), but for $\text{Bi}_{12}\text{TiO}_{22}$ (BTO), recording in an AC field is in common use. Recent investigations of holographic recording in semi-insulating GaAs:Cr ($N_{\text{Cr}} = 1.06 \mu\text{m}^{-1}$) [4,5] have demonstrated remarkable superiority of the moving grating mechanism.

In this paper, we give for the first time, to our knowledge, the results on direct experimental comparison of these two techniques for ETO and PSC crystals. Probable reasons for their different efficiencies are also discussed.

Two samples of PTO grown at the Department for Quantum Electronics of A.F. Ioffe Physical Technical Institute were used in the experiments. Both of them (PTO^{#1} and PTO^{#2}) were grown under similar conditions, but the initial mixtures of PbO_2 of different purities were used. As indicated by the preliminary chemical analysis, the concentration of impurities (Cr) in the mixture used for preparation of the PTO^{#2} crystal was approximately one order of magnitude higher.

The experiments were performed in the conventional two-wave mixing geometry. All the crystals were cut in the

92-18731



(110) plane and oriented in such a way that the [110] axis was in the incidence plane. The external fields were also applied along this crystallographic axis. The AC field of a frequency 70 Hz had a step-like form. For recording a HeNe (λ 633 nm) and a Ar-ion (λ 514 nm) lasers were used for ETO and BSO crystals respectively.

The experimental gain factors Γ as functions of DC (○) and AC (●) field amplitudes for different samples are presented in Figs.1-3. Note that in each measurement, the data for recording in DC field were obtained for the optimal, resonance, speed of the interference pattern V_0^{Γ} . These figures show that the gain factors observed for different mechanisms in ETO^{#1} and BSO samples are more or less comparable. On the other hand, ETO^{#2} demonstrates a high gain for recording of moving gratings and an extremely low efficiency of two-wave energy transfer that slowly grows with a spatial frequency K for recording in AC field (Fig.4). In addition, the gain factor observed in this sample for moving gratings grows linearly with K while ETO^{#1} and BSO samples exhibit a quadratic dependence.

Figs.5,6 show the experimental dependences of Γ on speed of the interference pattern V , obtained for ETO^{#1}, and ETO^{#2} samples under a DC field. A nearly ideal symmetry of the curve for ETO^{#2} indicates that the low efficiency of energy transfer for this crystal in an AC field can be attributed to:

- A. a bipolar photoconductivity resulting in a nearly complete compensation of the diffusion-like shifted gratings formed by the carriers of opposite signs (for recording in DC field, gratings recorded by different carriers have resonance speeds of different signs and for this reason do not compensate each other to such an extent)
- B. short drift length of carriers in a crystal with a monopolar photoconductivity.

A nearly linear dependence of the gain factor on spatial frequency observed in the AC field speaks in favour of the second model. This model for ETO^{#2} is also supported by symmetrical curves for the diffraction efficiency $\eta(V)$ with

only one maximum at $V=0$ (Fig.6).

Using values of half-wave voltage (2.2, 2.8, and 3.3 kV for BTO^{*1} , PTO^{*2} , and BSO respectively) and initial quadratic portions of the experimental $\Gamma(E_{ac})$ dependences (Figs.1,2,3), one can estimate the diffusion lengths, L_D , of the photocarriers in BTO^{*1} , PTO^{*2} , and BSO as 0.16, 0.03, and 0.8 μm ($\mu\tau=10^{-8}$, $3 \cdot 10^{-10}$, and $2.8 \cdot 10^{-7} \text{ cm}^2/\text{V}$).

From the physical point of view, it is quite understandable why recording of a moving grating in BTO^{*2} is superior to recording in an AC field. Short drift length of photocarriers makes impossible efficient recording of the photorefractive gratings in the AC field which can only be of a shifted type. On the other hand, a fairly efficient conventional drift recording of unshifted gratings in the DC electric field needs no long drift lengths. The phase shift of the recorded grating required for observation of two-wave energy transfer can be induced by moving of interference pattern. It is important to note that the grating amplitude is not increased in this situation.

It is also worth noting that in the long drift approximation, the maximum diffraction efficiency, η , and the $\pi/2$ phase shift of the recorded grating are reached for nearly the same resonance velocity of the pattern V_0^η . On the contrary, in the short drift length approximation, V_0^η goes to zero, and the resonance velocity V_0^Γ , necessary to obtain the maximum gain factor, reaches the maximum possible value $(K\tau_n)^{-1}$ (K is the spatial frequency, and τ_n is the Maxwell relaxation time). BTO^{*2} investigated in our experiments clearly demonstrates this limiting case (Fig.6). For BTO^{*1} V_0^η is not equal to zero, but the difference between these two resonance velocities is appreciable (Fig.5), and for BSO these velocities are approximately equal.

REFERENCES

1. J.P.Huignard, A.Marrakchi, Opt.Comm.,38, 249 (1981)
2. S.I.Stepanov, M.P.Petrov, Opt.Comm.,53, 292 (1985)
3. S.I.Stepanov, M.P.Petrov, in "Photorefractive Materials & Their Applications 1", ed by P.Gunter, J.P.Huignard (Springer-Verlag, London, 1988)
4. J.Kumar et al., Opt.Lett.,12, 120 (1987)
5. E.Imbert et al., Opt.Lett.,13, 327 (1988)

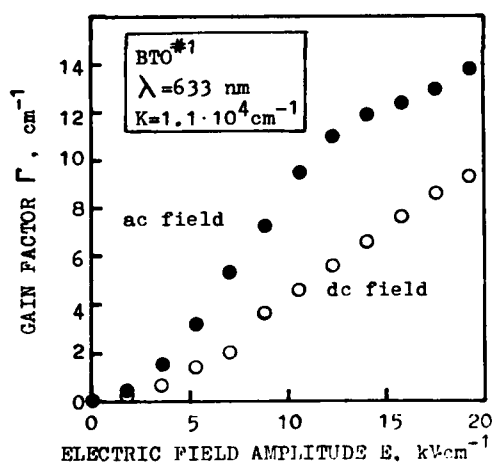


Fig. 1

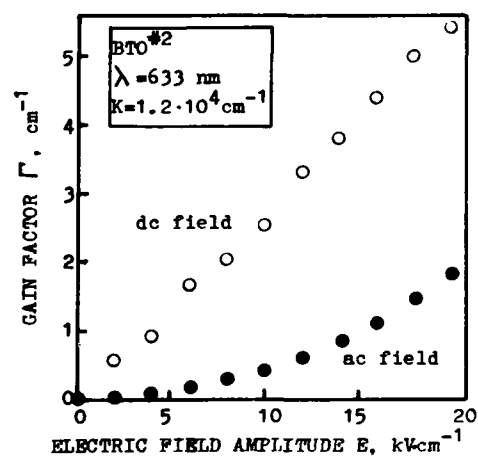


Fig. 2

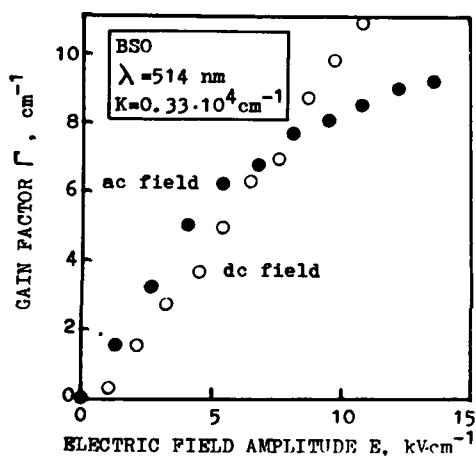


Fig. 3

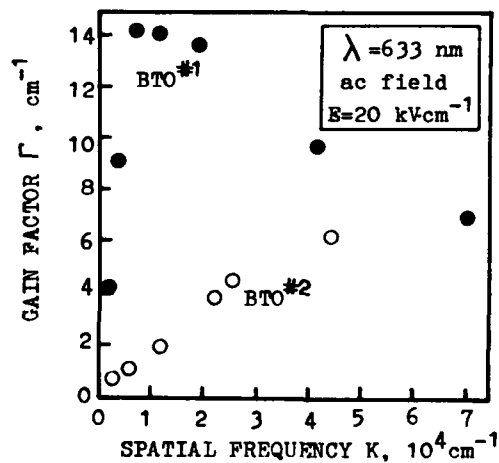


Fig. 4

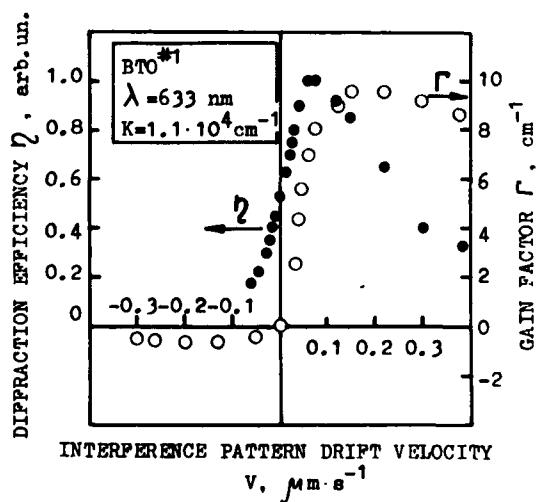


Fig. 5

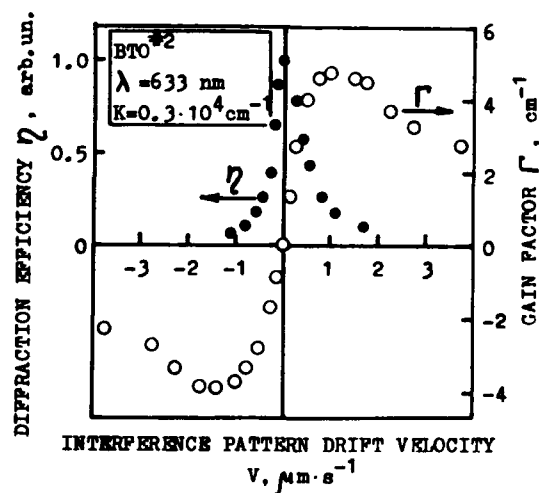


Fig. 6



Polarization properties of $\text{Bi}_{12}\text{SiO}_{20}$ crystals.

T. Panchenko, A. Kudzin, Y. Potapovich, G. Snezhny
 Physics Department Dnepropetrovsk State University
 Gagarin av., 72, 320625, Dnepropetrovsk,
 Uk.S.S.R
 ph. (056-2) 391401

Dnepropetrovsk

Photorefractive crystals $\text{Bi}_{12}\text{SiO}_{20}$ (BSO) are particular interest for applications such as spatial light modulators, image amplification and the like. Some properties are connected to distribution of space charge induced in the crystal both by an applied (or intrinsic) electric field and illumination. Many electrical and optical properties as BSO dependence on density and kind of localized states. In these paper the results of study of both photoelectret and thermoelectret state (PES and TES) and intrinsic charge distribution as were are presented.

The many features of electrets state was carried out by thermally stimulated depolarization (TSD) in temperature range 300-800 K. The potential distribution was determined by point electrical probe method - with 30 μm accuracy. The thermo- and photoelectrets was formed by polarization in external electric field ($U_p = 0.01-1$ kV) in temperature range 300-600 K in dark or under illumination ($\lambda_p = 0.38-0.63$ μm).

The experiments were carried out with plane-parallel wafer 3x5 mm big and about 3-5 mm thick cut from the crystal BSO, grown by the Czochralski method. It has long been recognized that electrical properties of such material as BSO strongly depends of kind of electrode. So in these experiments the different electrodes were used: Pt-BSO-Pt, Pt-D-BSO-Pt, where D - thin film of mica.

The dependence of the TSD response $I(T)$ on temperature is complex and consist of many separate parts of $I_i(T)$. Provided that the every part of $I(t)$ has Haussian form

$$I_i(T) = I_{oi} \exp(-(T-T_{oi})^2 / (\Delta T_i / 1.657)^2),$$

here T_{oi} -temperature of maximum, ΔT_i - half-width, and I_{oi} - maximum of $I_i(T)$.

Both PES and TES have sharply inhomogeneity electric field distributions with charge oscillations (c.o.) near contacts (fig.1). The amplitude of c.o. and their distribution depends on conditions of PES or TES formation. The features of spatial distribution both of internal electric field and charges after polarization in low field $U_p < 0.2$ kV of the samples with Pt-BSO-Pt electrodes may be explained by process of exclusion and blocked contact. Monopolar exclusion model [3] is valid for explanation of TSD current oscillation. The feature of

92-18732



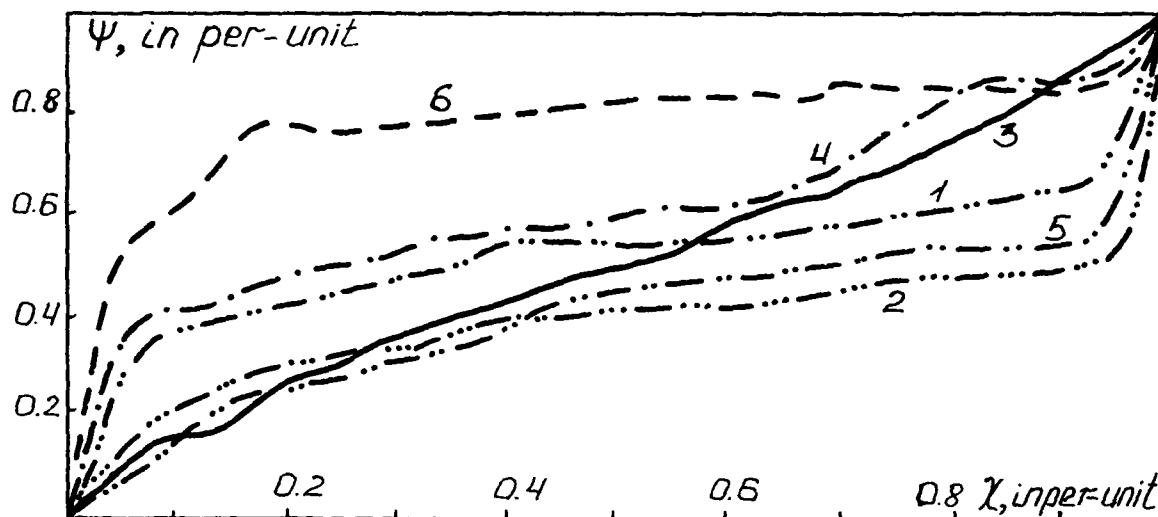


Fig.1. Potential distributions $\Psi(x)$ measured for $U_p = 0.2$ kV (1,2,6); 0.5 kV (3); 1.0 kV (4,5) at different wavelengths ($\lambda_p = 0.66 \mu\text{m}$ (1,4,6); $0.43 \mu\text{m}$ (2,5); white light (3)) in Pt-BSO-Pt (1-5) structure and with interlayer of mica (6).

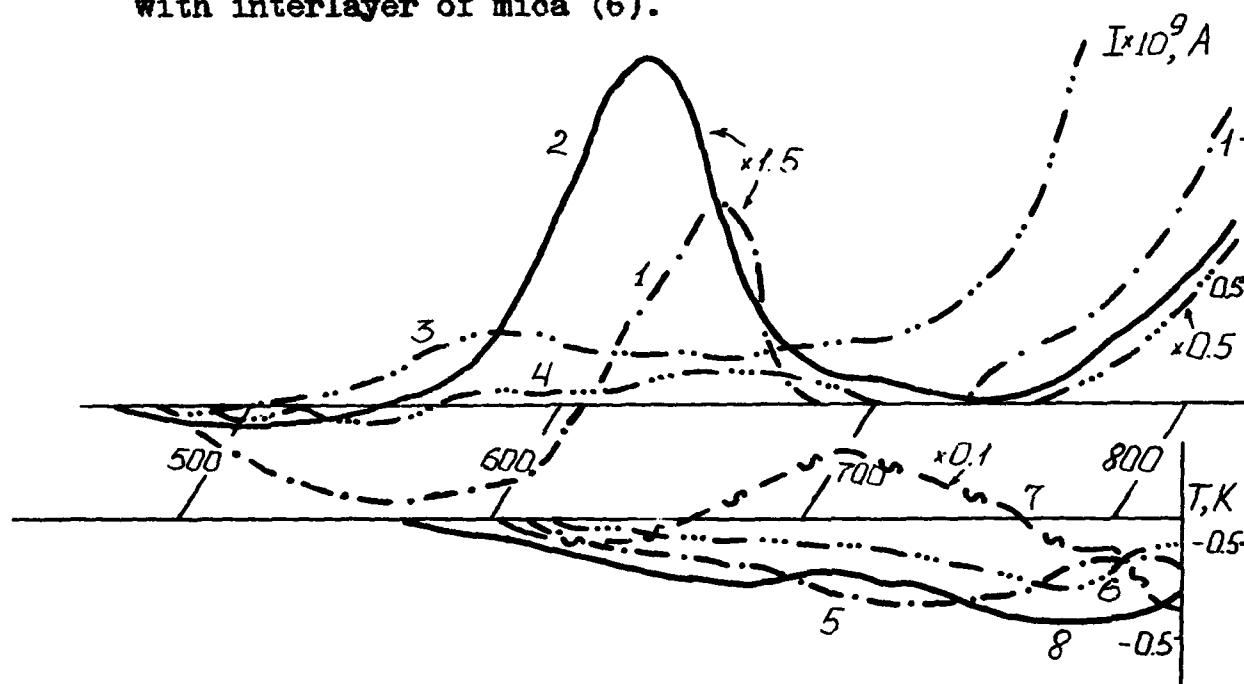


Fig.2. The currents TSD for electret state in BSO crystals for different structure at $T_p = 300$ K.

Pt-BSO-Pt: 1- $E_p = 3$ kV/cm; 2- $E_p = 3$ kV/cm, $\lambda_p = 0.42 \mu\text{m}$;

3- $E_p = 20$ kV/cm; 4- $E_p = 20$ kV/cm, $\lambda_p = 0.42 \mu\text{m}$;

Pt-D-BSO-D-Pt: 5- $E_p = 3$ kV/cm; 6- $E_p = 20$ kV/cm, $\lambda_p = 0.42 \mu\text{m}$;

Pt-D-BSO-Pt: 7- $E_p = 3$ kV/cm, blocked cathode;

8- $E_p = 3$ kV/cm, blocked anode.

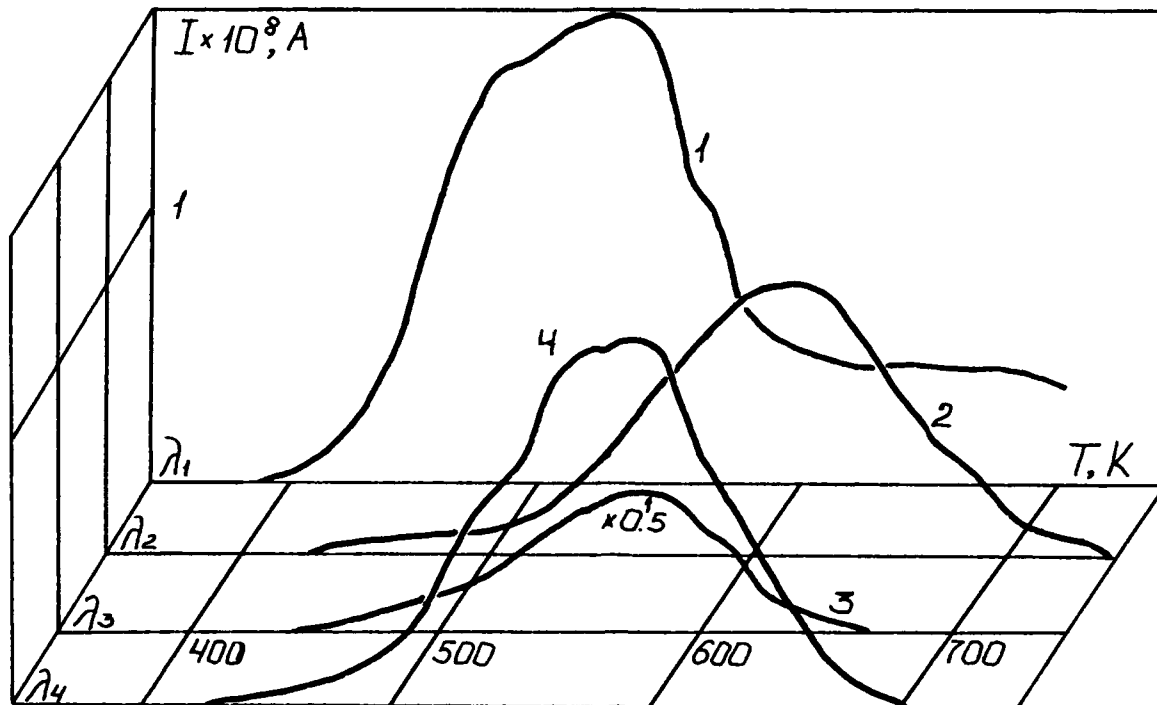


Fig.3. The current TSD for photoelectret state in BSO crystals for $U_p = 0.6$ kV, $T_p = 473$ K at different wavelength: $\lambda_p = 0.38$ μm (1); 0.42 μm (2); 0.53 μm (3); 0.66 μm (4).

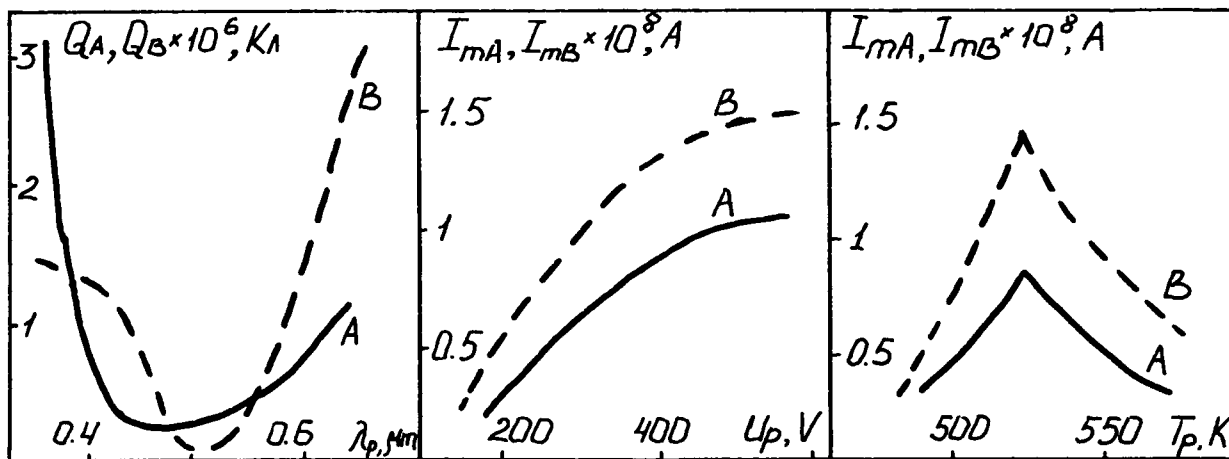


Fig.4. Influence of the intensity I_{ma} , I_{mb} and charge Q_a , Q_b of peaks A and B on the condition polarization.
a) Dependence of the charge on the wavelength for $U_p = 0.6$ kV, $T_p = 473$ K.
b) Dependence of the intensity peaks on the applied voltage for $T_p = 523$ K.
c) Dependence of the intensity peaks on the temperature for $U_p = 0.6$ kV.

current oscillation depends also on polarization condition and kind of electrodes.

The concurrence between both charge injection and charge exclusion in external field $U_p > 0.2$ kV takes place in the sample. There were shown that charging cause accumulation of homocharge and inversion of TSD for Pt-BSO-Pt and Pt-D-BSO-Pt structures. But there is inversion of TSD caused by repeated many times polarization in internal electric fields of TES and PES for Pt-D-BSO-D-Pt structure (fig.2).

Analysis of TSD in PES was performed which correspond in condition write down and read out optical information in PROM devices. It reveals thin structure of localized states at 0.55-1.50 eV interval below conductivity zone and quasi continuous distributed in 1.2-1.3.eV interval.

The dependence of amplitude I_{oi} and release charge Q_{oi} under thermally depolarization for individual components of spectrums $I(T)$ from condition of polarization λ_p, U_p, T_p are studied.

There are no applicability explain these results by two-levels model [4]. It was shown that two quasidipoles mechanisms of TSD with activation energies 0.93 eV and 1.06 eV (fig.4), about ten space charge mechanisms take place.

Much more likely this dipoles are caused by unstoichiometry and existence of Bi^{3+} and Bi^{5+} ions in tetrahedral Si^{4+} sites. Recharging of these ions lead to photochromic effect of BSO crystals and dipole maxima of TSD current $I(T)$.

References

1. Gorohovatskiy U.A. // Osnovi termodepolyarizatsionnogo analiza, M., Nauka, 1981, 173 p.
2. Glebovskiy D.N. // Jurnal prikladnoy spektroskopiy, 1983, v.35, N 3, p. 25-29.
3. Gudaev O.A., Malinovskiy V.K. // Fizika tverdogo tela, 1981, v.15, N 5, p. 868-873.
4. Astratov V.N., Ilinskiy A.V., Furman A.S. // Phys. stat. sol.(b), 1988, v.150, N 2, p.611-615.



HOLOGRAM RECORDING IN GaAs THROUGH EL2 INTRACENTRE ABSORPTION.

Andrei L.Khromov, Michael P.Petrov.

USSR, 194021, Leningrad, Politechnicheskaya 26,

A.F.Ioffe Physico-Technical Institute.

Phone: 515-67-65.

Deep donor centre, referred to as EL2, is the dominant deep level in melt-grown GaAs crystals. Photoionization of EL2, the subsequent space charge redistribution, and refractive index modulation through the electrooptic effect are responsible for what we call below the photorefractive (PR) gratings observed in GaAs semi-insulating crystals, see e.g. [1]. EL2 centre is also distinguished by a number of specific features including the existence of the excited metastable state $EL2^*$ of the same charge. $EL2 \Rightarrow EL2^*$ transitions take place under light excitation with photon energy $h\nu$ between 1.0 and 1.3 eV. At low temperatures $T \approx 100$ K the corresponding cross section σ and lifetime τ are sufficiently large ($\sigma \approx 10^{-17} \text{ cm}^2$, $\tau \approx 10$ s according to [2]) and hence the metastable state EL2 strongly affects the absorption and photocurrent spectrums, some photoelectrical properties of the material, etc. [3,4]. Nevertheless, the probable influence of $EL2 \Rightarrow EL2^*$ transitions on the properties of GaAs crystals as a reversible holographic medium is still in question.

The aim of the study reported here was to investigate the possibility of the hologram recording in semi-insulating crystals through a new physical mechanism namely the local modulation of the optical properties of the crystal caused by $EL2 \Rightarrow EL2^*$ transitions.

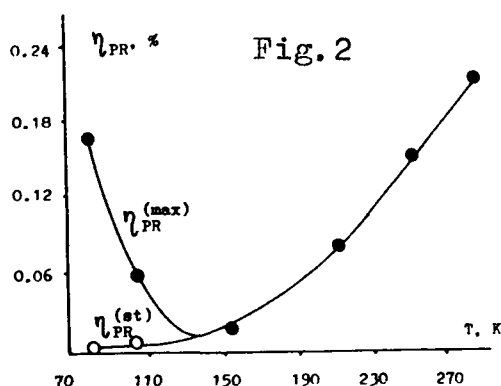
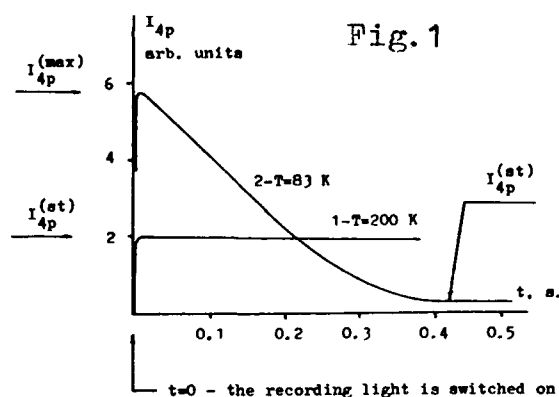
One of the versions of the degenerate four-wave mixing scheme was used. Diffraction of the s-polarized readout wave off the PR hologram is accompanied by the rotation of its polarization plane by 90° i.e. the polarization state is changed from s- to p-. Meanwhile the wave diffracted off the hologram of any other physical origin contains s-polarized component as well. Thus, the diffracted wave I_4 polarization state analysis allows different mechanisms of hologram formation to be distinguished.

Holograms were both recorded and reconstructed with pulse sequences (period $T_p = 50 \mu\text{s}$ and pulse duration $\tau_p \approx 500$ ns) at the wavelength $\lambda = 1.06 \mu\text{m}$ which is close to the optimum one for $EL2 \Rightarrow EL2^*$ transitions. The pulse intensity I_p was on the order of 4 kW/cm^2 corresponding to the average intensity $\langle I \rangle = 4 \text{ W/cm}^2$. A cubic $5 \times 5 \times 5 \text{ mm}^3$ GaAs sample was placed inside the optical cryostat where temperature could be varied from 77 to 300 K. Detector D detected the envelope of the amplitude modulated diffracted light pulse sequences.

Our experiment proved the PR grating formation dynamics to be monotonous within the temperature range 300-120 K, (see curve 1 in fig.1), while at temperatures T below 110 K the hologram formation dynamics changed drastically. We observed nonmonotonous transient consisting of the initial rapid growth of the diffraction effi-

92-18733





We managed to discover the non-PR grating formed in GaAs at temperatures below 180 K. At $T > 120$ K the recording occurred monotonically while at $T < 110$ K a curious nonmonotonous transient was observed (see fig.3,4). The non-PR hologram recording at $T < 110$ K is also irreversible in the sense explained above and regenerating also is achieved after heating under the same conditions.

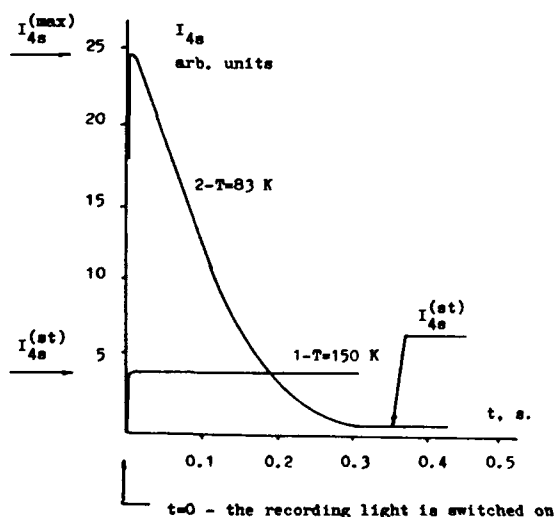
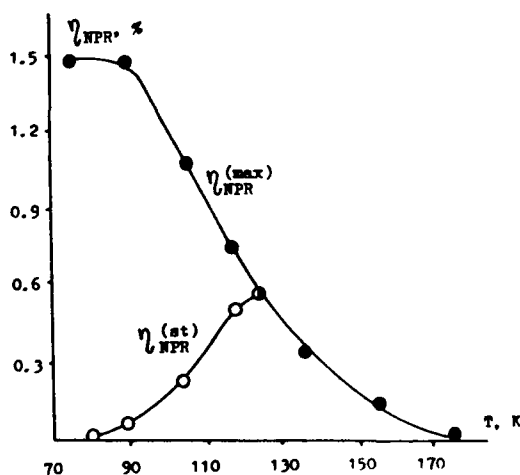


Fig.3

ciency from 0 up to $\eta_{PR}^{(max)} \sim I_{4p}^{(max)}$ followed by the slow relaxation to the stationary value $\eta_{PR}^{(st)} \ll \eta_{PR}^{(max)}$ equal to zero in some cases (see curve 2 in fig.1). Both $\eta_{PR}^{(max)}$ and $\eta_{PR}^{(st)}$ plotted as functions of temperature are shown in fig.2. In addition, at $T < 110$ K the PR hologram recording became irreversible. We mean that the signal shown in fig.1 curve 2 was observed only once when the light was switched on for the first time after cooling the sample. Switching the light on for a second time about 20 s later resulted in no signal at all. We found that heating the sample above 120 K for a few minutes resulted in regeneration of its initial properties



We suppose $EL2 \Rightarrow EL2^*$ transitions to be the most probable reason for the non-PR hologram formation and present the following qualitative model of the processes that occur in GaAs at low temperatures under light excitation.

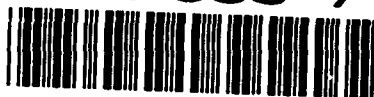
Before the light is switched on all EL2 centres are in the ground state and the occupancy of the metastable $EL2^*$ level is negligible. After introducing N -the ground EL2 state density and N^* -that of the metastable state the initial conditions can be written in the form $N = N_D - N_A$, $N^* = 0$, where $N_D \approx 10^{16} \text{ cm}^{-3}$ is the total impurity level density, $N_A \approx 10^{15} \text{ cm}^{-3}$ is compensating acceptor density. Under the illumination with interference pattern $I(x)$ spatially non-uniform densities $N(x)$ and $N^*(x)$ are formed. $EL2 \Rightarrow EL2^*$ transitions cause lattice relaxation around the centre which in turn results in the refractive index variations $\Delta n = \Delta n(x) = \Delta n(N(x), N^*(x))$ and thus give rise to the spatially periodic refractive index profile (estimated to be on the order of 10^{-5}) and the diffracted s-polarized wave I_s . Since $T \gg \tau_p$ N^* is steadily increasing and N decreasing. At last we find all $EL2$ transferred into $EL2^*$ everywhere within the crystal's volume i.e. $N = N_D - N_A$, $N^* = 0$. In that final state refractive index variations amplitude Δn is obviously zero and also the diffracted beam intensity (see fig.3.4). Moreover, according to [2,6] in this final state the crystal loses sensitivity to light that well explains the observed holographic response quenching. As it was mentioned above the regeneration of the initial properties can be achieved by heating the sample above 120 K for a time required for all $EL2^*$ to relax back to $EL2$. This conclusion is in good agreement with the statement made in [2] concerning the regeneration of the photocapacitance response.

To summarize we have reported the first observation of the non-PR grating established in GaAs under light excitation at low temperatures. Its main features can be explained by using the assumption that the photoinduced $EL2 \Rightarrow EL2^*$ transitions cause local refractive index variations, probably due to the piezoelectric effect. If so, the detailed analysis of the optically induced anisotropy in GaAs may produce the possibility of getting the experimental insight into the microscopic structure of EL2 point defect.

REFERENCES

1. A.L.Smirl, G.C.Valley, K.Bohnert, T.F.Boggess. IEEE J. Quantum Electron. 24 (1988) 289.
2. G.Vincent, D.Bois, A.Chantre. J. Appl. Phys. 53 (1982) 3643.
3. M.Kaminska, M.Skowronski, J.Lagowski, J.M.Parsey, H.C.-Gatos. Appl. Phys. Lett. 43 (1983) 302.
4. M.Kaminska, M.Skowronski, W.Kusko. Phys. Rev. Lett. 55 (1985) 2204.
5. A.L.Khromov, A.A.Kamshilin, M.P.Petrov. Sov. Phys. Solid State 32 (1990) 278.
6. G.Vincent, D.Bois. Solid State Commun. 27 (1978) 431.

AD-P006 746



Single Crystal Growth of Photorefractive Sillenites

Volkov V.V., Kargin Yu.F., Skorikov V.M.

The Kurnakov Institute of General and Inorganic Chemistry, USSR Academy of Sciences.

USSR, 117907 Moscow, GSP-1, Leninsky Pr., 31, phone 232-10-21

The compounds, crystallized in the cubic form similar to sillenite structure, occur in a number of isomorphs [1]. The well-known representatives of this family are bismuth germanium (BGO) and bismuth silicon oxides (BSO), both of which can be grown from their stoichiometric melts using Czochralsky technique. The optical examination and utilization of the isomorphs are difficult because of their incongruent melting or decomposition in solid state.

At our laboratory single crystals of BSO, BGO incorporated with a variety of elements of I-VIII Periodic Table groups, as well as $\text{Bi}_{12}\text{TiO}_{20}$ (BTO), $\text{Bi}_{38}\text{ZnO}_{58}$ (BZnO), $\text{Bi}_{25}\text{FeO}_{39}$, $\text{Bi}_{25}\text{GaO}_{39}$ (BGaO), $\text{Bi}_{24}\text{AlPO}_{40}$, $\text{Bi}_{24}\text{GaPO}_{40}$, $\text{Bi}_{24}\text{FePO}_{40}$ and BTO doped with Zn, Fe, V, P, Ga have been grown. The present report deals with heterovalent Ti^{4+} ion substitutions of the host BTO influence on the visible transmission spectra, photoconductivity, optical power rotation and linear electrooptic factors.

From our previous investigation of the phase diagrams we found out that solutions containing 5 to 6 molar % Fe_2O_3 , 8 to 9 molar % Ga_2O_3 and 9 to 10,5 molar % ZnO could be used to grow crystals. The attempts were successful adopting the top seeded solution technique. The best conditions for growth were the seed rotation at rates between 30 and 40 rpm, cooling rate between 3 and 5 degrees per day. In order to eliminate the discrepancy dislocations generated by the seed and thermal strains, the crystallization of $\text{Bi}_{25}\text{FeO}_{39}$ and $\text{Bi}_{25}\text{GaO}_{39}$ was carried out onto the seed cut from BTO along $\langle 100 \rangle$ and $\langle 110 \rangle$ axes. The constant lattice of BTO is determined to be $a = 10,1738 \pm 0,0008 \text{ \AA}$. Furthermore, the solid solution $\text{Bi}_{12}\text{Ti}_{0,72}\text{V}_{0,28}\text{O}_{20}$ crystal with the constant lattice $a = 10,195 \text{ \AA}$ has been prepared for

92-18734



growth $\text{Bi}_{38}\text{ZnO}_{58}$. Using 300 g charge, crystals weighing up to 20 and 30 g have been grown. Neutron diffraction patterns accomplished on the spherical samples with 6 mm diameter reveal the following: a) there are regulated vacancies in the oxygen sublattice for O(3) sites; b) Bi^{3+} ions occupy tetrahedral locations with formation $[\text{BiO}_3]^{3-}$ umbrella structure units. In Table 1 the concentration of M elements in tetrahedral position is showed.

Table 1

| Compound | $\text{Bi}_{25}\text{FeO}_{39}$ | $\text{Bi}_{38}\text{ZnO}_{58}$ | $\text{Bi}_{25}\text{GaO}_{39}$ |
|---------------------------------|---------------------------------|---------------------------------|---------------------------------|
| Concentr. M, mas. % theoret. | 0,9 | 0,7 | 1,2 |
| exper. | 1,1 | 0,7 | 1,3 |
| Unit cell, Å | 10,169 | 10,201 | 10,176 |

The crystallochemical formula of these crystals based on the experimental data, should be written: $\text{Bi}_{12}[\text{Bi}_{0,5}^{3+}\text{Fe}_{0,5}^{3+}]_{0,19,5}$, $\text{Bi}_{12}[\text{Bi}_{0,66}^{3+}\text{Zn}_{0,33}^{2+}]_{0,19,33}$ and $\text{Bi}_{12}[\text{Bi}_{0,5}^{3+}\text{Ga}_{0,5}^{3+}]_{0,19,5}$ [2-4].

The BTO single crystals were pulled from solutions containing 6-8 molar % TiO_2 in excess Bi_2O_3 under lateral growth kinetics, in contrast to BSO and BGO, which could be grown relatively easily from stoichiometric starting composition under continuous growth kinetics. Reduction of axial temperature gradients up to 8 and 10 degrees cm^{-1} under supersaturation leads to faceted crystal growing. Fig.1 shows typical as grown BTO crystals. The best conditions for growth were pulling rate of 0,9 mm hr^{-1} and seed rotation rate of 40 rpm. Crystals up to 400 g, 30 mm square, with (100) major facets were grown on $\langle 100 \rangle$ oriented seeds. A spherical neutron diffraction pattern defined the numerical data for Ti^{4+} and $\text{O}^{2-}(3)$ ions packing factor equal to $0,91 \pm 0,01$ and $0,97 \pm 0,01$, respectively.

In order to investigate the photorefractive characteristics samples of 5x2x10, 5x4x10, 5x8x10 mm with polished plates (100)x(011)x(011) and (100)x(010)x(001) oriented have been prepared, see Fig.1. The data listed in Table 2 for elements tetrahedrally coordinated in $\text{Bi}_{12}\text{Ti}_{1-x}\text{M}_x\text{O}_{20}$ have been achieved by means of bulk chemical analysis, X-ray microprobe and differential IR-spectrometry.

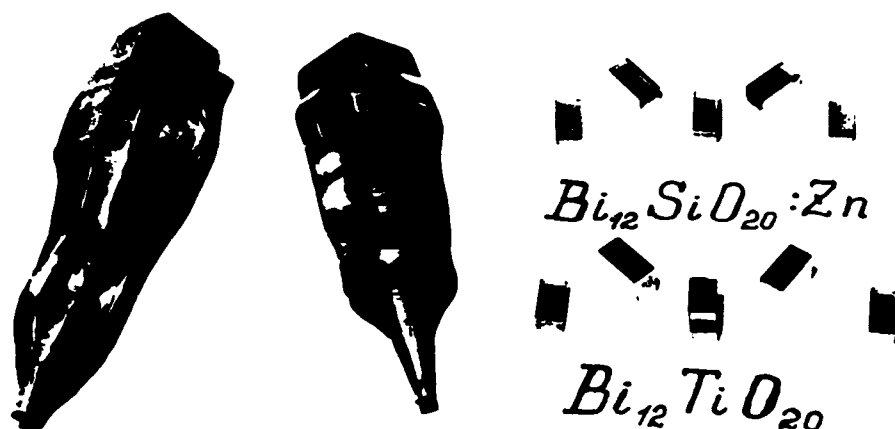


Fig.1. The single crystals of BTO; polished samples.

Table 2

| Tetrahedrons | Concentr. M, mas. % | Substitution % | Segreg., K_{eff} | Unit _{cell} A |
|----------------|------------------------|-------------------|-----------------------|---------------------------|
| $[ZnO_4]^{6-}$ | 0,15 | 6 | 0,2 | 10,176 |
| $[FeO_4]^{5-}$ | 0,13 | 7 | 0,2 | 10,176 |
| $[VO_4]^{3-}$ | 0,50 | 28 | 2,4 | 10,195 |
| $[PO_4]^{3-}$ | 0,18 | 20 | 0,4 | 10,177 |

The incorporation of 0,05 mas.% Zn, Ga or less is expected to enhance the maximum photocurrent as compared with the host crystal. For greater concentration values the amount of $[BiO_3]$ structural clusters seems to quench the photoconductivity significantly. IR-spectrometry analysis of $[MO_4]$ phonon oscillations shows that P and V ions with 5+ valency yielded appreciable changes in the photoconductivity spectra and relaxation time kinetics. For example, V^{5+} ions maintenance increases sensitivity of the material in the long wavelength visible spectrum. Such effect is caused by the sensitive 1,9 eV level of the band gap.

From previous study [2] $Bi_{12}VO_{20,5}$ reveals additional oxygen anion which binds four coupling Bi polyhedrons, as a result of Bi-O(3) bonding break in $[Bi_2O_8]$ dimeric units. Formation of such clusters under $[TiO_4]^{4-} \rightarrow [VO_4]^{3-}$ substitution

is, moreover, found to be a considerable effect both on photosensitivity and optical activity. Table 3 gives the values of the optical power rotation and linear electro - optic coefficients for some crystals. Note that

$\text{Bi}_{12}\text{Ti}_{0,72}\text{V}_{0,28}\text{O}_{20}$ reveals the least optical activity, what may lead to application of this material in photorefractive devices.

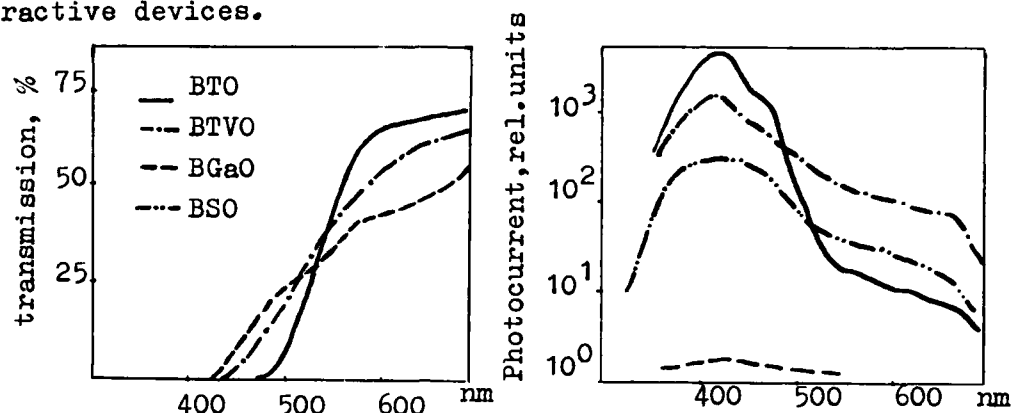


Fig.2. The transmission and photoconductivity spectra.

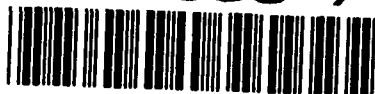
$\lambda = 630 \text{ nm}$

Table 3.

| Composition | Optical power rotation, °/mm | $(n_0^3 r_{41}), 10^{-12} \text{ m/B}$ | $r_{41}, 10^{-12} \text{ m/B}$ |
|-------------|------------------------------|--|--------------------------------|
| BSO | 21 | 75 | 4,5 |
| BTO | 7 | 95 | 5,9 |
| BGaO | 21 | 65 | ... |
| BTO:Zn | 8 | 90 | 5,9 |
| BTVO | 4,6 | 100 | ... |

References :

1. Kargin Yu.F., Mar'in A.A., Skorikov V.M. // Sov. Inorg. Mat. 1982. V. 18. No. 10. P. 1605.
2. Radayev S.F., Muradyan A.A., Kargin Yu.F. // Reports of USSR Acad. of Sci. 1989. V. 307. P. 606.
3. Radayev S.F., Muradyan A.A., Kargin Yu.F. // Reports of USSR Acad. of Sci. 1989. V. 307. P. 1381.
4. Radayev S.F., Muradyan A.A., Kargin Yu.F. // Reports of USSR Acad. of Sci. 1989. V. 306. P. 624.



Temperature dependence of the two beam coupling gain coefficient of photorefractive GaP

K. Kuroda, Y. Okazaki, T. Shimura, and M. Itoh

*Institute of Industrial Science, University of Tokyo
Roppongi, Minato-ku, Tokyo, 106 Japan
Phone: +81-3-3402-6231*

1. Introduction

Undoped semi-insulating GaP is photorefractive material which is sensitive to the laser light of the wavelength between $0.6 \mu\text{m}$ and $0.9 \mu\text{m}$ ¹⁾. He-Ne lasers and GaAlAs laser diodes belong to this spectral region. This material is important for constructing compact systems with laser diodes.

Since semi-insulating GaP has no significant application in electronics yet, enough data are not available. In this paper, we describe the measurement of the two beam coupling gain coefficient and the time constant at various temperature. The decrease of the gain coefficient is observed both at high and low temperature. We also observed the photochromic effect, that is, intensity dependent absorption at low temperature.

2. Experimental Setup

The experimental setup is shown in Fig.1, which is similar to the previous one¹⁾. The sample is contained in a cryostat cooled by liquid nitrogen. The temperature can be varied from 100 K to 400 K.

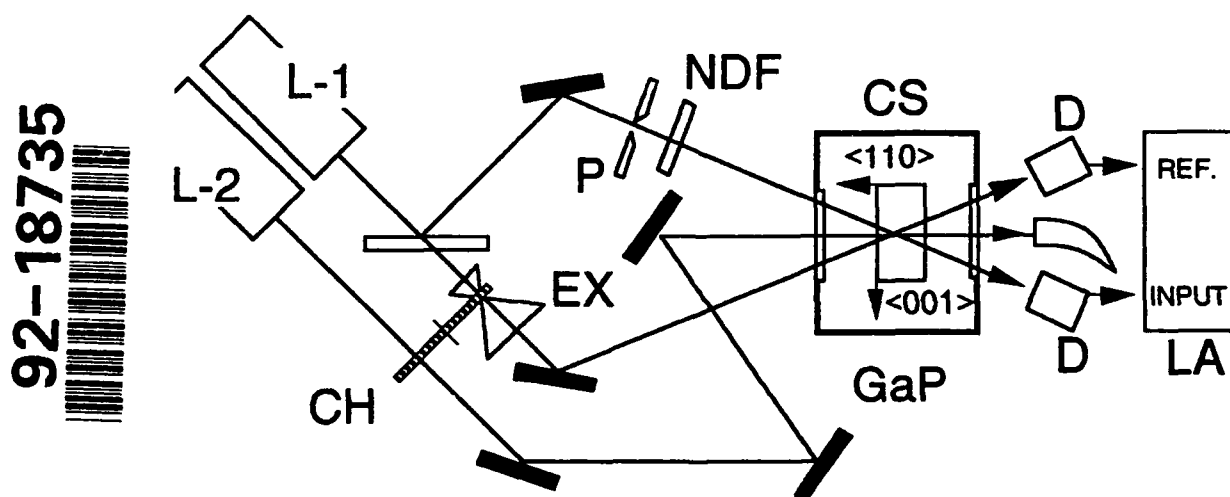


Fig.1 Experimental setup. L-1, L-2 : He-Ne lasers; CH: chopper; EX: beam expander, P: pinhole, NDF: neutral density filter; CS: cryostat; D: photodetectors; LA: lock-in amplifier.

Two 633-nm He-Ne lasers were used: laser 1 to form the refractive index grating and laser 2 to erase the grating. A chopper cut the pump beam and the erase beam alternatively. The chopping frequency was varied from 5 to 30 Hz. A lock-in amplifier was used to improve the S/N ratio. The Fourier transform method was used to determine both



the gain coefficient and the time constant from the lock-in amplifier data. The detail of this method was described in the previous paper¹). Another function of laser 2 was to cancel the photochromic effect, that is, the dependence of the absorption on the intensity. If the pump and erase beams have same intensity, the increase of the absorption is also same in the pump and the erase period.

3. Experimental Results and Discussions

3.1 Photorefractive effect

The temperature dependence of the coupling gain coefficient is shown in Fig.2. The grating period was 1.1 μm , which is almost equal to the Debey shielding length at $T = 300$ K. Maximum gain coefficient was 0.41 cm^{-1} at $T = 360$ K. As the temperature elevates beyond 360 K, the thermally excited electrons sweep out the grating and the gain coefficient decreases rapidly.

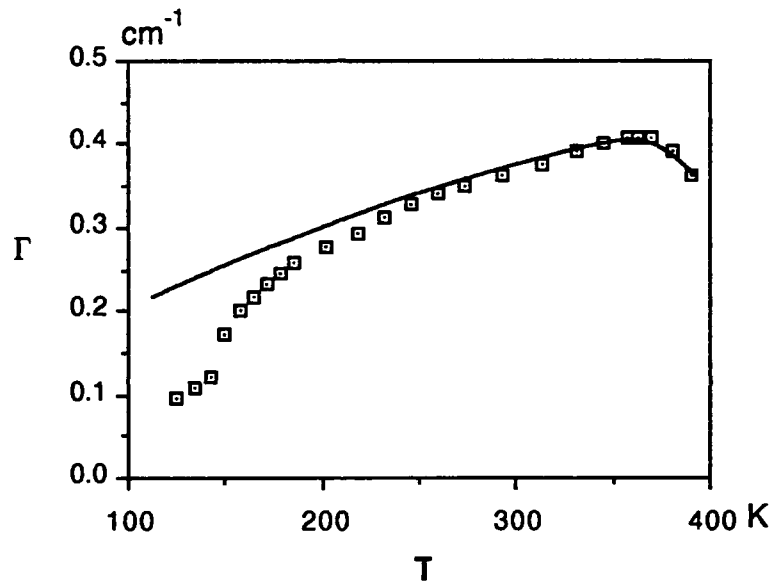


Fig.2 Temperature dependence of the coupling gain coefficient.

The solid curve is calculated from the standard theory of the photorefractive effect with single carrier, which is given by

$$\Gamma = \frac{2\pi n^3 r_{41}}{\lambda \cos \theta} \frac{2\pi k_B T}{e \Lambda \left(1 + \frac{4\pi^2 \epsilon k_B T}{e^2 N_E \Lambda^2} + \zeta_{sc} \right)} \frac{1}{1 + \frac{\sigma_d}{\sigma_{ph}}} \quad (1)$$

Notations are listed below:

n : refractive index

r_{41} : the component of the electro-optic coefficient

λ : wavelength

θ : the Bragg angle inside the crystal

k_B : Boltzmann constant

T : temperature

e : elementary charge

Λ : grating period
 ϵ : dielectric constant
 N_E : equivalent density of trap
 γ : recombination coefficient
 n_{th} : thermal equilibrium density of electron
 s : absorption cross section
 I : intensity of light
 ζ_{sc} : correction term due to the screening effect by minority carriers²⁾

We used the following numerical equation to plot the solid curve in Fig.2,

$$\Gamma = \frac{0.00217T}{1 + 0.0025T} \frac{1}{1 + 1.6 \times 10^8 T^2 \exp\left(-\frac{12700}{T}\right)} \quad (2)$$

where T is in K. Temperature dependence of the last factor in eq.(2) mainly comes from the recombination coefficient and thermal electron density³⁾. Above 200 K, the experimental results are well fitted to the theoretical curve. But below 200 K, there exists discrepancy between the experiments and the simple theory.

As the temperature decreases, thermal coupling between shallow acceptors and valence band becomes weak, and then the shallow acceptors begin to contribute to the photorefractive effect. The space charge density produced by the acceptor screens that by the deep donor. This effect is expressed by the screening term ζ_{sc} which is the ratio of the effective trap density of the shallow acceptors to that of the deep donors²⁾.

3.2 Time constant

Time constant as a function of temperature is plotted in Fig.3.

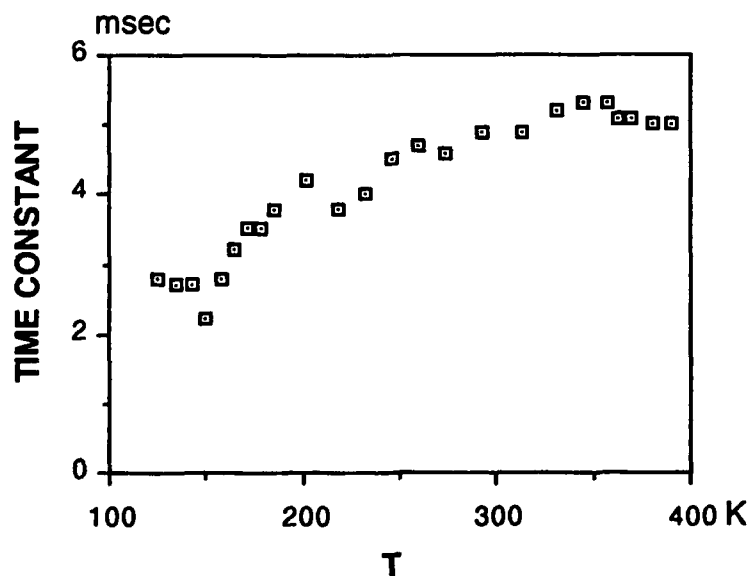


Fig.3 Time constant.

At lower temperature, time constant becomes short. This is mainly because that the mobility of carriers increases as the temperature decreases. The increase of mobility makes the dielectric relaxation time short.

At the temperature where the photochromic effect becomes significant, multi-trap levels contribute to the transfer of the charges. This makes the evolution of the space charge complicated, and as a result, the formation of the internal electric field does not obey the simple exponential law. Therefore the measured time constants are not accurate in this temperature region.

3.3 Photochromic effect

At temperature from 120K to 140K, photochromic effect was observed. The absorption is plotted as a function of intensity in Fig.4.

The photochromic effect is frequently observed in BaTiO_3 ⁴⁾ and cooled GaAs^{3,5)}. This effect is originated by the existence of shallow donor levels.

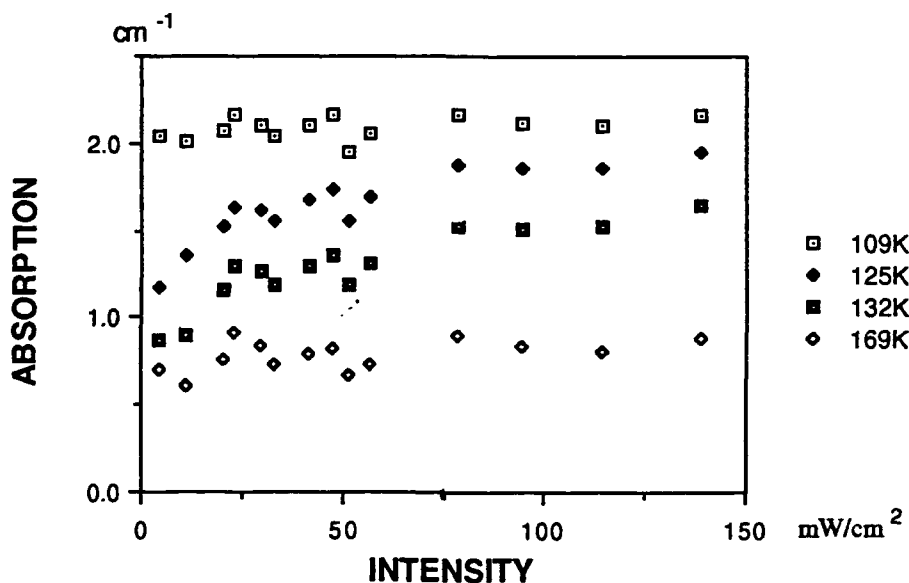


Fig.4 Absorption coefficient as a function of intensity. Photochromic effect is observed at $T = 125$ and 132 K.

4. Conclusion

The two wave coupling gain coefficient and its time constant were measured. The screening effect was observed around 150 K. Photochromic effect was also observed between 120 and 140 K. These results indicate the existence of shallow acceptor (screening) and shallow donor (photochromic) levels. Energy depth of these shallow acceptor and donor is estimated 100 - 150 meV from the temperature dependence.

References

- 1) K. Kuroda, Y. Okazaki, T. Shimura, H. Okamura, M. Chihara, M. Itoh, and I. Ogura, *Opt. Lett.* **15** (1990) 1197.
- 2) D. D. Nolte, D. H. Olson, and A. M. Glass, *Phys. Rev. Lett.* **63** (1989) 891.
- 3) Y. Tomita, thesis (California Institute of Technology, 1989)
- 4) A. Motes and J. J. Kim, *J. Opt. Soc. Am. B* **4** (1987) 1379.
- 5) D. D. Nolte and A. M. Glass, *Opt. Quantum Electron.* **22** (1990) S47.



Non-steady-state photoEMF in crystals with long relaxation times of photoconductivity

I.A.Sokolov, S.I.Stepanov

(A.F.Ioffe Physical Technical Institute, 194021, Leningrad, USSR)

Introduction

The recently discovered effect of non-steady-state photo(EMF) is a powerful technique for the measurement of different parameters of photorefractive crystals [1-3]. The photoEMF is observed as an alternating electric current J^ω through a short-circuited sample of photoconductor illuminated by a vibrating pattern of interference between two coherent waves, one of which is phase modulated with frequency ω (Fig.1). It results from a periodic modulation of the spatial shift between the distribution of photoconductivity that follows movements of the interference pattern and the distribution of the space-charge electric field recorded through the conventional diffusion holographic mechanism in photorefractive crystals.

As shown in [3], the expression for the first harmonic of the photocurrent at high excitation frequencies comparable with the inverse lifetime of photocarriers τ is given by

$$J^\omega = - \frac{S \sigma_0 m^2 \Delta E_D \omega \tau_H}{2\{(1-\omega^2 \tau \tau_H)^2 + \omega^2 (\tau_H (1+K^2 L_D^2) + \tau)^2\}^{1/2}} \quad (1)$$

Here, S is the cross-section of the sample, σ_0 is the average photoconductivity, m is the contrast, Δ is the vibration



amplitude of the interference pattern, $E_D = Kk_B T/e$ is the so-called diffusion field, $K = 2\pi/\Lambda$ is the spatial frequency of the interference pattern, and τ_H is the Maxwell relaxation time.

We measured the frequency transfer function of the effect of the non-steady-state photoEMF for the $\text{Bi}_{12}\text{TiO}_{20}$ crystal ($4 \times 10 \times 5 \text{ mm}^3$) at the wavelength of a HeNe laser (for $KL_0 \approx 0.3$, $L_0 \approx 0.9 \text{ } \mu\text{m}$) for two illumination levels ($P_1 = 20 \text{ mW}$, $P_2 = 10 \text{ mW}$) (Fig.2). As seen in Fig.2, there are two characteristic points on the transfer function of the effect. From the position of the first point, the Maxwell relaxation times were found to be $\tau_{H1} \approx 230 \mu\text{s}$, $\tau_{H2} \approx 460 \mu\text{s}$. The second characteristic point is associated with the finite lifetime, τ , of photoelectrons in the conduction band that was estimated to be $\approx 5 \mu\text{s}$. No variations in the position of the second characteristic point for the light powers used were observed.

An average photoconductivity of the $\text{Bi}_{12}\text{TiO}_{20}$ crystal was estimated to be $\sigma_{01} \approx \epsilon \epsilon_0 / \tau_{H1} \approx 1.8 \cdot 10^{-6} (\text{Ohm} \cdot \text{m})^{-1}$. Using a well known relation $L_0 = (\mu \tau k_B T/e)^{1/2}$, the $(\mu \tau)$ -product and the mobility of photocarriers μ can be determined: $\mu \tau \approx 3.2 \cdot 10^{-7} \text{ cm}^2 \text{ V}^{-1} \text{ s}^{-1}$, $\mu \approx 0.06 \text{ cm}^2 \text{ V}^{-1} \text{ s}^{-1}$. The mean diffusion length of photocarriers $L_0 \approx K_0^{-1}$ was found from the position of the maximum amplitude on the spatial frequency dependence of the photo EMF $J^\omega (\Lambda^{-1})$ measured for a high excitation frequency $\omega \gg \omega_0 \approx (\tau_H (1 + K^2 L_0^2))^{-1}$ (Fig.3).

Earlier [3] we reported the measurements of average

lifetimes of photocarriers in the $\text{Bi}_{12}\text{SiO}_{20}$ crystals ($\tau \approx 3 \mu\text{s}$, $\lambda = 633 \text{ nm}$; $\tau \approx 100 \mu\text{s}$, $\lambda = 442 \text{ nm}$).

In the work reported here a sample of the $\text{Bi}_{12}\text{SiO}_{20}$ crystal ($5 \times 2 \times 10 \text{ mm}^3$) at the wavelength of an Ar-ion laser ($\lambda = 514 \text{ nm}$, $I_0 \approx 0.24 \text{ mW/mm}^2$) was investigated.

For excitation frequencies $(1 + K^2 L_0^2) / \tau \gg \omega \gg \omega_0$ the signal of the non-steady-state photoEMF peaks at spatial frequency $K_0 = L_0^{-1}$ (Fig.4), inversely proportional to the mean diffusion length of photocarriers, which was found to be $\approx 1.3 \mu\text{m}$ for the light intensity $I_0 \approx 0.3 \text{ mW/mm}^2$. The frequency transfer function of the photoEMF signal is shown in Fig.5. The Maxwell relaxation time was found to be $\approx 10 \text{ ms}$, the average lifetime of photocarriers was estimated to be $\approx 19 \mu\text{s}$.

Without going into detail, we note here that the position of the second characteristic point on the transfer function of the effect was found to be intensity-dependent. We observed also the sublinear dependence of the average photoconductivity on the light intensity for higher intensity levels. These facts are interesting and require more thorough investigation.

Literature

1. M.P.Petrov, S.I.Stepanov, and G.S.Trofimov, Sov.Tech.Phys.Lett., 12, 379 (1986).
2. M.P.Petrov, I.A.Sokolov, S.I.Stepanov, and G.S.Trofimov, J.Appl.Phys., 68, 2216 (1990).
3. I.A.Sokolov, S.I.Stepanov, Electron.Lett., 26, 1275 (1990).

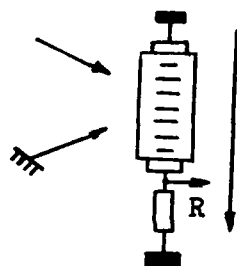


Fig. 1

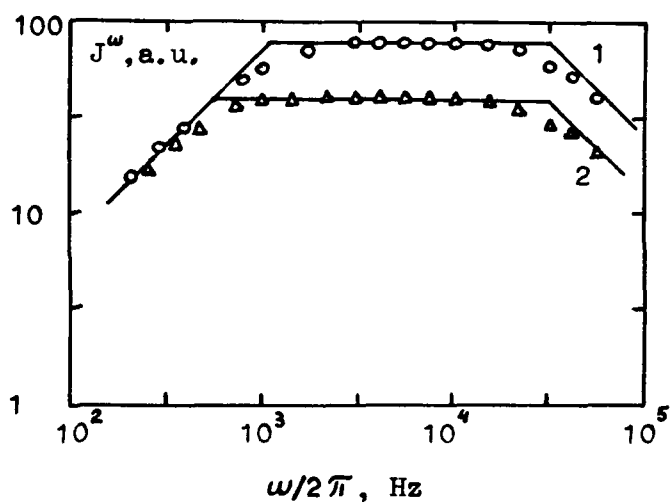


Fig. 2 Transfer function

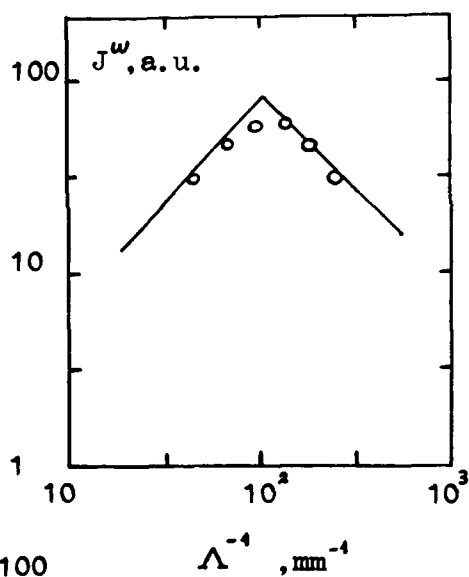
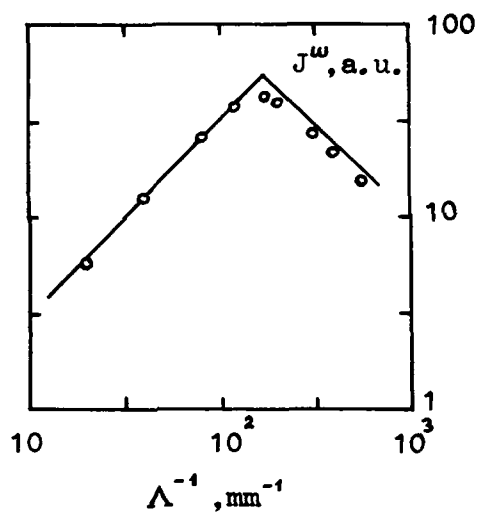


Fig. 4

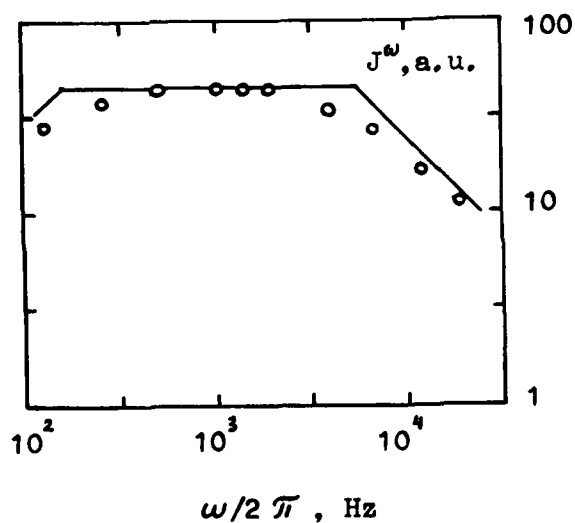


Fig. 5



CHARGE TRANSPORT IN HIGH-RESISTIVITY PHOTOREFRACTIVE CRYSTALS

(Bi₁₂SiO₂₀, ZnSe, GaAs)

A.V. Ilinskii

A.F. Ioffe Physical-Technical Institute,
Academy of Sciences of the USSR, Leningrad

Introduction. The paper reviews our studies^[1-7] concerned of photoinduced charge dynamics and electric field evolution in the case of external field screening. The experimental methods providing possibility of electric field distribution direct measurements are considered. It is found that there are two different regimes of electric field screening which depend on experimental conditions (kind of crystal, temperature): narrowing of major carriers depletion region and stratification effect (numerous space charge layers of alternating sign) with increasing charge density - regime 1 and the slow broadening of single layer with constant charge density may occur in bulk of a sample - regime 2. These regimes were experimentally investigated in Bi₁₂SiO₂₀, ZnSe and GaAs crystals. A theoretical description is given of a sufficiently general charge transfer model involving the photogeneration of free carriers, their drift and trapping throughout the depth of the material.

Experimental methods. Bi₁₂SiO₂₀ and ZnSe crystals were investigated by the method based on Pockels effect - fig.1. A sample is

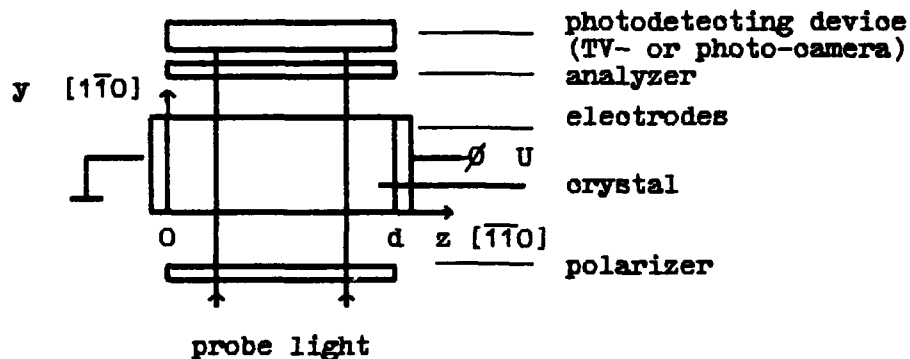


FIGURE 1

probed with linearly polarised light in the direction y perpendicular to that of the applied field. Because of the linear transverse electro-optic effect the probe light undergoes phase

92-18737



spatial modulation in the crystal volume in accordance with the pattern of electric field distribution $E(z,t)$ (the field is assumed to be parallel to the z -axis). The light emerging from the crystal is passed through an analyzer (a polaroid) transforming phase in to intensity modulation, and light intensity modulation $I(z,t)$ is measured. The crystal symmetry, sample orientation and geometry of the experiment were taken into account for the quantitative field measurements^[1].

Method for investigation GaAs crystals is based on Franz-Keldysh effect. It also includes probing a sample in the direction "y" perpendicular to electric field by a light beam with photon energies below the band gap of GaAs crystals ($\lambda = 0.904 \mu\text{m}$). From the shift of band edge to longer wavelengths (caused by electric field) the relation between space-time distribution of probe light intensity $I(z,t)$ and electric field $E(z,t)$ may be evaluated.

Experimental results. Electric field distribution patterns in $\text{Bi}_{12}\text{SiO}_{20}$ at $T = 262 \text{ K}$ measured at different times after voltage application ($t(\text{s})$: 1-0, 2-6, 3-60)^[2,3] are shown in fig.2. It can

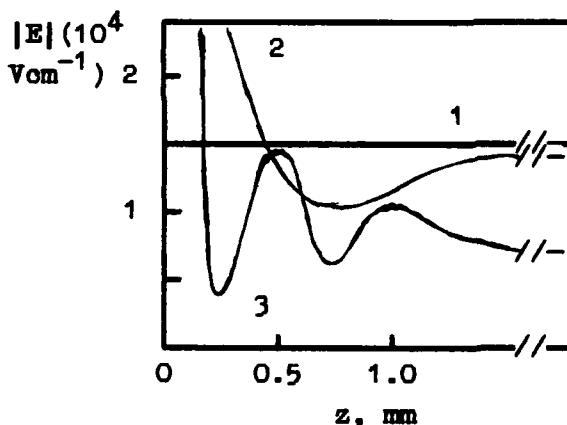


FIGURE 2

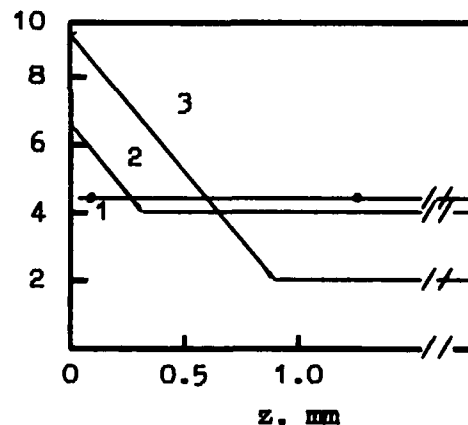


FIGURE 3

be seen that after voltage application and uniform photoexcitation a region is formed in the sample near the negative electrode where the field absolute value decrease with distance from the electrode. Such field behavior shows that electrons are a major charge carriers and positive space-charge layer with density $\sim 10^{12} \text{ cm}^{-3}$ occurs near the negative electrode. The thickness of the layer decreases in time. In late evolution stages an unusual qualitative

feature of field distribution appears: spatial oscillations of the electric field take place in the sample (regime 1). It means that a multilayer sign alternating space charge structure (i.e. space charge stratification) is built up in the sample; the charge layers move towards the negative electrode and their density increases. Electric field distribution patterns in ZnSe crystals at $T = 329$ K ($t(s)$: 1-0, 2-0.08, 3-0.24)^[4,5] is presented on fig.3. Electric field localized region formed near blocking positive contact evidence for hole type of conductivity and for the creation of positive space charge in the a sample volume. In contrast to the previous case of stratification a broadening with constant charge density p_0 (regime 2) instead of depleted region narrowing takes place. It is important to note that regime 1 was observed in ZnSe at $T=212$ K, and regime 2 in $Bi_{12}SiO_{20}$ at $T=161$ K [4,5].

The space-time electric field evolution in i-layer of GaAs p-i-n structure at $T=173$ K ($t(s)$: 1- 10^{-5} , 2- $35 \cdot 10^{-3}$, 3-steady state) is shown on fig.4. Electric voltage is applied to the structure in an reverse direction. Electric field is localized in the volume of high-resistivity i-layer. In this sample negative space-charge region is built up near n-layer boundary, that determine hole type of charge transport.

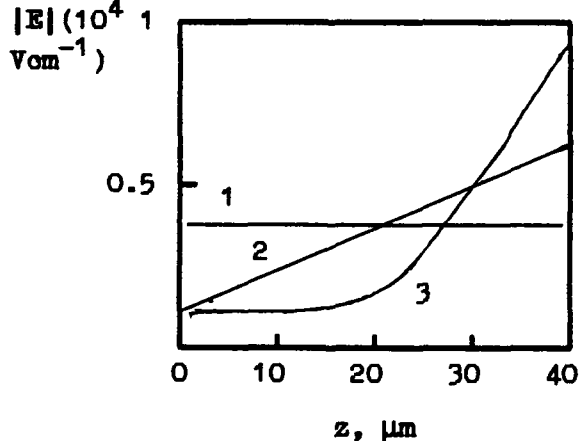


FIGURE 4

Theory. Theoretical observations show^[6,7] that all experimental results for $Bi_{12}SiO_{20}$ and ZnSe can be explained by taking into account the recharging of deep levels L1 and L2 which have different ionisation energies ($\epsilon_1 < \epsilon_2$), ionization time and trapping times ($\tau_{i1} < \tau_{i2}$, $\tau_1 \ll \tau_2$). (The theoretical analyses of experimental results for GaAs is in progress). The type of screening regime depends on the relation between τ_M , τ_{i1} , τ_{i2} and $\tau^* = \tau_{i1}\tau_{i2}/\tau_1$, where τ_M - Maxwellian time. For regime 1 at linear stage of the process ($t \ll \tau_M$) the internal field evolution is given

by:

$$\frac{E - E_0}{E_0} = \left(\frac{t l_0}{\tau_M z} \right)^{1/2} \exp(-z/l_0) I_1 \left(2 \sqrt{\frac{z t}{l_0 \tau_M}} \right).$$

Here $I_1(y)$ - is the Bessel function, $E_0 = U/d$ - applied el. field, d - sample length, $l_0 = \mu_d \tau E_0$ - free carrier drift length, μ_d - free carrier mobility, τ - their average lifetime ($\tau \ll \tau_M$). For the nonlinear stage of field screening ($t \gg \tau_M$) the numerical methods were used for the equations solution [2,3].

For regime 2 the transient process is a slow broadening of a single depletion layer with constant charge density ρ_0 . The increasing of its thickness z_0 from zero to the steady-state value W is given by

$$z_0 = W \operatorname{th}(t/\tau_0)$$

$$W = \left(\frac{2\epsilon U}{\rho_0} \right)^{1/2}; \quad \tau_0 = \frac{1}{\mu_d} \left(\frac{2\epsilon d}{\rho_0 E_0} \right)^{1/2}$$

In the course of this process the local equilibrium between the ionization and retrapping is stated. Thus boundary charge dynamics is described as the motion of an effective free electron gas with drift mobility $\mu_d = \mu \tau / \tau_i \ll \mu$, μ_d value determines the broadening velocity $v = \mu_d E_0$.

References.

1. V.N.Astratov and A.V.Ilinskii, Soviet Phys.- Solid State, v. 24, 61, (1982).
2. V.N.Astratov, A.V.Ilinskii and V.A.Kiselev, Soviet Phys.- Solid State v.26, 1720, (1984)
3. V.N.Astratov and A.V.Ilinskii, Ferroelectrics v.75, 251 (1987).
4. V.N.Astratov, A.V.Ilinskii, S.M.Repin and A.S.Furman, Soviet Phys.- Solid State, v. 32, (1990)
5. V.N.Astratov, A.V.Ilinskii and A.S.Furman, Phys. Stat. Sol.(b), v.150, 611-615 (1988).
6. V.N.Astratov, A.V.Ilinskii, and A.S.Furman, Soviet Phys.- Solid State, v.31, 1396 (1989)
7. V.N.Astratov, A.V.Ilinskii, A.S.Furman and S.M.Repin Phys. Stat. Sol.(b), v.163, 135 (1991).



Transport-induced-grating interferometry:
application to photorefractive $\text{Bi}_{12}\text{TiO}_{20}$

Ping Xia, J. P. Partanen and R. W. Hellwarth

Departments of Electrical Engineering and Physics, University of
Southern California, Los Angeles, CA, 90089-0484

We have developed a technique to measure interferometrically charge-transport-induced refractive index gratings in photoconductive insulators. All four parameters needed to describe fully the interaction between the two beams Bragg matched to the grating can be determined. We use the method to find that the complex optical polarizability of an occupied charge trap equals that of an unoccupied trap plus $(0.7 - i4.5 \pm 0.7 \pm i0.4) \times 10^{-22} \text{ cm}^3$ in photorefractive $\text{Bi}_{12}\text{TiO}_{20}$.

A spatially sinusoidal "grating" of optical intensity can produce a sinusoidal grating of occupied deep traps in photorefractive crystals. This intensity grating is essentially proportional to $\vec{E}^* \cdot \vec{E}$ where the electric field amplitude \vec{E} at the optical frequency ω equals $\hat{e}_1 \vec{E}_1 \exp(i\vec{k}_1 \cdot \vec{x}) + \hat{e}_2 \vec{E}_2 \exp(i\vec{k}_2 \cdot \vec{x})$, the superposition of two optical plane waves ($\hat{e}_1^* \cdot \hat{e}_1 = 1$, etc.). Under a wide variety of experimental conditions, a steady trap grating is produced, after sufficiently long times, that results in a change $\Delta\epsilon$ of the optical dielectric tensor of the form

$$\Delta\epsilon = m a e^{i\vec{k} \cdot \vec{x}} + m^* b e^{-i\vec{k} \cdot \vec{x}} \quad (1)$$

Here m represents the usual complex modulation index defined as

$2(\hat{e}_1 \cdot \hat{e}_2^*) E_1 E_2^* (|E_1|^2 + |E_2|^2)^{-1}$; $\vec{k} \equiv \vec{k}_1 - \vec{k}_2$. The result (1) requires that $|m| \ll 1$, so in experiments either beam 1 or 2 is made to be much weaker than the other. The small complex dielectric variations a and b are independent of optical intensity over a wide range of intensities for the mechanisms that commonly predominates; for example, charge gratings operating through the electro-optic effect¹ and optical polarizability differences of occupied and unoccupied deep traps.² It is well known that under these conditions one can

92-18738



solve for $\Delta\epsilon$ and for the weak beam amplitude $E_1(\vec{x})$ that is caused by scattering of the relative unaffected strong beam, with the amplitude E_2 , from this dielectric variation (1).

We have employed a new experimental technique that measures unambiguously the real and imaginary parts of the elements of the tensors \vec{a} and \vec{b} . Further theory can be used to interpret the results in terms of screening lengths, electrogalvanic effects, absorption gratings, etc., as we do below for a nominally undoped single crystal of optically active cubic $\text{Bi}_{12}\text{TiO}_{20}$ (grown by the Hughes Research Laboratories) which we call HRL1. Our apparatus is shown in Fig. 1. Two counterpropagating beams having identical (circular) eigenpolarizations create the steady state grating. The neutral density filter defines the weak beam ($|m| \sim 0.2$). The polarizing beamsplitter P3 deflects the transmitted weak beam to photodiode D which records its intensity I_w . Once the steady state is reached, a

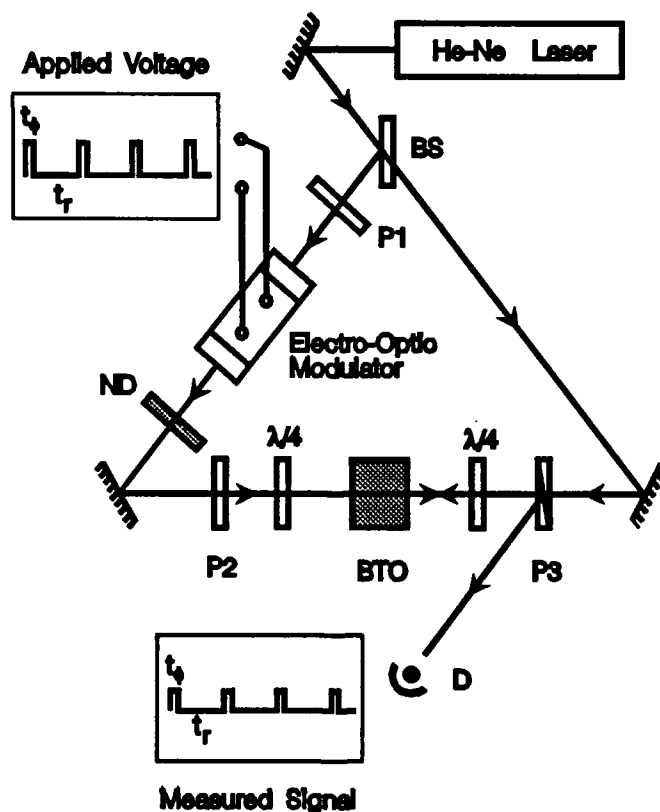


Fig. 1 Transport-induced-grating inteferometer apparatus.

constant voltage V applied to the electro-optic modulator changes the weak beam phase by φ for a time t_φ , too short for the trap grating or $\Delta \epsilon$ to change its value ($t_\varphi \approx 1000 \times t_\varphi$ in Fig. 1). Again an analytic (slowly varying envelope) solution for the transmitted intensity $I_w(\varphi)$ with this phase change can be obtained. We measure the ratio of this intensity normalized to $I_w(0)$ for zero phase shift and plot the result as in Fig. 2. The theory gives for the case that beam 1 is the weak beam

$$I_w(\varphi)/I_w(0) = |e^{i\varphi} + e^A - 1|^2 / |e^A|^2 \quad (2)$$

where

$$A = i\omega d (\hat{e}_1^* \cdot \hat{a} \cdot \hat{e}_2) (\hat{e}_1 \cdot \hat{e}_2^*) / (nc) \quad (3)$$

The refractive index of beam 1 is n and d is the thickness of the sample. With the beam roles interchanged, (1) gives the prediction (2) for experiment except that \hat{a} is replaced by \hat{b} and \hat{e}_1 and \hat{e}_2 are interchanged in the expression of (3). The four parameters (the real

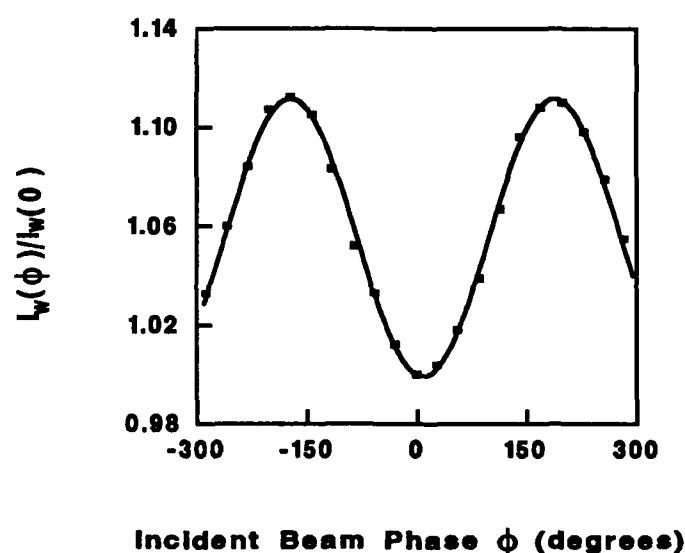


Fig 2. Transmitted probe beam intensity as a function of incident probe phase angle φ .

and imaginary parts of the tensor elements $(\hat{e}_1^* \cdot \overset{\leftrightarrow}{a} \cdot \hat{e}_2)$ and $(\hat{e}_2^* \cdot \overset{\leftrightarrow}{b} \cdot \hat{e}_1)$ fully describe the interaction between beams 1 and 2. Other polarizations and other interaction geometries can be used for other tensor elements.

The counterpropagating geometry illustrated here is used to eliminate the electro-optic contribution to $\overset{\leftrightarrow}{a}$ and $\overset{\leftrightarrow}{b}$ so that other contributions can be isolated. We expect the largest contributions to $\overset{\leftrightarrow}{a}$ and $\overset{\leftrightarrow}{b}$ to be caused by the difference α in polarizability between occupied and unoccupied trap sites and by the electrogyratory effect. In the preliminary experiments we did not observe measureable difference when the roles of weak and strong beams were interchanged indicating an insignificant contribution from the electrogyratory effect. With the help of the parameters found from Ref. 3 we can estimate an upper limit for the electrogyratory coefficient $|g_{41}| < 2.2 \times 10^{-11}$ cm/V which is slightly smaller than the upper limit given in Ref. 1 but in strong disagreement with the interpretation of Ref. 4. We estimate the polarizability difference between occupied and unoccupied trap sites to be $(0.7 - i4.5 \pm 0.7 \pm i0.4) \times 10^{-22}$ cm³. The negative value for the imaginary part of α means with the present sign convention that unoccupied traps absorb more than occupied traps.

REFERENCES

1. N. V. Kukhtarev, V. B. Markov, S. G. Odoulov, M.S. Soskin and V. L. Vinetskii, *Ferroelectrics* **22**, 949 and 961 (1979).
2. P. Xia, J. M. C. Jonathan, J. P. Partanen and R. W. Hellwarth, CLEO 1991 in Baltimore, paper CWD6.
3. J. P. Wilde, L. Hesselink, S. W. McCahon, M. B. Klein, D. Rytz and B. A. Wechsler, *J. Appl. Phys.* **67**, 2245 (1990).
4. M. S. Brodin, V. I. Volkov, N. V. Kukhtarev and A. V. Privalko, *Opt. Commun.* **76**, 21 (1990).



DETERMINATION OF THE MOBILITY AND TRANSPORT PROPERTIES OF
PHOTOCARRIERS IN BGO BY THE TIME-OF-FLIGHT TECHNIQUE

M. TAPIERO, A. ENNOURI, J.P. ZIELINGER, J.P. VOLA
IPCMS, Groupe d'Optique Non Linéaire et d'Optoélectronique
5, rue de l' Université 67000-STRASBOURG, FRANCE (Tel: 88358000)

J.Y. MOISAN

CNET LANNION B OCM/TAC BP 40, 22301 LANNION. FRANCE

J.C. LAUNAY

Laboratoire de Chimie du Solide du CNRS
351 Cours de la Libération , 33405-TALENCE, FRANCE

Sillenites are potentially a promising class of photorefractive materials for specific applications provided that crystals, insuring the corresponding optimal and reproducible operating characteristics, could be prepared. The first step in this direction is to measure and to check the reproducibility of the involved properties of the as-grown material obtained by the usual Czochralski technique which in fact works under relatively well defined conditions. In this respect, the determination of the mobility of photocarriers (electrons in BGO) and the knowledge of the mechanism of charge transport are of fundamental importance.

Values for the mobility, mostly in BSO, ranging from 10^{-6} to a few $\text{cm}^2 \cdot \text{V}^{-1} \cdot \text{s}^{-1}$ have been reported (1)(2)(3)(4). Mobilities between 10^{-2} and $1 \text{ cm}^2 \cdot \text{V}^{-1} \cdot \text{s}^{-1}$ usually indicate trap-limited band motion whereas lower values are more likely characteristic of multiple-trapping or hopping (5). This large scattering of the results can be attributed to the various measuring techniques used (steady-state or transient photoconductivity, holographic determination...etc) but it may also be due to a possible variable degree of disorder in the investigated samples. Indeed it is well known that the microscopic mobility μ_0 of free charge carriers is a very sensitive probe of the crystalline quality and chemical purity of the material. In addition the actually measured macroscopic drift mobility μ_d is reduced from μ_0 by a factor taking into account the proportion of time spent in traps especially under steady state conditions (5). This last difficulty may however be avoided by using a suitable transient measuring technique.

The classical time-of-flight (TOF) technique that we used offers the necessary experimental flexibility to access directly the true mobility of photoelectrons in BGO. A sheet of electron-hole pairs is formed close to the front surface of a wafer of thickness L (0.2 - 1 mm) on which a semi-transparent Pt contact had been deposited. A 20 ns duration N_2 -laser pulse (337 nm) is used to this purpose. When a negative voltage V is applied across the specimen, a certain amount of photoelectrons are extracted from the irradiated region (IR) and drift through the non irradiated region (NIR) inducing a transient signal in a 50Ω load resistor connected to the Pt contact on the rear surface. The measuring system comprises a fast storage oscilloscope from which the recorded data are transferred to a computer for further numerical processing.

92-18739



A general observation is that the amplitude and shape of the TOF signal are very sensitive to the optical history of the sample prior to the application of the laser pulse, but an experimental procedure could be worked out which allows us to get reproducible transients and a correct determination of the drift mobility as well as of different characteristic time constants.

A measurable and usable signal can only be obtained when the sample is permanently illuminated by an additional white or monochromatic source (intensity I_s), the intensity of the laser pulse is kept sufficiently small and the repetition period ΔT of the pulse is not too short (typically a few seconds). If ΔT is fixed (or more generally $\Delta T \cdot I_s = K = \text{constant}$) a remarkably reproducible current transient is observed. As a rule if K is increased, the signal is multiplied by a fairly time independent gain factor which tends to an upper limit for high values of K .

The shape of the decay depends on the wavelength λ_s of the additional illumination.

a) For $\lambda_s < 550$ nm a clear break is observed at a time $t = t_f$. Depending on the values of L and V , the initial portion of the curve $I(t)$ may be either a constant

$$I(t) = \frac{Q}{t_f} \quad \text{for} \quad t \leq t_f \quad (1)$$

or a slowly decreasing exponential function (Fig. 1)

$$I(t) = \frac{Q}{t_f} \exp \left(- \frac{t}{\tau_c} \right) \quad (2)$$

where Q represents the charge injected in the NIR

For $t > t_f$ the decay becomes steeper but is still fairly exponential. The corresponding time constant τ_f is typically $90 \mu s$

The most important point however is that t_f does not depend on K , but varies as $1/V$ and L^2 . Consequently t_f is the mean transit time of electrons across the specimen. Depending on the sample values for μ_d in the range 0.3 to $1 \text{ cm}^2 \cdot V^{-1} \cdot s^{-1}$ (± 0.02) were found.

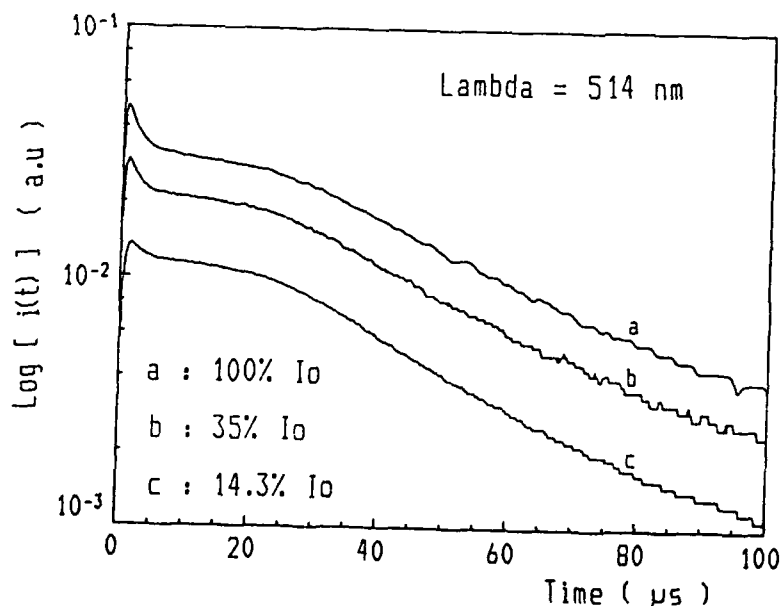


Figure 1.

Semilogarithmic plot of the TOF signal : sample illuminated at 514 nm with three different intensities

b) For $\lambda_s > 550$ nm a completely different shape is observed (Fig.2) : the decay can now be fitted to a single exponential. The time constant τ_c is typically 70 μ s. Under these conditions, the transit time cannot be determined.

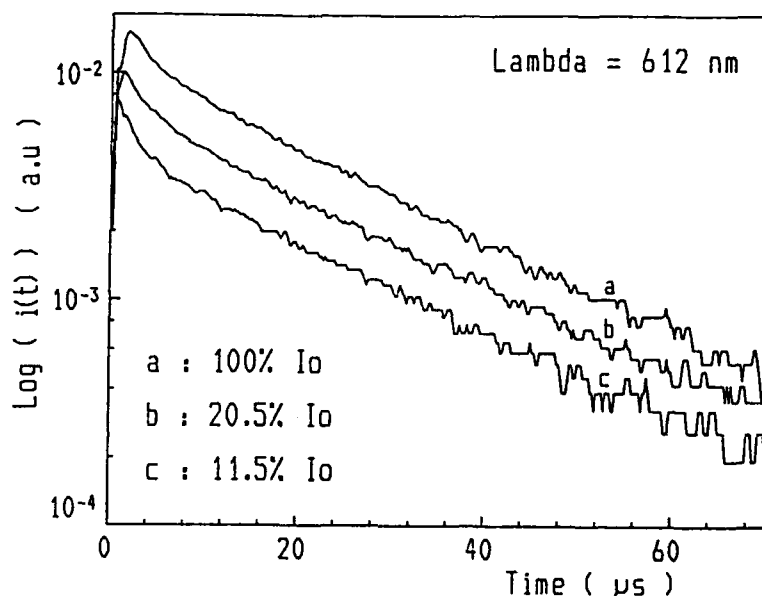


Figure 2.

Semilogarithmic plot of the TOF signal : sample illuminated at 612 nm with three different intensities

The relatively large value of μ_d and the characteristic shape of the current transient allow us to rule out (at least in undoped BGO) a dispersif charge transport mechanism i.e. hopping and multiple trapping. The most likely process is a one trapping-center limited band motion. Indeed, elementary theory of such a model predicts transients of the observed form.

The different actions of short and long wavelengths additional illuminations on the shape of the transient can be clearly correlated with charge transfer between absorption centers (A) and deep traps (B) involved in photorefractivity. Indeed, there is a striking similarity between these effects and the corresponding observations in photorefractivity, photoconductivity and optical absorption (6).

Assuming that photorefractive sites also play a key role in TOF measurements, a very simple and coherent explanation can be proposed for all the described effects. On the other hand K and λ_s are the determining experimental factors.

1) If K is small compared to the integrated number N_{uv} of UV photons, a stable space charge field rapidly builds up (positive A centers in the IR, trapped electrons near the boundary between the IR and NIR) which prevents further electron penetration into the NIR ($Q=0$ in equations 1 and 2).

2) When the sample is illuminated with photons of $\lambda_s < 550$ nm, a certain amount of B traps will be permanently and uniformly occupied in the bulk. The space charge field is reduced and consequently more electrons can enter the NIR and move across the wafer without being captured. Since L is large compared to the depth of the IR, the electrical field in the NIR remains unaffected when a more or less important space charge is built up near the front surface. This explains why the transit time does

not depend on K (Fig.1). So the amplitude of the TOF signal is determined solely by the injected charge Q (equations 1 and 2). The origin of the exponential decay for $t > \tau_1$ is yet not quite clear but it probably corresponds to the thermal release of carriers from a shallow trap.

3) Previous work (6) has shown that photons of $\lambda > 550$ nm excite electrons from B levels (previously filled by short wavelength excitation) to the conduction band from where they return to unoccupied A sites. The main action of the additional illumination is to neutralize the space charge during the waiting time ΔT of the laser. Thus appreciable charge can enter the NIR when the laser pulse is applied, but the totality of the electrons are retained in the B centers. The transient can be described by equation (2); τ_c can be considered as the mean free drift time or trapping time which can be expressed as

$$\tau_c = 1 / N_B * S_B * v \quad (3)$$

where N_B is the concentration of traps, S_B the thermal capture cross section and v the thermal velocity. N_B is known to be of the order of a few 10^{15} cm^{-3} . Knowing $\tau_c = 70 \text{ } \mu\text{s}$, S_B can be estimated to about 10^{-18} cm^2 .

In conclusion, the drift mobility can be measured by the classical TOF method in presence of a bias short wavelength illumination (e.g. 514 nm) generating a high enough concentration of free photocarriers in order to prevent the formation of a space charge (in a photorefractive material this effect is particularly important) and to keep filled the active deep traps. These conditions insure a quasi-unhindered migration of the injected extra carriers. Consequently we believe that the measured mobility, which is of the order of $1 \text{ cm}^2 \cdot \text{V}^{-1} \cdot \text{s}^{-1}$ in undoped BGO, is the microscopic mobility. This value is in agreement with the expected one (3).

This work is partially supported by CNET LAB/OCM/TAC under contract number 89 8B 078 00 790 92 45.

REFERENCES.

- (1) S.L. HOU, R.B. LAUER and R.E. ALDRICH
J.Appl.Phys. 44, 2652 (1973)
- (2) B.Kh. KOSTYUK, A. Yu KUDZIN and G.Kh. SOKOLYANSKII
Sov.Phys.Sol.State, 22, 1429 (1980)
- (3) R. OBERSCHMID, Ph.D. Thesis, Technical University, München, 1981
- (4) G. PAULIAT, A. VILLING, J.C. LAUNAY and G. ROOSEN
J. Opt.Soc.Am. B, 7, 1481 (1990)
- (5) J.M. MARSHALL
Rep.Prog.Phys., 46, 1235-1282 (1983)
- (6) M. TAPIERO, J.G. GIES, N. BENJELLOUN, J.C. LAUNAY and J.P. ZIELINGER,
Topical Meeting on Photorefractive Materials, Effects and Devices, Technical Digest, January 17-19, (1990), Aussois (FRANCE)



Conduction band and trap limited mobilities in $\text{Bi}_{12}\text{SiO}_{20}$

P. Nouchi, J. P. Partanen and R. W. Hellwarth

Departments of Electrical Engineering and Physics,
University of Southern California, Los Angeles, CA, 90089-0484

The mobility of photoexcited charge carriers in photorefractive insulators can be measured with a holographic time-of-flight technique.¹ By illuminating the crystal with two interfering 30 ps laser pulses at the wavelength of 532 nm, we create an instantaneous sinusoidal pattern of photoexcited charge carriers. A strong electric field E_0 is applied across the crystal causing the sinusoidal pattern of charge carriers to drift with a velocity μE_0 , where μ is the mobility. With a proper choice of the interference fringe spacing Λ , the superposition of this drifting charge pattern on the complementary pattern of photo-ionized traps creates an observable oscillating space charge field. We probe this oscillation by diffracting a weak cw He-Ne beam from the refractive index grating that is created via the electro-optic effect. The period P_t of the observed oscillation is the time required for photoexcited charge carriers to drift over one spatial period Λ . A time-of-flight mobility μ can therefore be simply determined using the equation

$$\mu = \frac{\Lambda}{P_t E_0} \quad (1)$$

We applied this technique to measure the mobility of photoexcited electrons in a $\text{Bi}_{12}\text{SiO}_{20}$ (BSO) sample.¹ A typical observed diffraction efficiency curve is shown in Fig. 1. It gives a mobility value $\mu = 0.24 \text{ cm}^2/(\text{Vs})$ with a 30 % error margin due to the uncertainty in E_0 . We also measured the mobility as a function of temperature in the same sample. We observed the temperature dependence to be of the Arrhenius form: $\mu \sim \exp(-E_a/k_B T)$ where $k_B T$ is the thermal energy and E_a is the activation energy. We determined E_a to be $320 \pm 40 \text{ meV}$.² The observed temperature dependence suggests that we are measuring a trap-limited mobility μ_t (controlled by the thermal excitation from shallow traps of depth E_a) rather than the conduction band mobility μ_c . For a simple shallow-trap model, the two mobilities are related by the expression

92-18740



$$\mu_t = \frac{\tau_s}{\tau_s + \tau_r} \mu_c, \quad (2)$$

where τ_s is the recombination time to the shallow traps and τ_r is the average time before release from a trap.

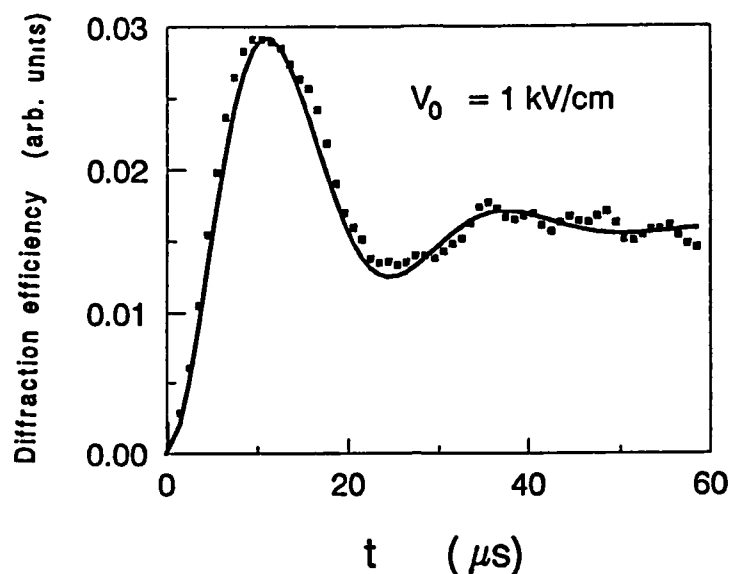


FIG. 1. Typical time development of the diffraction efficiency. The solid curve is the best fit of Equ. (3) to the data, with $\Gamma' = 8.6 \times 10^4 \text{ s}^{-1}$ and $\Gamma' = 2.42 \times 10^5 \text{ s}^{-1}$ (see Ref. 1).

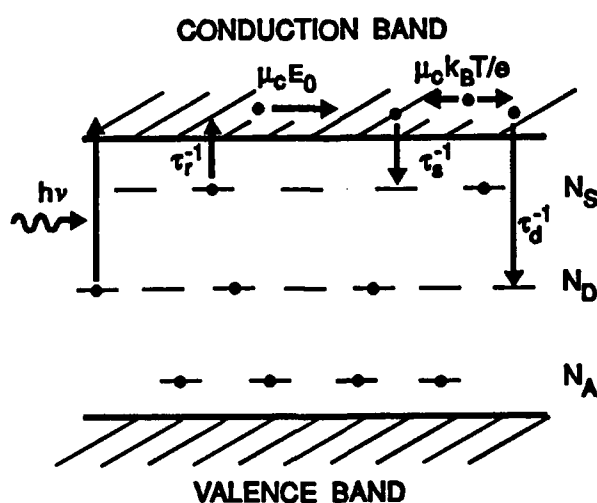


FIG. 2. Schematic diagram of the processes included in the shallow-trap model.

We have developed a shallow-trap model to describe the grating efficiency in time. As illustrated in Fig. 2, in addition to the usual photorefractive sites, the model includes thermally excitable shallow traps of constant depth. Excited electrons are free to move by drift or diffusion in the conduction band before recombining to both shallow and deep trap levels. The material equations are the same as in Ref. 3 with an additional rate equation for the shallow traps and the corresponding change in the continuity equation. We have found an analytic solution for the amplitude of the space charge field in the case of an instantaneous sinusoidal excitation in the limit of small modulation and low excitation. The space charge field amplitude E_1 has two components which both approach exponentially their steady state values. With our experimental conditions only one of the two components is significant, resulting in the following time dependence for the diffraction efficiency I_d :

$$I_d \sim |1 - e^{-\Gamma t}|^2 \quad (3)$$

where

$$\Gamma = \Gamma' + i\Gamma'' = \frac{\tau_r}{\tau_s \tau_d} + k^2 \mu_t \frac{k_B T}{e} + \tau_r (k \mu_t E_0)^2 - i(k \mu_t E_0) \quad (4)$$

Here $1/\tau_d$ is the recombination rate from the conduction band to the deep trap levels and $k = 2\pi/\Lambda$. We see from (4) that the imaginary part Γ'' is a direct measure of trap limited mobility μ_t as explained in the description of the experimental method. The real part Γ' has a quadratic dependence on E_0 . If we plot our measured values of Γ' as a function of Γ'' and fit the points with a constant and a second order term (Fig. 3) the coefficient for the second order term is τ_r . From this, we find $\tau_r = 800 \pm 50$ ns. With our earlier photocurrent measurements³ which gave $\tau_s = 26$ ns, we obtain from (2) the conduction band mobility value $\mu_c = 7 \pm 3$ cm²/(Vs). The large uncertainty reflects experimental difficulties in reaching the low-intensity limit. This value is consistent with the lower-limit of 2 cm²/(Vs) which we got directly from photocurrent measurements,³ and also with the lower limit 3.24 cm²/(Vs) inferred from photocurrent measurements by Le Saux, *et al.*⁴ We are presently preparing to measure μ_c directly in a time-of-flight experiment.

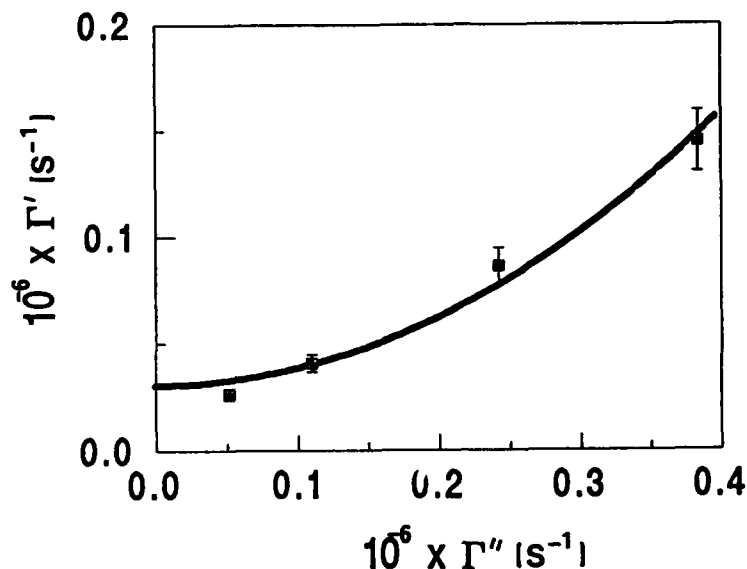


FIG. 3. Γ' versus Γ'' as determined by fitting Eq. (3) to four experimental curves such as shown in Fig. 1. The solid curve is a best fit to the data with the second order term equal to 804 ns.

REFERENCES

- ¹J. P. Partanen, J. M. C. Jonathan and R. W. Hellwarth, Appl. Phys. Lett. 57, 2404 (1990).
- ²P. Nouchi, J. P. Partanen and R. W. Hellwarth, CLEO 1991 in Baltimore, paper CWD4.
- ³J. P. Partanen, P. Nouchi, J. M. C. Jonathan and R. W. Hellwarth, submitted to Phys. Rev. B, 1990.
- ⁴G. Le Saux and A. Brun, IEEE J. Quantum Electron. QE-23, 1680 (1987).

AD-P006 753



Breaking of the electrooptic and dielectric tensor symmetries by space charge electric fields.

G. Pauliat, P. Mathey, G. Roosen

Institut d'Optique Théorique et Appliquée,

Unité Associée au Centre National de la Recherche Scientifique,

Centre Scientifique d'Orsay,

Bât. 503, B.P. 147, 91403 ORSAY Cedex, FRANCE.

Tel. (33) 1 69 41 68 31

Fax (33) 1 69 41 31 92

Introduction

The space charge electric field associated with a photorefractive grating generates deformations (through piezoelectricity) which in turn, modify both the electrooptic and dielectric constants. These modifications are of importance and must be taken into account¹. For instance, in BaTiO₃ samples the dielectric constant ϵ_{11} , determined using spatially uniform applied electric fields, varies by a factor of two between clamped and unclamped crystals. Hereafter, we demonstrate that these differences are even more important for space charge electric fields because these non uniform fields induce strain components which are not produced by uniform fields. Therefore, the effective electrooptic coefficient can be different from zero in a configuration in which both the clamped and unclamped coefficients for uniform fields vanish.

Analysis of the induced deformation

Because of piezoelectricity, the space charge electric field \underline{E} inside the sample modifies the stress $\underline{\sigma}$ and the strain $\underline{\delta}$. With Einstein summation convention, we have²:

$$\sigma_{ij} = c_{ijkl} \delta_{kl} - e_{kij} E_k \quad (1)$$

where δ_{ij} , σ_{ij} , c_{ijkl} , e_{ijk} , E_i are the components of the strain, stress, rigidity and piezoelectric tensors and of the electric field.

The influence of the induced deformation on the electric displacement \underline{D} (whose components are D_i) and on the change $\Delta\eta_{ij}$ of the impermeability tensor are given by:

$$D_i = e_{ijk} \delta_{jk} + \epsilon_o \epsilon_{ij}^{\delta=0} E_j \quad (2)$$

$$\Delta\eta_{ij} = r_{ijk}^{\delta=0} E_k + p_{ijkl}^{E=0} \delta_{kl} \quad (3)$$

92-18741



where $r_{ijk}^{\delta=0}$ are the components of the totally clamped electrooptic tensor, $p_{ijkl}^{E=0}$ are the components of the elastooptic tensor, $\varepsilon_{ij}^{\delta=0}$ are the components of the relative static dielectric tensor for strain free crystal and ε_0 is the free space permittivity.

It should be noted that these equations (1-3) are valid for both uniform or spatially modulated electric fields. However, they are not sufficient and must be completed in order to determine the electrooptic and dielectric coefficients. For instance, for uniform fields, the boundary conditions on the sample faces (clamped or unclamped conditions) must be known.

We will now, solve the set of equations (1-3) for non uniform fields like the space charge field gratings associated with the photorefractive effect.

To complete equations (1-3), we use the first principle of dynamics. If the sample is at equilibrium, the forces due to stress vanish³:

$$F_i = \frac{\partial \sigma_{ij}}{\partial x_j} = 0 \quad (4)$$

The boundary conditions fix the values of the σ_{ij} on the crystal faces but not inside the sample. To determine these values everywhere, we can remark that for most photorefractive experiments, the fringe spacing of the induced grating is much smaller than the dimensions of the crystal. We thus restrict our analysis to quasi infinite crystal. The grating wave vector (which is parallel to the electric field) is an axis of symmetry for the induced deformation. Therefore we conduct the calculation in a set of axes where the first axis x' is parallel to the electric field. All the components in this new set of axes are denoted by a prime. The space derivatives with respect to y' and z' vanish and Eq. (4) reduces to:

$$\frac{\partial \sigma_{x'x'}}{\partial x'} = 0 \quad (5)$$

Therefore the spatially modulated part of $\sigma_{x'x'}$, which is induced by the space charge field grating, equals zero. From Eq. (1), one immediately finds that there is a single non zero strain component: $\delta_{x'x'}$. This result is similar to previous derivations for acoustic waves or entropy fluctuations in bulk materials⁴. We get:

$$\begin{cases} \delta_{x'x'} = \frac{e_{x'x'x'}}{c_{x'x'x'x'}} E \\ \delta_{x'y'} = \delta_{x'z'} = \delta_{y'z'} = \delta_{y'y'} = \delta_{z'z'} = 0 \end{cases} \quad (6)$$

where E denotes the modulus of the applied field \underline{E} .

If the a_i are the direction cosines of the electric field \underline{E} in the crystallographic axes, then $\delta_{x'x'}$ is expressed as a function of the piezoelectric and rigidity tensor components given in those axes:

$$\delta_{x'x'} = HE \quad (7)$$

with

$$H = \frac{\sum_{i,j,k=1}^3 a_i a_j a_k e_{ijk}}{\sum_{l,m,n,o=1}^3 a_l a_m a_n a_o c_{lmno}} \quad (8)$$

The strain components can also be expressed in the crystallographic axes:

$$\delta_{ij} = a_i a_j H E \quad (9)$$

Eq. (9) demonstrates that a photorefractive grating can generate strain components which can not be induced by a uniform electric field (and conversely). For instance, for cubic crystals and according to Eq. (1) a spatially uniform electric field along the [111] crystallographic direction can only induce shear deformations ($\delta_{ij} \neq 0$ if $i \neq j$ only). However, if the field is spatially modulated then, all the strain components are equal and differ from zero (Eq. (9)).

We may thus consider that the piezoelectric tensor symmetry (and therefore the dielectric and electrooptic tensor symmetries) is modified in presence of an electric field grating.

Determination of the photorefractive dielectric and electrooptic constants

Expressions for the photorefractive dielectric $\underline{\underline{\epsilon}}^{pr}$ and electrooptic $\underline{\underline{r}}^{pr}$ tensors are derived inserting Eq (9) for δ_{ij} in equations (2) and (3). However, the expressions we thus obtain are misleading because $\underline{\underline{\epsilon}}^{pr}$ and $\underline{\underline{r}}^{pr}$ directly depend on the electric field through its direction cosines (coefficient H). Therefore, we prefer to define an effective photorefractive dielectric constant ϵ_{eff}^{pr} and an effective photorefractive electrooptic constant r_{eff}^{pr} .

Poisson's law that links the modulated electric charge grating to the electric field displacement is used to define ϵ_{eff}^{pr} :

$$\text{div}(\underline{\underline{\epsilon}}^{pr} \underline{E}) = \epsilon_{eff}^{pr} \text{div} \underline{E} \quad (10)$$

so that we immediately get:

$$\epsilon_{eff}^{pr} = a_i \left(\epsilon_{ij}^{\delta=0} + e_{ikj} a_k \frac{H}{\epsilon_o} \right) a_j \quad (11)$$

We used the usual definition for the effective photorefractive electrooptique coefficient which is obtained from the expression of the coupling strength between two optical beams whose polarization vector components are v_i and w_j :

$$r_{eff}^{pr} = v_i^* \frac{n_i^2 n_j^2 \Delta \eta_{ij}}{E} w_j \quad (12)$$

with n_i^2 the square of the refractive indices.

From this definition (12) we get:

$$r_{eff}^{pr} = v_i^* \left(r_{ijk}^{\delta=0} + p_{ijkl} a_l H \right) a_k w_j n_i^2 n_j^2 \quad (13)$$

Equations (11) and (13) show that the valid constants to describe the photorefractive effect are neither the clamped nor the unclamped ones. According to Eq. (5), the crystal must indeed be always considered as internally unclamped along the field axis x' whatever the applied external forces are. Conversely the other stress components may be different from zero. One should point out the fact that the breaking of the crystal symmetry by the spatially modulated field allows a non zero r_{eff}^{pr} coefficient (Eq. (13)) in a configuration (given field direction and optical beam polarizations) where a uniform field would not induce any index change. For example, for crystal belonging to the point group symmetry $\bar{4}3m$, a modulated field grating along the $[111]$ crystallographic direction induces an isotropic coupling between two optical waves polarized along one crystallographic axis. Such an isotropic coupling in these materials is forbidden by the usual symmetry of the electro-optic tensor ($r_{ijk}^{\delta=0} = 0$ if $i = j$).

Conclusion

In the presence of a uniform electric field the dielectric and electrooptic constants depend on externally applied forces. However, those to be used for a spatially modulated field are independent of external forces. Therefore, to describe the photorefractive effect in the presence of an externally applied voltage, quite different values must be used for both the dielectric and electro-optic constants: the first ones for the uniform part of the field and the others for its modulated component. Experimental evidence of this phenomenon will be given at the conference.

References

- 1_ " Photoelastic contribution to the photorefractive effect in cubic crystals."
S.I. Stepanov, S.M. Shandarov and N.D. Khat'kov.
Sov. Phys. Solid State 29, 1754 (1987).
- 2_ " Physical properties of crystals"
J.F. Nye.
The Clarendon Press, Oxford (1957).
- 3_ " Théorie de l'élasticité."
Landau, Lifchitz.
Ed. Mir Moscow (1967).
- 4_ " A note on the polarization of light scattered from entropy and LA fluctuations in solids"
D.W. Pohl.
Solid State Comm. 23, 447 (1977).



INFLUENCE OF PIEZOELECTRIC AND PHOTOELASTIC EFFECTS ON PULSE HOLOGRAM RECORDING IN PHOTOREFRACTIVE CRYSTALS

R. Litvinov, S. Shandarov

Institute of Automatic Control Systems and Radioelectronics
40 Lenin av., Tomsk 634050, USSR

In paper¹ the effective recording of hologram gratings in photorefractive crystals by short light pulses was studied experimentally. The self-diffraction theory of light pulses for the time of Maxwell's relaxation τ_m which was negligible compared with the pulse duration τ_u was investigated by Kuchtarev and Semenetz². Here we did not take into account the influence of piezoelectric and photoelastic effects that might have a strong influence on hologram recording and restoration³. The results of the analysis of hologram grating pulse recording in photorefractive crystals accounting for piezoelectric and photoelastic effects for $\tau_u \ll \tau_m$.

A hologram grating was assumed to be formed in boundless medium by two interfering light pulses of the same frequency ω with the wave vectors \vec{k}_1 and \vec{k}_2 . We neglected the photogalvanic effect and self-diffraction and considered the intensity of the light field to have the rectangular time envelop

$$I(\vec{r}, t) = I_0(1 + m \cos \vec{k} \cdot \vec{r}) \cdot [\theta(t) - \theta(t - \tau_u)], \quad (1)$$

where I_0 is the mean light intensity; m is the depth of modulation; $\vec{k} = \vec{k}_1 - \vec{k}_2$; $\theta(t)$ is Heaviside step.

While analyzing we used the system of equations from paper¹ generalized for anisotropic media in the case when the spatial dependence of all functions was defined by the coordinate η along the grating vector \vec{k} .

$$\rho_0 \frac{\partial^2 U_i}{\partial t^2} = C_{ik} \frac{\partial^2 U_k}{\partial \eta^2} - e_i \frac{\partial E}{\partial \eta}, \quad (2)$$

$$e \frac{\partial E}{\partial t} + \frac{\partial^2 U_i}{\partial \eta^2} = Q, \quad (3)$$

$$\delta_k = e \mu_{ki} m_i N E - e D_{ki} m_i \frac{\partial N}{\partial \eta}, \quad (4)$$

$$\frac{\partial Q}{\partial t} + \frac{\partial \delta_k}{\partial \eta} = 0, \quad (5)$$

$$\frac{\partial N}{\partial t} = \frac{\beta \alpha I}{h \omega} - \frac{N}{\tau_r} - \frac{m_k}{e} \frac{\partial \delta_k}{\partial \eta}, \quad (6)$$

where U_i , δ_k are vector components of the elastic displacement and electric current density, respectively; E is a vector module of the electric intensity; Q is a volume charge density; N is a concentration of non-equilibrium charge carriers; ρ_0 is a substance density; τ_r is a recombination time; $C_{ik} = C_{ikl} m_l$,

92-18742



$e_{ij}' = e_{mij} m_m m_j$, $\epsilon' = \epsilon_{mn} m_m m_n$; C_{ijkl} , e_{mij} , ϵ_{mn} , μ_{ki} , D_{ki} are tensor components of elasticity modyles, piezoelectric factors, dielectric permittivity, mobility, diffusion coefficient; m_k are guide cosines of the vector $\vec{m} = \vec{k}/|\vec{k}|$; α is an absorption coefficient; β is a quantum efficiency.

Neglecting the conduction currents that is true for an initial section of recording at $\tau_m \gg \tau_u$, we may obtain the following equations for the complex amplitudes $U_i(t)$ and $E(t)$ of the first spatial harmonics of the induced elastic and electric fields

$$\rho_0 \frac{\partial^2 U_i^m}{\partial t^2} + k^z P_{ik} U_k^m = \frac{e e_i' k^z}{\epsilon'} \int_0^t N^m(t') dt', \quad (7)$$

$$E^m = \frac{ik}{\epsilon'} \left[e D' \int_0^t N^m(t') dt' - e' U_k^m \right], \quad (8)$$

where $P_{ik} = C_{ik} + e_i' e_k'$; $D' = D_{ik} m_i m_k$.

The right sides of Eq.(7) and (8) are determined by the amplitude of the first spatial harmonic N in the distribution of the non-equilibrium charge carriers that may be represented in the form

$$N^m(t) = 2 \frac{\beta \alpha m I_0}{h \omega} \tau_N \left\{ \theta(t) \left[1 - \exp\left(-\frac{t}{\tau_N}\right) \right] - \theta(t - \tau_u) \left[1 - \exp\left(-\frac{t - \tau_u}{\tau_N}\right) \right] \right\}, \quad (9)$$

where $\tau_N^{-1} = \tau_r^{-1} + D' k^z$.

Using proper solution of equation of piezoacoustics for waves the propagation direction of which is given by the grating vector \vec{k} , the solution of Eq.(7) may be found in the form

$$U_a^m = 2 F p_i^a e_i' C_a^{-1} \left\{ \theta(t) [f_a(t) - A_a \sin(\omega_a t - \varphi_a)] - \theta(t - \tau_u) [f_a(t - \tau_u) - A_a \sin(\omega_a(t - \tau_u) - \varphi_a)] \right\}, \quad (10)$$

where $F = [e L_D \beta \alpha m I_0 \tau_N] / [\epsilon' (1 + k^z L_D^z) h \omega]$; $L_D = D' \tau_r$; p_i^a are guid cosines of the unit vectors \vec{p}^a ($\alpha = 1, 2, 3$) of proper elastic

waves; $C_a = \rho v_a^2$; $\omega_a = k v_a$; $A_a = [\omega_a \sqrt{1 + \omega_a^2 \tau_N^2}]^{-1}$; $\varphi_a = \arctg(\omega_a \tau_N)$; v_a are phase velocities of proper elastic waves; $f_a(t) = (t/\tau_N) - 1 + [\omega_a^2 \tau_N^2 \exp(-t/\tau_N)] / [1 + \omega_a^2 \tau_N^2]$.

Eq. (10) is a superposition of a stationary wave, it depends on the time of the elastic field. Let us consider below the case when $\omega_a \tau_N \gg 1$ that is true for $\text{Bi}_{12}\text{SiO}_{20}$ crystals. We do not take into account the influence of the acoustic wave with a negligible amplitude A_a . Accounting for the correlation (10) from Eq.(8) we obtain the expression for intensity of the induced electric field

$$E^m = 2ikF [\theta(t) f^E(t) - \theta(t - \tau_u) f^E(t - \tau_u)], \quad (11)$$

where $f^E(t) = [1 - \sum_{\alpha=1}^3 K_\alpha^z] \left[\frac{t}{\tau_N} - 1 \right] + [1 - \sum_{\alpha=1}^3 K_\alpha^z \frac{\omega_a^z \tau_N^z}{1 + \omega_a^z \tau_N^z}] \exp(-t/\tau_N)$; $K_\alpha^z = \frac{(p_i^a e_i')^z}{C_a \epsilon'}$.

The found expressions (10) and (11) allow us to define the tensor perturbations of dielectric impermeability of the crystal Δb_{mn} by the induced field accounting for piezoelectric and pho-

toelastic effects

$$\Delta b_{mn} = ikF(B_{mn}\exp(ik\eta) + \text{c.c.}) \quad (12)$$

where $B_{mn} = B_{mn}^E + B_{mn}^U$; $B_{mn}^E = r_{mnk} m_k [\theta(t)f^E(t) - \theta(t-\tau_u)f^E(t-\tau_u)]$; r_{mnk} , p_{mnkl} are components of the electrooptic and photoelastic tensors, respectively.

The calculated results of kinetics of increasing values B_{mn} for the vector \vec{k} orientation in the plane (110) of $\text{Bi}_{12}\text{SiO}_{20}$ crystal are represented in Fig.1,2,3,4 (curves 1,3). Here there is also noted the value B_{mn}^0 calculated without photoelastic and piezoelectric effects (curve 2). In calculations we used the values of the parameters $\mu' = 2.9 \cdot 10^{-10} \text{ m}^2/(\text{V}\cdot\text{s})$, $\mu'\tau_r = 10^{-11} \text{ m/V}$, $\epsilon' = 56$ and indicated in τ_u values of the remain material constants $\text{Bi}_{12}\text{SiO}_{20}$. The period of hologram grating is equal to $\Lambda = 5 \mu\text{m}$, the the lenght of recording light pulses is about $\tau_u = 20 \text{ ns}$.

At the initial section of the recording the increasing of the components B_{mn} , B_{mn}^0 is due to the square law (see Fig.1,3). The time of the grating output to the steady level is much more the recording pulse duration (see Fig.2,4) and it is defined by the constant τ_N .

The contribution of piezoelectric and photoelastic effects to the non-diagonal components Δb_{mn} at the orientation $\vec{k} \parallel [110]$ (see Fig.1,2) and $\vec{k} \parallel [111]$ (see Fig.3,4) is less the order than defined by the electrooptic effect and weakly decreases the absolute value Δb_{mn} (compare curves 1 and 2).

For orientation $\vec{k} \parallel [111]$ (see Fig.3,4), all diagonal components by the module are equal ($|B_{11}| = |B_{22}| = |B_{33}|$), and they are determined by the photoelastic addition B_{mm}^0 (curve 3) that has similar order as a value $B_{23}^0 = |B_{13}^0|$ defined by the electrooptic effect.

The performed calculation show the necessity of taking into account the additional contribution of the photoelastic and piezoelectric effect to the perturbations of the tensor of dielectric impermeability Δb_{mn} while hologram recording by short light pulses.

References

1. J.M.C. Jonathan, G. Roosen, Ph. Poussignol, Optics Letters, 13,224 1988.
2. N. Kuhtarev, T. Semenetz, Ukr. Fiz. Zh., 35(4), 538 1990.
3. V. Deev, P. Pyatakov, Zh. of Tech. Fiz., 56(10), 1909 1986
4. M.P. Petrov, S.I. Stepanov, A.V. Khomenko, Photosensitive electrooptic media in holography and optical information processing, Nauka, Lenigrad, 1983.
5. V. Shepelevich, S. Shandarov, A. Mandel, Ferroelectrics, 110, 235 1990.

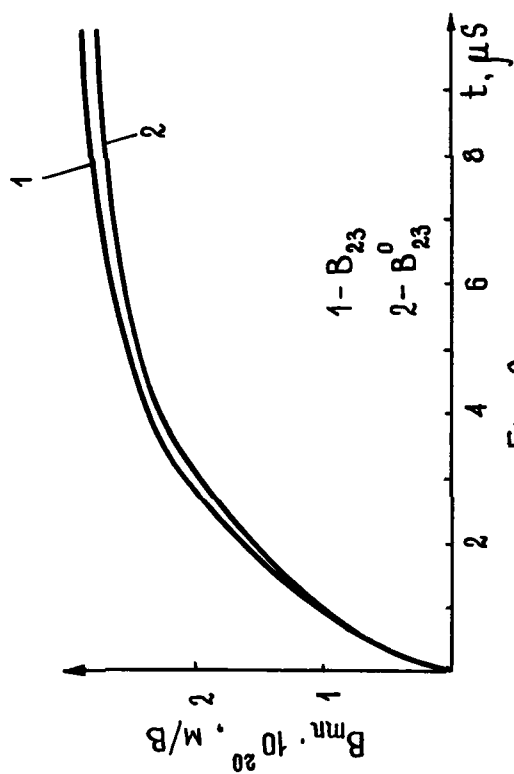


Fig. 2.

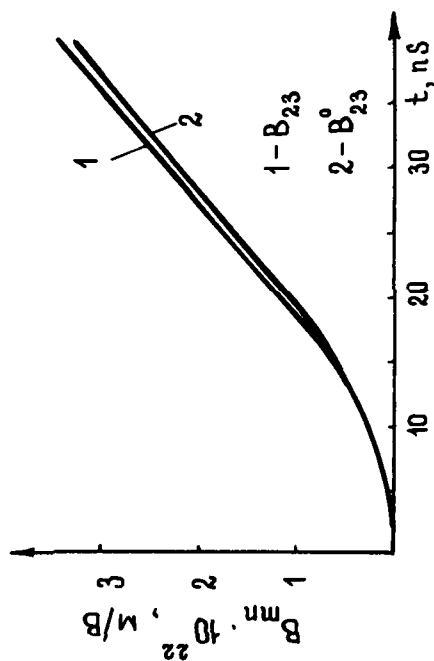
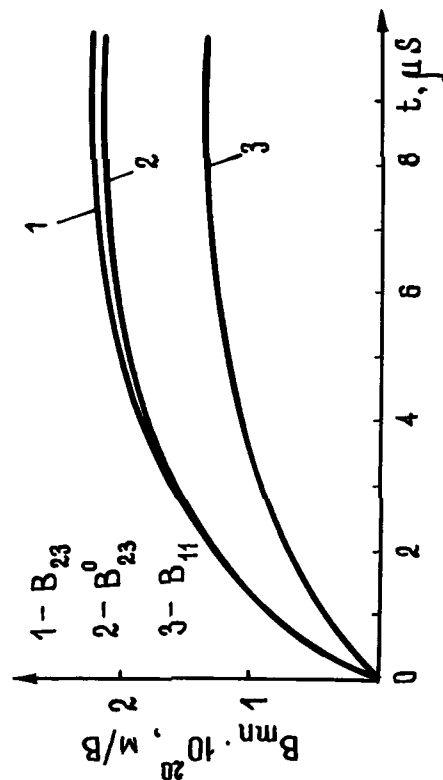


Fig. 1.

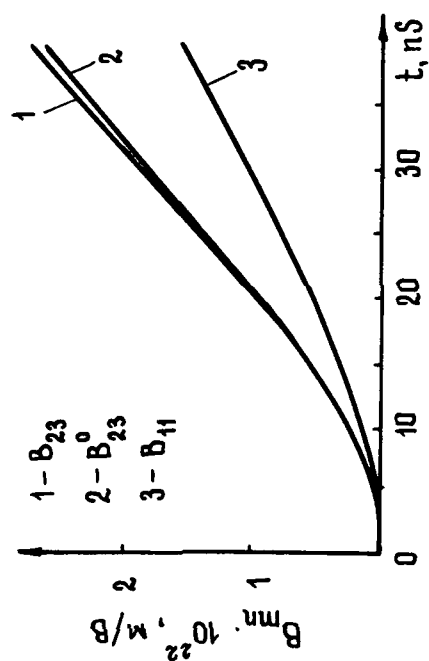


Fig. 3.



Elasto-optic and roto-optic contribution to the photorefractive effect

M. Zgonik* and P. Günter

Institute of Quantum Electronics, Swiss Federal Institute of Technology,

ETH Hönggerberg, CH-8093 Zürich, Switzerland

phone 41-1-377 2332, fax 41-1-371 5989

**and J. Stefan Institute, Jamova 39, YU-61111 Ljubljana, Slovenia*

In a photorefractive experiment the space-charge grating is built-up along a certain axis and it modulates the refractive indices via the linear electro-optic (EO) effect. In many of the works in the field there is an on-going dilemma which EO coefficient and also dielectric constants to use in order to model the photorefractive effect.^[1] The relevance of the question lies in the fact that the unclamped (stress-free) and the clamped (strain-free) values typically differ by more than a factor of two. Experiments in KNbO_3 ^[2] and BaTiO_3 ^[3] tend to indicate that the unclamped values are more appropriate. In this contribution we show that neither the clamped nor the unclamped linear EO coefficients are to be used without caution but the appropriate effective coefficients must be calculated for every particular crystal symmetry and sample orientation.

As all the crystals showing linear EO effects are also piezoelectric the piezoelectric coupling will produce a crystal deformation. The grating period of typically $1 \mu\text{m}$ is much smaller than the dimensions of the crystal in which the grating is built, therefore for symmetry reasons the modulated component of the deformation which can be described by a displacement vector field $\vec{u}(\vec{r})$ must have the form

$$\vec{u}(\vec{r}) = \vec{u}^A \sin \vec{K} \vec{r} , \quad (1)$$

where \vec{u}^A is the amplitude of the displacement and \vec{K} is the wavevector of the photorefractive grating.

To describe the photo-elastic contribution to the refractive index change in a photorefractive experiment the contribution was taken erroneously as being proportional to the strain tensor. As shown by Nelson and Lax^[4] in the case of inhomogeneous deformation the antisymmetric part of the strain tensor can not be neglected as it produces the rotation of the optical index ellipsoid and therefore influences the



light propagation. The change in the optic index ellipsoid is therefore written as

$$\Delta\left(\frac{1}{n^2}\right)_{ij} = r_{ijk}^S E_k + p'_{ijkl} u_{kl} , \quad (2)$$

where r_{ijk}^S is the linear EO tensor in a clamped crystal, E_k are the components of the electric field and u_{kl} are the displacement gradients

$$u_{kl} = \frac{\partial u_k}{\partial x_l} , \quad (3)$$

and the modified elasto-optic tensor p'_{ijkl} has no symmetry upon interchange of the last two indices and can be expressed as the sum of the conventional elasto-optic (Pockels) tensor p_{ijkl} ^[5] and the rotational part $p_{ij[kl]}$ ^[6] as

$$p'_{ijkl} = p_{ijkl} + p_{ij[kl]} , \quad (4)$$

where the second summand is antisymmetric in the last two indices. In a coordinate system that coincides with the principal axes of the index ellipsoid this second summand is equal to

$$p_{ij[kl]} = \frac{1}{2} \left[\left(\frac{1}{n^2}\right)_{ii} - \left(\frac{1}{n^2}\right)_{jj} \right] (\delta_{il} \delta_{kj} - \delta_{ik} \delta_{lj}) \quad (5)$$

In order to calculate the deformations produced by the electric field $\vec{E} = \vec{E}^{SC} \cos \vec{K}\vec{r}$ we write the equation for the stress T_{ij} with the strain S_{kl} and the electric field as independent variables:^[6]

$$T_{ij} = C_{ijkl}^E S_{kl} - e_{kij} E_k , \quad (6)$$

where C_{ijkl}^E is the tensor of the elastic constants at constant electric field and e_{kij} is the piezoelectric stress tensor. In a static case the equilibrium conditions are given by a vanishing divergence of the stress tensor expressed as:

$$\frac{\partial T_{ij}}{\partial x_j} = 0 = C_{ijkl}^E \frac{\partial S_{kl}}{\partial x_j} - e_{kij} \frac{\partial E_k}{\partial x_j} \quad (7)$$

and are further reduced by inserting the strain expressed with displacement gradients $S_{ij} = \frac{1}{2}(u_{ij} + u_{ji})$ (3) and the expressions for the modulated components of the electric field. After rearranging the summation in the elastic part we get the equation:

$$C_{ijkl}^E u_k^A n_j n_l - \frac{E^{SC}}{K} e_{kij} n_k n_j = 0 , \quad (8)$$

where n_i are the components of a unit vector parallel to \vec{K} which is also parallel to \vec{E} . (8) can be rewritten as a set of three inhomogeneous linear equations:

$$A_{ik} u_k^A = B_i, \quad (9)$$

with

$$A_{ik} = C_{ijkl}^E n_j n_l \quad \text{and} \quad B_i = \frac{E^{SC}}{K} e_{kij} n_k n_j. \quad (10)$$

The determinant of A_{ik} is different from zero as known from the eigen value problem for the acoustic waves^[6]. Therefore the solution for the displacements u_k^A is unique and can be written as

$$u_k^A = A_{ki}^{-1} B_i, \quad (11)$$

and the final dependence of the variations of the optical indicatrix is described by

$$\Delta \left(\frac{1}{n^2} \right)_{ij} = \left(r_{ijk}^S n_k E^{SC} + p'_{ijk} n_l u_k^A K \right) \cos \vec{K} \vec{r}. \quad (12)$$

Let us now see the consequences of the previous conclusions to the photorefractivity of crystals that belong to the tetragonal 4mm system, e.g. BaTiO₃, and to the orthorhombic mm2 system, e.g. KNbO₃ and Ba₂NaNb₅O₁₅. We will investigate two special cases, one with the space charge field directed along the polar c axis (z) and the second case with the space-charge field perpendicular to c and directed along the b axis (y).

In the case of $\hat{n} = (0, 0, 1)$ the equation (11) gives the amplitude u_3^A of the displacement along the z -axis as the only nonzero one. The final result for the refractive index changes is then given as

$$\Delta \left(\frac{1}{n^2} \right)_{ii} = \left(r_{iis}^S + \frac{p_{iis33} e_{333}}{C_{3333}^E} \right) E^{SC} \cos Kz, \quad (13)$$

showing that only the contribution of the deformation along the z -axis is present while in a totally unclamped situation with a homogeneous electric field also the deformations along x - and y -axis would contribute to the refractive index change. As no shear deformation is allowed in this geometry the elasto-optic tensor components that appear in (13) are just the usual elements of the Pockels tensor p_{iis33} .

In the second example we study the situation with the space charge field directed along the y -axis. The result show that just a shear displacement along the

z -axis is induced by the electric field. The only component of the index ellipsoid that is influenced in this geometry is

$$\Delta\left(\frac{1}{n^2}\right)_{23} = \left(r_{232}^S + \frac{p'_{2332}e_{232}}{C_{3232}^E}\right) E^{SC} \cos Ky = \left(r_{232}^S + 2p'_{2332}d_{232}\right) E^{SC} \cos Ky \quad (14)$$

The result is expressed both with the piezoelectric e_{232} and d_{232} tensor element. It can be seen that when the electric field is aligned along the y -axis the same deformation u_{23} influences the refractive index in an unclamped sample in a homogeneous external field and in a photorefractive experiment. However, the modified elasto-optic tensor (4) should be used in the case of the photorefractive effect.

In conclusion we repeat the procedure to be followed when calculating the optic response to a periodic space-charge electric field. First, the amplitude u_k^A of the elastic deformation which has the form of a static plain wave (1) and follows the periodicity of the electric field has to be calculated from (11). Inserting u_k^A in the expression (12) the changes in the optical indicatrix are obtained. The modified elasto-optic tensor p'_{ijkl} as defined in (4) and (5) has to be used in order to account for the changes produced by the shear deformation which imperatively rotates the axes of the optical indicatrix.

References

- [1] P. Günter and J.-P. Huignard eds.: *Photorefractive materials and applications I*, Springer-Verlag (Berlin 1988)
- [2] P. Günter, Phys. Rep. **93**, 199 (1982)
- [3] M. B. Klein, *Photorefractive properties of BaTiO₃*, in Ref. [1]
- [4] D. F. Nelson and M. Lax, Phys. Rev. Lett. **24**, 379 (1970)
- [5] J. F. Nye, *Physical properties of crystals*, Clarendon (Oxford 1957)
- [6] J. Sapriel, *Acousto-optics*, J. Wiley & Sons (Chichester 1979)



**SIMULTANEOUS DIFFRACTION OF TWO LIGHT WAVES IN CUBIC
OPTICALLY ACTIVE PHOTOREFRACTIVE PIEZOCRYSTALS**

V.V. Shepelevich, M.N. Egorov

**Mozyr Pedagogical Institute, 247760 Mozyr, Gomel Region,
U.S.S.R. Tel.: 2.40.91**

The influence of optical activity on two-beam coupling in a (110)-cut cubic photorefractive $\text{Bi}_{12}\text{SiO}_{20}$ crystal has been investigated in a number of papers (e.g., [1,2]) for the case of two typical configurations $\vec{K} \parallel [001]$ and $\vec{K} \parallel [001]$, where \vec{K} is the grating vector. The simultaneous diffraction of two light beams has been considered in [3] for arbitrary orientation of the vector \vec{K} from the point of view of the electrooptic grating model. However, the results of [4] testify to the necessity of taking into account the piezoelectric and photoelastic properties of the crystal during the process of refractive index grating formation.

This communication is devoted to the theoretical and experimental investigation of simultaneous diffraction of two light waves by holographic gratings recorded in $\text{Bi}_{12}\text{SiO}_{20}$ of (110)-cut, taking into account the optical activity, electro-optical, piezoelectrical and photoelastic properties of the crystal. To focus on the above effects, we digress from the dynamic model of diffraction [5], considering the phase grating in the crystal as a given one. This permits obtaining analytical expressions of the relative intensities of the diffracted light waves, which are in good agreement with the experimental results.

The consideration was based on the following equations of coupled waves

92-18744



$$\begin{aligned} R_1' &= b_1 S_1 + b_2 S_2 + b_3 R_2, & R_2' &= b_3 S_1 + b_4 S_2 - b_1 R_1, \\ \text{where } S_1' &= -b_1 R_1 + b_2 R_2 + b_3 S_1, & S_2' &= -b_2 R_1 + b_4 R_2 - b_3 S_1, \end{aligned} \quad (1)$$

$$\begin{aligned} \epsilon_1 &= -\frac{\epsilon_0}{\cos \theta_0} \left(\frac{b_{11} + \Delta b_{22}}{2} - b_{12} \right) \cos^2 \theta + \Delta b_{33} \sin^2 \theta + \\ &+ \sqrt{2} \Delta b_{23} \sin 2\theta, \end{aligned}$$

$$\begin{aligned} \epsilon_{2,3} &= -\frac{\epsilon_0}{2} \left[(\Delta b_{12} + \Delta b_{33} - \frac{\Delta b_{11} + \Delta b_{22}}{2}) \frac{\sin 2\theta}{2} + \right. \\ &+ \sqrt{2} \Delta b_{23} \cos 2\theta \left. + \frac{\Delta b_{11} - \Delta b_{22}}{2} \cos \theta \operatorname{tg} \varphi_0 \right], \end{aligned} \quad (2)$$

$$\begin{aligned} \epsilon_4 &= -\frac{\epsilon_0}{\cos \theta_0} \left[\left(\frac{\Delta b_{11} + \Delta b_{22}}{2} - b_{12} \right) \sin^2 \theta + \Delta b_{33} \cos^2 \theta - \right. \\ &- \left(\frac{\Delta b_{11} + \Delta b_{22}}{2} + b_{12} \right) \sin^2 \theta_0 - \sqrt{2} \Delta b_{23} \sin 2\theta \cos^2 \theta_0, \end{aligned}$$

$$\epsilon_0 = \frac{\pi}{2\lambda} n_0^3, \quad n_0 \text{ is the crystal refractive index, } \frac{\Delta}{\cos \varphi_0},$$

Δ is the specific rotation of the crystal, Δb_{ij} are the components of change of the reverse dielectric permeability tensor, defined in [4], θ is the angle between the grating vector \vec{K} and the direction [001], θ_0 is the Bragg angle inside the crystal.

Unlike [4], expressions (2) can be used in the case of large Bragg angles, $\theta_2 \neq \theta_3$ in equations (1). Besides, the equality $b_{13} = -b_{23}$ taking place for (110)-cut crystals in question [6], has been taken into account.

To confirm the phenomenological model of the diffraction process, we have made an experimental study of simultaneous diffraction of light waves. The experimental results for the case where the light waves are polarized in the vibration

plane orthogonal to the plane of incidence as compared with the theoretical curves are given in Fig. 1. The ratio χ of the S-beam light intensity in the presence of the grating to that without the grating are plotted on the ordinate. The best agreement of the experimental results with the theoretical curve 1 is achieved with the electric field of the grating $E_g = 0.625$ kV/cm. It follows from Fig. 1 that the neglect of the piezoelectric effect leads to a qualitative change in the shape of the curve $\chi(\theta)$. Especially pronounced qualitative distinctions take place at $\theta \simeq 140^\circ$ and $\theta \simeq 310^\circ$. In the presence of the piezoeffect at these points the intensity pump is practically absent, whereas in the case where the piezo-effect is neglected it can reach 2%.

The experiment was also carried out at an angle of 112° between the beams in the air. In this case the character of the dependence $\chi(\theta)$ remained unaltered, but the maximum value $\chi(\theta)$ increased up to 1.12.

Fig. 1 also shows the plots of the maximum values $\chi^m(\theta)$ (curves 3 and 4), each of which is reached at a certain value of azimuth ψ_0^m of the reading waves. The analytical expressions for $\chi^m(\theta)$ and $\psi_0^m(\theta)$ will be presented in the report.

1. P.D. Foote, T.J. Hall, Optical Communications. 57, 201 (1986)
2. S. Mallick, D. Rouede, Appl. Phys. B43, 239 (1987)
3. V.V. Shepelevich, E.M. Khramovich, Opt. Spektrosk. (in press)
4. V.V. Shepelevich, S.M. Shandarov, A.E. Mandel, Ferroelectrics 110, 235 (1990)
5. N.V. Kukhtarev, V.B. Markov, S.G. Odulov, M.S. Soskin, V.L. Vinetskii, Ferroelectrics 22, 949 (1979)
6. S.M. Shandarov, V.V. Shepelevich, N.D. Khat'kov, Opt. Spektrosk. (in press)

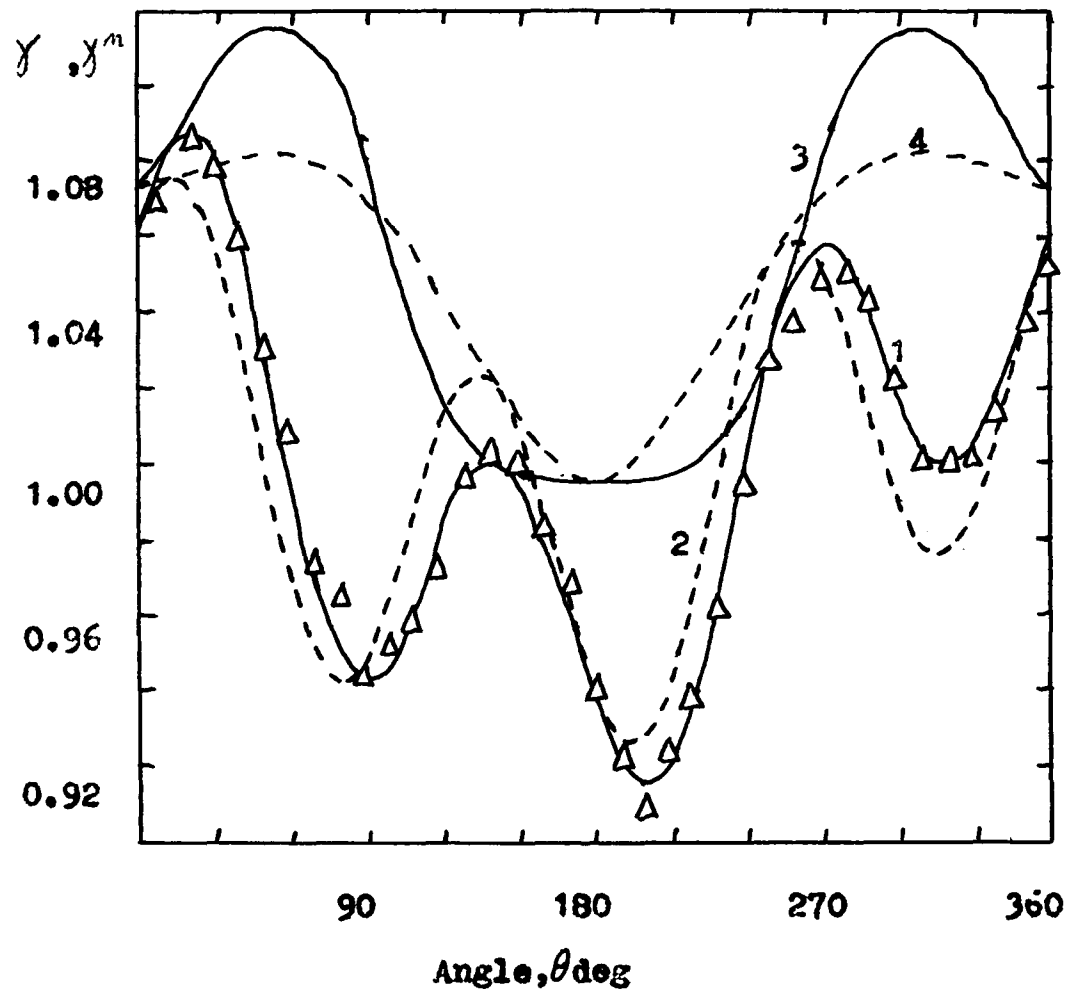


Figure 1. γ and γ^m vs angle θ . The ratio of the R-to-g-beam intensity at the entrance to the crystal is 2. The specific rotation of the crystal is 0.372 rad/mm, crystal thickness is 2.19 mm. The other parameters of crystal coincide with those of [4]. 1,2 - γ ; 3,4 - γ^m ; 1,3 - with regard to the piezoelectric effect; 2,4 - without regard to the piezoelectric effect; Δ - is experimental points.



PHOTOGYRATION AND PHOTOINDUCED STRUCTURE DISTORTIONS
IN DOPED LiNbO_3 AND LiTaO_3 .

S.M. Kostritskii

Department of Physics, Kemerovo State University, 650043 USSR

In this work photoinduced phenomena in iron-doped ($C = 0,01; 0,038; 0,05; 0,07$ wt.%) and copper-doped ($C = 0,01; 0,025; 0,04$ wt.%) lithium niobate and lithium tantalate single crystals have been investigated using the Raman scattering (RS) and IR-reflection spectroscopy. The following types of lasers were used as illumination sources: YAG:Nd^{3+} ($\lambda = 10640 \text{ \AA}$); He-Ne (6328 \AA); Ar^+ ($5145, 4880 \text{ \AA}$); He-Cd (4416 \AA).

A number of studies shows the existence of photovoltaic effect (PVE) in these crystals consisting of high voltage electric field appearance in illuminated regions. The PVE field is 10^3 V/cm in nominally pure crystals and that is 10^5 V/cm in the doped crystals. At the same time it is known that the electrogyration effect could take place with the external electric field imposed on the crystal. Besides, these crystals (C_{3v} point symmetry group) do not possess any intrinsic first order optical activity, it making the task of photogyration experimental observation much easier. It should be noted that the given effect can be observed only in the direction close to the optical axis, which is connected with the masking influence of linear birefringence. Therefore at photogyration studies the laser radiation was directed along the optical axis and was polarized along one crystallographic axis (x or $y \parallel \sigma_v$). The PVE fields along the axes y and z are to appear in crystals under condition mentioned above. Their magnitude is determined by the PVE tensor components β_{22} and β_{31} , respectively. The electric field along the y -axis results in the appearance of the component of a symmetric part of gyration pseudotensor G_{23} [1]:

$$G_{23} = k \cdot A_{14} E_y = k A_{14} \beta_{22} \alpha I (\sigma_{ph} + \sigma_d)^{-1}; \quad \sigma_{ph} = f \cdot I \quad (1)$$

where: A_{14} - electrogyration effect tensor component; σ_{ph}, σ_d - photo and dark conductivity; α - absorption coefficient; I - intensity.

92-18745



As is known the G_{23} component will determine the elliptical birefringence value. The magnitude of the induced biaxiality would be insignificant as the value of the angle between the binormals is $0,8 - 2,5^\circ$, depending on the light frequency and impurity concentration. Therefore the polarization ellipticity degree will be small and light polarization will be close to the linear one. The large ellipse axis of the light polarization for the light that has gone through the crystal will be deflected from the direction of the incident light polarization on the ψ angle, whose magnitude is largely determined by the induced gyrotropy: $\psi = hG_{23}L$, where L - the way length of laser irradiation in crystal; h - const.

Using the data of RS measurements we get: $\rho_1 = [hG_{23}] = 0,3^\circ/\text{mm}$, $\rho_2 = 0,9^\circ/\text{mm}$ for $\text{LiNbO}_3:\text{Fe}$ ($C = 0,05 \text{ wt.}\%$) at $\lambda_1 = 6328 \text{ \AA}$, $\lambda_2 = 4416 \text{ \AA}$; $\rho_1 = 0,15^\circ/\text{mm}$, $\rho_2 = 0,7^\circ/\text{mm}$ for $\text{LiNbO}_3:\text{Fe}$ ($C = 0,01 \text{ wt.}\%$); $\rho_1 \approx \rho_2 \approx 0$ for nominally pure crystals. In the $\text{LiTaO}_3:\text{Fe}$ and $\text{LiNbO}_3:\text{Cu}$ the magnitudes of ρ is significantly less ($\leq 0,4^\circ/\text{mm}$). By substituting the experimental values into (1) we obtain:

$$(A_{14})_{\text{LT}} > (A_{14})_{\text{LN}} \approx 2 \cdot 10^{-12} \text{ M/V.}$$

The experimental measurements of the RS asymmetry [1] at different L indicates that the dependence ψ on L is described by theoretical expressions at large values L ($\geq 6^\circ/\text{mm}$) only approximately, which points to the inhomogeneity of the photovoltaic field along the light beam.

It was experimentally established that inhomogeneous illumination in visible and UV ranges induced distortions in the structure of these crystals. Moreover in doped crystals photoinduced structure distortions results in lowering of symmetry in a unit cell. The latter is the cause of additional lines in RS and IR spectra connected with the forbidden activity of A_2 -phonons. The distortions become most significant when laser irradiation was directed perpendicularly the optical axis. In the polarization geometry $x(zx)z$ for angle $\theta = 45^\circ$ between the wave vector of the phonon and optical axis, Raman spectra show a line with $\omega = 187(164) \text{ cm}^{-1}$ for LiNbO_3 (LiTaO_3), fig.1. This line is due to the phonon with the mixed symmetry ($A_2 + E$), its frequency

changing from $152(141)\text{cm}^{-1}$ ($E(\text{TO})$) at $\theta=0$ to $223(186)\text{cm}^{-1}$ ($A_2(\text{TO})$) at $\theta=90^\circ$, fig.2.

This changings can be described by the following expression:

$$\omega^2(\theta) = \omega^2(E(\text{TO})) \cos^2\theta + \omega^2(A_2(\text{TO})) \sin^2\theta \quad (2)$$

The frequencies of A_2 -phonons is determined by neutron inelastic scattering [2] in LiNbO_3 and by RS in defected LiTaO_3 [3].

There is also one more line which shows up simultaneously with the first. Now it is a E-symmetry phonon $172(153)\text{cm}^{-1}$, changing frequency from $152(141)\text{cm}^{-1}$ at $\theta=0$ to $198(165)\text{cm}^{-1}$ ($E(\text{LO})$ -phonon) at $\theta=90^\circ$. Such spectral simultaniety of extraordinary phonons with frequencies $172(153)$ and $187(164)\text{cm}^{-1}$ indicates that the whole RS spectrum of a real crystals results from overlapping spectra from regions with the distorted and intact structure. This is corroborated by the RS study along the spectrum. It was established that the forbidden activity of A_2 -phonons is caused by a distortion entailing lowering of symmetry in a unit cell from C_{3v} to C_3 . Due to this effect 5 initially inactive A_2 -modes get activated and their RS-tensor tends to have analogy to A_1 -modes. Intensification of the spectral lines respondent to activity of A_2 -phonon, at C_{Fe}

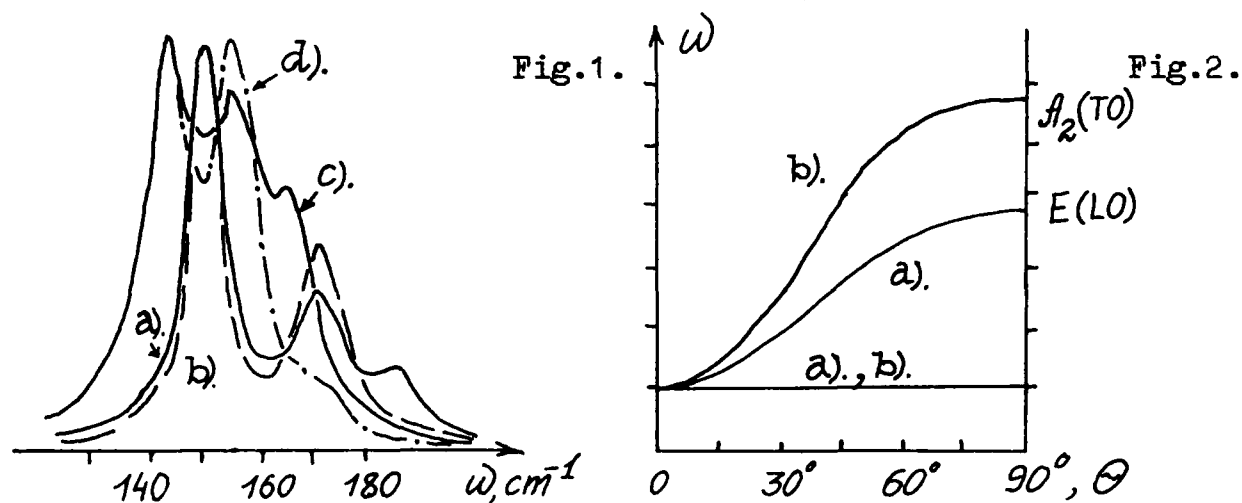


Fig.1. Raman spectra of $\text{LiNbO}_3\text{:Fe}$ at $C=0,05\text{ wt.}\%$ (a), $C\cong 0$ (b); $\text{LiTaO}_3\text{:Fe}$ at $C=0,038\text{ wt.}\%$ (c), $C\cong 0$ (d). $\lambda=4416\text{ \AA}$, $P=60\text{ mW}$, $t=15-20\text{ min}$.

Fig.2. The dependences of phonons frequencies from the angle θ for regions with distorted (a) and with intact structure (b).

and C_{Cu} increasing and λ decreasing, reveals the photoinduction mechanism about these structure distortions. This dependence, in turn, was found to be strongly correlated with the corresponding behavior of the PVE [5]. Further investigation of photoinduced RS demonstrated that structure distortions would occur in the border zone of the illuminated region, which is due to inhomogeneity of the distribution of photoinduced space-charge [4]. These distortions which located in the region space-charge concentration survive for a long time ($10^2 - 10^5$ hh) after ending illumination, depend on the exposure time t and are characterized by saturation. The kinetic can be described by the exponent with Maxwell's relaxation time $\tau_m = \epsilon \epsilon_0 / (\sigma_{ph} + \sigma_d)$:

$$I_{RS}(A_2) = [I_{RS}(A_2)]_{\text{sat}} (1 - e^{-t/\tau_m}) \quad (3)$$

Besides, the second type of distortions featuring independence of exposure time were detected. They are dependent on the illumination intensity, nonlocated and disappear immediately after the illumination is stopped. The results of experimental and theoretical investigation are in favor of supposition that microscopic mechanism of structure distortion consists in pseudo Jahn-Teller effect which is motivated by connection of photoexcited nonequilibrium electrons with optical modes. The split of the $E^1(TO)$ phonon into two lines ($\Delta\omega = 3 - 5 \text{ cm}^{-1}$) proves that in a crystals there are some local strained states, which connected with excitation of photorefractive centers. The comparison of the Raman spectra damages in LiNbO_3 and LiTaO_3 indicates that their magnitude is proportional to the square of the electron-phonon interaction constant.

REFERENCES

1. S.M. Kostritskii, *Ferroelectrics* 83, 75 (1988).
2. M.R. Chowdhury, G.E. Peckman, D.H. Saunderson, *J. Phys. C: Sol. St. Phys.* 11, 1671 (1978).
3. A.F. Penna, A. Chaves, P.R. Andrade, S.P.S. Porto, *Phys. Rev. B* 13, 4907 (1976).
4. N. Ohnisi, *Jap. J. Appl. Phys.* 16, 1451 (1977).
5. H.G. Festl, P. Hertel, E. Kratzig, R. von Baltz, *Phys. Stat. Sol.* (b) 113, 157 (1982).



Investigation of photorefractive self pumped phase conjugators in the presence of loss and high modulation depth.

James E. Millerd, Steffen D. Koehler, Elsa M. Garmire

Center for Laser Studies, University of Southern California,

University Park, DRB 17, Los Angeles, Ca. 90089

(213) 740-4235

Marvin B. Klein

Hughes Research Laboratories, Malibu, Ca. 90265

We have recently demonstrated large two beam coupling gains in InP:Fe by combining the band-edge resonance technique with a second resonant enhancement involving temperature stabilization.¹ While loss increases near the band-edge, the gain increases much more dramatically. Net gain coefficients larger than 20 cm⁻¹ have been measured making semiconductor gains comparable to those in ferroelectric materials. We present here an investigation of this material as a self pumped phase conjugator.

The two beam coupling gain in the limit of small modulation index is ²,

$$\frac{I_s(l)}{I_s(0)} = \frac{(\beta+1) e^{\Gamma l}}{\beta + e^{\Gamma l}} \quad (1)$$

where l is the interaction length, β is the ratio of pump to signal beam and,

$$\Gamma = \frac{2\pi n_o^3 r_{41}}{\lambda \cos \theta} \frac{\text{Im}(E_{sc})}{m}, \quad m = \frac{2\sqrt{I_p I_s}}{I_s + I_p}, \quad (0 < m < 1). \quad (2)$$

Here $\text{Im}(E_{sc})$ represents the imaginary part of the space charge field and m is the modulation index. According to this theory, Γ is independent of m since E_{sc} is linear in m .

Figure 1 shows that, while using the band-edge resonance and temperature stabilization enhancement techniques in InP:Fe¹, the two wave mixing gain drastically decreases at large modulation depths. Similar results have been reported in BSO and GaAs when using applied fields and moving gratings.^{3,4} Refregier *et al*,³ have introduced a simple empirical formula to model this behavior:

$$\text{Im}(E_{sc}) \sim f(m) = \frac{1}{a_f} (1 - \exp(-a_f m)) \quad (3)$$

92-18746



where a_f is a fitting parameter. In our InP experiments a_f is approximately 8 when the saturated gain, in the limit of small m , is taken as 30 cm^{-1} (see solid line in Figure 1).

The theory for self pumped phase conjugation using photorefractive four-wave mixing has been described by Cronin-Golomb *et al.*⁵ Coupled wave equations describing the interaction have been derived and then solved by assuming that the linear absorption, α , is negligible and the modulation depth is small. In many applications, including the case of band edge resonant enhancement, these assumptions are not valid. Wolffer *et al.*⁶ have studied the effects of absorption and large modulation index on the double pumped phase conjugate mirror. We present here an investigation of the effects on self pumped phase conjugators.

We have included both the effects of linear absorption and non-linearities of the space charge field at high modulation index in the coupled wave equations and solved them numerically. The results of these calculations for the ring mirror are shown in figures 2-4. We have introduced a figure of merit η , defined as the absorption coefficient divided by the gain coefficient (α/Γ), to better describe the effects of loss. Figure 2 shows the decrease in reflectivity as the linear absorption becomes significant, (η gets large). The maximum reflectivity is limited and there exists an optimum coupling strength.

The large signal effects were modeled by replacing the linear dependence of the space charge field ($E_{sc} \sim m$) with $f(m)$ of equation 3. Figure 3 shows the effects for several values of the fitting parameter a_f . The reflectivity is clearly reduced with increasing a_f , however, it continues to grow with increasing coupling strength.

Figure 4 shows the combined effects of absorption and the non-linear space charge field. The reflectivity is drastically reduced and again an optimum coupling strength is evident for the case of high absorption. We will also report on the theoretical effects on the linear mirror⁵ when absorption and large signal effects are included. These results indicate that the high gain produced by enhancement techniques such as the band-edge resonance may not be useful for phase conjugate mirrors. We will present experimental results of InP:Fe and $\text{Bi}_{12}\text{TiO}_{20}$ ring mirrors to compare to theory.

1. J. E. Millerd, S. D. Koehler, E. M. Garmire, A. Partovi, A. M. Glass and M. B. Klein, "Photorefractive gain enhancement in InP:Fe using band edge resonance and temperature stabilization", *Appl. Phys. Lett.* **57**, 2776 (1990).
2. P. Gunter and J.-P. Huignard, "Photorefractive materials and their applications I.", Springer - Verlag, New York, 1988.
3. Ph. Refregier, L. Solymar, H. Rajbenbach, and J.P. Huignard, "Two beam coupling in photorefractive $\text{Bi}_{12}\text{SiO}_{20}$ crystals with moving grating: Theory and experiments." *J. Appl. Phys.* **58**, 45 (1985).

4. B. Imbert, H. Rajbenbach, S. Mallick, J.P. Herriau and J.P. Huignard, "High photorefractive gain in two beam coupling with moving fringes in GaAs:Cr crystals." *Optics Lett.* **13**, 327 (1988).
5. M. Cronin-Golomb, B. Fisher, J. O. White and A. Yariv, "Theory and applications of four-wave mixing in photorefractive media", *IEEE J. Quant. Elect.*, QE-20, 12 (1984).
6. N. Wolffer, P. Gravey, J.Y. Moisan, C. Laulan and J.C. Launay, "Analysis of double phase conjugate mirror interaction in absorbing photorefractive crystals: Application to BGO:Cu", *Opt. Comm.*, **73**, 351 (1989).

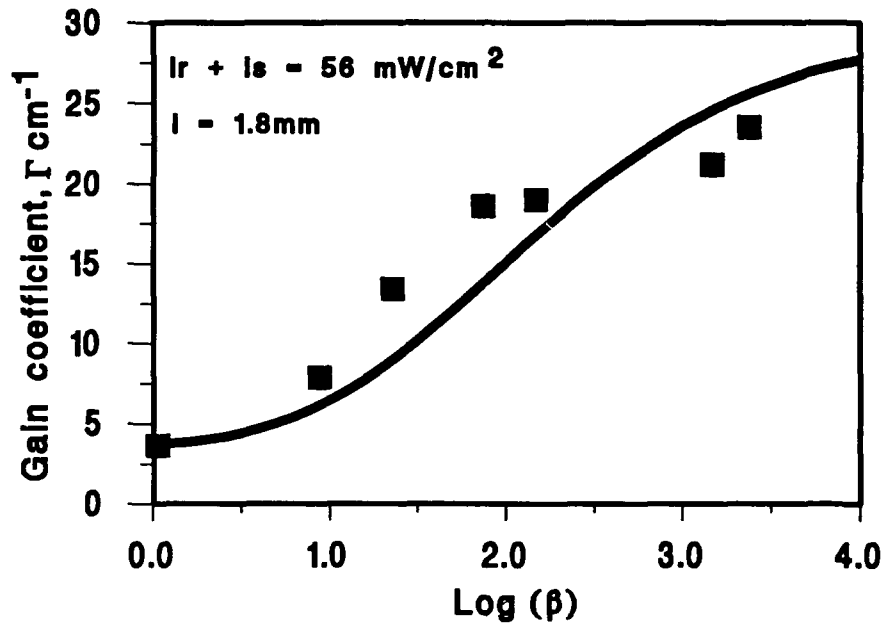


Figure 1. Gain coefficient vs Beam ratio.

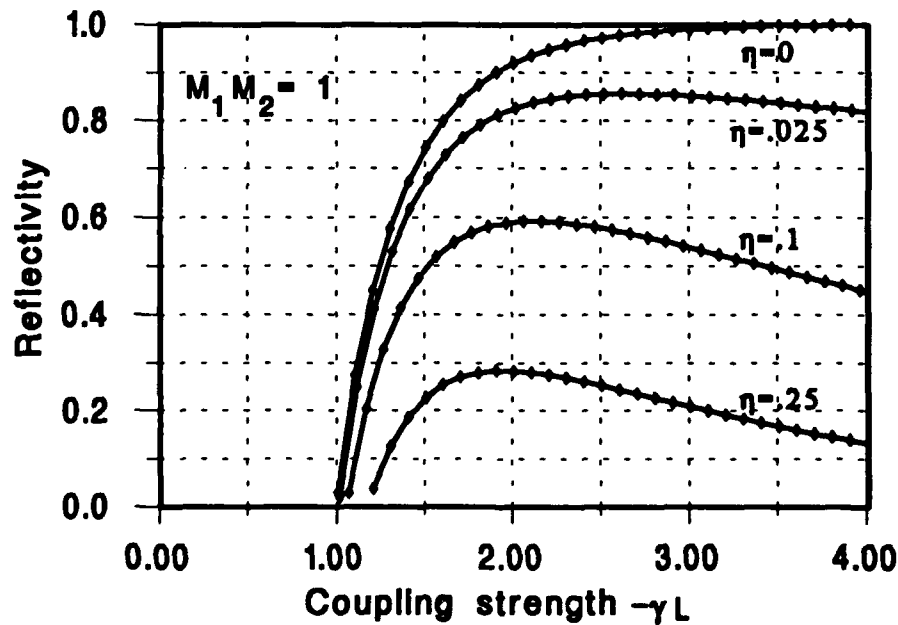


Figure 2. Effects of absorption on the ring mirror.

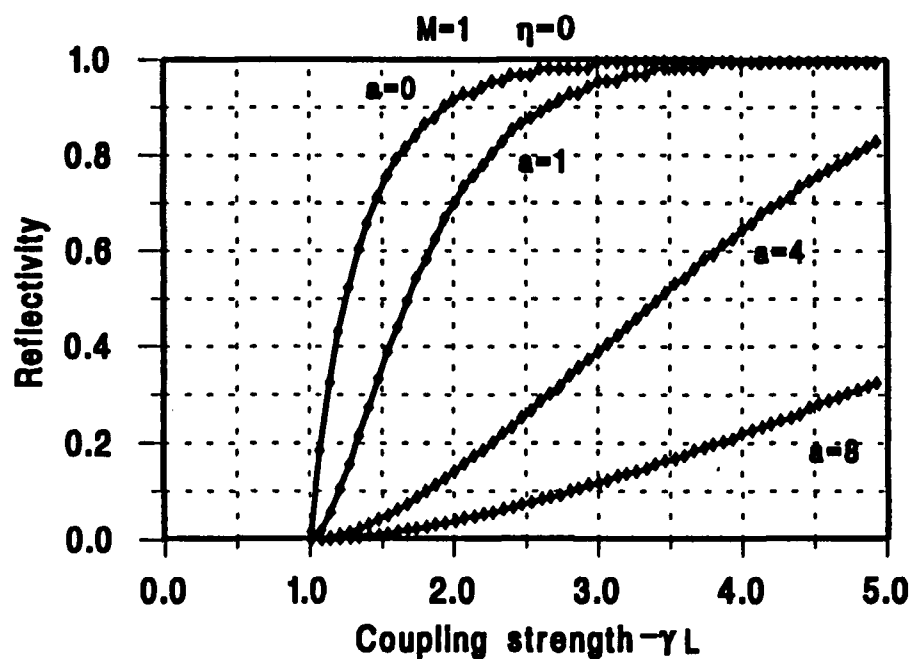


Figure 3. Large signal effects on ring mirror.

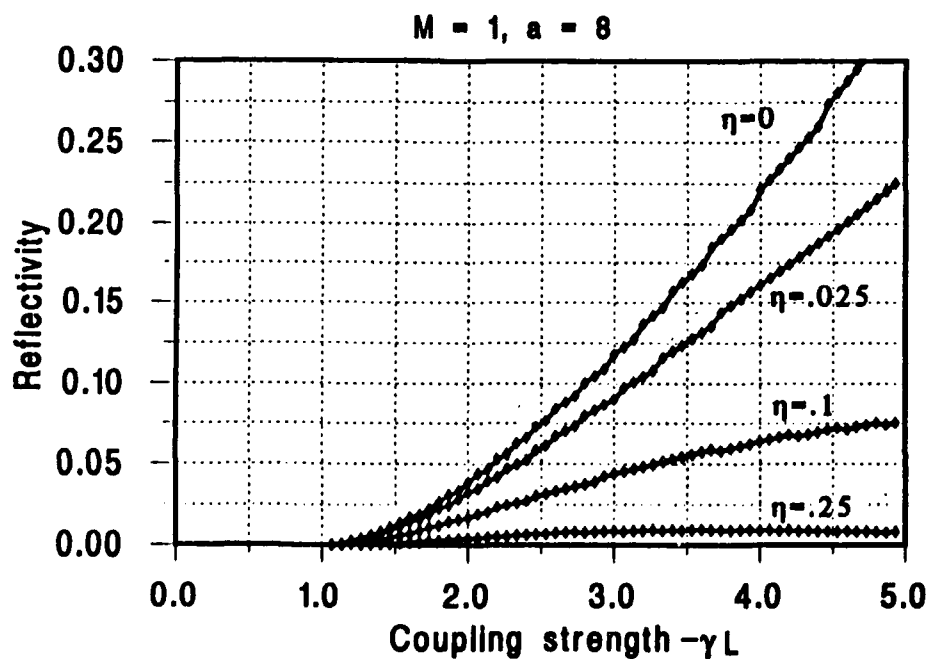


Figure 4. Combination of large signal and linear absorption.

AD-P006 759



Perturbative Analysis of Higher Order Photorefractive Effect

R. Saxena and T. Y. Chang

Rockwell International Science Center

1049 Camino Dos Rios, Thousand Oaks, CA 91360

(805) 373 - 4157

Abstract

Analytic expressions are derived for second- and third-order photorefractive effect. The dependence on spatial frequency, applied field, and velocity of moving grating is examined.

92-18747



Summary

The response of photorefractive media to sinusoidal intensity patterns is described by the band-transport model of Kukhtarev *et al.*¹ The set of nonlinear coupled equations contained in this model cannot be solved exactly. For small modulation depth of the interference pattern, the equations can be solved by linearizing them.^{1,2} A sinusoidal index grating, with a spatial frequency equal to that of the incident light, is predicted by the linearized solutions. These solutions are adequate for explaining most of the experimental results obtained from two-beam coupling and four-wave mixing in photorefractive materials. In general, however, the space charge field has a spectrum of spatial harmonic frequencies at integral multiples of the spatial frequency of incident intensity. Exact numerical solutions of the nonlinear equations have been obtained for large modulation depths by expansion of the variables into their Fourier components, with analytic results for drift dominated recording.³ An intelligent guess to the solutions must be initially known for numerical convergence.⁴ Perturbative approach developed by Ochoa *et al.*⁵ is valid for diffusion field much smaller than the saturating field.

We extend the perturbative approach of Refregier *et al.*⁶ to obtain explicit expressions for the second- and third-order space charge fields at steady-state for moving gratings and applied fields. The perturbation expansion parameter is the modulation depth of the fringe pattern, assumed to be much smaller than unity. The analytic results are valid for arbitrary strengths of characteristic fields in the photorefractive material and applied field. Higher-order harmonics for hole density and the ionized acceptor density are also calculated, and the dependence of the amplitudes of higher harmonics on applied field, spatial frequency, and velocity of moving grating is examined. Refregier *et al.*⁶ obtained the second-order correction to the amplitude of the fundamental harmonic of the space charge field, and used it to explain the dependence of photorefractive gain on the beam ratio

of the writing beams in two-beam coupling experiments. A knowledge of the higher order space charge fields would be relevant for experiments that examine the nonlinear photorefractive response specifically, like second-harmonic phase conjugation,⁷ high-bandwidth image correlation,⁸ etc.

References

1. N. V. Kukhtarev, V. B. Markov, S. G. Odulov, M. S. Soskin and V. L. Vinetskii, *Ferroelectrics* **22**, 961 (1979).
2. G. C. Valley, *J. Opt. Soc. Am.* **B1**, 868 (1984).
3. F. Vachss and L. Hesselink, *J. Opt. Soc. Am.* **A5**, 690 (1988).
4. L. B. Au and L. Solymar, *J. Opt. Soc. Am.* **A7**, 1554 (1990).
5. E. Ochoa, F. Vachss, and L. Hesselink, *J. Opt. Soc. Am.* **A3**, 181 (1986).
6. Ph. Refreiger, L. Solymar, H. Rajbenbach and J. P. Huignard, *J. Appl. Phys.* **58**, 45 (1985).
7. T. Y. Chang and P. Yeh, *J. Opt. Soc. Am.* **A3**, 33 (1986).
8. M. P. Petrov, S. V. Miridonov, S. I. Stepanov, and V. V. Kulikov, *Opt. Commun.* **31**, 301 (1979).

The Effect of Large Signals in Photorefractive Media

A.K.Powell, D. Fish, G.R. Barrett and T.J. Hall

Department of Physics

King's College London

Strand, London WC2R 2LS, UK

Photorefractive materials remain of interest as optically nonlinear elements, because of the large saturated nonlinear effects that they exhibit at low continuous wave optical power levels. They can be used to give large optical amplification to image bearing beams by utilising the nonlinear process of two-wave mixing. Four-wave mixing can also be achieved, and phase conjugate reflectivities of signal beams can be substantially greater than unity. Self-pumped phase conjugation is also possible in those photorefractive materials with nonlinearities that are suitably large.

The range of photorefractive materials with, usefully large nonlinear effects has increased in recent years with the development of both DC and AC applied electric field enhancement techniques. The modelling of the effects of applied fields with the band transport model of Kukhtarev shows that large enhancements (P) of the photorefractive effect are possible, with an applied symmetrical square waveform being optimum. There is, however, a limiting process termed a 'Large Signal Effect' that limits these large enhancements to a regime where the signal beam is small, as compared to the pump beam [1,2]. This effect can be described quantitatively by developing the band transport model. If the small modulation solutions are extrapolated to $m > 1/P$, one predicts a negative free carrier concentration, which clearly is unphysical. In practice the space charge field saturates at a value which preserves a positive carrier density. The peak magnitude of the space charge field is limited as a consequence, to the same order of the peak applied field.

We show new results for the case of applied AC fields and model the effect of large signal saturation upon the performance of an optical resonator system based upon the ring passive phase conjugation.

- [1] G.A. Swinburne, T.J. Hall, A.K. Powell, 'Large Modulation Effects in Photorefractive Crystals'. IERE Proc. Int. Conf. on Holographic Systems, Components and Applications, Bath, U.K., 11-13 Sept., 1989, pp.175-184.
- [2] L.B. Au, L. Solymar, 'Space-charge field in photorefractive materials at large modulation. ', Opt. Lett. 13, 8, (Aug. 1988)

LARGE SIGNAL GAIN EFFECTS IN
PHOTOREFRACTIVE $\text{Bi}_{12}\text{TiO}_{20}$ AT 633 nm

M.B. Klein, F.P. Strohkendl and B.A. Wechsler
Hughes Research Laboratories
3011 Malibu Canyon Road
Malibu, CA 90265

AD-P006 760

(213) 317-5247



G.A. Brost
Photonics Center
Rome Laboratory
Griffiss AFB, N.Y. 13441

J.E. Millerd and E.M. Garmire
Center For Laser Studies
Univ. of Southern California
Los Angeles, CA 90089-1112

$\text{Bi}_{12}\text{TiO}_{20}$ (BTO) is a photorefractive material in the same structural class (sillenite) as $\text{Bi}_{12}\text{SiO}_{20}$ (BSO) and $\text{Bi}_{12}\text{GeO}_{20}$ (BGO). However, BTO offers some unique advantages over BSO and BGO: (1) larger electro-optic coefficient (5.7 pm/V)¹, and (2) lower optical activity ($6^\circ/\text{mm}$ at 633 nm)^{1,2}. Previous photorefractive measurements^{3,4} have shown that gain coefficients on the order of $10\text{--}15 \text{ cm}^{-1}$ can be produced through the use of an applied AC field. In this work we show that the largest gain values can only be obtained for large values of the pump/probe intensity ratio β . As β approaches unity (large signal regime), higher spatial order gratings become prominent, and the gain is reduced from its large- β value.⁵⁻⁸ Our results are similar to those obtained by other researchers for BSO⁵ and GaAs⁶ with an applied field. We have analyzed this and related phenomena using a finite difference method to model the photorefractive grating

92-18748



formation. This method yields accurate numerical solutions which are valid for all values of β .

Typical plots of the measured intensity gain as a function of the input beam ratio are given in Figure 1. Since the beam ratio varies through the sample, the gain coefficient also varies. In order to obtain the intrinsic variation of the gain coefficient with beam ratio from the data of Figure 1, we require solutions to the wave equations that account for optical activity and pump depletion, and which include a physical model for the variation of the local space charge field with beam ratio. These modifications can be avoided if a sufficiently thin sample is used.

We will compare our gain data with full solutions of the wave equation that account for the dependence of the gain coefficient with beam ratio. In addition, we will present direct measurements of the strength of the higher spatial order gratings for the conditions of our experiment.

REFERENCES

1. J.P. Wilde, L. Hesselink, S.W. McCahon, M.B. Klein, D. Rytz and B.A. Wechsler, J. Appl. Phys. 67, 2245 (1990).
2. A. Feldman, W. Brower and D. Horowitz, Appl. Phys. Lett. 16, 201 (1970).
3. S.I. Stepanov and M.P. Petrov, Opt. Comm. 53, 292 (1985).
4. D. Rytz, M.B. Klein, B.A. Wechsler, R.N. Schwartz and K. Kirby, "Growth And Characterization of Photorefractive $\text{Bi}_{12}\text{TiO}_{20}$," OSA Topical Meeting on Photorefractive Materials, Effects and Devices, Los Angeles, Ca, August 12-14, 1987.
5. P. Refregier, L. Solymar, H. Rajbenbach and J.P. Huignard, J. Appl. Phys. 58, 45-57 (1985).
6. B. Imbert, H. Rajbenbach, S. Mallick, J.P. Herriau and J.P. Huignard, Opt. Lett. 13, 327-329 (1988).

7. G.A. Swinburne, T.J. Hall and A.K. Powell, "Large Modulation Effects in Photorefractive Crystals," IERE Proc. Int. Conf. on Holographic Systems, Components and Applications, Bath, U.K. Sept. 11-13, 1989, pp 175-184.
8. L.B. Au and L. Solymar, J. Opt. Soc. A13, 1554 (1990).

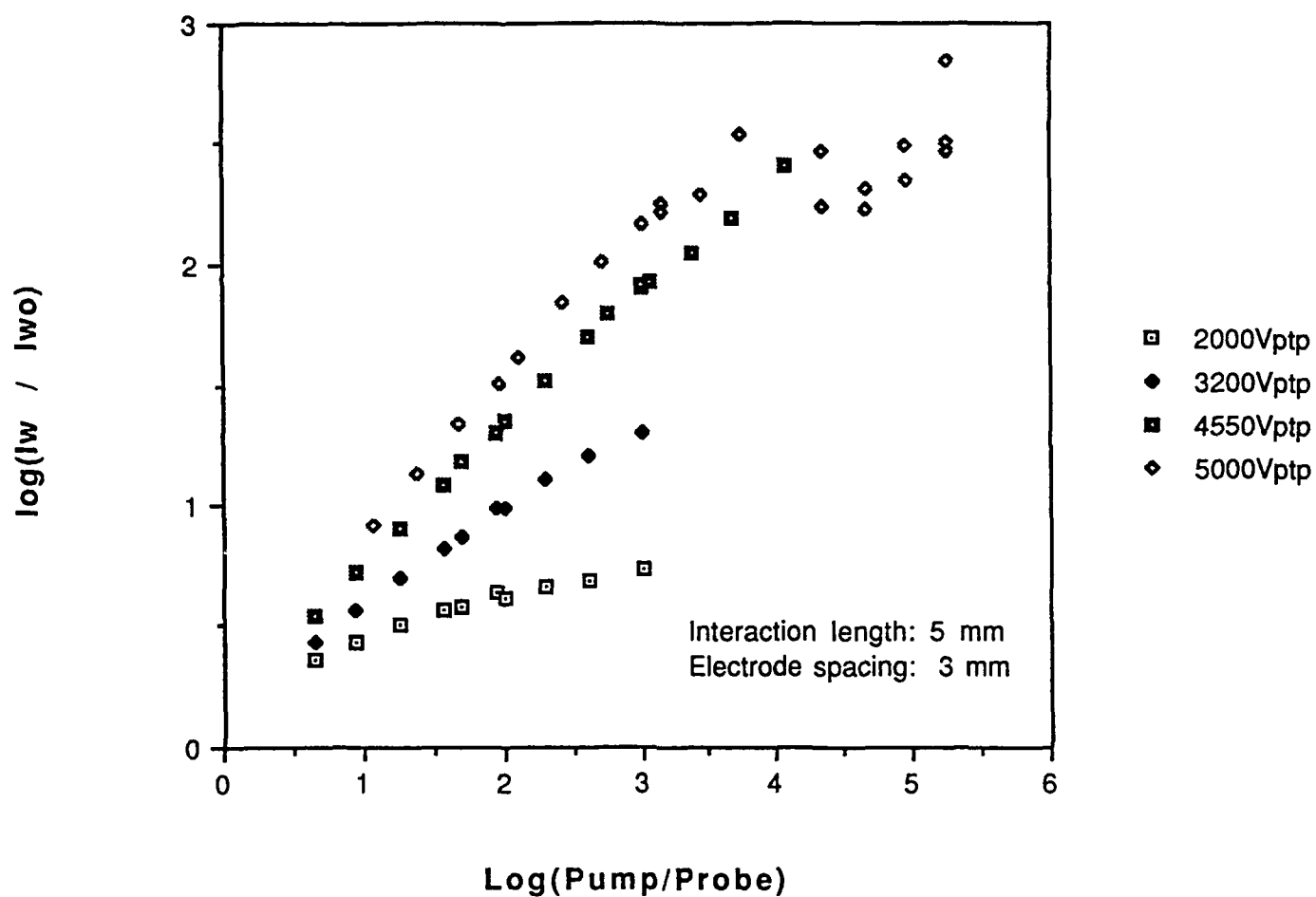


Fig. 1 Measured intensity gain vs. input beam ratio for four values of AC peak-to-peak voltage. The grating period is $4 \mu\text{m}$, and the AC square-wave frequency is 60 Hz.

**Numerical Analysis of Photorefractive Grating Formations
at Large Modulation**

George A. Brost
Photonics Center
Rome Laboratory
Griffiss AFB, NY 13441

AD-P006 761


Enhancements in the two-beam coupling gain can be achieved in cubic crystals of the BSO type by the use of nonstationary external conditions such as the application of a dc field along with a moving interference pattern or by the application of an alternating electric field[1,2,3,4,5]. However, for modulation index, m , greater than about 0.1 the performance falls off significantly with increasing m [1,5]. Some success has been achieved in obtaining steady-state solutions of the nonlinear equations in the presence of moving fringes[1,6,7,8]. These numerical calculations were accomplished by expansion of the variables into their Fourier components or by perturbation techniques. In this paper we model the photorefractive grating formation by a finite difference method. This approach is quite general. The numerical solutions predict the photorefractive behavior at large modulation for stationary and nonstationary photorefractive recording techniques.

In our calculations we assume that the spatial symmetry of the grating formation is one dimensional and periodic in the grating period. We apply the band transport model with a single set of

92-18749



recombination centers and one species of free carrier. A grating period is divided into N elements. The electric field and free carrier, current, and charge densities are determined for each element. The distribution of charge among free carriers and traps is calculated from the rate equations and the current flow between elements is determined by the continuity equation. This method provides time-dependent field and charge distribution characteristics without requiring the small modulation index approximation.

We have used this numerical method to calculate the grating formation in BSO under conditions of moving fringes and also applied alternating electric fields. At low modulation the numerical results agree with analytical results, derived from a linearized theory[1,2,3,4]. At high modulation, the calculations predict the saturation of the fundamental component of the space charge field which has been observed experimentally. This is demonstrated in Figure 1 where we plot results of calculations for moving fringes at the optimum velocity[1] for 3 and 30 μm grating periods and an applied field of 10 KV/cm. The function $f(m)$ is proportional to the imaginary part of the fundamental component of the space charge field and expresses the relationship between the fundamental component and the modulation index. The solid lines are a fit to the functional form of $f(m) = 1/a[1-\exp(-am)]$ found phenomenologically by Refregier et al[1]. Similar results were obtained for square wave alternating electric fields. The magnitude of the saturation effect depended on the type of external conditions. The harmonic

content of the space-charge field depended not only on the modulation index, but also on the grating period and on the method of nonstationary recording.

The temporal evolution of the space charge field was also studied. At high modulation the calculations predicted an "apparent" decrease in the response time, but with a time dependence that departed from that of a single real exponential time constant (plus an imaginary component for moving fringes). The temporal dependencies of the higher harmonics did not follow that of the fundamental, and were in general more complicated.

In summary, we have used a finite difference method to model the photorefractive behavior of BSO at high modulation index.

REFERENCES

1. P. Refregier, L. Solymar, H. Rajbenbach, and J.P. Huignard, J. Appl. Phys. **58**, 45 (1985).
2. S.I. Stepanov and M.P. Petrov, Optics Comm. **53**, 292 (1985).
3. X. Gan and S. Ye, Optics Comm. **66**, 155 (1988).
4. K.Walsh, A.K. Powell, C. Stace, and T.J. Hall, J. Opt. Soc. Am. B **7**, 288 (1990).
5. S.I. Stepanov and M.P. Petrov, Sov. Phys. Tech. Phys. **32**, 1054 (1987).
6. L.B. Au and L. Solymar, J. Opt. Soc. Am. A **7**, 1554 (1990).
7. G.A. Swinburne, T.J. Hall, and A.K. Powell, IEE 2nd Int. Confernce on Holographics, Systems, Components, and Applications, Sept. 1989.
8. F. Vachss and L. Hesselink, J. Opt. Soc. Am. B **5**, 1814 (1988)

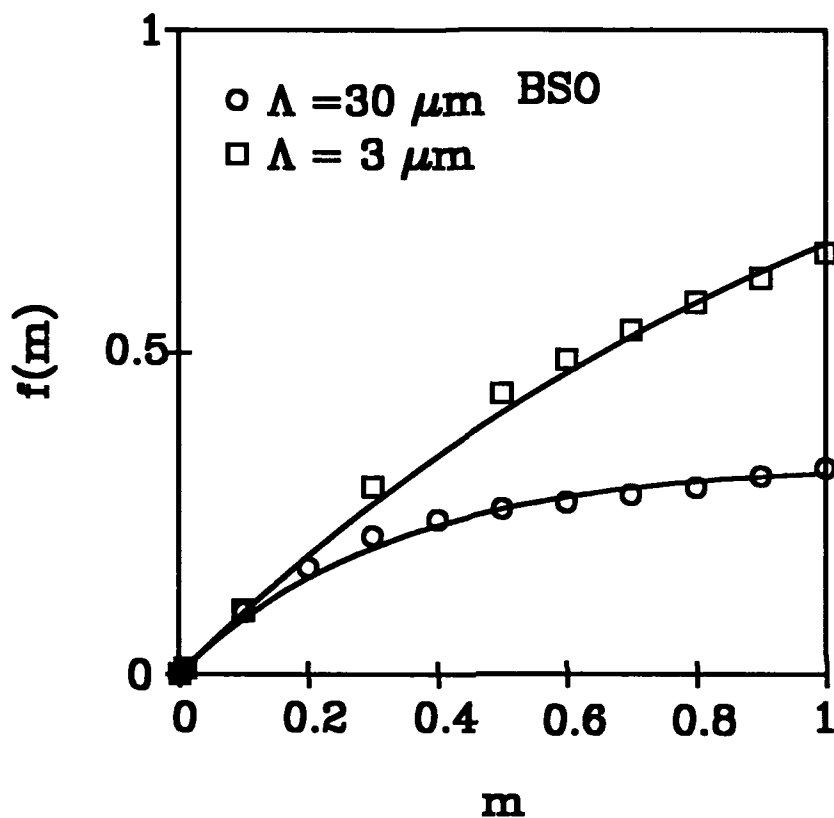


FIGURE 1. Calculated correction function $f(m)$ which relates the magnitude of the fundamental component of the spaced charge field to the modulation index. The lines are a fit of the calculated results to the functional form $f(m) = (1/a)[1 - \exp(-am)]$.

Dynamic Solutions and Instabilities of the Four-wave Mixing Interaction Utilising the Underlying SU(2) Group Symmetry

G. R. Barrett, A. K. Powell and T. J. Hall
Department of Physics
King's College London
Strand, London WC2R 2LS

Abstract

Optical phase conjugation is an important nonlinear process, with many applications in the areas of optical communications and optical processing. This is as a result of the wave-front correction properties that phase conjugation offers and this has generated much interest in the area. A common method of producing phase conjugated wavefronts is the four-wave mixing interaction and many publications on the steady state solution to this problem have appeared over the last decade. More recently, however, interest has been focussed upon the temporal behaviour of four-wave mixing systems, with instabilities and chaos being both demonstrated by Gauthier et al [1] and predicted by Królikowski et al [2].

To date, the analysis for the temporal behaviour of anisotropic four wave mixing, in the transmission grating regime, has involved the direct numerical integration of the equations describing four wave mixing. This analysis however, does not utilise the symmetries of the four wave mixing process, and thus results in a more complex problem. Through exploitation of these symmetries the complexity of the problem has been reduced from one containing four complex variables, to one containing three real variables. This has been accomplished through the use of the Special Unitary Group 2, a group providing a two dimensional matrix, whose elements are functions of three real variables. The multiplication of this matrix, together with one containing the boundary conditions for the problem, thus enables the four complex beam amplitudes to be reexpressed in terms of three real quantities. Using this technique, the temporal nature of anisotropic four wave mixing has been studied, and shown under certain conditions, to exhibit chaotic behaviour when an electric field is present. The effect of any material absorption on the chaotic nature is also demonstrated.

[1] Daniel J Gauthier, Paul Narum, and Robert W. Boyd, Phys. Rev. Let. Vol. 58 No. 16, 1640 (1987)

[2] W. Królikowski, M. R. Belc' M. Cronin-Golomb, Aleksander Bledowski, J. Opt. Soc. Am. B7, 1204 (1990)

AD-P006 762



Holographic recording and parametric scattering due to orthogonally polarized beams in BaTiO₃

L. Holtmann, E. Krätzig

FB Physik, Universität Osnabrück, W-4500 Osnabrück, FRG, tel. (0541) 6082653

M. Goukov, S. G. Odoulov

Institute of Physics, Ukrainian SSR Academy of Sciences,
252 650, Kiev, USSR, tel. (044) 2650818

B. Sturman

Institute of Automation and Electrometry, Siberian Branch of USSR
Academy of Sciences, 650 090, Novosibirsk, USSR, tel. (3832) 355270

Among the variety of photorefractive crystals BaTiO₃ distinguishes by its large nondiagonal electrooptic coefficient $r_{42} = 1600 \text{ pm/V}$ which enables efficient anisotropic diffraction [1, 2].

We report the first observation of anisotropic selfdiffraction from gratings arising in BaTiO₃ when two copropagating orthogonally polarized waves (ordinary and extraordinary) impinge in the crystal at an arbitrary angle in the plane perpendicular to the optical axis and discuss the possible origins of this effect. A nominally pure BaTiO₃ single crystal of dimensions $6.6 \times 4.4 \times 2.6 \text{ mm}$ is used. Two expanded beams of an argon laser ($\lambda = 515 \text{ nm}$) intersect inside the sample with the \vec{c} -axis directed normally to the plane of incidence (Fig. 1); both beams have nearly equal intensities (total intensity $\approx 6.5 \text{ kWm}^{-2}$).

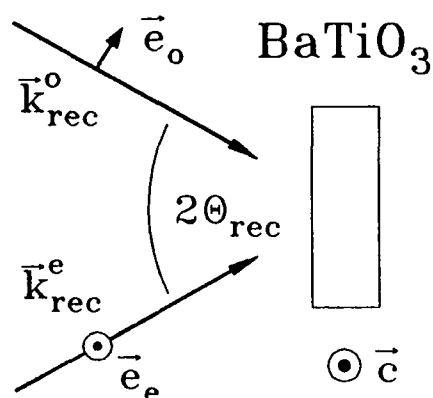


Figure 1: Experimental arrangement (schematically); an ordinary wave (wave-vector \vec{k}_{rec}^o , polarization \vec{e}_o) and an extraordinary one (\vec{k}_{rec}^e , \vec{e}_e) impinge on a BaTiO₃ crystal at an angle $2\theta_{rec}$.

Under these conditions the gradual development of a coupling between the two recording beams is observed. The largest steady-state diffraction efficiency of about 2×10^{-2} is reached for $2\theta_{rec} = 22^\circ$ (in air).

All observations indicate that a volume grating with the wavevector

$$\vec{K} = \vec{k}_{rec}^o - \vec{k}_{rec}^e$$

92-18750



is recorded in the crystal, where \vec{k}_{rec}^o , \vec{k}_{rec}^e are the wavevectors of the recording beams, and *o* and *e* denote ordinary and extraordinary polarization, respectively. Three different physical processes may lead to such a coupling.

1 Direct coupling of two orthogonally polarized waves

As BaTiO₃ crystals belong to the noncentrosymmetric point group 4mm they may exhibit a bulk photovoltaic effect [3, 4]. Particular spatially-oscillating currents may contribute to the recording of a grating with wavevector \vec{K} when two orthogonally polarized waves impinge in the crystal [5]. Such a type of recording is known for iron or copper doped LiNbO₃ and for LiTaO₃:Cu crystals [6].

Recording of gratings by those spatially-oscillating photovoltaic currents is most effective when the two waves intersect in the plane normal to the polar axis of the crystal.

2 Coupling of two incident waves via two-step diffraction from gratings recorded by similarly polarized waves

When studying anisotropic recording in BaTiO₃ we observe also a light-induced scattering cone [7] (Fig.2). This scattering appears due to *isotropic (diffusion type)* recording of pairs of gratings with wavevectors

$$\vec{K}_1 = \vec{k}_{rec}^o - \vec{k}_{sc2}^o \quad \text{and} \quad \vec{K}_2 = \vec{k}_{sc1}^o - \vec{k}_{rec}^o \quad (2)$$

with subsequent anisotropic readout of those gratings by another recording wave (Fig. 3)

$$\vec{k}_{sc1}^o = \vec{k}_{rec}^e + \vec{K}_1 \quad \text{and} \quad \vec{k}_{sc2}^o = \vec{k}_{rec}^e - \vec{K}_2 \quad (3)$$

where \vec{k}_{sc1}^o , \vec{k}_{sc2}^o are the wavevectors of scattered light.

When the gratings with wavevectors \vec{K}_1 and \vec{K}_2 appear, the two-step Bragg-matched diffraction of an ordinary wave into an extraordinary one (or vice versa) becomes possible. The two-step diffraction from gratings with wavevectors \vec{K}_1 and \vec{K}_2 produces a wave propagating in the same direction as the wave diffracted directly from the grating with wavevector \vec{K} . It has been shown recently that the two-step diffraction of similar nature couples two extraordinary waves intersecting in the plane normal to the \vec{c} -axis of LiNbO₃:Fe, i. e. in a geometry where neither direct photovoltaic recording nor direct readout are possible [8].

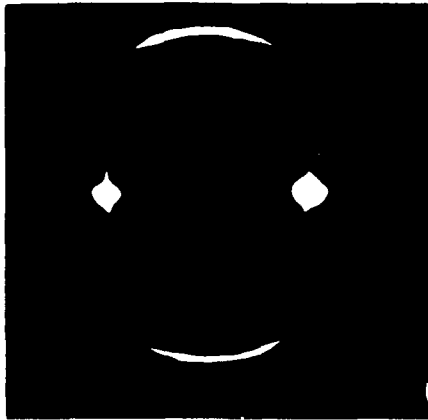


Figure 2: Typical scattering patterns obtained with the arrangement of Fig. 1.

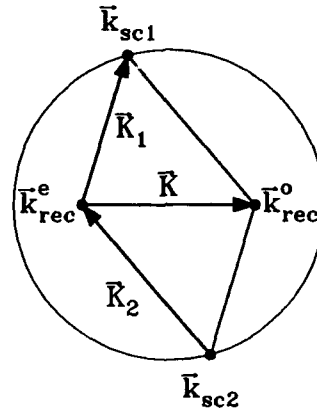


Figure 3: Schematic representation of the model for the scattering and diffraction processes

3 Coupling of two incident waves arising from nonlinear mixing of scattering gratings

Due to the nonlinearity of the recording process in photorefractive crystals the appearance of two gratings with wavevectors \vec{K}_1 and \vec{K}_2 will result in recording of additional gratings with sum and difference spatial frequencies, $\vec{K}_1 \pm \vec{K}_2$ [9]. The sum gratings for various pairs of scattered waves along the cone will be all individual, while the difference gratings will superimpose and result in a grating with the wavevector (Fig. 3)

$$\vec{K} = \vec{K}_1 - \vec{K}_2. \quad (4)$$

4 Discussion

To distinguish between the two possibilities of diffraction (two-step or one-step) we measure the angles of Bragg diffraction at another wavelength $\lambda = 633$ nm. If a grating with the wavevector \vec{K} does exist in the crystal it may be read by a wave with another wavelength. From Bragg's condition one can deduce the relations between the angles Θ_{rec} , Θ_{rd}^o and Θ_{rd}^e . In Fig. 4 the calculated and the measured dependences of $\Theta_{rd} = f(\Theta_{rec})$ are compared for recording at 515 nm and readout at 633 nm. Perfect agreement is quite evident clearly indicating the existence of the grating with wavevector \vec{K} in the sample.

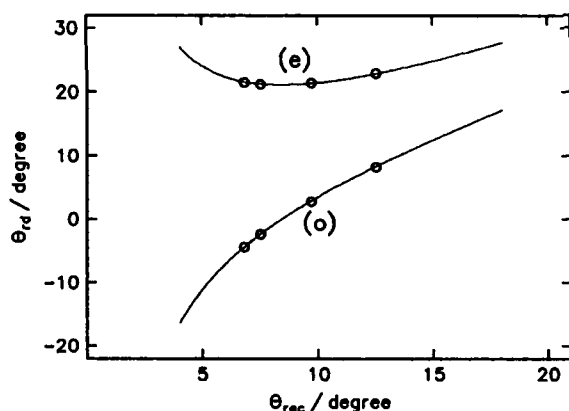


Figure 4: Dependence of the anisotropic readout angles $\Theta_{rd}^{o,e}$ (o and e denote ordinary and extraordinary polarization) on the recording angles Θ_{rec} for a recording wavelength of 515 nm and a readout wavelength of 633 nm.

Furthermore, it is necessary to clarify whether this grating is recorded by spatially oscillating photovoltaic currents or by a nonlinear mixture of the gratings recorded by the incident waves with the scattered waves. To answer this question we study the dynamics of coupling of the incident light waves while vibrating the crystal in the direction of its \vec{c} -axis.

The sample is mounted on a piezodriver and shifted periodically in the direction normal to the plane of incidence of the pump waves. A sinusoidal voltage with amplitude U is applied to the piezoelement providing a displacement of several microns. The intensity of the light scattered into the cone of ordinary waves and the diffraction efficiency of the recorded grating are monitored continuously (Figs. 5,6).

For $U = 0$ V the diffraction efficiency η is rapidly increasing up to a certain comparatively small saturation value at the initial stage of recording. Then, with increasing time we observe a continuous but more slow rise of η reaching a much larger saturation value. The comparison

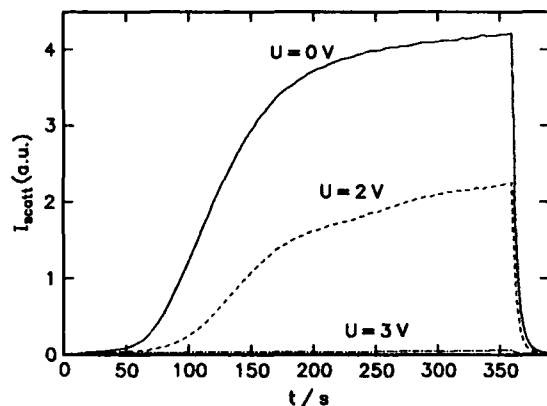


Figure 5: Intensity I_{scatt} of scattered light versus time t for different piezodriver voltages U

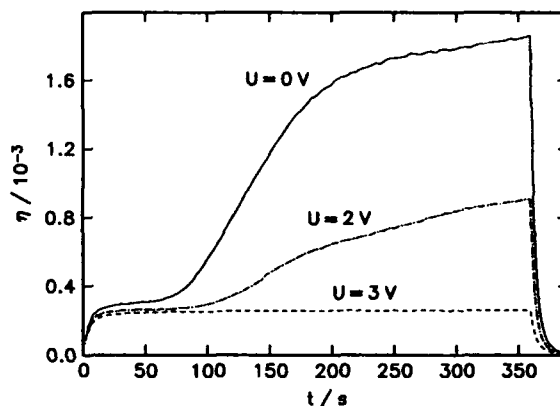


Figure 6: Diffraction efficiency η of a grating with the wavevector \vec{K} versus time t for different piezodriver voltages U

with the dynamics of the scattered light shows that the second increase of η just coincides in time with the development of the light-induced scattering. This partial correlation suggests the hypothesis of two different mechanisms of coupling, one connected and another not connected with the light-induced scattering.

The experiment with the vibrating crystal proves this hypothesis more clearly. When the piezo-driver is moving during the recording the steady-state intensity of scattered light is diminishing; also the saturation value of diffraction efficiency is decreasing. But the diffraction efficiency obtained in the initial part of recording is practically not affected by the vibrations of the crystal. For a piezodriver voltage of $U = 3$ V the scattered light is no more visible and the diffraction efficiency saturates at the level reached before the onset of scattering. The scattering gratings \vec{K}_1 and \vec{K}_2 and also the difference grating $\vec{K}_1 - \vec{K}_2$ cannot appear. Thus we conclude that for the nominally pure BaTiO₃ crystal we really observe grating recording by spatially-oscillating photovoltaic currents excited by two orthogonally polarized waves.

Acknowledgement. Financial support by the Deutsche Forschungsgemeinschaft (SFB 225) is gratefully acknowledged.

References

- [1] M. P. Petrov, S. I. Stepanov, A. A. Kamshilin, *Optics and Laser Technology* **79**, 149 (1979).
- [2] N. V. Kukhtarev, E. Krätzig, H. C. Külich, R. A. Rupp, J. Albers, *Appl. Phys. B* **35**, 17 (1984).
- [3] A. M. Glass, D. v. d. Linde, T. J. Negran, *Appl. Phys. Lett.* **25**, 233 (1974).
- [4] V. Belinicher, B. Sturman, *Sov. Phys: Uspekhy* **23**, 199 (1980).
- [5] S. Odoulov, *Sov. Phys.: JETP Lett.* **35**, 10 (1982).
- [6] S. Odoulov, *Ferroelectrics* **91**, 213 (1989).
- [7] S. Odoulov, B. Sturman, L. Holtmann, E. Krätzig, accepted by *Appl. Phys.* (1991).
- [8] M. Goulikov, S. Odoulov, *Ukrainian Phys. J.* **36**, 530 (1991).
- [9] R. Rupp, H. C. Külich, U. Schürk, E. Krätzig, *Ferroelectrics Lett.* **8**, 25 (1987).

PARAMETRIC SCATTERING OF LIGHT IN PHOTOREFRACTIVE LiNbO_3 CRYSTALS

K.N.Zabrodin, A.N.Penin, N.M.Rubinina

*Department of Physics/Quantum Radiophysics, Moscow State
University, Moscow, 119899, USSR*

1. A few years ago in photorefractive crystals of $\text{LiTaO}_3:\text{Cu}$ [1] and $\text{LiNbO}_3:\text{Cu}$ [2] a new nonlinear optic phenomenon, called the parametric scattering of "holographic type", has been observed. As in the case of well-known [3] wide-angle species of photoinduced scattering, this process was degenerate. But it occurred under condition of phase-matching for four coupling waves:

$$2\mathbf{K}_L(\omega) = \mathbf{K}_{S1}(\omega) + \mathbf{K}_{S2}(\omega), \quad (1)$$

and hence had narrow spatial spectrum, where $\mathbf{K}_L, \mathbf{K}_{S1}, \mathbf{K}_{S2}$ are the wave vectors of the pump and two phase-conjugated scattered waves on frequency ω . The scattered radiation was polarized orthogonally in respect to the laser beam. So in LiNbO_3 ($n_o < n_e$) the scattering $ee \rightarrow oo$ took place at the angle $\theta_s = \hat{\mathbf{K}}_L \hat{\mathbf{K}}_{S1} = \hat{\mathbf{K}}_L \hat{\mathbf{K}}_{S2} = \arcsin \sqrt{n_o^2 - n_e^2} \approx 42^\circ$ for $\lambda = 0.5 \mu\text{m}$ (o-ordinary, e-extraordinary polarized waves).

As it has been ascertained by Odulov, Sturman, Obukhovskii [1-5], the degenerate parametric scattering is connected with electrooptic refractive index modulation by an internal electrostatic field. This latter is being formed over Maxwell time $\tau_M = \epsilon / 4\pi\sigma_{ph}$ (σ_{ph} -photoconductivity) as a result of a bulk spatially-oscillating photovoltaic current. Its magnitude depends on polarization and intensity of light in the crystal.

This paper is mainly concerned with the study of temporal dynamics of the degenerate parametric scattering setting up. Besides that a number of the scattering new properties have been observed.

2. To clear up the question of holographic parametric scattering existence, the plates of LiNbO_3 monocrystals doped with different activators (Fe, Cu, Mg, Zn, Nd, Sn, Ti-ions) have been investigated. The scattering was only noted when illuminated x- or y-cuts of the crystals doped with Cu (0.5 wt.%) and in the samples with binary doping with Cu(0.5 wt.):Ti(0.5 wt.%). Adding of titanium ions not affected much on the scattering characteristics. The excitation by

92-18751

an Ar-laser (TEM₀₀-mode, $\lambda=514.5\text{nm}$) was turned out to be of maximum efficiency. The reverse process of $oo \rightarrow ee$ type was detected in the samples doped with Fe. Two o-polarized beams intersected at the synchronism angle $2\theta_s = \hat{K}_{L1} \hat{K}_{L2}$ caused the appearance after the crystal of normally propagated e-waves:

$$K_{L1}(\omega) + K_{L2}(\omega) = 2K_S(\omega)$$

This fact supports the conclusion of [2] that the effective nonlinearity χ_{eff} imaginary part sign is determined by an activator species, i.e. $\text{Im}\chi_{eff}(:\text{Fe}) = -\text{Im}\chi_{eff}(:\text{Cu})$.

3. The results of the measurements of stationary scattering intensity $I_{S1}=I_{S2}=I_S$ versus pump intensity I_L are shown on Fig.1. The curves have a highly nonmonotonic character, the maximum of transformation conforms to $I_L \approx 5 \text{ W/cm}^2$ for all samples.

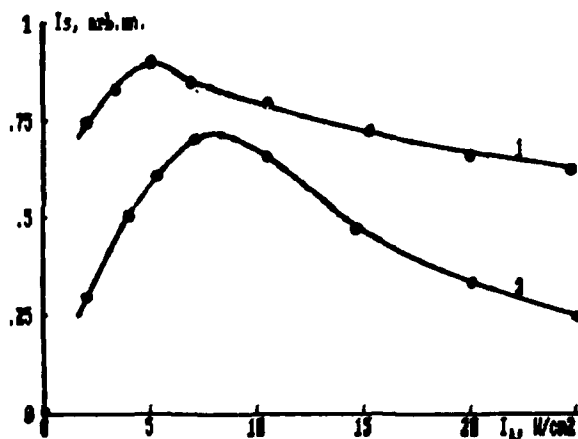


Fig.1. Plot of stationary scattering intensity I_S versus pump intensity I_L : 1-LiNbO:Cu, 2-Cu:Ti

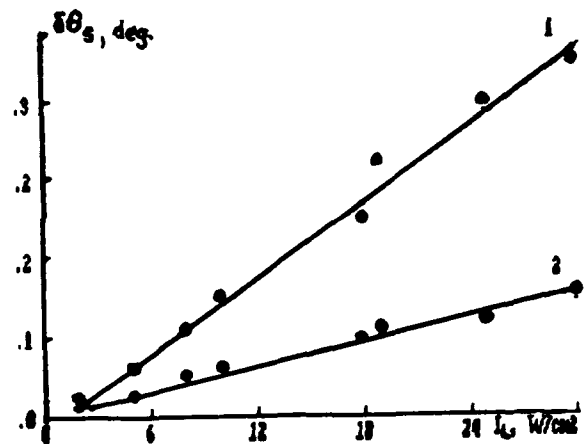


Fig.2. Plot of angle of phase mismatching $\delta\theta_s$ versus pump intensity I_L : 1-LiNbO:Cu, 2-Cu:Ti

Next, we have observed a significant decreasing, by 0.4° , of the scattering angle θ_s and, hence, of the birefringency $\Delta(n_o - n_e)$ by $1 \cdot 10^{-3}$ as the pump intensity I_L increases by 30 W/cm^2 . The measurement of $\delta\theta_s(I_L)$ allows to estimate the magnitude of $\text{Re}\chi_{eff}(:\text{Cu}) = 2\text{Re}\chi_{eff}(:\text{Cu:Ti}) \approx 10^{-2} \text{ cm}^3/\text{erg}$. Again, it is interesting that $\Delta(n_o - n_e)$ was linear with I_L , even though $\sigma_{ph} \gg \sigma_d$ (σ_d -dark conductivity). This result conforms well with the model of photovoltaic effect in lithium niobate proposed by Pashkov [6], according which, first occurs the excitation of carriers from a deep level into a shallow one and next the ionisation of the latter takes place.

4. At Fig.3 the experimental measurements of the scattering dynamics $I_s(t)$ are displayed by the circles. The parameter of the curves is the pump intensity I_L . The solid lines here shows the results of numerical solution of the coupled waves equations and of the relaxation equation for the space charge field obtained in [7] in approximation of the linear photogeneration $\sigma_{ph} \propto \sigma_d I_L$.

For the scattering dynamics analysis the nonlinear optics consideration is useful. Hence, the effective third order non-linearity χ_{eff} may be thought of as a function of time. This approach is justified by an experiment. In that the dependence of normalized intensity versus exposed energy, i.e. $I_s(I_L t)/I_L$, turned out to be the universal characteristic of the crystal. The curves 1-5 Fig.3 plotted in coordinates $(I_L t)$, (I_s/I_L) are coincide. At the initial moment χ_{eff} is small and subsequently increases by four or five orders.

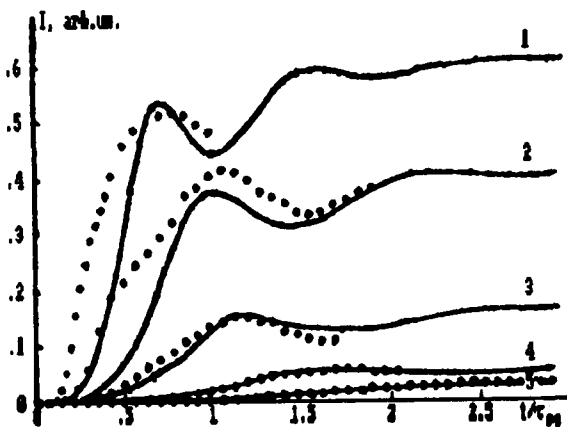


Fig.3. Plot of scattering dynamics, i.e. signal intensity I_s vs time t , curves parameter-pump intensity I_L , 1-5.0; 2-3.2; 3-1.7; 4-0.9; 5-0.6 mW/cm²

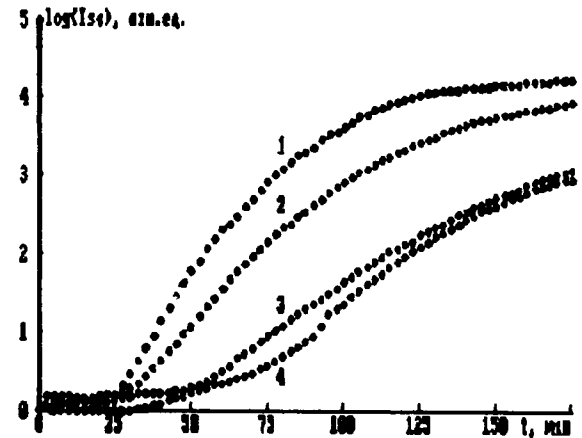


Fig.4. Scattering dynamics, i.e. signal intensity I_{s1} vs time t , curves parameter-additional beam intensity I_{s0} : 1-3.5; 2-1.7; 3-0.2; 4-0 mW/cm².

In view of the mentioned above facts, by analogy with another nonlinear processes, we may separate three characteristic sections in $I_s(t)$ dependence. At the initial *spontaneous* stage the scattering intensity is slightly time dependent. It is determined exclusively by an interaction of the pump wave and some optical noise that plays a role of the "seed" for the scattering. Later, after χ_{eff} reached the value great enough for I_s to become of order of the primary noise intensity, the positive feedback of the scattering is "switching on". Now the velocity of χ_{eff} increasing,

that is the velocity of the holographic grating writing, is depends on the laser and scattered waves intensity. The parametric scattering converts to the *stimulated* regime followed by an exponential signal enlarging. Finally at the last stage the scattering *saturates*. The nonlinearity mounts up to its stationary magnitude depended on photoconductivity.

5. To define the mechanism which is the noise inducing spontaneous scattering due to, the dynamics of signal intensity $I_{s1}(t)$ (Fig.4) was measured with the additional external illumination by o-polarized coherent wave in the direction of K_{s2} . The illumination intensity I_{s2}^o is curves parameter here and the pump was fixed $I_L \approx 0.3 \text{ W/cm}^2$. For $I_{s2}^o \geq 5 \text{ mW/cm}^2$ the parametric process was suppressed and a usual two beam coupling took place. For $I_{s2}^o \approx 0.2 \text{ mW/cm}^2$ the illumination had no effect on temporal dynamics of the scattering (compare curves 3 and 4). This fact gives us opportunity to suppose the primary noise intensity to be of the same order. An estimate of the spectrum brightness $I_{\omega\Omega} = I / \Delta\omega\Delta\Omega$ ($\Delta\omega$ -frequency-response, $\Delta\Omega$ -angular spectrum width of radiation) of laser Rayleigh scattering from the crystal bulk and volume inhomogeneities gives $I_{\omega\Omega}^{RL} \ll I_{\omega\Omega}^o$, $I_{\omega\Omega}^o$ -the brightness of the additional illumination. On the other hand $I_{\omega\Omega}^o \sim I_{\omega\Omega}^{vac} = \hbar\omega / 2\pi\lambda^2$, where $I_{\omega\Omega}^{vac}$ -the brightness of the quantum noise, known to induce three- and four-wave parametric oscillator luminiscence [8].

-
- [1]. S. Odulov, K. Belabaev, I. Kiseleva, *Opt. Letts.*, **10**, 31 (1985).
 - [2]. I. Kiseleva, V. Obukhovskii, S. Odulov, *Sov. Phys.-Solid State*, **28**, 1673 (1986).
 - [3]. J. Marotz, K. H. Ringhofer, A. R. Rupp, S. Treichel, *IEEE J. of QE*, **QE-22**, 1376 (1986)
 - [4]. B. Sturman, *Sov. J. Quantum Electron.*, **10**, 276 (1986),
 - [5]. V. Obukhovskii, *Ukrainskii Fizich. Zh.*, **31**, 67 (1986) (in Russian).
 - [6]. A. Onischenko, V. Pashkov, S. Topchii, *Sov. Phys.-Solid State*, **28**, 1784 (1986),
 - [7]. N. Kukhtarev, B. Pavlic, T. Semenets, *Phys. Stat. Sol. (a)*, **94**, 623 (1986).
 - [8]. D. Klyshko, "*Photony i nelineynaya optika*", Moskva, Nauka, (1980) (in Russian).



Forward Phase-Conjugate Wave in Degenerate Four-Wave

Mixing (DFWM) in Photorefractive Crystalline Slab

H. Y. Zhang and X. H. He

Department of Physics, Beijing University

Beijing, P. R. China

S. H. Tang

Department of Physics, National University of Singapore

Singapore 0511, Singapore

DFWM as an useful tool to generate phase conjugate waves has recently been the subject of intensive study. In particular, photorefractive crystals such as LiNbO_3 , KNbO_3 , BaTiO_3 and SBN are widely used^[1]. Among the published papers on DFWM most are concerned with backward phase conjugate waves and only a few with forward phase conjugate waves.^[2,3] In both of these papers the intensity of the forward phase conjugate wave has not been investigated. We report here a systematic study of the intensity of forward phase conjugate wave.

The geometry of interaction for DFWM inside a P.R. crystal is shown in Fig. 1. A He-Ne laser was used as the light source. Two pump beams A_1 and A_2 impinge on the crystalline slab perpendicularly along opposite directions +Z and -Z respectively. The thickness of the P.R. crystalline slab is $L = 0.8$ mm along the Z axis. The signal beam A_4 with incident angle $\theta = 33^\circ$ is reflected by the rear surface of the crystal (at the $Z = L$ surface). The interaction of A_1 , A_2 and A_4 through four-wave mixing processes gives rise to the backward phase conjugate wave A_{pb} . Similarly A_r can be considered as a signal beam. The four-wave interaction of A_1 , A_2 and A_r gives rise to the forward phase conjugate wave A_{pf} .

The phase conjugation of the signal beam can be verified by placing a film containing an image in the path of the signal beam. Good quality real images were observed in the planes S_r and S_b at same distances from the crystalline slab as shown in Fig 1. The build-up curves for the backward phase conjugate wave P_{pb} and the forward phase conjugate wave P_{pf} are shown in Fig 2. The backward phase conjugate wave is reflected off by the beam splitter BS_3 . The intensity of backward phase conjugate wave is equal to $P_{pb} = P'_{pb}/R =$

$$\frac{1}{0.45} P'_{pb}$$

92-18752



The behavior of the intensity of forward phase conjugate wave is studied by blocking pump beam P_1 , or pump beam P_2 , or both of them. When the pump beam P_1 is blocked, the intensity P_{pb} of the backward phase conjugate wave decreases by only 5% of its original intensity. When P_1 is blocked the intensity of the forward phase conjugate wave P_{pr} decreases by a large margin, to a low value of $13 \mu\text{W}$. This contribution arises from the reflection of the backward phase conjugate wave P_{pb} at the front surface of the crystalline slab. It can be estimated by considering the reflectivity $R_s = 14\%$ of the front surface, the attenuation due to the absorption α of $\text{LiNbO}_3\text{:Fe}$ crystal and the reflection loss at the rear surface. The intensity P_{pb} is equal to $P'_{pb} = \frac{75 \mu\text{W}}{0.45} = 166 \mu\text{W}$. The absorption coefficient of the $\text{LiNbO}_3\text{:Fe}$ crystal is $\alpha = 4 \text{ cm}^{-1}$ at $\lambda = 633 \text{ nm}$. The intensity of the reflected wave is estimated to be $166 \times R_s \times e^{-\alpha L} (1 - R_s) = 14 \mu\text{W}$, which is very close to the measured value of $P_{pr} = 13 \mu\text{W}$.

When pump beam P_2 is blocked, P_{pr} sheds off nearly 30% of its original intensity whereas P_{pb} becomes negligibly small. This loss of 30% is attributed mainly to the absence of contribution from P_{pb} reflected off by the front surface. With P_2 blocked the intensity of P_{pr} is measured to be $47 \mu\text{W}$. It arises from the diffraction of P_1 by the transmission grating formed by A_2 and A_r .

The analysis leads to the conclusion that the observed forward phase conjugate wave contains two main contributions: the major one is the phase conjugate wave of P_r and the lesser one the reflection of the backward phase conjugate wave P_{pb} at the front surface of the crystalline slab.

The relationship of the ratio P_{pr}/P_{pb} against the ratio P_1/P_2 was investigated. The results are shown in Fig. 3. Fig. 3 shows a linear relationship between $\frac{P_{pr}}{P_{pb}}$ and $\frac{1}{P_2}$. The relationship $P_{pr} \propto P_{pb}$ further implies

that when the ratio $\frac{P_1}{P_2}$ is sufficiently large P_{pr} will be stronger than P_{pb} . This is demonstrated in Fig. 3 where it is seen that when $\frac{P_1}{P_2} = 6.5$, $P_{pr} = 2P_{pb}$. The build-up traces of P_{pr} and P_{pb} against time for $\frac{P_1}{P_2} = 6.5$ is shown in Fig. 4.

References

- 1 P. Günter
Physics Reports 93 No 4 (1982) 199.
- 2 Vladimir Kondilenko, Serguer Odoulov and Marat Soskin
Ferroelectrics Letters 1 (1983) 19
- 3 A. Bledowski, W. Krodikowski and A. Kujawski
Optics Communications 61 (1987) 71-74

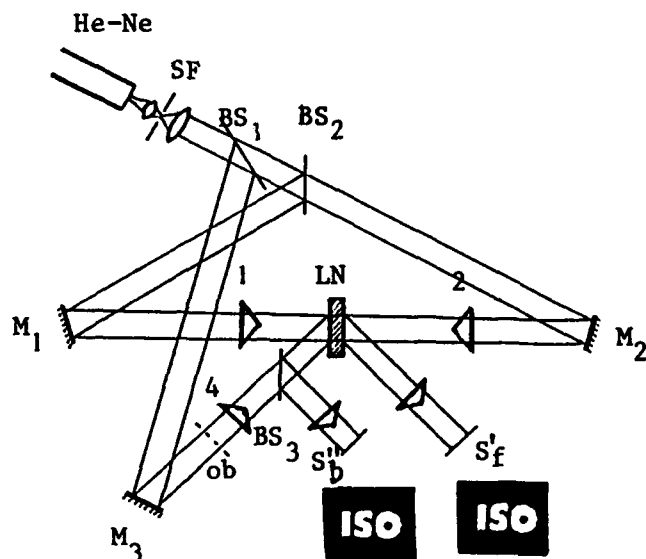


Fig 1 : Experimental set-up, LN is $\text{LiNbO}_3\text{:Fe}$ Crystal.

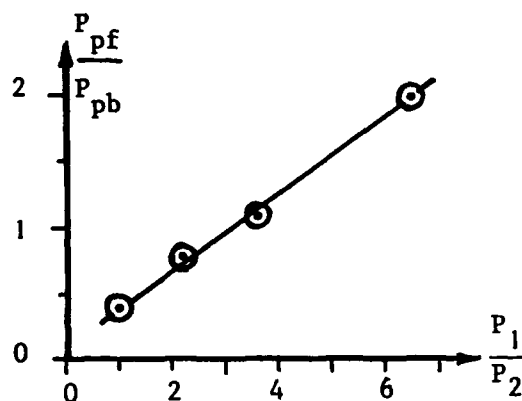


Fig 3 : The diagram of ratio $\frac{P_{pf}}{P_{pb}}$ against pumping P_{pb} power ratio $\frac{P_1}{P_2}$.

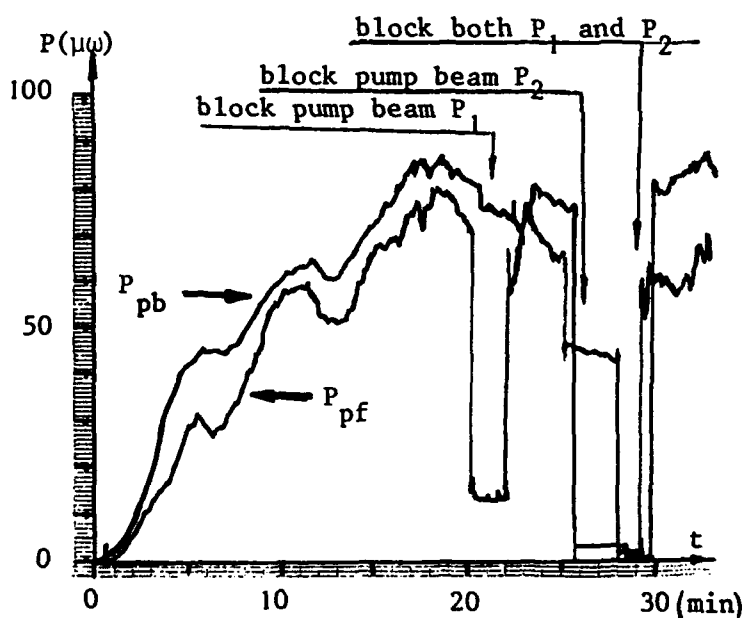


Fig 2 (a) : The recording traces of forward phase conjugation wave P_{pf} and backward phase conjugation wave P_{pb} , while pump beam $P_1=P_2=1.7$ mW. The contributions of different refractive index gratings to P_{pf} and P_{pb} are showed by blocking pump beam P_1 , P_2 and both P_1 and P_2 respectively.

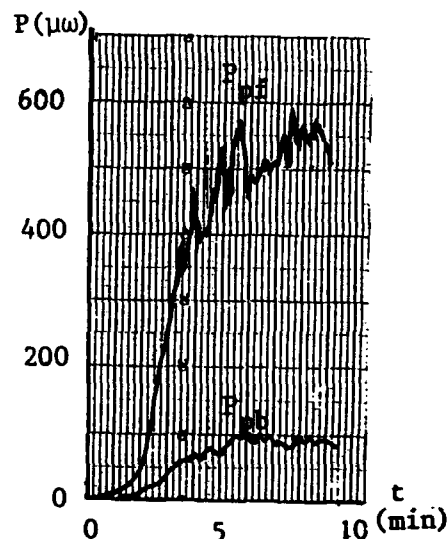


Fig 2 (b) : The recording traces of P_{pf} and P_{pb} for pumping power ratio $P_1/P_2 = 65$.

AD-P006 765



PHOTOINDUCED CHARGE TRANSPORT IN OPTICAL DAMAGE RESISTANT
LiNbO₃:Me (Me = Mg,Zn)

T.R.Volk, M.A.Ivanov, F.Ya.Shchapov, N.M.Rubinina*

Institute of Crystallography SU Acad Sci 117333 Moscow
Moscow State University,

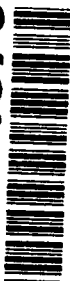
Photoinduced charge transport in LiNbO₃ is defined by presence of a Fe-like impurity, Fe²⁺ being the donor, Fe³⁺ - the acceptor of electrons¹. Two level scheme gives the linear dependence of photoconductivity (that is of inverse response times of photorefraction) on the light intensity².

We discuss the influence of Me impurities (Me = Mg,Zn), provided for optical damage resistance in LiNbO₃, on photoelectric phenomena. Me impurity affects photoconductivity of LiNbO₃ rather than photovoltaic properties^{3,4}. Investigations of charge transport phenomena in LiNbO₃:Me reveal some threshold Me concentrations (5.5 mol.%Mg³ or 7.7 mol.%Zn⁴) which coincide with those in optical measurements.

Firstly we describe the results for LiNbO₃:Me with Me concentrations lower than the thresholds. The dependence of photorefraction on exposure time obeys the usual law $\delta\Delta n(t) = \delta\Delta n_0(1 - \exp(-t/\tau_m))$, where $\tau_m = \epsilon/4\pi\sigma$, σ - photoconductivity. In light intensity range $10^{-3} - 5 \cdot 10^2$ Wt/cm² photoconductivity shows sublinear dependence on light intensity $\sigma \propto I^X$ ($0.5 < X < 1$). However if these crystals are additionally doped with low Fe concentration, then σ on intensity obeys linear law. For example in LiNbO₃:2mol.%Zn $\sigma = 9 \cdot 10^{-14} I^{0.75}$ cm/Ohm*Wt, while in LiNbO₃:2mol.%Zn:0.02mol.%Fe $\sigma = 0.7 \cdot 10^{-13} I$ cm/Ohm*Wt (fig.1). Photoconductivity in LiNbO₃:Me is higher than in pure LiNbO₃.

These results are explained as follows. Sublinear dependence σ vs I in LiNbO₃:Me as in BaTiO₃⁷ is due to shallow traps. As photoconductivity in LiNbO₃:Me significantly increases compared to pure LiNbO₃, so shallow trap levels are Me²⁺ centers substituting for Li⁺ sites. In LiNbO₃ and obviously in LiNbO₃:Me charge transport phenomena are defined by accidental Fe-like impurities with concentration $< 10^{17}$ cm⁻³ (correspondingly to ESR data). In LiNbO₃:Me where Me

92-18753



concentration is of about 10^{20} cm^{-3} (fig.1) exceeding essentially that of Fe-like acceptors. Me^{2+} traps influence electron transport process. However in $\text{LiNbO}_3:\text{Me}:\text{Fe}$ with Fe concentration of about 10^{18} cm^{-3} (fig.1), the dependence σ vs I is described by linear law coinciding with the dependence for $\text{LiNbO}_3:\text{Fe}^6$. Thus in $\text{LiNbO}_3:\text{Me}:\text{Fe}$ Me^{2+} -traps are not involved in charge transport. That means that their capture cross-section of electrons is much lower than that of Fe^{3+} -like acceptors. Hence in $\text{LiNbO}_3:\text{Me}$ photoconductivity can be described by 'three-level' scheme including Fe-like donor-acceptor pair and Me^{2+} -traps with extremely low capture-cross section of electrons. Solving the kinetics equation we obtain a photoconductivity increase compared to pure LiNbO_3 and its sublinear dependence on light intensity in accordance with experimental results.

Doping with Me exceeding the thresholds, followed by photorefractive decrease by two orders of the value, leads to sharp change of capture centers. It was demonstrated in experiments in X-ray induced optical absorption^{3,5}.

X-irradiating at room temperature induces in LiNbO_3 and $\text{LiNbO}_3:\text{Fe}$ a stable broad band in visible revealing two maxima (fig.2). Maximum at about 500 nm is due to increase of Fe^{2+} concentration because of trapping interband electrons by Fe^{3+} acceptors: $\text{Fe}^{3+} + e^- = \text{Fe}^{2+}$. Maximum at 380 nm seems to be connected with some intrinsic hole-trapped centers (for example V_{Li}^-). X-ray induced spectra in $\text{LiNbO}_3:\text{Me}:\text{Fe}$ and $\text{LiNbO}_3:\text{Me}$ with Me up to the thresholds demonstrate the same behaviour (fig.2) in accordance with above scheme of levels.

If Me concentrations exceed the thresholds, X-ray induced spectra sharply differ from those. Now they demonstrate the single unstable maximum 380 nm (fig.2) quickly fading in darkness. Thus in these crystals X-irradiation does not induce Fe^{2+} . That means that capture cross-section of electrons by Fe^{3+} center is sharply reduced so that Fe^{3+} loses its acceptor properties.

These results are in agreement with the data on X-irradiation at liquid nitrogen temperature (LNT). LNT X-ray induced spectrum of LiNbO_3 (and of low-doped $\text{LiNbO}_3:\text{Me}$) is a

broad non-resolved band in visible⁸ due to electron capturing both by Fe^{3+} -like acceptors and by shallow traps which are ionized at room temperature (fig.3). If Me concentration exceeds the threshold, the intensity of this band is by the order of the value lower than that in LiNbO_3 (fig.3). These results also indicate that high-level Me doping reduces cross-sections of capture Fe^{3+} centers in LiNbO_3 and creates new ones.

In summary in $\text{LiNbO}_3:\text{Me}$ with Me lower than the thresholds Me centers take part in photoinduced charge transport as shallow traps, while at higher concentrations they alterate the types of electron acceptors involved in charge transport. Mg^{2+} was supposed to be the electron acceptor in highly-doped $\text{LiNbO}_3:\text{Mg}^{3+}$.

-
1. E. Kratzig, R. Orlovski Appl. Phys. 15, 133, 1978
 2. N. V. Kukhtarev Sov. Tech. Phys. Letts. 2, 437, 1976
 3. D. A. Bryan, R. Gerson e. a. Appl. Phys. Lett. 44, 847, 1984
 4. T. R. Volk, N. M. Rubinina e. a. Ferroelectrics 109, 345, 1990
 5. T. R. Volk, N. M. Rubinina Phys. Stat. Solidi (a) 108, 437, 1988
 6. A. M. Glass, D. von der Linde e. a. J. Electr. Mater. 4, 915, 1975
 7. S. Ducharme, J. Feinberg J. Appl. Phys., 56, 839, 1984
 8. D. von der Linde, O. F. Shirmer, H. Kurz Appl. Phys. 15, 153, 1078

Fig. 1

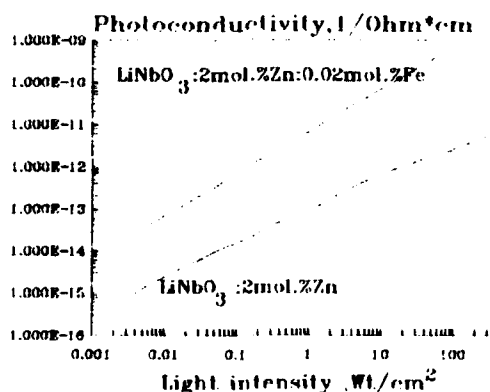


Fig.2 (room temperature)

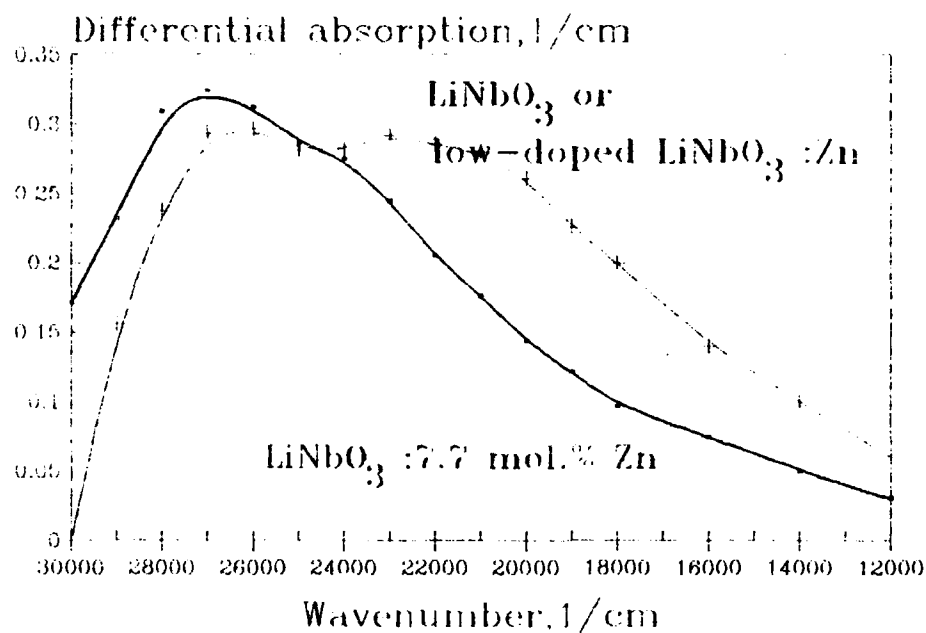
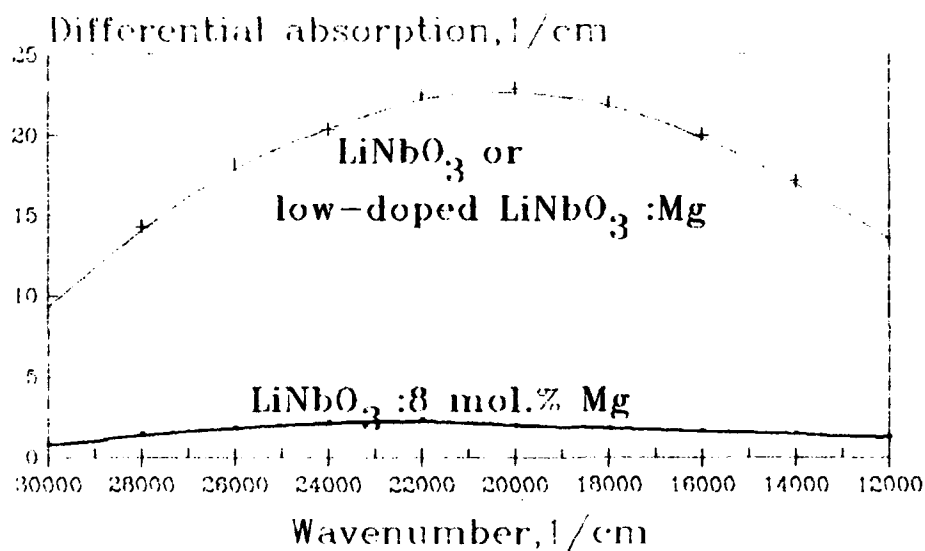


Fig.3 (liquid nitrogen temperature)



(differential spectra are obtained by
subtracting the initial spectra from
the spectra of X-irradiated crystals)



OPTICAL DAMAGE RESISTANT IMPURITIES IN LITHIUM NIOBATE.

T.R. Volk, N.M. Rubinina* and S. Stizza**

Institute of Crystallography Acad.Sci., Moscow

117333 Moscow USSR, Leninsky prospect 59

*Moscow State University, **Universita di Camerino (Italy)

Magnesium¹⁻³, zinc⁴⁻⁶ and some other impurities (substituting mainly for the lithium sites) drastically change optical properties of LiNbO_3 . In particular the value of optical damage (photorefraction) in $\text{LiNbO}_3:\text{Me}$ ($\text{Me} = \text{Mg}, \text{Zn}, \dots$) is sharply reduced compared with undoped LiNbO_3 ²⁻⁶. Similarly Me impurities tend to suppress so-called "dark trace" effect⁴⁻⁶ (that means stable darkening under intensive visible laser radiation).

The dependences of optical properties on Me concentrations demonstrate some common features. First of all they reveal 'threshold' concentration values (5.5 mol.% Mg²⁻⁴ or 7.7 mol.% Zn⁴⁻⁶ for congruent LiNbO_3) which correspond to step like change of optical properties such as IR-absorption and ESR spectra²⁻⁶, luminescent characteristics^{7,8} and nonlinear-optical parameters³⁻⁶ (fig.1).

The dependences of phasematching temperatures vs Me concentrations reveal maxima in the threshold concentration ranges (fig.1). In $\text{LiNbO}_3:\text{Zn}$ the maximum is more flat than in $\text{LiNbO}_3:\text{Mg}$. In threshold concentration ranges photorefraction both in $\text{LiNbO}_3:\text{Mg}$ and $\text{LiNbO}_3:\text{Zn}$ is decreased at least by two orders of magnitude compared with pure crystal (fig.2). Thus optical damage resistant $\text{LiNbO}_3:\text{Me}$ crystals with over-threshold Me concentrations can be used as frequency doublers at about room temperature.

In threshold Me concentration ranges the OH^- absorption band 2.87 μm , which is characteristic of LiNbO_3 shifts toward 2.83 μm (fig.3). In $\text{LiNbO}_3:\text{Mg}$ the shift takes place in the concentration range 4.8 - 5.5 mol.% Mg while in $\text{LiNbO}_3:\text{Zn}$ the

92-18754



band shifts in more wide range 6.7 - 7.7 mol.%Zn^{4,5}. In the intermediate concentration range IR spectra reveal simultaneously the both bands (fig.3).

The most pronounced threshold effects are manifested in ESR measurements²⁻⁶. In LiNbO₃:Me:Fe up to Me thresholds the positions of ESR lines connected obviously⁹ with axially symmetric Fe³⁺ are the same as in LiNbO₃:Fe whereas the shape of lines smoothly changes with Me concentration increasing. At 5.5 mol.% Mg or 7.7 mol.%Zn the shape of the spectra changes in a step-like manner revealing a set of new lines, whose intensities are proportional to Fe concentration in the crystal. Note that these Me concentrations correspond to whole 'over-pumping' IR absorption to the short-wave bands (fig.3). Exactly these Me concentrations in LiNbO₃ suppress the acceptor properties of Fe³⁺-like centers and of other capture levels^{4,10} resulting in sharp alteration of photoinduced charge transport. Simultaneously the intensity of UV-excited luminescence in LiNbO₃:Mg⁷ and LiNbO₃:Zn⁸ begins to increase, when Me concentrations exceed the thresholds.

The results allow to conclude that 'threshold' Me concentrations mean a change of Me location in LiNbO₃ lattice. In low-doped LiNbO₃:Me Me²⁺ ions seem to substitute for Li⁺. At Me concentrations exceeding the thresholds, Me ions can be supposed to substitute for Nb⁵⁺ sites. The change of ESR spectrum might mean the alteration of Fe³⁺ location in the lattice. In contrast as photovoltaic properties and optical absorption in visible are not influenced by Me presence^{9,10}, so Fe²⁺ location seems to be unaffected. In LiNbO₃:Zn all the 'threshold' phenomena are less pronounced than in LiNbO₃:Mg (fig.1,3). As Zn is more amphoteric than Mg, the former is likely to substitute simultaneously both for Li and Nb sites in a respectively large concentration range.

The investigations of Mg and Zn parameters in LiNbO₃ lattice by means of EXAFS method are in progress.

References:

1. Gi Guo Zhong, Jin Jian, Zhong Kong Wu Proc. 11 Int. Quantum Electronic Conf. IEEE Cat.N 80,CH 1561-0,1980, 631
2. Bryan D.A.,Gerson R.,Tomaschke Appl.Phys.Letts. 1984 44,847
3. Bryan D.A.,Rice R.R., Gerson R.,Tomaschke H.E.,Sweeney K:L., Halliburton L.E.//Opt.Eng. 1985 24, 138
4. Volk T.R.,Rubinina N.M.,Pryalkin V.I.,Krasnikov V.V., Volkov V.V.// Ferroelectrics .1990.109, 345
5. Volk T.R.,Rubinina N.M.,Pryalkin V.I.// Sov.J.Quant.Electr. 1990, 17, N3,262
6. Volk T.R.,Rubinina // Opt.Lett.1990, 15,N18,996
7. F.Kloze, M.Wohlecke, S.Kapghan// Ferroelectrics. 1989.92,181
8. M.Wohlecke, N.M.Rubinina, T.R.Volk// in press
9. R.Sommerfeldt,L.Holtmann,E.Kratzig,B.Grabmayer Phys.Stat.Sol.(a) 106,89,1988
- 10.T.R.Volk,N.M.Rubinina Phys.Stat.Sol.(a) 108, 437,1988

Phasematching temperatures in LiNbO₃:Mg and LiNbO₃:Zn

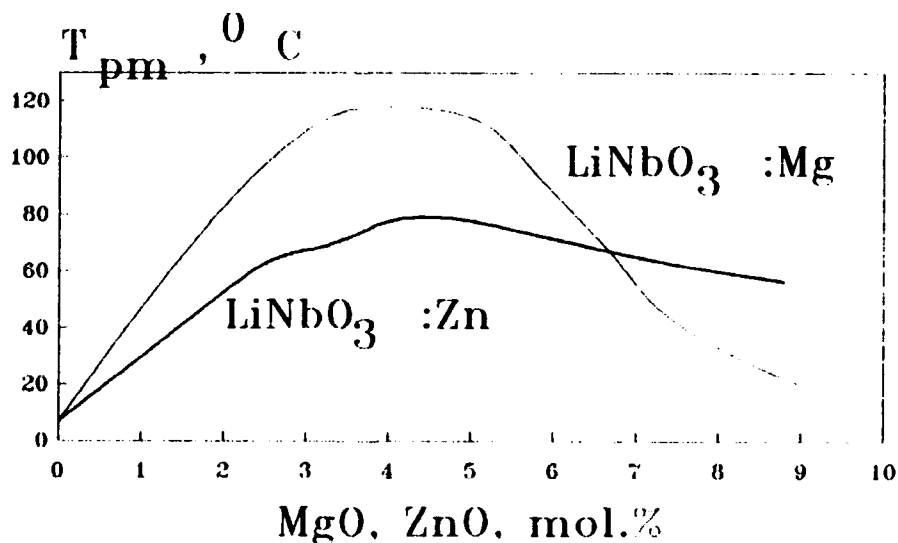


Fig.1

Photorefraction in $\text{LiNbO}_3:\text{Zn}$
(488 nm, 20 W/cm²)

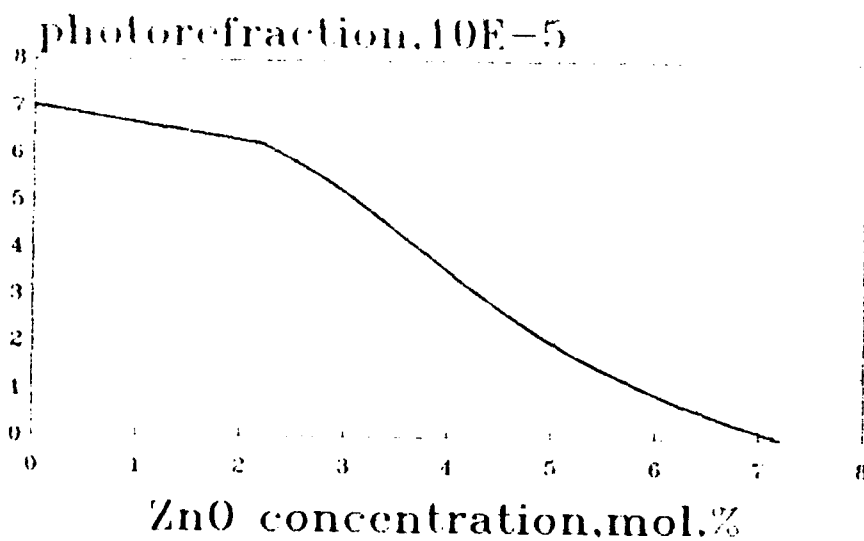


Fig. 2

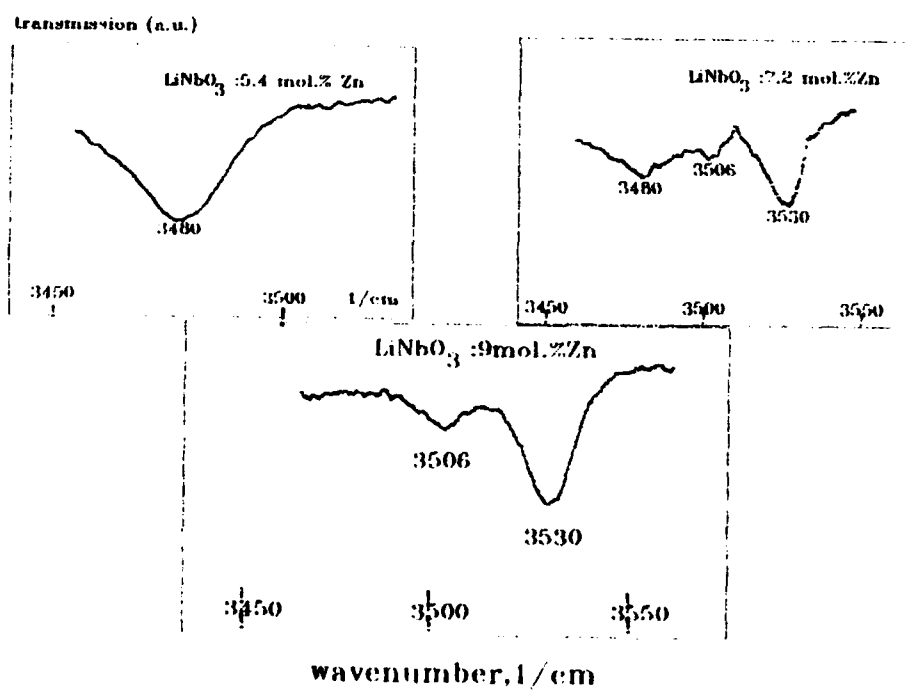


Fig. 3

Tuesday, July 30, 1991

Plenary Session on Optical and Electronic Signal Processing

TuD 7:30pm–8:30pm
Academic Center Auditorium

Alastair Glass, Presider
AT&T Bell Laboratories

Electronics, Optics, and the Photorefractive Effect

Richard C. Williamson
MIT Lincoln Laboratory
PO Box 73
Lexington, MA 02173

Optics, Electronics, and the Photorefractive Effect

Demetri Psaltis
California Institute of Technology
Pasadena, CA 91125

Wednesday, July 31, 1991

Beam Fanning and Self- Pumped Phase Conjugation

WA 8:00am–10:00am
Academic Center Auditorium

Jack Feinberg, *Presider*
University of Southern California



REFLECTION GRATING MUTUAL CONJUGATOR
IN THE GEOMETRY OF TWO INTERCONNECTED RING MIRRORS.

A. V. Mamaev^{*} and A. A. Zozulya^{**}

^{*} Institute for Problems in Mechanics, pr. Vernadskogo 101, Moscow 117526, USSR

^{**} P. N. Lebedev Physics Institute, Leninsky pr. 53, Moscow 117924, USSR

Geometry for conjugation of mutually incoherent laser beams, consisting of two interconnected passive ring mirrors, was proposed in Ref.[1]. This is the only geometry among all known mutual conjugators, that can work equally well with either transmission, or reflection gratings recording. A detailed theory of this geometry and its experimental realization in the photorefractive SBN crystal in the case, when transmission gratings were operating, can be found in Ref.[1]. Here we report on the experimental investigation of a reflection grating mutual conjugator in the geometry of two interconnected ring mirrors in cw regime with the characteristic relaxation times of the order of several milliseconds.

Experimental arrangement is shown in Fig.1. Radiation of an argon ion laser ($\lambda = 0.488\mu\text{m}$), operating at several longitudinal modes, was divided into two beams with the help of a halfwave plate $\lambda/2$ and a polarizer P (Glan prism). Path difference between these beams considerably exceeded the coherence length of laser

92-18755



radiation (about 5cm), but was less, than the round-trip laser cavity length, so the beams might be considered mutually incoherent. Polarization of one of the beams was rotated by 90 degrees by a $\lambda/2$ plate and the beams were focused by a lens L_1 in a photorefractive crystal $\text{KNbO}_3\text{:Fe}$ along its optical axis without intersecting each other.

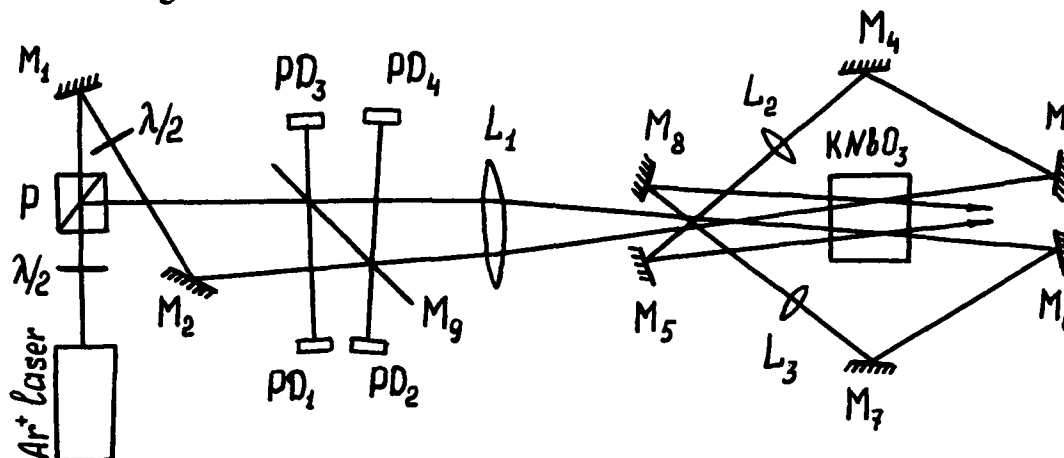


Fig.1

Thickness of the crystal was about 6.5mm, and diameters of the beams in the crystal were about 0.2mm. After passing through the crystal the beams were redirected by metal mirrors $M_3 - M_8$ and again entered the crystal, as the secondary beams, at an angle $\approx 0.04\text{rad}$ in the air to the primary beams. First secondary beam intersected second primary one and vice versa, as shown in Fig.1. Lenses L_2 and L_3 , placed in the feedback loops, made diameters of secondary beams in the crystal approximately equal to those of primary beams. All the interacting beams in the crystal were linearly polarized in the plane of their intersection. Lengths of the feedback loops were approximately the same and exceeded the coherence length of laser radiation, hence all the beams in the crystal were mutually incoherent. Crystal was oriented in such a

way to utilize electrooptic coefficient r_{13} . Part of incident and backreflected radiation with the help of semitransparent mirror M_9 was directed to photodetectors $PD_1 - PD_4$, that measured the powers of incident and backreflected beams.

Dynamics of one of the backscattered beams for approximately equal powers of incident beams ($\approx 40\text{mW}$ each) is shown in Fig.2, demonstrating characteristic relaxation time of several milliseconds. Dynamics of second backscattered beam was analogous to that, depicted in Fig.2.

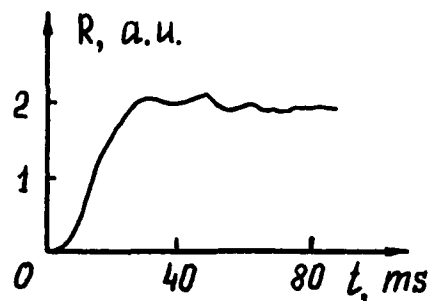


Fig.2

Nonlinear reflectivities R_1 and R_2 of two incident beams versus their power ratio are shown in Fig.3.

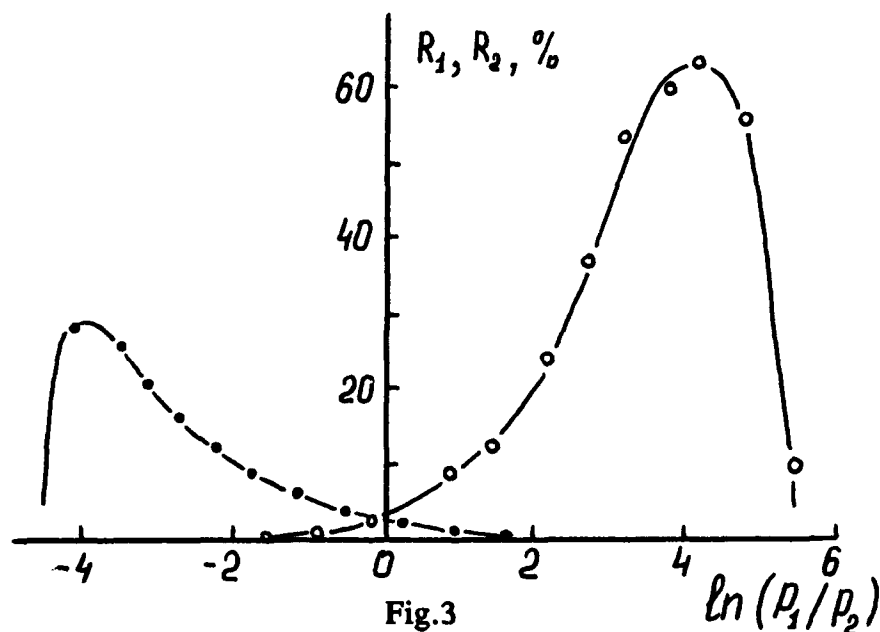


Fig.3

Some asymmetry of these curves is probably due to the different

ratio of diameters of incident and secondary beams in two interaction regions and/or different values of coupling constant in these regions.

References

1. A. A. Zozulya and A. V. Mamaev. Pis'ma Zh. Eksp. Teor. Fiz. **49**, 483 (1989) [Sov. JETP Lett. **49**, 553 (1989)]; Zh. Eksp. Teor. Fiz. **97**, 101 (1990) [Sov. Phys. JETP **70**, 56 (1990)].



Crystal noise limited holographic interferometry in BSO

R. C. Troth and J. C. Dainty

Applied Optics Section, Blackett Laboratory,
Imperial College, London SW7 2BZ, U.K.

Tel : (+44)(71)5895111 Ext(6823) Fax : (+44)(71)5899463

S. L. Sochava and S. I. Stepanov

A. F. Ioffe Physicotechnical Institute,
Academy of Sciences of the USSR, Leningrad.

March 8, 1991

There are two geometries that are generally used for real-time interferometry, the four wave mixing (FWM)^{1,2} and two beam coupling (TBC)^{3,4} geometries. There is, however, a geometry which incorporates features of both FWM and TBC proposed by Petrov *et.al.*⁵ and it is this geometry which is easiest to implement and gives good results. In this geometry the anisotropic self diffraction properties of sillenite crystals such as $\text{Bi}_{12}(\text{Ge}, \text{Si}, \text{Ti})\text{O}_{20}$ are used to produce a polarization rotation between the incident and diffracted beams. Thus if one of the above crystals is placed in the standard FWM orientation, with the $[1\bar{1}0]$ crystallographic direction in the plane of the incident beams, such that the axes of charge induced birefringence are at $\pm 45^\circ$ to the $[001]$ direction (*Fig.1*), then the transmitted object (signal) beam can be cancelled by using two orthogonal polarizers placed in front of and behind the crystal. This enables the diffracted image to be isolated from the signal so reducing the effective noise in the output hologram. Rather good time-average and double exposure interferograms can be produced^{6,7}, (*Fig.2*), with, however, a restriction on the size of the object that can be investigated, when the object is diffusely reflecting. In the case of the time-average interferogram shown in (*Fig.2*) the object was only 40 mm in diameter. The restriction on object size is partly due to geometrical considerations but is also strongly dependent on the noise and sensitivity characteristics of the crystal used. For this reason we present here an analysis of two samples of $\text{Bi}_{12}\text{SiO}_{20}$ (BSO) crystals grown in different laboratories, based on a simple theory for the determination of maximum viewable object size, from material considerations.

There are two material characteristics of a PRC which can be used to quantify how good it will be in an interferometric arrangement such as that described in references 6 and

92-18756



7. These are the coefficient of scattered noise distribution, $\vartheta(\mathbf{K})$, of the crystal and the exposure sensitivity to the illuminating radiation, $W_H = I_R \tau_{sc}$; where I_R is the reference beam intensity ($I_R \gg I_S$) and τ_{sc} is the characteristic time for steady state hologram formation. By consideration of the brightness (radiance) of a signal wave from a diffusely reflecting object, and a noise wave generated by light scattering within the volume of a crystal the following equation describing the relation between object area and experimental parameters can be derived:

$$A \simeq \frac{P_0 \tau_{sc}}{\pi \vartheta W_H \mathcal{R}_N} \quad (\text{m}^2), \quad (1)$$

where A is the object area, P_0 the power illuminating the object and \mathcal{R}_N is the signal to noise ratio (SNR) required from the interferometer. The diffraction efficiency of the interferogram, η_I , does not appear in the above equation but is also an important parameter in describing the maximum object area. In fact the interferogram diffraction efficiency can be written in terms of an idealized hologram diffraction efficiency, η_H , as;

$$\eta_I \approx 4\beta_0 \eta_H, \quad (2)$$

where β_0 is the intensity ratio of signal to reference beams. The diffraction efficiency can also be written in terms of the SNR and the extinction ratio, T_P , of the crossed polarizers on either side of the crystal as:

$$\eta_H \approx \frac{\mathcal{R}_N T_P}{4}. \quad (3)$$

Using equations (1) and (2) it is possible to obtain a value for the maximum object area which can be viewed using a CCD camera. In order to do this it is necessary to measure the scattered noise distribution of the crystal at the working wavelength, the sensitivity of the crystal and the steady state diffraction efficiency.

Two crystals of BSO (BSO^{#1} and BSO^{#2}) were investigated to characterize their suitability for use in an interferometric system. The noise distribution was measured for both crystals at wavelength $\lambda = 514$ nm, and also for the BSO^{#1} sample at $\lambda = 633$ nm. The results are presented in *Fig.3* showing the spatial frequency dependence of the scattered noise coefficient $\vartheta(\mathbf{K}) = P/P_0\Omega$, where P and P_0 are the scattered and incident powers respectively and Ω is the solid angle. There is quite a marked difference between the noise distributions for the BSO samples at $\lambda = 514$ nm with the BSO^{#1} sample having a much larger coefficient at high spatial frequencies than the BSO^{#2} sample. From equation (1) this obviously acts to decrease the observable object area relative to the BSO^{#2} sample. The overall limit on the object size is, however, determined by the product of the noise and sensitivity characteristics of each crystal.

In order to measure the variation in sensitivity, at $\lambda = 514$ nm of the crystals with respect to spatial frequency, the characteristic time for steady state hologram formation was measured. For BSO, illuminated with mW cm^{-2} incident intensities, τ_{sc} is quite low which makes it difficult to measure by conventional means. For this reason a two beam coupling method, using a sinusoidal phase modulation of the signal beam, was used to form a non-stationary grating inside the crystal^{8,9}. This method produces good amplitude modulation at the second harmonic of the frequency, ω , of the phase modulation. When the frequency of phase modulation is such that $2\pi/\omega \geq \tau_{sc}$ a steady state grating is produced so the amplitude of intensity modulation becomes zero. Thus the cut off frequency, ω_c , can be found and from this τ_{sc} ($\tau_{sc} = \omega_c^{-1}$). However, the cut off frequencies are typically of the order of 2 to 50 Hz which makes the exact cut off very difficult to find due to mechanical vibrations and air movement. For this reason a two frequency technique was used¹⁰ in which

the signal beam was modulated by a low amplitude high, "signal", frequency $\omega_h \geq \omega_c$, and a high amplitude variable, "jamming", frequency $\omega_j \leq \omega_c$. The signal frequency was kept constant at some arbitrary value, 150 Hz, and the jamming frequency was varied from 1 to 100 Hz for a series of different spatial frequencies, with the jamming frequency amplitude, $\Delta\omega_j$, varied to produce a suppression of signal amplitude of 0.7. By plotting the amplitude of jamming signal against jamming frequency ω_c can be obtained for each spatial frequency, as shown in *Fig. 4* for two spatial frequencies. The cut off frequency corresponds to the point at which $\Delta\omega_j$ has to be increased to give the same signal suppression. From the values of ω_c obtained from the jamming frequency curves the dependence of exposure sensitivity with spatial frequency has been plotted for both BSO crystals and is shown in *Fig. 5*. From this, BSO#¹ is half an order of magnitude more sensitive than BSO#². Using data obtained from *Figs. 3, 5* and using equation (1) it is found that interferograms of objects with areas of $A \simeq 1 \text{ m}^2$ may be produced if the incident power illuminating the object is $\geq 1 \text{ W}$.

The idealized hologram diffraction efficiency dependence on spatial frequency is plotted in *Fig. 6* for both BSO crystals. Using the values of η_H corresponding to the optimum spatial frequencies for noise minimization obtained from *Fig. 3* the intensities of interferograms imaged onto a CCD camera are found to be $I_I \simeq 2 \times 10^{-5} \text{ mW cm}^{-2}$ for BSO#¹ and $I_I \simeq 7 \times 10^{-5} \text{ mW cm}^{-2}$ for BSO#² for imaging by a lens of sensible numerical aperture through a $20 \times 20 \text{ mm}^2$ crystal aperture. These intensities are above the typical limiting intensities of modern CCD cameras so it should be possible to investigate vibrating or displaced objects as large as 1 m^2 .

1. J.P. Huignard, J.P. Herriau and T. Valentin, *Appl. Opt.* **16**, 2796 (1977).
2. A. Marrakchi, J.P. Huignard and J.P. Herriau, *Optics. Comm.* **34**, 15 (1980).
3. J.P. Huignard and J.P. Herriau, *Appl. Opt.* **16**, 1807 (1977).
4. J.P. Huignard and A. Marrakchi, *Optics. Lett.* **6**, 622 (1981).
5. M.P. Petrov, S.V. Miridonov, S.I. Stepanov and V.V. Kulikov, *Optics. Comm.* **31**, 301 (1979).
6. A.A. Kamshilin and M.P. Petrov, *Optics. Comm.* **53**, 23 (1985).
7. R.C. Troth and J.C. Dainty, *Optics. Lett.* **16**, 53 (1991).
8. A.A. Kamshilin and E.V. Mokrushina, *Sov. Tech. Phys. Lett.* **12**, 149 (1986).
9. Y. Barmenkov, V.V. Zosimov, N.M. Kozhevnikov, L.M. Lyamshev and S.A. Serushchenko, *Sov. Phys. Dokl.* **31**, 817 (1987).
10. S.I. Stepanov, I.A. Sokolov and G.S. Trofimov, *Sov. Phys. Tech. Phys.* **34**, 1165 (1990).

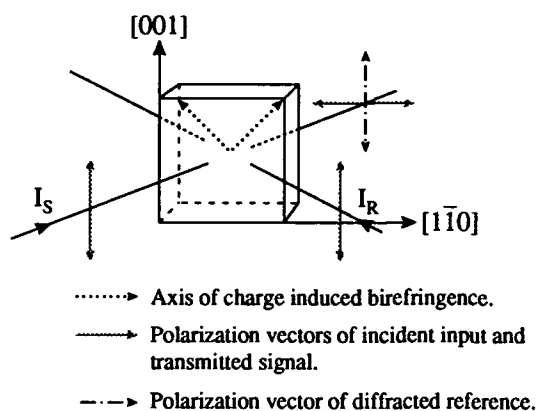


Fig.1 Schematic of the crystal orientation used for real-time interferometry showing the input and diffracted output polarization vectors, and the axes of charge induced birefringence.

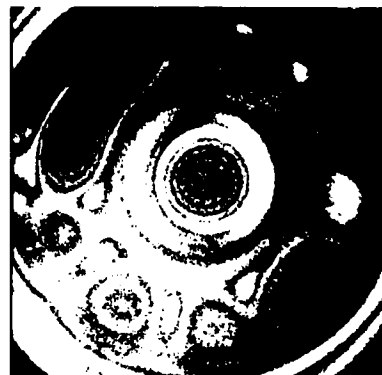


Fig.2 Time-average interferogram of a loudspeaker vibrating at a frequency of 10 KHz.

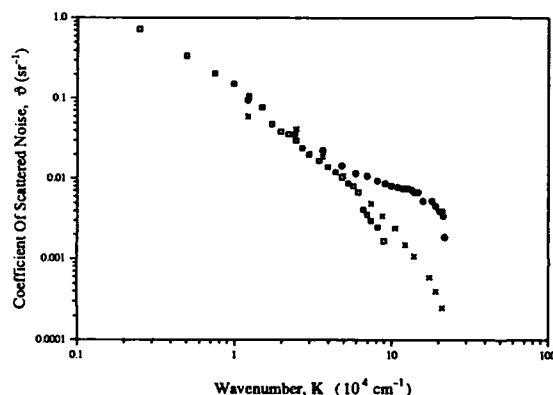


Fig.3 Dependence of the coefficient of scattered noise on spatial frequency. BSO#1 sample at $\lambda = 514$ nm (\bullet), and $\lambda = 633$ nm (\square); BSO#2 sample at $\lambda = 514$ nm (\times)

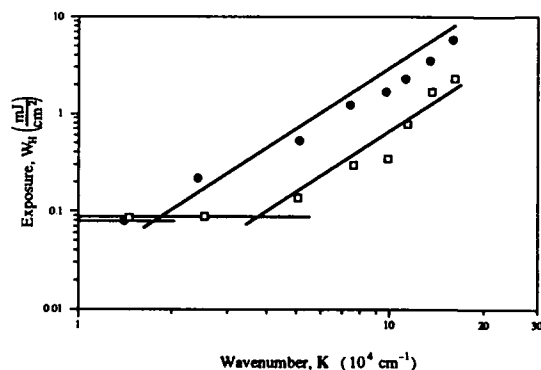


Fig.5 Dependence of the exposure sensitivity, W_H , on spatial frequency for BSO#1 sample (\square) and BSO#2 sample (\bullet).

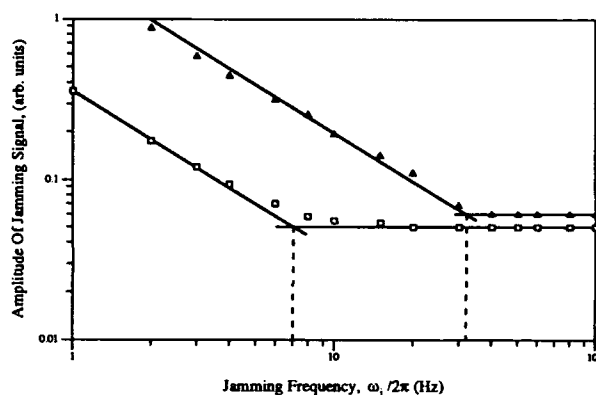


Fig.4 Dependence of the amplitude of jamming, Δ^0j , on jamming frequency for BSO#1 sample at spatial frequencies of $K = 2.55 \mu\text{m}^{-1}$ (Δ) and $K = 11.42 \mu\text{m}^{-1}$ (\square).

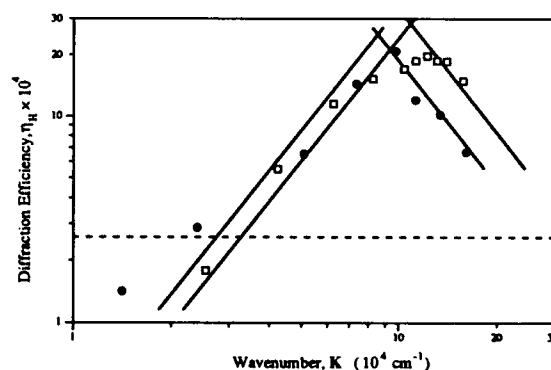


Fig.6 Dependence of the idealized hologram diffraction efficiency, η_H , on spatial frequency for BSO#1 sample (\square) and BSO#2 sample (\bullet).



**DOUBLE PHASE CONJUGATED MIRROR AND DOUBLE COLOUR
PUMPED OSCILLATOR USING BAND-EDGE PHOTOREFRACTIVITY IN InP:Fe**

N.Wolffer, P.Gravey, G.Picoli and V.Vieux

CNET Lannion B/OCN/TAC - Route de Trégastel BP40

22301 LANNION France (33)96053287

I-INTRODUCTION

The Double Phase Conjugated Mirror (DPCM)¹ and the Double Colour Pumped Oscillator (DCPO)² are particularly interesting devices for reconfigurable optical interconnects^{2,3,4,5}. In a DPCM two mutually incoherent pump beams (at nearly identical wavelengths) incident on the opposite faces of a photorefractive (PR) crystal share a common grating which diffracts them into the phase conjugated of the opposite one. When the wavelength difference of the interacting beams is important (larger than the grating selectivity), they can still induce a common grating (DCPO). Recently DPCM has been observed in InP:Fe⁶ and GaAs:EL2⁷ at 1.06 μm and DCPO has been achieved in InP:Fe using 1.06 and 1.32 μm wavelengths⁸.

This paper presents new results on both DPCM and DCPO obtained in InP:Fe at wavelengths close to its band edge. More precisely, we have observed DPCM at wavelength down to 970 nm and DCPO between a fixed wavelength of 1.047 μm and a variable one down to 965 nm. Using a wavelength close to the band edge has two major implications for PR devices. There is indeed an increase of the optical absorption α , but the effective electro-optic coefficient is greatly enhanced through the Franz-Keldysh effect which has already been exploited to achieve large 2WM gains in GaAs⁹.

II-EXPERIMENTAL SET-UP AND SAMPLE CHARACTERISTICS

The source used for the DPCM experiments was a Ti:Sapphire laser; for DCPO studies one of the two beams entering the crystals (the pump beams) has been replaced by another one issued from a diode pumped Nd:YLF laser emitting at 1.047 μm . The results reported here have been obtained with InP:Fe sample 169QC4, grown at CNET. The optical interaction length L and the distance d between the two silver pasted electrodes are both equals to 6.0 mm. The sample temperature is stabilized through a Peltier cooling element. An external dc field is applied along the $\langle 001 \rangle$ axis. The sign of this field is chosen in order to maximise the 2WM gain by addition of the contributions of Pockels and Franz-Keldysh effects. The two vertically polarized pump beams enter the opposite 110 faces which are uncoated. Figure 1 shows the absorption spectra. α increases from 1.2 cm^{-1} at 1.047 μm to 5.4 cm^{-1} at 0.965 μm . For a given applied field E_0 , the influence of the Franz-Keldysh effect can be described¹⁰ through an effective linear electrooptic coefficient $r_{\text{eff}} = r_{41} + r_{\text{Franz-Keldysh}}$. Separate 2WM experiments (gain measurements for two opposite signs of the

92-18757



applied field) have been performed with the same sample in order to measure the wavelength dependence of the ratio $r_{\text{Franz-Keldysh}}/r_{41}$. The results are shown in figure 2 (for $E_0 = 10$ kV/cm). At 965 nm, $r_{\text{eff}} = 2.28 \cdot r_{41}$.

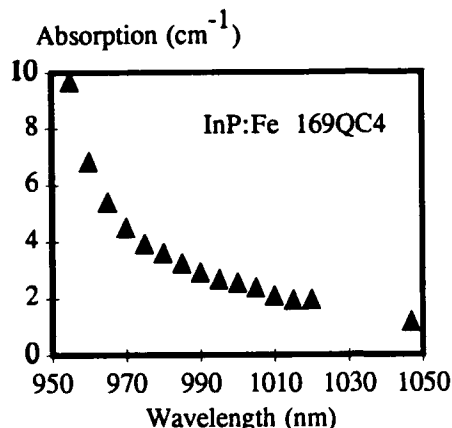


Figure 1

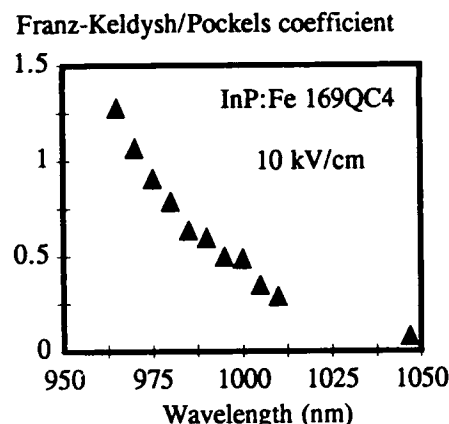


Figure 2

III-CALCULATION PROCEDURE FOR DPCM AND DCPO CONVERSION EFFICIENCIES

The experimental characteristics reported in figures 1 and 2 enable to predict the performances of this same sample in DPCM and DCPO experiments. For this, numerical simulations have been performed. The calculation method used in the DPCM case has already been described in previous works on BGO¹¹ and InP:Fe⁶. We simply recall that this calculation requires to take into account the non linearity of the space charge field E_1 at high fringe contrast m . We followed Refregier et al.¹² by assuming that E_1 is proportional to $f(m)E_{\text{sc}}$ with $f(m) = (1 - e^{-am})/a$. E_{sc} is the saturated space charge field value calculated in the low m limit.

The method used for the DCPO is an extension of the previous one; we shall just indicate here the main modifications. We consider in this case two distincts interference patterns (supposed to be in phase) at wavelengths λ_1 and λ_2 defined by

$$I^1(x) = I_0^1 (1 + m_1 \cos Kx); \quad I^2(x) = I_0^2 (1 + m_2 \cos Kx) \quad (1)$$

Standard techniques allow to derive the first Fourier component E_1 of the space-charge field under the form

$$E_1 = m_1 E_{\text{sc}1} + m_2 E_{\text{sc}2} \quad (2)$$

where $m_1 E_{\text{sc}1}$ (resp. $m_2 E_{\text{sc}2}$) is the solution corresponding to interference pattern $I^1(x)$ (resp. $I^2(x)$) in presence of an uniform illumination I_0^2 (resp. I_0^1). The coupling coefficients for both wavelengths λ_1 and λ_2 are then as usual (for small angles inside the crystal):

$$C(\lambda) = (\pi/\lambda) (n^3(\lambda) r_{\text{eff}}(\lambda)/2) E_1 \quad (3)$$

As for the DPCM, we have to take into account that for large conversion efficiencies (i.e. the ratio of the diffracted beam intensity

over the total transmitted one) m_1 and m_2 are not negligible when compared to 1. To evaluate the space-charge field non-linearities we have used an heuristic extension of the formula of Refregier et al. by introducing a normalized fringe modulation m'

$$m' = (m_1 E_{sc1} + m_2 E_{sc2}) / (E_{sc1} + E_{sc2}) \tag{4}$$

and modifying E_1 as follows

$$E_1 = (f(m')/m') (m_1 E_{sc1} + m_2 E_{sc2}) \tag{5}$$

IV-EXPERIMENTAL RESULTS

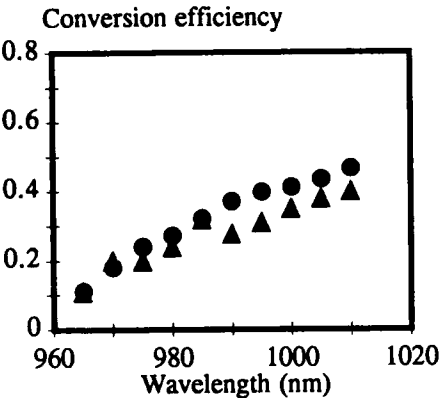


Figure3

Conversion efficiency for $\lambda_1 = 1,047$ nm
vs $\lambda_2 = 965$ to $1,010$ nm
(exp:triangles, calc: circles)

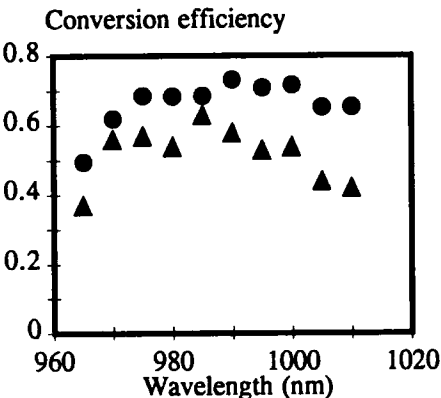


Figure4

Conversion efficiency
for $\lambda_2 = 965$ to $1,010$ nm vs λ_1
(exp:triangles, calc: circles)

We first measured the DPCM conversion efficiency η for different wavelengths with $E_0 = 10$ kV/cm and fringe spacing Λ of about $6.7 \mu m$. The sample temperature was 281 K and the pump intensities were adjusted to maximise the efficiency as predicted by the model of PR effect in InP:Fe¹³. The results were obtained by measurement of the pump depletion (after checking that fanning was negligible), and are summarized below, together with the calculated values:.

| | | | |
|-----------------|-------|------|------|
| Wavelength (nm) | 970 | 980 | 1000 |
| η (exp) | ~0.50 | 0.58 | 0.58 |
| η (calc) | 0.60 | 0.64 | 0.67 |

The theoretical values have been calculated with the set of material parameters used in ref13, with $[Fe^{2+}] = 1.5 \cdot 10^{16} \text{ cm}^{-3}$, $[Fe^{3+}] = 4.5 \cdot 10^{16} \text{ cm}^{-3}$ and $a = 1.9$. The value of a has been chosen according to previous studies of DPCM in InP:Fe at $1.06 \mu m^8$. Experimental datas are smaller than calculated ones. This can be explained by the transverse unhomogeneity of the pump intensities (leading to non optimum illumination in some parts of the crystal) and by internal reflections reducing the fringe contrast. Moreover the value obtained at 970 nm was not stable

because at this wavelength the maximum efficiency required an higher illumination, increasing the photocurrent. An improvement of the cooling system efficiency should overcome this problem.

Figures 3 and 4 show the measured and calculated conversion efficiencies for both beams in the case of DCPO. Results concerning the fixed wavelength (1,047 nm) pump are given in figure 3. Those concerning the variable wavelength (965 to 1010nm) are plotted on figure 4. The sample temperature was 279 K. The intensity of the 1,047 nm beam was optimized in presence of the 1,010 nm beam and then kept constant, while the intensity of the other was optimized for each wavelength. The mean grating period was the same as previously and the applied field 10 kV/cm. The difference between measured and calculated datas is slightly larger than in the DPCM case. We suppose that this arises from still less uniformity in the low power 1,047 nm beam. In contrast to the DPCM case the efficiency was very stable, even for the lower wavelengths.

V-CONCLUSION

We have demonstrated that mutually incoherent PR interactions like DPCM and DCPO can be realized in InP:Fe at wavelengths near the band edge with conversion efficiencies exceeding 50%, owing to the Franz-Keldysh effect. They could find, for exemple, applications with 0.98 μm laser diodes, which are used for pumping some fibre optical amplifiers.

REFERENCES

- [1] S.Weiss, S.Sternklar, and B.Fischer, *Opt.Lett.* 12, 114 (1987)
- [2] S.Sternklar, and B.Fischer, *Opt.Lett.* 12, 711 (1987)
- [3] H.J.Caufield, J.Shamir, and Q.He, *Appl.Opt.* 26, 2291 (1987)
- [4] S.Weiss, M.Segev, S.Sternklar, and B.Fischer, *Appl.Opt.* 27, 3422 (1988)
- [5] M.Cronin-Golomb, *Appl.Phys.Lett.* 54, 2189 (1989)
- [6] P.Gravey, N.Wolffer, G.Picoli, and C.Ozkul
Technical Digest of the Topical Meeting on Photorefractive Material, Effects, and Devices II, Aussois-France (1990), p.164
- [7] P.L.Chua, D.T.H.Liu, and L.J.Cheng, *Appl.Phys.Lett.* 57, 858 (1990)
- [8] V.Vieux, P.Gravey, N.Wolffer and G.Picoli, *Appl.Phys.Lett.*, to be published
- [9] A.Partovi, A.Kost, E.M.Garmire, G.C.Valley, and M.B.Klein, *Appl.Phys.Lett.* 56, 1089 (1990)
- [10] G.Picoli, P.Gravey, N.Wolffer and V.Vieux
Technical Digest of the Topical Meeting on Photorefractive Material, Effects, and Devices II, Aussois-France (1990), PD5
- [11] N.Wolffer, P.Gravey, J-Y.Moisand, C.Laulan and J-C.Launay, *Opt.Comm.* 73, 351 (1989)
- [12] Ph.Refreqier, L.Solymer, H.Rajbenbach, and J.P.Huignard, *J.Appl.Phys.* 58, 45 (1985)
- [13] G.Picoli, P.Gravey, C.Ozkul, and V.Vieux, *J.Appl.Phys.* 66, 3798 (1989)



**Application of Beam Fanning in a Photorefractive BaTiO₃ Crystal:
Measurement of Light Scattering at Zero Degrees by a Single Glass Fiber**

G. G. Padmabandu, Choonghoon Oh and Edward S. Fry

Department of Physics, Texas A & M University

College Station, TX 77843. Ph. (409)-845-6876.

Introduction:

The photorefractive effect in BaTiO₃ has been the subject of extensive research in recent years. Because of very large electro-optic coefficients, BaTiO₃ has become a unique candidate for a variety of nonlinear optical devices which operate at very low light intensities. Most of these devices use energy transfer between coherent optical beams that interfere inside the crystal while some devices use the extinction of a single beam through beam fanning¹⁻³.

In this letter, we will discuss the use of a BaTiO₃ beam fanning limiter to make quantitative measurements, and will present the first measurement of zero degree scattering from micron sized glass fibers.

A coherent light beam that propagates through a BaTiO₃ crystal fans out in a direction determined by the c- axis of the crystal. With proper choice of the angle of incidence more than 99% of the input intensity can be removed from the incident beam using a 5 mm crystal⁴. Beam fanning occurs due to a refractive index gradient that is formed across the the illuminated area and which causes the beam to be deflected. The index gradient is produced by optically induced charge migration, which in turn induces an anisotropic electric field inside the crystal. For BaTiO₃ this process takes a fraction of a second to a few seconds depending on the input beam intensity and thus it has been recognized as a slow response medium. If a phase or an amplitude change of the input beam occurs in a time shorter than the response time, it will not be diffracted by the photoinduced grating but will be transmitted instead.

Light scattering by small particles has been the subject of intense investigations for many decades but all experimental work to date has been limited to angles from the near forward direction⁵ to the back scattering direction. The limiting experimental factor in the forward direction, $\theta = 0^\circ$, is the unscattered plane wave which is superposed with the scattered spherical wave. Separation of the two waves is not impossible but is very difficult. Therefore, there has been little previous experimental success in attempts to separate the two waves in the forward direction.

The identifying characteristic of the light scattered at zero degree is its shift in phase. However, linear interferometric techniques to separate the scattered light from

92-18758



the unscattered have been unsuccessful due to systematic problems. In our new approach, using beam fanning to separate the scattered and unscattered light, a time dependance to the scattered light is introduced by moving the scatterer in and out of the incident beam. The response time of the crystal is controlled by adjusting the incident intensity of the laser beam. The motion of the scatterer is set so that it can cross the laser beam in a time shorter than the crystal response time. When all these conditions are met, the time dependant scattered light and the time independent unscattered light are separated due to beam fanning as they propagate through a BaTiO_3 crystal.

The Experiment:

Fig. 1 shows the schematic of the experimental set up. The cw Ar^+ laser (514.5nm) is polarized in the plane of incidence and parallel to the plane of the c- axis of each BaTiO_3 crystal. The first crystal is 45° cut and the second is 0° cut. For all measurements the laser power was kept below 10 mW in order to maintain a longer response time. Adjustable apertures A1, A2 and A3 shield the two crystals and the detector from stray light. The lens collects the light that is transmitted through the two crystals and focuses it onto the detector.

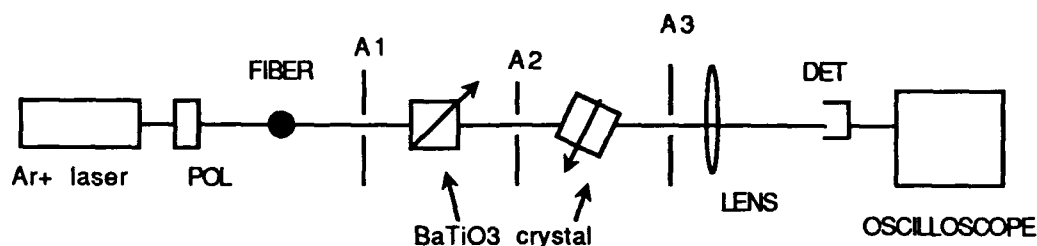


Fig. 1. Experimental Set-up

The scattering sample is a micron sized glass fiber positioned normal to the incident laser beam. The fiber is mounted on a 12 rpm synchronous motor so that it could be rotated in circle of radius 3 cm. In each rotation, the fiber crosses the laser beam twice producing two pulses of scattered light. The forward scattered portion of these pulses together with the strong unscattered beam is then sent through two successive BaTiO_3 crystals as in Fig.1. Since the unscattered portion of the beam has a constant phase, most of it is removed from the transmitted beam through beam fanning in each crystal.

Beam fanning in a 5 mm BaTiO_3 single crystal cut at 45° to the c- axis can produce over 99% extinction of the incident beam when near normal incidence is used. This

extinction is not sufficient for scattering measurements since the scattered component of the beam is weak compared to the unscattered component. By using two BaTiO₃ crystals as shown in Fig. 1, we achieved about 99.9% extinction of the unscattered beam.

In addition to the large extinction of the unscattered beam there are other advantages of using two crystals instead of one longer crystal. The most important of all is the suppression of the crystal generated scattering noise. The strong incident beam can undergo scattering in the first crystal and send some light in the forward direction. Since the phase of this scattered light is constant in time, the second crystal conveniently subtracts it from the transmitted beam when two crystals are used. However, there is a significant loss of the signal due to large Fresnel reflections at the four faces of the two crystals.

After filtering through the two crystals, the transmitted light is collected and focused on to a photodiode and is measured in a sampling oscilloscope. Measurements for several glass fibers of radii between 1 μm and 35 μm will be presented.

Conclusion:

In conclusion, we have successfully used the photorefractive technique to isolate the forward scattered light from a single micron sized glass fiber. This novel technique may be used to measure forward scattering from aerosols as well as from particles suspensions. They all are in constant Brownian motion and will produce a time dependent phase in the scattered light so that the beam fanning can isolate the scattered light from the unscattered. Finally, the measurement of forward scattering from a single fiber can be used to calibrate light scattering apparatus.

References:

1. J. Feinberg and K. R. McDonald in "Photorefractive Materials and Their Applications, vol. II", P. Gunter and J. P. Huignard ed. (Springer-Verlag 1988)
2. R. S. Cudney, R. M. Pierce and J. Feinberg, "Transient Detection Microscope", *Nature* **332** 424 (1988)
3. D. Z. Anderson, D. M. Lininger and J. Feinberg, "Optical tracking novelty filter", *Opt. Lett.* **12** 123 (1987).
4. Mark Cronin-Golomb and Amnon Yariv, "Optical Limiters Using Photorefractive Nonlinearities" *J. Appl. Phys.* **57** 4906 (1985).
5. R. W. Spinrad, "Measurements of the volume scattering function near forward angles for suspended oceanic particulates", *SPIE vol. 60, Ocean optics V* 18 (1978).

AD-P006 771



FREQUENCY SHIFT IN A MUTUALLY PUMPED PHASE CONJUGATOR OF BaTiO₃

Dadi Wang, Zhiguo Zhang and Peixian Ye

(Institute of Physics, Chinese Academy of Sciences

Box 603, Beijing 100080, China, Tel. 86-01 2569066)

92-18759



Summary

Since the observation of self-frequency scanning with a passive phase-conjugate mirror coupled to a dye-laser cavity in 1984, much attention has been paid to frequency detuning in photorefractive (PR) wave mixing. Such a phenomenon has been widely studied in various photorefractive oscillators.⁽¹⁾ In this paper, we present the experimental results of frequency shift (f-shift) in our mutually pumped phase conjugator (Bridge conjugator)⁽²⁾ and demonstrated to be dramatically dependent upon the power density of pumping beams.

The experimental setup was similar to that we used in our previous investigation on bridge conjugator.⁽²⁾ The configuration is schematically shown in Fig.1. Two mutually incoherent beams, beam 1 and beam 2, with the same wavelength ($\lambda = 514.5$ nm) and e-polarization were input on the two adjacent surfaces of BaTiO₃, respectively. To observe the frequency shift between phase conjugate (PC) outputs and their relevant incident ones, i.e., PC beam of beam 1 noted as beam 1* and its energy source beam, beam 2, as well as another pair of beam 2* and beam 1, we built two interferometers. That is, let beam 1* (or beam 2*) and beam 2 (or beam 1) interfere each other to produce fringes on a screen and then the frequency shift can be read out from the movement of the fringes.

Our previous results on bridge phase conjugator showed that a stable and strong PC output for each input beam can be generated in a rather wide geometric and optical parametric regime. However, the frequency shift occurred in this configuration exhibited a critical dependence upon the initial conditions, which included positions, angles, optical intensities and divergencies of the incident beams. It also showed a favorable choice even for the incident faces of the crystal. These

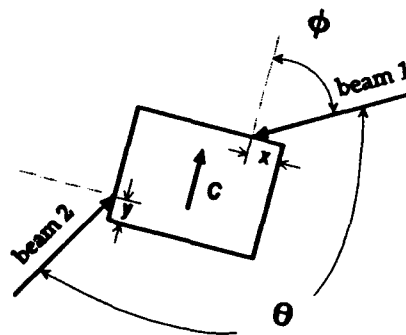


Fig. 1

facts imply that f-shift relates tightly with both the formation of the coupling channel in crystal and the surface aspect of the crystal. Nevertheless, once the f-shift appeared under a given condition, it was repeatable. The following is a summary of our experimental results under the incident condition: $\theta = 62^\circ$, $\phi = 156^\circ$, $x = 3.9\text{mm}$, $y = 5.6\text{mm}$, the definitions of θ , ϕ , x , y , are shown in Fig.1.

(1) The f-shift in each PC output was very stable once it was established. Usually, a f-shift state could last for a few hours, which ruled out the possibility that frequency shift effect was originated from the influence of the environment.

(2) By monitoring the movement directions of the two sets of interference fringes ($1^* + 2$, $2^* + 1$), we inferred that the frequency shifts of two PC beams had an identical sign.

(3) The speeds of the two sets of travelling fringes were always the same in the experiment, which proved that the magnitudes of the two PC f-shifts were also the same. This relationship is obviously to be seen in Fig.2, a typical record of two sets of beats. There, the upper curve corresponds to the beat between beam 1^* and beam 2, and the lower one between beam 2^* and beam 1. Evidently, the beat frequency is what we called the PC output detuning or the frequency shift of the PC output.

(4) The intensity observed for each PC beam was approximately steady, except that there was a very weak modulation with a frequency equal to the f-shift of the PC output.

(5) A peculiar phenomenon found in the measurement of power dependence of f-shift was that in a certain power range of the input beams, the f-shift deviated dramatically from the linear dependence law that was observed in PR oscillators⁽¹⁾. As shown in Fig.3, when the total power of the two input beams was low, the f-shift increased linearly with the power. Nevertheless, when the power reached to a 'critical' value of 16.8 mW the f-shift suddenly fell down instead of linearly increasing, as shown at point B in figure 3. When the power was increased further, the f-shift began to rise again and went up quickly to

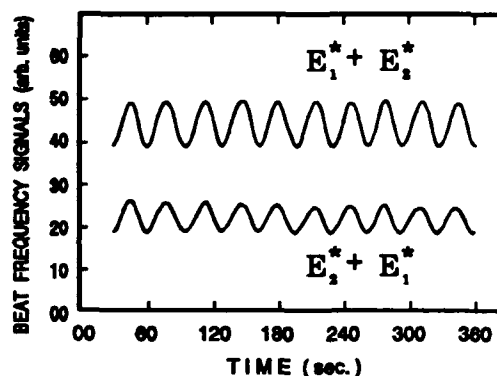


Fig. 2

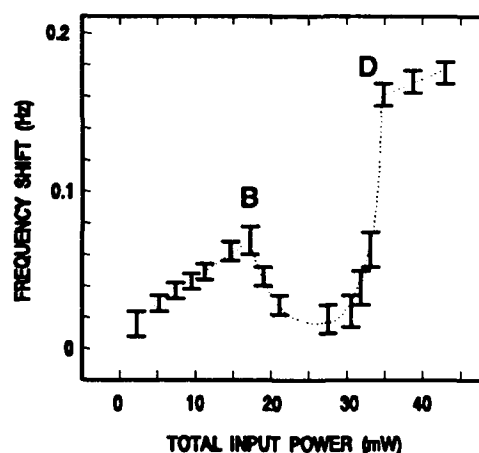


Fig. 3

a pretty high value (point D in figure 3). After that its increase followed with the power linearly. Similar curves with the above behaviour were obtained for several occasions in the experiment which indicated that this extraordinary dependence might be an inherent character of the frequency shift process.

We now address some possible explanations for the frequency shift in the bridge phase conjugator. Firstly, a Doppler frequency shift from the moving gratings formed in the crystal can be responsible for this frequency shift. According to our previous model for this configuration⁽²⁾, these gratings formed in the interaction regions are shared for both PC outputs, therefore, the f-shift due to the movement of the gratings should be identical for both PC outputs. Our experimental results (2) and (3) are consistent with this analysis. On the other hand, even a tiny grating motion, because of the very large response time τ (1 - 10 ms) of BaTiO₃, it can drive a considerably large lag of the spatial phase $\Delta = \tan(2k_g V_g \tau)$, which may significantly affect the wave mixing in the crystal. From this point of view, the tendency to self-optimize the four-wave-mixing process in the crystal induces a grating motion.

Secondly, by referring to the model proposed by P. Yeh et al.⁽³⁾ for their mutually pumped phase conjugators, an internal ring cavity might be formed in our configuration. Suppose inside the crystal there is such a beam which passes through the two interactions where it gets a photorefractive gain from wave coupling and runs a ring path by total internal reflection at the surfaces of the crystal. After each round-trip of this beam, assume, the intensity condition for oscillating can reach due to the large PR coupling efficiency, but due to this cavity is fixed the phase condition seems no other choice to be exactly fulfilled except for oscillating at a detuning frequency. As a result a f-shift on PC output will predict. Following this model, the dramatic drop of f-shift with the power (Fig.3), can be understood as a mode jumping during the ring oscillation. Of course, the cause of the mode jumping is still a puzzle. So far, this model, in principle, can interpret the physical mechanism of f-shift existed in the bridge conjugator. Unfortunately, we have not yet observed any ring channels inside the crystal, which was suggested to support this model as Yeh et al. did in their example.

The other possible origin of f-shift should be pointed out here is the existence of an internal electric field and photovoltaic field in BaTiO₃ crystal, because the magnitudes of the f-shift in our results is almost on the same order of that reported by S. Sternklar etc. in their zero external field situation. No doubt, the electrical field may play a crucial role in producing frequency shifts, to prove it should be the next subject.

REFERENCES

- 1. B. Fischer, S. Sternklar and S. Weiss; *J. of Quantum Electro.* 25, 550 (1989)
- 2. D. Wang, Z. Zhang, Y. Wu, S. Zhang and P. Ye; *Opt. Communi.* vol. 73, 495 (1989)
- 3. P. Yeh, T.Y. Chang and M.D. Ewbank; *J. Opt. Soc. Am. B*, vol. 5, 1743 (1988)
- 4. S. Sternklar, S. Weiss, and B. Fischer; *Opt. Lett.*, vol. 11, 165 (1986)



PARAMETRIC OSCILLATION IN PHOTOREFRACTIVE CRYSTALS WITH LOCAL RESPONSE IN UNCLOSED OPTICAL CAVITIES

A.P.Mazur, A.D.Novikov, S.G.Odulov and M.S.Soskin

Institute of Physics, Ukrainian SSR Academy of Science,
252 850, Kiev, USSR
tel. (044) 285 55 63

Steady-state coherent oscillation in the ring-loop and double-side mirror geometries is first observed and studied in media with local nonlinear response. The results of calculation are presented stating that the oscillation becomes possible providing two necessary conditions are met: the oscillation waves appear 1) misaligned with respect to strictly backward to pumps directions to restore the phase matching, and 2) they are shifted in frequency with respect to the pump waves. By appropriate choice of frequencies of two incident waves in double-side mirror geometry one of oscillating waves may be done a perfect conjugate replica of an input wave with limited spatial spectrum.

Experiment. The oscillation was obtained in iron doped lithium niobate crystals in double-side mirror and ring-loop geometries (Fig.1a,b) with unexpanded pump beams from CW TEM₀₀ Ar or He-Cd lasers. All interacting waves (the pumps 2 and 4, the oscillation waves 1 and 3) were polarized in the plane of incidence, the optical axis of the sample was in the same plane. The LiNbO₃:Fe 0.02 wt.% samples were Y-cut and measured 8 x 6 x 3 mm³. In double-side mirror configuration two independent lasers were used mounted on different optical tables. The aberrator (ground glass) was placed close to the input face $z = l$ increasing the beam divergence inside the sample to nearly 20°.

The dynamics of oscillation development was as follows: a long (≈ 20 min) preoscillation interval, an intense spike of oscillation switch-on and a smooth transition to the steady-state behavior; the diffraction efficiency at saturation reached ≈ 0.003 . The angular divergence of oscillation wave 3 and wave 1 after the aberrator in the plane of interaction was $\approx 15'$ and approximately three-four time larger in perpendicular direction. In such a way the compensation for severe phase aberrations was achieved; the smaller was the distance between the sample and the aberrator the better was the quality of reconstructed wavefront.

Each oscillation wave was propagating not exactly in backward with respect to the pump wave direction. The angular deviation was increasing when the angle between two pump waves was set smaller (Fig.2).

The oscillation with similar characteristics was obtained also in ring-loop configuration, no aberrator was necessary in this arrangement to produce the collimated oscillation wave.

For both geometries the oscillation was possible for two opposite orientations of crystal axis thus proving that the main process of amplification originates from local response of the material.

Calculation of oscillation threshold. To consider the possibility of oscillation we analyzed the standard set of equations for complex amplitudes A of four interacting waves [1]. In undepleted pumps approximation the complete set can be reduced to two equations, one for the reflectivity of nonlinear sample, $\eta = |A_1/A_3|$, and other for the generalized phase, $\Phi = \phi_1 + \phi_2 - \phi_3 + \phi_4 - \Delta k_z z$, taking into account possible angular misalignment $\Delta\theta$ of interacting

92-18760



waves:

$$\begin{aligned} d\eta/dz &= -\gamma''\eta - \gamma''\cos\Phi (1+\eta^2) \frac{\sqrt{r}}{1+r} - \gamma'\sin\Phi (1-\eta^2) \frac{\sqrt{r}}{1+r}, \\ d\Phi/dz &= \gamma''\sin\Phi (1-\eta^2) \frac{\sqrt{r}}{1+r} - \gamma'\cos\Phi (1+\eta^2) \frac{\sqrt{r}}{1+r} - \gamma'\eta - \Delta k_z \eta, \end{aligned} \quad (1)$$

where $r = |A_2/A_4|^2$ is the pump intensity ratio, $\Delta k_z = (2\pi\Delta\theta\sin 2\theta/\lambda)(n^2 - \sin^2\theta)^{-1/2}$, γ' and γ'' are the coupling constants for unshifted and $\pi/2$ -shifted gratings in the material. For the considered case [3]

$$\gamma' + i\gamma'' = \gamma^0 \left[\frac{1}{1 + (\tau\delta\omega)^2} + i \frac{\tau\delta\omega}{1 + (\tau\delta\omega)^2} \right], \quad (2)$$

where $\gamma^0 = -\pi r_{33} n_e^3 \beta_{33} / \kappa \lambda \cos\theta$ is a real coupling constant corresponding to purely local nonlinear response, r_{33} and β_{33} are the electrooptic and photovoltaic constants, κ is the specific photoconductivity, λ is the wavelength, $\delta\omega$ is the frequency detuning and τ is the photorefractive relaxation time. One can analyze the solution of Eqs.1 for arbitrary $\gamma'/\gamma'' = \tau\delta\omega$; considering the oscillators we will find $\tau\delta\omega$ ensuring the maximum gain and therefore minimum threshold of oscillation.

In the limit of $r = 1$, $\gamma' = 0$ the solution of Eq.1 gives the oscillation threshold $\gamma'' = 2$ and no oscillation is predicted for purely local response, $\gamma'' = 0$, $\gamma' \neq 0$ in agreement with the previous results [2]. The new solutions for oscillation were found for combined local/nonlocal response, i.e. for the gratings, shifted for intermediate angles in the interval $(0 + \pi/2)$.

With the initial condition $\eta(0) = 0$ (no input wave 1 at the entrance face $z = 0$) one can get from the equation for phases that $\Phi(0) = \tan^{-1}(\gamma'/\gamma'')$ and calculate further $\eta(z)$ and $\Phi(z)$ with Runge-Kutta technique. For properly choiced sign of frequency detuning $\delta\omega$ the infinite grows of η occurs at certain critical thickness of the nonlinear layer which correspond to mirrorless oscillation. To determine the threshold for ring-loop oscillator we take $\eta(0) = 1/\sqrt{r}$. The necessary condition for oscillation in both cases is the compensation for nonlinear dephasing which is due to local response by geometrical dephasing due to misalignment of oscillation waves.

Fig.3 represents the dependencies of η and Φ on the coupling strength $\gamma'l$, (i.e. for the fixed coupling constant γ' on the thickness l of nonlinear sample) for γ''/γ' equal to 0.8, 0.1 and 0.01 (curves 1, 2 and 3 respectively). The infinite grows of η occurs for all possible γ''/γ' ; the smaller is nonlocal constant γ'' , the larger becomes the threshold thickness. Note also that at critical thickness the phase Φ takes the same absolute value but is opposite in sign to its input value.

The dependence of $\gamma''l/(\gamma'l)_{th} = f(\tau\delta\omega)$ is presented in the Fig.4 for $\gamma^0 l = 15, 10$ and 1.66 (curves 1, 2 and 3 respectively). The maximum above threshold gain is reached for $\delta\omega = 0.8/\tau$ for arbitrary initial $\gamma^0 l$.

Discussion. The considerations presented above can be supported by the following numerical estimates. Eq.1 contains the photovoltaic constant β_{33} and the specific photoconductivity κ ; both this quantities were measured from the

two-beam coupling experiments at $\lambda = 0.44 \mu\text{m}$: $\beta_{33} = 3.2 \cdot 10^{-9} \text{ A/W}$ and $\kappa = 1.6 \cdot 10^{-13} \text{ cm/Ohm.W}$. From this data the local coupling constant $\gamma^0 = -65 \text{ cm}^{-1}$, and the optimum frequency detuning of oscillation wave, $\delta\omega = 3 \cdot 10^{-8} \text{ Hz}$, were evaluated. By fitting the experimental points of the Fig.3 to calculated dependence

$$\Delta\theta = -\gamma'\lambda \sqrt{n^2 - \sin^2\theta} \left[2\pi \sin 2\theta \right]^{-1}, \quad (3)$$

one can deduce $\gamma' = -50 \pm 10 \text{ cm}^{-1}$, i.e. the value close to the results of direct measurements. Unfortunately, the measurement of so small frequency deviation superposed to technical noise because of imperfect mechanical stability looks impossible. It should be underlined that nonlinear change of refractive index in $\text{LiNbO}_3:\text{Fe}$ is negative which results in positive Δk_z and $\Delta\theta$ in agreement with the experimental results.

Phase conjugation. As it follows from the described experiments and calculations the oscillating beams are not strictly phase conjugate to the incident beams because of the angular misalignment (see Eq.2). Nevertheless if the lateral shift of oscillation wave is small compared with the characteristic size of optical inhomogeneities of aberrator in this interaction even the strong distortion of the wavefront can be compensated for.

For the pump waves with different temporal frequencies the angular deviation of one oscillating wave can be completely compensated for. Fig.5 represents the schematic explanation of this idea with the wavevector diagrams. If all four interacting waves have the same frequencies and are sent in the sample from outside at the angles $\pm\theta$ (Fig.5a) the dephasing exists, determined by the local part of nonlinear response, γ' . In the geometries discussed above the oscillation waves selfdevelop from the noise at a certain angle $\Delta\theta$ just to compensate for this nonlinear dephasing (Fig.5b). And finally in the Fig 5c the wavevector diagram for interaction with nondegenerate pumps is shown, where $\lambda_1 = \lambda_4$ and $\lambda_2 = \lambda_3$ are adjusted in such a way that the wavevectors of wave 4 and wave 3 become parallel. Note that the misalignment of the waves 1 and 2 is approximately doubled as compared with the case of degenerate pumps.

Pump frequency detuning necessary to compensate for the angular deviation of oscillating wave can be found from the relation

$$(\Delta\lambda/\lambda) = (\Delta n/n) \cot^2\theta, \quad (4)$$

where $\Delta n = \gamma\lambda/2\pi$ is the nonlinear change of refractive index, which we will take for simplicity equal for both pump waves. At $\theta = 30^\circ$, $\lambda = 0.44 \mu\text{m}$ and $\Delta n \leq 10^{-3}$ one can get $\Delta\lambda \leq 6 \text{ A}$. It is obvious that the pump frequency detuning necessary for compensation depends on the angle between two incident waves, that is why this technique may be applied for phase conjugation of the beams with the limited spatial content only.

REFERENCES

- 1 M.Cronin-Golomb, B.Fisher, J.White and A.Yariv,
IEEE J.Quantum Electronics, QE-20, 12 (1984)
- 2 S.Sternklar, S.Weiss and B.Fisher,
Opt. Lett. 11, 165 (1986)
- 3 J.P.Huignard and A.Marrakchi, Opt. Lett. 6, 622 (1981)

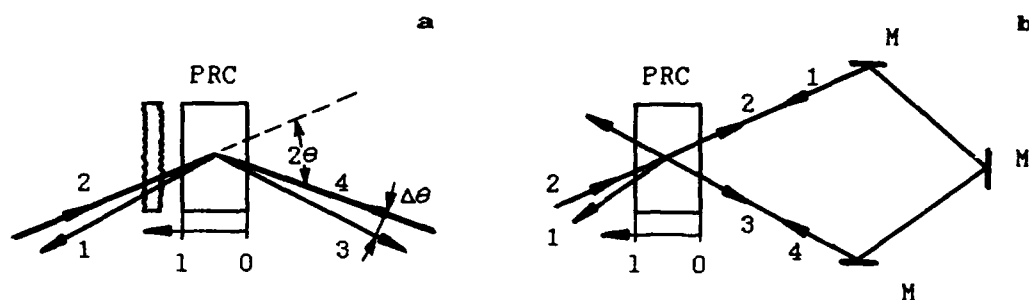


Fig. 1

Angular deviation,
 $\Delta\theta$, min

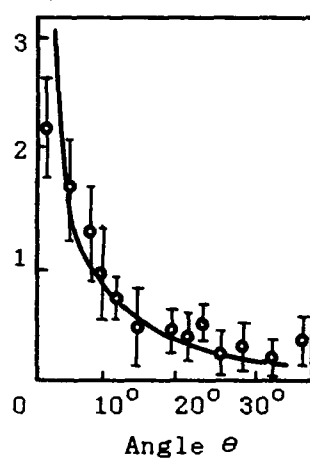


Fig. 2

Reflectivity, phase

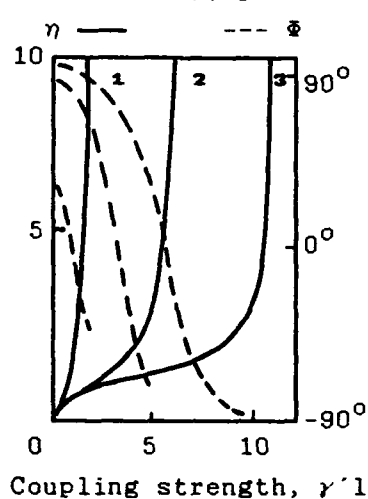


Fig. 3

Normalized gain,
 $\gamma''1/(\gamma''1)_{th}$

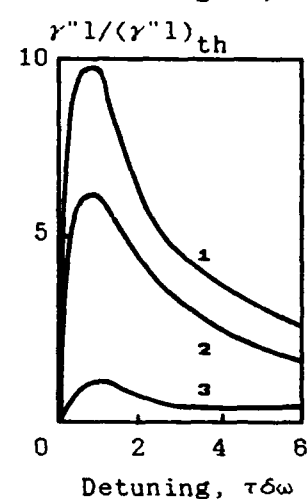


Fig. 4

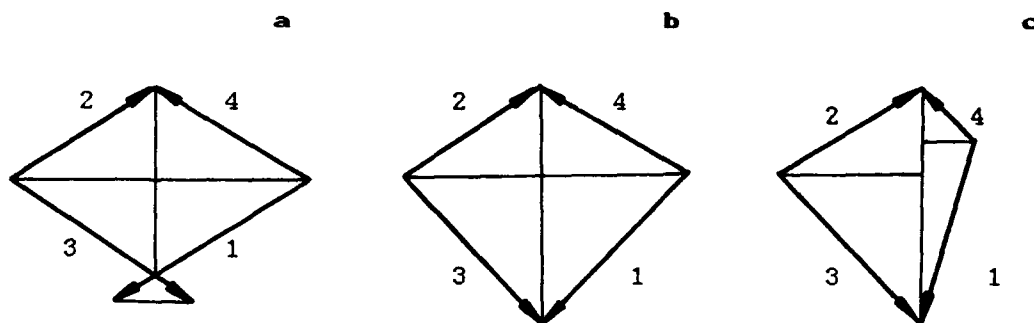


Fig. 5

AD-P006 773



Anisotropic Diffraction in Photorefractive Volume Hologram

CHING-CHERNG SUN AND MING-WEN CHANG

Institute of Optics Sciences
National Central University
Chung-Li, Taiwan 32054, R.O.C.

Recently, there are extensive studies on applying the photorefractive effect for optical data storage and processing[1][2]. One of the most important applications is for the volume holographic storage. In this paper we report theoretical derivations and experimental results on the important properties of the anisotropic diffraction in a photorefractive volume hologram in a $BaTiO_3$. As we shall see, the diffraction efficiency, the angular sensitivity, and the optimal reconstructing angle for obtaining the maximum diffraction efficiency depend very much on the grating vector and crystal orientations. The crystal orientation and the light beam directions are shown in Fig.1. In order to avoid the beam coupling phenomena[3], we use S-polarized light for writing holograms and P-polarized light for reconstruction. These two writing light beams interfere and induce a corresponding phase grating in the $BaTiO_3$ through the photorefractive effect. Now suppose the reconstructing and the diffracted beams are written as \vec{E}_a and \vec{E}_b respectively, we apply the slowly-varying amplitude approximation to solve the coupled-wave equation with the boundary conditions that $E_a(0)=1$ and $E_b(0)=0$. We obtain the formula for diffraction efficiency as

$$\eta = \left| \frac{E_b(l)}{E_a(l)} \right|^2 = \left[\frac{1}{1 + \frac{\sigma^2}{4|\Gamma|^2}} \right] e^{-\alpha y'} \sin^2(\sqrt{\sigma^2 + 4|\Gamma|^2} y'), \quad (1)$$

where α is the bulk absorption constant,

$$\sigma = \frac{1}{2}(k_b^2 - \omega^2 \mu \epsilon_b),$$

$$|\Gamma| = \frac{\omega^2 m}{4C^2} \gamma_{eff} E_{sc},$$

E_{sc} is the space charge field [4], m is the light modulation depth and

$$\gamma_{eff} = n_o^4 \gamma_{13} \cos \beta \sin \alpha_a \sin \alpha_b + n_o^2 n_e^2 \gamma_{42} \sin \beta \cos(\alpha_a - \alpha_b) + n_e^4 \gamma_{33} \cos \beta \cos \alpha_a \cos \alpha_b.$$

92-18761



Equation (1) is similar to the well known Kogelnik formula [5]. However, the anisotropic nature of γ_{eff} and σ makes the photorefractive diffraction different from that of the isotropic case. Since $\gamma_{42} = 8pm$, $\gamma_{33} = 28pm$ and $\gamma_{42} = 820pm$ [6], hence the $\gamma_{42}\sin\beta$ term dominates in γ_{eff} . As the grating tilt angle β increases, γ_{eff} and thus $|\Gamma|$ and η also increase until the argument in $\sin^2()$ in eq.(1) reaches $\frac{\pi}{2}$. Figure 2 shows the dependence of diffraction efficiency on the grating tilt β . In our experiments, we use an argon laser at the wavelength 488nm for writing and a HeNe laser at 633nm for reading. The writing power is $10 \frac{mw}{cm^2}$ and the reading power is $1 \frac{mw}{cm^2}$ to keep the effect on the grating minimum. We rotate the crystal to change β . It can be seen from the figure that the experimental results agree with our calculation. We also change the amplitude of the grating vector by adjusting the angle between the writing beams. This shows that the diffraction efficiency η depends on the grating vector.

Next, we consider the angular sensitivity (AS) of a photorefractive hologram. We define the AS as the angles deviate from the angle for maximum diffraction efficiency for the diffraction efficiency down to -20dB (instead of -3dB for easily experimental observation). At this large angular deviation, the diffraction efficiency is governed by the asymptotic behavior of the fractional part in eq.(1), which is determined by the ratio of $\frac{\sigma^2}{4|\Gamma|^2}$. As β increases, Γ increases, but σ remains relatively constant. This causes the ratio $\frac{\sigma^2}{4|\Gamma|^2}$ to decrease and therefore the AS is increased. The dependence of the AS on β is calculated and plotted in Fig.3 together with the experimental data. The figure shows that the AS increases as β is increased.

The third characteristic of the anisotropic diffraction is that the maximum diffraction efficiency may not happen at the exact Bragg match, and it also depends on β . We define the angular deviation (AD) as the angle apart from the Bragg angle to reach the maximum diffraction efficiency for a grating angle β , i.e., AD=0 means the maximum diffraction efficiency occurs at the Bragg angle. The theoretical calculation is shown in Fig.4. It shows that AD is β dependent in a $BaTiO_3$ crystal.

In conclusion, we have presented important properties of photorefractive volume hologram including diffraction efficiency, angle sensitivity and angle deviation apart from the Bragg match to reach the maximum diffraction efficiency. All these properties relate to the grating vector and the orientation of the crystal, and are different from the cases in an isotropic volume hologram.

We acknowledge the helpful discussions with Professors T.C.Hsieh and K.Y.Hsu of National Chiao Tung University.

REFERENCES

- [1] P.Yeh, A.E.Chiou, J.Hong, T.Chang & M.Khoshnevisan, "Photorefractive nonlinear optics and optical computing", Opt.Eng. 28(4), 3328 (1989).
- [2] P.Staebler & J.J.Amodei, "Couple-wave analysis of holography storage in $LiNbO_3$ ", J. Appl. Phys. 43(3), 1042 (1972).

- [3] A.E.Chiou and P.Yeh, "Symmetry filters using optical correlation and convolution", Opt. Eng. 29(9), 221 (1990).
- [4] J.Feinberg, D.Heiman, A.R.Tanguay & R.W.Hellwarth, "Photorefractive effects and light-induced charge migration in barium titanate", J. Appl. Phys. 51, 1297 (1980).
- [5] H.Kogelnik, "Coupled wave theory for thick hologram gratings", Bell. Syst. Tech. J. 48, 2909 (1969).
- [6] I.P.Kaminow, "Barium Titanate light modulator, II", Appl. Phys. Lett. 8(11), 305 (1966).

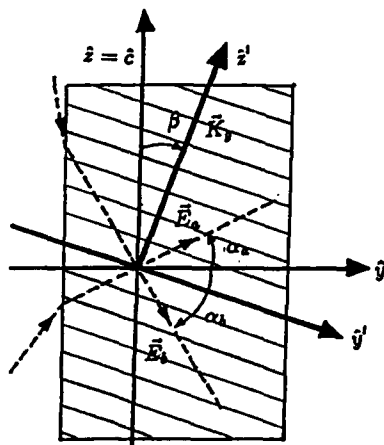


Fig.1

Geometrical configuration of the diffraction in $BaTiO_3$. \vec{E}_a and \vec{E}_b are the reconstructing and diffracted beams; β is the angle between optical axis (\hat{c}) of the crystal and grating vector \vec{K}_g ; α_a , α_b are the incident angles inside the crystal with respect to surface normal.

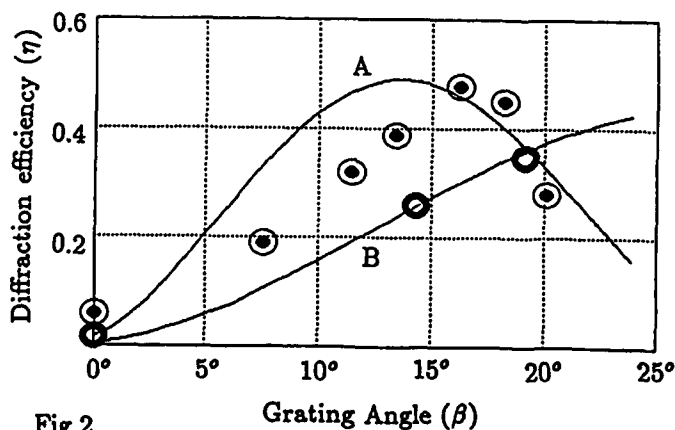


Fig.2

Diffraction efficiency (η) vs grating angle (β). Two lines with theoretical calculation with respect to two different angles between constructing beams, i.e., line A : 4° and line B : 8°.

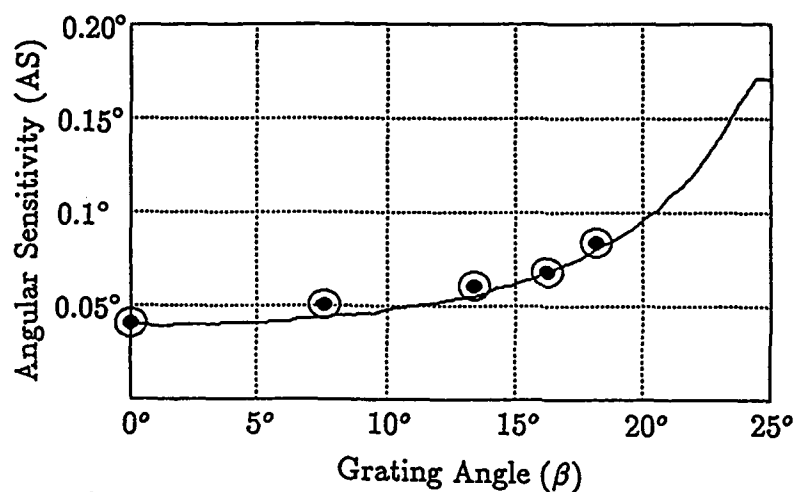


Fig.3

The β dependence of the angular sensitivity (AS). The angle between two writing beams is 8° and the solid line is the theoretical calculation.

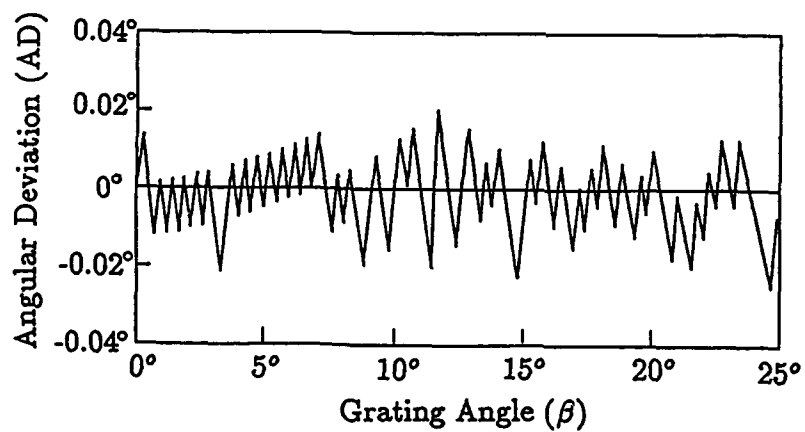


Fig.4

The β dependence of the angular deviation (AD). The angle between two writing beams is 8° and the line is the theoretical calculation.



92-18762

Low-Frequency Noise and Photoinduced Scattering in Photorefractive Crystals

B.I. Sturman

Institute of Automation and Electrometry Siberian Branch
of the USSR Acad.Sci., Novosibirsk, 630090, USSR

Introduction

Photoinduced scattering (PS) is inherent in a varying degree in any photorefractive crystal. The origin of the PS is quite clear: this is an amplification of the weak seed scattering. A number of papers, for example [1-3], deal with a description of the effect. The pump and scattered waves supposed usually to have the same frequency. In the framework of that approach, a steady-state PS may only be caused by the nonlocal photorefractive response (i.e. by shifted gratings). However, in many cases experiments show the steady-state PS to be abnormally large and this can not be accounted for by the nonlocal response. $\text{LiNbO}_3\text{:Fe}$ crystals, where the local response (i.e. unshifted gratings) exceed in value the nonlocal one by 10^1 - 10^2 times, can be pointed out as an example.

We suggest a new interpretation of the PS for crystals with a predominant local response.

Model

The main factor that gives rise to the amplification of the seed scattering is low-frequency noise of optical system elements, namely the fluctuation of the laser intensity and that of the refractive index of the crystal. A well known fact underlies the interpretation: the dependence of the exponential gain $\Gamma(\Omega)$ on the detuning $\Omega = \omega_0 - \omega$ between frequencies of pumping and testing beams is very sharp [4]. Schematically, this dependence is shown in Fig.1. Usually, the value Γ reaches its maximum Γ_m at $\Omega \approx \gamma$, where γ is the inverse dielectric relaxation time.

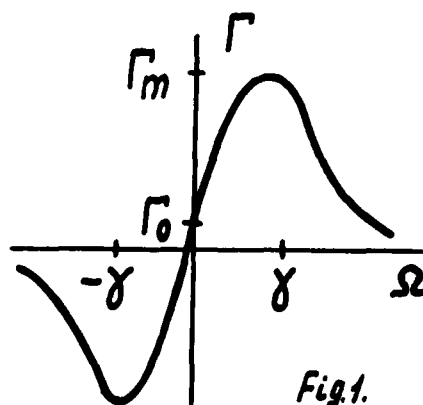


Fig.1.

The value Γ_0 characterises the local photorefractive response. If the seed scattering is elastic and the pump intensity is constant, then the steady-state scattering is given by

$$I_s \approx I_s^{\text{el}} \exp(\Gamma_0 l). \quad (1)$$

However, if only one of the above conditions is violated, the intensity will be expressed as follows:

$$I_s \approx I_s^{\text{inel}} \exp(\Gamma_m l), \quad (2)$$

where the value I_s^{inel} depends on the character of the LF noise. As far as $\text{LiNbO}_3\text{:Fe}$ is concerned, the exponent index $\Gamma_m l$ often reaches the value $\sim 10^2$, while $\Gamma_0 l \sim 1$. Even though the value I_s^{inel} is several orders of magnitude less than I_s^{el} , the exponential factor in Eq.(2) still dominates.

Let us consider the factors determining the value of I_s^{inel} . One of such factors is low-frequency ($\Omega \approx \gamma$) fluctuations of the incident intensity. In fact, such fluctuations exist in any experiment, being often out of control. Phase fluctuations due to the large laser line width ($\Delta\nu \gg \gamma$) do not contribute to I_s^{inel} . The other factor is temporal fluctuations of the refractive index. It is well known from statistical physics [5] that the frequency spectrum of fluctuations is proportional to $(\Omega^2 + \gamma^2)^{-1}$ for any equilibrium physical system that can be characterised by the only relaxation constant γ . Then the fluctuations that have the frequency $\Omega \approx \gamma$ are comparable with the static ones. Of course, the situation in question is ideal. Apart from the above mentioned electrical fluctuations, there are static volume and surface imperfections in any photorefractive crystal which have infinitely large relaxation time. For this reason the contribution of the inelastic seed scattering may be relatively small and pattern specific.

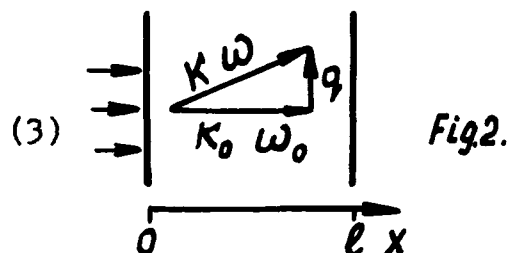
Moreover, it should be born in mind that non-equilibrium so called $1/f$ noise, proportional to Ω^{-1} , occurs in any physical system, in particular, in lasers and crystals [6].

Description

The starting equations for the PS have the form:

$$\left(\frac{d}{dx} + i\Delta\right)a_k = ik_0 a_0 (P_q + P_q^0)$$

$$\left(\frac{d}{dt} + \gamma\right)P_q = \beta a_k a_0^* .$$



Here a_0 and a_k are the complex amplitudes of pumping and scattered waves, \vec{k}_0 and \vec{k} are the respective wave vectors (see Fig.2), $\vec{q} = \vec{k} - \vec{k}_0$ is the grating vector, $\Delta = k - k_0$, P_q and P_q^0 are the amplitudes of the light induced and spontaneous gratings of the refractive index and β is a coupling constant (being real for the local response). Boundary conditions for a_k can incorporate scattering on the input surface. Eqs. (3) are valid when the length of light coherence is well above the crystal thickness l .

It is important that relaxation parameter γ depends on $|a_0|^2$ and it fluctuates in time. The typical approximation $\gamma \propto |a_0|^2$ corresponds to the situation where the dark conductivity of a crystal is negligible and the photoconductivity σ_{ph} is proportional to $|a_0|^2$.

When the fluctuations of the pump intensity I_0 are negligible, Eqs.(3) give the following formula for the light intensity dI scattered into solid angle do :

$$\frac{dI}{I_0} \approx \frac{\gamma k_0^4}{\Gamma_m} K_{q\gamma} \exp(\Gamma_m l) do. \quad (4)$$

Here $K_{q\Omega}$ is the Fourier-component of the correlation function $K(\vec{\rho}, \tau) = \langle \Delta n(\vec{r} + \vec{\rho}, t + \tau) \Delta n(\vec{r}, t) \rangle$, which is the main characteristic of the fluctuations of the refractive index Δn . It is quite clear that $K_{q\Omega}$ is connected with photocurrent fluctuations. An information about $K_{q\Omega}$ can be derived either from an independent experiment or from a microtheory.

An interesting situation takes place when we want to consider the intensity fluctuations as the main cause of the PS. Whenever

$\gamma \propto |a_0|^2$, no amplification of the seed scattering occurs. The intensity fluctuations can stimulate the PS provided the dependence $\gamma(|a_0|^2)$ is not linear. The origin of that nonlinear behaviour may lie with sub- or superlinear dependence of the photoconductivity $\sigma_{ph}(I_0)$ or with the dark conductivity being sufficiently large. The scattered light intensity can be expressed in terms of the Fourier-component of the correlation function $L(\tau) \equiv \langle I_0(t+\tau)I_0(t) \rangle$.

Numerical estimations of the value I_s^{inel} in Eq.(2) are highly sensitive to the choice of model parameters. Nevertheless, the estimations demonstrate efficiency of the mechanisms.

Conclusions

Anomalously large PS is possible in a photorefractive crystal with a predominant local response.

It is possible to consider such a crystal as an amplifier of the well-known $1/f$ noise.

The LF noise amplification may be important for treatment of any photorefractive phenomenon that requires a seed scattering.

The frequency shift $\Omega \approx \gamma$ should exist between the pumping beam and the scattered waves.

A suppression of the PS is possible by stabilizing of the laser intensity.

References

1. I.F.Kanaev, V.K.Malinovskii and B.I.Sturman, Opt.Comm., V.34, p.95, 1980.
2. J.Marotz, K.Ringhofer, R.A.Rupp and S.Treichel, IEEE, V.22, p.1376, 1986.
3. V.V.Obukhovskii, A.V.Stoyanov and V.V.Lemeshko, Kvant. Electron., V.14, p.113, 1987.
4. Photorefractive Materials and Their Application (Springer, 1989), V.62, p.5, p.101.
5. L.D.Landau and E.M.Lifshits, Statistical Physics, Part I, Moscow, 1976, p.406.
6. F.Hooge, Physica, V.60, p.130, 1972.

Wednesday, July 31, 1991

Defects and Charge Transport

WB 10:30am–12:00m
Academic Center Auditorium

Thomas Pollak, *Presider*
Sanders Associates



Identification of light induced charge transfer processes in BaTiO₃ by combined ESR and optical measurements

O.F. Schirmer, E. Possenriede, H. Kröse, P. Jacobs

Fachbereich Physik, Universität Osnabrück
Barbarastr. 7, W-4500 Osnabrück, Federal Republic of Germany
Tel. (0541) 608-2630, Fax: (0541) 608-2670

Introduction

What are the defects responsible for the photorefractive effect in BaTiO₃? What charge conversion processes involving these defects are taking place during illumination? Along which energetic paths are charges transported? These questions have to be answered if one wants to understand the outstanding photorefractive properties of BaTiO₃ on a microscopic basis.

The necessary information can be obtained from ESR studies, if these are combined with optical investigations. We report on such measurements. It was found that the optical behavior of the defects identified by ESR varied from specimen to specimen, even if these were nominally undoped. Even for the same crystal the results depended strongly on the history of illumination and heat treatments. We can give so far only representative results, mostly obtained with crystals cut from one boule, which was nominally undoped.

ESR investigations of defects in BaTiO₃ in relation to the photorefractive behavior of the material have been performed earlier [1, 2]. We extend such measurements by observing ESR with BaTiO₃ single crystals also at low temperatures and by simultaneously monitoring the light induced changes of ESR and optical absorption.

Methods

ESR was measured at 9 and 34 GHz. In most cases low temperatures, down to 6 K, had to be applied in order to prevent too short spin lattice relaxation times and thermal instabilities of the defects in their light induced metastable configurations.

The changes of the ESR, mostly at such low temperatures, were observed under the following illumination program: monochromatic light of successively shorter wavelengths, starting near 1100 nm, was shone onto the crystal fixed in the ESR cavity. The wavelength dependence of the light induced changes of the ESR signals was monitored. By this method the threshold energies for charge conversion can be determined. At the low temperatures used the charge changes are mostly metastable. By repeating the above measurement cycle without heating after the first run the energies of the metastable states can thus be determined. For more details see below.

In order to establish a correlation between light induced changes of ESR and optical absorption we have combined an optical spectrometer with the ESR setup. In this way we can monitor both changes simultaneously. By this method the microscopic information obtained from ESR at low temperatures is transferred to optical absorption bands, which mostly are observable also at room temperature, where photorefractive experiments are carried out usually. Our aim is to attribute all major absorption bands in BaTiO₃ to definite microscopic centers, including diamagnetic ones, in order to have the tools to unravel the light induced processes occurring at room temperature.

92-18763



Results

a) ESR

We first list here all the paramagnetic defects, which we have identified so far in the crystals studied. For details of the interpretation of the basic ESR results, we refer to the listed publications. In most cases paramagnetic cations are concerned, substituting for Ti^{4+} .

Table 1: ESR centers identified in various BaTiO_3 single crystals

| | |
|---|---|
| $3d^1$: Cr^{5+} [3], Ti^{3+} – ass. with defect [4] | $3d^7$: Co^{2+} [8], $\text{Co}^{2+}-\text{V}_0$ [4] |
| $3d^3$: Fe^{5+} [5], Mn^{4+} [6], Cr^{3+} [7] | $5f^3$: Nd^{3+} [9] |
| $3d^4$: $\text{Fe}^{4+}-\text{V}_0$ [5] | $5d^7$: Pt^{3+} [10, 4] |
| $3d^5$: Fe^{3+} , $\text{Fe}^{3+}-\text{V}_0$ [5] | $2p^5$: O^- ass. with Al^{3+} and with unkn. def. [3, 4] |

Fig. 1 shows the model consistent with the ESR data on the latter O^- centers. Their concentration is strongly enhanced by suitable illumination of the crystals. They originate from light induced holes, captured near defects on Ti sites, which are charged negatively with respect to the lattice (acceptor centers). The nature of A_{Ti} in Fig. 1 is not known yet. Because oxygen orbitals are involved, these centers have energy levels rather close to the valence band.

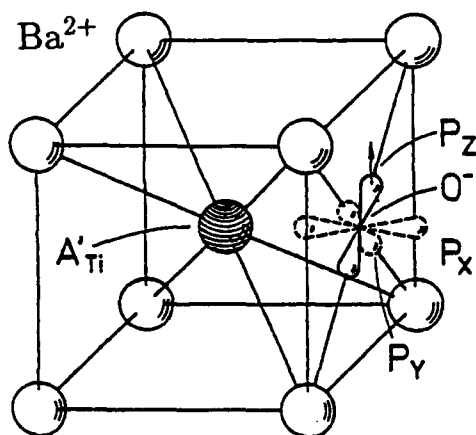


Fig. 1: Model of O^- trapped hole center in nominally undoped BaTiO_3 . For clarity only one of the six oxygen ions surrounding Ti is shown. The groundstate orbital of the hole, p_z , and the next excited states, p_x and p_y , are indicated. The nature of the acceptor defect A_{Ti} , replacing Ti, is not yet known.

b) Photoinduced valence changes

As an example only the results obtained with a single specimen, nominally undoped, are shown in detail. Fig. 2 shows the variation of the concentrations of the indicated centers under illumination. Fe^{3+} and O^- are the mainly occurring paramagnetic entities in this crystal. It is known from holographic studies [11] that the mobile charge carriers in this crystal for illumination with $\lambda = 514$ nm and 633 nm are holes. Accordingly Fig. 2a can be interpreted in the following way: For $\lambda \lesssim 850$ nm, Fe^{3+} is created by hole photoionisation of Fe^{4+} ; in the range $650 \text{ nm} \lesssim \lambda \lesssim 850$ nm holes are captured at unknown sites; for $\lambda \lesssim 650$ nm they appear partly in the form of the O^- center shown in Fig. 1. The processes occurring are lumped together in the inset of this figure. In Fig. 2b the behavior of the charge states metastably created during the first run are studied. It is seen that already at rather long wavelengths holes are photoionised from O^- . In fact this occurs already for $\lambda \approx 1500$ nm (~ 0.8 eV). So this center is rather shallow. The freed holes are captured by Fe^{3+} , forming Fe^{4+} . At shorter wavelengths the same processes occur as in Fig. 2a. It is seen that in this crystal at low temperatures a spatial hole transfer

between Fe^{4+} and O^- takes place. The threshold energies are indicated.

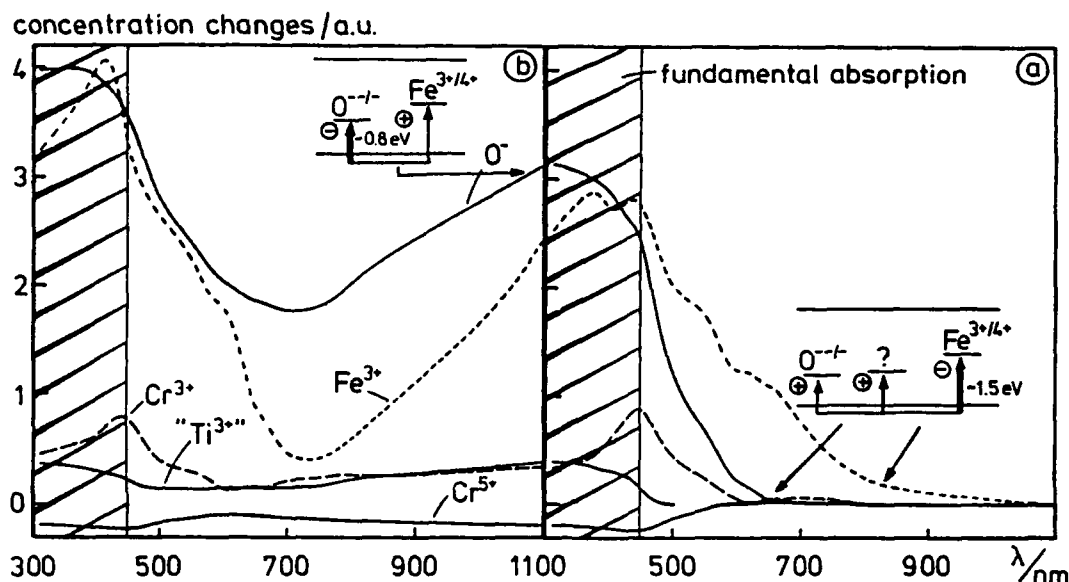


Fig. 2: The changes of the concentrations of ESR centers identified in a nominally undoped BaTiO_3 crystal under illumination with light of varying wavelengths. O^- and Fe^{3+} are the paramagnetic entities whose charges are changing in the most prominent way. In Fig. 2a the crystal, cooled to ~ 20 K in the dark, is illuminated with light of successively shorter wavelengths, starting near 1100 nm. The inset summarizes the essential charge transfer processes occurring. In Fig. 2b the first cycle is repeated without prior warming of the crystal. Now O^- , metastably created during the first run, is photoionized at long wavelengths. For explanation see inset.

c) Simultaneous measurement of ESR and absorption changes

With the same crystal the absorption changes shown in Fig. 3 were measured – simultaneously with the ESR data of Fig. 2a. The charge conversion light, wavelength Λ , was applied just before the ESR- and absorption measurements. The total absorption spectra, wavelength λ , were obtained with rather low level light intensities of short duration, ~ 170 ms, using a diode array as detector.

The most prominent features in Fig. 3 are the absorption bands denoted O^- and Fe^{3+} . Fe^{3+} rises strongly for $\lambda \lesssim 850$ nm, O^- for $\lambda \lesssim 650$ nm, corresponding to the same behavior as in Fig. 2a. Fig. 3 thus identifies the wide band peaked near 690 nm as caused by O^- . This assignment is in accord with previous experience on the mechanism of the absorption of such O^- trapped hole centers [12]. It is furthermore seen in Fig. 3 that a band peaked at 440 nm, denoted Fe^{4+} , changes its intensity as expected for Fe^{4+} according to Fig. 2a. The corresponding Fe^{4+} absorption in SrTiO_3 , as identified by correlation with ESR [13], has its maximum near the same wavelength. This band is also rather wide in SrTiO_3 , extending down to 800 nm. The remaining bands in Fig. 3 could not yet be identified.

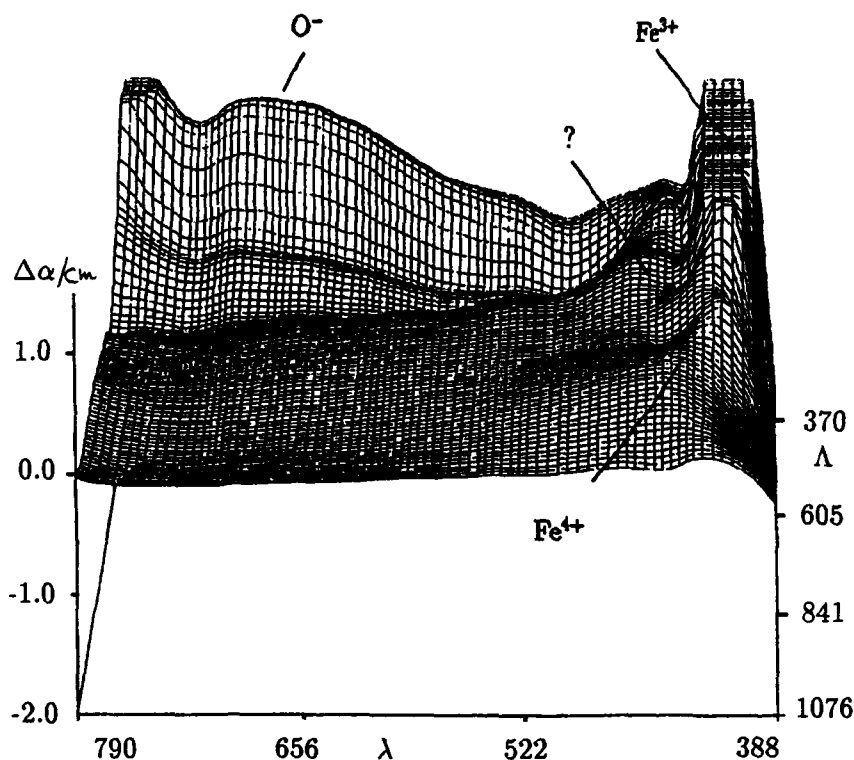


Fig. 3: Changes of the optical absorption during the illumination cycle of Fig. 2a. The optical absorption is scanned with the wavelength λ . The charge conversion light is denoted Λ , the Λ -axis corresponds to the abscissa in Fig. 2a.

Conclusion

Using combined ESR and optical absorption measurements it is seen that illumination of the investigated specimen leads to hole transfer from Fe^{4+} to O^- . It is expected that this method, applied here for the first time, will lead to an explanation on the atomic level of charge transfer paths, light induced optical absorptions and possibly also the phenomenon of sublinear dependence [14] of photoconductivity on light intensity in BaTiO_3 .

References

- [1] R.N. Schwartz, B.A. Wechsler, (to be published)
- [2] M.B. Klein, in "Photorefractive materials and their applications", *Topics in Applied Physics* 61, ed. by P. Günter and J.P. Huignard (Springer, Berlin, Heidelberg 1988), pp. 195-236
- [3] E. Possenriede, O.F. Schirmer, J. Albers, G. Godefroy, *Ferroelectrics* 107, 313 (1990)
- [4] E. Possenriede, O.F. Schirmer, (to be published)
- [5] E. Possenriede, O.F. Schirmer, H. Donnerberg, G. Godefroy, A. Maillard, *Ferroelectrics* 92, 245 (1989)
- [6] K.A. Müller, W. Berlinger, K.W. Blazey, J. Albers, *Solid State Commun.* 61, 21 (1987)
- [7] K.A. Müller, W. Berlinger, J. Albers, *Phys. Rev. B* 32, 5837 (1985)
- [8] M. Aguilar, *Solid State Commun.* 50, 837 (1984)
- [9] E. Possenriede, O.F. Schirmer, G. Godefroy, *phys. stat. sol. (b)* 161, K55 (1990)
- [10] Z. Šroubek, K. Ždánkský, E. Šimánek, *phys. stat. sol.* 3, K1 (1963)
- [11] L. Holtmann, private communication
- [12] O.F. Schirmer, *Z. Physik B* 24, 235 (1976)
- [13] K.W. Blazey, O.F. Schirmer, W. Berlinger, K.A. Müller, *Solid State Commun.* 16, 589 (1975)
- [14] see, e.g.: L. Holtmann, *phys. stat. sol. (a)* 113, K89 (1989)



SPECTROSCOPY OF LIGHT SENSITIVE DEFECT/IMPURITY CENTERS IN PHOTOREFRACTIVE BaTiO₃

Robert N. Schwartz, Barry A. Wechsler, and Ross A. McFarlane
Hughes Research Laboratories
Malibu, CA 90265

Control and optimization of the behavior of photorefractive crystals requires first, a thorough understanding of the nature (charge state, local symmetry, and electronic structure) of the defects/impurities present in these materials, and of their interaction with light.^{1,2,3} Toward this end, we have carried out electron paramagnetic resonance (EPR), photo-EPR, and optical absorption measurements on a variety of BaTiO₃ samples doped with transition metal ions. These crystals were grown by top-seeded solution growth from a melt with an excess of TiO₂.

In order to identify the charge states of transition metal dopants and to correlate them with the processing conditions (annealing in oxidizing and reducing atmospheres), we have carried out extensive EPR measurements as a function of temperature on both single crystals and polycrystalline samples. We describe in detail our EPR results on polycrystalline samples for various oxidation-reduction conditions. From these measurements we are able to establish a relative energy scale for the positions of the various charge states of the transition metal dopants in the bandgap of BaTiO₃ (Fig. 1).

We have also carried out extensive photo-EPR measurements on cobalt-doped BaTiO₃ single crystals. This technique allows one to monitor the change in the charge state of a paramagnetic defect/impurity center under illumination. Furthermore, with this technique new defect centers that are created under illumination may be identified.⁴ Measurements of the steady-state photo-EPR response as a function of wavelength, intensity and temperature have been carried out. Figure 2 shows the photo-EPR signal at 25 K as a function of incident light intensity at 647 nm. We will report measurements for excitation wavelengths covering the range from 488 nm to beyond 900 nm. To investigate the dynamics of the photogenerated charges, we have

92-18764



measured the time response of the photo-EPR signal at fixed light intensity over a range of wavelengths and temperatures.

REFERENCES

1. B.A. Wechsler and M.B. Klein, *J. Opt. Soc. Am. B* **3**, 1711 (1988).
2. D. Rytz, B.A. Wechsler, M.H. Garrett, C.C. Nelson, and R.N. Schwartz, *J. Opt. Soc. Am. B* **7**, 2245 (1990).
3. R.N. Schwartz, B.A. Wechsler, and D. Rytz, *J. Am. Ceram. Soc.* **73**, 3200 (1990).
4. E. Possenriede, O.F. Schirmer, J. Albers, and G. Godefroy, *Ferroelectrics* **107**, 313 (1990).

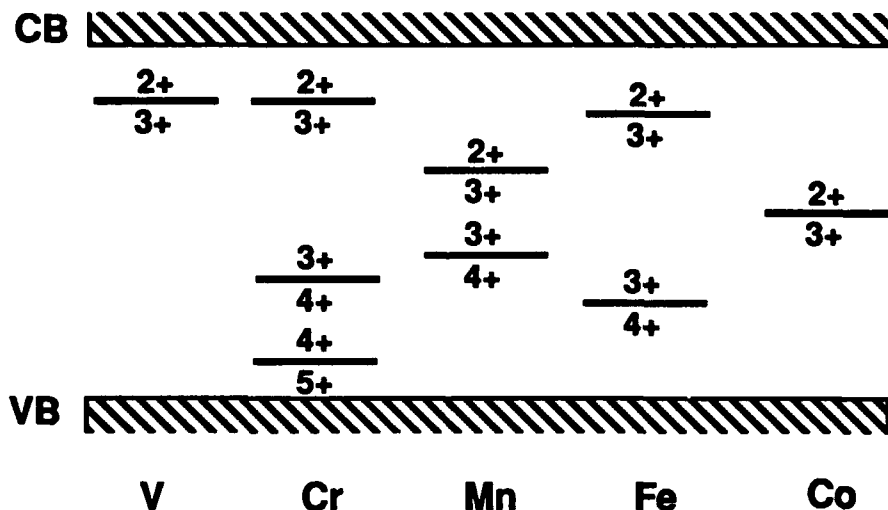


Figure 1. Schematic energy level diagram illustrating the relative positions of the ionization levels of various transition metals in BaTiO₃, as inferred from EPR studies. Other levels may be present but were not detected in our EPR experiment. The Cr (3+/4+) and (4+/5+) levels may be close together, since 3+ and 5+ states are sometimes observed simultaneously. The two Mn levels are probably also closely spaced, since the 2+ and 4+ states may be present simultaneously.

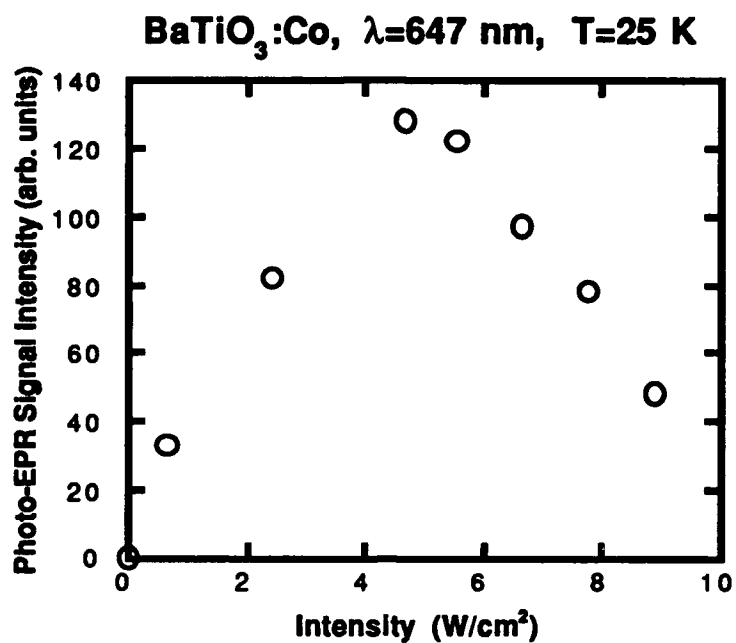


Figure 2. Variation of the photo-EPR signal intensity as a function of incident light intensity for BaTiO₃.



Two-center model explains photorefractive properties of $\text{KNbO}_3\text{:Fe}$

L. Holtmann, G. Kuper, K. Buse, S. Loheide, H. Hesse, E. Krätzig
 FB Physik, Universität Osnabrück, W-4500 Osnabrück, FRG, tel. (0541) 6082752

KNbO_3 has favourable photorefractive properties for applications in fast nonlinear optics such as image processing, coherent light amplification, [1] or self-pumped phase conjugation [2]. Desirable is the optimization of the sensitivity connected with the response time and the refractive index change. Only little is known about the centers involved in the photorefractive effect of KNbO_3 . Previous models were based on the assumption of iron impurities occurring in two valence states, Fe^{2+} and Fe^{3+} , as sources and traps for the redistribution of charges [1]. But these models cannot explain a nonlinear response of photoconductivity on light intensity already observed earlier [3, 4].

Measurements of photoconductivity, light-induced absorption, refractive index change and grating phase shift in a $\text{KNbO}_3\text{:Fe}$ crystal are carried out. As suggested for BaTiO_3 we use a charge transport model including deep and shallow traps to explain both the photoconductivity and light-induced absorption in $\text{KNbO}_3\text{:Fe}$ looking for a complete set of model parameters.

1 Photoconductivity

With the help of an argon laser ($\lambda = 515\text{ nm}$) elementary phase holograms are formed within a $\text{KNbO}_3\text{:Fe}$ crystal and erased by a separate off-Bragg erasure beam of adjustable intensity. The photoconductivity σ_{ph} is deduced from the hologram decay times τ via $\sigma_{ph} = \epsilon\epsilon_0/\tau$ with $\epsilon = \epsilon_{33} = 55$ [5]. The measured photoconductivities do not scale linearly with light intensity I nor can be described by a fractional power law dependence $\sigma_{ph} \propto I^x$. It is advantageous to plot σ_{ph}/I as a function of light intensity I because regions of linear photoconductivity versus light intensity result in horizontal lines (Fig. 1). The photoconductivity becomes linear in I at higher light intensities. This effect is most pronounced when the crystal temperature is 25°C . In Fig. 1 results of conventional current-voltage measurements are also included coinciding favourably with those determined holographically.

2 Light-induced absorption

In $\text{KNbO}_3\text{:Fe}$ we observe light-induced absorption similar to that reported for BaTiO_3 [7, 8, 6] when the sample is subjected to intensive illumination of a strong pump beam. The temporal evolution of the light-induced absorption coefficient α_{li} is shown in Fig. 2 for light polarization perpendicular to the c -axis. The absorption rises exponentially with rate $\gamma_{li} = 12\text{ s}^{-1}$ for $I = 29\text{ kWm}^{-2}$. The rate γ_{li} depends on light intensity but not on the crystal temperature. The decay process of α_{li} cannot be described by a simple exponential law especially when the value of α_{li} reached during the illumination is close to the maximum of $\alpha_{li} = 12\text{ m}^{-1}$. The initial decay rate strongly depends on temperature but also slightly on the steady state value of α_{li} . From the temperature dependence of the initial decay process starting from equal steady state values of α_{li} we may deduce an activation energy of $E_2 = 0.8 \pm 0.1\text{ eV}$ for the decay rate of the light-induced absorption. Figure 3 shows the steady state value of the light-induced absorption α_{li} as a function of pump light intensity. At lower temperatures the light-induced absorption saturates for light intensities of about 10 kWm^{-2} .

92-18765



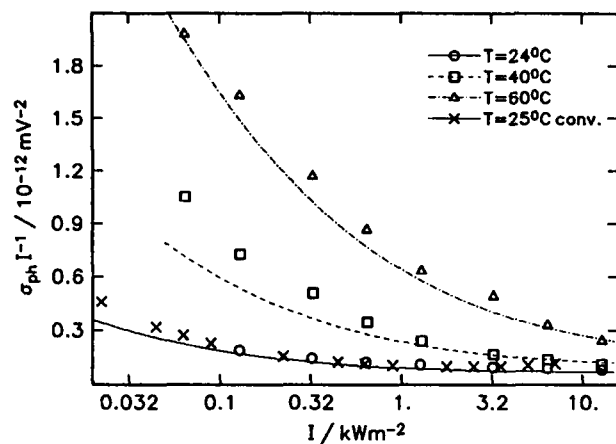


Figure 1: Specific photoconductivity σ_{ph}/I versus light intensity I for different crystal temperatures T . Values denoted by x are obtained from conventional current-voltage measurements. The curves are calculated from the two-center model (see text).

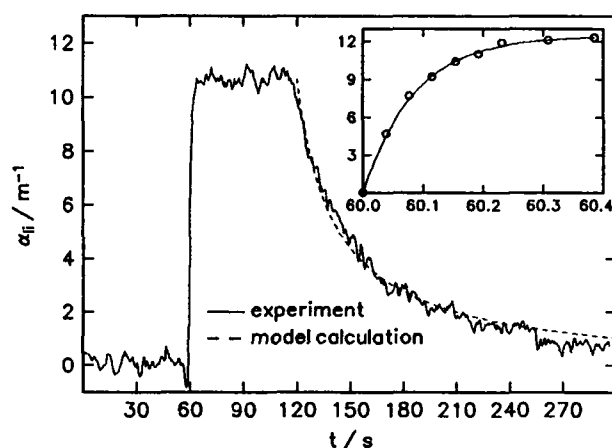


Figure 2: Light-induced absorption coefficient α_{li} for $\lambda = 514 \text{ nm}$ versus time t . At $t = 60 \text{ s}$ the pump is switched on and switched off at $t = 120 \text{ s}$. The pump beam intensity is $I = 3 \text{ kWm}^{-2}$ and the temperature is 25°C . The inset shows the rise of α_{li} for $I = 29 \text{ kWm}^{-2}$. The decay of α_{li} is calculated from the two-center model (see text).

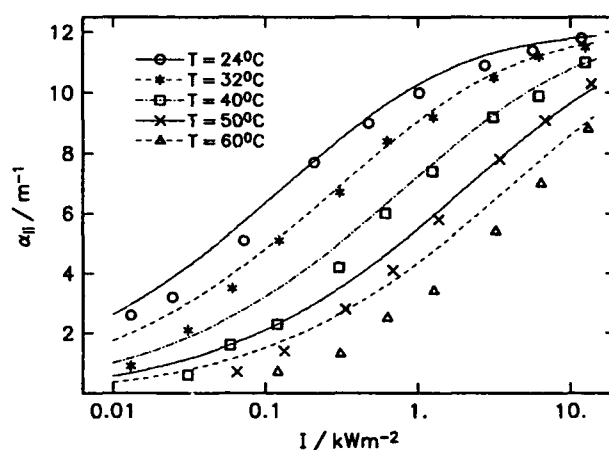


Figure 3: Light-induced absorption coefficient α_{li} for $\lambda = 515 \text{ nm}$ as a function of light intensity I with the crystal temperature T as a parameter. The curves are calculated from the two-center model (see text).

3 Refractive Index Change

Elementary gratings are recorded in our $\text{KNbO}_3\text{:Fe}$ crystal using an argon laser (515 nm) and simultaneously read with a helium neon laser (633 nm). From the diffraction efficiency η of the gratings we deduce the refractive index change Δn . The steady state value of Δn depends on light intensity and crystal temperature (see Fig. 4). At $T = 25^\circ\text{C}$ the refractive index change Δn increases with increasing light intensity within the interval investigated whereas at $T = 60^\circ\text{C}$ we obtain a decrease of Δn with growing I .

We analyse the steady state refractive index change of different recording cycles when applying external electric fields to the crystal. With growing field strength we first observe a decrease of Δn reaching a minimum before Δn increases continuously with E_{ext} . We attribute this behaviour

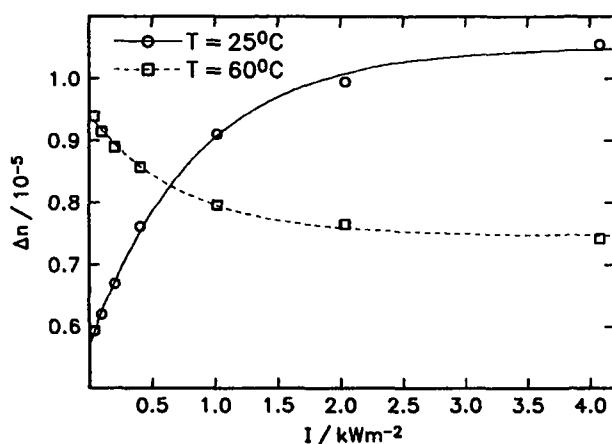


Figure 4: Steady state refractive index change Δn versus intensity I of the writing beams for different temperatures T . The modulation index is about 0.9 and the grating spacing $\Lambda = 1.2 \mu\text{m}$. The reading beam with wavelength 633 nm is polarized parallel to the c -axis. The lines are only for orientation.

to a compensation mechanism of the external electric field and the internal photovoltaic field E_{phv} . Therefore we can derive the photovoltaic field strength as a function of light intensity and temperature. At room temperature the photovoltaic field increases with I up to $8 \times 10^4 \text{ Vm}^{-1}$.

4 Grating phase shift

A two-beam interference arrangement similar to that described earlier is used to form elementary gratings in $\text{KNbO}_3:\text{Fe}$. In front of the crystal one of the beams is periodically phase-modulated with the help of an electrooptic modulator leading to small vibrations of the light interference pattern with respect to the sample. Due to beam coupling the output signals consist of harmonic terms in the modulation frequency [9]. From the first- and second harmonic parts the phase shift of the hologram can be evaluated as a function of recording time.

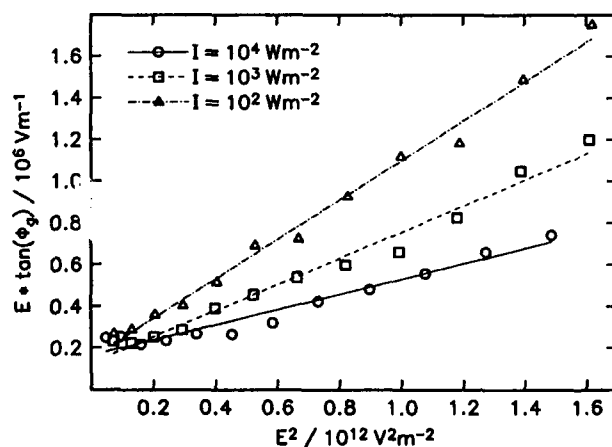


Figure 5: Plot of $E \tan(\Phi_g)$ versus E^2 allowing the determination of E_d and E_q according to ref.[10]. The lines are linear fits to the data.

$I = 10^4 \text{ Wm}^{-2}$: $E_d = 1.6 \times 10^5 \text{ Vm}^{-1}$, $E_q = 2.7 \times 10^6 \text{ Vm}^{-1}$;

$I = 10^3 \text{ Wm}^{-2}$: $E_d = 1.3 \times 10^5 \text{ Vm}^{-1}$, $E_q = 1.6 \times 10^6 \text{ Vm}^{-1}$;

$I = 10^2 \text{ Wm}^{-2}$: $E_d = 1.5 \times 10^5 \text{ Vm}^{-1}$, $E_q = 1.1 \times 10^6 \text{ Vm}^{-1}$

We measure the dependence of the steady state phase shift Φ_g versus the applied electric field E_{ext} for different light intensities and crystal temperatures. Figure 5 shows the dependence of $E \tan \Phi_g$ versus E^2 for $T = 60^\circ\text{C}$ and different intensities where E is determined by $E = E_{ext} - E_{phv}$. This type of plot allows the determination of the diffusion field E_d and the limiting space charge field E_q [10]. The measured diffusion fields coincide favourably with the theoretical value $E_d =$

$1.6 \times 10^5 \text{ Vm}^{-1}$. The limiting space charge field E_q increases with increasing light intensity. At $T = 25^\circ\text{C}$ we obtain no dependence of E_q on the light intensity ($E_q = 2.7 \times 10^6 \text{ Vm}^{-1}$).

5 Discussion

The nonlinear dependence of the photoconductivity versus light intensity and the light-induced absorption may be explained in terms of a two-center charge transport model [8, 6]. Two "saturation" effects appear: The photoconductivity becomes linear in the light intensity and the light-induced absorption saturates when the light intensity is high enough. Just this behaviour may be inferred from the two-center model [11]. The mentioned effects appear when the thermal generation rate compares with the light-induced generation rate at the second center. From the transient behaviour of the light-induced absorption and a correlation of the photoconductivity with the steady state light-induced absorption coefficient we deduce different parameters of the two-center model [6]. A complete set of parameters may be evaluated describing reasonably the behaviour of the photoconductivity and the light-induced absorption. Results of our model calculations are included in the Figs. 1, 2, 3.

As the photovoltaic field is small compared to the diffusion field $E_d = 1.35 \times 10^5 \text{ Vm}^{-1}$ ($T = 25^\circ\text{C}$, grating spacing $\Lambda = 1.2 \mu\text{m}$) the intensity dependence of the refractive index change Δn in Fig. 4 cannot be explained in terms of an intensity dependent photovoltaic field. This conclusion is also supported by the intensity dependence of Δn at 60°C which also excludes significant effects of the dark conductivity. According to ref.[10] the nonlinear dependence of the photoconductivity on light intensity has to be taken into account in the interpretation of holographic experiments. The maximum refractive index change may be reduced when the photoconductivity is nonlinear in light intensity.

The transport of charges from deep level impurities to shallow levels within the two-center model is connected with a change of the concentration ratio of occupied to empty centers [8, 12]. Consequently, the effective trap concentration N_{eff} and the limiting space charge field E_q vary with light intensity and temperature.

Financial support by the Deutsche Forschungsgemeinschaft is gratefully acknowledged.

References

- [1] P. Günter, *Phys. Rep.* **93**, 199 (1982).
- [2] D. Rytz, S. De Zhong, *Appl. Phys. Lett.* **54**, 2625 (1989).
- [3] A. E. Krumins, P. Günter, *Phys. Stat. Sol.(A)* **55**, K185 (1979).
- [4] P. Günter, F. Micheron, *Ferroelectrics* **18**, 27 (1978).
- [5] E. Wiesendanger, *Ferroelectrics* **6**, 263 (1974).
- [6] L. Holtmann, M. Unland, E. Krätzig, G. Godefroy, *Appl. Phys. A* **51**, 13 (1990).
- [7] A. Motes, J. J. Kim, *J. Opt. Soc. Am. B* **4**, 1379 (1987).
- [8] G. A. Brost, R. A. Motes, J. R. Rotgé, *J. Opt. Soc. Am. B* **5**, 1879 (1988).
- [9] P. M. Garcia, L. Cescato, J. Frejlich, *J. Appl. Phys* **66**, 47 (1989).
- [10] R. A. Rupp, A. Maillard, J. Walter, *Appl. Phys. A* **49**, 259 (1989).
- [11] L. Holtmann, *phys. stat. sol. (a)* **113**, K89 (1989).
- [12] D. Mahgerefteh, J. Feinberg, *Phys. Rev. Lett.* **64**, 2195 (1990).

AD-P006 778



Electron-Hole-Transport in Photorefractive Media

M.C. Bashaw

Department of Applied Physics, Yale University,
New Haven, Connecticut 06520-2157

T.-P. Ma and R.C. Barker

Department of Electrical Engineering, Yale University,
New Haven, Connecticut 06520-2157

(Telephone: M.C.B. 415 723-9127, T.-P.M. 203 432-4211,
R.C.B. 203 432-4308)

Recently, electron-hole transport in photorefractive media has received much interest. Many observations which cannot be accounted for by simple single-carrier single-level transport can be explained by electron-hole transport. This summary describes electron-hole transport by two different models and describes a regime in which both models give similar results.

For the single-level electron-hole-transport model considered, one species of traps exists in the band gap, and charge transfer occurs by both electron and hole transport. For the two-level electron-hole-transport model, two species of traps exist in the band gap, and charge transfer occurs by electron transport for the species closest to the conduction band and by hole transport for the species closest to the valence band.

For most regimes, the two models give significantly different results. Saturation space-charge fields depend on the model used; for the single-level model, the field depends on the relevant rate constants, but for the two-level model, it depends on the relevant limiting space-charge fields. The number of time constants depends on the model used; the single-level model yields one time constant, whereas the two-level model yields two. And only the two-level electron-hole-transport model allows the presence of complementary gratings [1].

For the case of large limiting space-charge fields, or equivalently, for the case of large grating periods, both the single- and two-level electron-hole-transport models give similar results. Using the quasi-steady approximation, both models reduce to the following expres-

92-18766



sion describing time evolution of the first-order Fourier harmonic of the space-charge field

$$\frac{\partial E_1}{\partial t} = -[m\Gamma_e(E_0 + iE_D) + \Gamma_e E_1] - [m\Gamma_h(E_0 - iE_D) + \Gamma_h E_1], \quad (1)$$

in which the response rates, Γ_e and Γ_h , which are functions of the grating period, assume the appropriate values for electron and hole transport for each model. Here E_D is the diffusion field and E_0 is the applied field.

Thus, in the large-grating-period limit for both models, the space-charge field, E_{sc} , is

$$E_{sc} = -im\xi E_D \quad (2)$$

where m is the modulation factor of the light interference pattern and the electron-hole competition factor, ξ , is

$$\xi = \frac{\Gamma_e - \Gamma_h}{\Gamma_e + \Gamma_h}. \quad (3)$$

The *sign* of the space-charge field depends on the properties of the electron- and hole-transport processes, in particular on the relevant time constants, and is in general a function of grating period. For large grating periods, or, equivalently, large charge transfer capacity, both Strohkendl *et al.* [2] and Valley [3] have shown that, for the single-level model, ξ simplifies to

$$\xi = \frac{\sigma_e - \sigma_h}{\sigma_e + \sigma_h}; \quad (4)$$

for the regime considered, this expression is valid for the two-level model as well.

This similarity has been demonstrated experimentally by Bernardo *et al.* [4]. They have shown in the same sample of $\text{Bi}_{12}\text{SiO}_{20}$ behavior described by the electron-hole competition factor, ξ , and have also shown grating recovery likely arising from complementary gratings due to two-level transport.

The approximation applies until the exposure time becomes appreciable with respect to the longer time constant. For this regime, the amplitude of the saturation space-charge field remains unchanged for the single-level case, but changes significantly for the two-level case, becoming a function of the limiting space-charge fields of both levels.

References

- [1] M.C. Bashaw, T.-P. Ma, R.C. Barker, S. Mroczkowski, and R.R. Dube, *J. Opt. Soc. Am. B*, **7**, 2329, (1990).
- [2] F.P. Strohkendl, J.-M.C. Jonathan, and R.W. Hellwarth, *Opt. Lett.*, **11**, 312, (1986).
- [3] G.C. Valley, *J. Appl. Phys.*, **59**, 3363, (1986).
- [4] L.M. Bernardo, J.C. Lopes, and O.D. Soares, *Appl. Opt.*, **29**, 12, (1990).



Determination of the Effective Trap Density of Ta:KNbO₃ and BaTiO₃ at 823 nm

A.E. Clement and G.C. Gilbreath
Optical Systems Section, Naval Research Laboratory, Washington, D.C. 20375-5000

S.N. Fugera
Sachs-Freeman Associates, Inc., 1401 McCormick Dr., Landover, MD 20785

Summary

There is considerable interest in finding a viable photorefractive coupler which operates in the near-infrared regime for use with laser diodes and laser diode arrays. A potential application for such a combination may be in laser spacecraft communications where a photorefractive coupler may serve as both an energy coupler and an adaptive optical component.[1] The III-V materials are undesirable components for a spacecraft environment due to the requirement to place large fields across the crystals and because the net gains in these materials remain quite low. Therefore, the study and potential development of existing diffusion-driven media toward increased infrared response may be useful. Two such materials of interest are BaTiO₃ and poled KNbO₃. The diffusion-driven response of the latter is of specific interest in this work.

The exponential gain coefficient, Γ , can be predicted as a function of geometry if all of the material properties of a photorefractive crystal are known for the wavelength of interest. At $\lambda=514.5$ nm, the effective trap density, N_A , for Ta:KNbO₃ is approximately $3.5 \times 10^{15} \text{ cm}^{-3}$. [2] For BaTiO₃, several groups have shown N_A to be of the order of 10^{16} cm^{-3} at this wavelength.[3,4] The trap density of neither crystal has been reported for wavelengths in the 820-830 nm region, which are typical of GaAs laser diodes. In this paper, we show a reduction of effective trap density in the near-IR for both crystals using a laser diode as a source, and show that this reduction in N_A must be taken into account, as well as the change of wavelength, when estimating Γ in the near-infrared regime.

Following the method of Klein and Valley, the effective trap density, N_A , and the scaling factor, F , can be determined from experimental two-wave mixing data if n and ϵ are known.[4] F is a scaling factor which may account for incomplete poling of the crystal, contributions from other charge carriers, or inhomogeneities in the crystal.[5] Two methods of determining these parameters have been used. The first method is to directly fit the data to the expression for exponential gain by using N_A and F as variables, where Γ is defined as:[4]

$$\Gamma = \frac{2\pi}{\lambda n \cos\theta_B} r_{\text{eff}} \left(\frac{E_{d0} E_{q0}}{\frac{E_{d0}}{\Lambda_g} + E_{q0} \Lambda_g} \right) \quad (1)$$

where Λ_g is the grating wavelength and $r_{\text{eff}} = F r_{\text{ang}} \sigma$. For a single type of charge carrier, the normalized conductivity, $\sigma = \pm 1$. The trap density is proportional to the



limiting space charge field, $E_{q0}\Lambda_g = 2q\Lambda_g N_A / \epsilon\epsilon_0$ and the diffusion field is given by $(E_{d0}/\Lambda_g) = k_B T 2\pi / q\Lambda_g$.

The second method fits the data to a straight line approximation of Γ in the form:[2]

$$\frac{K_g}{\Gamma} = \frac{q n \lambda \cos\theta_B}{2 \pi k_B T r_{eff}} + \frac{n \lambda \cos\theta_B \epsilon \epsilon_0}{2 \pi q r_{eff} N_A} K_g^2 \quad (2)$$

where $K_g = 2\pi/\Lambda_g$. The value of r_{eff} , and therefore F , can be determined from the intercept and the value of N_A can be determined from the slope and intercept of the line. Two assumptions must be made to use this approach. First, that r_{eff} is not dependent on grating spacing, and second, that Λ_g is large enough so that $\cos\theta_B \approx 1$. This assumption has inherent problems. Our analysis shows that if it is assumed that r_{eff} is a constant, predicted values for Γ can vary from actual values by as much as 90% over internal Bragg angles from 0° to 15° .

The necessity of taking into account the carrier density in addition to the change of wavelength is illustrated in Fig 1. In (1a), Γ is computed for various grating spacings, Λ_g , at $\lambda = 514.5$ nm and 823 nm, using Eqn. 1 for a fixed carrier concentration in Ta:KNbO₃, where $N_A = 3E(13) \text{ cm}^{-3}$. Values for other parameters can be found in Refs. [6] and [7]. The value of F is estimated to be 0.91 based on the assumption that $\theta_B = 0^\circ$.

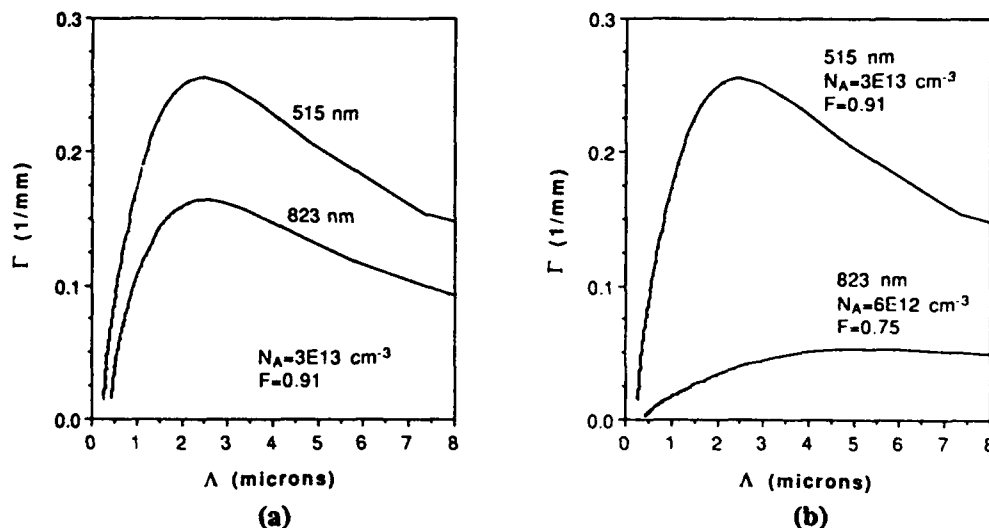


Fig. 1 Exponential gain coefficient for Ta:KNbO₃. (a) trap density and scaling factor are assumed to be constant; (b) trap density and scaling factor are assumed to change with λ .

As can be seen from the curves, a change in wavelength predicts a lower gain at 823 nm but the integrity of the curve is generally maintained and the magnitude at optimum grating spacings is reduced by $\approx 35\%$. However, when the carrier concentration and scaling factors are taken into account, the change in wavelength illustrates a dramatic difference. The magnitude of the exponential gain at the optimum geometry for $\lambda = 514.5$ nm is reduced by $\approx 85\%$ and the shape of the curve changes. In this sample of Ta:KNbO₃ it is evident that the gain in the IR will not be

enhanced by coupling at large Bragg angles as is the case at $\lambda=515$ nm. The values for N_A and F used to generate these curves are derived from experimental data discussed below.

Experimental data was generated using standard two-beam coupling in the bench configuration shown in Fig. 2, which illustrates how the laser diode was mode-stabilized and monitored. Two wave mixing gain, G , was measured as $S(\text{pump})/S(\text{no pump})$ [8] where measurements were made using samples of BaTiO_3 and poled Ta:KNbO_3 , provided by Sanders and Virgo Optics, respectively. The KNbO_3 was doped with a 1% concentration of tantalum. Gains vs. grating spacing were measured at 514.5 nm using an Ar+ source with a temperature-stabilized etalon. Similar measurements were taken using a single stripe 100 mW laser diode. Due to mode-hopping, the laser diode was temperature stabilized and monitored for frequency stability during all runs using an optical spectrometer from Candela.

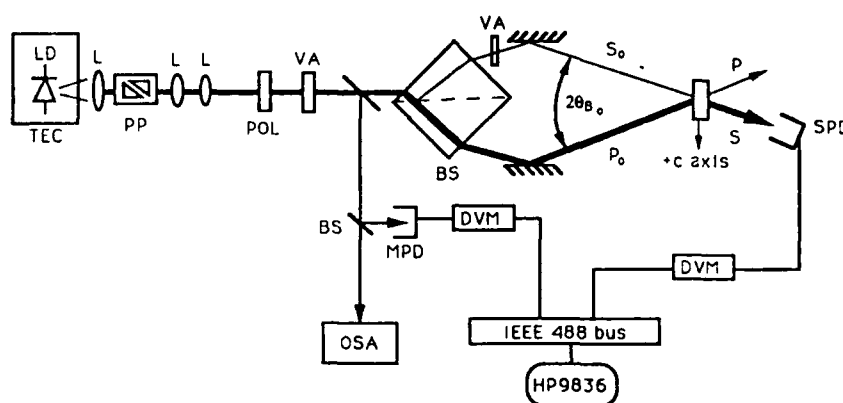


Fig. 2 Experimental bench configuration for two-wave mixing using a mode-stabilized laser diode

The beam ratio was set to 200 in order to achieve saturated gains. The signal and the pump intensities were $167 \mu\text{W}/\text{cm}^2$ and $33 \text{ mW}/\text{cm}^2$ respectively at both wavelengths. The light was predominantly extraordinarily polarized with an extinction ratio of 20:1. For both materials, the beams were incident on the b-face of the crystal. The maximum measured gains at $\lambda=514.5$ nm and $\beta=0^\circ$ were 25.6 for Ta:KNbO_3 at $\theta_B=5.0^\circ$ and 15.5 for BaTiO_3 at $\theta_B=9.7^\circ$. At $\lambda=823$ nm the maximum gain produced in both crystals was ≈ 2 . The size of the clear apertures of the two crystals prevented measurement of gain for grating spacings smaller than $1.5 \mu\text{m}$. It should be pointed out that both of these crystals have high r_{42} coefficients, and can yield higher gains for nonzero values of β [6] but such an orientation is not used in the computation of N_A .

In each of the four experiments, the data fit to a least squares approximation in the form of Eqn. (2) with a correlation coefficient of $R^2 \geq 0.97$, indicating that the second method should produce reliable results. However, the error between the predicted Γ and the experimental data ranges from a minimum of a few percent at $\Lambda_g=7 \mu\text{m}$ to 90% at $1\text{--}2 \mu\text{m}$. Figure 3 illustrates how using the straight line method can lead the experimenter to miscalculate the predicted gain coefficient. In this figure, the experimental data points for Ta:KNbO_3 and BaTiO_3 at $\lambda=823$ nm are plotted against the curves predicted by the two methods. For both BaTiO_3 and Ta:KNbO_3 , a remarkably

better fit is enabled using the first method, where values of N_A and F are iteratively changed. Even small changes in either value can have a dramatic effect on the shape of the curve. The values for N_A and F , determined with method 1, are given in Table 1, along with corresponding response times.

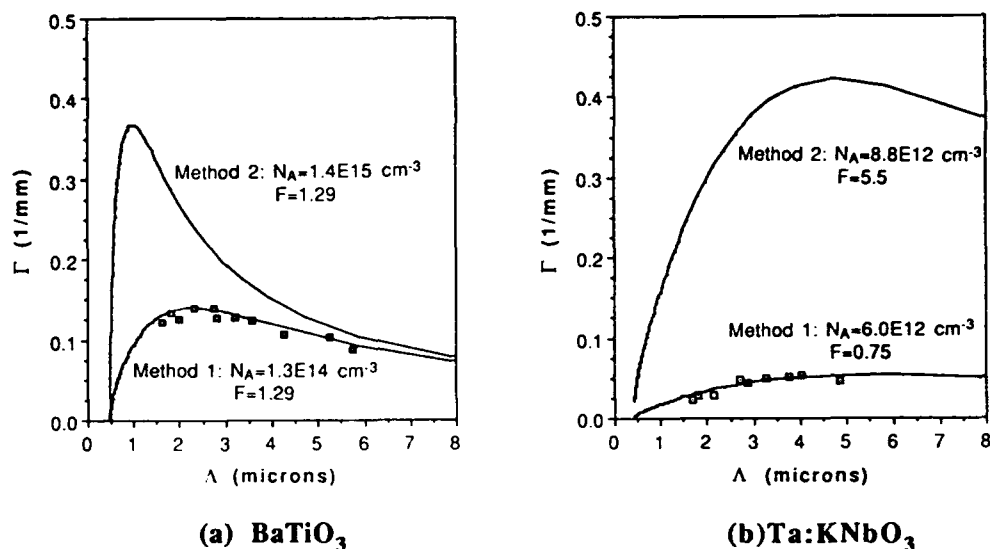


Fig. 3 Comparison of the two methods for determining the trap density and scaling factor for each crystal at $\lambda=823$ nm. Method 1 is the more accurate estimation technique.

Table 1. Material Parameters

| Crystal | N_A (cm ⁻³) | | F | | τ (sec) | |
|----------------------|---------------------------|--------|--------|--------|--------------|--------|
| | 515 nm | 823 nm | 515 nm | 823 nm | 515 nm | 823 nm |
| BaTiO ₃ | 5.7E14 | 1.3E14 | 1.55 | 1.29 | 12 | 40 |
| Ta:KNbO ₃ | 3.0E13 | 6.0E12 | 0.91 | 0.75 | 18 | 514 |

In conclusion, we have shown that the effective trap density in both Ta:KNbO₃ and BaTiO₃, is reduced as the wavelength used for photorefractive coupling is increased to $\lambda=823$ nm. We have also demonstrated that the most reliable method of determining N_A and the scaling factor is to vary these two parameters until an analytic curve of Γ vs Λ_g is produced which fits the two-wave mixing data.

References

1. G.C. Gilbreath and F.M. Davidson, SPIE Proc., 1136, 290 (1989).
2. R.J. Reeves, M.G. Jani, B. Jassemnejad, R.C. Powell, G.J. Mizell, and W. Fay, Physical Review B, 43, 71 (1991).
3. J. Feinberg, D. Heiman, A.R. Tanguay, and R.W. Hellwarth, J. Appl. Phys., 51, 1297 (1980).
4. M.B. Klein and G.C. Valley, J. Appl. Phys., 57, 4901 (1985).
5. C. Medrano, E. Voit, P. Amrhein, and P. Gunter, J. Appl. Phys., 64, 4668 (1988).
6. A.E. Clement and G.C. Gilbreath, Appl. Optics, 30 (1991).
7. J.C. Baumert, J. Hoffnagle, and P. Gunter, SPIE Proc., 492, 374 (1984).
8. A. Marrakchi and J.P. Huignard, Appl. Phys., 24, 131 (1981).



Photorefractive and Photochromic Effects in Barium Titanate

M. H. Garrett, *J. Y. Chang, †T. M. Pollak, H. P. Jenssen and †C. Warde

Massachusetts Institute of Technology

†Departments of Electrical Engineering and Computer Science, the *Materials Science and Engineering Department and the Crystal Physics Laboratory, 77 Massachusetts Ave. Rm 13-3157, Cambridge, MA 02139, (617) 253-6622

1.0 Introduction

Nominally undoped p-type BaTiO_3 was grown that exhibits interesting intensity dependent photorefractive and photochromic properties. When its photochromism is activated the absorption increases at the activating wavelength and there is a concurrent and proportional reduction in photorefractive response time. Three photoactivated and thermally reversible absorption conditions and the difference spectra of the photochromic crystal are shown in Figure 1.

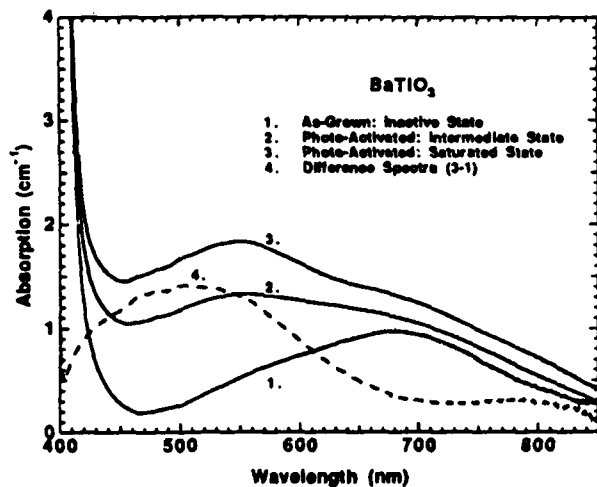


Figure 1.

2.0 Experiments

The photochromism is activated with high intensity ($\sim 3.5 \text{ W/cm}^2$) argon ion laser illumination ($\lambda=514.5 \text{ nm}$). A concomitant change in the crystals' light-induced absorption/transparency properties also originate with the photochromic change. In our photorefractive experimental setup we are able to measure light-induced changes in the absorption by shuttering the incoherent pump beam. Shown in Figure 2 are three signal transmissions corresponding to the three

absorption states shown in Figure 1 and for various pump and signal beam conditions.

Initially, only the signal transmission is observed. Then the pump beam shutter is opened while the pump beam is being vibrated over several grating periods at a rate much greater than the grating formation time (incoherent pump) and thus absorption effects are now observed. When the crystal is in the inactive photochromic state light-induced absorption is observed, in the saturated state it shows light-induced transparency and little or no light-induced absorption is observed in the intermediate state since it is a combination of the inactive and saturated state.

These photochromic states were also examined by measuring the effective gain which is the ratio of the steady-state transmitted signal intensity when both the signal and pump beams are coherently present within the crystal

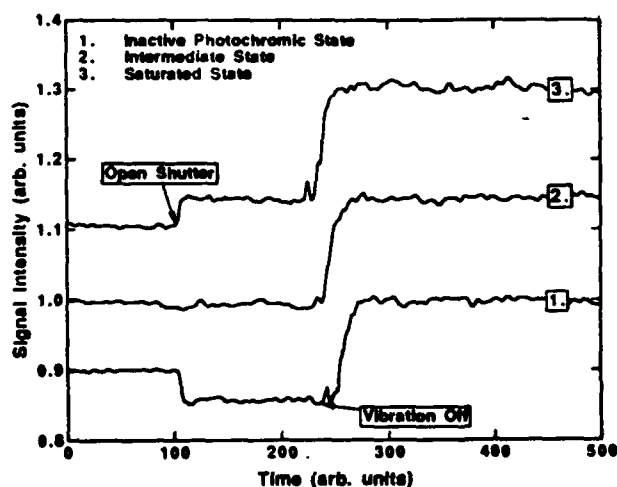


Figure 2.

to the signal intensity transmitted when the pump beam is incoherent with the signal. With this technique, the pump beam continuously illuminates the crystal and the temperature and the absorption are constant in both measurement conditions (coherent versus



incoherent). The measurements were made at 500 mW/cm^2 , low enough to preserve the initial photochromic state. In addition, to determine possible contributions from both electrooptic and absorptive beam coupling [1] we determined the gain for the $\pm C$ -axis orientations of the crystal where the effective gain is given by,

$$\gamma_0^\pm \equiv \frac{I_c(L)}{I_{inc}(L)} = \frac{I_s \text{ with Coherent Pump}}{I_s \text{ with Incoherent Pump}} \quad (1)$$

and, for an undepleted pump and small modulation, is equal to,

$$\begin{aligned} \gamma_0^\pm &= \exp[\pm \gamma] / \cos \theta \\ &= \exp[\pm \gamma_{eo} + \gamma_{abs}] / \cos \theta. \end{aligned} \quad (2)$$

Where, l is the crystal thickness and θ is the internal half-angle between the beams. We note that γ is the gain coefficient which is the sum of the electrooptic gain coefficient, $\pm \gamma_{eo}$, (whose sign is dependent on the orientation of the C -axis and sign of the majority charge carriers), and γ_{abs} the absorptive "gain" coefficient from trap gratings [1]. To reduce errors from physically reorienting the crystal we simply exchange the roles of the pump and signal beams by changing their relative intensities with the crystal in a fixed position,

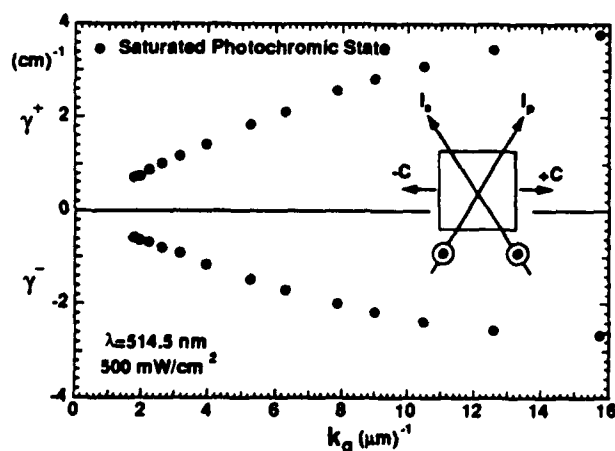


Figure 3. Beam coupling dependence on grating wavevector and c -axis orientation.

(where their beam ratio is 800). Shown in Figure 3 is the gain as a function of grating wavevector for $\pm C$ -axis crystallographic orientations. There is an asymmetry in the beam coupling gain, i.e. $+\gamma \neq -\gamma$, that cannot be attributed to light-induced absorption effects as described by Motes and Kim [2] but could be ascribed to absorptive coupling previously described by A. V. Knyaz'kov and M. N. Lobanov [3] and by Pierce et al. [1].

The intensity dependence of the gain was also determined between 1 mW/cm^2 and 1 W/cm^2 and the sublinear dependence of the response time on intensity was measured over this same interval.

3.0 Theory

In the inactive or saturated photochromic state the crystals absorptive and photorefractive properties are described by the deep and shallow trap model of Tayebati and Mahgerefteh [4] where the absorption due to two levels is,

$$\alpha = s_D N_{DA} + (s_T - s_D) M_0, \quad (3)$$

where s_D and s_T are the excitation cross-sections of the deep and shallow traps, N_{DA} is the difference between the donor and acceptor concentrations and M_0 is the occupied shallow trap concentration. The absorption can be modified by charge transfer from the deep level into the shallow level and depending on its absorption cross-section and concentration it will also modify the absorption characteristics of the material. In the inactive photochromic state light-induced absorption implies that $s_T > s_D$. When a new deep level (2.41 eV) absorbing center is activated to the saturated state light-induced transparency occurs and $s_D > s_T$.

The possible deep and shallow-trap charge gratings, N_1 and M_1 respectively, are,

$$-eN_1 = -meN_E \frac{k_g^2}{(k_g^2 + k_0^2)} -$$

$$meM_E \frac{1}{(1 + s_T I_0 / \beta)} \frac{k_{0D}^2}{(k_g^2 + k_0^2)} \text{ and,}$$

$$eM_1 = -meM_E \frac{1}{(1 + \beta / s_T I_0)} \frac{k_g^2}{(k_g^2 + k_0^2)} + meM_E \frac{1}{(1 + s_T I_0 / \beta)} \frac{k_{0D}^2}{(k_g^2 + k_0^2)} \quad (4)$$

I_0 is the intensity, β is the thermal excitation rate of the shallow traps, m is the modulation index, and N_E and M_E are the effective deep and shallow trap densities.

The spatial modulation of the absorption, (giving rise to absorptive coupling), is given by,

$$\hbar\omega(s_D N_1 - s_T M_1), \quad (5)$$

and the space-charge field is intensity dependent where,

$$E_1 = -im \frac{k_B T}{e} \frac{k}{1 + k^2 / k_0^2} \eta(I), \quad (6)$$

where the intensity dependent term has a value between 0 and 1 and is equal to,

$$\eta(I) = \frac{1}{k_0^2} \left[k_{0D}^2 + \frac{k_{0T}^2}{1 + \beta / s_T I_0} \right]. \quad (7)$$

The Debye screening wavevector, k_0 , (which is equal to the square root of the sum of the squares of the deep and shallow trap Debye screening wavevectors, k_{0D} and k_{0T}), is also intensity dependent because of the redistribution of charge between deep and shallow levels.

4.0 Results

From our measurements we are able to determine the electrooptic and absorptive coupling gain coefficients where,

$$\gamma_{\infty} = (\gamma^+ + |\gamma^-|) / 2 \text{ and } \gamma_{\text{abs}} = (\gamma^+ - |\gamma^-|) / 2 \quad (8)$$

Relatively small percentage changes in the electrooptic gain occurred between the three

photochromic states. However, the absorptive gain varied in proportion to the magnitude of the light-induced absorption effects (since they are related through equations 3 and 5). For instance, the intermediate photochromic state, with no light-induced absorption, had virtually no absorptive coupling.

Shown in Figure 4 is a plot of the electrooptic and absorptive gain as a function of grating wavevector with the crystal in the saturated photochromic state. The electrooptic gain approaches zero for small grating wavevectors but the absorptive gain coefficient remained finite as $k_g \rightarrow 0$. (Absorptive coupling was measured at a grating period of 10 μm while no electrooptic coupling was measured. This behavior is predicted by the deep and shallow trap model where the second terms of the charge gratings remain finite at small k_g .

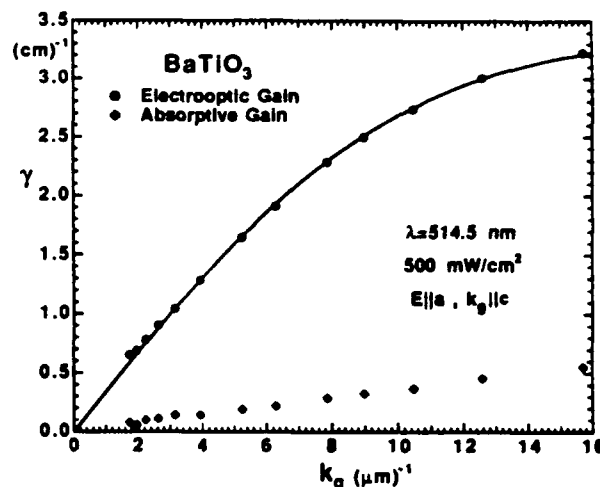


Figure 4. Electrooptic and absorptive gain dependence on grating wavevector.

From the electrooptic gain data of Figure 4 the Debye screening wavevector k_0 and $\eta(I)$ were determined by fitting the equation for the gain as a function of grating wavevector where, $\gamma_{\infty} = (i2\pi\epsilon_{\text{eff}} / n\lambda m)E_1$. The relevant electrooptic coefficient is r_{13} and n in the index of refraction. Here, k_0 equals $17.2 \mu\text{m}^{-1}$ and $\eta(I)$ equals 0.38. The intensity dependence of the space-charge field (eqn. 6), in all photochromic states are nearly identical, where the saturated state gain dependence on intensity is shown in Figure 5.

Measurements of the sublinear dependence of the response time on intensity,

in the saturated photochromic state, give the coefficient of intensity as $x=0.57$. The sublinear dependence of the response time on intensity is predicted by the deep and shallow trap model used here [4] and for a two trap model described by Mahgerefteh and Feinberg [5] and Brost and Motes [6]. The nominally undoped sample is a type B crystal as described by Margerefteh and Feinberg [5]. The crystal has high dark conductivity with a grating storage time that is *intensity* dependent and decays in less than a second at a writing intensity of $\sim 3.4 \text{ W/cm}^2$.

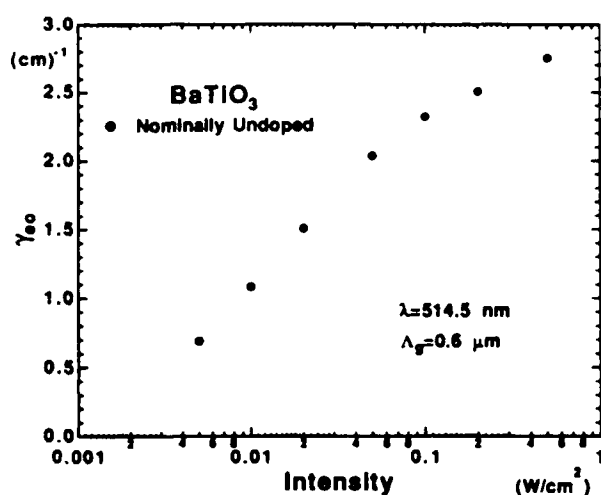


Figure 5. Intensity dependence of the beam coupling gain in the saturated photochromic state.

The response time of the saturated compared to the inactive photochromic state, (or the light-induced decay of the space-charge field), is reduced by a factor of four at 1 W/cm^2 . In one sample the response time was as low as 60 msec at 1 W/cm^2 when the photochromism is saturated (where the $1/e$ intensity decay of the diffracted probe beam was 30 msec). This crystals' sensitivity is believed to be higher than previously reported in the literature at $0.17 \text{ cm}^3/\text{kJ}$.

Similar photochromic and photorefractive changes were observed in LiNbO_3 [7,8]. For those crystals the photochromic behavior was observed only when co-doping the crystal with transition metal ions. However, as was the case for those samples, the changes in the two

visible absorption features of our BaTiO_3 , (at 690 nm and 515 nm), are not proportional implying the interaction of more than two species. When we reduce these crystals, ($P_{\text{O}_2} < 10^{-15} \text{ atm}$), the photochromism is eliminated and thus we suspect that co-doping and oxygen play a role in the photochromism observed here. Mass spectroscopy is being conducted to determine the impurity ions in our samples.

In conclusion, we have reported the photochromic properties of BaTiO_3 that lead to an increase in the absorption and to a proportional decrease in response time. We find light-induced absorption/transparency in the same crystal depending on the photochromic state. The electrooptic and absorptive beam coupling effects were resolved by our measurement technique and characterized in terms of a deep and shallow trap model. In particular, the absorptive coupling is finite for small k_g and for this photochromic crystal when no light-induced absorption changes are observed also no absorptive coupling is observed (and vice-versa).

Acknowledgment

This work supported by NASA under agreement NAG 1-996.

[†]T. M. Pollak, Lockheed Sanders, 130 Daniel Webster Hwy., Merrimack Nashua, NH 03054

References

1. R. M. Pierce, R. S. Cudney, G. D. Bacher, and J. Feinberg, *Opt. Lett.* **15**, 414, (1990).
2. A. Motes and J. J. Kim, *J. Opt. Soc. Am. B* **4**, 1379 (1987).
3. A. V. Knyaz'kov and M. N. Lobanov, *Sov. Tech. Phys. Lett.* **11**, 365, (1985).
4. P. Tayebati and D. Margerefteh, *J. Opt. Soc. Am. B*, May, (1991).
5. D. Mahgerefteh and J. Feinberg, *Phys. Rev. Lett.* **64**, 2195, (1990).
6. G. A. Brost and R. A. Motes, *Opt. Lett.* **15**, 1194 (1990).
7. D. L. Staebler and W. Phillips, *Appl. Phys. Lett.* **24** (6), 268, (1973).
8. E. Krätzig and H. Kurz, *J. Electrochem. Soc.: S. S. Science and Tech.*, 131, (1977).

Wednesday, July 31, 1991

Poster Session: Wave Interactions and Devices

WC 1:00pm–2:30pm
Academic Center Classrooms



Picosecond Nonlinear Optical Responses in
Photorefractive Crystals

H. Liu, R.J. Reeves, and R.C. Powell

Center for Laser Research

Oklahoma State University, Stillwater, OK 74078

(405) 744-6575

Picosecond-pulse laser excitation was used to establish and probe refractive index gratings in KNbO_3 , KTaO_3 , and mixed crystals of $\text{KTa}_{1-x}\text{Nb}_x\text{O}_3$. The purpose of this work was first to identify the physical processes contributing to fast nonlinear optical responses in these samples, and second to determine how these processes evolve with time into the space-charge field photorefractive effect observed with continuous wave excitation. The techniques of pulse-probe degenerate four-wave mixing and nondegenerate four-wave mixing with a continuous wave probe laser were both employed to obtain information about the photorefractive processes that take place after fast pulse excitation. The measurements were made as a function of laser fluence, crossing angle of the write beams, sample orientation with respect to the grating wavevector, polarization directions of the write and probe beams, and write beam wavelength. Mixed crystals with the niobium concentration parameter x varying from 0 to 1.0 were investigated along with KNbO_3 samples containing a variety of dopant ions.

In undoped KNbO_3 samples, three types of signals were identified that we classify as having fast, intermediate, and long characteristic times. On very long time scales (i.e.



milliseconds), the normal photorefractive process associated with the relocation of charge carriers is observed. On the time scale of 100 ps to 10 ns, a signal associated with a population grating of a transient ionic species is observed. On the time scale of 0 to 100 ps, a signal is observed with possible contributions from bound charges, free carriers, and scattering from a Nb^{5+} hopping mode. In mixed crystals, the signals observed on the intermediate and fast time scales were found to vary significantly with laser beam wavelength and polarization, sample orientation, niobium concentration, annealing conditions, and poling. At a concentration of 1 mol %, the dopant ions were found to have little effect on the fast and intermediate signals but to significantly effect the long time photorefractive signal.

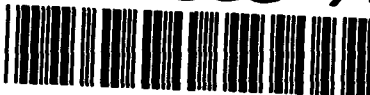
For excitation at 532 nm, the intermediate time signal builds up to a maximum in a time equal to the free carrier lifetime while for 1064 nm excitation, this signal component is not observed. The decay of this signal is of the order of 10 ns which corresponds to the time scale of the fluorescence lifetime of Nb^{4+} ions in these crystals. The grating decay rate of this nonlinear optical response decreases as the grating spacing is increased indicating that a diffusion processes is shortening the lifetime of the grating. This signal component has a maximum at intermediate niobium concentrations in the region of KTN where a structural phase transition occurs at room temperature. From these observations, a lattice relaxation model has been developed to interpret the results. This contribution to the signal is attributed to the polarizability change associated with a Nb^{4+} excited state population grating. These excited states are

mobile and migrate as small polarons.

The fast component of the signal is present for both 532 and 1064 nm excitation. For the latter the signal is less intense and decays with a relaxation time only slightly longer than the convolution of the three 18 ps pulses. For the former, the signal decay at low excitation fluences is of the order of 100 ps which is the free carrier lifetime. Thus, these results show that there are contributions to the fast nonlinear optical response from both free carriers and from processes that have response times less than or equal to the convolution width of the laser pulses. Theoretical estimates of the bound carrier response indicate that this is not the dominant contribution to the fast signal. The most probable origin of the additional contribution to the fast signal is stimulated scattering from the niobium hopping mode. Scattering intensity calculations, temperature dependences, and polarization dependences appear to confirm this hypothesis.

The results of this comprehensive investigation provide a clear picture of the time evolution of the nonlinear optical response of this class of material from the ultrafast to the continuous wave time scale. The instantaneous response has contributions from bound charges, niobium hopping modes, and free carriers. The first two of these disappear within the convolution time of the 18 ps pulses while the third one decays away in 100 ps as the free carriers become trapped on niobium ions creating mobile Nb^{4+} polarons. The signal from the population grating of these polarons decays through diffusion and

recombination on the time scale of several nanoseconds. The charges are then left in shallow traps and move more slowly through trap-modulated mobility until they encounter deep traps. The charges in these deep traps establish the space-charge field that produces the long time photorefractive effect observed on the millisecond time scale.



Self-Pumped Phase Conjugation in Barium Titanate with High Intensity Nanosecond Pulses

M.J.Damzen and N.Barry

Optics Section, The Blackett Laboratory, Imperial College,
London SW7 2B7, U.K.

Telephone no. :071 589 5111

Summary

An investigation of self-pumped phase conjugation in barium titanate is made using nanosecond pulses (15 ns) derived from a repetitively pulsed (10 Hz) and frequency-doubled Nd:YAG laser system (532 nm wavelength). It is experimentally shown that high reflectivity ($> 20\%$) can be achieved. It is also shown that there is a progressive decrease in the reflectivity of both the corner-pumped and ring-passive geometries at pulse intensities of $> 4 \text{ MW/cm}^2$. At these intensity levels a high photo-carrier population is induced, altering the relative concentrations of Fe^{2+} and Fe^{3+} centres and leading to a strong intensity-dependent competition between hole and electron photoconductivity.

For the corner-pumped geometry (Figure 1) the intensity-dependence of the phase conjugate reflectivity is shown in Figure 2. The reflectivity increases with pulse intensity up to 20% . Small change in reflectivity occurs in the range 0.5 to 4 MW/cm^2 but a dramatic decrease in the reflectivity occurs at intensity $> 4 \text{ MW/cm}^2$.

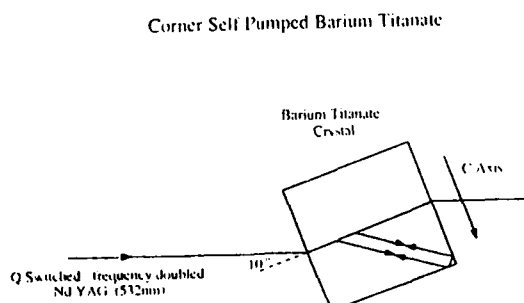


Figure 1.

Graph of Phase Conjugate Reflectivity against Pulse Intensity for Corner Self Pumped Barium Titanate

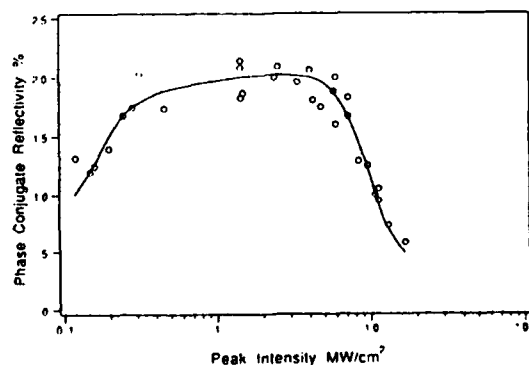


Figure 2.

92-18770



In the ring-passive geometry (Figure 3) the phase conjugate reflectivity has an intensity dependence as shown in Figure 4. The reflectivity also shows a decrease in the vicinity of 4 MW/cm^2 . The change in reflectivity is more gradual than in the corner-pumped case until approximately 10 MW/cm^2 where the reflectivity decreases rapidly. In this intensity range the self-generated counter-rotating loop beam switches from a TEM_{00} type mode into a twin-lobed profile in the vertical direction. Interferometric investigation reveals that there is a π phase shift between the two lobes. The twin-lobed beam can therefore be identified as a TEM_{01} mode in correspondence to standard laser resonator theory.

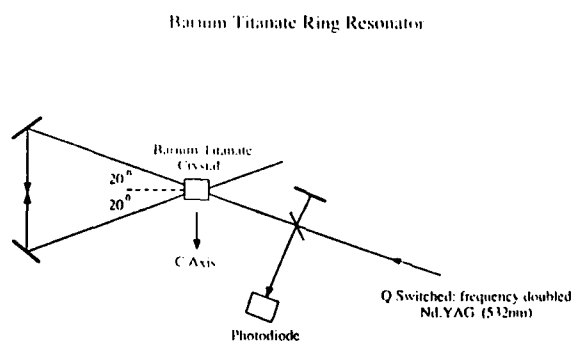


Figure 3.

Graph of Phase Conjugate Reflectivity against Pulse Intensity for a Barium Titanate Ring Resonator

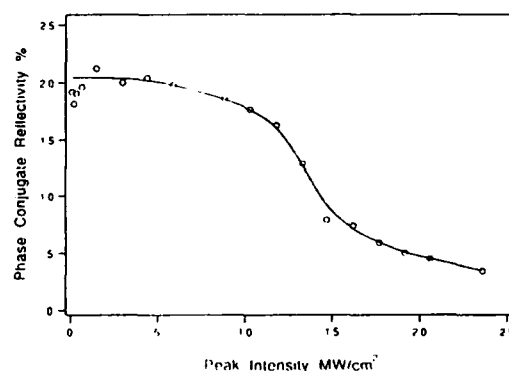


Figure 4.

To understand the intensity-dependent reflectivity and spatial mode behaviour of these self-conjugating geometries we have analysed a high-intensity theory of photorefraction. Although carrier saturation due to the limited number of photoionisable dopants can lead to gain suppression we have calculated that this effect is insufficient to explain the gain suppression observed.

A more adequate explanation requires consideration of simultaneous hole and electron conductivity. We have developed an expression for the exact solution for the space-charge field valid even at high intensities. Using this expression we have plotted the normalised two-beam coupling gain coefficient (proportional to space-charge field) as a function of intensity in Figure 5.

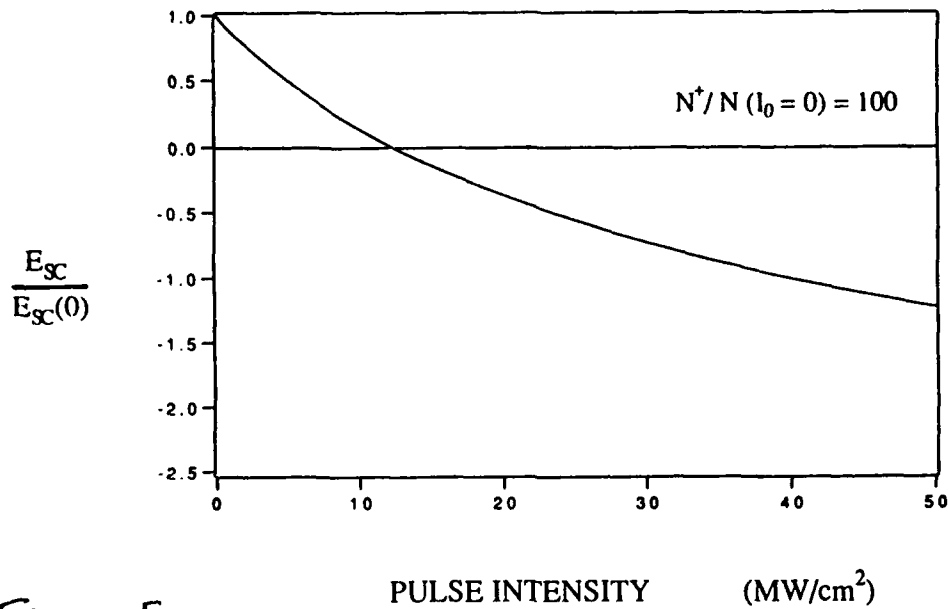


Figure 5.

At low intensities, for our crystal parameters the grating formation is hole dominated. According to theory, with estimated crystal parameters, the gain (and space-charge field) reverses sign (see Figure 5) above approximately 13 MW/cm^2 , indicating a change to electron dominated conductivity. This intensity-dependent gain variation would account for the high intensity experimental observations.

The physical explanation for the intensity-dependent hole / electron competition is primarily due to the high photocarrier production, predominately holes ($n_h \gg n_e$) in barium titanate. Photoionisation alters the relative concentrations of the dopant centres $N = [\text{Fe}^{2+}] = N(0) + n_h$ and $N^+ = [\text{Fe}^{3+}] = N^+(0) - n_h$ where $N(0)$ and $N^+(0)$ are the dopant concentrations under dark conditions. The ratio of electron to hole conductivity is given by

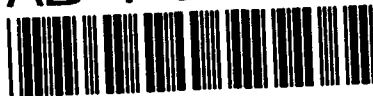
$$\frac{\sigma_e}{\sigma_h} = \frac{e \mu_e n_e}{e \mu_h n_h} = \frac{s_e \mu_e \gamma_h}{s_h \mu_h \gamma_e} \left(\frac{N}{N^+} \right)^2$$

where s_e (s_h), μ_e (μ_h) and γ_e (γ_h) are the photoionisation cross-section, mobility and recombination coefficient for electrons (holes). The dopant ratio (N/N^+) increases with intensity due to photoionisation leading to a relative increase in electron conductivity compared to hole conductivity.

We have experimentally confirmed this switch from hole to electron dominated conductivity by observation of a switch in the direction in beam fanning above approximately 30 MW/cm². We have also achieved corner-pumping into the opposite corner compared to the direction of corner-pumping at low intensity.

The intensity-dependent gain suppression also explains the the spatial switch from the TEM₀₀ to TEM₀₁ mode of operation in the ring-passive geometry. The TEM₀₀ pump beam has highest intensity, and hence strongest gain suppression, on axis. The TEM₀₁ mode has a node on axis and hence will receive higher gain than the TEM₀₀ mode and will consequently become the dominant mode.

In conclusion, we have demonstrated that high conjugate reflectivity (> 20 %) can be obtained with repetitively-operated nanosecond pulses in self-pumped geometries. A strong intensity dependent competition in the relative electron-hole conductivity is predicted at megawatt/cm² intensities and explains the reflectivity and spatial mode behavior in self-pumped phase conjugate experiments.



Nanosecond Photorefractive Effects in KNbO_3

I. Biaggio, M. Zgonik, P. Günter

Institute of Quantum Electronics

Swiss Federal Institute of Technology

ETH-Hönggerberg

CH-8093 Zürich, Switzerland

(Phone: 41-1-377 2338, Fax: 41-1-371 5989)

Two laser beams interfering in a photorefractive crystal ionize light absorbing impurities and produce two initially overlapping concentration gratings. These two gratings consist of ionized donors that are immobile and of free charges that can move due to diffusion in a concentration gradient and drift in an external or internal electric field. Spatial separation between the two gratings produces a space-charge field which modulates the refractive indices of the crystal via the linear electro-optic effect. The photorefractive effect can be efficiently employed for two-wave and four-wave mixing already at the low light-intensities obtained with CW lasers [1]. The trade-off connected with low power optical beams is a decrease in response time. The photorefractive index change depends on the optical energy absorbed and not on the instantaneous optical intensity. In order to increase the speed of response beyond the limit given by the photogeneration rate one must use high intensity laser pulses. Photorefractive diffraction gratings with sub-microsecond response-times were already measured in LiNbO_3 [2], BaTiO_3 [3,4], KNbO_3 [5,6,15], and $\text{Bi}_{12}\text{SiO}_{20}$ [7,8]. KNbO_3 is known for its large linear electro-optic (EO) and second-order nonlinear optical coefficients. When chemically reduced the photorefractive response time decreases[9-11].

In order to explore the potentials of KNbO_3 in fast-response four-wave mixing and to find the ultimate limit of the photorefractive response-time we investigate the evolution of the photorefractive grating by a pump-and-probe technique using strong sub-nanosecond light pulses in the green spectral range.

We use a mode-locked (ML) and Q-switched (100 Hz) Nd:YAG laser frequency doubled to 532 nm and a Pockels-cell to select a single 75 ps ML pulse out of the Q-switch envelope. The probe pulse - derived by a 10% reflector - passes six times through a variable time-delay path consisting of a fixed and a moving right angle prisms to produce a maximum delay difference of 20 ns. The probe beam is focused into the sample to a beam-waist of 40 μm . The alignment of the probe beam is controlled by a four-quadrant photodiode and the orientation of the moving prism is electronically corrected during translation. The writing beams are focused by a variable focal-



length lens system to produce beam-waists from 50 μm to 300 μm in the sample. The probe beam is counterpropagating to one of the writing beams. With the sample cut along the orthorhombic axes and adjusted symmetrically to the two writing beams the phase-matching condition is satisfied also for different polarizations of the read-out (horizontal) and the write beams (vertical). The diffracted beam is reflected by a beam-splitter, is detected by a photomultiplier and a boxcar integrator and is fed to a computer, also used for controlling the stepper-motor in the time-delay line. The maximum total energy per writing pulse is 2.5 μJ producing a maximum energy density of about 25 mJ/cm^2 in the sample.

Fig. 1 shows a typical measurement in a reduced KNbO_3 crystal. In Fig. 1 the maximum intensity I_0 is about 50 MW/cm^2 , the intensity modulation index m is 0.75. Slower spatial variations of I due to beams of limited diameter are not taken into account. Negative times in the figure mean that the probe pulse traverses the crystal before the write-pulses. The residual diffraction observed at negative times is due to incomplete erasure of the photorefractive grating written 10 ms earlier by the previous pair of write-pulses. The peak at zero time-delay, shown enlarged in the inset, is attributed to third order nonlinear processes. Its form exactly follows the convolution of the write and the probe pulses with the probe delay as a parameter. This feature has also been observed in KNbO_3 in [15]. After the write-pulses have terminated the diffraction efficiency steadily increases and reaches a steady state value in approximately 5 ns.

The inset in Fig. 1 also shows the results of a subsequent measurement with the crystal turned by 90 degrees. The grating wavevector K is in this case parallel to the b-axis of the crystal. The photorefractive effect vanishes by symmetry in this configuration. Here once again one observes the zero-delay peak of a similar height as in the first arrangement, but after the end of this peak only a very small diffraction efficiency is measured. This signal will decay to zero within 10 ns. With $K//c$ a higher scatter of measured values was generally observed, as seen in Fig. 1, which we believe is caused by interference effects with the residual photorefractive grating present in the crystal because of incomplete erasure within the 10 ms interval between the pulses.

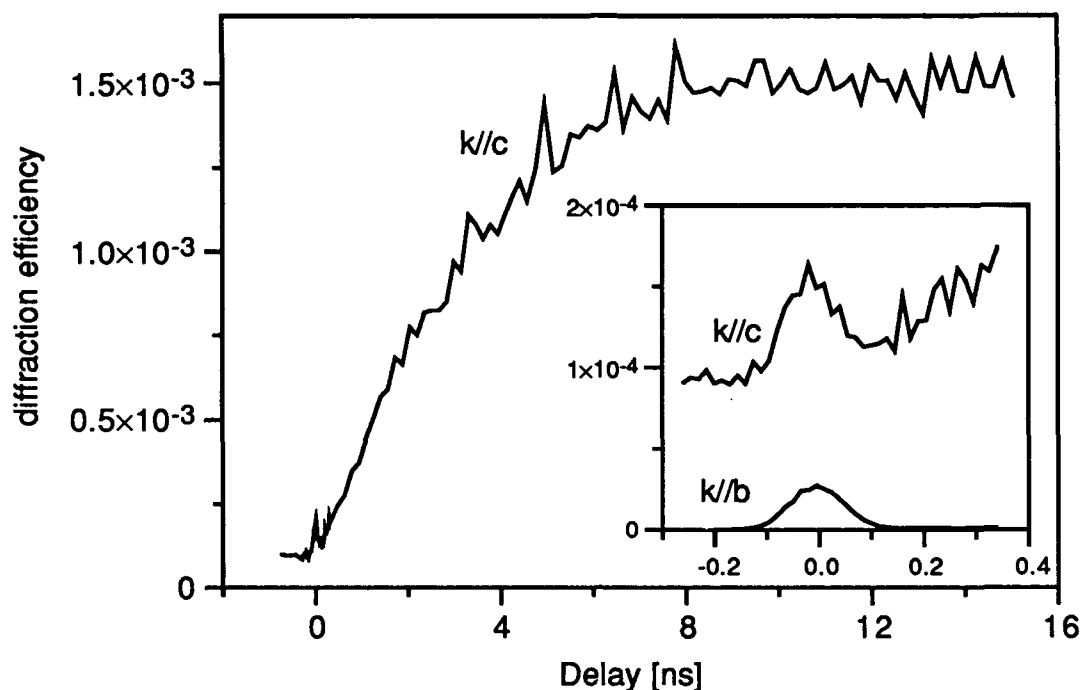


Fig.1. Picosecond and nanosecond response in a reduced KNbO_3 crystal. The grating period is $0.8 \mu\text{m}$ ($K = 7.9 \mu\text{m}^{-1}$), the intensities of the writing beams are 8 MW/cm^2 and 40 MW/cm^2 . The inset shows the peak at zero time-delay which is due to a degenerate four-wave mixing process for two different geometries.

K/c : After the zero time-delay peak the photorefractive diffraction efficiency reaches a constant value in some ns. The background and noise come from the incompletely erased previously written photorefractive gratings.

K/b : After the zero time-delay peak no build-up of the diffraction efficiency is observed. An approximately 3000 times lower diffraction efficiency compared to the K/c measurement is measured.

We believe that the zero-delay peak is due to an intrinsic dissipation-less third order process. If the process leading to the zero time-delay peak was connected with the generation of free charge carriers it should depend strongly on the concentration of photo-sensitive centers assuming that most of the absorbed photons produce free charge carriers. We measured similar efficiencies at zero delay also for pure, unreduced samples. The absorption constant of the reduced sample of about 0.6 cm^{-1} at 532 nm is more than ten times larger than that of an untreated one.

In our experiments no external electric field was applied to the crystal. In this case the model[11,12,13] predicts that the initial charge displacement following the excitation is mainly due to diffusion with the characteristic time

$$\tau_d = \frac{e_0 K^2}{\mu k_B T}$$

where e_0 is the unit charge, k_B is the Boltzman constant, T is the absolute temperature and μ is the mobility of free carriers. The space-charge field E_{SC} follows the charge transport process and does not interfere with it as long as $E_{SC} \ll E_d$, with $E_d = Kk_B T/e_0$ denoting the diffusion field. In this case the build-up time of E_{SC} is expected to be given by τ_d if the recombination time of free charge carriers is large enough. For efficient photorefractive recording the charges should displace approximately half a grating period before they recombine^[14].

In reduced KNbO_3 the expected trapping time is of the order of μs [5,6,10] and the build-up time should be given by τ_d . According to Eq. (1) the build-up time should follow the $1/K^2$ dependence. However, for a decrease of K by a factor of four the measured response time did not change significantly.

The material properties of ferroelectric KNbO_3 that can give rise to the observed build-up time, and other possible limitations of the response time of the photorefractive effect will be discussed at the meeting. The measured response functions for different experimental conditions and differently prepared crystals will be presented.

References

1. P. Günter and J.-P. Huignard eds.: Photorefractive materials and their applications, (Springer, Berlin 1988)
2. C. T. Chen, D. M. Kin, and D. von der Linde, IEEE J. Quantum Electron. QE-16, 126 (1980)
3. L. K. Lam, T. Y. Chang, J. Feinberg, and R. Hellwarth, Opt. Lett. 6, 475 (1981)
4. A. L. Smirl, K. Bohnert, G. C. Valley, R. A. Mullen, and T. F. Boggles, J. Opt. Soc. Am. 6, 606 (1989)
5. M. Zgonik, I. Biaggio, P. Amrhein, and P. Günter, Ferroelectrics 107, 15 (1990)
6. I. Biaggio, M. Zgonik, and P. Günter, Opt. Comm. 77, 312 (1990)
7. J.-L. Ferrier, J. Gazengel, X. Nguyen Phu, and G. Rivoire, Opt. Comm. 58, 343 (1986)
8. J. M. C. Jonathan, G. Roosen, Ph. Roussignol, Opt. Lett. 13, 224 (1988)
9. E. Voit, M. Z. Zha, P. Amrhein, and P. Günter, Appl. Phys. Lett. 51, 2079 (1987)
10. C. Medrano, E. Voit, P. Amrhein, and P. Günter, J. Appl. Phys. 64, 4668 (1988)
11. P. Günter and F. Micheron, Ferroelectrics 18, 27 (1978)
12. N. V. Kukhtarev, Sov. Tech. Phys. Lett. 2, 438 (1976)
13. N. V. Kukhtarev, V. B. Markov, S. G. Odulov, M. S. Soskin, and V. L. Vinetskii, Ferroelectrics 22, 949 (1979)
14. A. M. Glass, M. B. Klein, and G. C. Valley, Appl. Opt. 26, 3189 (1987)
15. R.J. Reeves, M.G. Jani, B. Jassemnejad, R.C. Powell, G.J. Mizell, W. Fay, Phys. Rev. B 43, 71 (1991)

AD-P006 784



Spectral Pulse Distortion from Two-Beam Coupling of Sub-Picosecond Pulses in a Photorefractive Crystal

X. Steve Yao and Jack Feinberg

Departments of Physics and Electrical Engineering

University of Southern California

Los Angeles, Ca 90089-0484

Telephone: (213) 740-1134

Consider the coupling between two trains of mode-locked pulses in a photorefractive crystal. Let each optical pulse be so weak that it takes a large number of pulses to built up a quasi-steady-state refractive-index grating in the crystal. In this case the shape of the pulses will change as the result of beam coupling.¹ The temporal pulse shape changes for two reasons. First, interference between the diffracted pulse and the transmitted pulse alters the pulse shape, as shown in Fig. 1. Second, only a portion of each pulse's full frequency spectrum is diffracted by the volume photorefractive grating.

In the simplest case, in which the laser pulses are long enough so that they can be considered quasi-monochromatic, there is only one photorefractive grating formed in the crystal, and its grating wavevector is

$$k=2(\omega_0/c) \sin 2\theta. \quad (1)$$

All of the frequency components in each pulse will be perfectly phase matched to this grating. In Eq(1), ω_0 is the center frequency of the laser pulses, c is the speed of light and 2θ is the external crossing angle between the two interfering beams.

Now consider the case incident pulses having sub-picosecond duration. Their spectral bandwidth is now larger than the phase-matching bandwidth of a single volume grating in a mm-sized crystal. In this case only

92-18772



a small portion of each pulse's frequency components is phase matched to any one photorefractive grating. One might think that the energy coupled between the two beams will be quite small and that the diffracted pulses will be temporally broadened. However, each frequency component ω of the light writes a separate photorefractive grating in the crystal with a wave number of $2(\omega/c)\sin 2\theta$, and the total photorefractive grating is the sum of these gratings. Each frequency component will always be perfectly phase matched to the grating it has written. As a result, the energy coupled between two beams of short optical pulses can be quite large, and pulse broadening due to phase mismatch is not particularly severe.

In this paper, we report the measurement and analysis of changes in the frequency spectrum of the laser pulses caused by two-beam coupling. It is easier to study the energy coupling and pulse shape distortion in the frequency domain; the time domain then can be analyzed by a Fourier transform. We block and unblock a pump beam and measure the difference in spectral shape and width of the pulses in the probe beam as a function of different delays between the two beams. The spectrometer has a resolution of 1 cm^{-1} . The zero delay between the two pulse trains is determined by translating the delay line until the two-beam coupling gain reaches a maximum, as shown in Fig. 2. Figure 3a shows how the spectrum of the probe beam changes when the pump beam is blocked, with no relative delay between the two beams. The spectral width of the transmitted probe clearly narrowed as a result of beam coupling. Qualitatively, the strength of the grating written by each frequency component is proportional to the intensity of that frequency component. The diffraction efficiency of a single frequency component is proportional to the amplitude of the grating phase-matched to that frequency. Consequently, the weaker optical frequency components are diffracted with relatively less efficiency. As a result, the spectral width of the probe beam narrows. Figure 3b shows the same data but now with the pump beam delayed by 0.81 picosecond. (Note: the spectrum from the dye laser changed somewhat between these two figures.) The appearance of the second peak in the spectrum of Fig. 3b will be explained in our presentation; it results

from the interference of the transmitted frequency components of the probe beam and the diffracted frequency components of the pump beam.

REFERENCES:

- 1) X. S. Yao, V. Dominic, and J. Feinberg, "Theory of beam coupling and pulse shaping of mode-locked laser pulses in a photorefractive crystal," J. Opt. Soc. Amer. B7, 2347-2355 (1990).

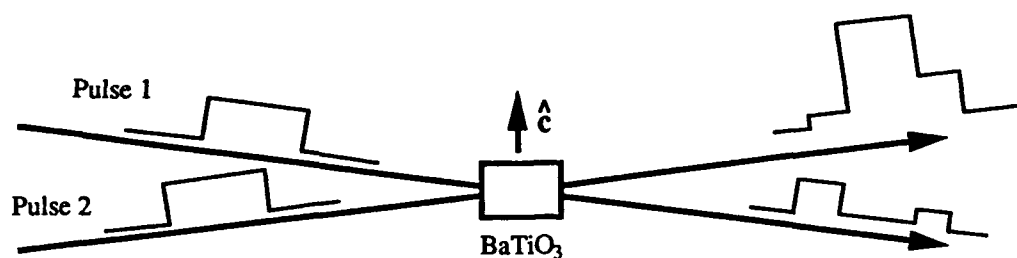


Figure 1) Pulse distortion from two-beam coupling in a photorefractive crystal.

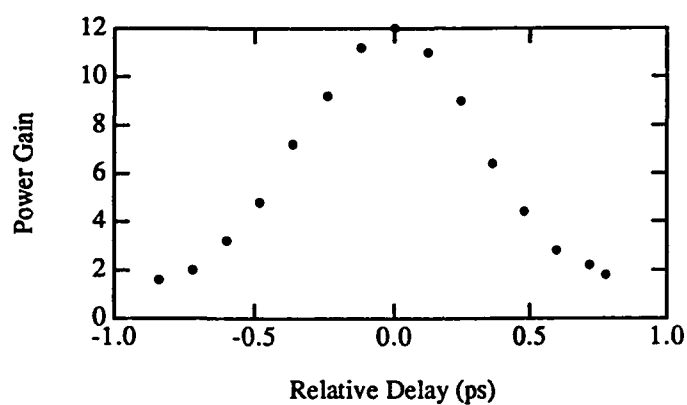


Figure 2) Two-beam coupling vs. the relative delay between the two beams.

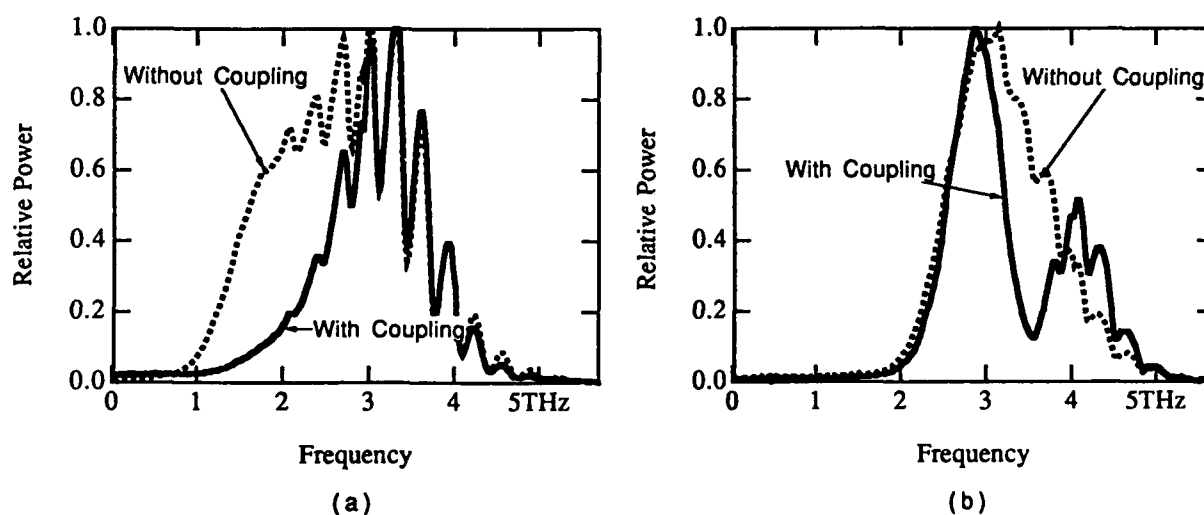


Figure 3) Spectral measurements of laser pulses with and without beam coupling. (a) Zero delay between two beams. (b) The relative delay between the two beams is 0.81 picosecond. Note that all spectral curves have been normalized to unity.

AD-P006 785

**Feature extraction by a self-organizing photorefractive system**

Claus Benkert, Verena Hebler, Ju-Seog Jang,

Shakil Rehman, Mark Saffman and Dana Z. Anderson

Department of Physics and Joint Institute for Laboratory Astrophysics, University of Colorado,

Boulder, CO 80309

Tel.: (303) 492-5129

An important feature of neural network processing lies in a network's ability to adapt to a given problem. The adaptation is accomplished by modifying its internal structure through some learning procedure. Neural network models may be classified in one of two types: The learning may be *supervised* by someone or something that indicates to the network what is expected of it, or the network may be governed by a *self-organizing* process in which it automatically develops an internal state that reflects the properties of its input environment. Self-organizing systems need no *a priori* knowledge supplied by a supervisor, and are particularly valuable when the task of the system depends only upon some property of the input data itself.

We here describe a self-organizing photorefractive system that extracts features from a collection of input patterns. The features are extracted according to a similarity criterion, which in our case is defined by an inner product. For example, if the collection of patterns consists merely of two images with orthogonal electric field patterns, the system will recognize the orthogonality and the extracted "features" will be the images themselves. If instead the two pictures are not orthogonal, the system will find a pair of best features, which, in different linear combinations, make up the images. When the system is subsequently presented with another picture it can recognize to what amount the learned features are present in the new input data.

The optical system is based on a multi-mode unidirectional photorefractive ring resonator [see Fig. 1] in which the modes are spatially distinct. An interesting property of this system is that

92-18773



the speed of the photorefractive materials employed govern the entire *learning* time, not the processing time. The gain for all of the resonator modes is supplied by a common photorefractive BaTiO₃ crystal which is pumped by a single frequency laser operating at 514 nm. The other two BaTiO₃ crystal provide mutual coupling between the resonator modes, which leads to the dynamical self-organization process.

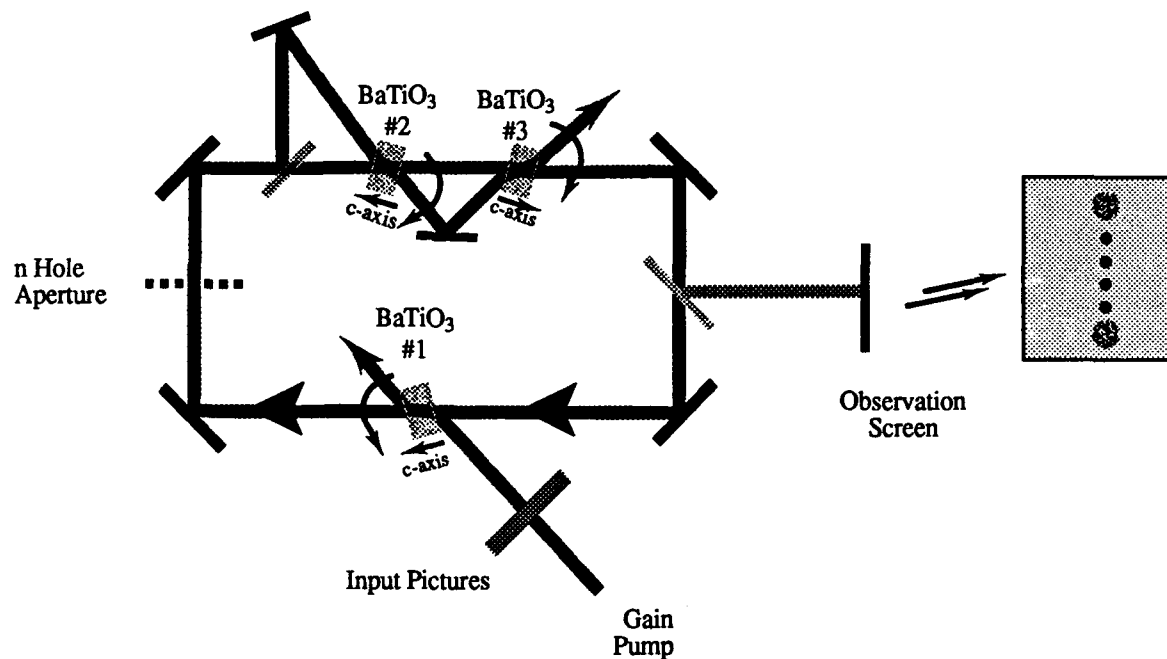


Fig. 1 Experimental set-up for a self-organizing photorefractive feature extractor.

The input patterns are sequentially impressed on the common pump beam. The set of patterns is repeatedly imposed onto the pump beam and the cycling time through the entire set is chosen to be smaller than the characteristic time constant of the BaTiO₃, which in our case is about one second. After some time, each mode of the resonator becomes maximally sensitive to a specific feature of the input pattern set, each mode choosing a different feature. In other words, the modes have become labels for the various features in the input pictures. As described above, for example, if two orthogonal pictures are presented to the system only two modes will oscillate, each mode synchronized with the appearance of its respective picture. The experimental results of this

particular case is shown in figure 2. Figure 2a and 2b depict a time sampling of the two orthogonal input pictures. Whenever one of the pictures is switched on at the input to the resonator, the orthogonal picture is switched off. Note that the actual exchange rate between the pictures is much higher than figure 2a and 2b suggest. The sampling rate is set such that the first picture is sampled for the first 20 cycles during its on state and for the following 20 cycles during its off state. The picture exchange rate in the experiment was 5 pictures per second. Figure 2c to 2e show a synchronized sampling of the mode intensities of three modes of the resonator. After a learning period the system has recognized the two orthogonal features in the input and has assigned two modes for their identification. The third mode does not respond because there are only two features in the input set. Thus the system has learned to distinguish between the two orthogonal input pictures in a self-organized process.

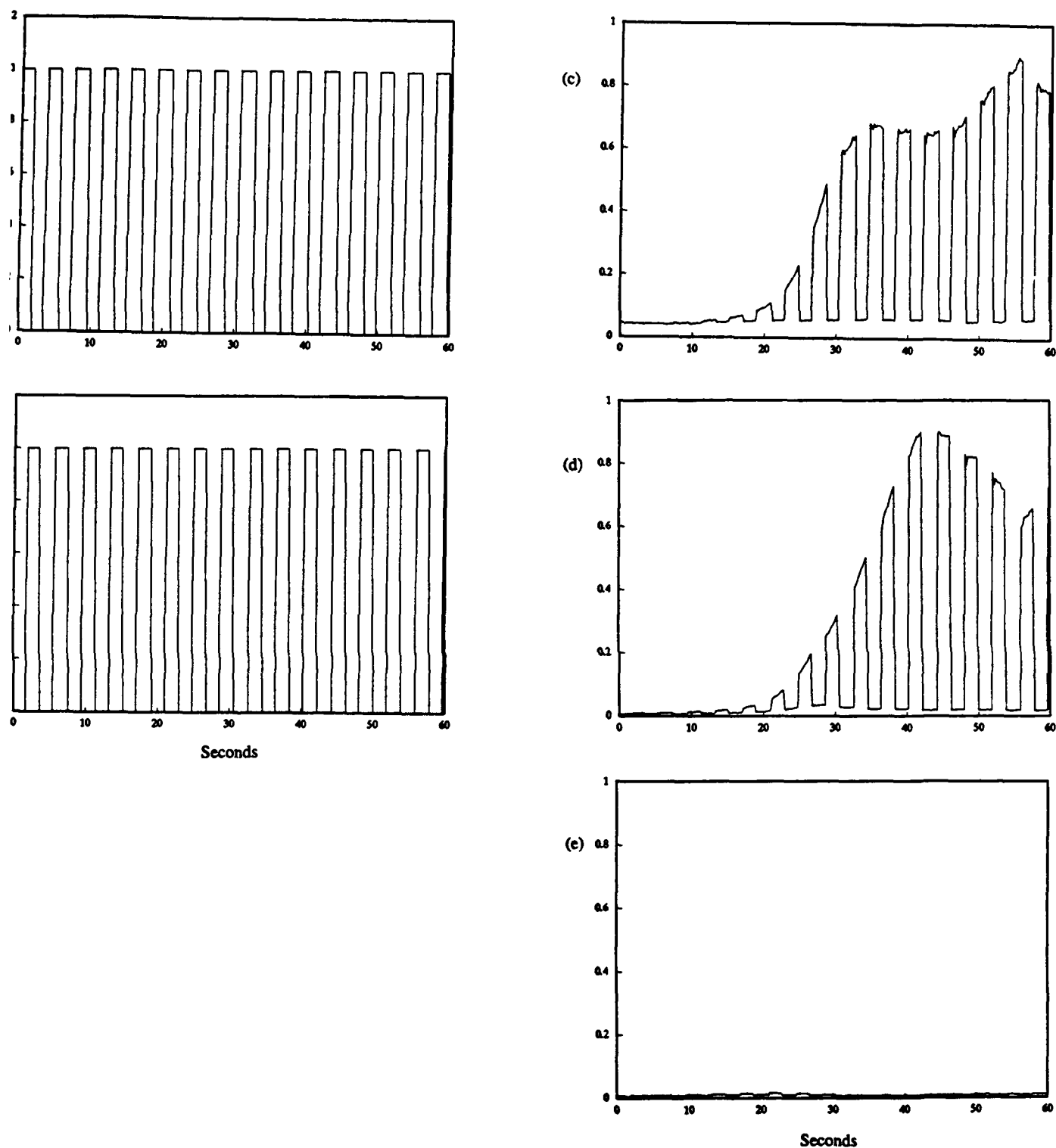


Fig. 2 Time sampling of an experiment, involving two orthogonal input pictures and a three mode resonator: (a) Intensity of picture A at the input to the resonator (b) Intensity of picture B (c) Output intensity of mode 1 (d) Output intensity of mode 2 (e) Output intensity of mode 3.



A Self-Organizing Photorefractive Frequency Decoder

Mark Saffman, Claus Benkert, and Dana Z. Anderson

Department of Physics and Joint Institute for Laboratory Astrophysics

University of Colorado, Boulder, CO. 80309-0440

SUMMARY

We demonstrate a self-organizing photorefractive circuit which decodes optical signals. The circuit is a pair of ring resonators with photorefractive gain and cooperative and competitive mode interactions. When a spatially multimode beam containing two optical carrier frequencies is used as the pump, the resonator self-organizes such that each frequency oscillates in spatially separate rings. Initial results, with a two crystal BaTiO₃ resonator, show a contrast ratio of better than 20:1 at the two outputs.

Consider the circuit shown schematically in figure 1. The photorefractive crystal in the center provides gain from a pump signal to two unidirectional, multi-mode ring resonators. Part of the energy in each ring is split off, and fed back into itself in a cooperative fashion by two beam coupling in a second photorefractive crystal. If the pump consists of a single optical frequency this configuration leads to a flip-flop behavior between the two resonators. This is similar to a previously reported flip-flop based on a competitive interaction between the rings¹. When the pump beam consists of two optical frequencies, in spatially orthogonal modes, the photorefractive gratings dynamically self-organize leading to a demultiplexing behavior.

92-18774



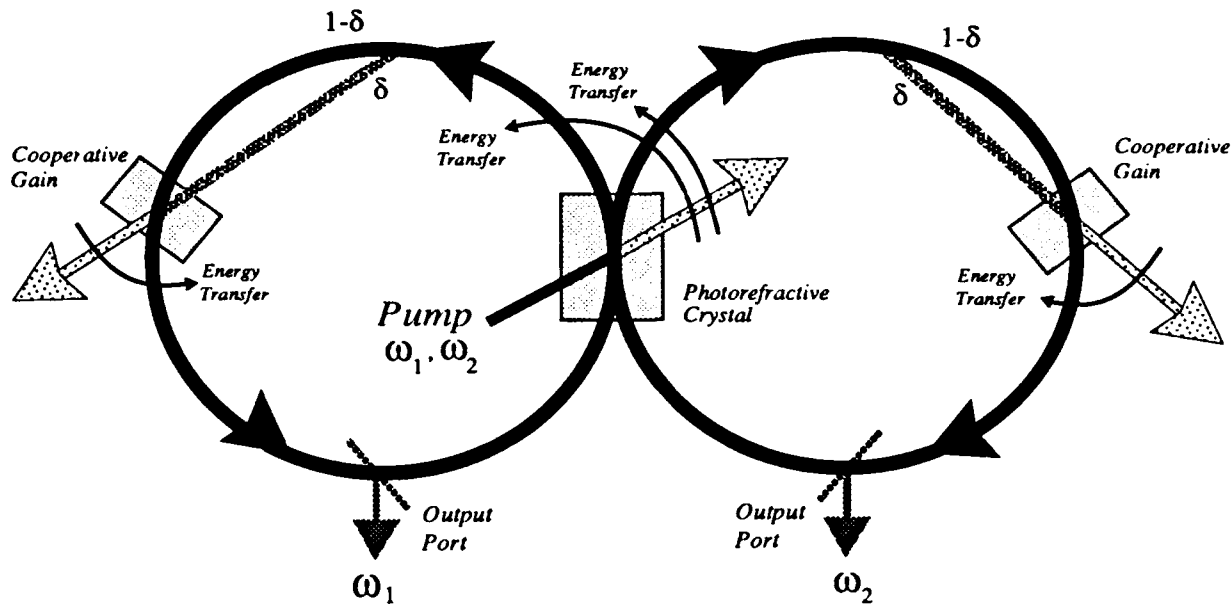


Figure 1. Self-Organizing frequency decoder.

The essential nonlinearity leading to the demultiplexing is the energy transfer in the cooperative gain crystal. In steady state, with one frequency oscillating in each ring, the cooperative crystal acts as a passive attenuator with a transmission

$$T = \frac{1 - \delta}{1 - \delta(1 - 1/G)}$$

where δ is the fraction of the resonating beam which is split off, and $G = e^{\Gamma}$ is the small signal gain in the crystal. If two frequencies attempt to oscillate in the same ring the modulation depth of the optical interference pattern is reduced. This in turn reduces the effective gain, which decreases T . Thus the cavity losses increase if two frequencies attempt to oscillate in a single ring. As long as the signals have a frequency separation greater than the inverse of the photorefractive response time additional cross gratings will not develop.

Combining the above nonlinearity, which encourages single frequency oscillation, with the pump crystal where both rings compete for energy results in each of the rings choosing one of the available frequencies. Since the pump

frequencies are in spatially orthogonal modes each grating in the pump crystal only transfers energy from a single input frequency to a single resonator ring.

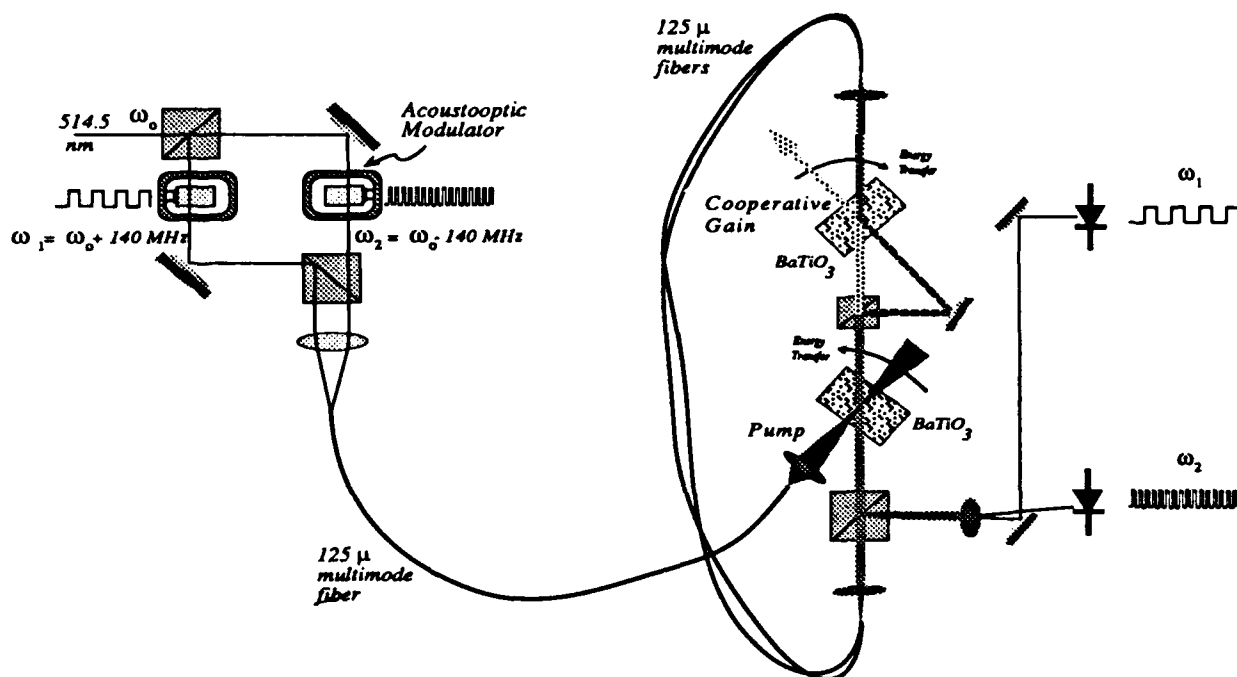


Figure 2. Experimental demonstration.

We have experimentally verified the behavior described above as shown in figure 2. Acoustooptic cells were used to split the output from an Ar^+ laser operating at 514.5 nm into two beams with a frequency separation of 280 MHz. The beams were then fed into a single multimode fiber, whose output pumped the photorefractive resonator. Each resonator ring had a length of about 1 meter, including 50 cm. of 125 μ multimode fiber. The pump and cooperative crystals were BaTiO_3 and the cooperative split off fraction δ , was about 0.9. The output from each ring was detected and displayed on an oscilloscope. By modulating the acoustooptic cells with low frequency square waves the frequency content in each ring was easily monitored. Preliminary results show a contrast ratio of better than 20:1 in each ring, as shown in figure 3.

References

1. Dana Z. Anderson, Claus Benkert, Beth Chorbajian, and Anno Hermanns, "Photorefractive flip-flop", Optics Letters, 16, 4, p.250, (1991)

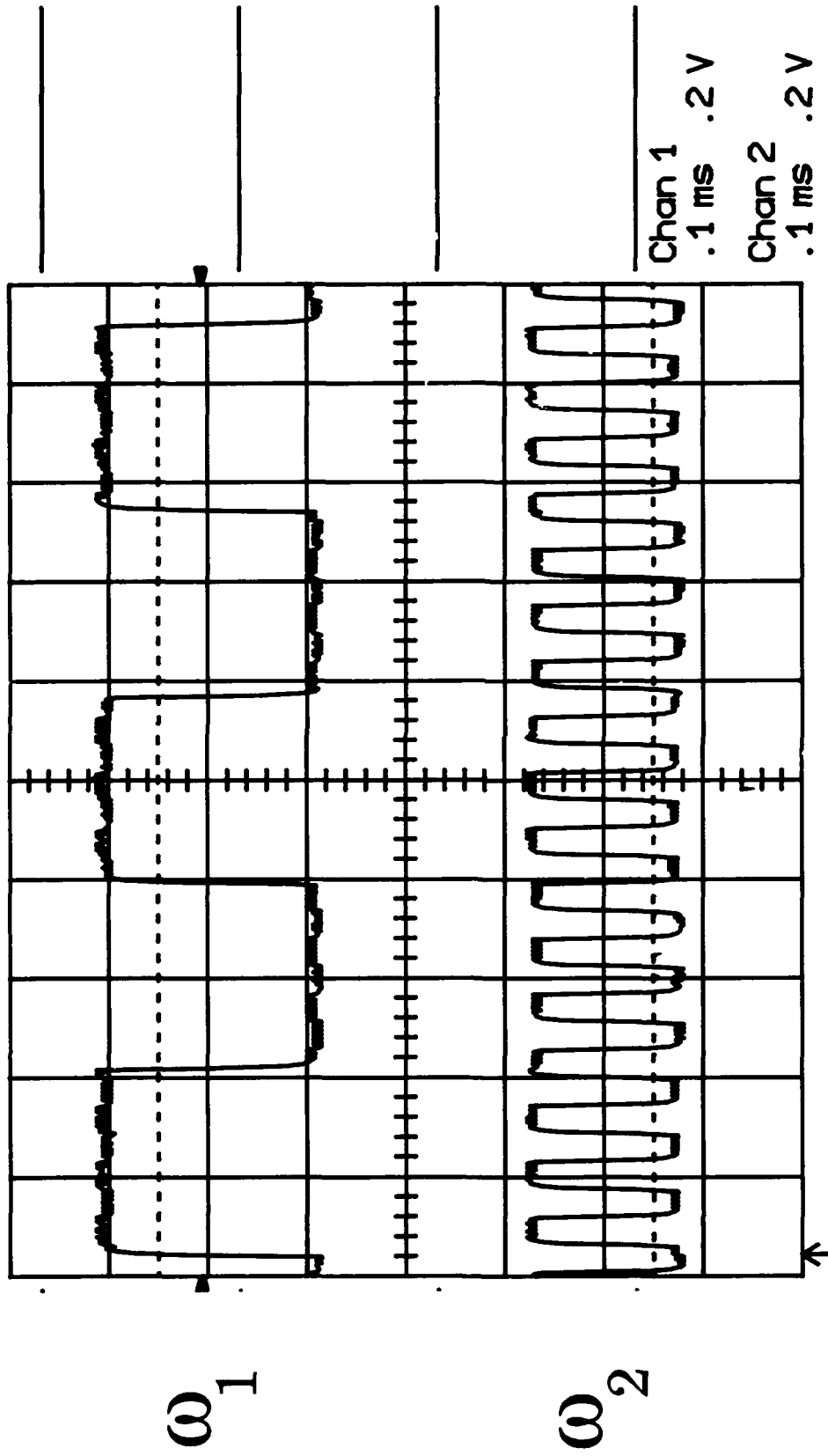


Figure 3. Experimental results. The traces show the outputs from the two resonator rings.

AD-P006 787



All-Optical Associative Memory based on a Nonresonant Cavity with Image Bearing Beams

M. Ingold, M. Duelli and P. Günter

Institute of Quantum Electronics, Swiss Federal Institute of Technology,
ETH - Hönggerberg HPF, CH-8093 Zürich, Switzerland. Phone: (0041) 1 377 23 37.

and

M. Schadt

Central Research Laboratory, F. Hoffmann-LaRoche Ltd., CH-4002 Basel, Switzerland.

1. Introduction

A new configuration of an all-optical, nonlinear holographic associative memory [1] is investigated. A multistable, content-addressable cavity is used, that performs image comparison, discrimination and read-out in one step. The required nonlinear processes are obtained by using a combination of a photorefractive KNbO_3 crystal and a nematic liquid crystal (NLC) in a feedback configuration with several beams.

2. Experimental

The associative memory is schematically drawn in Fig. 1. It consists of two or three signal beams that are focused on the NLC, amplified by the photorefractive crystal, refocused and fed back to the NLC. The birefringent NLC is positioned between crossed polarizers. Due to the birefringence induced by the feedback beams through molecular reorientation, the output intensity of each signal beam can switch between two stable states [2], [3]. Thus the output of all signal beams is a multistable function of the pump intensity. The signal beams are intensity modulated by the permanently stored images and the pump beam carries the selected input image. The photorefractive crystal is used for image comparison by photorefractive two-wave mixing of several signal beams with one pump beam. Each signal amplification depends on the amount of overlap between the stored and the input image. The stored image which is most similar to the input image is amplified best and switched on by the NLC. Thus the signal beam containing the associated image is discriminated from the other beams. In the output extracted from the cavity the associated image is bright and the other stored images remain dark.

92-18775



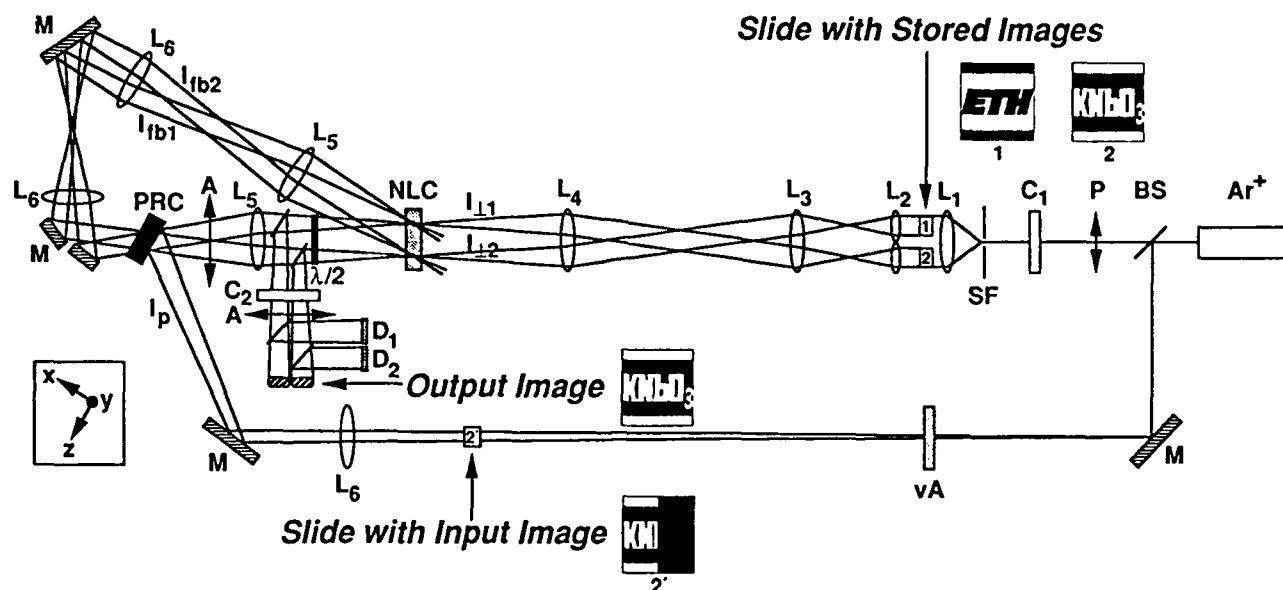


Fig. 1. Ar^+ : argon ion laser ($\lambda=515$ nm), BS: beam splitter, P: polarizer oriented under $+45^\circ$, where the horizontal polarization lies in the plane of the cavity, C_1 , C_2 : linear compensators, SF: spatial filter consisting of a microscope objective and a pinhole, lenses: L_1 ($f=175\text{mm}$), L_2 =microlenses ($f=68\text{mm}$), L_3 ($f=300\text{mm}$), L_4 ($f=500\text{mm}$), L_5 ($f=150\text{mm}$), L_6 ($f=300\text{mm}$), M: mirrors, vA: variable attenuator, NLC: homeotropically aligned nematic liquid crystal cell of thickness $d=500\mu\text{m}$, $\lambda/2$: half wave plate transforming -45° into H polarization, A: analyzers oriented horizontally, D_1 , D_2 : detectors, PRC: photorefractive crystal. The principal axes of the first compensator and the nematic liquid crystal are horizontal and vertical and those of the second compensator are parallel to $+45^\circ$ and -45° . The use of two compensators allows to choose appropriate intracavity starting intensities while compensating the output images to complete darkness before read-out. The distance between two succeeding lenses is always equal to the sum of their focal lengths. The NLC and the PRC are positioned at the focal planes of the lenses L_4 and L_5 respectively. The optical rays involved are named as follows: I_{11} , I_{12} = signal beams, I_{fb1} , I_{fb2} = feedback beams, I_p = photorefractive pump beam. The slide with the stored images is put in the focal plane of the microlenses and is imaged into the PRC. The slide with the input image is illuminated by the pump beam and also imaged into the PRC.

3. Results

Fig. 2a - 2c display measurements of associative read-out. Three different input images on the pump beam evoke the most similar stored image, that is characterized by the largest overlap with the input image. Photographs of associative recall are presented in Fig. 3a - 3c. Two black and white images are shown in the off-state (Fig. 3a) and after bistable switching with two incomplete input images (Fig. 3b - c). In these measurements the pump intensity is used as an easily adjustable control parameter which assures, that only one signal image wins in the beam competition and is switched on.

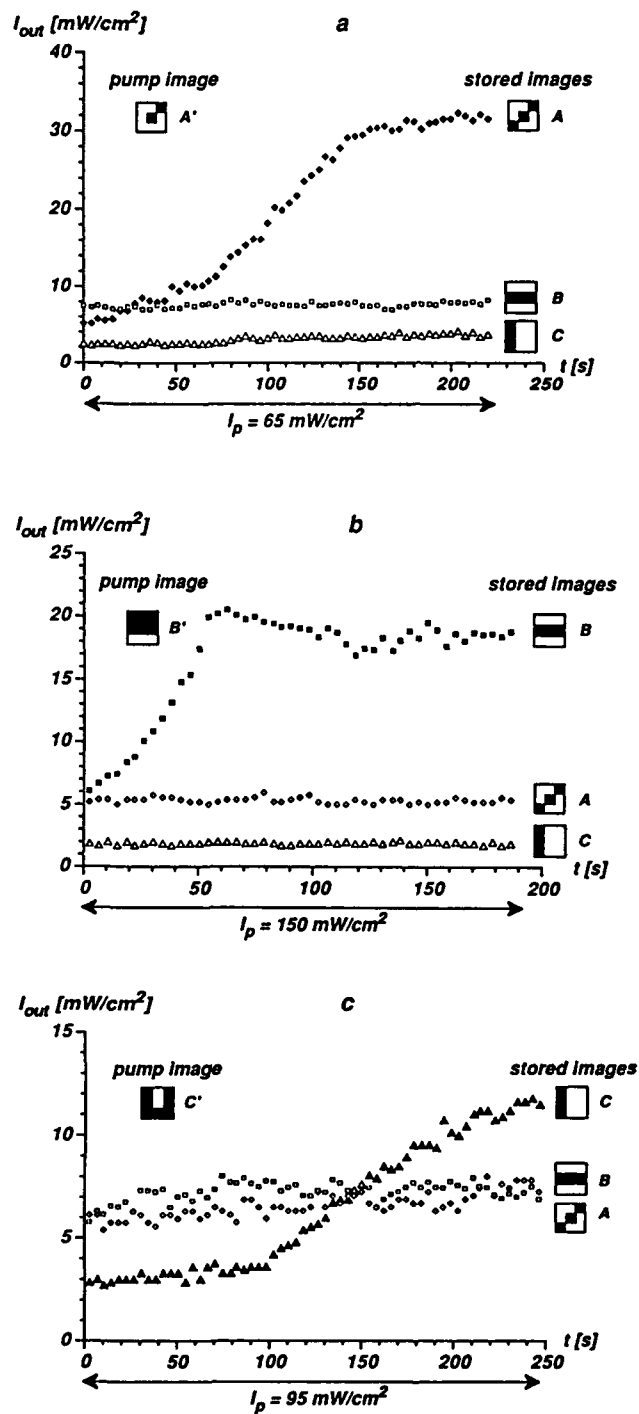


Fig.2. Associative read-out with three stored patterns, named A, B, C, and partial or erroneous input. The output intensities I_{out} of three injected signal beams are shown as a function of time after the pump beam is turned on. The intensities of the output beams and the pump beam refer to the bright areas of their images in the photorefractive crystal. The most similar image switches on, because it is amplified best and wins in the beam competition by depleting the pump. 2a - 2c: The input images A', B' and C' evoke the most similar images A, B and C respectively.



Fig.3. Output of associative memory with two stored images and partial input images. 3a: The off-state of the associative memory is shown, with the pump beam turned off. 3b - 3c: Image completion is demonstrated. The half input image, shown at the top of the photograph, evokes the associated complete image. The associative read-out is achieved with high contrast.

4. Discussion

Several requirements must be fulfilled in order to obtain a correct association: All signal beams must have identical optical hystereses, i.e. same injected power, same cross sections in the NLC and same losses in the cavity. Since the Fourier transforms of the signal images appear in the NLC, both on the signal and the feedback beams, the wavevectors of the images should be concentrated around a narrow and flat part of the Fourier spectrum in order to achieve an efficient and spatially homogeneous phase shift across the signal beam cross section by the feedback beam. In the photorefractive crystal the images must have perfect overlap, pump depletion should be not too strong and the photorefractive effect must be homogeneous in the whole crystal volume. Furthermore during read-out the NLC acts as a Fourier filter for the signal images. This limits the resolution of the output images to approximately 1.5 linepairs per mm under our experimental conditions. Presently new configurations are under investigation, that allow to separate the beams bearing images from those, that are switched in the NLC.

5. References

- [1] Y. Owechko, IEEE J. Quant. Electronics **25**, 619-632 (1989).
- [2] M. Ingold and P. Günter, J. Opt. Soc. Am. B **7**(12), 2380-2386 (1990)
- [3] M. Ingold, J. Keller, G. Pauliat and P. Günter, Ferroelectrics **92**, 269 (1989)



Detection of the transient motion of a scattering surface
by two-wave mixing in a photorefractive crystal.

R. K. Ing* and J.-P. Monchalin

National Research Council Canada, Industrial Materials Institute,
75 De Mortagne Boulevard, Boucherville, Québec J4B6Y4, Canada.

* UltraOptec Inc., 27 de Lauzon Street, Boucherville, Québec J4B1E7, Canada.

Telephone: (514) 641-2280 ext. 214

Optical detection of the transient surface motion of objects is an area of far reaching practical importance. Applications include the vibration monitoring of many engineering structures (power plants, aircrafts, engines of various kinds...) and more recently the detection of ultrasound produced by pulse laser excitation. This technique, now in active development in our laboratory and elsewhere, extends ultrasonic inspection of materials to conditions otherwise difficult or impossible (complex geometries, hot products on a production line...). Various optical systems have been devised for detecting surface motion and have been recently reviewed¹. We are reporting here the novel use of two wave mixing in a photorefractive crystal for detecting such a motion and in particular ultrasonic displacement produced by pulsed laser excitation. This approach has the merit of being applicable to a rough surface by integrating over many speckles and of having a very broad frequency detection bandwidth. The use of two-wave mixing for coherent homodyne detection of arbitrary wavefronts was previously reported and applied to the detection and amplification of an intensity modulated wave². In the case of interest here of the detection of surface motion, the signal wave which has been scattered off the surface is instead phase modulated, and the scheme previously reported cannot be directly used since the transmitted signal wave and the diffracted pump wave, which acts as local oscillator, are in phase. Linear and sensitive detection of phase shifts requires instead the interfering light fields to be in quadrature. Before describing an optical configuration which satisfies this requirement, we analyze the effect of a small phase shift applied to the signal wave in a two-wave mixing configuration.

In our experiment we use a BaTiO₃ crystal without applied field. In this material, charge separation is essentially caused by diffusion and the stationary spatial phase shift between the interference pattern and the recorded hologram is $\pi/2$. In general, this phase shift is determined by the following equation:

$$\tau_d \frac{\partial E_{sc}}{\partial t} + A E_{sc} = B E_q P^* S \quad (1)$$

where E_{sc} is the space charge field, P and S are the complex amplitudes of the pump wave and of the signal wave inside the crystal, respectively. A , B , E_q and τ_d can be found from the standard theories of the photorefractive effect^{3,4}.

The steady state space charge field is readily derived and is equal to $(B/A)E_q P^* S$. If a small sinusoidal phase modulation of frequency ω and of amplitude ϕ_0 ($\phi_0 \ll 1$) is applied upon S before the crystal, eq. (1) can be rewritten as:

$$\tau_d \frac{\partial E_{sc}}{\partial t} + A E_{sc} = B E_q P^* S (1 + j \phi_0 \cos(\omega t)) \quad (2)$$

which gives the solution:

$$E_{sc} = \frac{B}{A} E_q P^* S (1 + j \alpha \cos(\omega t + \psi))$$



complex amplitude transmission coefficients through the index grating of the two polarization components S^X_0 and S^Y_0 of the signal beam respectively. γ_3 is different from γ_1 because light propagation indexes for X and Y polarizations are different. These coefficients can be easily derived from the results of Vahey⁶ and Kogelnik⁷ on fixed index gratings.

As shown in *figure 1*, a retardation plate is introduced at the exit of the crystal. This plate gives a phase shift noted ϕ between the X and Y axis-components of S and is followed by a polarizing cube beam splitter which makes the X and Y polarizations of S to interfere along new X' and Y' polarization directions oriented at 45° with respect to X and Y. The complex amplitudes along X' and Y', $S^{X'}$ and $S^{Y'}$ are:

$$\sqrt{2}S^{X'}(t) = |\gamma_1| |S^X_0| e^{-j(\phi_0 + \phi_1)} + |\gamma_2| |P^X_0| e^{-j\phi_2} + |\gamma_3| |S^Y_0| e^{-j(\phi_0 + \phi_3 + \phi)}$$

and

$$\sqrt{2}S^{Y'}(t) = |\gamma_1| |S^X_0| e^{-j(\phi_0 + \phi_1)} + |\gamma_2| |P^X_0| e^{-j\phi_2} - |\gamma_3| |S^Y_0| e^{-j(\phi_0 + \phi_3 + \phi)}$$

to which correspond the intensities $I^{X'}(t)$ and $I^{Y'}(t)$:

$$I^{X'}(t) = \frac{|\gamma_1|^2 |S^X_0|^2 + |\gamma_2|^2 |P^X_0|^2 + |\gamma_3|^2 |S^Y_0|^2}{2} + |\gamma_1| |S^X_0| |\gamma_2| |P^X_0| \cos(\phi_0 + \phi_1 - \phi_2) \\ + |\gamma_1| |S^X_0| |\gamma_3| |S^Y_0| \cos(\phi_0 - \phi_3 + \phi_1 - \phi_3 + \phi) + |\gamma_2| |P^X_0| |\gamma_3| |S^Y_0| \cos(-\phi_0 + \phi_2 - \phi_3 + \phi)$$

$I^{Y'}$ is given by an identical expression with the exception of a negative sign (-) in front of the two last terms. To simplify calculations, let us take $\phi^X_0 = \phi^Y_0 = \phi_0 + \phi_u$, where ϕ_u represents the rapid phase modulation. In the experiment to detect ultrasonic motion, ϕ_u is equal to $4\pi\delta/\lambda$ where δ is the ultrasonic amplitude displacement and λ the laser wavelength. Taking the difference between $I^{X'}$ and $I^{Y'}$, we obtain

$$\Delta I = 2 |\gamma_1| |S^X_0| |\gamma_3| |S^Y_0| \cos(\phi_1 - \phi_3 + \phi) + 2 |\gamma_2| |P^X_0| |\gamma_3| |S^Y_0| \cos(-\phi_0 - \phi_u + \phi_2 - \phi_3 + \phi)$$

In order to maximize the sensitivity of detection of ϕ_u , ϕ should be adjusted so $-\phi_0 + \phi_2 - \phi_3 + \phi = \pi/2$. Then, $\phi_1 - \phi_3 + \phi = \phi_1 + (\pi/2 + \phi_0 - \phi_2)$. Since we have a $\pi/2$ shift between gratings, perfect phase matching between signal and diffracted pump wavefronts is realized which means $-\phi_0 + \phi_2 - \phi_1 = 0$. In this case, it follows

$$\Delta I = 2 |\gamma_2| |P^X_0| |\gamma_3| |S^Y_0| \sin(\phi_u) \approx 2 |\gamma_2| |P^X_0| |\gamma_3| |S^Y_0| \phi_u \text{ for } \phi_u \ll 1.$$

Note that if grating shift is different from $\pi/2$, a DC offset will have to be added in this expression of ΔI .

These expressions show that a high photocurrent signal ΔI can be achieved if the diffraction efficiency $|\gamma_2|$ of the index grating is large. This parameter depends upon the grating build-up which, in turn, depends on the total incident intensity, on the incident beam ratio and on the grating spatial frequency⁵. If optimal conditions are achieved, an exponential intensity gain of 20 cm⁻¹ can be obtained in a BaTiO₃ crystal. That leads the ratio $(|\gamma_2| |P^X_0|)/(|\gamma_1| |S^X_0|)$ in the undepleted pump approximation to reach a maximum value of 150 with a crystal thickness of 5 mm.

We also observe that a DC component is present in $I^{X'}$ and on $I^{Y'}$. For a grating shift of $\pi/2$, this DC value is equal to $|\gamma_1|^2 |S^X_0|^2 + |\gamma_3|^2 |S^Y_0|^2 + |\gamma_2|^2 |P^X_0|^2$. The high gain which can be achieved with BaTiO₃ permits more easily one to reach the shot noise limited detection regime.

Additional elements of the setup for ultrasound detection are shown in *figure 1*. We note that pump beam does amplify only the signal beam during its first transmission through the crystal and not after multiple reflection by the crystal faces. To achieve a better gain by making use of the large value of r_{42} , the index grating direction is not along the c-axis. The spatial frequency of the index grating is chosen to correspond to the maximum value of E_{sc} . Following values found in the literature, the angle difference between the two incident beams is taken to be approximately 40°. The beam ratio is chosen to be optimal so that the exponential gain reaches its saturation limit.

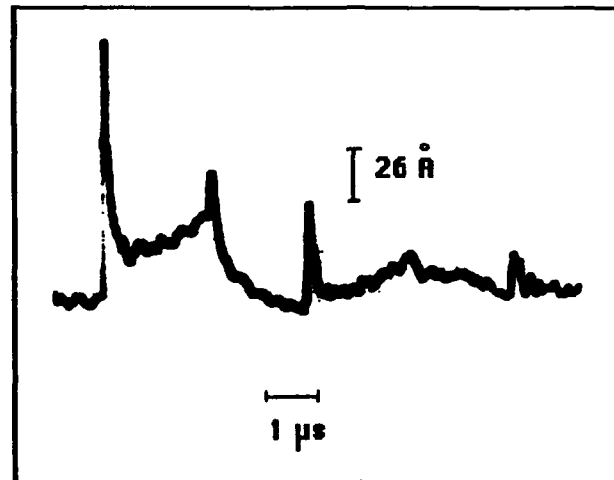


Figure 2. Ultrasonic displacement generated by a Q-switch Yag laser beam in the vaporization regime. Thickness of the aluminium plate: 12.5 mm. Recorded bandwidth: 1kHz-20 MHz.

We are showing in *figure 2* an experimental result obtained with this setup. This data shows the on-axis ultrasonic displacement generated by a Q-switch YAG laser beam of short time duration (10 ns), focused to 1 mm diameter spot, detected on the opposite side of a plate 12.5 mm thick. The detection surface is not polished. Generation is done in the vaporization regime, the surface being coated by a thin oil layer. We can observe in this figure, the arrival of the various longitudinal and transverse wavefronts directly propagating from the source and after multiple reflections.

Work is presently continuing in order to evaluate the minimum ultrasonic displacement which can be detected with such a setup for various signal beam intensity levels and to estimate its étendue (throughput) by varying the spot size on the surface or the opening of the pupil of the collecting lens.

References

1. J.-P. Monchalín, IEEE Trans. Ultrason. Ferroelectrics and Freq. Contr. **UFFC-33**, 485, 1986
2. G. Hamel de Monchenault and J. P. Huignard, J. Appl. Phys. **63**, 624, 1988.
3. J. M. Heaton and L. Solymar, Optica Acta **32**, 397, 1985.
4. N. V. Kukhtarev, V. B. Markov, S. G. Odulov, M. S. Soskin and V. L. Vinetskii, Ferroelectrics **22**, 949, 1979.
5. D. Rak, I. Ledoux and J. P. Huignard, Optics Comm. **49**, 302, 1984.
6. D. W. Vahey, J. Appl. Phys. **46**, 3510, 1975.
7. H. Kogelnik, Bell Syst. Tech. J. **48**, 2909, 1969.

AD-P006 789



Velocity filtering using complementary gratings in photorefractive BSO

Ghazanfar Hussain and Robert W. Eason

Department of Physics and Optoelectronics Research Centre
University of Southampton, Southampton SO9 5NH, UK.

Motion detection, velocity filtering and the detection of change in a given scene are all important aspects for optical processing architectures and systems. So far several different techniques have been reported in the literature that use either all optical [1-4], or hybrid (optical plus electronic) [5-6], schemes to implement novelty filter [1] type operations. The electronic techniques however may have only limited applications due to the sequential nature of the process. For essentially all-optical schemes the intrinsic advantages of parallel image subtraction are clear. In this paper we report a different scheme for motion detection and velocity filtering which uses two spatially multiplexed gratings with a relative phase shift of 180 degrees, (known as complementary gratings). Such grating recording has already been implemented in a LiNbO₃ crystal [7].

Optical motion detection however can benefit considerably from the use of a reasonably fast material, such as photorefractive BSO. Here we have recorded complementary gratings by applying a periodic phase modulation to the reference beam. The two gratings recorded in this way produce a photoinduced index modulation Δn_A and Δn_B with a 180° phase shift. The resultant superposed index modulations are thus

$$\Delta n_A = N_A \cos [Kx + \phi_A(x)]$$

$$\Delta n_B = N_B \cos [Kx + \phi_B(x)]$$

Subtraction is realized when both multiplexed gratings are of identical strength and $\phi_A - \phi_B = 180^\circ$ so that $\Delta n_A + \Delta n_B = 0$

In the case of a static object these grating profiles are almost identical and the phase conjugate output is ideally reduced to zero. If any movement occurs in the object plane however these multiplexed gratings will undergo dynamic change and any resultant output will indicate motion within the object plane.

Figure 1, shows the details of the experimental arrangement for motion detection via this multiplexed degenerate four wave mixing configuration. An Argon Ion laser operating in multi-longitudinal mode at 514.5 nm was spatially filtered and expanded to a diameter of ≈ 5 mm and split by beam splitter BS₁. The reflected beam was directed towards a piezo-electric mirror M₂ driven by a variable frequency square wave AC voltage. Mirror M₂ reflected the incident beam towards the BSO crystal as a reference beam I₁. Beam splitter BS₂ split the incoming beam to form an object beam I₂ and a mutually incoherent counter propagating readout beam I₃. Beam I₂ was incident on the BSO, after traversing an object, beam splitter BS₃, and imaging lens L₁ (f=15 cms).

The intensities of the beams I₁, I₂ and I₃ were arranged to be 7.0 mW, 3.5 mW and 1.7 mW respectively. Lens L₁ was used for 1:1 imaging of the input light distribution into the BSO crystal. The angle between the beams I₁ and I₂ outside the crystal was 40°. To write the complementary gratings a square wave AC voltage was applied to the piezoelectric pusher in the reference beam with a controllable frequency in the range of 0-100 Hz and driving voltage 0-30 volts.

92-18777



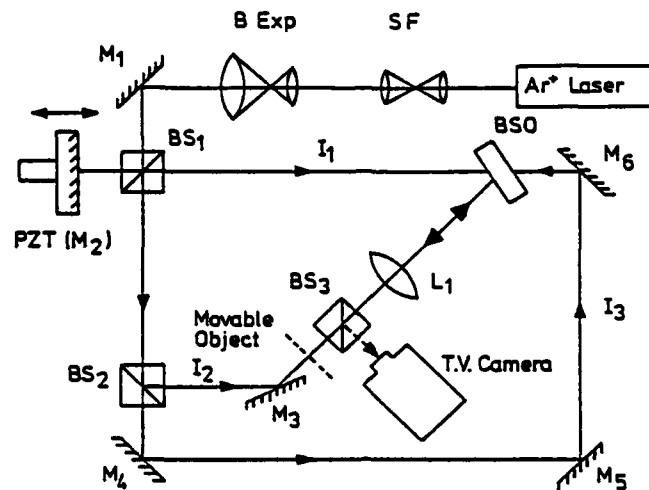


Figure [1]. The experimental arrangement for velocity filtering using complementary gratings in photorefractive BSO.

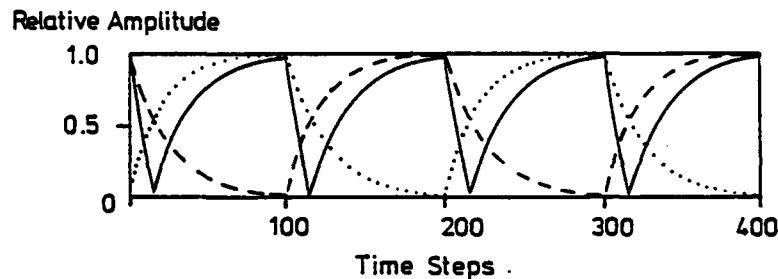


Figure [2]. Result of simulation for the complementary gratings build up, decay and the differential output.

Subtraction by these complementary gratings can be illustrated via a model shown in figure 2, which considers the simultaneous presence of two multiplexed gratings. For this simulation decay and growth of the two gratings (dashed and dotted lines) follows the relationship for grating strength

$$A(t) = A_0 \exp(-t/\tau_1)$$

$$B(t) = B_0 [1 - \exp(-t/\tau_2)]$$

The differential output is shown by the solid line.

Figure 3 column (i) shows oscilloscope traces, recorded on a storage scope of the phase conjugate output from the complementary gratings detected at the image plane by a photodiode. Trace (a) shows the output when a square AC voltage of 1 Hz was applied to the pusher while trace (b) shows the output for 30 Hz. Figure 3 column (ii), shows simulation results at corresponding pushing frequencies. It is clear that simulation and experiment are in close agreement.

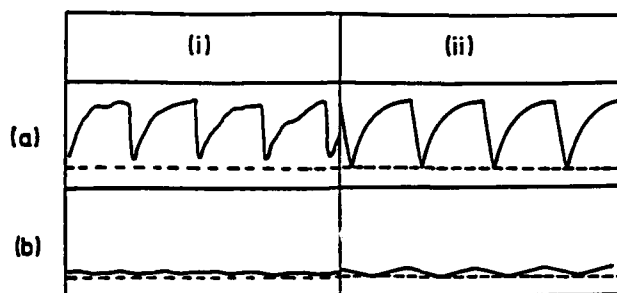


Figure [3] Column (i) oscilloscope traces of the phase conjugate output for piezo-electric pusher frequencies of 1 Hz (a) and 30 Hz (b). Column (ii) shows simulations for corresponding frequencies.

Figure 4 (a) shows the photograph of a resolution test chart whose phase replica was placed in the object plane, to demonstrate velocity filtering. Fig. 4 (b) shows the result of image subtraction when complementary gratings are recorded at a frequency of 30 Hz. Results of a sequence of output images are shown in figures 4(c) and 4(d). In these figures the motion of the object was simple harmonic (pendulum-like behaviour) and all parts of the test chart were moved with identical speeds, however the subtraction process has isolated particular features within the general field of motion. Photograph (c) and (d) show the moving objects at specific times within the cyclic oscillatory motion for the same input phase object. The feature sizes shown here, vary from $70\text{ }\mu\text{m}$ width in fig. 5(c), to the smallest features observable, with the limited numerical aperture in our experimental arrangement, of $20\text{ }\mu\text{m}$ in fig. 4(d). It can therefore be concluded that the observed features depend on a unique combination of size and velocity.

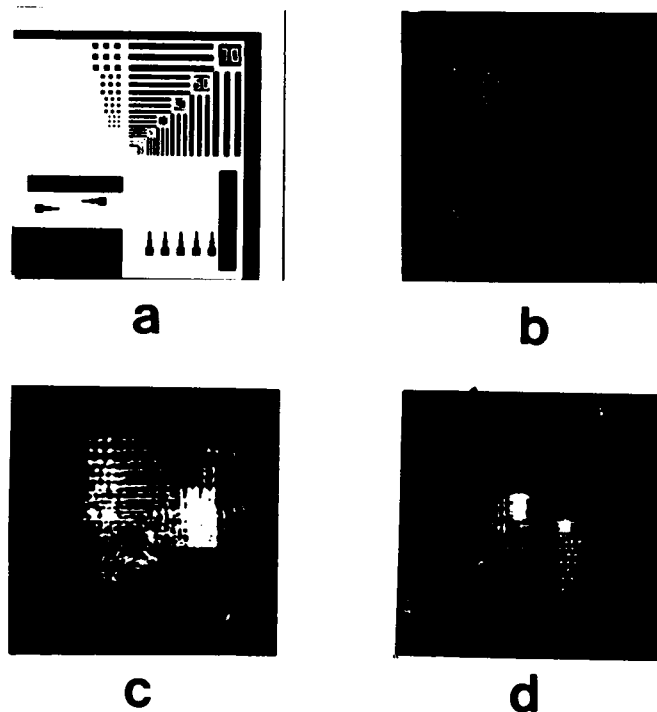


Figure [4]: (a) shows a resolution test chart whose phase replica was placed in the object plane. (b) shows the result of image subtraction when complementary gratings are recorded at a pushing frequency of 30 Hz. (c) and (d) are from a sequence of photographs showing velocity filtering detection of features of particular dimensions, which are only observed at specific speeds.



Figure [5]. Results of directional motion detection via a Fourier transformation stage. (a) Fourier transform of subtraction of static resolution chart. (b) shows higher horizontal orders which correspond to lower speed.

Another aspect of this technique illustrates the implementation of a Fourier transform stage. Figure 5(a) shows the Fourier transform of subtraction achieved via complementary gratings while fig. 5(b) for example show that the higher horizontal orders appearing are directly interpretable as a distinct feature size within the output image plane.

References

1. D. Z. Anderson, D. M. Liniger and J. Feinberg, Opt. Lett. 12, 128 (1987).
2. J. A. Khoury, G. Hussain and R. W. Eason, Opt. Comm. 71, 138 (1989).
3. M. Cronin-Golomb, A. M. Biernacki, C. Lin and H. Kong, Opt. Lett. 12, 1029 (1987).
4. R. S. Cudney, R. M. Pierce and J. Feinberg, Nature, 332, 424 (1988).
5. T. Aida, K. Takizawa and M. Okada, Opt. Lett. 14, 835 (1989).
6. Y. Li, A. Kostrzewski, D. H. Kim and G. Eichmann, Appl. Opt. 28, 4861 (1989).
7. J. P. Huignard, J.-P. Herriau, and F. Micheron, Ferroelectrics, 11, 393 (1976).



Phase-locked detection of running interference pattern in photorefractive SBN.

O. P. Nestiorkin, Ye. P. Shershakov, B. Ya. Zel'dovich

Nonlinear optics laboratory, Polytechnic Institute,
prosp. Lenina 76, Chelyabinsk, 454080, USSR
phone.3512-39-91-40

N. V. Bogodaev, L. I. Ivleva, N. M. Polozkov

General Physics Institute, Academy of Sciences of USSR 38
Zavilov Street, Moscow 117942, USSR, telex 411074 LIMEN SU,
phone 095 135-77-44.

Holographic grating in a photorefractive crystal may be recorded due to the diffusion of electrons or their drift in external or intrinsic photovoltaic dc field as a result of illumination by a static interference pattern. Those traditional mechanisms are well studied [1]. Running interference pattern may be registered by the phase-locked detection in the externally applied ac field. That mechanism was realized in the paraelectric crystal $\text{Bi}_{12}\text{TiO}_{20}$ (BTO) [2,3]. In this work we have performed the phase-locked detection mechanism in the ferroelectric photorefractive crystal SBN:Ce.

The scheme of the experiment is shown in Fig.1. The crystal was illuminated by two waves S and P_S . The frequency of P_S wave was shifted by $\omega/2\pi=20\text{Hz}$ as a result of motion of the piezomirror with a saw-tooth voltage applied to it. The He-Ne laser with 10 mW power was used as a source of radiation. Polarizations of the waves coincided with the plane of incidence. Intensity ratio at the entrance of the crystal $\rho^2=|S|^2/|P_S|^2$ was varied from 10^{-3} to 1. The frequency and the phase of external field applied to the crystal was synchronized with the saw-tooth voltage. The diffraction efficiency η of the recorded static hologram was measured experimentally versus the intensity ratio ρ^2 , amplitude E_0 of the externally applied field

92-18778



and the grating period Λ . The value of η was determined by the measurement of the intensity of the diffracted signal in the absence of the input one.

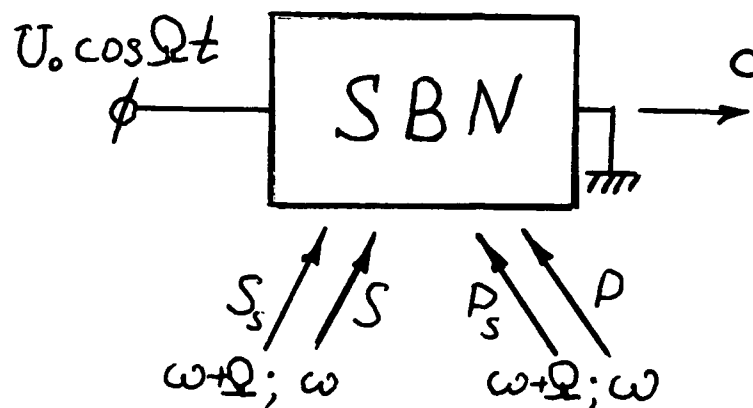


Fig.1. Scheme of the experiment

Some new waves appear during the record as a result of the diffraction on the static hologram: S_s with shifted frequency and P with undisturbed frequency. Pairs of waves $(S;P)$ and $(S_s;P_s)$ record the gratings due to the diffusion mechanism. Analysis shows, that if optical axis is directed as shown in Fig.1 the grating of S_s and P_s waves is in phase with the one recorded by S and P_s waves by means of the phase-locked detection mechanism. In contrast the grating of waves S and P is counterphase to the one of S and P_s waves. The sign of that effect is opposite for the reversed optical axis direction. In agreement to said if $\beta^2=1$ the two gratings caused by the self-diffraction of S and P_s waves and by following diffusion recording exactly compensate each other. Therefore the diffraction efficiency does not depend on optical axis direction. For small intensity ratio $\beta^2=|S|^2/|P_s|^2 \ll 1$ the diffraction efficiency is larger if the energy exchange due to degenerate interaction results in the amplification of the weak beam S_s . That corresponds to the optical axis direction shown in Fig.1. The higher is the efficiency of degenerate beam coupling caused by diffusion recording, the larger is the difference

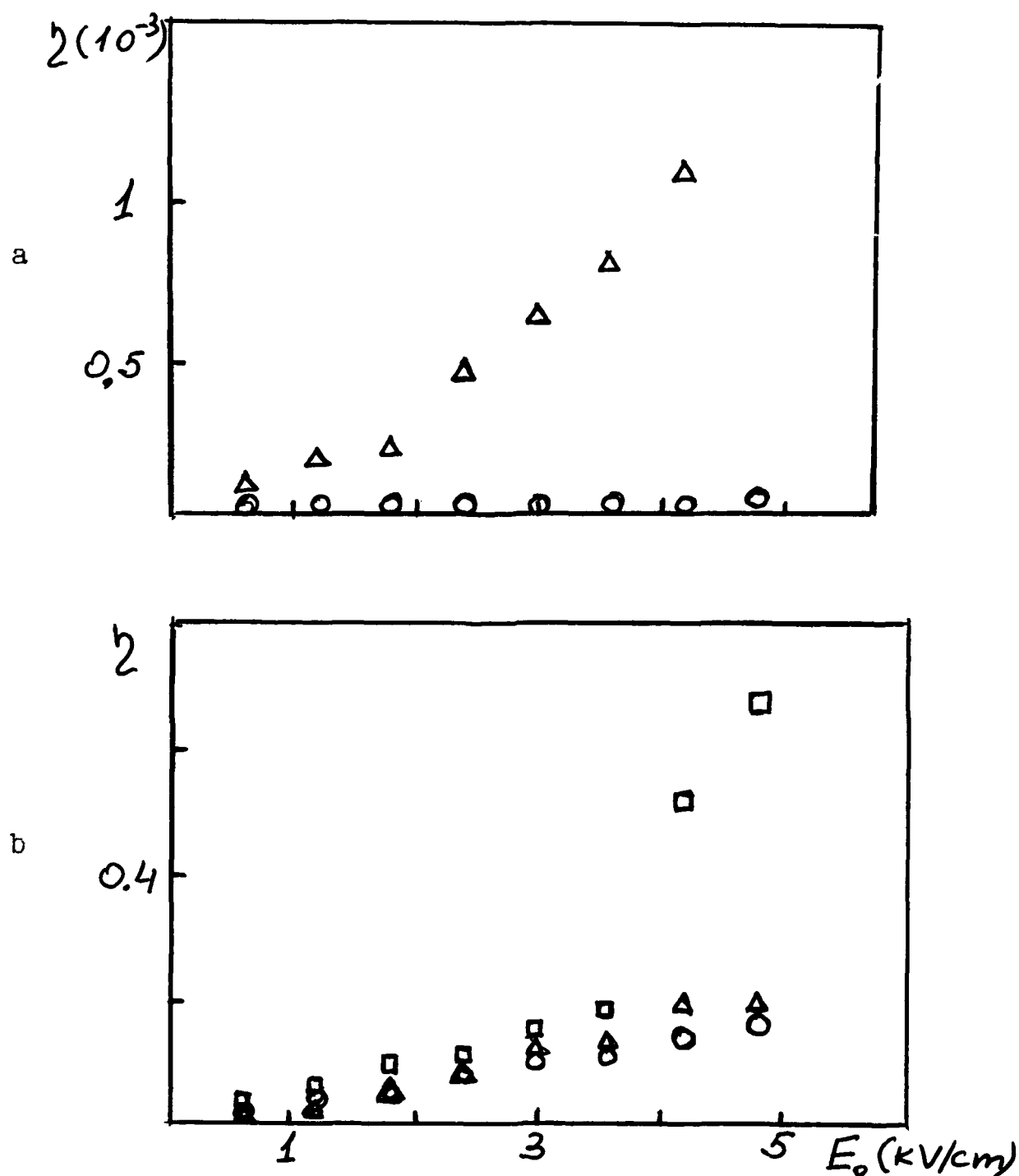


Fig.2. Diffraction efficiency of hologram η versus external field amplitude E_0 . a) intensity ratio $\beta^2 = 10^{-3}$, grating period $\Lambda = 2 \mu\text{m}$. Different marks correspond to different optical axis direction b) Δ and \circ correspond to $\Lambda = 2 \mu\text{m}$, $\beta^2 = 1$, and two different optical axis directions; \square - corresponds to $\Lambda = 50 \mu\text{m}$, $\beta^2 = 1$ and optimum optical axis direction.

between diffraction efficiencies for the two optical axis directions. In the other words that difference must grow if the grating period decreases. All the above conclusions were confirmed by experiment (see Fig.2). The maximum diffraction efficiency $\eta=0.7$ was realized for $\beta^2=1$, $\Lambda=50\mu\text{m}$, $E_0=4.8\text{kV/cm}$ and strongly exceeds the corresponding value for phase-locked detection mechanism in $\text{Bi}_{12}\text{TiO}_{20}$ crystal [3].

Maximum amplitude of field which may be applied to the crystal without destruction of its monodomain structure was 5kV/cm .

In this work we have also developed the nonlinear theory of four-wave mixing (S, P_s, S_s, P) including the depletion of all the waves, and its results are in a reasonable agreement with the experiment.

References

1. P. Gunter and J. -P. Huignard, Ed., *Photorefractive Materials and Their Applications*, vols I and II, Berlin: Springer-Verlag, 1988, 1989.
2. P. N. Ilinykh, O. P. Nestiorkin, and B. Ya. Zel'dovich, *Opt. Comm.* **80**, 249 (1990).
3. P. N. Ilinykh, O. P. Nestiorkin, and B. Ya. Zel'dovich
Recording a static hologram with laser beams of different frequencies in photorefractive crystals. *JOSA B*, 1991, to be published.



Time-Integrating Self-Pumped Phase Conjugator

Erik Oldekop and Asad Siahmakoun
Center for Applied Optics Studies
5500 Wabash Ave.
Terre Haute, IN 47803
Phone: (812) 877-8309

1. Introduction

Huignard *et al.* presented a speckle-free imaging processor using a BSO crystal and four-wave mixing. The input beam passed through a diffuser screen which was mounted on a step by step rotation motor. Four-wave mixing generated a phase-conjugated beam which was time-integrated with a Polaroid camera [1].

Ford and coworkers investigated the effect of a photorefractive (PR) fanout on a time-varying input. When a time-varying input was imaged into the PR gain medium the time-independent portion of the input signal fanned out while the time-varying portion transmitted. Thus, the PR gain medium acted as a novelty filter, transmitting the changes in the input immediately and fanning out the portion which was stationary for a time longer than the PR gain medium response time τ [2].

In this paper a time-integrating filter using self-pumped phase conjugation (SPPC) is described. When a time-varying input is sent into the PR crystal, SPPC will occur for the constant portions of the input. The PR crystal acts as a novelty filter, causing SPPC for the stationary input and transmitting the changes in the input which are varying in time shorter than τ , the PR crystal response time.

The time variation of the speckle pattern is governed by the characteristic time constant T . The characteristic time T of a moving specklegram is defined as the time for which an average speckle grain needs to displace itself. The characteristic time T is defined by $T = s/v$ where v is the speed of the specklegram and s the grain size. Since the crystal response time is inversely proportional to the intensity [3], at a certain intensity level I_0 the crystal response time can be made equal to the characteristic time of the specklegram. If the intensity is reduced below I_0 , the response time of the PR crystal will be longer than the characteristic time T of the speckle pattern. This implies that the SPPC signal will be time-integrated while for $\tau < T$ time-integration is not achieved.

A minimum speed, v_{min} , was found to characterise the limitations of this process. Assuming that the beam waist at the input plane of the PR medium does not change with a variation in intensity, one can express a linear relationship between the v_{min} and the incident power P , given by $v_{min} = gP$, where g denotes a proportionality factor.

2. Experiment and Analysis

The specklegrams are bleached photographic recordings of speckle patterns [4]. The speckle grain size was measured with a Zeiss microscope and calculated. The measured speckle size s_m , and the calculated s_c can be found in Tab.1.

The experimental setup is shown in Fig.1. An Ar^+ laser at $\lambda = 514nm$ was used with extraordinary polarisation in the plane of a $BaTiO_3$ crystal. The laser beam was expanded 25X, spatially filtered, and collimated. The expanded beam, having a diameter of 3.0cm was sent through a photographic slide. It then passed through the specklegram which was mounted on a step motor. Finally, the light was imaged into the PR crystal. The SPPC signal was monitored in the output plane by a CCD camera, and the video output was sent via an Epix image processing board to a monitor.

For inputs of 1.3 – 4.7mW the rise time of the SPPC signal was recorded from which the response time τ was extrapolated.

The time-integration due to the crystal can be described as a smearing of the speckles in the SPPC output. While the speckles were moved by the step motor in a discrete fashion, the SPPC signal revealed a continuous movement of the speckles (smearing). Moving the specklegrams at minimum speed resulted in a temporary stop of the continuous movement of speckles in the SPPC signal. While moving the specklegrams

92-18779



| specklegrams | 1 | 2 | 3 |
|--------------------------------|---------------|--------------|--------------|
| speckle size s_c [μm] | 39 ± 9 | 77 ± 17 | 116 ± 26 |
| speckle size s_m [μm] | 48 ± 21 | 106 ± 62 | 139 ± 68 |
| $g \cdot s_e$ [μm] | 70 ± 5 | 190 ± 5 | 250 ± 40 |
| proportionality factor g | 1.7 ± 0.2 | | |
| speckle size s_e [μm] | 41 ± 5 | 113 ± 13 | 148 ± 18 |

Table 1: Speckle grain sizes for three different specklegrams, The calculated and measured speckle sizes are denoted as s_c , and s_m , respectively. g is the proportionality factor of the response time, inverse power expression, and s_e is the speckle size deduced from the slope of Fig.2

at speeds greater than this threshold speed caused smearing of the speckles in the SPPC signal and thus producing a time-integrated signal.

The specklegrams speed required to interrupt the time-integration was recorded for different power levels ($1.3mW - 3.0mW$). The data from the power versus response time measurement and the data from the power versus minimum speed measurement were combined to produce a plot of v_{min} versus the incident power P and it can be seen in Fig.2. The proportionality factor g and the speckle size s_e deduced from the slope of Fig.2 are given in Tab.1.

In order to compare the output of the time-integration self-pumped phase conjugator with the output of a digital averaging routine 12 frames were stored in the Epix board. Then, a digital averaging routine was performed on the frames. Figure 3 shows the input, the digitally averaged input, the SPPC signal, and the digitally averaged SPPC signal. It can be seen that digital averaging does not significantly remove the speckle pattern.

3. Conclusions

A time-integrating filter was presented. Speckles were removed with the time-integrating self-pumped phase conjugator. In contrast to the four-wave mixing setup used by Huignard the setup of the time-integrating self-pumped phase conjugator is simple and requires practically no alignment.

It was shown that the time-integrating SPPC was superior to a software averaging routine. More importantly, the SPPC filter performs in real-time.

An equation relating the minimum speed of the specklegrams to the input power was given and the experimental results are in good agreement with the theoretical prediction ($v_{min} \propto P$).

Further applications of this setup include a novelty filter which only transmits time-varying portions of the input signal, and returns a SPPC of the time-independent portions. This work is completed and will be published elsewhere.

4. References

- [1] J.Huignard, J.Herriau, L.Pichon, A.Marrakchi, Speckle-free imaging in four-wave mixing experiments with BSO crystals, Opt. Lett., Vol.5, No.10, pg 436-437, Oct 1980
- [2] J.Ford, Y.Fainman, S.Lee, Time-integrating interferometry using photorefractive fanout, Opt. Lett., Vol.13, No.10, pg 856-858, Oct 1980
- [3] *Photorefractive materials and their applications II*, editors: P.Günther, J.Huignard, Springer Verlag, 1989
- [4] P.Hariharan, C.Chidley, Photographic phase holograms: the influence of developer composition on scattering and diffraction efficiency, Appl. Opt., Vol.26, No.7, pg 1230-1234, April 1987

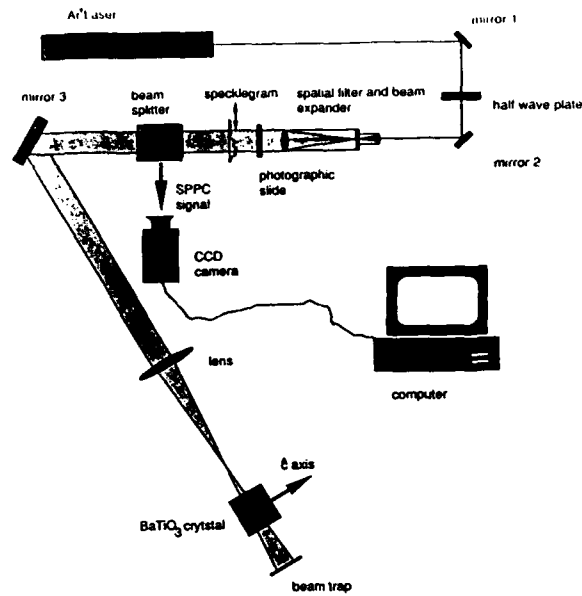


Figure 1: Experimental apparatus of the SPPC time-integrating filter

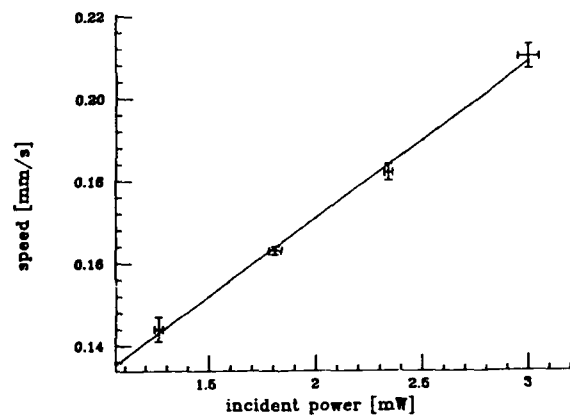


Figure 2: Minimum speed v_{min} over incident power P for distorter 2

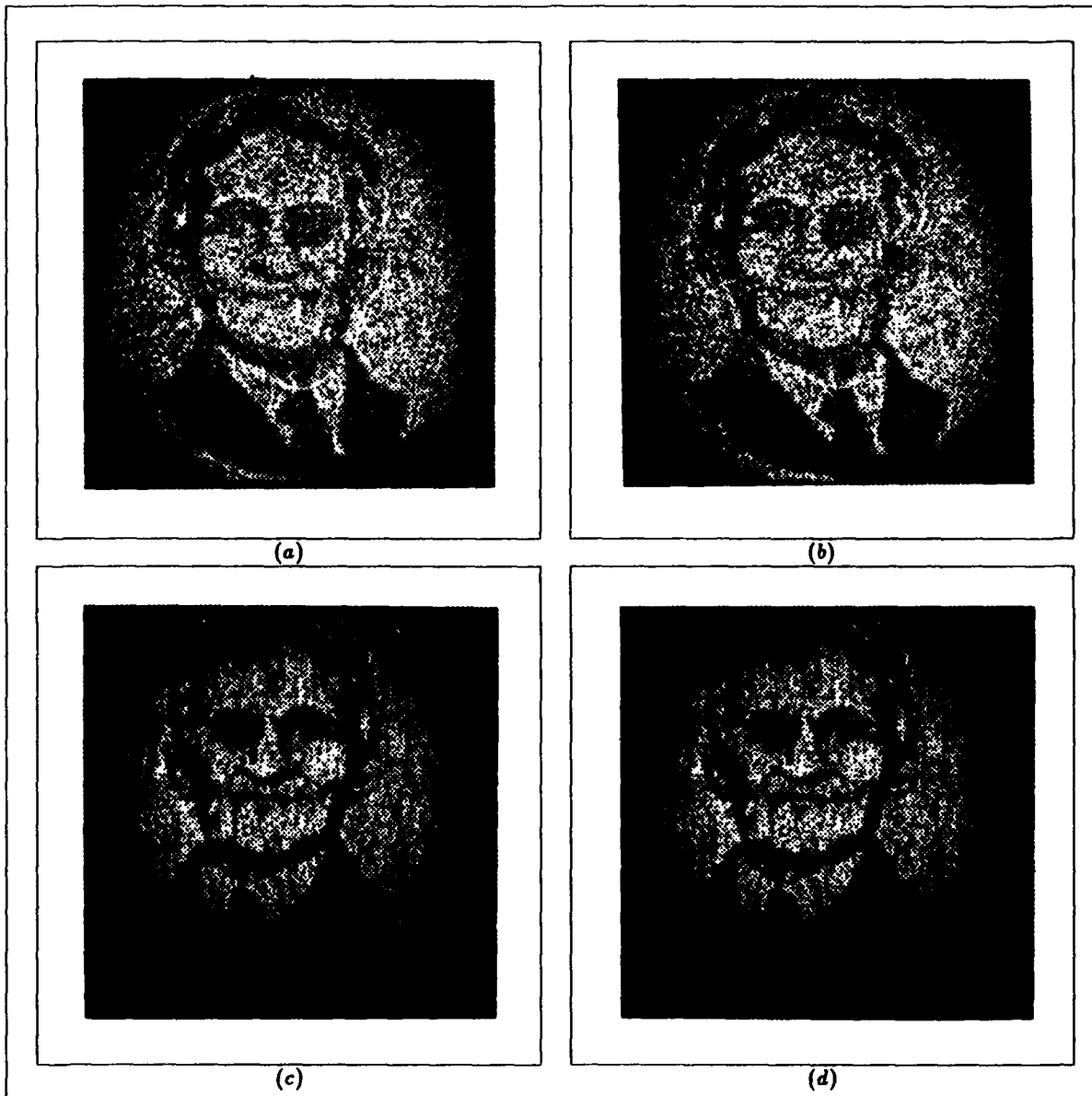


Figure 3: (a) input, (b) software averaged input, (c) SPPC signal, (d) software averaged SPPC signal



Photorefractive Deamplification for Artifact Noise Reduction

Jehad Khoury and Mark Cronin-Golomb

Electro-Optics Technology Center
Tufts University
Medford, MA 02155

92-18780

Charles L. Woods

Rome Laboratory
Solid State Sciences Directorate
Hanscom AFB, MA 01731

Mailing address: RL/ESOP/Woods
Hanscom AFB, MA 01731

Telephone: (617) 377-4922

Summary:

Many optical image processing operations such as edge enhancement may be performed by suitable linear spatial filters. A broader class of operations is made available by extending this technique to nonlinear filters. An example of this is the use of a logarithmic nonlinearity for conversion of multiplicative to additive noise [1]. In this work, we demonstrate that phase preserving thresholding in the Fourier plane which linearly transmits signals above a certain intensity, reduces additive signal dependent noise, such as noise from coherent artifacts, image defects and uniformity noise.

Coherent artifact noise, defect noise and film grain noise are often important limitations in the operation of coherent optical processing devices. It can be shown that both of these noise sources contribute a similar spectral effect in the Fourier transform plane: addition of signal dependent noise to the signal transform. This enables a nonlinear optical thresholding mechanism operating in the Fourier plane to separate the relatively intense signal peaks from the noise related smear. This noise reduction even works with input amplitudes which have a small signal relative to noise. We use the thresholding mechanism of photorefractive two-beam coupling to reduce strong artifact noise in plane wave illumination of a bar chart transparency. There is no noticeable reduction in the resolution of the signal in our measurements. Furthermore, no reference signal is used in this noise reduction technique.

This approach is an extension of previous work which also used a transmission threshold to reduce additive speckle noise [2]. The new feature of this analysis is that the arbitrary spectrum of the additive noise [2] (for example, flat for white noise) is replaced in the Fourier plane by the convolution of the artifact noise and the signal, which has an envelope similar to that of the signal spectrum. In the special case of artifact noise, it is often possible to approximate the radial distribution of the signal by a $1/f$ (or some other suitable generic shape) spectrum for use in the Fourier plane thresholding. In

the nonlinear optical process of two-beam coupling, it is possible to shape a reference or pump beam to spatially tune this optical threshold. In contrast, additive white noise (or white spectrum signal dependent noise) requires a constant fixed intensity threshold provided by a uniform reference intensity.

For an amplitude modulated plane wave signal which is accompanied by any additive signal dependent noise with a broadened power spectrum, the noisy image may be represented by

$$(1-a)s + n'(s) \quad 1)$$

where the plane wave incident on the signal modulator has lost a dc energy equivalent to the quantity a and is producing an equal or lesser energy of noise with spatial distribution $n(s)$. The Fourier transform of the amplitude modulation of the signal s will be sharply peaked and reduced by amplitude, while that of $n'(s)$ will in general be weak and dispersed. In particular, the noise for coherent artifact noise, defect noise and input uniformity (or grain) noise is linearly dependent on the signal, and may be represented by

$$i = A s + n(x) s \quad 2)$$

where A is approximately unity, and the noise term $n(x)$ is a zero mean fluctuation for coherent artifact noise. Opaque defects in the input plane, will produce an input term of,

$$(1-a) s + (a-d(x)) s \quad 3)$$

where the defect distribution $d(x)$ has a value of 1 over the area of the defects and 0 elsewhere, and the constant a is chosen to give $(a-d)$ a mean value of zero (representing a loss of energy in the plane wave in Equation 3). Uniformity or grain noise produced in the input plane may be similarly represented by Equation 2.

The Fourier transform of an input with noise which is linearly dependent on the signal is given by,

$$I = A S + N*S \quad 4)$$

where the noise dependent term (the convolution of the noise and signal spectrums) acts to statistically distribute energy around the sharp peaks of the signal transform.

This noise term cannot simply be removed by band (high or low) pass spatial filtering without significantly changing the image. However, nonlinear filtering acts as an adaptive filter to reduce noise while preserving the image.

In the Fourier plane, the noise term is generally much less intense than the respective spectrum peaks of the signal, as is clear from Equation 4. This enables the thresholding mechanism in the Fourier transform plane to reduce this noise. In two beam coupling [2] with signal deamplification [3], the reference beam intensity profile R selects the threshold level. The asymptotes of the two beam coupling filter transmittance, F , is given by

$$F = \begin{cases} 1, & \text{for } I \gg R, \\ \exp(-g), & \text{for } I \ll R \end{cases} \quad 5)$$

If the filter is to remove the noise from the signal according to Equation 5, the spatial profile of the reference beam must satisfy the inequality

$$|A|^2 \gg R/|S|^2 \gg |S \cdot N|^2 / |S|^2 \quad 6)$$

where the Fourier transform of noise is characteristically broad and weak [3]. In Equation 6, the left inequality is required to preserve the signal fidelity, and the right inequality is required to reduce the noise. Since the noise spectrum is widely spread relative to the sharp signal spectrum peaks, substantial noise reduction may be achieved with a plane wave reference. White noise reduction requires a flat reference, which may reduce high frequency resolution.

If the envelope of the noise spectrum envelope is narrower than that of the signal, the reference beam profile is chosen to be approximately proportional to the signal intensity envelope. The signal spectrum amplitude often has a $1/f$ envelope, providing a generic best-shape for the reference profile.

Results of a preliminary experiment using two-beam coupling thresholding (deamplification) for reducing coherent artifact noise are shown in Figure 1. Figure 1a) shows the noisy input image produced by scattering of the incident plane wave from dust on a slide. Figure 1b) shows the noise reduced image after nonlinear spatial filtering. This grating developed in the crystal works as an adaptive noise cancelling hologram.

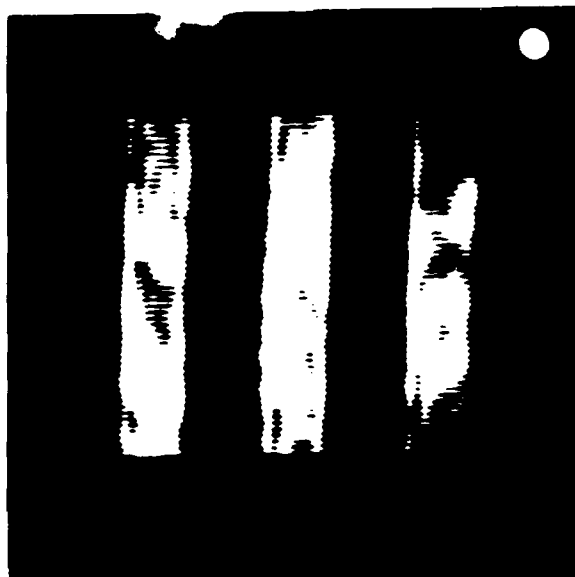
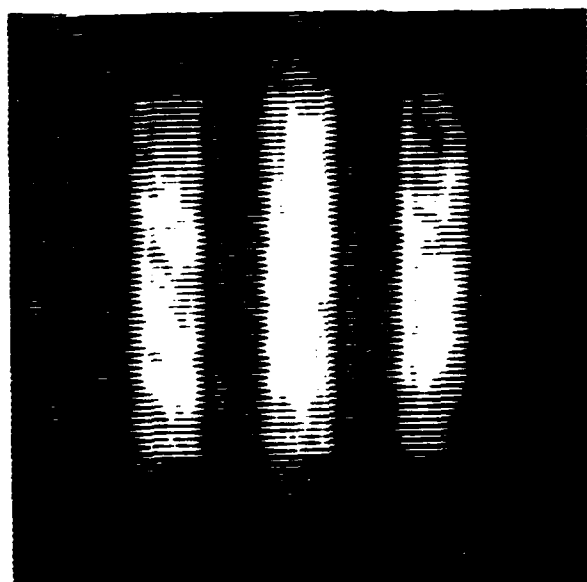
These results show that it is possible to reduce additive signal dependent noise without significantly affecting the resolution of the object by using nonlinear optical thresholding. Using linear low pass spatial filtering to remove this noise would have increased the degradation of the bar edges and corners.

REFERENCES

- 1) H.Kato and J.W.Goodman, Appl.Opt. 14,1813 (1975)
- 2) J.Khoury, C.Woods and M.Cronin-Golomb, to appear Opt.Lett.
- 3) Y.Fainman, E.Klancik and S.H.Lee, Opt.Eng. 25, 228 (1986)

FIGURE 1. Photograph illustrating signal dependent noise reduction using photorefractive two beam coupling:

- A) Three bar pattern with initial coherent artifact noise; and
- B) Noise reduced image.

A**B**



Stability of Information Readout by Self-pumped Phase Conjugation in Barium Titanate

F. C. Lin, D. Sun, G. Leu, and M. A. Fiddy

Department of Electrical Engineering, University of Lowell, Lowell, MA 01854

Tel: (508) 934-3359

Fax: 0101-508-458-8289

T. Yang and Y. Y. Teng

Department of Physics and Applied Physics, U. of Lowell, Lowell, MA 01854

SUMMARY

For real-time optical image storage and processing, we have systematically studied self-pumped phase conjugation (SPPC) [1] in barium titanate (BaTiO_3) crystals (from Sanders Associates Inc., Merrimack, NH) in terms of the incident angle θ , the impact position l on the crystal surface, the distance L between the imaging lens and the impact point on the crystal face [Figure 1], the argon-ion laser power P (p-wave with various wavelengths), and the ambient temperature T . We found that the stability of the temporal SPPC intensity $I_{\text{PC}}(t)$ strongly depends on these geometrical parameters, θ , l , and L . The objective in this paper is to identify optimal conditions in order to stabilize and maximize the temporal evolution of the SPPC reflectivity $R(t)$ which is defined as the ratio of $I_{\text{PC}}(t)$ to the intensity I_{M} retro-reflected by a mirror at the position of the crystal to the detector. We have defined the optimal (or stable) condition for the SPPC as $|R_{\text{max}} - R(t)|/R_{\text{max}} \leq 0.1$, where R_{max} is the maximum value of $R(t)$ (recorded within 10 minutes to 1 hour) and also the maximum value in terms of the above geometrical and physical parameters.

When $P = 100$ mW, $T = 10^\circ\text{C}$, and $L = 9.7$ cm (the focal length f of the imaging lens is 10 cm), the optimal orientation consistently occurred at large θ (around 70°) and $l \approx 2$ mm on the 4.8 mm side for crystal sample #1359-D ($4 \times 4.5 \times 4.8$ mm³), at medium θ (about 55°) and $l \approx 2.4$ mm on the 4.2 mm side (parallel to the c-axis) for sample #88-A ($4.2 \times 4.2 \times 5$ mm³), and at small θ ($\sim 25^\circ$) and $l \approx 3$ mm on the 4 mm side for sample #159-C ($4 \times 4.8 \times 5$ mm³). The tolerance range for θ is within $\pm 10^\circ$ from the above optimal value for all crystals but the available range for l is very restrictive (less than ± 0.5 mm from the above optimal value). These rather specific combinations of θ and l reflect two effects: (1) different geometrical constraints imposed on BaTiO_3 crystals with different dimensions and (2) the distinct optical property of individual

92-18781



crystal due to the concentration variation of defect and impurity centers. When L was varying from 8.2 cm to 11.2 cm with increment 0.5 cm ($P = 100$ mW, $T = 10$ °C, $\theta = 70^\circ$, $l = 2$ mm, $f = 10$ cm, and sample #1359-D), the stable pattern of $I_{PC}(t)$ is confined within a narrow range $L = 9.7 \pm 0.5$ cm. When the focal length f is changed to 17 cm and the rest of the parameters remain the same, $I_{PC}(t)$ is stable over a wider L range. Since the depth of focus is longer for larger f , a larger interaction volume in the crystal is induced for generating stable SPPC. Meanwhile, the response time of the SPPC grating formation and the quality of the SPPC image are also improved for larger f [2].

The multiple-image storage and readout using the SPPC in BaTiO₃ have been achieved by illuminating the image-bearing beam at various crystal heights on the incident face. It is very difficult to store and recall images at the same height either by changing the incident intensity or the incident angle. Previously stored images can be erased by the beam fanning pattern which is induced by another input image for storage at the same height. Furthermore, if images are to be recalled from different incident angles, the image recall is always hindered by the violation of the Bragg condition. The angular selectivity in this case is not as simple as that described in the coupled wave theory [3]. When the spatial frequency content of the image-bearing incident beam has high complexity, the pattern of volume reflection gratings is also very complicated such that the diffraction efficiency drops very rapidly to zero once the incident angle for the image readout deviates slightly from the exact Bragg angle [4].

A good isolator (combination of two polarizers and a quarter-wave plate with an isolation ratio of 10^4) was used to minimize optical feedback into the laser cavity. With laser power fluctuation less than 0.2%, we found that R_{max} (recorded at every 10 minutes) is slightly dependent on P [Figure 2]. In all temporal measurements of $I_{PC}(t)$ for the sample #1359-D, the parameters P , θ , L , l , and f were fixed at 25 mW, 70° , 16.6 cm, 2.5 mm, and 17 cm, respectively. Each measurement of $I_{PC}(t)$ was taken at 5-second interval in order to ensure sufficient sampling of the fluctuation pattern. In Figure 3, it is shown that $I_{PC}(t)$ is more unstable after the crystal was exposed, intentionally, to the minimum laser illumination for almost 6 hours at the same ambient temperature $T = 10$ °C. This indicates that the local heating effect on $I_{PC}(t)$ is equivalent to the thermal effect caused by the ambient temperature variation as shown in Figure 4.

We believe that the SPPC instability is caused by the thermal ionization of secondary photorefractive centers such as shallow traps [5] rather than by optical feedback and any frequency shift in the phase-conjugate beam. Notice that the

measurements described above were achieved without the control on the crystal temperature. We have used a thermocouple controller and a thermocouple to control the crystal temperature in order to improve the response time of the grating formation [6], to demonstrate the thermal effect on the SPPC instability and, more importantly, to explore the optimal temperature range in order to stabilize the information readout.

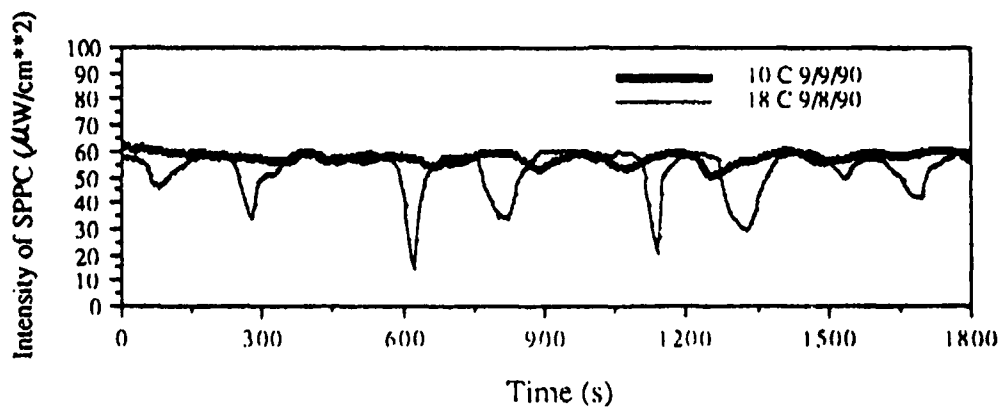
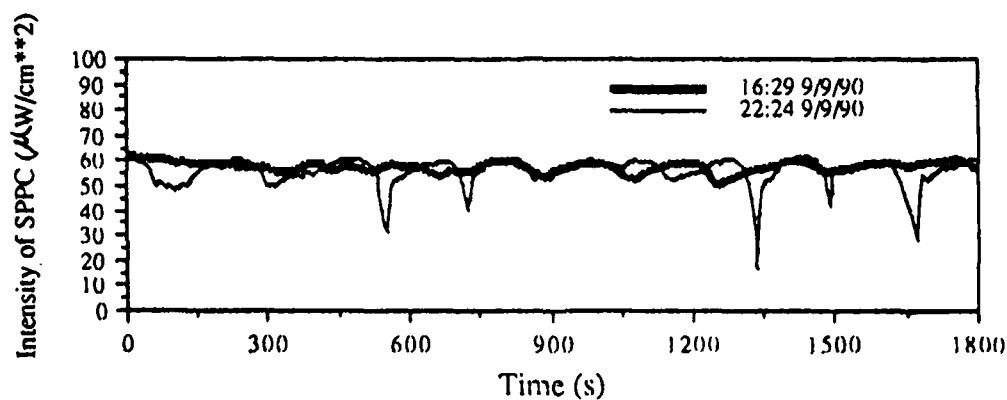
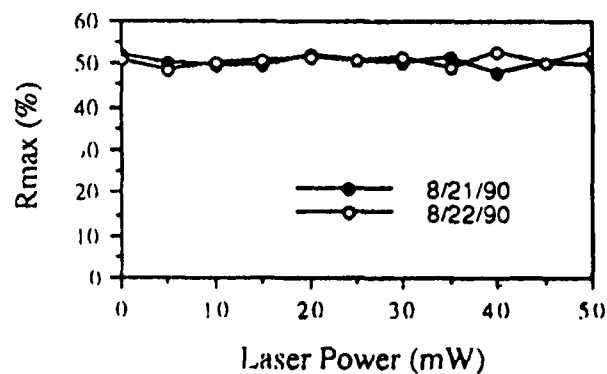
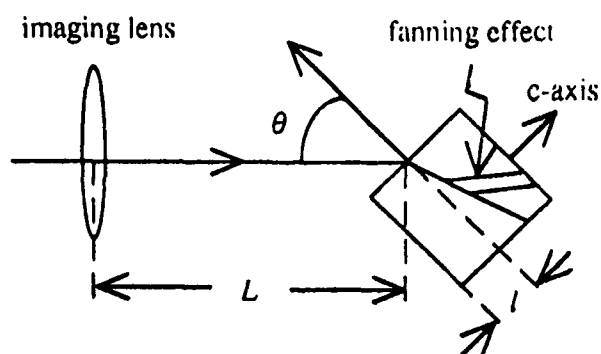
REFERENCES

- [1] J. Feinberg, *Opt. Lett.*, 7, 486, 1982.
- [2] K. H. Fielding, S. K. Rogers, M. Kabrisky, and J. P. Mills, *Opt. Eng.*, 28, 849, 1989; G. J. Dunning, D. M. Pepper, and M. B. Klein, *Opt. Lett.*, 15, 99, 1990.
- [3] H. Kogelnik, *Bell System Tech. J.*, 48, 2909 (1969).
- [4] A. M. Glass, *Opt. Eng.*, 17, 470 (1978).
- [5] G. A. Brost, R. A. Motes, and J. R. Rotge, *J. Opt. Soc. Am.*, B5, 1879, 1988; D. Mahgerefteh and J. Feinberg, *Phys. Rev. Lett.*, 64, 2195, 1990; G. A. Brost and R. A. Motes, *Opt. Lett.*, 15, 1194, 1990; P. Tayebati and D. Mahgerefteh, to appear in *JOSA-B*.
- [6] D. Rytz, M. B. Klein, R. A. Mullen, R. N. Schwartz, G. C. Valley, and B. A. Wechsler, *Appl. Phys. Lett.*, 52, 1759, 1988.

FIGURE CAPTIONS

- Figure 1. (top left) delineates the orientation of the barium titanate in the experimental setup and the fanning effect which generates the SPPC in the crystal.
- Figure 2. (top right) presents the SPPC reflectivities at two different days for a collimated laser beam with no information coded (raw beam) as a function of the laser power. All of measurements were taken after the crystal (sample #1359-D) was warmed up for around 1/2 hour.
- Figure 3. (middle) shows temporal evolutions of the measured SPPC intensities taken at two different starting time with other parameters fixed at ($P = 25\text{mW}$, $T \approx 10^\circ\text{C}$, $L = 16.6\text{cm}$, $\theta = 70^\circ$, $l = 2.5\text{mm}$, $f = 17\text{cm}$, and sample #1359-D); the first one started at 16:29 (thick curve) and the second one at 22:24 (thin curve) after the crystal was intentionally illuminated by the incident beam coded with the image of the US Air Force resolution chart at minimum laser power for almost 6 hours.
- Figure 4. (bottom) shows temporal evolutions of measured SPPC intensities taken at two different days with ambient temperatures 10°C (thick curve) and 18°C (thin curve) with other parameters fixed at

($P = 25\text{mW}$, $L = 16.6\text{cm}$, $\theta = 70^\circ$, $l = 2.5\text{mm}$, $f = 17\text{cm}$, and sample #1359-D) for the incident beam coded with the image of the US Air Force resolution chart.





Effects of Grating Erasure on Beam Fanning and Self-Pumped Phase Conjugation

Gary L. Wood, William W. Clark, III, and Edward J. Sharp

CECOM Center for Night Vision and Electro-Optics
Fort Belvoir, Virginia 22060-5677
(703) 664-1432

Gregory J. Salamo

92-18782



Department of Physics
University of Arkansas
 Fayetteville, Arkansas 72701

The photorefractive phenomena of beam fanning and phase conjugation have been used to demonstrate such operations as optical limiting, interconnecting, tracking, and a wide variety of applications utilizing phase conjugate mirrors. Many other applications can be realized when two laser beams interact in a photorefractive crystal since one of the beams can be used to control the other. For example, it is possible to amplify, deplete, direct, switch, or modulate one of the beams with the other. The photorefractive effect provides the underlying mechanism for these demonstrations of all-optical light by light control. These applications depend upon the formation of particular photorefractive gratings and the perturbation of those gratings. Only recently has attention been given to the importance of the physical location of the gratings within the crystal.^{1,2,3}

Depending upon the application it may be desirable to have very little or no erasure take place (reading out holographic memories, for example). Partial erasure of well organized photorefractive gratings has formed the basis of several important applications in the past, most notably that of spatial light modulation or incoherent to coherent conversion.^{4,5} Finally, complete grating erasure may be the desired goal. Complete grating erasure by light is routinely used to refresh crystals between experiments. All traces of any previous gratings are removed leaving the crystal with a spatially uniform distribution of photoexcitable charge carriers.

In this work the effects of erase beams (including grating disturbances) on the photorefractive behavior of cerium doped strontium barium niobate (SBN:60) are determined. The beam fanning response time, throughput intensity, self-pumped phase conjugate start-up time, and phase-conjugate reflectivity are determined for different erasure conditions.

The experimental situation used to establish the gratings of interest consisted of a single crystal of SBN which was illuminated with an extraordinary polarized argon-ion laser (writing beam) to establish either beam fanning (stimulated,

forward photorefractive scattering) gratings or the gratings necessary to produce self-pumped phase conjugation in the "cat" mirror⁶ geometry. The write beam at 488 nm had a spot diameter at the crystal of 0.8 mm ($\text{HW1/e}^2\text{M}$) and intensity $I_{wb} = 0.038 \text{ W/cm}^2$. The crystal was maintained at near normal incidence for all the measurements.

The time response and throughput intensity for beam fanning was monitored for the following erasure conditions: (1) laser light (polarized ordinary) at an intensity of 0.048 W/cm^2 with a spot size equal to that of the writing beam which propagates over the same beam path as the writing beam; (2) flooding the crystal with white light (incoherent) at an intensity of 0.038 W/cm^2 perpendicular to the plane of incidence of the write beam (i. e. from the top); and (3) selectively probing the crystal from the top with an ordinary polarized laser beam at 0.15 W/cm^2 .

The time response for beam fanning has been shown experimentally to exhibit an intensity dependence given by, $t_r = AI^{-x}$, where $x \sim 1$, from cw to nanosecond excitation.^{7,8} Here, A is a material dependent constant with units of J/cm^2 . The dramatic and surprising effect on the beam fan response time as a result of incomplete erasure using erasure conditions (1) and (2) is shown in Fig. 1. For example, when 85% of the gratings are erased with the incoherent source the time response is ~ 7.9 seconds. For 85% erasure with the coherent source the time response is ~ 22 seconds. However, when the gratings were 70% erased by either beam the time responses are nearly equal.

Figure 2 shows the results obtained when erasure condition (3) was used to examine the steady-state beam fan. The extraordinary polarized writing beam was introduced into a grating free crystal at time $t = 0$ and allowed to come to steady state. The signal gain was increased by 10 and a shutter was opened to introduce the erase beam from the top of the crystal at several spots indicated (a, b, c, and d) in the insert of Fig. 2. For the locations indicated by, d, there was no observed change in the steady state transmission. For locations, a, and b, there was an initial increase in the transmission which subsequently returned to steady state. The shutter was then closed producing another, but smaller, increase in the transmission which again returned to the steady state after a short period of time. Illumination at location c produced a slight increase in the transmission which did not return to steady state until the shutter was closed.

The self-pumped phase conjugate start-up time and reflectivity were also determined for erasure condition (2). These results are shown in Fig. 3 as a function of erasure time. For erasure times longer than 30 seconds the conjugate signal requires time to start-up (i. e. the time from when the shutter is opened until a signal is first observed). For erasure times shorter than 30 seconds a

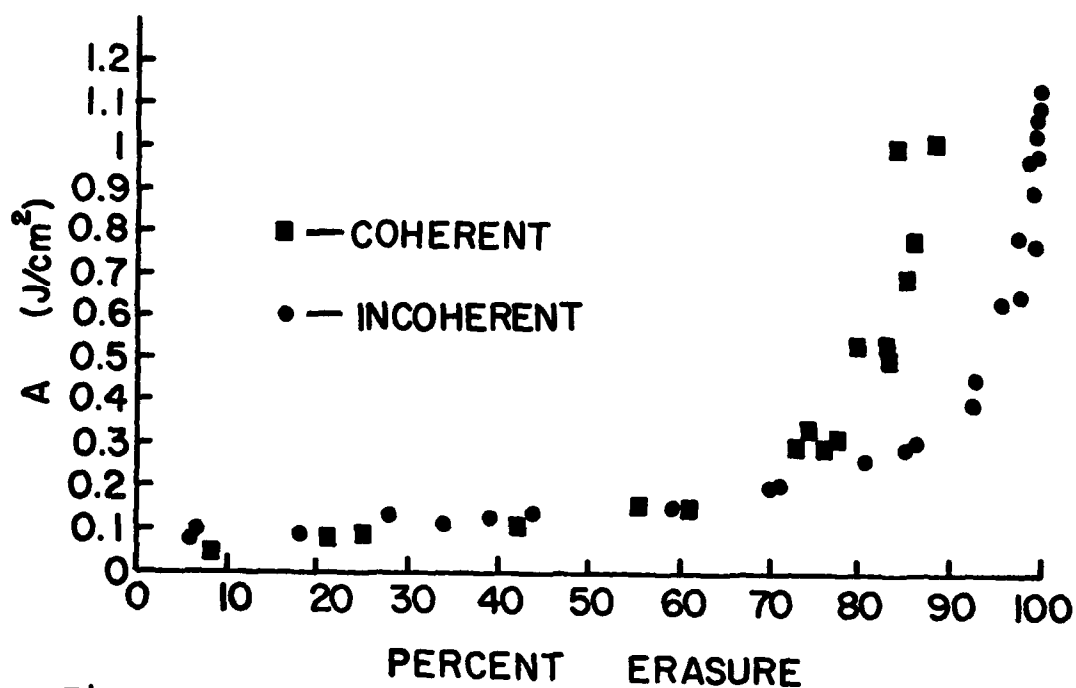


Fig. 1. Beam fanning time response versus percent of erasure for incoherent and coherent erasure.

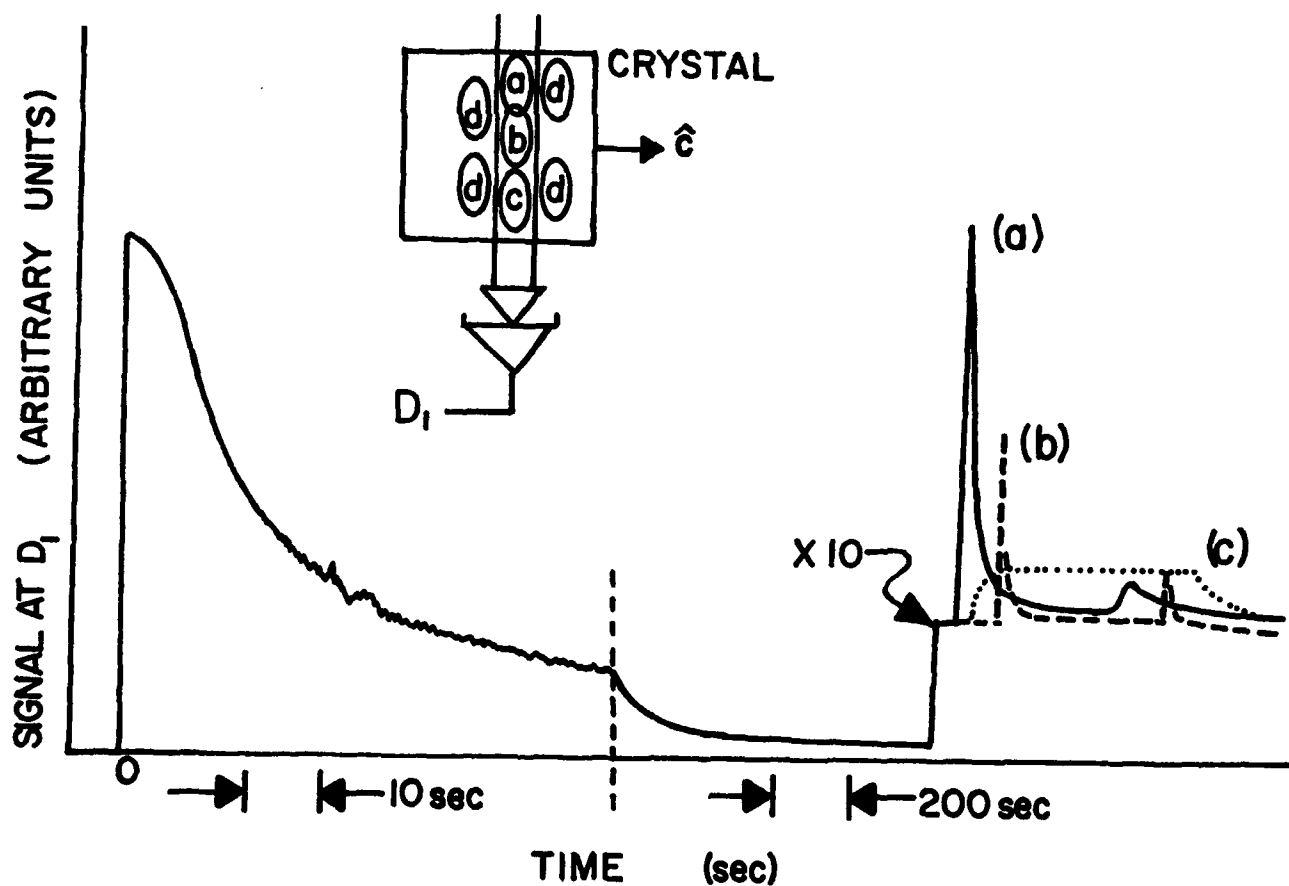


Fig. 2. Effect of preferential erasure on the transmitted intensity in a crystal of SBN while in the process of beam fanning.

conjugate signal was observed instantaneously when the shutter was opened. This value, which is some percentage of the steady state value, is plotted on the left ordinate axis in Fig. 3. The squares, dots, and triangles are for the same writing intensity of 0.038 W/cm^2 using different input locations on the crystal and the x's are for a writing intensity of 0.38 W/cm^2 .

The significance of these and other results will be discussed in detail.

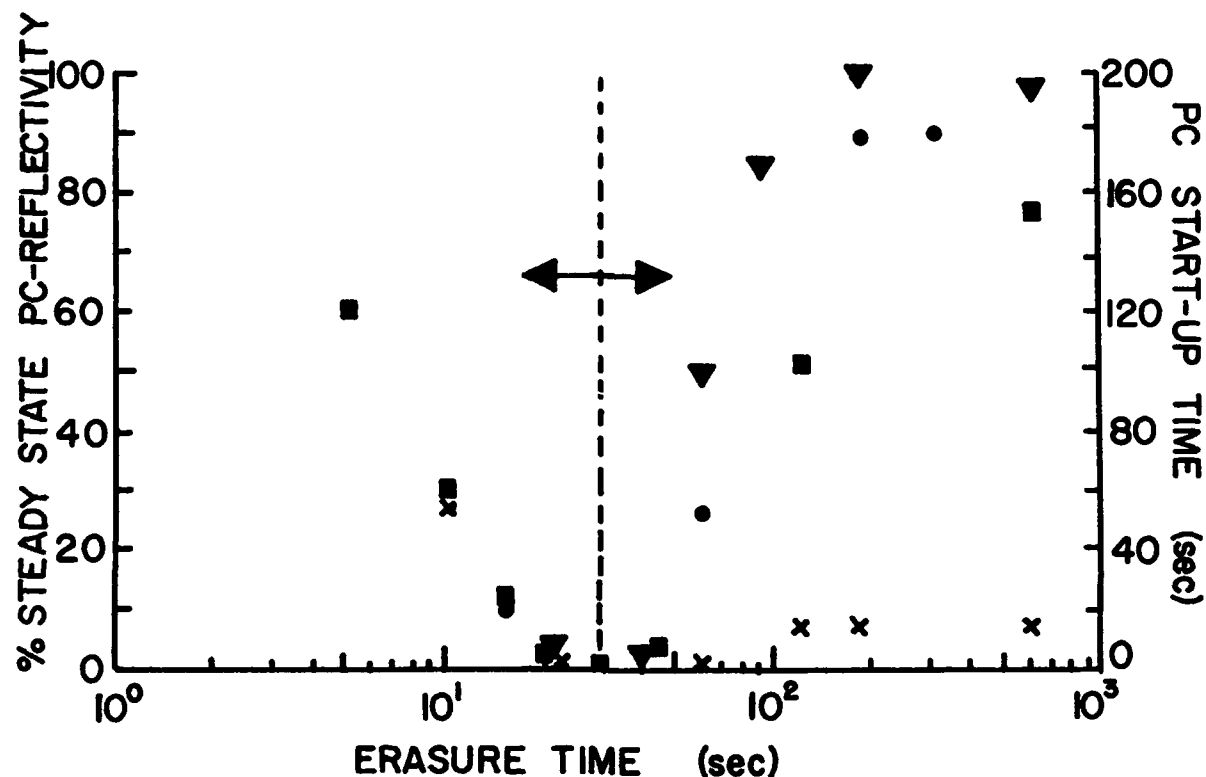


Fig. 3. The self-pumped phase conjugate start-up time and the percent of steady-state conjugate reflectivity as a function of erasure time.

-
1. P. S. Brody, Appl. Phys. Lett., 53:262 (1988).
 2. D. Pepper, Phys. Rev. Lett., 62:2945 (1989).
 3. G. J. Dunning, D. M. Pepper, and M. B. Klein, Opt. Lett., 15:99 (1990).
 4. A. A. Kamshilin and M. Petrov, Sov. Tech. Phys. Lett., 6:144 (1980).
 5. Y. Shi, D. Psaltis, A. Marrakchi, and A. R. Tanguay, Jr., Appl. Opt., 22:3665 (1983).
 6. J. Feinberg, Opt. Lett., 7:486 (1982).
 7. M. J. Miller, E. J. Sharp, G. L. Wood, W. W. Clark, III, G. J. Salamo, and R. R. Neurgaonkar, Opt. Lett., 12:341 (1987).
 8. B. Monson, G. J. Salamo, A. G. Mott, M. J. Miller, E. J. Sharp, W. W. Clark, III, G. L. Wood, and R. R. Neurgaonkar, Opt. Lett., 15:12 (1990).



Intensity Dependent Thresholding and Switching in the Photorefractive
"Bridge" Mutually Pumped Phase Conjugator

Stephen W. James and Robert W. Eason

Department of Physics, University of Southampton, Southampton SO9 5NH, U.K. (tel.0703 592098)

The large electro-optic coefficient of photorefractive materials such as BaTiO_3 has allowed the observation of exotic phase conjugators such as the Self-Pumped Phase Conjugator (SPPC)¹ and, more recently, the Mutually Pumped Phase Conjugator (MPPC), in which two simultaneous phase conjugate (PC) outputs are produced by the interaction of two mutually incoherent beams within a photorefractive crystal. Several generic MPPC configurations have been reported, differing more in their exact beam geometry rather than the physical mechanism responsible for the effect. These geometries include the Double Phase Conjugate Mirror (DPCM)², the Mutually incoherent beam coupler (MIBC)³, the Bird-Wing Phase Conjugator (BWPC)⁴, the Frogs Legs Conjugator⁵ and the Bridge Conjugator^{6,7}. Both the DPCM and MIBC have been shown to possess input beam intensity ratio dependent reflectivities and thresholds^{8,9}, and these properties have been utilised in the DPCM for image processing applications⁸.

Here we report the observation of total input intensity, rather than intensity ratio, dependent reflectivity from the Bridge MPPC, which has allowed the investigation of effects such as optical thresholding, bistable and hysteretic switching, and optical flip-flop type behaviour.

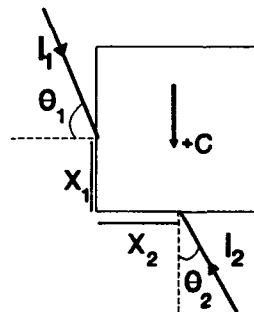


Figure 1: Schematic diagram of the Bridge MPPC

A schematic diagram of the Bridge MPPC is shown in figure 1. The two input beams were derived from the output of an Ar^+ ion laser, operating multi-longitudinal mode at 514.5 nm, and were directed toward the 6mm x 6mm x 6mm crystal of BaTiO_3 , their path length difference arranged to ensure their mutual incoherence. The input beam intensity ratio was kept constant, while the total input power could be varied via a variable neutral density filter. The precise form of the total intensity dependence of the PC reflectivity could be modified by alteration of the input beam geometry.

An example of the thresholding behaviour of the PC output is shown in figure 2, which shows the PC reflectivities obtained for both beams as a function of the total input power. The reflectivities are constant at higher powers, falling off at 30 mW, showing a threshold at 12 mW below which no PC output was observed.

92-18783



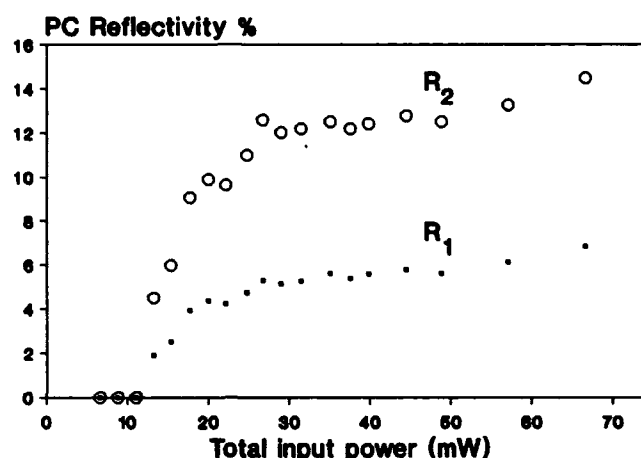


Figure 2: PC reflectivity, R , as a function of total input power, obtained from the Bridge MPPC with input beam intensity ratio $=0.93$, $\theta_1=70^\circ$, $\theta_2=10^\circ$, $x_1=4\text{mm}$, $x_2=2\text{mm}$.

Optical thresholding of this sort could be useful in schemes involving, for example, correlation effects and associative memories. Variation of the input geometry allowed the threshold to be altered. No hysteresis was observed between upward and downward cycling of the input power.

Further changes to the input geometry allowed a different type of thresholding to be observed, in which the Bridge conjugator gave way to an SPPC output from beam 1. This allowed the investigation of optical bistable/hysteretic switching, as is shown in figure 3. On the downward cycle a threshold of 18 mW was reached below which the Bridge conjugator was destroyed by the onset of SPPC from beam 1. On the upward cycle SPPC persisted until the power reached 42 mW before the original bridge configuration was restored, the reflectivity being the same as that obtained on the downward cycle. Thus we have a device which allows the switching of the PC output of beam 2 in a bistable/hysteretic fashion, and, perhaps more interestingly, a method for changing the source of the light for the PC of beam 1, from beam 2 in the bridge configuration, to beam 1 itself in the SPPC geometry, which due to the difference in the pump beam path lengths for these two options, provides a "coherence switch" for subsequent wave mixing processes involving the PC output of beam 1.

It is likely that these effects are a result of competition between the Bridge conjugator and SPPC, arising from the difference in the intensity dependent response times of these two processes.

Figure 4 shows the response times (10%-90%) obtained for i) beam fanning, ii) SPPC (both for an input angle of 60°) and iii) Bridge MPPC ($\theta_1=60^\circ$, $\theta_2=40^\circ$, $x_1=3\text{mm}$, $x_2=2\text{mm}$). The Fanning and Bridge graphs have a similar form, with $\tau_{\text{Fanning}} \propto I^{-0.75}$, $\tau_{\text{Bridge}} \propto I^{-0.79}$, while $\tau_{\text{SPPC}} \propto I^{-0.38}$.

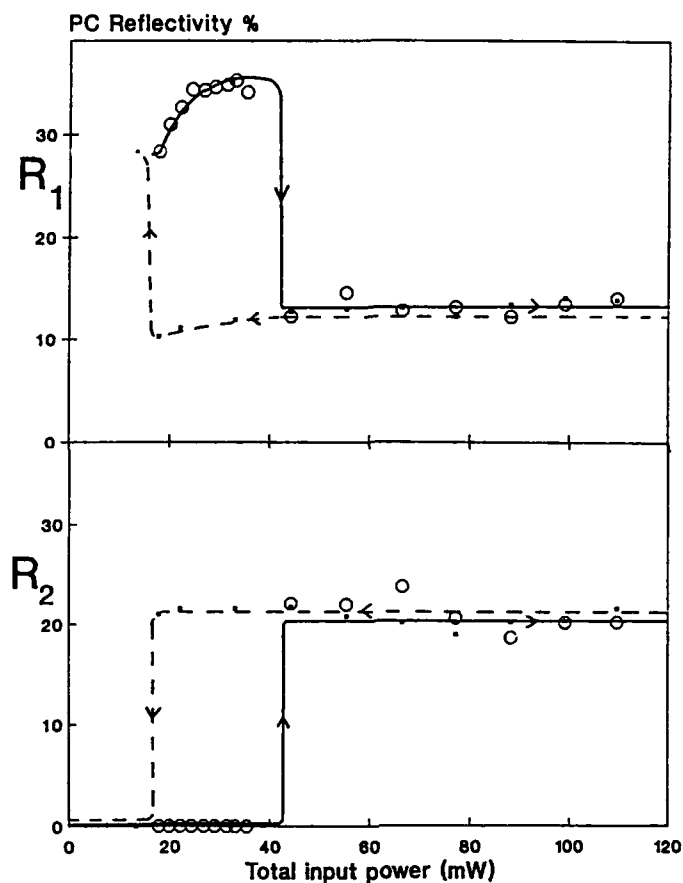


Figure 3: PC reflectivity, R , obtained from the Bridge MPPC as a function of the total input power, with $\theta_1=60^\circ$, $\theta_2=20^\circ$, $x_1=4\text{mm}$, $x_2=4\text{mm}$. x, downward cycle, O, upward cycle.

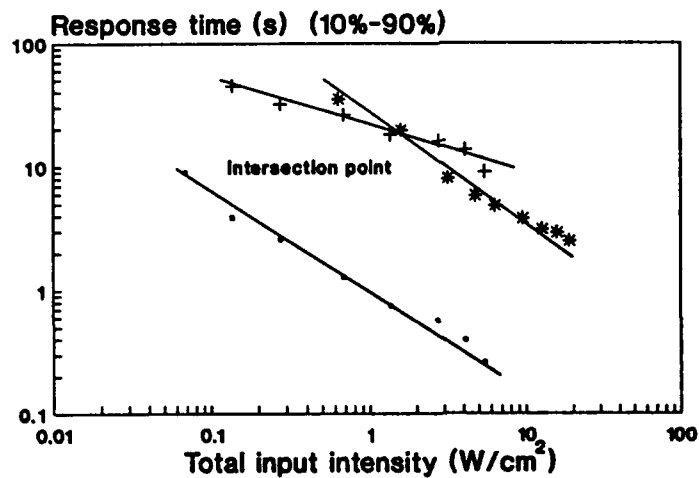


Figure 4: Response times (10%-90%) of beam fanning (\bullet), SPPC, (+), and the Bridge MPPC, (*), as a function of the total input intensity.

The significant feature of the curves for the Bridge and the SPPC is that they show an intersection point. On the high intensity side of this point the bridge will form fastest and might be expected to dominate, possibly preventing the Bridge conjugator from forming, while on the low intensity side SPPC grows first, similarly preventing SPPC from forming. In the vicinity of the intersection point one might expect competition between the processes, leading to experimentally observed fluctuations in the PC output.

In summary therefore we have observed total input intensity dependent thresholding and switching within a photorefractive Mutually Pumped Phase Conjugator. A qualitative argument based upon competition between SPPC and Bridge Conjugator, resulting from the difference in the exponents in the intensity dependent response times of the two processes, namely $\tau_{\text{Bridge}} \propto I^{-0.79}$, and $\tau_{\text{SPPC}} \propto I^{-0.38}$, has been presented to account for these effects.

Acknowledgements

The authors are grateful to the Science and Engineering Research Council for research funding under the U.K. Phase Conjugation Consortium grant no. GR/F 84256.

References

1. J. Feinberg, Opt.Lett. 7, 486 (1982).
2. S. Sternklar, S. Weiss, M. Segev and B. Fischer, Opt.Lett. 11, 528 (1986).
3. R.W. Eason and A.M.C. Smout, Opt.Lett. 11, 51 (1987).
4. M.D. Ewbank, Opt.Lett. 13, 47 (1988).
5. M.D. Ewbank, R.A. Vazquez, R.R. Neurgaonkar and J. Feinberg, J.O.S.A. B 7, 2306 (1990).
6. D. Wang, Z. Zhang, Y. Zhu, S. Zhang and P. Ye, Opt.Comm. 73, 495 (1989).
7. E.J. Sharp, W.W. Clarke III, M.J. Miller, G.L. Wood, B. Monson, G.J. Salamo and R.R. Neurgaonkar, Appl.Opt. 26,743 (1990).
8. S. Sternklar, S. Weiss and B. Fischer, Opt.Eng. 26, 423 (1987).
9. A.M.C. Smout and R.W. Eason, Opt.Lett. 12 498 (1987).



**Extraordinary polarised light does not always yield the highest reflectivity from
Self-Pumped BaTiO₃**

Stephen W. James and Robert W. Eason

Department of Physics, University of Southampton, Southampton SO9 5NH, U.K. (tel. 0703 592098)

The 'Cat-Mirror' Self Pumped Phase Conjugator, SPPC, has continued to stimulate research since its discovery in 1982¹. Surgical erasure of photorefractive gratings has been used in attempts to locate principle interaction regions in the conjugator^{2,3}, and also to control the magnitude and temporal behaviour of the phase conjugate output⁴.

The SPPC has been shown to possess a well defined value of gain-interaction length product¹. In order to obtain sufficient gain in BaTiO₃ it is necessary to access the r_{42} electro-optic coefficient by using an extraordinary (\hat{e}) polarised input beam. As the plane of polarization of the input beam is rotated only the \hat{e} component will contribute to the PC output, since the ordinary \hat{o} component does not see sufficient gain, and is not phase matched to the gratings written by the \hat{e} component. Thus the \hat{e} component, I_e , and hence the PC output, would be expected to follow:

$$I_e(\theta) = I_{inc} \cos^2(\theta) \quad (1)$$

$$I^*(\theta) = R_{PC} I_{inc} \cos^2(\theta) \quad (2)$$

where I_{inc} is the input power, $I^*(\theta)$ is the PC output power, R_{PC} is the PC reflectivity and θ is the angle of the plane of polarisation with respect to the extraordinary polarisation direction. Equation (2) would be expected to represent the upper limit on the PC output, since the co-propagating (and virtually co-linear) \hat{o} component would be expected to erase the SPPC gratings, thereby reducing the PC output.

Here, however, we will show that for *certain* input geometries it is possible to increase the PC reflectivity (by up to a factor of 2) through the inclusion of an \hat{o} component, and that by controlling the \hat{o} component it is possible to achieve optical gain in the PC output.

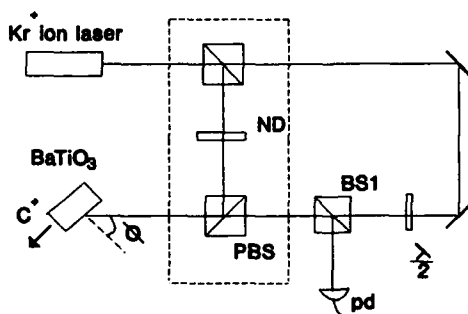


Figure 1: Schematic diagram of the experimental arrangements. Additional components required for the second experiment are shown in the dashed box.

The experimental arrangements are shown in figure 1. The output from a Kr⁺ ion laser operating at 647 nm was directed toward the 6mm x 6mm x 6mm crystal of BaTiO₃. The plane of polarization could be rotated via



the half-waveplate with the total input power kept constant, or, as in the second experiment (additional components shown in the dashed box) the \hat{e} input power kept constant, and the \hat{o} component, arranged to be co-propagating with the \hat{e} component off the polarizing beam splitter (PBS), could be controlled via the variable neutral density filter (VND).

Figure 2 shows the PC reflectivity (defined here as $\Gamma/(I_e + I_o)$, where Γ is the PC output, and I_e and I_o are the intensities of the \hat{e} and \hat{o} components of the input beam) obtained at an angle of incidence, ϕ , of 58° , as the plane of polarization, θ , was rotated.

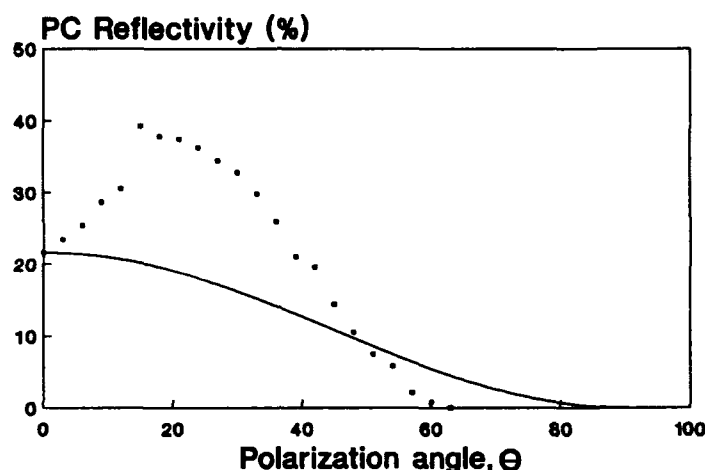


Figure 2: Normalised reflectivity as a function of Polarisation angle, θ , for an angle of incidence, ϕ , = 58° . The expected $\cos^2(\theta)$ dependence is shown by the solid line.

Here we see that, as θ is increased, the output exceeds the expected $\cos^2(\theta)$ dependence at all angles out to $\theta = 45^\circ$, and that the inclusion of an \hat{o} polarized component in the input beam produces a 75% enhancement in the PC reflectivity at $\theta = 15^\circ$.

The key to understanding this behaviour lies in the time dynamics of the SPPC process for these geometries, which, for the previous data set, is shown in figure 3. Here we see that when the input beam is totally \hat{e} polarised ($\theta = 0$) there is an initial exponential increase in the PC output, followed by a decay to a steady state value. As the \hat{o} component is increased, by rotating the input plane of polarisation, the amplitude of the subsequent decay is reduced before being eliminated completely.

This has led to the conclusion that the onset of SPPC is accompanied by a secondary, parasitic, process of longer time constant, which extracts power from the SPPC geometry. The \hat{o} component erases the parasitic gratings, reducing their deleterious effect, in a similar way to that noted in ref. 4

In the previous experiment the useful \hat{e} component of the input was decreased for increasing θ . We have therefore recorded data sets where the power of the \hat{e} component was kept constant at 10 mW, and the \hat{o} component, introduced off the PBS shown in figure 1 was controlled via a variable neutral density filter.

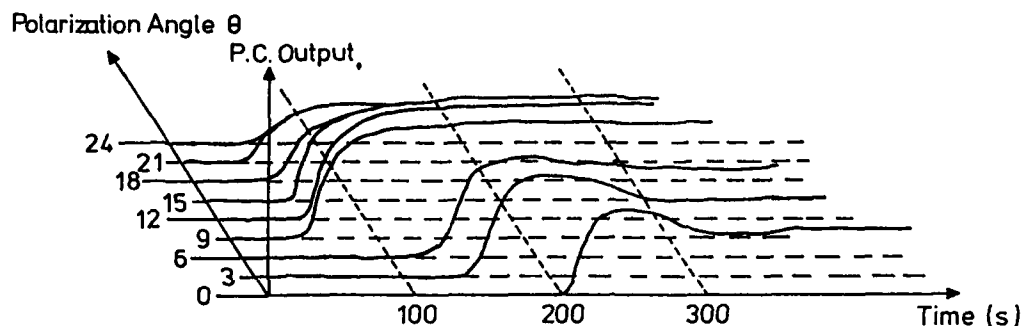


Figure 3: Time dependence of the PC output for the data set of figure 2

Figure 4 shows the PC output obtained as a function of the ratio I_0/I_e . The region A, shown in the insert, replotted as the PC output Vs the δ polarised input power, I_0 , is the area of interest here, since it shows a gradient of 2.8, and hence it is possible to control the PC output with net optical gain. It is believed that by optimisation of the input parameters it should be possible to increase the value of gain seen here.

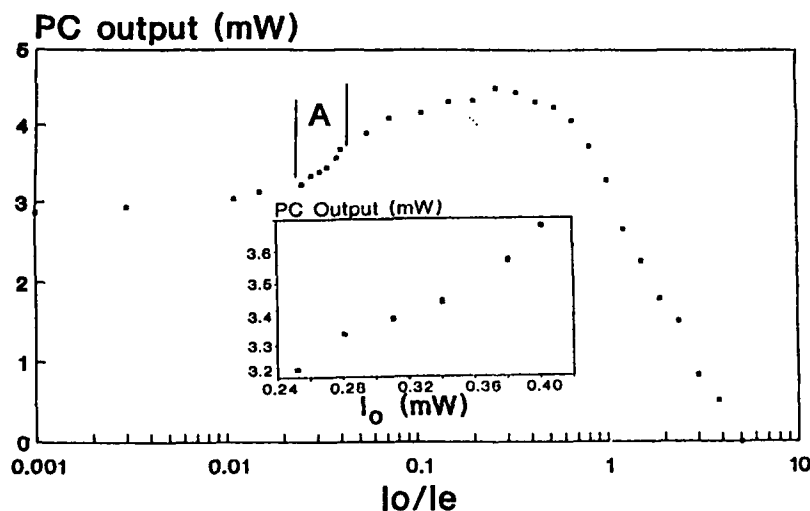


Figure 4: PC output as a function of ratio I_0/I_e . The insert shows region A re-plotted as the PC output Vs I_0 .

A typical trace of the temporal behaviour of the PC output during a switching run is seen in figure 5. The PC output was allowed to reach its steady state value of 2.95 mW. At $t=220$ s a 2.6 mW co-propagating δ polarised beam was introduced and the PC output immediately began to grow, reaching its enhanced value of 4.37 mW after 30 s.

P.C. Output (mW)

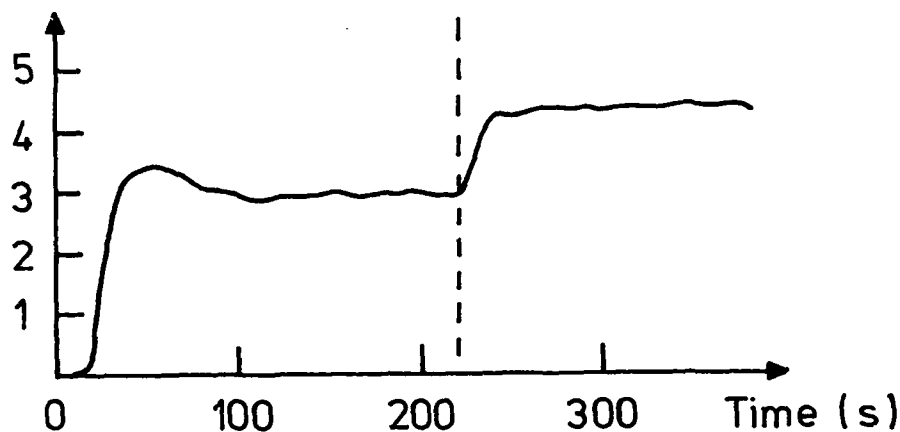


Figure 5: Time dynamics of switching process.

In summary therefore, we have observed that, for certain input geometries, δ polarization is not necessarily the optimum polarization for SPPC in BaTiO₃. Inclusion of an δ polarized component can as much as double the PC reflectivity. Observation of the time dynamics of the process for these geometries has led to the conclusion the erasure of parasitic gratings by the δ component is responsible for the effect. We have also shown that it is possible to switch the power in the PC output with net optical gain.

Acknowledgements

The authors are grateful to the Science and Engineering Research Council for research funding under the U.K. Phase Conjugation Consortium grant no. GR/F 84256.

References

1. J. Feinberg, Opt.Lett. 7, 486 (1982).
2. P.S. Brody, Appl.Phys.Lett. 53, 262 (1988).
3. D.M. Pepper, Phys.Rev.Lett. 62, 2945 (1989).
4. G.J. Dunning, D.M. Pepper and M.B. Klein, Opt.Lett. 15, 99 (1990).



Self-Pumped Phase Conjugation in BaTiO₃:Ce

Chitra Guruswamy and Doyle A. Temple

Department of Physics and Astronomy

Louisiana State University

Baton Rouge, Louisiana 70803-4001

Introduction

Barium titanate is important as a nonlinear optical material primarily because of its large photorefractive gain. This gain is large enough to give rise to self-pumped phase conjugation at low optical power.¹ Several studies have been conducted on enhancing the gain of the crystal through controlled doping²⁻⁵ and annealing.^{3,6,7} These dopants have, till now, been confined to transition metals such as iron,^{2,3} chromium,⁴ iron + nickel,⁵ and cobalt.⁵ In this talk, we report preliminary results of the self-pumped phase conjugate reflectivity in cerium doped barium titanate.

Experiment

The optical setup used for the reflectivity measurements is shown in Fig.1. The laser source was a multi-longitudinal mode, single transverse mode argon ion laser polarized in the plane of the figure (extraordinary) and operating at 514.5 nm. The self-pumped phase conjugate reflectivity was measured by placing a beam splitter in the path of the incident beam and monitoring the phase conjugate beam with a silicon photodetector. The crystal was mounted on a precision rotator and aligned such that the surface normal and the incident beam wave vector were coplanar. The data reported here was taken using a 100 mW incident beam collimated to a diameter of 5 mm at the crystal surface.

92-18785



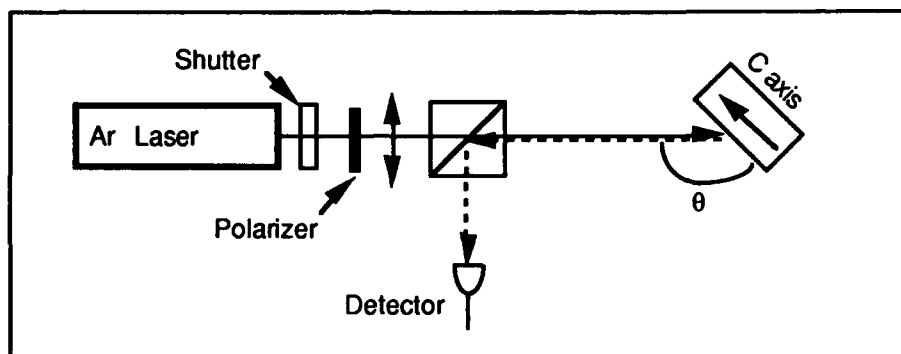


Figure 1. Schematic diagram of the setup used to measure the self-pumped phase conjugate reflectivity and the surface reflectivity in BaTiO₃:Ce.

Results and Discussion

As shown in Fig. 2, self-pumped phase conjugation was found to occur over a wide range of incident angles. The phase conjugate reflectivity was found to reach 50% for an incident angle of 80°, comparable to that of BaTiO₃:Co.⁶ It was also observed that the reflectivity became unstable for angles below 60°. However, the latter observation is inconclusive as the laser was not optically isolated from the phase conjugate reflection. We were unable to observe any of the ring structures in the crystal that are characteristic of self-pumped phase conjugators. This was probably due to the deep red color of the crystal and the strong fanning. We are presently conducting measurements to further characterize the optical properties.

References

1. J. Feinberg, Opt. Lett. **7**, 486 (1982)
2. G. Godefroy, G. Ormancey, P. Jullien, W. Ousi-Benommar, and Y. Semanou, Digest of IEEE International Symposium on Applications of Ferroelectrics (ISAF) (IEEE, New York, 1986, paper PA-1).
3. P. G. Schunemann, D. A. Temple, R. S. Hathcock, C. Warde, H.L. Tuller, and H. P. Jenssen, J. Opt. Soc. B **5**, 1685 (1988)
4. R. S. Hathcock, D. A. Temple and C. Warde, IEEE J. Quantum Electron. **QE-23**, 2122 (1987)
5. D. Rytz, B. Wechsler, M. H. Garrett, C. C. Nelson, and R. N. Schwartz, J. Opt. Soc. Am. B **7**, 2245 (1990)
6. S. Ducharme and J. Feinberg, J. Opt. Soc. Am. B **3**, 283 (1986)
7. M. B. Klein and R. N. Schwartz, J. Opt. Soc. Am. B **3**, 293 (1986)

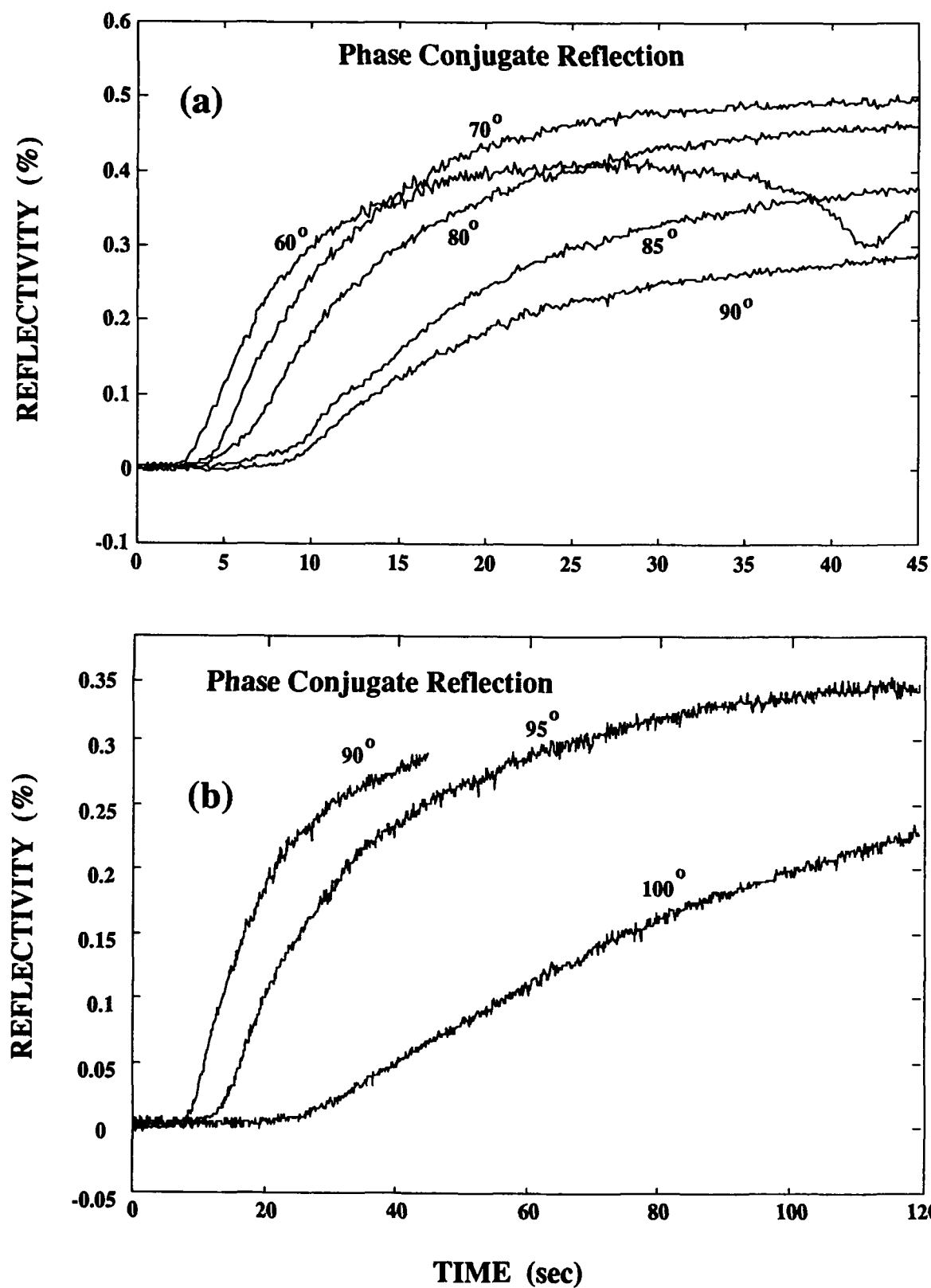


Figure 2. Time dependence of the phase conjugate reflectivity in cerium doped barium titanate. Angles less than 90 degrees are plotted in figure (a) while angles greater than 90 degrees are plotted in figure (b).



Multiple Grating Optical Processing in Barium Titanate

S.A.Boothroyd, P.H.Beckwith, L.Chan, and J.Chrostowski

National Research Council Canada
Institute for Information Technology
Ottawa, Ont., Canada K1A OR6
Tel. 613 993 2524

92-18786

Nonlinear optical image subtraction and Boolean XOR operations have been demonstrated in Michelson interferometers with phase conjugate mirrors [1-3]. The two interferometer arms each contain a light modulating transmission or reflection element which must be carefully registered and imaged at the interferometer output. Destructive interference between the output images of the two arms arises because one image undergoes a extra π phase change on reflection from a dielectric interface. Image subtraction has also been achieved in photorefractives via double exposure holography [4] where two gratings are formed by displacing the reference beam in phase by π . A π phase shift on one of the writing beams in four wave mixing has also been used to selectively erase volume holograms in photorefractive media [5-7].

We describe a new approach using phase conjugation in barium titanate by which image subtraction, the logic XOR, and also the logic OR operation are achieved. Our simple arrangement uses only two mutually coherent input beams for four-wave mixing phase conjugation. Unlike phase conjugate Michelson interferometry the two input images arise from the same modulation element and are automatically registered. In contrast to double exposure interferometry a steady state optically processed image, representing image subtraction, logic XOR, or logic OR, can be produced.

The method involves writing a time averaged photorefractive grating which represents two different images with a controlled phase difference between them. The two images are impressed on a laser beam by transmission through an electrically addressed spatial light modulator (SLM). The transmission of the SLM is alternated between two patterns at video rate, each pattern existing for one frame period before the other pattern is displayed. A piezo electric mirror is stepped between two positions in synchronization with changes in the SLM transmission and directs the image beam to the photorefractive crystal. Phase conjugate readout of this grating is an optically processed image which gives image subtraction or the logic XOR when the phase difference is π and the OR operation when the phase shift is $2\pi/3$ and $4\pi/3$.

The experimental arrangement is shown in figure 1. Laser radiation at 514.5 nm was split into a weak image and a strong reference beam, the image beam was reflected from a piezo mirror onto

a modified Panasonic colour TV, model no. PC-3T20. The pixel size of the SLM liquid crystal TV is $120 \times 135 \mu\text{m}$, each pixel was covered by a red, blue, or green filter. The red pixels blocked the laser light but both the green and blue pixels allowed transmission. The reference beam formed a self-pumped phase conjugator and in doing so generated counterpropagating beams within the crystal which are exact phase conjugates of each other and which interact with the weak image beam to generate its phase conjugate. In this way only two input beams were needed and four-wave mixing phase conjugation of the image beam was achieved with minimal alignment. The strong beam provides a stable reference throughout the formation and readout of the composite grating. The Bragg condition is satisfied for each part of the image beam however the strength of the gratings depend on the direction of the grating wave vector and the crystal c-axis. The piezo mirror and the SLM were under computer control, a frame grabber card provided two patterns to the SLM and a synchronization signal to the piezo mirror. A square wave voltage signal enabled the piezo mirror to be stepped between two positions imparting a calibrated phase shift to the reflected beam. The phase conjugate image was detected by a CCD camera or could be photographed directly.

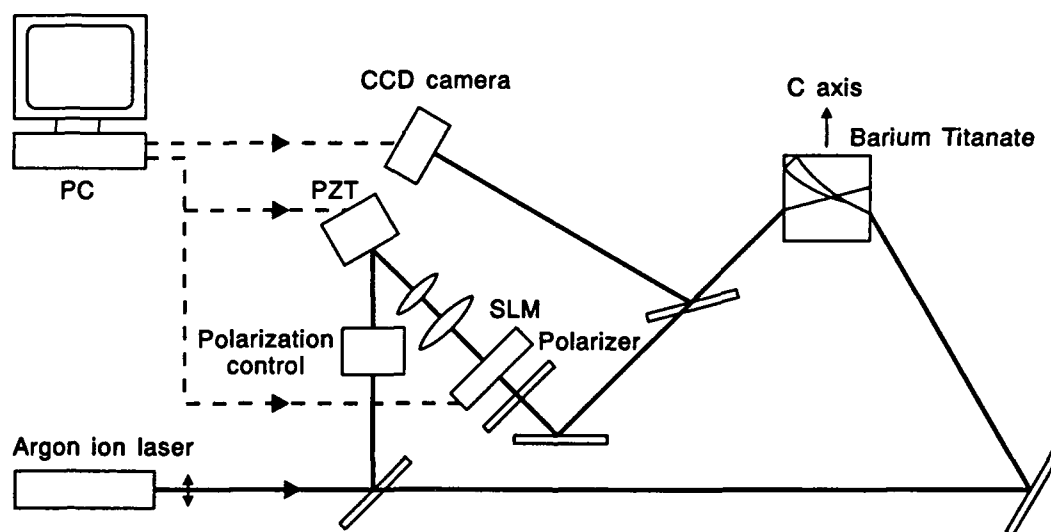


Figure 1. Experimental arrangement

Figure 2 shows a series of photographs demonstrating multiple image optical processing in barium titanate. Figures 2(a) and 2(b) are the phase conjugate images of two transmission patterns on the SLM. Individual pixels are easily resolved although the relatively poor contrast between 'on' and 'off' pixel states is evident, illustrating a limitation of this device. When these two patterns are alternated on the SLM without any phase shift from the piezo mirror then the phase conjugate image in figure 2(c) is seen. Three levels of output are generated, the most intense pixels result when the pixel in both figures 2(a) and 2(b) is 'on', the intermediate level arises when either

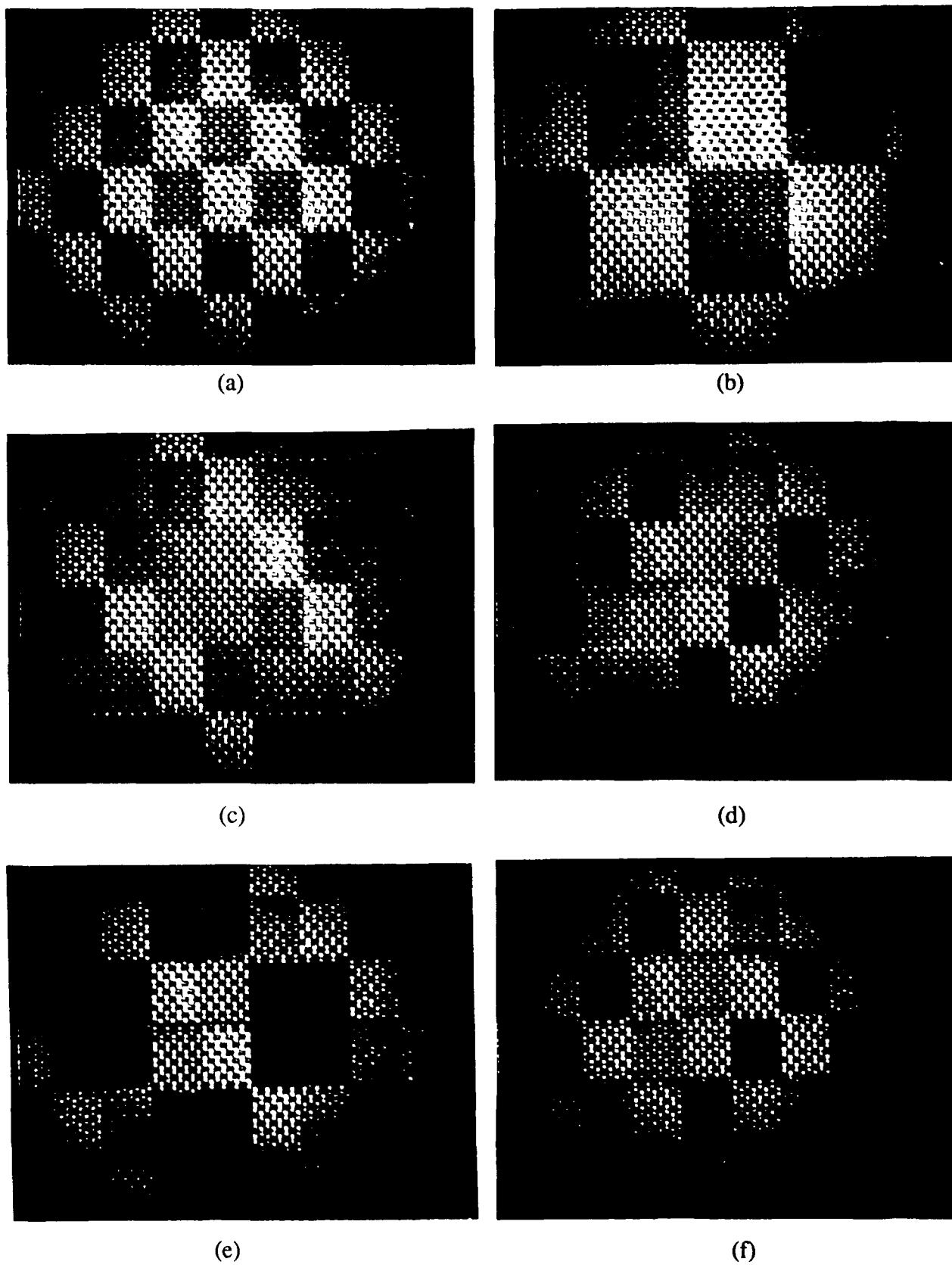


Figure 2. Phase conjugate output

of the registered pixel images in figures 2(a) and 2(b) is 'on' but not both, and when both pixels are 'off' the output is weak. With thresholding, allowing only the most intense pixel images to be recorded, figure 2(c) represents the logic AND operation. The image in figure 2(d) was produced when the relative phase shift between the two patterns was $2\pi/3$. In this case two output levels are seen giving the logic OR operation. Increasing the phase shift to π the output represents image subtraction or the logic XOR, figure 2(e). Here pixels in the 'on' state in both input patterns interfere destructively and the output is dark, furthermore for pixels in the 'off' state in both inputs the residual transmission also leads to destructive interference and the dark regions in figure 2(e) are black. In the case of a π phase shift between the two input images any static phase inhomogeneity introduced on transilluminating the SLM or other optical components is represented in the gratings from both images and thus where destructive interference takes place the cancellation is exact. The optical quality of the SLM is not a concern in this application. Increasing the phase shift between the two images still further to $4\pi/3$ leads again to the OR operation, figure 2(f).

Nonlinear image processing has potential for industrial application. A video signal from a production line can be compared with an image stored in memory and the processed image developed within the material response time. Time averaged interferometry with a video rate SLM allows more than two images to be cycled as the grating develops and the exposure time and relative phase for each individual image is variable giving enhanced processing potential. We are currently evaluating this scheme for neural network applications [6,7].

References

1. A.E.Chiou, P.Yeh, "Parallel image subtraction using a phase-conjugate Michelson interferometer", *Opt. Lett.* **11**, 306, (1986).
2. S.K.Kwong, G.A.Rakuljic, A.Yariv, "Real time image subtraction and exclusive or operation using a self-pumped phase conjugate mirror", *Appl. Phys. Lett.* **48**, 201, (1986).
3. S.A.Boothroyd, J.Chrostowski, "Interferometer", U.S. patent allowed, 1991.
4. Y.H.Ja, "Real-time image subtraction in four-wave mixing with photorefractive $\text{Bi}_{12}\text{SiO}_{20}$ crystals", *Opt. Comm.* **42**, 377, (1982).
5. J.P.Huignard, J.P.Herriau, F.Micheron, "Coherent selective erasure of superimposed volume holograms in LiNbO_3 ", *Appl. Phys. Lett.* **26**, 256, (1975).
6. J.H.Hong, S.Campbell, P.Yeh, "Optical implementation of perceptrons using photorefractive media", OSA Topical Meeting on "Photorefractive materials and devices II", 1990.
7. B.H.Soffer, Y.Owechko, G.J.Dunning, "A photorefractive optical neural network", *SPIE* **1347**, 2, (1990).

**ACOUSTOOPTIC MODULATOR CORRECTION
BY HOLOGRAMS IN THE PHOTOREFRACTIVE CRYSTALS.**

*A. Gnatovskii, N. Kukhtarev, V. Maglevanii,
A. Pigida, V. Verbitskii.*

Institute of Physics, Academy of Science of the Ukr. SSR,
Kiev, 252650, Prospekt Nauki 46, USSR.

Possibility of holographic correction of the aberration caused by the acoustooptic modulation was demonstrated using photorefractive crystals as holographic recording media. Correction was realized using simple two-wave mixing scheme which allow to wash out aberrations but save useful information which may be carried by acoustical wave.

Correcting holograms were written in the photorefractive crystals $\text{LiNbO}_3:\text{Fe}$ with orthogonally polarized signal and reference beams of HeNe laser ($\lambda=0.633\mu$) and with holographic grating vector \vec{q} perpendicular to the crystal \vec{c} -axis. In this configuration vectorial photogalvanic gratings anisotropic diffraction were responsible for correction process. Several orders of diffraction by acoustical waves were used as signal waves with two configuration: plane of acoustical diffraction were perpendicular or parallel to the plane of correcting hologram.



PHASE CONJUGATION WITH SATURABLE GAIN AND SATURABLE ABSORPTION

Milivoj Belić and Dejan Timotijević
 Institute of Physics (tel. -11-107-107)
 P.O. Box 57, 11001 Belgrade, Yugoslavia
 and

Robert W. Boyd
 The Institute of Optics (tel. -716-275-2329)
 University of Rochester, Rochester, NY 14627, USA

We have investigated 2WM and 4WM processes in photorefractive crystals in the nonsaturated regime, *i.e.* when the coupling between beams and the absorption depend on the light intensity. Different models of saturable absorption in 2WM via reflection grating are considered, and the corresponding wave equations are solved exactly. The solutions are written in terms of hypergeometric functions or in quadratures. From the solutions it was found that the energy transfer between the waves is less effective in the nonsaturated stage of the process.

Further, a model of multigrating 4WM is investigated, with intensity dependent coupling coefficients. A system of four nonlinear differential equations for the steady-state energy transfer is solved in terms of quadratures, and a boundary-value fitting procedure devised in the parameter space. Stable and unstable solutions are found, depending on the strength of the coupling.

For g negative only stable solutions exist. In this region our procedure rapidly and accurately converges to a unique solution satisfying given boundary conditions. As compared to standard shooting or other methods, our procedure is found superior, especially when multiple solutions occur in the system.

We find that energy transfer is adversely affected when the mixing of waves proceeds in the nonsaturated regime. This conclusion is perhaps obvious, however, we also find that the stability of the PC process is enhanced in this regime. The stability is also enhanced by turning the absorption on, but this influence is also expected. Globally, absorption suppresses instabilities, but it also suppresses the processes of interest.

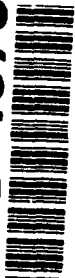
For g positive, sooner or later, instabilities set in. Different types of unstable behavior are observed: quasiperiodic motion on a torus, and a period doubling cascade to chaos. Chaotic behavior in this context means that the intensity reflectivity does not settle onto any particular value, but wanders on a strange attractor in the parameter space. In general, the nonsaturated regime is more stable than the saturated regime, *i.e.* higher values of g are needed in order to destabilize the system.

Finally, it should be pointed out that instabilities found in a steady-state numerical analysis (such as ours), should be viewed with suspicion. They may not exist in the real crystal. The existence of such instabilities should be verified experimentally.

Our procedure consists in the following. Wave equations for intensities considered here are of the form:

$$I_1' + \alpha(I)I_1 + 2g(I) \frac{I_1 I_2}{I} = 0 \quad (1a)$$

92-18787



$$I_2' - \alpha(I)I_2 + 2g(I) \frac{I_1 I_2}{I} = 0, \quad (1b)$$

for 2WM, /1/ and:

$$II_1' = 2\gamma(I)I_1 I_2 - 2g(I)I_1(I_4 - I_3) - \alpha(I)II_1, \quad (2a)$$

$$II_2' = 2\gamma(I)I_1 I_2 + 2g(I)I_2(I_4 - I_3) + \alpha(I)II_2, \quad (2b)$$

$$II_3' = 2g(I)I_3(I_1 + I_2) + 4g(I)(I_1 I_2 I_3 I_4)^{1/2} + \alpha(I)II_3, \quad (2c)$$

$$II_4' = 2g(I)I_4(I_1 + I_2) + 4g(I)(I_1 I_2 I_3 I_4)^{1/2} - \alpha(I)II_4, \quad (2d)$$

for 4WM. /2, 3/ Here I is the total intensity, and $\alpha(I)$, $\gamma(I)$ and $g(I)$ are the corresponding intensity dependent absorption and wave coupling coefficients. The prime here denotes the derivative along the propagation (z) direction. We assume standard 2WM (reflection) and 4WM (multigrating) geometry, with two-point boundary conditions. According to the model of Townsend and La Macchia, /4/ an appropriate functional form for gain coefficients is:

$$\gamma(I) = \gamma \frac{I}{C + I}, \quad g(I) = g \frac{I}{C + I}, \quad (3)$$

where γ and g are the values of the saturated gain, and C a constant dependent on the material. We investigated two models of saturable absorption, two-level and photorefractive, introduced by Brost, Motes and Rotge: /5/

$$\alpha(I) = \frac{\alpha_0}{C + I}, \quad \alpha(I) = \alpha_0 + \alpha \frac{I}{C + I}, \quad (4)$$

which allow analytic treatment. Here α_0 is the linear absorption, and α a material parameter. The method of solution of Eqs. (1) and (2) is presented in Refs. /3/ and /6/.

The solution for photorefractive absorption with $\alpha_0=0$, is given in terms of two functions $F(z)$ and $f(F)$:

$$I_1 = f \exp \left(\frac{F}{2} \right), \quad I_2 = f \exp \left(-\frac{F}{2} \right), \quad (5)$$

which are found by evaluating a system of two quadratures:

$$\int_{F_0}^F \frac{dx}{\beta - \tanh x} = \ln \frac{f}{f_0}, \quad C \int_{F_0}^F \frac{dx}{f(x)(\sinh x - \cosh x)} - \ln \frac{f}{f_0} = gz, \quad (6)$$

where $\beta = \alpha/g$. As it happens often with nonlinear equations and implicit

relations, Eqs. (6) allow multiple solutions which satisfy the same boundary conditions. Typical situation is presented in Fig. 1. Such solutions complicate the analysis, especially when there is no clear criterion which distinguishes physically relevant (allowed) from the irrelevant solutions. Here, by simple inspection, one solution is discarded. However, in 4WM there is no such criterion, and multiple solutions appear, leading to chaotic response of the system.

The solution of Eqs. (2) for 4WM is similarly written in terms of two functions v and w :

$$I_1 = I_{4d} \frac{u(v)-(v+\delta)}{2}, \quad I_2 = I_{4d} \frac{u(v)+(v+\delta)}{2}, \quad (7a)$$

$$I_3 = I_{4d} \frac{\cosh w - 1}{2}, \quad I_4 = I_{4d} \frac{\cosh w + 1}{2}, \quad (7b)$$

which are also given as quadratures:

$$w(v) = \int_1^v \frac{f(x)}{xu(x)} dx, \quad (8a)$$

$$\ln v(z) + c \int_1^v \frac{dx}{xu(x)} + \int_1^v \frac{\cosh w(x)}{xu(x)} dx = 2g(z-d), \quad (8b)$$

where $f(v) = av^{3/2g}$ and $u(v) = [(v+\delta)^2 + f^2]^{1/2}$. Parameters a and δ , which depend on the missing boundary values, are evaluated iteratively, in a self-consistent procedure. It is during this iterative procedure that unstable situations arise, leading to chaotic output.

One such instance is presented in Fig. 2, which depicts the bifurcation diagram obtained by sampling the saturation constant C as the control parameter. Evidently, the system becomes more stable as C is increased, which is equivalent to having less and less saturated crystal.

References:

- /1/ Y. H. Ja, Opt. Quant. Electron. **17**, 291-295 (1985).
- /2/ T. K. Das, K. Singh, Opt. Quant. Electron. **22**, 167-174 (1990).
- /3/ M. R. Belić, Phys. Rev. **A37**, 1809-1812 (1988).
- /4/ R. L. Townsend, J. T. LaMacchia, J. Appl. Phys. **41**, 5188-5192 (1970).
- /5/ G. A. Broost, K. A. Motes, J. R. Rotge, J. Opt. Soc. Amer. **B5**, 1879-1885 (1988).
- /6/ M. R. Belić, Opt. Quant. Electron. **16**, 551-557 (1985); W. Krolikowski, M. R. Belić, Opt. Lett. **13**, 149-151 (1988).

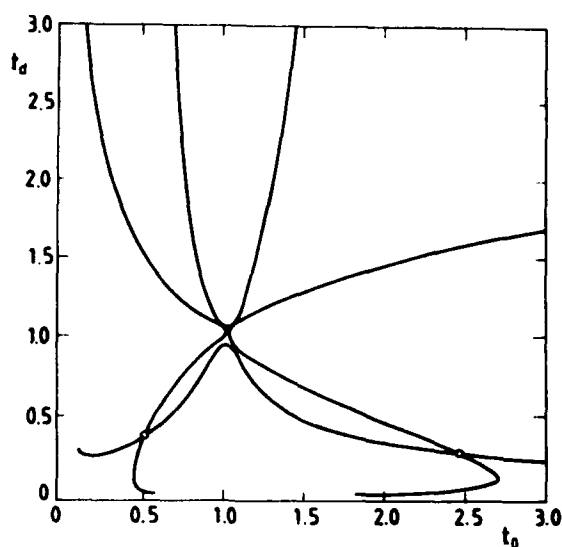


Figure 1: Multiple solutions of 2WM. The curves are obtained when boundary conditions are applied to Eqs. (6). The crossing points define the values of the arguments t_0 and t_d for which boundary conditions are satisfied. Here $t = (g - \alpha) / (g + \alpha) \exp(2F)$. Of the two points visible, the point to the left leads to negative z , and must be discarded. The unique solution corresponds to the point to the right. Note also the "avoided crossing" nature of the singularity at $t_0 = t_d = 1$.

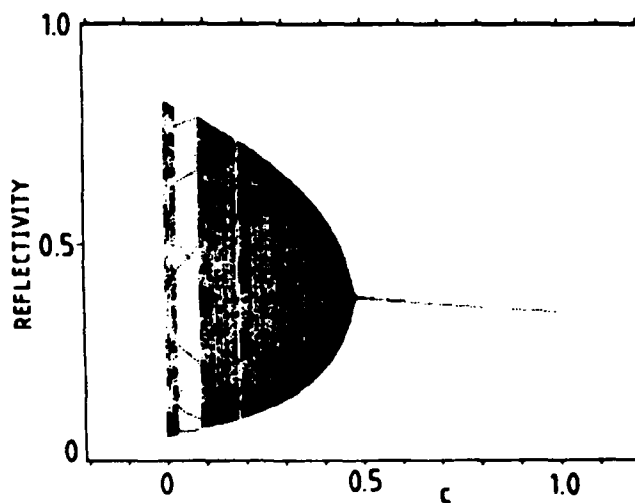


Figure 2: Multiple solutions in 4WM. The figure presents bifurcation diagram as the saturation parameter C is varied. The system is chaotic for $C=0$ (saturation), and then proceeds through a series of changes until a unique solution is obtained for $C=1$ (nonsaturated system).



Instabilities in Coupled Photorefractive Ring Cavities and Self-Pumped Phase Conjugators

Li-Kuo Dai and Yih-Shun Gou

Institute of Electric-Optical Engineering

National Chiao Tung University, Hsinchu, Taiwan, R.O.C.

Claire Gu

Rockwell International Science Center

1049 Camino Dos Rios, Thousand Oaks, CA 91360

Pochi Yeh*

Department of Electrical and Computer Engineering

University of California, Santa Barbara, CA 93106

SUMMARY

Photorefractive mode coupling between resonators provides a simple model for self-pumped phase conjugators [1] where instabilities may occur due to energy transfer between different oscillation modes inside the crystal. In this paper, we consider the dynamical behaviors of mode coupling between two unidirectional ring resonators [2]. The first resonator is driven by an external laser beam via photorefractive two-wave mixing. The internal oscillating beam is then employed to drive the second ring resonator via the same mechanism (see Fig.1).

The dynamics of the coupled system is described by a set of spatial-temporal equations [3] with appropriate boundary conditions. To investigate the instability behaviors, we use the mean-field approximation [4] to simplify the transient analysis.

We first solve for the steady states of the system. When the gain of the two cavities are below certain threshold, there is no self-oscillation in the system. If the gain for the primary cavity is increased above its threshold while the gain for the secondary cavity remains low, self-oscillation will occur in the primary cavity only. If the gain in the secondary cavity is gradually increased, self-oscillation will occur in the secondary cavity. At the same time, the oscillation intensity in the primary cavity will decrease, since the secondary cavity acts like a loss mechanism for the primary one. If the gain for the secondary cavity is further

92-18788



increased, the coupled system will become unstable. We will analyze the stability of all possible steady states as well as the dynamics of unstable oscillations.

Fig. 2 shows the results of linear stability analysis, where C_1 and C_2 represent the relative gain in the primary and secondary cavities respectively. It can be noticed that as the gain for the primary cavity is increased while the gain for the secondary cavity is fixed, the system will first experience unstable oscillations then the oscillations will become more and more stable. During the unstable oscillations, chaos and self-pulsations may occur. The instabilities of the coupled cavity is due to the competition for energy between the two cavities, which is similar to what occurs in self-pumped phase conjugators.

Numerical results of the unstable oscillations are shown in Fig. 3 and Fig. 4 with different sets of parameters. Fig. 3 shows that as the gain for the primary cavity increases, the self-pulsation will first experience period doubling and then chaos. This is clearly seen in the intensity power spectrum with the appearance of subharmonic and a broadband spectrum. Fig. 4 shows another type of unstable oscillation — pulsed oscillation [5].

We conclude that self-oscillation, coupling and competition for energy are the origin for our coupled system and this can be extended to explain the instabilities in self-pumped phase conjugators.

* Pochi Yeh is also a Principle Technical Advisor at Rockwell International Science Center.

REFERENCES

- [1] M.D.Ewbank and P.Yeh, Proc. SPIE, **613**, 59(1986).
- [2] P.Yeh, IEEE J. Quantum. Electron., Vol. **QE-25**, 484(1989).
- [3] D.M Lininger, D.D.Crouch, P.J.Martin, and D.Z.Anderson, Opt. Comm. **76**, 89(1990).
- [4] N.B.Abraham, P.Mandel, and L.M.Narducci, in:Progress in Optics, Vol. **XXV**, ed. E.Wolf p.104, 1988.
- [5] S.Weiss, and B.Fischer, Opt. Comm. **70**,515(1989).

Fig. 1 Schematic drawing of two coupled unidirectional photorefractive ring cavities.

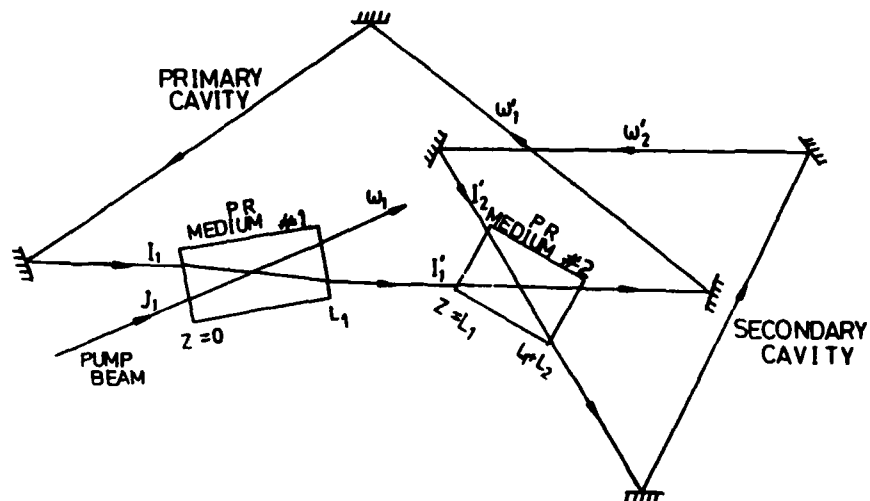


Fig. 2 Results of linear stability analysis. S and H stand for stable steady state and Hopf bifurcation respectively.

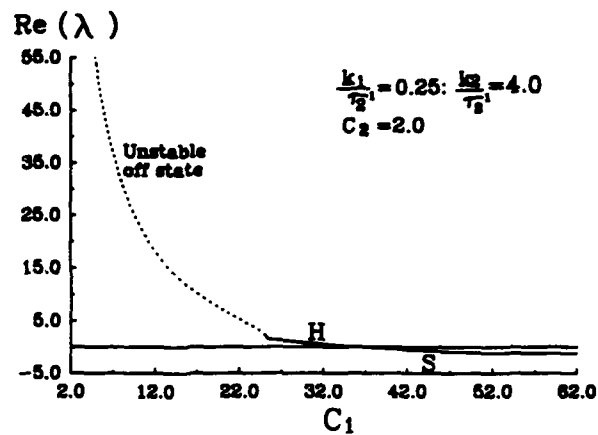


Fig. 4 Pulsed oscillation.

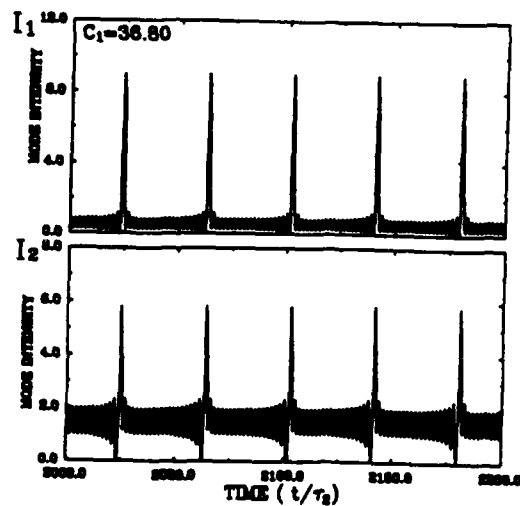
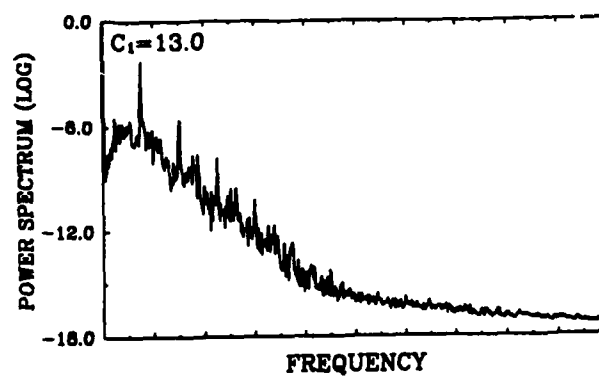
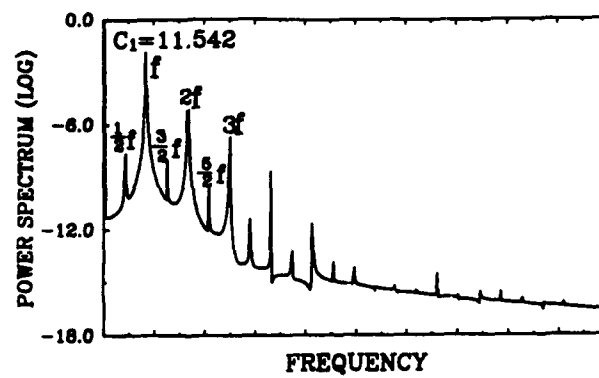
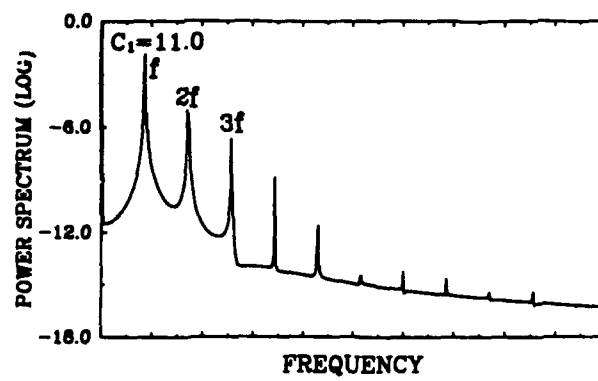


Fig. 3 Intensity power spectrum showing self-pulsation, period doubling, and chaos.



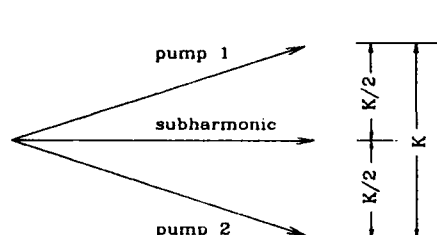
AD-P006 801



Analytic and Numeric Results on Subharmonics in BSO

A. Bledowski¹, B. Sturman², J. Otten and K. H. Ringhofer¹

Recently, experiments with $\text{Bi}_{12}\text{SiO}_{20}$ (BSO) initiated by Mallick et al.[1] and continued by the Oxford group[2, 3, 4, 5, 6] have shown that, under certain conditions, one or more spatially subharmonic beams may arise between two pump beams (see Fig. 1).



Two mechanisms have been identified which contribute to this effect:

- selective amplification[7, 8] of a signal scattered in the right direction
- spontaneous generation [9, 6], made possible by the nonlinearities in the materials equations [10].

Figure 1: Geometry for the generation of a subharmonic.

In this paper we concentrate on the second mechanism, but first we comment on a paper by Au and Solymar[11] Fig. 2 of that paper shows the real and the imaginary part of the space-charge field for a BSO crystal with frequency detuning as the curve parameter. The curves for higher values of the modulation show kinks which have not been explained by Au and Solymar.

We have recalculated these curves for a value of the electron mobility μ three times higher ($\mu = 10^{-5} \text{ m}^2/\text{Vs}$), as has been recommended in Refs. [12, 6] and found not only kinks but even discontinuities. The curves A, B, and C of Fig. 2 show the absolute value of the space-charge field for modulation 1 as a function of frequency detuning and one has to accept the conclusion that hysteresis is involved.

The dimensionless variables used in Fig. 2 are the following:

$\lambda = q(N_D - N_A) / \epsilon_r \epsilon_0 K E_0$ with q the elementary charge, N_D and N_A the concentration of donors and compensators, ϵ_r the relative dielectric constant, ϵ_0 the permittivity of the vacuum, K the grating vector and E_0 the external field. Furthermore, $\epsilon = \lambda / \omega$, where $\omega = \Omega / s I_0$ with Ω the frequency detuning, s the cross-section for the creation of mobile carriers, and I_0 the average intensity. Finally, $\gamma = 1 / K l_d$ where l_d is the drift length in the external field.

Further analysis shows that behind hysteresis another effect is hidden, namely instability against period doubling as documented by the (dotted) curve B of Fig. 2.

¹FB Physik der Universität, PF 4469, D-4500 Osnabrück, F.R.G.

²Institute of Automation and Electrometry, USSR Academy of Sciences, Siberian Branch, Universitet-skii Pr., 1, Novosibirsk, 630090, U.S.S.R.

92-18789



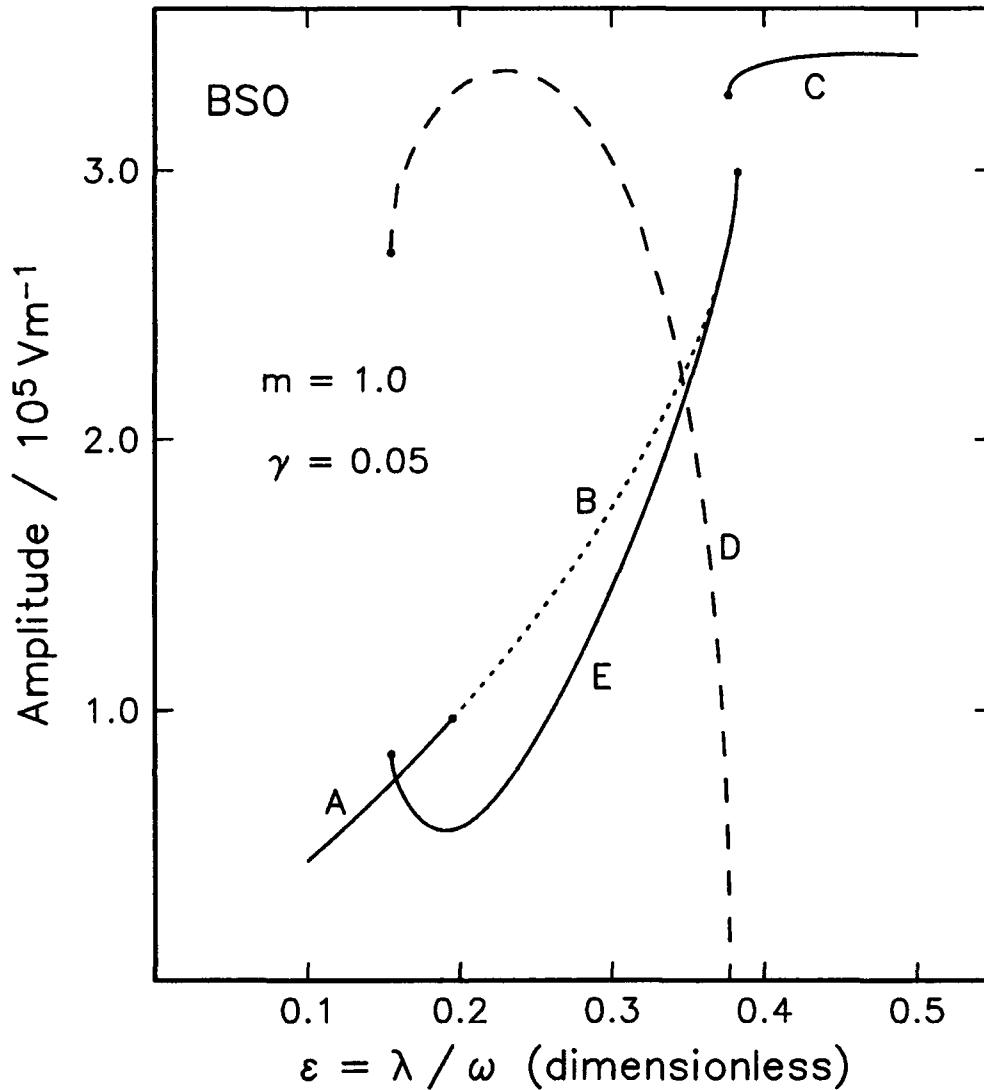


Figure 2: Amplitudes of the Fourier components 1 and 1/2. For details see the text.

We have found instability already in the simplest possible model taking into account only a minimum number of Fourier components. In this model, the instable stationary solution, showing the period of the light-intensity pattern, is described by

$$e_{stat}(Kx - \omega t) = e_1^* e^{-i(Kx - \Omega t)} + 1 + e_1 e^{i(Kx - \Omega t)} \quad (1)$$

where e is the space-charge field divided by the external field. Stability is analyzed by adding terms exponentially growing or decaying depending on the sign of the real part of the parameter Γ :

$$e(x, t) = e_{stat}(Kx - \Omega t) + \delta e(Kx - \Omega t) e^{\Gamma s I_0 t} \quad (2)$$

and by allowing for subharmonic terms $\delta e_{\pm 1/2} \exp(\pm i(Kx - \Omega t))$ in the Fourier expansion of $\delta e(Kx - \omega t)$. Here $sI_0 t$ is a dimensionless time parameter with s the cross section for the excitation of electrons and I_0 the average intensity. Assuming the amplitudes $\delta_{\pm 1/2}$ to be small one obtains an explicit equation for Γ [13]:

$$\left(\frac{\epsilon}{\lambda}\gamma\Gamma - \frac{1}{4} + \epsilon\right)^2 + \frac{1}{4}\left(\frac{\epsilon}{\lambda}\Gamma + \gamma\right)^2 = \left(\left(\frac{1}{4} + \epsilon\right)^2 + \left(\gamma + \frac{1}{2}\frac{\epsilon}{\lambda}\Gamma\right)^2\right) \frac{1}{4} \frac{m\epsilon}{(1-\epsilon)^2 + \gamma^2} \quad (3)$$

The real part of Γ changes sign for

$$\left(\frac{1}{4} - \epsilon\right)^2 + \frac{\gamma^2}{4} = \left(\left(\frac{1}{4} + \epsilon\right)^2 + \gamma^2\right) \frac{1}{4} \frac{m\epsilon}{(1-\epsilon)^2 + \gamma^2}. \quad (4)$$

This formula defines the region of instability. The dashed line in Fig. 3 shows this region in the ϵ - γ plane. The full line shows the same region in an approximation which also allows for Fourier components $\pm 3/2$. The dotted line shows the result of our exact numeric calculation. There is a minimum as well as a maximum value of ϵ and of γ for the region of instability.

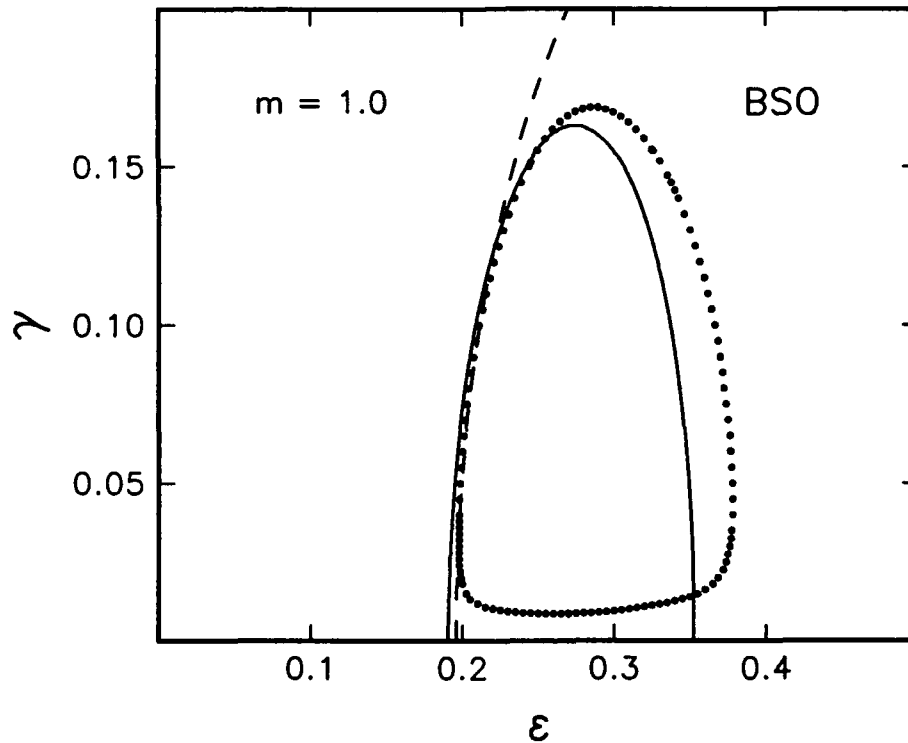


Figure 3: Region of instability against generation of subharmonics. For details see the text.

Finally, curves E and D of Fig. 2 show the absolute value of the Fourier component one and $1/2$, respectively. The crossing point of curves A and E refers to different stable states, one with and one without subharmonics.

Acknowledgements: Three of the authors (A. B., J. O. and K. H. R.) have been supported by Deutsche Forschungsgemeinschaft within the program of the SFB 225 "Oxide Crystals for Electro- and Magneto-optical Applications".

References

- [1] S. Mallick, B. Imbert, H. Ducollet, J. P. Herriau, and J. P. Huignard. Generation of spatial subharmonics by two-wave mixing in a nonlinear photorefractive medium. *J. Appl. Phys.*, 63:5660-5663, 1988.
- [2] D. R. Erbschloe and L. Solymar. Linear resonator in photorefractive BSO with two pump beams. *Electr. Lett.*, 24:683-684, 1988.
- [3] D. R. Erbschloe and L. Solymar. Unidirectional ring resonator in photorefractive bismuth silicon oxide with two pump beams. *Appl. Phys. Lett.*, 53:1135-1137, 1988.
- [4] D. C. Jones and L. Solymar. Competition between subharmonic and resonating beams for photorefractive gain in bismuth silicon oxide. *Opt. Lett.*, 14:743-744, 1989.
- [5] D. J. Webb and L. Solymar. Observations of spatial subharmonics arising during two-wave mixing in BSO. *Opt. Comm.*, 74:386-389, 1990.
- [6] D. J. Webb, L. B. Au, D. C. Jones, and L. Solymar. Onset of subharmonics generated by forward wave interactions in $\text{Bi}_{12}\text{SiO}_{20}$. *Appl. Phys. Lett.*, 57:1602-1604, 1990.
- [7] K. H. Ringhofer and L. Solymar. New gain mechanism for wave amplification in photorefractive crystals. *Appl. Phys. Lett.*, 53:1039-1040, 1988.
- [8] K. H. Ringhofer and L. Solymar. Three-wave and four-wave forward mixing in photorefractive materials. *Appl. Phys.*, B 48:395-400, 1989.
- [9] L. B. Au, L. Solymar, and K. H. Ringhofer. Subharmonics in BSO. In *Proceedings of the topical conference on "Photorefractive Materials, Effects and Devices II"*, Aussois, France, 1990.
- [10] N. V. Kukhtarev, V. B. Markov, S. G. Odulov, M. S. Soskin, and V. L. Vinetskii. Holographic storage in electrooptic crystals. *Ferroelectrics*, 22:949-960 and 961-964, (1979).
- [11] L.-B. Au and L. Solymar. Space-charge field in photorefractive materials at large modulation. *Opt. Lett.*, 13:660-662, 1988.
- [12] G. Lesaux, G. Roosen, and A. Brun. Observation and analysis of the fast photorefractive process in bso. *Opt. Comm.*, 56:374-378, 1986.
- [13] B. Sturman, A. Bledowski, J. Otten, and K. R. Ringhofer. Subharmonics in photorefractive crystals. to be published.



SPATIAL SUBHARMONIC GENERATION IN BaTiO₃

A. Novikov, S. Odoulov

Institute of Physics, Ukrainian SSR Academy of Science,
252 650, Kiev, U S S R
tel.(044) 265 08 18

R. Jungen and T. Tschudi

Institut fuer Angewandte Physik,
Technische Hochschule,
W 6100, Darmstadt,
Federal Republic of Germany,
tel.(06151) 16 20 22

Generation of spatial subharmonics is considered as a consequence of convective instability in parametric nonlinear mixing of two copropagating coherent waves of the same frequency: two incident pump waves and the scattered wave, propagating at the bisector of pump waves.

Efficient amplification of the seed, scattered radiation can be achieved only for phase matched nonlinear mixing. For BaTiO₃ it may be the mixing of two orthogonally polarized pump waves, ordinary and extraordinary, and the scattered extraordinary wave, all propagating in the plane normal to crystal C-axis and meeting the following phase matching condition [1,2]

$$\mathbf{k}_p^o - \mathbf{k}_{\text{subh}}^e = \mathbf{k}_{\text{subh}}^e - \mathbf{k}_p^e = \mathbf{K}, \quad (1)$$

where \mathbf{k} is the wavevector, the indices o and e denote ordinary and extraordinary polarization, p and subh denote pump waves and subharmonic, respectively, \mathbf{K} is the wavevector of the grating recorded in the sample by extraordinary pump wave and extraordinary subharmonic (Fig.1).

Subharmonic generation in BaTiO is the inverse process to the light-induced conical scattering of unique extraordinary wave [1-3]. It can be described by the same equations as for anisotropic selfdiffraction [4] but with the changed initial conditions [5].

It can be shown that in undepleted pumps approximation the intensity of the subharmonic, I_{subh} , will grow exponentially with the sample thickness x

$$I_{\text{subh}}(x) = I_{\text{subh}}(0) \exp \left[\pm \frac{2\pi \Delta n x}{\lambda} \frac{\sqrt{r}}{1+r} \right], \quad (2)$$

where $r = I_p^e / I_p^o$ is the pump intensity ratio, λ is the wavelength and Δn is the nonlinear change of refractive index.

The sign \pm in the exponent correspond to two different combinations of phases ϕ of interacting waves

92-18790



$$2\phi_{\text{subh}} - \phi_p^m - \phi_p^e = 0 \text{ or } \pi. \quad (3)$$

Only the component of seed radiation with the phase necessary to provide the positive increment will be amplified and will give rise to the development of subharmonic.

Analytical solution for subharmonic intensity can be obtained also with the depletion of pump wave taken into account [5].

We describe in this report the first observation and the study of the subharmonic generation, of the amplification of signal beam in the direction of subharmonic, and of the use of this amplification process to obtain the selfoscillation in linear and ring cavities in nominally pure BaTiO_3 crystals.

The sample of BaTiO_3 was used to observe and to study the described processes. The experimental arrangement is shown schematically in Fig.2. The light beam from Ar laser (TEM_{00} , $\lambda = 0,51 \mu\text{m}$, $P \approx 100 \text{ mW}$) was splitted in two parts with equal intensities by the beamsplitter BS and directed by mirrors M symmetrically to the input face of photorefractive crystal PRC making an angle 2θ in air. The $\lambda/2$ retarder was placed in one lag of interferometer to change the polarization of the beam to orthogonal one.

The exposure of the sample by beams at angle $\theta = 23^\circ$ determined by the phase matching condition

$$\sin\theta = \sqrt{n_o(n_o - n_e)}, \quad (4)$$

($n_{o,e}$ are the refractive indices) resulted in gradual development from the noise of the extraordinary wave propagating just along bisector of two pump waves. Fig.3 represents the angular distribution of light after the crystal, photographed from the screen SC (see Fig.2) placed at 40 cm from the sample. Bright spot between two pump waves corresponds to the first spatial subharmonic. In the same picture one can see also additional wave (with wavevector k_s^o), the ordinary one, diffracted from the same subharmonic grating in accordance with the phase matching condition (see Fig.1).

$$k_s^o = k_p^e - K. \quad (5)$$

We studied the temporal behavior of the signal (extraordinary) wave aligned in the direction of subharmonic. Typical temporal evolution of amplified signal intensity is shown in the Fig.4. Qualitatively it corresponds to calculated dependence of $I_{\text{subh}} = I_{\text{subh}}(\Gamma x)$ if we take into account that the coupling strength is smoothly increasing in time from zero up to the saturation value. From the data similar to those presented in the Fig.4 one can calculate the steady state gain,

$$\Gamma_o = (1/x) \ln \left[I_{\text{subh}}(x) / I_{\text{subh}}(0) \right], \quad (6)$$

which is plotted in the Fig.5 as a function of pump intensity ratio. In agreement with the result of calculation (see (Eq.2)) the maximum gain is achieved for $r = 1$. The solid line represent the best fit to theoretical dependence

$$\Gamma(r) = \Gamma_0^{\max} \frac{\sqrt{r}}{1 + r}, \quad (7)$$

a good qualitative agreement with the experiment is obvious.

Maximum gain factor achieved in the experiment, $\Gamma = 3 \text{ cm}^{-1}$, was large enough to use this parametric amplifier as an active medium of a coherent oscillator. Various optical cavity arrangements have been tested: closed linear oscillator, unidirectional closed ring oscillator (Fig.6a) and unidirectional unclosed ring oscillator (Fig.6b). In the last case the angle of pump incidence has been larger then necessary for the selfdevelopment of subharmonic and the oscillation was observed in two conjugate directions along the phase-matching cone.

REFERENCES

1. R.Rupp and F.Drees, Appl Physics,B, **39**, p.223 (1986)
2. D.Temple and C.Warde, J.O.S.A. B, **3**, p.337 (1986)
3. M.Ewbank, P.Yeh and J.Feinberg, Opt. Com. **59**, p.423 (1986)
4. N.Kukhtarev, E.Kraetzig, H.C.Kulich, R.A.Rupp and J.Albers
Appl. Phys. **B35**, 17 (1984)
5. S.Odoullov, Ukranian Phys.J.(in Russian), **32**, p.145 (1987)
6. A.Novikov, S.Odoullov,
Ukranian Phys.J.(in Russian) ,**32**, p.1514 (1987)

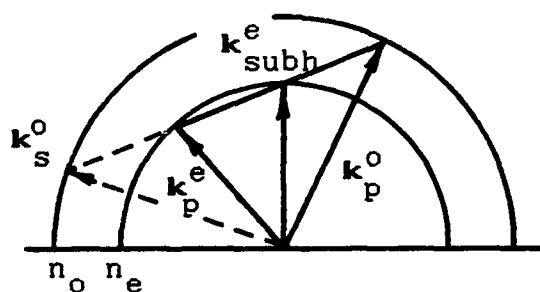


Fig.1

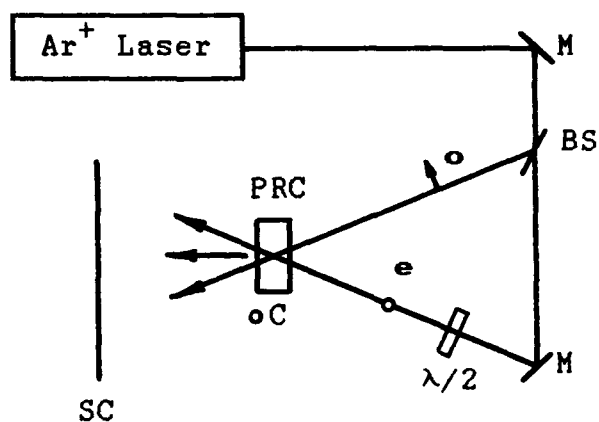


Fig.2

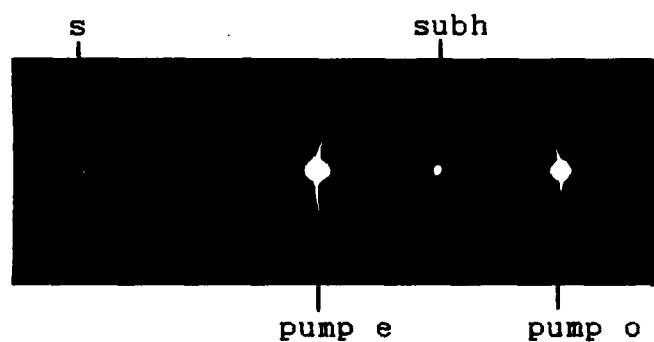


Fig.3

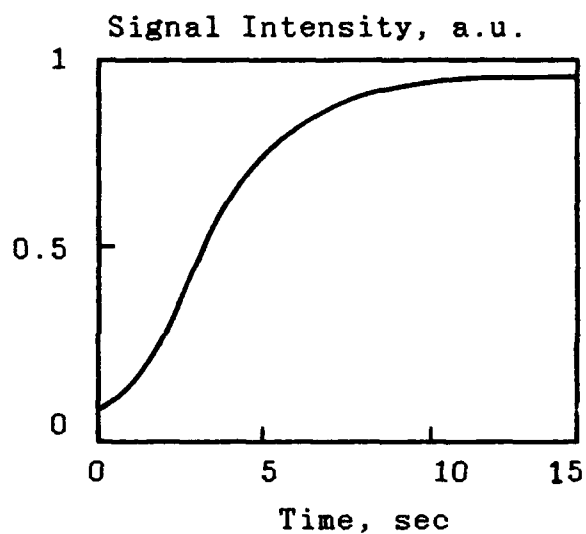


Fig.4

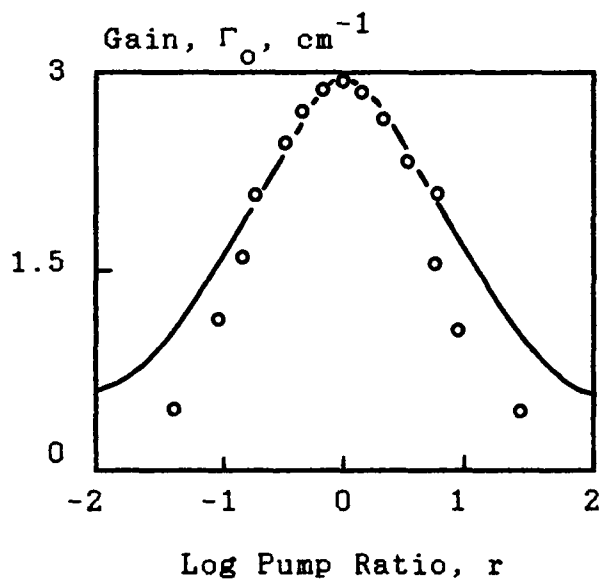


Fig.6

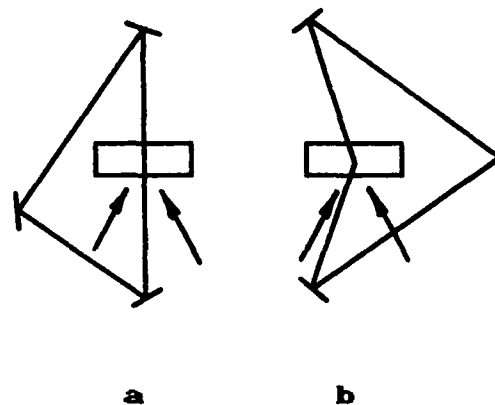


Fig.6



92-18791



Instability of spatial subharmonic under hologram recording in a photorefractive crystal.

O. P. Nestiorkin

Nonlinear optics laboratory, Polytechnic Institute, *politekhnikeskii*
prosp. Lenina 76, Chelyabinsk, 454080, USSR *inst*

112

Wave mixing experiments in photorefractive crystals (PRC) have resulted in the observation of large number of interesting phenomena. Communications about spatial subharmonic generation were published in [1,2]. Subharmonic gratings with a wave vector q/n (n - integer) have been occurring during the illumination of PRC $\text{Bi}_{12}\text{SiO}_{20}$ by moving interference pattern with a wave vector q (Fig.1). Authors of [3] suggested the mechanism of generation of subharmonic at the expense of noise component amplification in the field of two pump waves. Amplification is caused by small off-Bragg vector Δq (see Fig.1). In this work we consider another possible mechanism of spatial subharmonic generation. By our opinion the particular mechanism which may lead to subharmonic generation is the following. Under illumination of PRC by interference pattern with intensity distribution $I(x,t) = I_0(1 + 0.5\exp[i(qx - \omega t)] + \text{c.c.})$ photoelectron concentration grating is generated there. That grating moves with the phase velocity $v = \omega/q$. Here I_0 is the average light intensity, m is a contrast of interference pattern, ω is the frequency detuning of interacting beams. Fluctuation of space charge field $\sim E_{1/2}\exp[i(qx/2 - \omega t/2)] + \text{c.c.}$ causes the generation of photocurrent wave $\sim j_{1/2}\exp[i(qx/2 - \omega t/2)] + \text{c.c.}$ That photocurrent wave has the same space-time structure as a space charge field wave and consequently may intensify the space charge separation under suitable phase relation between those two waves. If that intensification exceeds the Maxwell relaxation, the space charge field amplitude of subharmonic will increase. The optimum condition for such instability is realized when the photocurrent wave is under resonance with trap charge exchange wave (TCEW) [4]. That wave occurs if electron drift length exceeds the

Eliminating the values N^+ and j , neglecting diffusion and trap saturation and considering electrostatic field and electron concentration as a sum of uniform and nonuniform parts $E_e = E_0 + E$ and $n_e = n_0 + n$ respectively one may receive:

$$\frac{n_t}{n_0} = - \frac{n}{\tau n_0} + \mu E_0 \frac{n_x}{n_0} + \mu E_x + m e^{i(qx - \Omega t)} \quad (2)$$

$$E_t = - \frac{E}{\tau_M} - \frac{E_0 n}{\tau_M n_0}$$

Here the terms proportional to nE are neglected, $\tau = (\nu N_A)^{-1}$ is the life time of electron in conduction band, n_0 is the average concentration of electrons $n_0 = SI_0 N_D / \nu N_A$, $\tau_M = \epsilon \epsilon_0 / e \mu n_0$ is the time of Maxwell relaxation. After eliminating the electron concentration n from (2) and neglecting by terms proportional to $(\tau/\tau_M)^2 \ll 1$ the equation for relaxation of subharmonic grating (without right-hand part) takes the following form:

$$E_t - L_D E_{xt} + \frac{1}{\tau_M} E = 0 \quad (3)$$

Here L_D is so called electron drift length $L_D = E_0 \mu \tau$. For harmonic space-charge field $E = E(t) e^{iqx}$ the equation (3) gives well known equation:

$$E_t(t) + [\tau_M (1 - iqL_D)]^{-1} E(t) = 0 \quad (4)$$

For next approximation it is necessary to take into account that Maxwell relaxation time is modulated by first harmonic of electron concentration with complex amplitude n_1 :

$$E_t - L_D E_{xt} + \left[1 + \frac{n_1}{2n_0} \exp[i(qx - \Omega t)] + \frac{n_1^*}{2n_0} \exp[-i(qx - \Omega t)] \right] E = 0 \quad (5)$$

grating period q^{-1} , i.e. $E_0 > E_p = (q\mu\tau)^{-1}$. Here $\mu\tau$ is a product of electron mobility μ and its life time τ in conduction band. Existence of such type instability was demonstrated by authors of [5] by numerical calculation for experimental condition for $\text{Bi}_{12}\text{SiO}_{20}$ used in [2]. The aim of the present work is to investigate analytically the conditons under which the discussed instability exists.

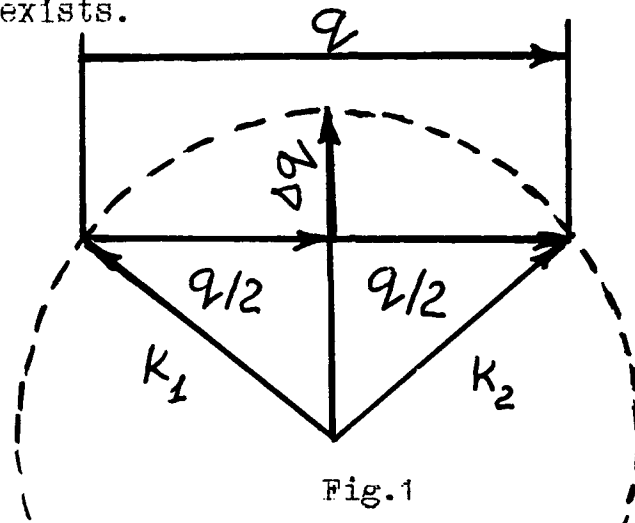


Fig.1

The process of the space charge grating formation is described by the system of equations [4]

$$\partial N^+ / \partial t = SI(N_D - N^+) - r n_e N^+$$

$$\partial N^+ / \partial t = \partial n_e / \partial t - \nabla j / e$$

(1)

$$j = e\mu n_e E_e + k_B T \mu \nabla n_e$$

$$\epsilon \epsilon_0 \nabla E_e = e(N^+ - n_e - N_A)$$

Here n_e , N^+ , N_D and N_A are the concentrations of electrons, ionized donors, all donors and acceptors respectively; S and r are the constants of photodetachment and electron-ion recombination respectively; j is the current density; E_e is electrostatic field, $e=|e|$ and $\mu=|\mu|$ are the absolute values of the charge and mobility of electron respectively; $k_B T$ is the temperature in energy units; ϵ and ϵ_0 are the static dielectric permittivities of crystal and vacuum respectively.

Here the Maxwell relaxation time is used as a unit of time measurement. It may be shown that equation (5) has exponentially increasing solution $\sim \exp(qx/2 - \alpha t/2)$ under condition:

$$|n_1/n_0| > [\alpha^2 + (Q\alpha - 4)^2]^{1/2} \quad (6)$$

Here $Q = qL_D$ is the Q-factor of trap-charge exchange wave. Considered instability of spatial subharmonic is analogous to the classical parametric resonance [6].

References

1. S. Mallick, B. Imbert, H. Ducollet, J. P. Herriau, and J.-P. Huignard, J. Appl. Phys. **63**, 5660 (1988).
2. D. J. Webb and L. Solymar, Optics Commun, **74**, 386 (1990).
3. R. H. Ringhofer and L. Solymar, Appl.Phys.Lett. **53**, 1039 (1988).
4. Ph. Refregier, L. Solymar, H. Rajbenbach and J. P. Huignard, J.Appl.Phys.**58**, 45 (1985).
5. L. B. Au, L. Solymar, and R. H. Ringhofer, Technical Digest of Topical Meeting in Photorefractive Materials, Effects & Devices II 1990, Aussois (France), paper B4.
6. L. D. Landau and E. M. Lifshits, Classical Mechanics, Moscow, Nauka, 1988 (in Russian).

SPATIAL SUBHARMONIC GENERATION AT INTERMODE
 INTERACTION IN PLANAR WAVEGUIDES

V. Popov, E. Shandarov, S. Shandarov

 Institute of Automatic Control Systems and Radioelectronics
 40 Lenin av., Tomsk 634050, USSR

 AD-P006 804


In papers ¹⁻⁴ the possibility of new light beam generation by interactions of light waves in photorefractive crystals is shown. New beams appear due to the subharmonic formation of the main holographic grating. The analysis of subharmonic generation was carried out for crystals with nonlocal response^{2,3} and circular photogalvanic mechanism of grating recording⁴. The vector diagram illustrating the latter type of interaction is represented in Fig.1. Here, the generated beam 1(3) has polarization orthogonal to polarization of exciting waves 2,4.

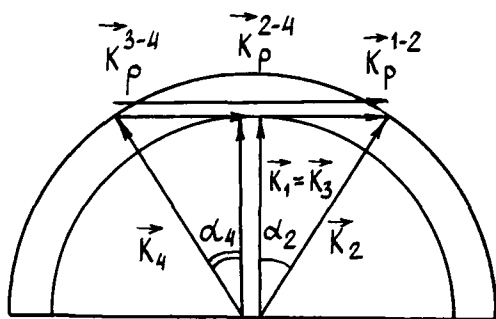


Fig. 1.

The intermode interaction of light beams in planar waveguides may be characterized by the same vector diagram. However, in this case the interacting waves may have similar polarization having different numbers of modes.

The given report is devoted to the analysis of generation of TE_p - modes 1 and 3 by exciting beams 2 and 4 (TE_{p-1} modes) in the planar waveguide on the Y cut of a $LiNbO_3$ crystal.

We assumed the angle α between the beams (Fig.1) to be small one that allowed us to consider TE modes to be polarized along the Z axis. The main contribution to holographic grating formation with the vectors

$\vec{K}_p^{1-2} = \vec{K}_p^{3-4}$ and $\vec{K}_p^{2-4} = \vec{K}_p^{1-2} - \vec{K}_p^{3-4}$ on the Y cut $LiNbO_3$ gives the constant of the linear photogalvanic current along the Z axis. So, the interaction mechanism of the modes in the given case is a local one. This analysis showed that the stationary time solution took place while application of the following condition to frequencies of interacting waves

$$\omega_2 - \omega_1 + \omega_4 - \omega_3 = 0 \quad (1)$$

and the system of equations for their complex amplitudes $C_i(x)$ may be represented in the form

$$\frac{dC_1}{dx} = -i\sqrt{\frac{h_2}{h_1}} \{ (\Gamma_{1,2} |C_2|^2 + \Gamma_{1,4} |C_4|^2) C_1 + (\Gamma_{1,2} + \Gamma_{1,4}) C_2 C_4 C_3^* \exp(2i\Delta Kx) \} \quad (2)$$

$$\frac{dC_3^*}{dx} = i\sqrt{\frac{h_2}{h_1}} \{ (\Gamma_{1,2} |C_4|^2 + \Gamma_{1,4} |C_2|^2) C_3^* + (\Gamma_{1,2} + \Gamma_{1,4}) C_2^* C_4^* C_1 \exp(-2i\Delta Kx) \} \quad (3)$$

$$\frac{dC_2}{dx} = -i\sqrt{\frac{h_1}{h_2}} \{ (\Gamma_{1,2}^* |C_1|^2 + \Gamma_{1,4} |C_3|^2) C_2 + (\Gamma_{1,2}^* + \Gamma_{1,4}) C_1 C_3 C_4^* \exp(-2i\Delta Kx) \} - i\Gamma_{2,4} |C_4|^2 C_2 \quad (4)$$

92-18792



$$\frac{dC_4^*}{dx} = i\sqrt{\frac{h_1}{h_2}} \{ (\Gamma_{1,2}^* |C_3|^2 + \Gamma_{1,4} |C_1|^2) C_4^* + (\Gamma_{1,2}^* + \Gamma_{1,4}) C_1^* C_3^* C_2 \exp(2i\Delta Kx) \} + i\Gamma_{2,4} |C_2|^2 C_4^* \quad (5)$$

Here one may designate $\Gamma_{mn} = \gamma_m / [1 + i(\omega_m - \omega_n)\tau]$; $2\Delta K = 2K_{1x} - K_{2x} - K_{4x}$; γ_m is a coupling factor taking into account the overlapping of the light fields $E(y)$ of the interacting modes and induced perturbations of dielectric permittivity $\Delta\epsilon_{33}(y)$ parallel with electro-optic and photogalvanic properties of the waveguide^{6,7}; h_1 and h_2 - effective thickness of the waveguide for TE_p and TE_{p-1} modes, respectively; K_{mx} are projections of the light wave vectors to the X axis; τ is the time of Maxwell relaxation.

The detuning by frequency between the interacting modes gives non-locality of the medium response necessary for exponential amplification of the waves 1 and 3. Let us use the low-signal approximation considering the exciting beams to be prescribed and equal in amplitude.

$$C_2 = C_4 = C_p \quad (6)$$

and put additional limitation to the frequency detunings

$$\omega_1 - \omega_2 = \omega_3 - \omega_4 = \Delta\omega \quad (7)$$

From Eq.7 we find the equality of the coupling factors

$$\Gamma_{1,2} = \Gamma_{1,4} = 1/2 \Gamma \sqrt{h_1/h_2} \quad (8)$$

With account for conditions (6) and (8) the equations (2) and (3) are simplified significantly

$$\frac{dC_1}{dx} = -i\Gamma |C_p|^2 C_1 - i\Gamma C_p^2 \exp(2i\Delta Kx) C_3^* \quad (9)$$

$$\frac{dC_3^*}{dx} = i\Gamma |C_p|^2 C_3^* + i\Gamma (C_p^*)^2 \exp(-2i\Delta Kx) C_1 \quad (10)$$

The solution of the system of equations (9) and (10) for initial conditions $C_1(0) = 0$, $C_3^*(0) = C_{3,0}$ may be found in the form

$$C_1 = -iC_{3,0} (\Gamma(C_p)^2/\beta) \exp(i\Delta kx) \sin(\beta x) \quad (11)$$

$$C_3^* = C_{3,0} (\exp(-i\Delta kx)/\beta) \{ \beta \cos(\beta x) + i(\Delta k + \Gamma |C_p|^2) \sin(\beta x) \} \quad (12)$$

$$\text{where } \beta = \sqrt{(\Delta kx)^2 + 2\Delta k\Gamma |C_p|^2}.$$

The analysis of Eq.(11) and (12) shows that the maximum amplification of waves 1 and 3 by the exciting beams takes place if the condition

$$\Delta k + 2\Gamma' |C_p|^2 = 0 \quad (13)$$

Here Γ' is a real part of the complex coupling factor $\Gamma = \Gamma' + i\Gamma''$.

Thus the amplification of the signal beam 3 with frequency ω_3 by the exciting beams 2 and 4 leads in the scheme under consideration (Fig.1) to the generation of the beam 1 with frequency ω_1 propagating collinearly with the beam 3. The output power in this case will have a constant component $P_0 = P_1 + P_3$ and the time modulation with frequency $2\delta\omega$ and the modulation depth $m = 2\sqrt{P_1 P_3}/P_0$. The dependences of the values P_0 and $2\sqrt{P_1 P_3}$, normalized at $P_{3,0} \sim |C_{3,0}|^2$, on the parameter $Z = 2\sqrt{h_1/h_2} \Gamma |C_p|^2 x$ are represented in Fig.2,3 and 4. The calculations were performed using formulae (11) and (12) with account for the condition (13).

The analysis of equations (11), (12) and curves in Fig.2-4 show that for the values of the parameter $Z < 1$ the amplification depends

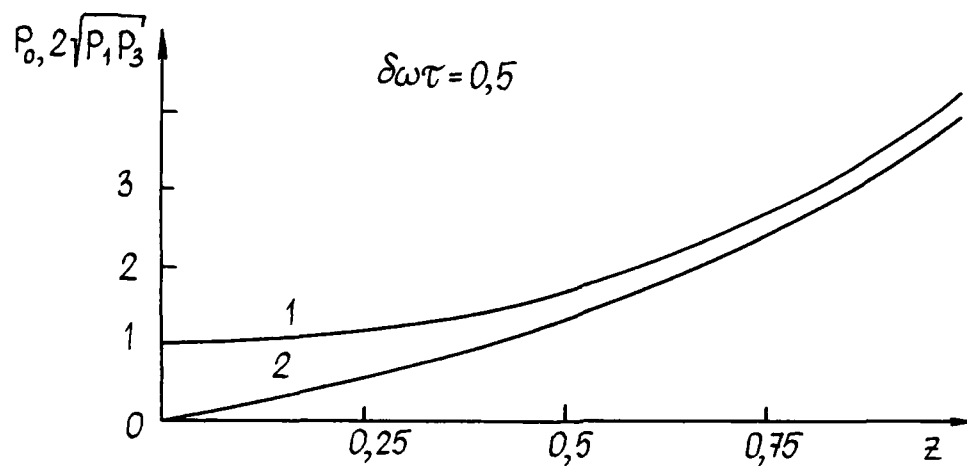


Fig. 2.

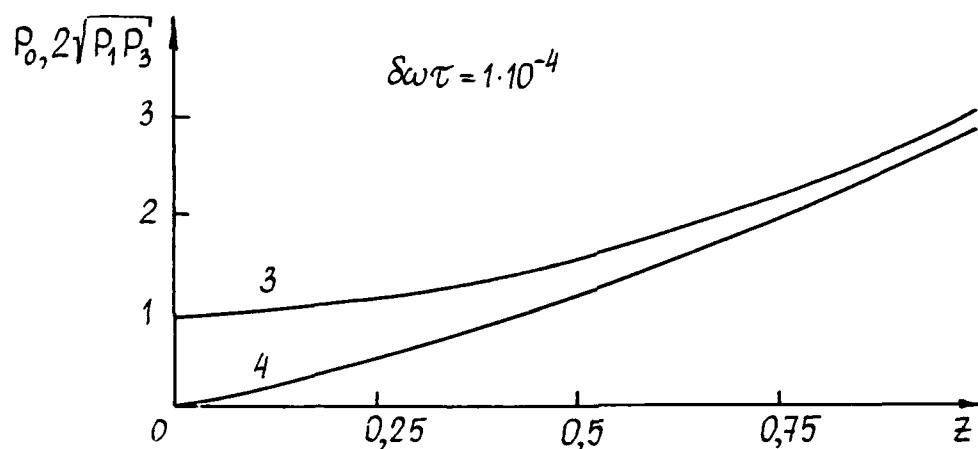


Fig. 3.

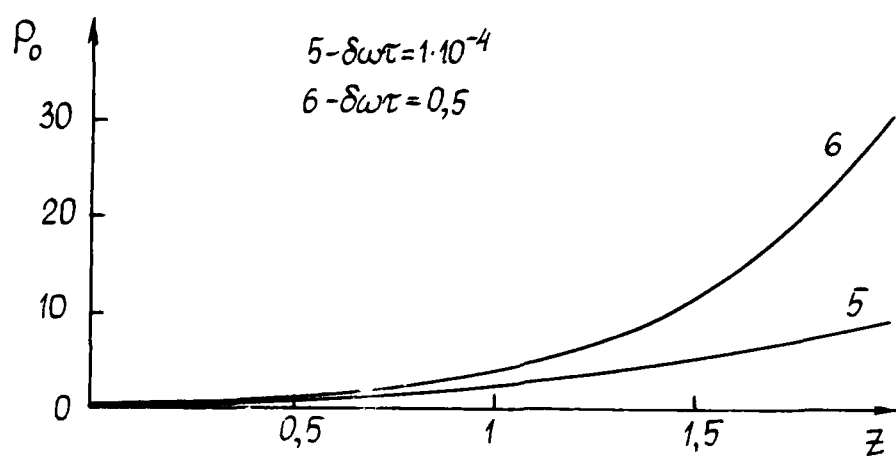


Fig. 4.

weakly on the value $\delta\omega\tau$ for both the constant component (curves 1 and 3) and the amplitude of oscillating part $2\sqrt{P_1 P_2}$ (curves 2 and 4). When increasing Z , the depth of the power modulation m is approximately a unit (1). However, for $Z > 2$ the maximum amplification of the signal beam takes place at $\delta\omega\tau = 0,5$ (curve 5).

The experimental investigation of the amplification of the signal beam 3(1) was performed for interaction TE_2-TE_3 at the light wavelength $\lambda = 633$ nm. In the experiments we used a planar waveguide $LiNbO_3$. The characteristics of this waveguide are shown in our previous papers^{5,6,9}. The powers of the exciting beams in the waveguide made up the values $P_2 \approx 0,15$ mW, $P_4 \approx 0,14$ mW. The power of the signal beam at the output in the absence of excitation was equal to $P_3(1) \approx 0,012$ mW. All beams were focused at the waveguide plane by external cylindrical lens with a focal distance $F \approx 250$ mm. Their aperture in the range of the interaction field of the waveguide was $\alpha \approx 50$ mkm. We estimated the length of the interaction field (the beam overlapping) as $l \approx 0,75$ mm.

While switching in the exciting beams coinciding with the signal beam by frequency (i.e. at $\delta\omega\tau=0$), the power of the latter was increased up to the value $P_{outp.}(1) \approx 0,018$ mW. In the experiments we found great sensitivity of the given interaction to the angle position asymmetry of the signal beam relative to the exciting beams. While tuning out the wave vector \vec{k}_3 from the central position, we observed the beam generation with the wave vector \vec{k}_1 that was not coincident with \vec{k}_3 .

From the experimental data and curve 3 represented in Fig.3 we estimated the value of the parameter $Z \approx 0,24$ for the case under investigation. With account for the pumping power and the interaction length, the estimation of the effective coupling factor gives the value $\gamma_1 \approx 2,6 \cdot 10^{-4}$ m/W. This value is in good agreement with the value $\tilde{\gamma} \approx (1-1,4) \cdot 10^{-4}$ m/W obtained in paper⁹ for the mode interaction TE_2-TE_3 in the given waveguide $LiNbO_3:Ti:Fe$.

References

1. S. Mallick, B. Imbert, H. Ducollet, J. P. Herriau, and J. P. Huignard, J. Appl. Phys., 63, 5660 1988.
2. L. B. Au and L. Solymar, IEEE J. Quant. Elect., 24(2), 163 1988.
3. L. B. Au, L. Solimar, K. H. Ringofer, Topical Meeting on Photorefractive materials, effects and devices.- January 17-19, Aussois, France, B4-1, 87 1990.
4. S. Odulov, Ukr. Fiz. Zh., 35(11), 1657 1990.
5. A. D. Novikov, S. G. Odulov, V. M. Shandarov, and S. M. Shandarov, Sov. Phys. Tech. Phys., 33(8), 969 1988.
6. G. Glazov, I. Itkin, V. Shandarov, E. Shandarov, S. Shandarov, J. Opt. Soc. Am., B7(12), 2279 1990.
7. I. Itkin, S. Shandarov, Zh. Tech. Fiz., 60(11), 147 1990.
8. I. Kuselyova, V. Obuhovskii, S. Odulov, Fiz. Tverd. Tela, 28(10), 2975 1986.
9. E. Shandarov, S. Shandarov, Opt. Spectrosk., (in press).

LIGHT-INDUCED SCATTERING IN PLANAR PHOTOREFRACTIVE WAVEGUIDES

A. Bashkirov, G. Glazov, I. Itkin,
N. Pankovetz and S. Shandarov

AD-P006 805
[Barcode]

The light-induced scattering is observed in photorefractive crystals due to noise hologram recording characterized by a complex angular spectrum¹. The formation of such holograms in planar waveguides has a number of peculiarities because the recording speed of a waveguide holographic grating depends on its period².

Let us consider the case (Fig.1), when in a planar waveguide a base wave with a plane wave front interacts with spatially fluctuating wave characterized by a complex angular spectrum

$$E_s = E_v(y) \sum_n A_n \exp[-i(k_0 x' \cos \alpha_n - k_0 z' \sin \alpha_n)], \quad (1)$$

where $E_v(y)$ is a field distribution of the mode by the depth of the waveguide; A_n - is amplitude of n -component of the angular spectrum propagating under the angle α_n ; k_0 is a module of the wave vector. The amplitude of a base wave A_0 was considered to increase significantly the amplitude of any angular components. Such model is close to the real case of radiation input to the waveguide by means of a prism when the waveguide scattering is determined, mainly, by inhomogeneities in the field of a gap "prism - waveguide layer".

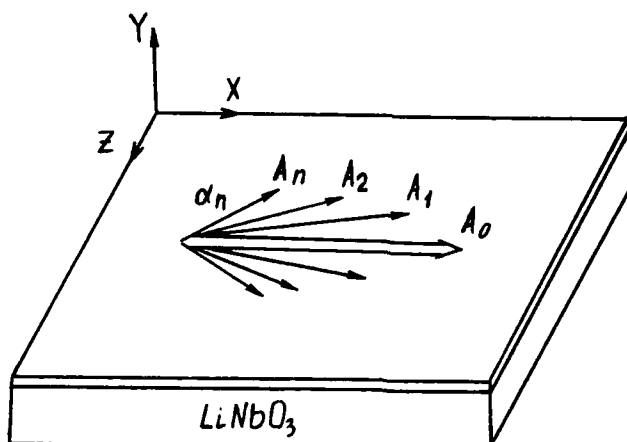


Fig.1. Scheme of light-induced scattering formation in planar waveguide.

In a photorefractive waveguide each scattered wave records a holographic grating with more powerful base beam. As a result of diffraction of the base beam at such gratings there is a redistribution of energy by the components of the angular spectrum. Equations of coupling waves in the case when E_s is a random function of the coordinate Z (Fig.1) have the form

92-18793



$$\begin{aligned}\frac{dC_0}{dx} &= -i \frac{k_0}{4n^*} \sum_m \Gamma_m C_m, \\ \frac{dC_n}{dx} &= -i \frac{k_0}{4n^*} \frac{\Gamma_n}{\cos \alpha_n} C_0.\end{aligned}\quad (2)$$

Here C_0 , C_n are complex amplitudes of a base wave and angular n -component; n^* is an effective refractive index of the waveguide mode; Γ_n is an overlapping integral² that characterizes a planar holographic grating formed by the base beam with each scattered wave. For initial section of the recording, when we may neglect the conduction currents of the overlapping integral is represented in the form

$$\Gamma_n = \gamma_n \frac{4n^* A_0 A_n t \cos \alpha_n}{k_0}.\quad (3)$$

In case when E_0 is a homogeneous random function of the coordinate Z , from Eqs.(2) we obtain the mean value of the intensities of the base and scattering beams

$$\langle |C_0(x)|^2 \rangle = A_0^2 \cos^2 \left[\frac{k_0}{4n^*} A_0^2 Q x t \right],\quad (4)$$

$$\langle |C_n(x)|^2 \rangle = \langle A_n A_n^* \rangle \left\{ 1 + \left[\frac{\gamma_n}{Q \cos \alpha_n} \right]^2 \sin^2 \left[\frac{k_0}{4n^*} A_0^2 Q x t \right] \right\}.\quad (5)$$

The constant $Q = \sqrt{\sum_m \frac{A_m^2}{A_0^2} \frac{\gamma_m^2}{\cos^2 \alpha_m}}$ defined the speed of the intensity decreasing of the base beam represents the generalized parameter that characterized the degradation properties of the given waveguide structure.

For modelling the processes of the light-induced waveguide scattering, the input angular distribution was prescribed in the form of discrete angular component set having complex random amplitudes non-correlated between each other with prescribed values of dispersions. The amplitude of the base wave A_0 exceeded 100 times the maximum value of any angular component $|A_n|$. The numerical calculation was performed for a model planar waveguide $\text{LiNbO}_3:\text{Fe}$ of YZ orientation parameters of which were cited in paper². As it was pointed out in this paper, the dependence of the overlapping parameter γ on the period of a holographic grating Λ .

The kinetics of the formation of the light-induced scattering picture in a model waveguide at the uniform distribution of dispersion of the angular spectrum component amplitudes is represented in Fig.2. While calculation the blending by ten input realizations was performed. As it is seen from Fig.2, while uniform distribution at the input, the energy of the base beam is transferred, mainly, to the components scattered under the maximum angles as holographic gratings formed by them have lesser period and are recorded quicker on the given cut².

There is one more case that is close to really observed picture of scattering which occurs in the waveguides on the Y cut of a LiNbO_3 crystal when the values of dispersions of angu-

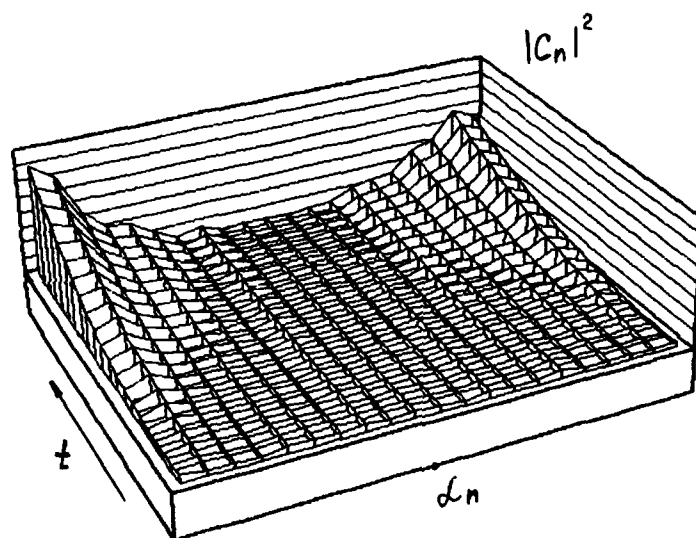


Fig.2. Kinetics of the formation of the light-induced scattering at the uniform distribution of dispersion of the angular spectrum component amplitudes.

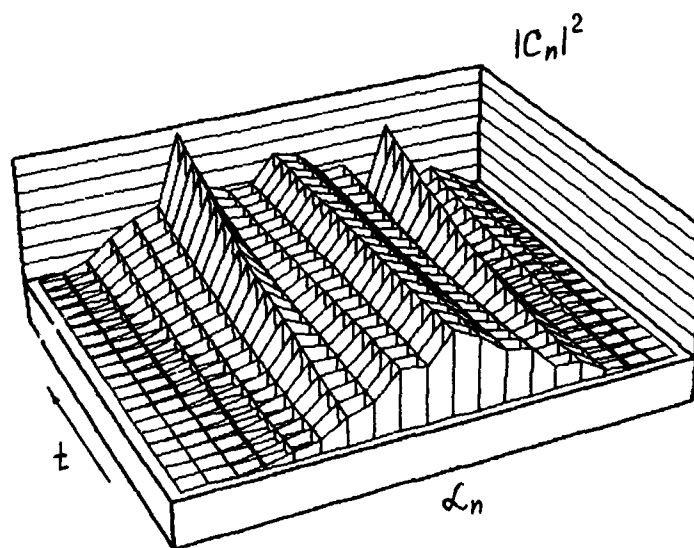


Fig.3. Kinetics of the formation of the light-induced scattering at the Gauss distribution of dispersion of the angular spectrum component amplitudes.

lar components have Gauss distribution. The time dependence of mean intensities for this case is represented in Fig.3. The marked optima in Figure are explained by the fact that some conflicting factors such as the initial amplitude and the period of the formed holographic grating act on the amplification of each angular component in the waveguide.

The degradation characteristics of photorefractive waveguide structures $\text{LiNbO}_3\text{:Ti:Fe}$ were studied experimentally. The waveguides were made at the plates on the Y cut LiNbO_3 by means of Ti diffusion ($t_d = 7$ h at $T = 1000^\circ\text{C}$) with a subsequent activation of the waveguide layer by Fe. The activation was performed by both thermodiffusion and implantation methods with additional annealing at $T = 950^\circ\text{C}$. Light with $\lambda = 633$ nm was injected into the investigated waveguides with the help of prisms from TiSrO_3 . Radiation power of the TE_0 mode propagation along the crystallophysic OX axis made up ~ 0.4 mW.

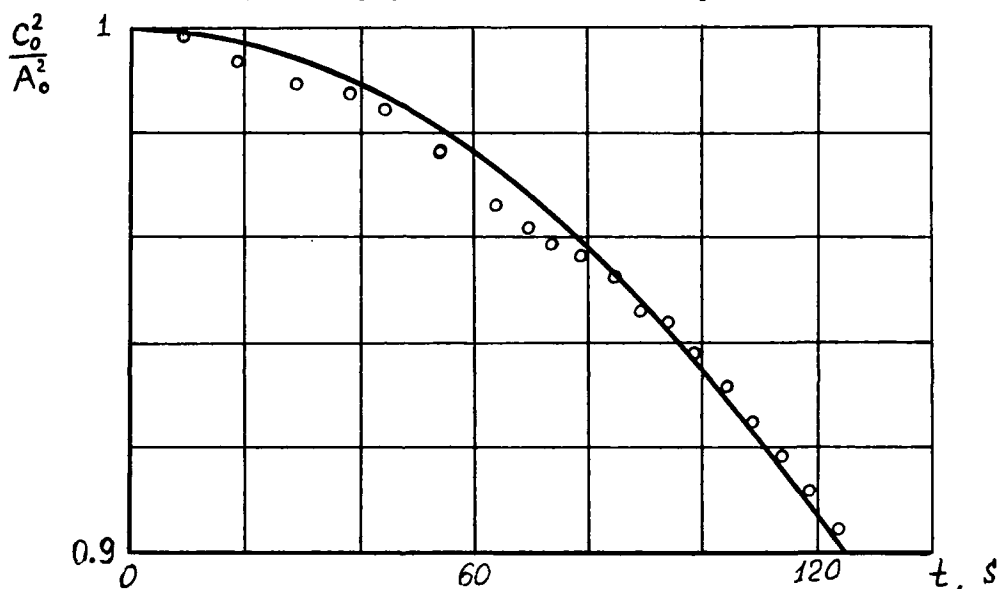


Fig. 4.

The kinetics of decreasing the light wave amplitude at the output was approximated by expression (4) (Fig.4). The parameter of degradation Q that formed the value equal to $\sim 3 \cdot 10^{-6}$ J/m for the TE_0 mode of $\text{LiNbO}_3\text{:Ti:Fe}$ waveguides and that was independent on the methods of activating impurity doping was determined by the method of the least squares. The parameter Q for TE_1 mode had a value by one order less that was explained by the non-uniform impurity distribution by the depth of the waveguide.

References

1. E.M.Avakjan, K.G.Belabaev, S.G.Odoulov Sov.Phys.Sol. Stat., v.25, N 11, 3274 1983.
2. G.Glazov, I.Itkin, V.Shandarov, E.Shandarov, S.Shandarov, J.Opt.Soc.Am., B7(12), 2279 1990.

PHOTOREFRACTIVE PARAMETRIC INTERACTION OF VOLUME
AND LEAKY OPTICAL WAVES IN PLANAR WAVEGUIDE ON
LITHIUM NIOBATE

V. M. Shandarov

Institute of Automatic Control Systems and
Radioelectronics
40 Lenin Avenue, 634050, Tomsk, USSR, Phone 382-496278

AD-P006 806



In optical waveguides with high photorefractive sensitivity the frequency - degenerate four - wave interactions are observed as well as in optical nonlinear materials [1]. Several types of interactions nonanalogous for the processes in volume materials, can be realized in optical waveguides because of specifics of their properties.

In this report the results of observation and investigation of the parametric interaction between volume and leaky waves in planar waveguide $\text{LiNbO}_3:\text{Ti:Fe}$ that have not been observed earlier are presented.

1. Schemes and conditions of experiments.

The optical waveguides were formed in LiNbO_3 Y - cut substrates by sequential Ti and Fe diffusion. In the direction of $X + 40^\circ$ at wavelengths of argon laser radiation in waveguides to 9 TE leaky waves could be excited. In experiments their excitation was performed while reflecting from waveguide surface of ordinary polarized light radiation in the substrate, if its incidence angle α corresponded to the condition:

$$\alpha = \arcsin(n_m/n_o),$$

where n_m is effective refractive index of leaky wave and n_o - the refractive index of ordinary light wave in substrate (Fig.1a).

The radiation of argon laser was nonpolarized, and two schemes for leaky waves excitation were used in experiments. Here were no special actions for radiation polarization in the first scheme, and extraordinary wave was reflected from the waveguide surface under the same angle as an ordinary one. In the second scheme the splitting of a laser beam into two rays polarization of which corresponded to the ordinary and extraordinary waves for the given waveguide orientation was used. The extraordinary wave incidence angle at waveguide surface in this case was non - equal of similar angle for ordinary wave and may be varied (Fig.1b).

2. Experimental results.

The effect of photorefractive parametric scattering was observed earlier in planar waveguide $\text{LiNbO}_3:\text{Ti:Fe}$ on

92-18794



waveguide modes and in $\text{LiNbO}_3\text{:Ti:Cu}$ waveguide on leaky modes in a coupling region of waveguide with prism [1,2]. Its main point consists in the parametric amplification of "noisy" holographic gratings that are formed due to photorefractive recording by interference of the incident light beam with secondary waves generated by the light scattering at waveguide perturbations. In [1,2] because of parametric amplification the development of diffraction spots on m - lines of lower - indices modes at excitation in waveguide of guide or leaky n - index mode has been observed.

For the first time the effect of leaky and volume light waves parametric interaction in waveguide $\text{LiNbO}_3\text{:Ti:Fe}$ was discovered in the first experimental scheme at excitation in the waveguide of TE_0 leaky mode. After a while after its excitation on m - lines corresponding to leaky TE_4 - TE_5 modes, the diffraction spots arranged almost symmetrically relative to the point of a cross section of these lines by the plane of incidence separated and developed (Fig.2). In stationary state these spots had the angular size as well as laser beam. Depending on the wavelength and radiation power they appeared on one or two m - lines. It should be noted that the light energy density in waveguide was not great because a laser beam was not focused. These parametric scattering pictures differed greatly from the observed ones earlier [1,2], when at excitation in the waveguide of some mode similar spots appeared on m - lines of lower indices modes.

This is our interpretation of this effect. In the process of TE_0 mode excitation there is photorefractive recording of many "noisy" gratings leading to the light scattering into all waveguide modes in a wide space angle. At the same time the presence of incident and reflected waves with extraordinary polarization may be considered as extraordinary wave propagation with propagation constant

$$\beta = k_0 n_e \cdot \sin(n_m/n_0),$$

where n_0 - refractive index of extraordinary wave, in waveguide region. The photorefractive interaction of this wave with scattered ones into various waveguide modes leads to the development of diffraction spots observed in experiments (Fig.3).

For explanation of this interpretation further experimental investigations were performed on the setup corresponding to the second scheme (Fig.1b). The following experiments are realized.

1. The nonpolarized argon laser radiation by polarizers was converted into linearly - polarized and conditions of these diffraction spots parametric generation were investigated. It is found that parametric generation of these spots is observed if in a laser beam there are components with polarization corresponding to polarization of ordinary

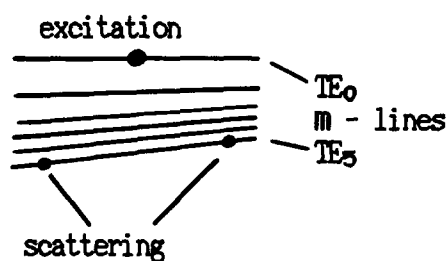
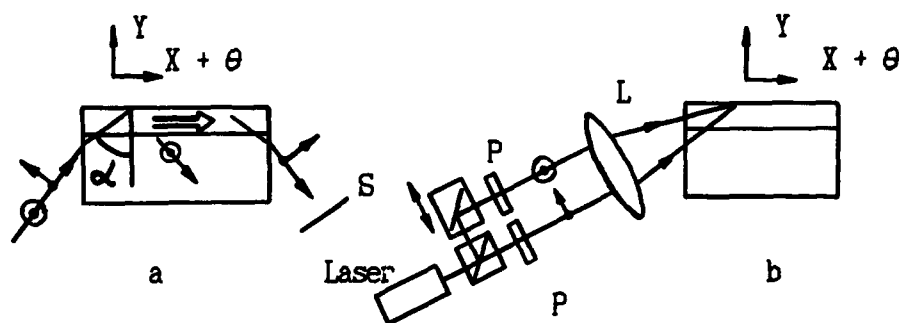


Fig.2. Schematic of scattering pattern on the screen

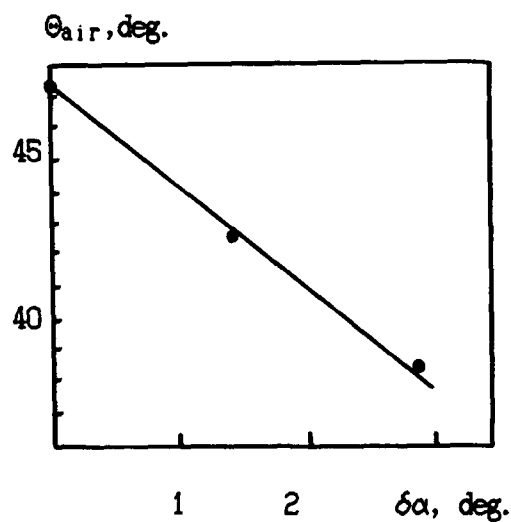
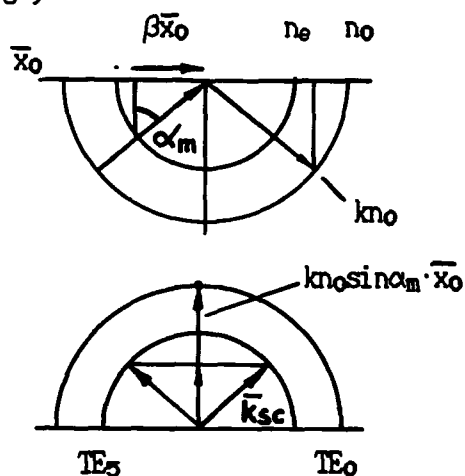


Fig.4. Scattering angle dependence on "o - e" sliding angles difference



and extraordinary waves in a waveguide substrate. These parametric effects were not observed for only ordinary or extraordinary polarization of light. However, in case when the light had ordinary polarization which then was changed into extraordinary one, also the parametric generation of spots was observed as well as in case of simultaneous influence of beams with orthogonal polarizations.

2. In second experimental scheme the spatial splitting of beams with both ordinary and extraordinary polarizations with possibility of the angle variation between these beams was realized (Fig.1b). The variation of this angle led to the change of diffraction parametric spots angular position. The calculations showed that a proposed interpretation of observed effects describes rather accurate the measured angular positions of these spots and the character of their variation while changing the angle between the beams with different polarizations. Here, the calculated dependence of the angular distance between the generated parametric spots corresponding to the TE_5 mode at excitation in waveguide of leaky mode TE_0 on sliding angle difference of ordinary and extraordinary beams relative to the waveguide surface at $\lambda = 488$ nm is represented in Fig.4. Here also the experimentally measured values of the given angles are represented.

3. Excitation in the waveguide of higher order leaky modes showed that this parametric effect is observed by excitation of modes $TE_0 - TE_3$. The variation of parametric spots angular place also good agreed with model calculations (in this case the first experimental scheme was used). It should be noted that while excitation in the waveguide of TE_3 leaky mode the "usual" parametric diffraction maxima described in [1] are observed as well as investigated ones in this research.

4. The described effect was also observed on the wavelength of He - Ne laser (633 nm) at excitation TE_4 leaky mode in the waveguide. The parametric spots on m -line of TE_3 mode were generated in this case.

In conclusion it should be noted that the studied effect for control of light waves in waveguide by external light beams may be of great interest.

R e f e r e n c e s

1. A.D.Novikov, S.G.Odoullov, V.M.Shandarov, S.M.Shandarov. JTF (USSR), 1988, V.58, N8, P. 1604 - 1606.
2. A.Novikov, S.Odoullov, V.Shandarov, S.Shandarov. Parametric intermode scattering in $LiNbO_3$ planar waveguides. In: Proc. Top. Meet. on Photorefractive Materials, Effects and Devices. Orsay, France, 1990.

AD-P006 807



**Investigation of Photorefractive Waveguides Fabricated by
Excimer Laser Ablation and Ion-Implantation.**

K.E.Youden and R.W.Eason

Optoelectronics Research Centre and Department of Physics

Southampton University, Southampton, U.K.SO9 5NH

Tel: 0703 595000

M.C.Gower

Central Laser Facility, Rutherford Appleton Laboratory,

Chilton, Didcot, Oxfordshire, U.K. OX11 0QX

Tel: 0235 821900

92-18795

The fabrication of thin films optical waveguides of photorefractive materials is particularly desirable for applications in integrated optics. It is also of interest because the guided-wave intensity-length product can be considerably larger than in bulk media because of the optical confinement within the waveguide. The increased intensity-length product may therefore allow much faster response times than in the bulk (typically by a factor of $\approx 10^3$ - 10^4). Thin crystalline films can be fabricated by a variety of techniques such as RF sputtering, flash evaporation,

molecular beam epitaxy and liquid phase epitaxy. However, the films grown are often of the incorrect (or variable) composition and phase and are rarely of good optical quality. We discuss here two methods that we have investigated for producing optical waveguides in several different photorefractive materials.

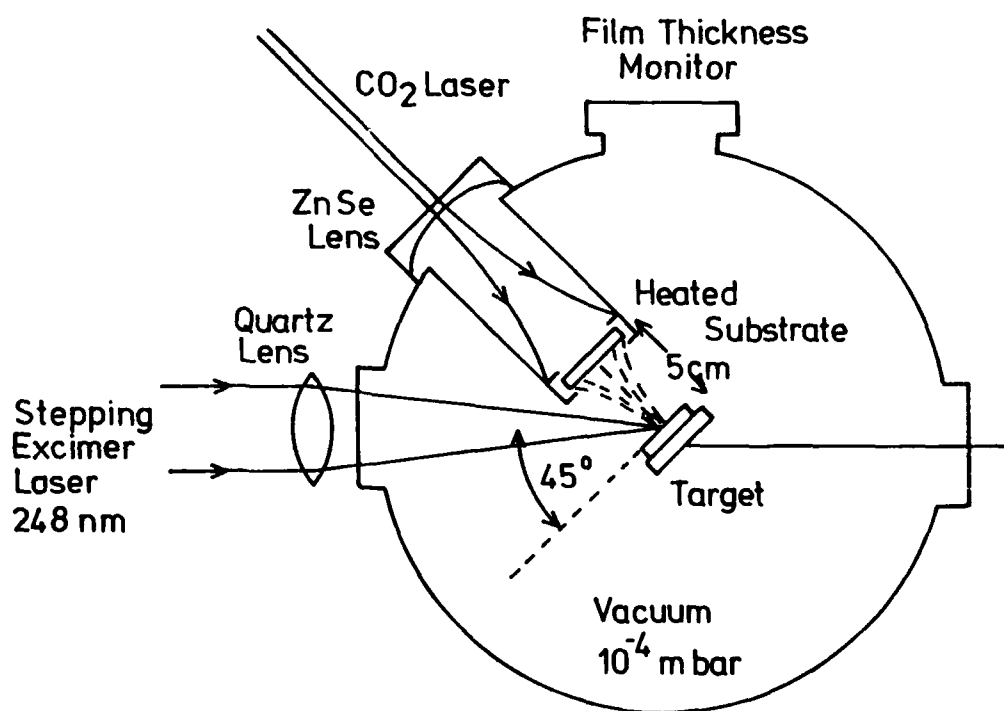


Figure 1. Experimental arrangement for excimer laser ablation.

Laser ablation provides a simple and convenient method for depositing films of a wide range of materials which allows the stoichiometry of a single target to be easily reproduced at the substrate. The experimental arrangement used to deposit such films is shown in figure 1. We

report the growth of waveguides of the photorefractive material Bi₁₂GeO₂₀ by the technique of excimer laser ablation. Using x-ray diffraction these films have been shown to be epitaxial

crystalline layers of [310] orientation and of the correct stoichiometry and phase. Two waveguide modes (one TE and one TM) have been observed using the arrangement in figure 2, corresponding to effective waveguide refractive indices of 2.40 and 2.37 respectively^[1].

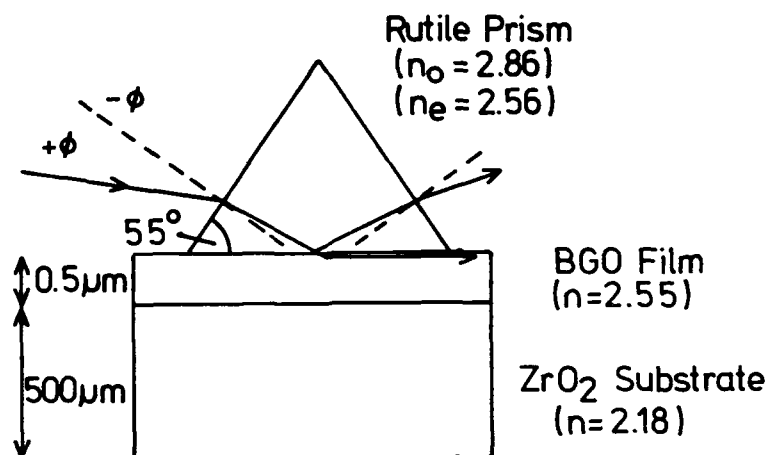


Figure 2. Arrangement for Prism Coupling Light into a Waveguide.

Secondly, work on waveguides formed by H^+ and He^+ ion-beam implantation of bulk crystals of $\text{Sr}_x\text{Ba}_{1-x}\text{Nb}_2\text{O}_6$ is also presented. Ion-beam implantation is an established technique for fabricating waveguides of depth in the range $1\mu\text{m}$ to $20\mu\text{m}$, via refractive index variations produced in the material due to interactions with the crystal lattice. Typically a barrier layer of lower refractive index occurs (see figure 3), which allows optical confinement within the waveguide layer^[2]. Photorefractive two-beam coupling, degenerate four-wave mixing and limited experiments on self-pumping, have been undertaken in Ce-doped crystals of SBN:52 and SBN:65, in multimode waveguides of typical dimensions of between $4\mu\text{m}$ and $15\mu\text{m}$. Results so far demonstrate that although problems may exist concerning changes to the bulk electro-optic coefficient, and anisotropic absorption may be induced via the ion-beam implantation process,

the technique can provide a useful means of achieving speed-up effects, via local intensity increase characteristic of the photorefractive nonlinearity.

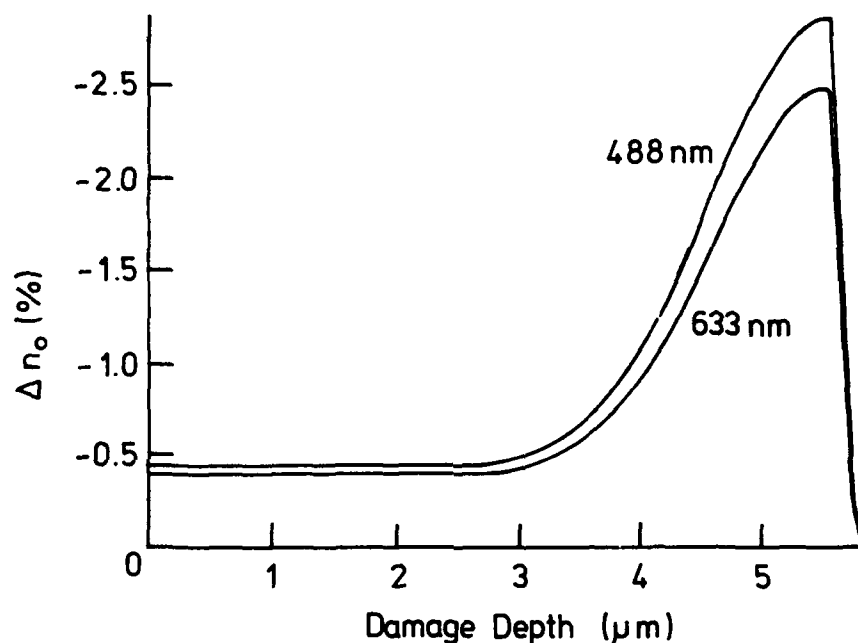


Figure 3. Refractive index profile for the ordinary ray in a He⁺ implanted waveguide.

We present results on the above techniques, and discuss the applications of such waveguide materials in the context of real-time integrated optical configurations.

[1] Epitaxial growth of Bi₁₂GeO₂₀ Thin Film Optical Waveguides Using Excimer Laser Ablation.

K.E. Youden, R.W. Eason, M.C. Gower. Submitted to Appl. Phys. Letts.

[2] Optical Effects of Ion Implantation. P.D. Townsend. Rep. Prog. Phys. **50** (1987) 501-558.

Agranat, A. — MA2
 Amrhein, P. — MB8, TuA8
 Anderson, D. Z. — WC5, WC6
 Austin, R. F. — MC1

Bacher, G. D. — MC4, MC12, TuA2
 Barker, R. C. — WB4
 Barman, D. — MA6
 Barrett, G. R. — TuC18, TuC21
 Barry, N. — WC2
 Bashaw, M. C. — WB4
 Bashkurov, A. — WC26
 Beckwith, P. H. — WC18
 Belić, Milivoj — WC20
 Benkert, Claus — WC5, WC6
 Biaggio, I. — WC3
 Biernacki, Anne Marie — TuB4
 Bledowski, A. — WC22
 Bogodaev, N. V. — MC10, TuA3, WC10
 Boothroyd, S. A. — WC18
 Boudebs, G. — TuA1
 Boyd, Robert W. — WC20
 Brost, George A. — TuC19, TuC20
 Burland, D. M. — MA1
 Buse, K. — WB3

Campbell, Scott — MB4
 Cartwright, C. M. — TuB3
 Chan, L. — WC18
 Chang, J. Y. — MC2, WB6
 Chang, Ming-Wen — WA7
 Chang, Tallis Y. — MC7, TuC17
 Chen, Huanchu — MA3, MA4
 Cheng, Li-Jen — TuA5
 Ching-Cherng, Sun — WA7
 Choonghoon, Oh — WA4
 Chrostowski, J. — WC18
 Clark, William W. III. — WC14
 Clement, A. E. — WB5
 Cronin-Golomb, Mark — MC9, TuA7, TuB4, WC12
 Cudney, R. S. — MC4, TuA2

Dadi, Wang — WA5
 Dai, Li-Kuo — WC21
 Dainty, J. C. — WA2
 Daliang, Sun — MA4, WC13
 Damzen, M. J. — WC2
 Delboubé, A. — MC6
 Denz, C. — MD1
 Domash, Lawrence H. — TuB6
 Ducharme, S. — MA1
 Duelli, M. — WC7
 D'yakov, V. A. — MC13

Eason, R. W. — TuB1, WC9, WC15, WC16, WC28
 Egorov, N. N. — TuC14
 Eliseev, V. V. — MC12
 Ennouri, A. — TuC9
 Ewbank, M. D. — MB3

Fainman, Yeshaiah — MD2, TuB2
 Feinberg, Jack — MC4, MC12, TuA2, WA, WC4
 Feldman, B. J. — MC8
 Feldman, R. D. — MC1
 Fiddy, M. A. — WC13
 Fischer, Baruch — MB2
 Fish, D. — MC11, TuC18
 Fogarty, Gerard — TuA7
 Ford, Joseph E. — MD2, TuB2
 Fredericks, George — MD4
 Fry, Edward S. — WA4
 Fugera, S. N. — WB5

Garmire, Elsa M. — TuC16, TuC19
 Garrett, M. H. — MC2, WB6
 Gilbreath, G. C. — MC8, WB5
 Gillespie, W. A. — TuB3
 Glass, A. M. — MC1, TuD
 Glazov, G. — WC26
 Gnatovskii, A. — MB1, MC15, TuA3, WC19
 Gou, Yin-Shun — WC21
 Goukov, M. — TuC22
 Gower, M. C. — MC28
 Gravey, P. — WA3
 Gu, Claire — MB4, MC7, WC21
 Guanyin, Zhang — MA3
 Günter, P. — MA5, MB8, TuA, TuA8, TuC13, WC3, WC7
 Guruswamy, Chitra — WC17

Haian, Miao — TuB5
 Hall, T. J. — MC11, TuC18, TuC21
 He, X.H. — TuC24
 He, Q. Byron — MB4
 Hebler, Verena — WC5
 Hellwarth, R. W. — TuC8, TuC10
 Hesse, H. — WB3
 Hesselink, Lambertus — MD, TuA4
 Hofmeister, R. — MA2
 Holtmann, L. — TuC22, WB3
 Hong, John — MC7
 Hongzhi, Kong — MC9
 Horowitz, Moshe — MB2
 Huanchu, Chen — MA3, MA4
 Huignard, J. P. — MC6, TuB
 Hussain, Ghazanfar — WC9

Ilnskii, A. V. — TuC7
 Ing, R. K. — WC8
 Ingold, M. — WC7
 Itkin, I. — WC26
 Ito, Fumihiko — MC14
 Itoh, Masahide — TuB5, TuC5
 Ivanov, M. A. — TuC25
 Ivleva, L. I. — MC10, WC10

Jacobs, P. — WB1
 Jae-Hoon, Kim — TuA5
 James, S. W. — WC15, WC16
 Jang, Ju-Seog — WC5
 Jenssen, H. P. — MC2, WB6
 Jian, Ma — MD2
 Jiang, Quanzhong — MA4
 Johansen, P. M. — TuB7
 Johnson, Kristina M. — MD4, MD6
 Jungen, R. — WC23
 Ju-Seog, Jang — WC5

Kargin, Y. F. — MB1, TuC4
 Khoury, Jehad A. — TuB4, WC12
 Khromov, Andrei L. — TuC3
 Kim, Jae-Hoon — TuA5
 Kitayama, Ken-ichi — MC14
 Klein, Marvin B. — TuA6, TuC16, TuC19
 Koehler, Steffen D. — TuC16
 Kong, Hongzhi — MC9
 Korol'kov, S. A. — MB5, MC13
 Korshunov, A. S. — MC10
 Kostritskii, S. M. — TuC15
 Kowarschik, R. — MB7
 Krätzig, E. — TuC22, WB3
 Królikowski, Wiesław — MC9
 Kröse, H. — WB1
 Kudzin, A. — TuC2
 Kukhtarev, N. V. — MB1, MC15, TuA3, WC19
 Kumar, J. — MA6
 Kuper, G. — WB3
 Kuroda, Kazuo — TuB5, TuC5
 Kuz'minov, Y. S. — MB5

Lahrichi, Adil — MD4
 Lapaeva, S. — MC15
 Launay, J. C. — TuC9
 Lecoq, J. P. — TuA1
 Lee, Sing H. — MD2, TuB2
 Leu, G. — WC13
 Leyva, Victor — MA2, MD3
 Li-Jen, Cheng — TuA5
 Li-kuo, Dai — WC21
 Lin, F. C. — WC13
 Litvinov, R. — TuC12
 Liu, Duncan T. H. — TuA5
 Liu, H. — WC1
 Liu, Simin — MA3
 Loheide, S. — WB3
 Lu, Xinliang — MA4

Ma, Jian — MD2
 Ma, T. P. — WB4
 MacCormack, Stuart — TuB1
 Maglevanii, V. — WC19
 Mamaev, A. V. — MB5, MC13, WA1
 Maniloff, Eric S. — MD6
 Mathey, P. — TuC11
 Mazur, A. P. — WA6
 McFarlane, Ross A. — WB2
 Melloch, M. R. — MA7, MA8
 Miao, Hai Yan — TuB5
 Midwinter, J. E. — MD5
 Millerd, James E. — TuC16, TuC19
 Ming-Wen, Chang — WA7
 Mobasher, B. — MD5
 Moerner, W. E. — MA1
 Moisan, J. Y. — TuC9
 Mokrushina, E. V. — TuC1
 Monchalin, J. P. — WC8
 Montemezzani, G. — MA5

Nestiorkin, O. P. — WC10, WC24
 Nolte, D. D. — MA7, MA8, MC3

Notni, G. — MB7
 Nouchi, P. — TuC10
 Novikov, A. D. — WA6, WC22

O'doulov, S. G. — TuC22, WA6, WC23
 Ogura, Iwao — TuB5
 Oh, Choonghoon — WA4
 Okamura, Hideki — TuB5
 Okazaki, Y. — TuC5
 Oldekop, E. — WC11
 Olson, D. H. — MC1
 Otten, J. — WC22

Padmabandu, G. G. — WA4
 Panchenko, T. — TuC2
 Pankovetz, N. — WC26
 Partanen, J. P. — TuC8, TuC10
 Partovi, A. — MC1
 Pauliat, G. — MD1, TuC11
 Peixian, Ye — WA5
 Penin, A. N. — TuC23
 Petersen, P. M. — TuB7
 Petrov, Michael P. — TuC3
 Pfändler, S. — MA5
 Phu, X. Nguyen — TuA1
 Picoli, G. — WA3
 Pierce, R. M. — MC4, TuA2
 Pigida, A. — TuA3, WC19
 Pollak, T. M. — WB, WB6
 Polozkov, N. M. — MC10, TuA3, WC10
 Poon, P. — MD5
 Popov, V. — WC25
 Possenriede, E. — WB1
 Potapovich, Y. — TuC2
 Powell, A. K. — MC11, TuC18, TuC21
 Powell, R. C. — WC1
 Prokof'ev, V. V. — TuC1
 Pryadko, L. — MB1
 Psaltis, Demitri — TuD2

Quanzhong, Jiang — MA4

Rabinovich, W. S. — MC8
 Rajbenbach, H. — MC6
 Rakuljic, George — MD3
 Rana, R. S. — MC3
 Reeves, R. J. — WC1
 Rehman, S. — WC5
 Ringhofer, K. H. — MB1, MC, WC22
 Rivoire, G. — TuA1
 Roosen, G. — MD1, TuC11
 Rubinina, N. M. — TuC23, TuC25, TuC26
 Rytz, Daniel — MA

Saar, Amir — MB6
 Saffman, M. — WC5, WC6
 Salamo, Gregory J. — WC14
 Sasaki, Hironori — MD2, TuB2
 Saxena, R. — TuC17
 Schadt, M. — WC7
 Schirmer, O. F. — WB1
 Schroeder, W. Andreas — MC5
 Schwartz, Robert N. — WB2
 Scott, J. C. — MA1
 Scott, S. — MA6

Segev, Mordechai — MB6
 Selviah, D. R. — MD5
 Semenets, T. — MB1
 Shandarov, E. — WC25
 Shandarov, S. — TuC12, WC25, WC26
 Shandarov, V. M. — WC27
 Sharp, E. J. — WC14
 Shchapov, F. Y. — TuC25
 Shepelevich, V. V. — TuC14
 Shershakov, Y. P. — WC10
 Shimura, Tsutomu — TuB5, TuC5
 Shkunov, V. V. — MB5, MC10, MC13
 Short, K. T. — MC1
 Siahmakoun, Azad — WC11
 Skettrup, T. — TuB7
 Skorikov, V. M. — TuC4
 Smirl, Arthur L. — MC5
 Snejnoy, G. — TuC2
 Sochava, S. L. — TuC1, WA2
 Sokolov, I. A. — TuC6
 Song, Yongyuan — MA3, MA4
 Soskin, M. S. — WA6
 Soutar, C. — TuB3
 Stark, Thomas S. — MC5
 Steier, William H. — TuA6
 Steiner, Bruce — TuA7
 Stepanov, S. I. — TuC1, TuC6, WA2
 Stizza, S. — TuC26
 Strohkendl, F. P. — TuC19
 Sturman, B. I. — TuC22, WA8, WC22
 Sun, Ching-Cherng — WA7
 Sun, Daliang — MA4, WC13
 Sylla, M. — TuA1

Taketomi, Yoshinao — MD2, TuB2
 Tang, S. H. — TuC24
 Tao, S. — MD5
 Tapiero, M. — TuC9
 Tayebati, Parviz — MA6, MC2, TuB6
 Temple, Doyle A. — WC17
 Teng, Y. Y. — WC13
 Timotijević, Dejan — WC20
 Trivedi, Sudhir — TuA6
 Troth, R. C. — WA2
 Tschudi, T. — MD1, WC23

Vachss, F. R. — MB3, MC7
 Valley, George C. — MC5
 Vazquez, R. A. — MB3
 Verbitskii, V. — TuA3, WC19
 Vieux, V. — WA3
 Vola, J. P. — TuC9
 Volk, T. R. — TuC25, TuC26
 Volkov, V. V. — TuC4
 Volyar, A. — MC15

Walsh, C. A. — MA1
 Wang, Dadi — WA5
 Wang, Q. N. — MA7

Wang, Z. Q. — TuB3
 Warde, C. — MC2, WB6
 Wechsler, Barry A. — TuC19, WB2
 Wilde, J. P. — TuA4
 Williamson, Richard — TuD1
 Wolffer, N. — WA3
 Wood, G. — WC14
 Woods, Charles L. — TuB4, WC12
 Wu, Yuanqing — MA3

Xia, P. — TuC8
 Xinliang, Lu — MA4
 Xu, Jingjun — MA3

Yanchuk, Z. — MB1
 Yang, T. — WC13
 Yao, X. Steve — WC4
 Yariv, Amnon — MA2, MB6, MD3
 Ye, Peixian — WA5
 Yeh, Pochi — MB4, WC21
 Yin-Shun, Guo — WC21
 Yongyuan, Song — MA3, MA4
 Youden, K. E. — WC28
 Yuanqing, Wu — MA3

Zabrodin, K. N. — TuC23
 Zel'dovich, B. Y. — WC10
 Zgonik, Marko — TuC13, WC3
 Zhang, Guanyin — MA3
 Zhang, H. Y. — TuC24
 Zhang, Zhiguo — WA5
 Zhiguo, Zhang — WA5
 Ziari, Mehrdad — TuA6
 Zielinger, J. P. — TuC9
 Zozulya, A. A. — MB, MB5, MC12, MC13, WA1
 Zydzik, G. J. — MC1

TECHNICAL PROGRAM COMMITTEE

Mark Cronin-Golomb, Cochair
Tufts University

Marvin Klein, Cochair
Hughes Research Laboratories

Materials

Vladimir Fridkin
Institute of Crystallography, USSR

Alastair Glass
AT&T Bell Laboratories

Peter Gunter
Swiss Federal Institute of Technology, Switzerland

Tom Pollak
Sanders Associates

Daniel Rytz
Sandoz Optoelectronique, Switzerland

Sergei I. Stepanov
Ioffe Institute, USSR

Physics of Photorefractive Effect

Milivoj Belic
Institut za Fiziku, Yugoslavia

Baruch Flecher
Technion-Israel Institute of Technology

Serguey G. Odulov
Ukrainian Academy of Sciences, USSR

Klaus H. Ringhofer
Universitat Osnabruck, Federal Republic of Germany

Gerald Roosen
Institut d'Optique, France

Peixian Ye
Chinese Academy of Sciences, China

Devices and Applications

Dana Z. Anderson
University of Colorado at Boulder

Jean-Pierre Hulgnard
Thomson-CSF, France

Kazuo Kyuma
Mitsubishi Electric Corporation, Japan

Abdelkhalil Marakchi
Bellcore

Min Mochizuki
Rockwell International Science Center

Henri Rajbenbach
Thomson-CSF, France